Volume 1

UPC 2023

Editors:
Tuomas Lappi, Daniel Tapia Takaki and Joakim Nystrand

Proceedings of
The First International Workshop
on the Physics of Ultra Peripheral Collisions
Playa del Carmen, Mexico
December 10-15, 2023

Proceedings of the International Workshop on the Physics of Ultra-Peripheral Collisions

Volume 1

UPC 2023

Editors: Tuomas Lappi, Joakim Nystrand and Daniel Tapia Takaki

Published by The University of Kansas Libraries

Impressum

Proceedings of the International Workshop on the Physics of Ultra-Peripheral Collisions: *Phys. Proc. Ultra-Peripheral Collisions*

UPC 2023 – *Proceedings of the International Workshop on the Physics of Ultra-Peripheral Collisions*

Online ISSN: 3064-8904
Print ISSN: 3064-8890

Published by The University of Kansas Libraries
Watson Library
1425 Jayhawk Blvd.
Lawrence, KS 66045

Conference Venue:
Hotel Iberostar Tucan/Quetzal, Playa del Carmen, Mexico
December 10–15, 2023

Links to Conference Resources
Online Proceedings: https://journals.ku.edu/upc/issue/view/2451
Indico Conference Website: https://indico.cern.ch/event/1263865

Editors: Tuomas Lappi, Joakim Nystrand and Daniel Tapia Takaki

Publication Date of Volume 1:
March 11, 2025

Acknowledgements

This conference was made possible in part through the support of the Inter-American Network of Networks of Quantum Chromo-Dynamics Challenges (I.ANN QCD), a National Science Foundation AccelNet program, and the University of Kansas Department of Physics and Astronomy. The Conference Proceedings are supported and published by the University of Kansas Libraries.

Committees and organization

International Program Committee (IPC):

Stan Brodsky (Stanford)

Guillermo Contreras (Prague)

David d'Enterria (Geneva)

Gerardo Herrera Corral (Mexico City)

Victor Goncalves (Pelotas)

Spencer Klein (Berkeley)

Tuomas Lappi (Jyvaskyla),

co-chairPaul Newman (Birmingham)

Joakim Nystrand (Bergen), co-chair

Marta Ruspa (Torino)

Eugenio Scapparone (Bologna)

Janet Seger (Omaha)

Anna Stasto (State College)

Peter Steinberg (Upton)

Mark Strikman (State College)

Antoni Szczurek (Krakow)

Daniel Tapia Takaki (Lawrence)

Samuel Wallon (Orsay)

Local Organizing committee:

Alexander Bylinkin (Bergen)

Amrit Gautam (Lawrence)

Martin Hentschinski (Puebla)

Gerardo Herrera Corral (Mexico City), co-chair

Tommaso Isidori (Lawrence)

Anisa Khatun (Lawrence)

Michael Murray (Lawrence)

John Ralston (Lawrence)

Kristin Rennells (Lawrence)

Mario Rodriguez Cahuantzi (Puebla)

Christophe Royon (Lawrence)

Daniel Tapia Takaki (Lawrence), co-chair

Scientific sessions conveners:

Session 1: Vector meson photoproduction

Alexander Bylinkin (Bergen)

Heikki Mantysaari (Jyvaskyla)

Session 2: Two-photon physics

James Daniel Brandenburg (Columbus, Ohio)

Mariola Klusek-Gawenda (Krakow)

Session 3: UPC and saturation

Renaud Boussarie (Orsay)

Michael Winn (Saclay)

Session 4: Inclusive photonuclear interactions

Aaron Angerami (Livermore)

Ilkka Helenius (Jyvaskyla)

Session 5: EM and peripheral events

Charlotte van Hulse (Madrid)

Wolfgang Schaefer (Krakow)

Session 6: MC and UPCs

Michal Broz (Prague)

Lucian Harlang-lang (Cambridge, UK)

Session 7: Future LHC experiments and EIC

Vadim Guzey (Jyvaskyla)

Zhoudunming Tu (Upton)

Scientific secretary:

Martin Hentschinski (Puebla)

Mario Rodríguez Cahuantzi (Puebla)

Secretariat and support from the University of Kansas:

Hanna Fontes (secretariat)

Anisa Khatun (publishing assistant)

Pramil Paudel (publishing assistant and graphic designer)

Prasamsha Pokhrel (secretariat)

Marianne A. Reed (production editor)

Kristin Rennells (Head of secretariat)

Matt Rennells (conference photographer)

Levi Van Ryder (publishing assistant)

Preface

We are pleased to present the *Proceedings of the First International Workshop on the Physics of Ultra-Peripheral Collisions (UPC 2023)*, held at the Iberostar Tucan/Quetzal Hotel in Playa del Carmen, Quintana Roo, Mexico, in the Riviera Maya, from December 10 to 15, 2023. This workshop marked the launch of an international conference series dedicated to ultra-peripheral collisions—an area of research at the forefront of photon-induced reactions in high-energy nuclear and particle physics.

UPC 2023 brought together approximately 90 participants, including a vibrant group of early-career researchers, who represented more than one-third of the attendees—a clear reflection of the community's growing breadth and dynamism. Over five days, participants engaged in a wide-ranging scientific program that encompassed experimental breakthroughs from RHIC and the LHC, theoretical advances in exclusive and inelastic photonuclear interactions, investigations of vector-meson photoproduction, and efforts to explore gluon saturation and low-x parton dynamics.

The conference began with a one-day student lecture event by Anna Stasto and Guillermo Contreras on December 10, 2023, offering early-career researchers the opportunity to discuss key topics in QCD and ultra-peripheral collisions processes.

The main workshop opened on December 11, 2023, with a plenary talk by Carlos Bertulani. His lecture traced the historical development of the field and included a heartfelt tribute to Gerard Baur who carried out early theoretical studies of ultra-peripheral nucleus-nucleus collisions.

Scientific sessions featured discussions on open-charm photoproduction, the use of UPCs to probe the quark–gluon plasma, and searches for axion-like particles and light-by-light scattering events. Theoretical contributions addressed several emerging frontiers, including vector-meson photoproduction as a probe of gluon saturation, double-parton correlations and generalized parton distributions, and studies of quantum entanglement in UPCs.

Looking to the future, the workshop also explored the potential of ultra-peripheral physics at the forthcoming Electron-Ion Collider (EIC) at Brookhaven National

Laboratory, while also reflecting on the significant legacy of photon-induced processes from experiments at HERA.

This volume compiles 25 contributions presented at UPC 2023. Together with additional presentation materials available on the conference's Indico page, including those not included in this volume, these proceedings serve as a valuable resource for researchers and reflect the dynamic progress of this rapidly evolving field.

We extend our sincere gratitude to all authors, session conveners, scientific secretaries, members of the local organizing committee, and the International Program Organizing Committee for their commitment and efforts in successfully launching this new conference series. We also gratefully acknowledge the support provided by the Inter-American Network of Networks of QCD Challenges, funded by the National Science Foundation AccelNet-Design program, as well as the University of Kansas for their partial financial support of the conference.

We look forward to reconvening at the next edition, UPC 2025, scheduled for June 9-13, 2025, in Saariselkä, Finland, and to witnessing the continued growth of this vibrant scientific community.

Tuomas Lappi
University of Jyväskylä

Joakim Nystrand
Bergen University

Daniel Tapia Takaki
The University of Kansas

Editors
Proceedings of the First International Workshop on the Physics of Ultra-Peripheral Collisions (UPC 2023)

Contents

Coherent Photoproduction of J/ψ Mesons in Ultraperipheral Pb–Pb Collisions at CMS
L.F. Alcerro (for the CMS Collaboration)

Impact Parameter Dependence of Dilepton Production: Wigner Function Approach and the Role of Photon Polarizations
Wolfgang Schäfer

Measurement of Dilepton Production from Photon Fusion Processes in Pb+Pb UPC with the ATLAS Detector
I. Grabowska-Bold (for the ATLAS Collaboration)

Four-Pion State in UPC
Mariola Klusek-Gawenda

Two-Body Densities as a Framework for Dynamical Imaging and Their Connection to Ultra-Peripheral Collisions
Zaki Panjsheeri, Joshua Bautista, Simonetta Liuti

The Ratio of Ψ(2S) and J/ψ Exclusive Photoproduction Cross-Sections as a Tool to Detect Non-Linear QCD Evolution
Martin Hentschinski, Marco Antonio Alcazar Peredo

Nuclear Shadowing in Inelastic Photon-Nucleus Scattering in UPCs with Forward Neutrons
Mark Strikman, Vadim Guzey, Massimiliano Alvioli

Inclusive and Diffractive Dijet Photoproduction in Ultraperipheral Pb-Pb Collisions at the LHC
Vadim Guzey

Collision Geometry in UPC Dijet Production
Petja Paakkinen, Kari J. Eskola, Vadim Guzey, Ilkka Helenius, Hannu Paukkunen

Axion Physics in UPC and LbyL Scattering
C.O. Ramírez-Álvarez, A. Fernández-Téllez, A.I. Hernández-Juárez

Photoproduction of J/ψ and Dileptons in Pb–Pb Collisions with Nuclear Overlap
N. Bizé (for the ALICE Collaboration)

Azimuthal Angular Correlations in Lepton Pair Production in Ultra-Peripheral Heavy Ion Collisions
F.S. Navarra, F.C. Sobrinho, C.A. Bertulani, I. Danhoni

Light-by-Light Scattering in Ultraperipheral Collisions of Heavy Ions with Future FoCal and ALICE 3 Detectors
Ya-jin Zhou

UPC Physics with ALICE in Run 3
Antoni Szczurek

Exclusive η_c Production by γ*γ Interactions in Electron-Ion Collisions

Anisa Khatun (for the ALICE Collaboration)

Photo-Nuclear Collisions in Pythia 8

I. Babiarz, V.P. Goncalves, W. Schäfer, A. Szczurek

Recent Results from Ultra-Peripheral Lead-Lead Collisions with ATLAS

I. Helenius, M. Utheim

Novel Aspects of Particle Production in Ultra-Peripheral Collisions

K. Maj (on behalf of the ATLAS Collaboration)

Phys. Proc. Ultra-Peripheral Collisions **1**, 001 (2024) 1-13

Historical introduction to ultra peripheral collisions

C.A. Bertulani
Department of Physics and Astronomy, Texas A&M University-Commerce
Commerce, Texas, 75025, USA

This is a brief history of photons, both soft and hard, real and virtual. About 150-100 years ago, Maxwell and Einstein discovered intriguing properties of electromagnetic fields and how to understand them both macroscopically and microscopically. Decades later, physicists developed the theory of renormalized quantum electrodynamics (QED), an incredibly accurate theory describing interactions of photons and other particles. Photons are used everywhere in academia and technological devices, from supermarket lasers and doors to academic studies in atomic, nuclear, and particle physics. In this article, I attempt to convey how the field of relativistic heavy ions rediscovered ultra-peripheral collisions (UPC) as a source of intense, almost real photons, and how it permits the study of a plethora of phenomena in the aforementioned academic fields. These phenomena are not always accessible by other means.

DOI: https://doi.org/10.17161/e6epmx12
Keywords: Heavy-Ion Physics, Ultra-peripheral collisions

1 Phriends and Photons

German professors used to wield significant influence. Today some still maintain their power while most lament its decline. Prior to 2002, most academic university departments operated under a hierarchical structure, with a principal C4 professor at the apex, overseeing a pyramid of other C2 and C3 professors (following the hierarchy $C4 > C3 > C2$). This was the landscape into which I stepped upon my arrival at the University of Bonn and the KFA-Jülich laboratory in Germany in 1984. Upon my arrival, the C4 professor instructed me to approach the offices of three $C_<$ professors and inquire if they had a PhD project for me. So, I followed his directive. The first $C_<$ professor filled the blackboard with numerous Feynman-like diagrams and equations for complex many-particle systems. Daunted by the complexity, I was relieved when, after an hour, he explained that if we published three papers in Nuclear Physics A or Physical Review C within the next four years, I could write my thesis.

The scenario repeated itself in the second office, leaving me in awe once more as the expectation remained: three papers → thesis. Can you see the significance? Three or more published papers signified both the achievement and the prestige of attaining a Doctorate in Philosophy. It was in the third office that I met Professor Dr. Gerhard Baur, a $C_<$ professor. He candidly admitted that he didn't have an immediate plan for a PhD student but instead handed me a paper to peruse and discuss with him later. Finding the paper intriguing, he proposed that we reach deeper into its concepts, suggesting that we could expand upon its physics together. The topic seemed absurd to my fellow PhD student colleagues: heavy ion collisions without actual collisions, C'mom are you kidding me?. Yet, over the course of the next four years, Gerhard and I published 15 (fifteen) papers on the topic. This is equivalent to 5 PhD theses, according to the reigning Jülich standards at that time.

Back in the mid-80s, the C4 Professor avidly followed the works of a Japanese physicist named T. Suzuki, frequently publishing his works in the Physics Review Letters. Determined to bring him to Jülich for a six-month period, the professor invested significant time and effort, only to discover that there were three T. Suzukis, and he had invited the wrong one. By then, it was too late. Such mishaps were not uncommon during that era. I vividly recall an encounter with the renowned T. Suzuki himself, who once stopped by my office and inquired about my PhD thesis. After my earnest attempt to convey the interest and significance of my research on ultra-peripheral heavy ion collisions (UPCs), he dismissed it as totally unimportant and undeserving of a conversation and left the room without saying goodbye.

In another occasion, in 1986, during a workshop in Erice, Italy, Gerhard and I faced harsh criticism from nuclear physics experts who loudly rebuked our proposal regarding a double giant resonance in nuclei within UPCs. I can still recall my former colleague Eric Ormand likening the situation to "opening a smelly can of worms." In 1987, in a significant twist of fate, the late Gerry Brown, who served as the editor of Physics Reports at the time, expressed interest in publishing my PhD thesis [1]. This time I felt vindicated, knowing that Gerry was a visionary man.

Over the years, despite facing numerous embarrassing situations while attempting to promote UPCs as a viable source of useful physics, we persevered in our work. Particularly, Gerhard's dedication led to

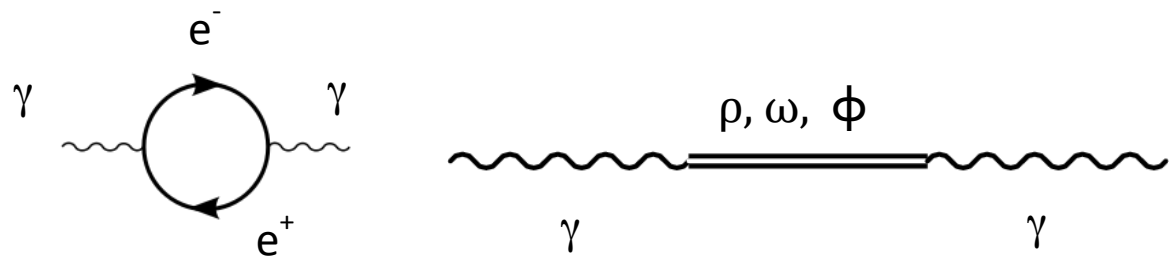

Figure 1 – The photon wavefunction contains "hidden" quantum fluctuations into pair of particles, very much like a Banksy drawing.

numerous contributions that extended beyond the 1990s. Gradually, UPCs emerged as a thriving field within both nuclear and particle physics.

I offer here a partial glimpse into the evolution of UPCs since the publication of my PhD thesis in 1988 [1]. Despite the prevailing skepticism at the time (as Mark Strickman recalled during this meeting, "in 1988, it looked like science fiction"), it's truly satisfying to witness how the predictions we put forth in works we published during the 1980s and 1990s have catalyzed a wealth of experimental findings and theoretical advancements. The domain of UPC physics has emerged as a focal point of extensive global research, playing a pivotal role in advancing our comprehension and consolidation of various phenomena within both QED and QCD realms [2–14].

Please note that this account is not exhaustive, and I may inadvertently overlook many references. Whenever feasible, I will include a selection of equations utilized to make estimates or even conduct rigorous calculations for cross sections and probabilities in UPC processes.

2 The Equivalent Photon Method

As Gerhard and I digged deeper into the topic of UPC, we stumbled upon Enrico Fermi's practical method formulated back in 1924 [15, 16]. He explored atomic ionization induced by α-particles. Fermi's work was published in German at the Zeitschrift für Physik and in Italian at the Nuovo Cimento. It's conceivable that Nuovo Cimento, established in 1923, initially functioned primarily as a repository of works by members of the Italian Physical Society (SIF) rather than adhering strictly to the norms of a traditional journal. In this context, Fermi might not have been influenced by the "publish or perish" philosophy as much as we do.

My first collaboration with Gerhard resulted in the publication of our work in 1985 [17]. Our objective was to extend Fermi's "equivalent photon method" using quantum mechanics and first-order perturbation theory. We demonstrated that the electromagnetic fields of a highly energetic charge can induce excitation processes in a nucleus and the matrix elements for the transition are equivalent to those induced by real photons. The final cross section can be expressed as a sum over multipoles,

$$\sigma = \sum_{E/M,L} \int \frac{d\omega}{\omega} n_{E/M,L}(\omega) \sigma_\gamma^{(E/M,L)}(\omega), \tag{1}$$

where $\sigma_\gamma^{(E/M,L)}(\omega)$ represents cross sections by (real) photons with energies ω. Electric (E) and magnetic (M) "multipolarities" include components of the photon angular momentum L. The $n_{E/M,L}(\omega)$ also depend on the beam energy $E_{\rm beam}$ and the photon energy ω. They are denoted by "equivalent (virtual) photon numbers" (EPN) [17]. For projectile bombarding energies below a few GeV/nucleon, the EPNs strongly depend on the $E/M, L$ multipolarity, e.g., $n_{E2} > n_{E1} > n_{M1}$, whereas at much larger energies they are approximately equal, $n_{E2} \sim n_{E1} \sim n_{M1}$, except for small excitation energies $\omega \ll \gamma/b$ [17]. $\gamma = (1 - v^2)^{-1/2}$ is the Lorentz factor, v is the projectile velocity, and b signifies the collision the impact parameter.

The UPC community primarily focuses on the high-energy limit, where the following relation holds:

$$\sigma \simeq \sum_{E/M,L} \int \frac{d\omega}{\omega} n(\omega) \sigma_\gamma^{(E/M,L)}(\omega) = \int \frac{d\omega}{\omega} n(\omega) \sum_{E/M,L} \sigma_\gamma^{(E/M,L)}(\omega) = \int \frac{d\omega}{\omega} n(\omega) \sigma_\gamma(\omega), \tag{2}$$

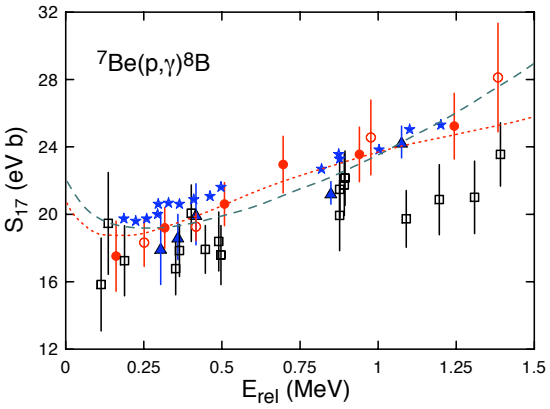

Figure 2 – Radiative capture reaction ^{7}Be(p,γ)^{8}B. The dashed line is the no-core shell-model calculation of Ref. [21] and the dotted line is from the resonant group method calculation of Ref. [23]. Experimental data are from Refs. [24–31].

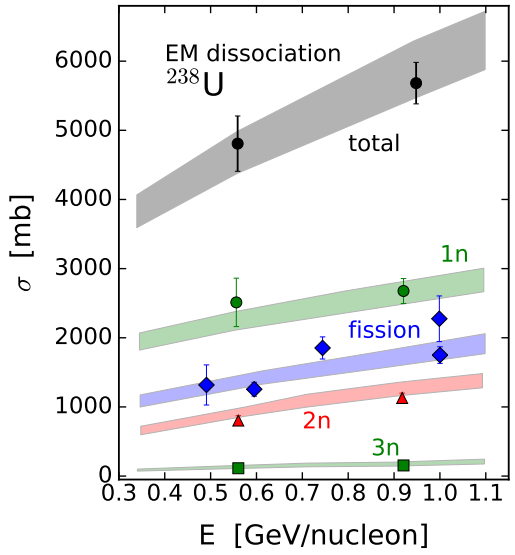

Figure 3 – Cross-section for EM dissociation of ^{238}U. The excited nucleus decays by fissioning (diamonds) and multiple neutron emission (xn) [39–42]. Theoretical calculations and their uncertainty bands are also shown [37].

with $\sigma_\gamma = \sum_{E/M,L} \sigma_\gamma^{(E/M,L)}$ representing the total cross section induced by a real photon. However, Eq. 1 possesses a certain elegance as it delineates how heavy-ion collisions facilitate the differentiation of various photon multipolarities $E/M, L$.

The prevalent belief that the EPN method, as described above for UPCs, is exclusively applicable to relativistic heavy ion collisions is erroneous. Equation 1 remains valid whenever first-order perturbation theory is accurately enough to describe the UPC process under examination. This validity stems from the fact that in UPCs, because the charged particle does not penetrate the nucleus, conditions are such that $\nabla \times \mathbf{B} = 0$ and $\nabla \cdot \mathbf{E} = 0$, with $\mathbf{E}$ and $\mathbf{M}$ being the fields generated by the moving charge.

Another common fallacy is the notion that it is impossible to separate pure electromagnetic processes from those involving the strong interaction. Various methodologies have been employed to differentiate between these processes including detailed studies of the cross sections dependencies on the projectile bombarding energy, angular distributions, and on the nuclear excitation energies. Notably, employing light nuclei (e.g., carbon) alongside heavy nuclei (e.g., lead) in measurements aids in isolating the contributions of the two interactions.

However, there's a caveat. Equations 1 and 2 hold true only to first order. The photon, unlike electromagnetic waves with cute little fish-like patterns, resembles more of a "Banksy" art piece [18], an intricate octopus-like entity (see Figure 1). It exhibits fluctuations into other particles through emission and re-absorption processes, imprinting its wave function with their characteristics:

$$|\gamma\rangle \quad = \quad C_{bare}\,|\gamma_{bare}\rangle + C_{ee}\,\left|e^-e^+\right\rangle + \cdots + C_{qq}\,|q\bar{q}\rangle + C_\omega\,|\omega\rangle + C_\phi\,|\phi\rangle + C_\rho\,|\rho\rangle + \cdots \tag{3}$$

Given the spin-parity $J^P = 1^-$, the photon can fluctuate into vector mesons $(\rho, \omega, \phi, J/\psi)$ comprised of quark-antiquark pairs (following the vector dominance model). Furthermore, the photon often manifests as multiple energy components, some of which are invisible or virtual, akin to the enigmatic nature of Banksy's works [18]. Multistep processes involving photon splitting, emission of its "parts," generation of intermediate states, or recycling are prevalent and integral to its nature.

3 Applications in Low Energy Nuclear Physics

3.1 The Coulomb dissociation method

In our proposal to employ UPC for nuclear physics, we introduced the Coulomb dissociation method in 1986 [19]. The differential Coulomb breakup cross section in UPC, where a projectile nucleus a interacts with a target nucleus A resulting in the reaction $a + A \longrightarrow b + c + A$, is expressed as:

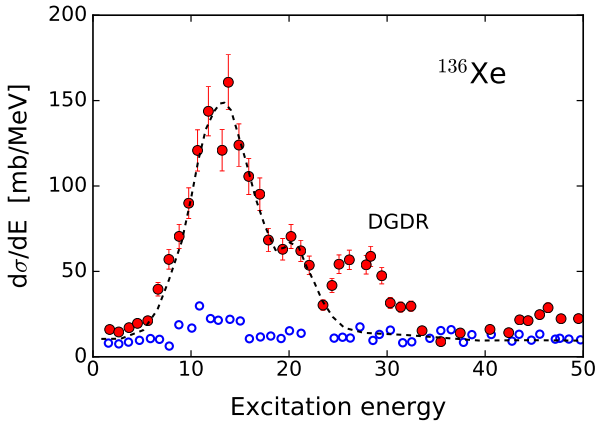

Figure 4 – Energy spectrum of giant resonances in ^{136}Xe projectiles in UPCs with a large-Z target. The Giant Dipole Resonance (DGDR) is evident as a distinct peak [50].

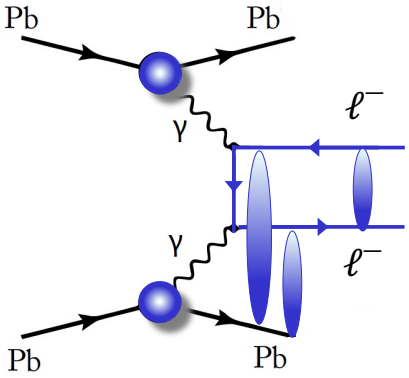

Figure 5 – Production of lepton-antilepton in UPCs. Higher-order processes, including the production of multiple pairs, might be important.

$$\frac{d\sigma_C^{E/M,L}(\omega)}{d\omega d\Omega} = \frac{dn^{E/M,L}(\omega;\theta;\phi)}{d\omega d\Omega} \cdot \sigma_{\gamma+a\to b+c}^{E/M,L}(\omega). \tag{4}$$

Here, ω denotes the excitation energy provided by the relative motion, and $\sigma_{\gamma+a\to b+c}^{E/M,L}(\omega)$ represents the photonuclear cross section for the photon energy ω and multipolarity $E/M, L$. The function $dn^{E/M,L}/d\omega d\Omega$ denotes the equivalent photon number, dependent on the scattering angle $\Omega = (\theta, \phi)$ [19].

Time reversal symmetry enables the deduction of the radiative capture cross section for the reaction $b+c \longrightarrow a+\gamma$ from the experimentally obtained $\sigma_{\gamma+a\to b+c}^{E/M,L}(\omega)$. This methodology has proven invaluable in determining radiative capture cross sections for various reactions pertinent to astrophysics. An illustrative example is the ^{7}Be$(p,\gamma)^8$B reaction, initially investigated in Ref. [20], followed by numerous subsequent experiments. This is shown in Figure 2, where the red dots were obtained using the Coulomb dissociation method and the experimental data are from Refs. [24–31]. Further discussions on the outcomes derived through this method can be found in Refs. [32–34].

Equation 4 is rooted in first-order perturbation theory and assumes that the nuclear contribution to the breakup is either negligible or separable under specific experimental conditions. The influence of nuclear breakup has been scrutinized by several researchers (see, e.g., Ref. [35]). Weakly-bound nuclei, such as "halo nuclei," characterized by very small neutron separation energies, exhibit significant multiple-step or higher-order effects, particularly through continuum-continuum transitions, as demonstrated in Ref. [35].

3.2 Giant Resonances

Another application of UPCs in low-energy nuclear physics was in investigating giant resonances within nuclei [36]. Typically, it decays by neutron emission, and for energies around 1 GeV/nucleon, such as those achievable at the GSI laboratory in Germany, the excitation cross sections can reach several barns [37, 38] (see Figure 3). At these energies, giant resonances can also be efficiently excited through nuclear interactions. However, it was soon recognized that for nuclei with high atomic numbers (large-Z), cross sections are significantly smaller compared to those induced by electromagnetic (EM) interactions [1, 39–42]. Presently, Coulomb excitation and decay of giant resonances serve as a valuable experimental tool, including in studies related to nuclear fission [43–45]. Because of its substantial cross section, this process has been proposed for use as a heavy-ion collider luminosity monitor [7, 46, 47].

3.3 Multiphonon giant resonances

In 1986, Gerhard and I proposed the excitation of multiple giant resonances in UPCs through multiple photon exchange [48, 49]. The non-perturbative treatment of this process can be achieved using coupled-channels equations. Additionally, Glauber methods offer a means to account for diffraction effects arising from nuclear interactions. Predictions indicated significantly large excitation probabilities for double,

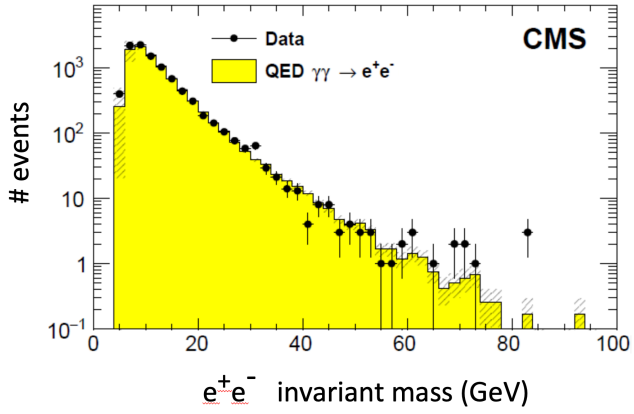

Figure 6 – e^+e^- pairs produced in UPCs observed with the CMS detector (from Ref. [66]).

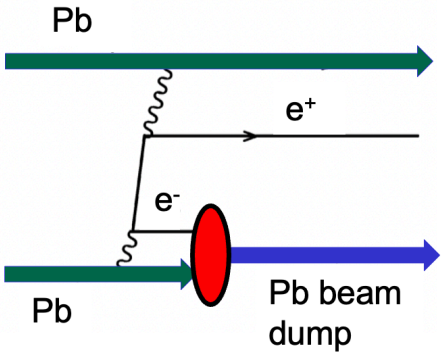

Figure 7 – Pair production with electron capture leading to possible beam losses [7].

triple, and multi-phonon resonances in nuclei [48,49]. Two pioneering experiments conducted at the GSI laboratory in Germany in 1993 provided empirical support for these predictions [50, 51]. One experiment employed gamma-gamma coincidences to identify the decay of the double giant dipole resonance (DGDR) [51], while the other observed predominantly neutron emission as a result of the decay of the multi-phonon giant resonances [50] (see Figure 4). The study of DGDR is particularly noteworthy as its strength and width offer valuable constraints for nuclear models regarding the absorption of multiple photons. Comprehensive reviews on this topic are available in references [52–54].

4 Pair production

One of the processes that called our attention in 1986 was the abundant production of electron-positron pairs in UPCs (Figure 5). The pioneering studies on the production of e^+e^- pairs in UPCs trace back to the 1930s. Bethe, Racah, Bhabha, Tomonaga, Nishina, Furry, among others, developed techniques to compute pair production employing the newly formulated Dirac equation. Dirac's equation famously predicted the existence of the positron, conceptualized as a void in the "vacuum sea" of electrons. Initially, the exploration for this "void" (positron) was pursued via UPCs involving cosmic rays possessing high kinetic energies E [55–60].

Under the assumption that the energy of produced pairs vastly exceeds the electron rest mass m_e, almost all theoretical forecasts [55–60] yielded a production cross section equal to

$$\sigma_{e^+e^-} = \frac{28}{27\pi} \left(Z_1 Z_2 \alpha r_e\right)^2 \ln^3\left(\frac{\gamma}{2}\right), \tag{5}$$

where the Lorentz factor is $\gamma \simeq E/M$, with M the mass of the cosmic ray ion, and $r_e = e^2/m_e$ fm is the classical electron radius (for a concise discussion, see Ref. [1]). The cross section reaches scandalous values of 200 kbarn for PbPb at LHC. In 1986, we revisited these computations employing contemporary methods in Quantum Electrodynamics (QED), beyond the scope of the physics known in the 1930s. We developed a theory incorporating final state interactions (depicted as blobs in Figure 5) utilizing Bethe-Maximon distorted waves [1]. Given the significantly large cross sections, on the order of kilobarns for standard collider energies like those at the LHC, we demonstrated the pertinence of exploring higher-order corrections [1, 61].

The simplest approximation we devised for multiple pair production assumed a Poisson distribution for the production probability for n pairs at a given impact parameter so that

$$P_{e^+e^-}(b) = \frac{[P_0(b)]^n}{n!} \exp\left[-P_0(b)\right], \tag{6}$$

where $P_0(b)$ is the probability for a single pair production, which can be calculated analytically [1],

$$P_0(b) = \frac{14}{9\pi^2 b^2} \left(Z_1 Z_2 \alpha r_e\right)^2 \ln^2\left(\frac{\gamma}{2m_e b}\right), \tag{7}$$

valid for $\gamma/m_e > b > 1/m_e$ [1]. The effect of final state interactions in multiple pair production was further investigated in numerous other publications and reviews [5, 6, 62–64].

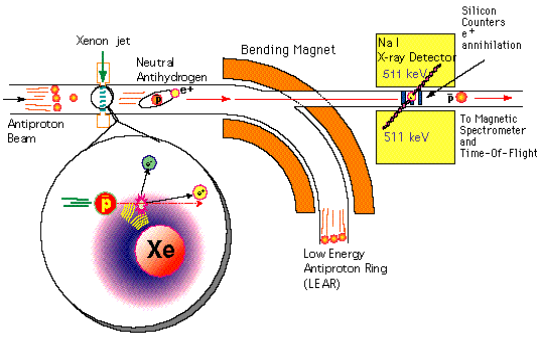

Figure 8 – Experimental setup employed in the identification of anti-atoms at the LEAR/CERN in 1996.

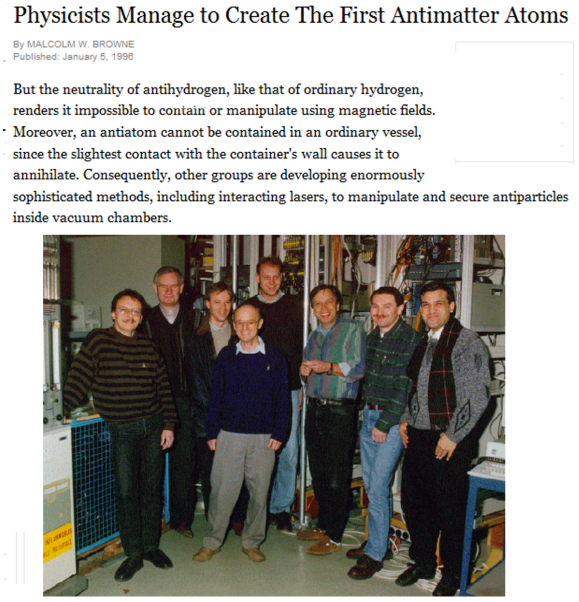
Physicists Manage to Create The First Antimatter Atoms

By MALCOLM W. BROWNE
Published: January 5, 1996

But the neutrality of antihydrogen, like that of ordinary hydrogen, renders it impossible to contain or manipulate using magnetic fields. Moreover, an antiatom cannot be contained in an ordinary vessel, since the slightest contact with the container's wall causes it to annihilate. Consequently, other groups are developing enormously sophisticated methods, including interacting lasers, to manipulate and secure antiparticles inside vacuum chambers.

Figure 9 – The New York Times report on the first ever production of an anti-atom in the laboratory (1996). Gerhard Baur (a theorist) stands in the center of the picture.

It is gratifying to witness current LHC experiments measuring the foundational pair-production cross sections initially calculated in the 1930s and later studied in References [1, 61–63]. These processes are now largely comprehended theoretically. Initial experiments validated predictions grounded in QED with the STAR detector at the Relativistic Heavy Ion Collider (RHIC) [65] and later that with the CMS detector at CERN (Figure 6). The generation of other particle-antiparticle pairs, such as (Figure 1), $\gamma\gamma \to \mu^+\mu^-$, $\gamma\gamma \to \pi^+\pi^-$, $\gamma\gamma \to W^+W^-$, etc., is not insignificant, as calculations in Refs. [61, 67, 68] have shown, and confirmed in subsequents works [1, 7, 67, 68]. For the production of $\mu^+\mu^-$ $(\pi + \pi^-)$ and $\tau^+\tau^-$ pairs we can use the equations above if $\gamma \gg 16$ for muon-pair production, or $\gamma \gg 200$ for tau-pair production. If these conditions are not satisfied, significant corrections to these equations are necessary, as shown in Ref. [1]. At the LHC, the Lorentz boost factor γ in the laboratory frame is about 7000 for p-p, 3000 for Pb-Pb collisions and the conditions above apply.

5 Anti-atoms and Exotic Atoms

Arguably, one of the most aesthetically captivating applications of UPCs involves the generation of lepton pair production, coupled with the capture of the negative lepton by one of the colliding ions [1, 69, 70] (see Figure 7). The cross section for electron-pair production with capture of the electron in an atomic K-shell orbit is [1]

$$\sigma_K = \frac{33}{20} Z_1^5 Z_2^5 \alpha^5 r_e^2 \ln\left(\frac{\gamma}{2}\right). \tag{8}$$

A factor $\sum_n 1/n^3 \simeq 1.202$ increases the value of this cross section when capture is considered for all other orbits. However, the effects of electron screening and distortions in heavy atoms modify the electron capture cross sections appreciably [1].

A groundbreaking adaptation of this method was developed for anti-hydrogen production at the LHC, initially proposed in Ref. [71], and later substantiated by a pioneering experiment conducted at CERN and documented in 1996 [72] (see Figure 8). Operating within the Low Energy Antiproton Ring

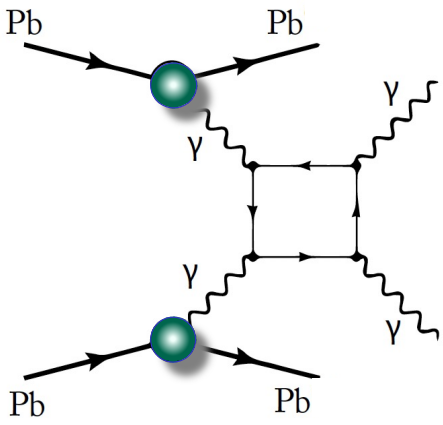

Figure 10 – Light-by-light scattering using UPCs.

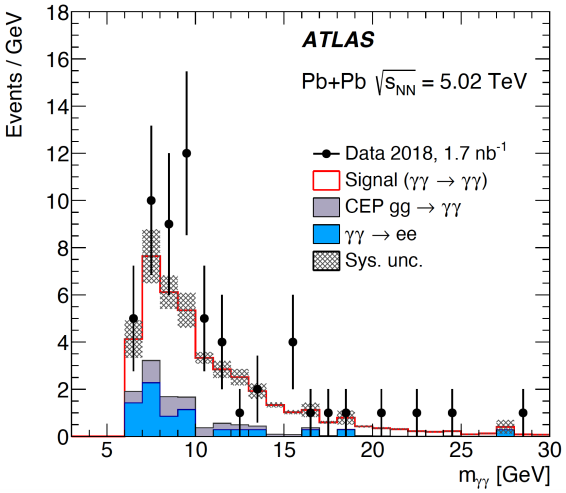

Figure 11 – Number of light-by-light scattering events observed with the ATLAS detector [101].

(LEAR), CERN's venture saw antiprotons colliding with protons, resulting in the capture of positrons into orbit around the antiproton. This landmark achievement marked the first terrestrial production of anti-atoms, with the detection of 11 anti-hydrogen atoms, attracting widespread attention from global media outlets including the New York Times [73] (see Figure 9). Gerhard used to say that it is not difficult for scientists to publish in Nature, Science, or Physical Review Letters, but it is very difficult to get their picture and achievements appearing in the New York Times. "I must have reached the apex of my career", he said.

Subsequently, a similar endeavor was undertaken at FERMILAB [74], yielding 57 identified events, aligning with perturbative calculations performed prior to the experiment [69] (see also Ref. [75]). Expanding horizons, investigations into the properties of anti-atoms are presently conducted utilizing ion traps, aimed at scrutinizing fundamental symmetries [76, 77]. Furthermore, the ambit of UPCs extends to the production of larger antimatter entities such as anti-deuterium, anti-tritium, and anti-helium [78]. Predictions made in Ref. [70] extend the potential of UPCs, envisioning the production of muonic, pionic, and other exotic atoms through coherent photon exchange between ions at the LHC.

It's noteworthy that as early as 1988, in Ref. [68], the process of electron-positron production, with subsequent capture of the electron into an atomic orbit of one of the ions, was proposed as a source of beam loss in relativistic colliders. Initial estimations indicated potential degradation of a high-Z ion beam within 2 hours at the LHC. Subsequent theoretical scrutiny [79] and recent experimental validation at the LHC [80] corroborate the earlier expectations [68]. Another intriguing facet lies in the production of ortho- and para-positronium in UPCs. Ref. [81] furnishes a theoretical framework within quantum field theory to compute positronium and other bound-states, such as mesons (bound $q\bar{q}$), through $\gamma\gamma$- and $\gamma\gamma\gamma$-fusion in UPCs [82–84].

One expects the existence of six leptonic atoms: (a) the positronium (e^+e^-), (b) the muonium (μ^+e^-), (c) dimuonium ($\mu^+\mu^-$), (d) tauonium (τ^+e^-), (e) tau-muonium ($\tau+\mu^-$), and (f) ditauonium ($\tau^+\tau^-$). Only positronium, muonium, and dipositron-positronium, and (e^+e^-)(e^+e^-) were observed experimentally [85–87]. Dimuonium has a radius a few hundred times smaller than the positronium and muonium. Because of its large mass, it is sensitive to physics beyond the standard model (BSM) [88] and unexplored time-like regions of quantum electrodynamics (QED). Therefore, the discovery of the dimuonium would be a significant one in physics [89]. The production of the dimuonium in UPC has been calculated and shown to be feasible to be measured at the LHC [90–93]. It has also been shown that the observation of the ditauonium at the LHC is possible [95]. In both cases, one expects the identification to proceed via its displaced vertex with a rather good control of the combinatorial dimuon background.

6 Light-by-light Scattering

The phenomenon of elastic scattering of light by light, $\gamma+\gamma\rightarrow\gamma+\gamma$, exclusively occurs through the fluctuation of a photon into an particle-antiparticle pair (Figure 10). This process bears a relatively minuscule probability, rendering a direct study with real photons unattainable. In our pioneering work [68],

Gerhard and I proposed the utilization of UPCs to probe $Z_1 + Z_2 \to Z_1 + Z_2 + \gamma + \gamma$, whereby two virtual photons scatter via a box diagram, producing two real photons. We underscored the theoretical uncertainty inherent in calculations reliant on the Delbrück scattering formalism [68]. To leading order, the cross section for $\gamma^*\gamma^* \to \gamma\gamma$ scattering events in UPCs leading to high energy photons is [68]

$$\sigma_D \sim 2.54 \times 10^{-2} Z^4 \alpha^4 r_e^2 \ln^3 \left(\frac{\gamma}{m_e R} \right), \tag{9}$$

where R is the radius of the colliding ions. For PbPb collisions at the LHC, one gets huge cross sections about $\sigma_D \sim 50$ b. But not all these photons can be detected as purely due to this process, due to background by similar processes such as Bremsstrahlung. For $E_\gamma > m_\mu$ and Pb + Pb collisions at the LHC, the cross section is much smaller, of the order of $\sigma_D \sim 30$ nb [94].

Light-by-light scattering was further studied in numerous other works where additional mechanisms for photon-photon scattering such as VDM-Regge, two-gluon exchanges, and meson resonances were considered (see, e.g., Refs. [96–100]). The ATLAS collaboration at the LHC achieved a breakthrough by observing this process experimentally (Figure 11) [101]. Such a revelation not only validates theoretical conjectures but also paves the path for exploring physics beyond the Standard Model (SM). An observed cross-section exceeding that predicted by the SM model could potentially signify the existence of new particles, such as axions [102–104]. This remarkable observation instigates a quest into realms of physics yet unexplored [104].

7 Meson production in UPCs

Gerhard and I devised a simple way to extend the EPN method to compute the production of a bound-particle denoted as X in UPCs (Figure 12) [68]. The cross-section for photon-photon fusion can be expressed as

$$\sigma_X = \int \frac{d\omega_1}{\omega_1} \frac{d\omega_2}{\omega_2} n_\gamma(\omega_1)\, n_\gamma(\omega_2)\, \sigma^X_{\gamma\gamma}(\omega_1\omega_2), \tag{10}$$

where $n_\gamma(\omega)$ represents the EPNs for photon energies ω, and $\sigma^X_{\gamma\gamma}(\omega_1\omega_2)$ stands for the photon-photon cross-section for producing particle X. It can be computed using Low's expression [105], derived from the detailed balance theorem, connecting the $\gamma\gamma$-production with the $\gamma\gamma$-decay,

$$\sigma^X_{\gamma\gamma}(\omega_1\omega_2) = 8\pi^2(2J+1)\frac{\Gamma_{m_X\to\gamma\gamma}}{m_X}\, \delta\left(\omega_1\omega_2 - m_X^2\right). \tag{11}$$

Here, m_X, J, and $\Gamma_{m_X\to\gamma\gamma}$ denote the mass, spin, and photon-photon $\gamma\gamma$ decay width of particle X, respectively. The delta-function ensures energy conservation. In Ref. [106], the significance of various meson models and exotic states is comprehensively discussed, encompassing states that were previously overlooked.

To segue, it's worth mentioning a proposal from 1989 aimed at detecting the Higgs particle using UPCs at the LHC [107]. This proposal elucidates the production mechanism through equations (10,11) while making appropriate assumptions regarding the Higgs properties. Our initial estimations in 1988 yielded a cross-section of 1 nb [68], closely aligning with the Higgs production cross sections at the LHC via hadronic processes, albeit with the advantage of minimizing the production of a multitude of other particles. However, it later became evident that the direct photon-photon production of $b\bar{b}$ pairs is significantly larger [108], although more optimistic scenarios for the Higgs production in UPCS have emerged later [109,110]. Since the primary mechanism for Higgs decay involves $b\bar{b}$ pairs, it can be inferred that the Higgs production in UPCs would be overshadowed by a background of directly produced pairs. The elusive Higgs was eventually observed at the LHC in hadronic interactions [111, 112].

8 Production of Exotic Mesons in UPCs

Multiquark states, including multiquark molecules such as $(q\bar{q})(q\bar{q})$, glueballs (gg), and hybrid mesons $(q\bar{q}g)$, hold significant role in meson spectroscopy [113]. UPCs offer a potential avenue for probing multiquark resonances by means of anomalous $\gamma\gamma$ couplings and multiquark energy spectra. They could serve as a means to test predictions concerning "abnormal" states [81–83]. The $\gamma\gamma$ width serves as a gauge of the charge of constituent quarks, facilitating differentiation between quark resonances and gluon-dominated resonances (termed "glueballs"). The failure to verify meson production via $\gamma\gamma$ fusion also serves as a significant indicator for the search for glueballs [81–83]. In UPCs, a glueball is formed by the annihilation of a $q\bar{q}$ pair into gluon pairs. In contrast, normal $q\bar{q}$ mesons are created directly.

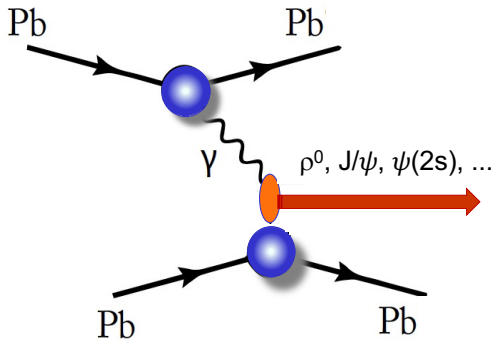

Figure 12 – Production of vector mesons in UPCs.

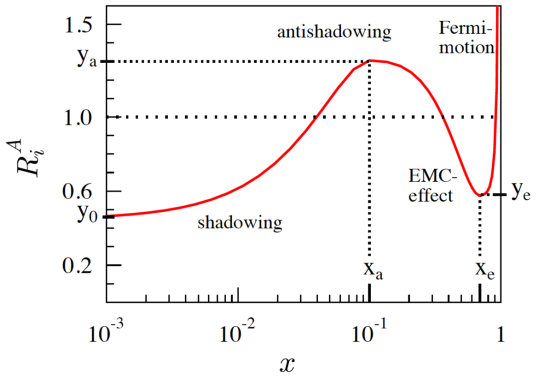

Figure 13 – Medium modification function displaying various effects as the momentum fraction x varies.

9 Probing Parton Distribution Functions with UPCs

The exploration of vector meson production, like J/ψ and $\Upsilon(1s)$, can be pursued utilizing Eq. (1) and first calculations and experiments on vector meson production we published in Ref. [114–119]. In 2001, we proposed [120] to use vector meson production for constraining generalized partonic distributions in nuclei, denoted as $F_A(x, Q^2)$, corresponding to a momentum fraction x, based on a formalism developed in Ref. [121]. For the mechanism induced by real photons, we employed the relation

$$\left.\frac{d\sigma^{\gamma A\to VA}}{dt}\right| t=0 = \frac{16\pi\alpha_s^2(Q^2)\Gamma_{ee}}{3\alpha M_V^5}\left[xF_A(x,Q^2)\right]^2, \tag{12}$$

where $\alpha_s(Q^2)$ represents the strong interaction coupling evaluated at the perturbative Quantum Chromodynamics (pQCD) factorization scale $Q^2 = W_{\gamma g}^2$, M_V denotes the vector meson mass, Γ_{ee} signifies its leptonic decay width, and $x = M_V^2/W_{\gamma p}^2$ denotes the fraction of nucleon momentum carried by gluons.

The nuclear Parton Distribution Function (PDF), denoted as $F_a^A(\mathbf{r}, x, Q^2)$, can be expressed as a folding of a medium modification function $R_a^A(\mathbf{r}, x, Q^2)$ with a nucleon PDF, represented as $f_a(x, Q^2)$. Here, the subscript a signifies a parton species, while the superscript A denotes a specific nucleus [122,123]. The variable $\mathbf{r}$ denotes the nucleon coordinate within the nucleus.

Nuclear modifications are encapsulated within $R_a^A(x, Q^2)$. For values of x less than 0.04, experimental observations reveal a shadowing effect, characterized by nuclear PDFs being smaller than the free nucleon distributions, denoted as $R_a^A < 1$ (Figure 13). In the range of $0.04 < x < 0.3$, an antishadowing effect is evident, with $R_a^A > 1$. The EMC effect manifests in the domain of $0.3 < x < 0.8$. Additionally, for $x > 0.8$, an enhancement also occurs attributed to the nucleonic Fermi motion. These effects are governed by distinct underlying physical principles.

In our previous works [122, 123], we investigated the influence of various gluon distributions on the production of J/ψ and $\Upsilon(1s)$ vector mesons in UPCs. Notably, UPCs involving pPb and PbPb collisions exhibit distinct production mechanisms termed "direct" and "resolved". Direct production entails the photon interacting directly with the nucleus, whereas the resolved mechanism entails the photon fluctuating into a quark-antiquark pair, which subsequently interact with the nucleus. At the leading order, direct production hinges on gluon distributions, that are particularly uncertain within the nucleus, especially at low x values (Figure 15). Conversely, the resolved mechanism probes the distributions of gluons and light quarks in both the photon and nucleus. The quadratic dependency of vector meson production in UPCs heightens sensitivity to gluon distributions in both cross-sections and rapidity distributions [120, 122, 123].

Our first computations for J/Ψ production, incorporating gluon distributions that account for nuclear gluon shadowing [122, 123], align well with experimental data from the ALICE [124–127] collaborations, as illustrated in Figure 14. It's evident that J/Ψ and Υ photoproduction in UPCs serves as a potent means to investigate nuclear gluon shadowing in the $x < 10^{-3}$ region.

In contrast to the claims of Refs. [122, 123], the currently most accepted hypothesis it that the resolved components of the photon are the most important for the production of vector mesons in UPCs. As mentioned in other works [128–134] many calculations illustrate the important role of hadronic fluctuations of the photon in the photoproduction of light vector mesons and the large leading twist nuclear

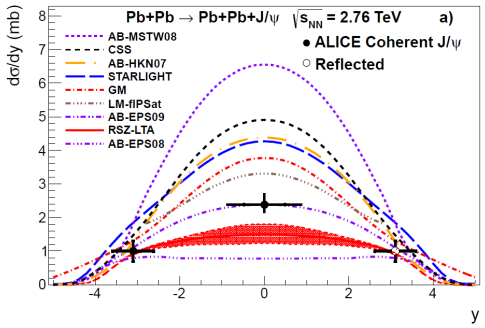

Figure 14 – Production of J/Ψ in UPCs at the LHC as a function of the rapidity y. It serves as a probe of different PDFs (adapted from Ref. [124]).

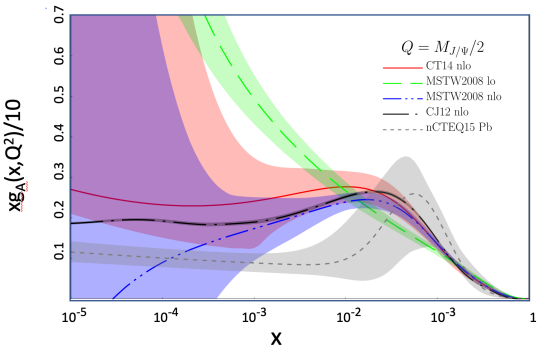

Figure 15 – Uncertainties in theoretical compilations of gluon distribution functions as a function of the momentum fraction x.

gluon shadowing in photoproduction of $q\bar{q}$ pairs off nuclei.

10 A History of the Future

I have illustrated how seemingly straightforward concepts, originating in the 1980s and 1990s, have blossomed into a fertile research domain at relativistic colliders. Experimentally verified unexpected phenomena induced in UPCs encompass a spectrum of discoveries, including double giant resonances, pioneering investigations with anti-atoms, beam loss attributed to capture of electrons, light-by-light scattering, exploration of PDFs, and quests for physics transcending the standard model. Could phenomena like $\gamma\gamma \rightarrow$ graviton [135] or axion-like particles [102, 103] be uncovered through this avenue? The verdict remains uncertain, contingent upon further strides in accelerator technology, beam physics, and novel detection methodologies.

But predicting is hard, especially if it is about the future! In my travels through numerous physics departments worldwide, I have often encountered the assertion that nuclear physics lacks the fundamental nature attributed to particle physics. Particle physicists often define "fundamental" as pertaining to answers regarding interactions, particles, and fields – like the Higgs – that bridge the gaps in theories concerning matter and forces in the Universe. To these critics, nuclear physics appears more akin to engineering with nucleons. However, it's evident that questions concerning the prediction of the Hoyle state in ^{12}C or the origin of elements and its implications for the existence of life must also be regarded as fundamental.

It seems plausible that if supersymmetric particles remain elusive at CERN in the next decade, particle physicists may need to focus on precision calculations and measurements or explore less "fundamental" avenues, such as the existence of exotic mesons or how medium modifications can modify parton distributions. Traditional particle physicists might feel ashamed. But, this could lead to a diversification of scientific endeavors in laboratory settings.

The future of big science may lie in what some still regard as "small science." The light source laboratories exemplify this trend, offering the potential to address some of the most pressing questions in nuclear and particle physics. Light, both on-shell and off-shell, proves to be an invaluable tool. It may be time for particle physicists to change their focus towards more practical pursuits and incorporate light-based research into their endeavors.

In my humble opinion, nuclear physics poses challenges at a significantly higher level compared to other physical sciences. This assertion stems from several factors: (a) The lack of comprehensive understanding of nucleon interaction, (b) the composite nature of nucleons, and (c) the complexity of the nuclear many-body problem arising from various aspects of the strong interaction. Perhaps due to the formidable nature of nuclear physics, senior nuclear physicists often exhibit skepticism and lack of support towards newcomers and new research endeavors.

Alan Bromley expressed in an essay that nuclear physicists are among the harshest referees, often rejecting meritorious papers out of jealousy or excessive criticism and destructiveness [136]. Conversely, colleagues in other physical disciplines tend to be more supportive of one another. This attitude must evolve for the survival of their own legacy, the nurturing of a new generation of young and talented nuclear physicists, and for the advancement of a science crucial for understanding the universe we inhabit.

Acknowledgments

I would like to thank Daniel Tapia Takaki for beneficial discussions and also for his leadership in this field. This work was partially supported by the U.S. DOE grant DE-FG02-08ER41533, the NSF grant no. 2114669 (Accelnet IAN-QCD https://www.iann-qcd.org) and the Helmholtz Research Academy Hesse for FAIR.

References

1. C. A. Bertulani and G. Baur, Phys. Rept. **163**, 299 (1988).
2. F. Krauss, M. Greiner, G. Soff, Prog. Part. Nucl. Phys. **39**, 503 (1997).
3. G. Baur, K. Hencken K, Trautmann D, S. Sadovsky and Y. Kharlov, Phys. Reports **364**, 359 (2002).
4. C.A. Bertulani, S. Klein and J. Nystrand, Annu. Rev. Nucl. Part. Sci. **55**, 271 (2005).
5. G. Baur, K. Hencken and D. Trautmann Phys. Reports **453**, 1 (2007).
6. A.J. Baltz et al. Phys. Reports **458**, 1 (2008).
7. C.A. Bertulani and G. Baur, "Relativistic heavy ion physics without nuclear contact", Physics Today **47**, 22 (1994).
8. S. Klein, J. Nystrand, "Ultraperipheral nuclear collisions", Physics Today **70**, 40 (2017).
9. Joakim Nystrand, Nucl. Phys. A **787**, 29 (2007).
10. J.G. Contreras and J.D. Tapia-Takaki, Int. J. Mod. Phys. A **30**, 1542012 (2015).
11. Spencer R. Klein, Nucl. Phys. A **967**, 249 (2017).
12. Spencer R. Klein, Joakim Nystrand, Janet Seger, Yuri Gorbunov, and Joey Butterworth, Comp. Phys. Comm. **212**, 258 (2017).
13. Spencer R. Klein and Peter Steinberg, Annual Reviews **70**, 323 (2020).
14. Peter Steinberg, ALICE, ATLAS, CMS and LHCb Collaborations at the LHC, STAR Collaboration at RHIC, Nucl. Phys. A **1005**, 122007 (2021).
15. E. Fermi, Zeit. Phys. **29**, 315 (1924).
16. E. Fermi, Nuovo Cimento **2**, 143 (1925).
17. C.A. Bertulani and G. Baur, Nucl. Phys. A **442**, 739 (1985).
18. https://www.banksy.co.uk
19. G. Baur, C. Bertulani and H. Rebel, Nucl. Phys. A **459**, 188 (1986).
20. T. Motobayashi, et al., Phys. Rev. Lett. **73**, 2680 (1994).
21. P. Navrátil, C.A. Bertulani, E. Caurier, Phys. Lett. B **634**, 191 (2006).
22. P. Navrátil, C.A. Bertulani, E. Caurier, Phys. Rev. C **73**, 065801 (2006).
23. P. Descouvemont, D. Baye, Nuclear Phys. A **567**, 341 (1994).
24. F.J. Vaughn, R.A. Chalmers, D. Kohler, L.F. Chase, Phys. Rev. C **2**, 1657 (1970).
25. B.W. Filippone, A.J. Elwyn, C.N. Davids, D.D. Koetke, Phys. Rev. C **28**, 2222 (1983).
26. L.T. Baby, et al., Phys. Rev. Lett. **90**, 022501 (2003).
27. A.R. Junghans, et al., Phys. Rev. C **68**, 065803 (2003).
28. N. Iwasa, et al., Phys. Rev. Lett. **83**, 2910 (1999).
29. B.Davids, et al., Phys. Rev. Lett. **86**, 2750 (2001).
30. F. Schümann, et al, Phys. Rev. Lett. **90**, 232501 (2003).
31. R.W. Kavanagh, T.A. Tombrello, J.M. Mosher, D.R. Goosman, Bull. Am. Phys. Soc. **14**, 1209 (169).
32. H. Esbensen, G.F. Bertsch, and K. Snover, Phys. Rev. Lett. **94**, 042502 (2005).
33. M. Gai, Phys. Rev. Lett. **96**, 159201 (2006).
34. E.G. Adelberger et al., Rev. Mod. Phys. **83**, 195 (2011).
35. C.A. Bertulani, Phys. Rev. C **108**, 054602 (2023).
36. G. Baur and C.A. Bertulani, Nucl. Phys. A **458**, 725 (1986).
37. T. Aumann, C.A. Bertulani and K. Suemmerer, Phys. Rev. C **51**, 416 (1995).
38. T. Aumann, K. Suemmerer, C.A. Bertulani and J.V. Kratz, Nucl. Phys. A **599**, 321 (1996).
39. S. Polikanov, et al., Z. Phys. A **350**, 221 (1994).
40. P. Armbruster, et al., Z. Phys. A **355**, 191 (1996).
41. T. Rubehn, et al., Z. Phys. A **353**, 197 (1995).
42. T. Aumann, et al., Nuclear Phys. A **599**, 321 (1996).
43. T. Aumann, K. Boretzky, J. Stroth, E. Wajda , Th. Blaich, J. Cub, and J. Holeczek, Acta Physica Polonica. B **1**, 375 (1997).

44. C.A. Bertulani, Y. Kucuk and R. Lozeva, Phys. Rev. Lett. **124**, 132301 (2020).
45. I. Stetcu, et al., Phys. Rev. Lett. **114**, 012701 (2015).
46. A.J. Baltz, C. Chasman and S.N. White Nucl. Inst. Meth. Phys. Res. A **41**, 1 (1998).
47. Spencer R. Klein, Nucl. Inst. meth. Phys. **459**, 1 (2001).
48. G. Baur and C.A. Bertulani, Phys. Lett. B **174**, 23 (1986).
49. G. Baur and C.A. Bertulani, Phys. Rev. C **34**, 1654 (1986).
50. R. Schmidt, et al., Phys. Rev. Lett. **70**, 1767 (1993).
51. J. Ritman, et al Phys. Rev. Lett. **70**, 533 (1993).
52. H. Emling, Prog. Part. Nucl. Phys. **33**, 729 (1994).
53. T. Aumann, P.F. Bortignon and H. Emling, Ann. Rev. Nucl. Part. Sci. **48**, 351 (1998).
54. C.A. Bertulani and V. Ponomarev, Phys. Reports **321**, 139 (1999).
55. W.H. Furry and J.F. Carlson, Phys. Rev. **44**, 238 (1933).
56. H.A. Bethe, Proc. Cambridge Philos. Soc. **30**, 524 (1934).
57. H.J. Bhabha, Proc. R. Soc. London Ser. A **152**, 559 (1935).
58. Y. Nishina, S. Tomonaga and H. Tamaki, Sci. Pap. Phys. Math. Res. Jpn **24**, 137 (1934).
59. Y. Nishina, S. Tomonaga and M. Kobayashi, Sci. Pap. Inst. Phys. Chem. Res. **27**, 137 (1935).
60. G. Racah, Nuovo Cimento **14**, 93 (1937).
61. G. Baur and C.A. Bertulani, Nucl. Phys. A **505**, 835 (1989).
62. K. Hencken, D. Trautmann, G. Baur, Phys. Rev. A **51**, 998 (1995).
63. G. Baur, K. Hencken, D. Trautmann, S. Sadovsky, Y. Kharlov, Phys. Reports **364**, 359 (2002).
64. A.J. Baltz, Phys. Rev. Lett. **100**, 062302 (2008).
65. J. Adams et al. (STAR Collaboration), Phys. Rev. C **70**, 031902 (2004).
66. W. Adam, et al., Phys. Lett. B **797**, 303 (2008).
67. G. Baur and C.A. Bertulani, Phys. Rev. C **35**, 836 (1987).
68. G. Baur and C.A. Bertulani, Z. Phys. A **330**, 77 (1988).
69. C.A. Bertulani C A and G. Baur, Phys. Rev. D **58** 034005 (1998).
70. C.A. Bertulani and M. Ellermann, Phys. Rev. C **81** 044910 (2010).
71. C. Munger and S. Brodsky Phys. Rev. D **49**, 3228 (1994).
72. G. Baur, et al, Phys. Lett. B **368**, 3 (1996).
73. Malcolm W. Browne, The New York Times, January 5 (1996).
74. G. Blanford et al., Phys. Rev. Lett. **80**, 3037 (1998).
75. C.A. Bertulani and D. Dolci, Nucl. Phys. A **683**, 635 (2001).
76. E.S. Reich, Nature News **11**, 17 (2010).
77. L. Grossman Phys. Rev. Focus **26** (2010).
78. H. Agakishiev, et al, Nature, **473**, 353 (2011).
79. S.R. Klein, Phys. Rev.: Accelerators and Beams **17**, 121003 (2014).
80. Schaumann, J.M. Jowett, C. Bahamonde Castro, R. Bruce, A. Lechner and T. Mertens, Phys. Rev.: Accelerators and Beams **23**, 121003 (2020).
81. C.A. Bertulani and F.S. Navarra Nucl. Phys. A **703**, 861 (2002).
82. B.D. Moreira, C.A. Bertulani, V.P. Goncalves and F. S. Navarra Phys. Rev. D **94**, 094024 (2016).
83. C.A. Bertulani, V.P. Goncalves, B.D. Moreira and F.S. Navarra Eur. Phys. J. **137**, 06019 (2017).
84. R. Fariello, D. Bhandari, C. A. Bertulani and F. S. Navarra, Phys. Rev. C **108**, 044901 (2023).
85. M. Deutsch, Proc. Am. Acad. Art. Sci. **82**, 331(1953).
86. V.W. Hughes, D.W. McColm, K. Ziock, R. Prepost, Phys. Rev. Lett. **5**, 63 (1960).
87. D.B. Cassidy, A.P. Mills, Nat.(Lond.) **449**, 195 (2007).
88. P.J. Fox, S. Jindariani, V. Shiltsev, FERMILAB-CONF-22-010-AD-PPD-T. arXiv:2203.07144 (2022).
89. V.W. Hughes, B. Maglic, Bull. Am. Phys. Soc. **16**, 65 (1971).
90. F. Ginzburg, U.D. Jentschura, S.G. Karshenboim, F. Krauss, V.G. Serbo, and G. Soff, Phys. Rev. C **58** 3565 (1998).
91. P.A. Krachkov, and A.I. Milstein, Nucl. Phys. A **971**, 71 (2018).
92. C. Azevedo, V. P. Gonçalves, and B. D. Moreira, Phys. Rev. C **101**, 024914 (2020).
93. R. Francener, V. P. Gonçalves, and B. D. Moreira, Eur. Phys. J. A **58**, 35 (2022).
94. C. A. Bertulani, D. Bhandari, F.S. Navarra, Eur. Phys. J. A **60**, 43 (2024).
95. David d'Enterria and Hua-Sheng Shao, Phys. Lett. B **842**, 137960 (2023).
96. D. d'Enterria and G.G. da Silveira, Phys. Rev. Lett. **111**, 080405 (2013).
97. M. Kłusek-Gawenda, P. Lebiedowicz, and A. Szczurek, Phys. Rev. C **93**, 044907 (2016).
98. P. Lebiedowicz and A. Szczurek, Phys. Lett. B **772**, 330 (2017).

99. M. Klusek-Gawenda, R. McNulty,, R. Schicker and A. Szczurek, Phys. Rev. D **99**, 093013 (2019).
100. P. Jucha, M. Klusek-Gawenda and A. Szczurek, Phys. Rev. D **109**, 014004 (2024).
101. G. Aaboud, et al., The ATLAS collaboration, Nature Physics **13**, 852 (2017).
102. V. Gonçalves and W. Sauter Phys. Lett. B **811**, 135981 (2020).
103. V.P. Gonçalves, D.E. Martins and M. Rangel, Eur. Phys. J. C **81**, 522 (2021).
104. L. Schoeffel, C. Baldenegro, H. Hamdaoui, S. Hassani, C. Royon, and M. Saimpert, Nucl. Phys. **1005**, 121840 (2021).
105. F.E. Low F E Phys. Rev. **120**, 582 (1960).
106. C.A. Bertulani, Phys. Rev. C **79** 047901 (2009).
107. E. Papageorgiu, Phys. Rev. D **40**, 92 (1989).
108. M. Drees, J. Ellis, D. Zeppenfeld, Phys. Lett. B **223**, 454 (1989).
109. David d'Enterria and Jean-Philippe Lansberg, Phys. Rev. D **81**, 014004 (2010).
110. David d'Enterria, Daniel E. Martins, and Patricia Rebello Teles, Phys. Rev. D **101**, 033009 (2020).
111. ATLAS Collaboration, Phys. Lett. B **716**, 1 (2012).
112. CMS Collaboration, Phys. Lett. B **716**, 30 (2012).
113. W-M Yao, et al., J. Phys. G **33**, 1 (2006).
114. Spencer R. Klein and Joakim Nystrand, Phys. Rev. C **60**, 014903 (1999).
115. Spencer R. Klein and Joakim Nystrand, Phys. Rev. Lett. **84**, 2330 (2000).
116. Anthony J. Baltz, Spencer R. Klein, and Joakim Nystrand, Phys. Rev. Lett. **89**, 012301 (2002).
117. C. Adler et al. (STAR Collaboration), Phys. Rev. Lett. **89**, 272302 (2002).
118. B. I. Abelev et al. (STAR Collaboration), Phys. Rev. C **77**, 034910 (2008).
119. PHENIX Collaboration, Phys. Lett. B **679**, 321 (2009).
120. V.P. Goncalves and C.A. Bertulani, Phys. Rev. C **65**, 054905 (2002).
121. L. L. Frankfurt, W. Koepf and M. Strikman, Phys. Rev. D **57**, (1998) 512
122. A. Adeluyi and C.A. Bertulani, Phys. Rev. C **84**, 024916 (2011).
123. A. Adeluyi and C.A. Bertulani, Phys. Rev. C **85**, 044904 (2012).
124. B. Abelev, et al. (ALICE Collaboration), Phys. Lett. B **718**, 1273 (2013).
125. J. D. Tapia Takaki; ALICE Collaboration, AIP Conf. Proc. **1523**, 221 (2013).
126. A. Abelev, et al., (ALICE Collaboration) Eur. Phys. J. C **73**, 2617 (2013).
127. D. De Gruttola D (ALICE Collaboration), Nucl. Phys. A **926**, 136 (2014).
128. V. Guzey, E. Kryshen, M. Strikman, M. Zhalov, Phys. Lett. B **726**, 290 (2013).
129. V. Guzey, M. Strikman and M. Zhalov, Eur. Phys. J. C **74**, 2942 (2014).
130. V. Guzey, E. Kryshen, and M. Zhalov, Phys. Rev. C **93**, 055206 (2016).
131. V. Guzey, M. Strikman, and M. Zhalov, Phys. Rev. C **95**, 025204 (2017).
132. V.P. Gonçalves, F.S. Navarra, and D. Spiering, Phys. Lett. B **791**, 299 (2019).
133. V. P. Gonçalves, D. E. Martins, and C. R. Sena, Eur. Phys. J. A **57**, 82 (2021).
134. Yuri V. Kovchegov, Huachen Sun, Zhoudunming Tu, [hep-ph] arXiv:2311.12208 (2023).
135. S. Ahern, J.W. Norbury and W. Poyser, Phys. Rev. D **62**, 116001 (2000).
136. D. Allan Bromley, Nuclear Physics News **11**, No. 3, (2001).

Phys. Proc. Ultra-Peripheral Collisions **1**, 002 (2024) 1-12

Vector meson production in ultraperipheral heavy ion collisions

Björn Schenke [a]
Physics Department, Brookhaven National Laboratory, Upton, NY 11973, USA

Heikki Mäntysaari
Department of Physics, University of Jyväskylä, P.O. Box 35, 40014 University of Jyväskylä, Finland
Helsinki Institute of Physics, P.O. Box 64, 00014 University of Helsinki, Finland

Farid Salazar
Institute for Nuclear Theory, University of Washington, Seattle WA 98195-1550, USA

Chun Shen
Department of Physics and Astronomy, Wayne State University, Detroit, Michigan 48201, USA
RIKEN BNL Research Center, Brookhaven National Laboratory, Upton, NY 11973, USA

Wenbin Zhao
Nuclear Science Division, Lawrence Berkeley National Laboratory, Berkeley, California 94720, USA
Physics Department, University of California, Berkeley, California 94720, USA

We review model calculations of exclusive vector meson production in ultraperipheral heavy ion collisions. We highlight differences and similarities between different dipole models and leading twist shadowing calculations. Recent color glass condensate calculations are presented with focus on effects from nuclear structure and azimuthal anisotropies driven by interference effects.

DOI: https://doi.org/10.17161/0mc43032
Keywords: ultraperipheral collisions, vector meson production, dipole models, color glass condensate

1 Introduction

Ultraperipheral heavy ion collisions (UPCs) at the Relativistic Heavy Ion Collider (RHIC) and the Large Hadron Collider (LHC) provide access to photonuclear events at high energy. They allow the study of processes that are otherwise only accessible by an electron- (or muon-) ion collider. While the kinematics is less controlled and versatile, because we cannot measure the momentum of a scattered electron, and the Q^2 is constrained to values close to zero, UPCs have the advantage of being able to probe very small momentum fractions x in the target. This is particularly useful for accessing the gluon saturation regime and exploring features of non-linear Quantum Chromodynamics (QCD) in dense systems [1].

One interesting process that is sensitive to the spatial parton distributions in the target as well as to saturation effects in the gluon distribution is the exclusive production of vector mesons. For coherent diffractive vector meson production, in which the target remains intact, measurements differential in the transverse momentum transfer squared $|t|$ contain information on the transverse (to the beam line) spatial structure of the target. In the case of incoherent production, for which the target breaks up, one is sensitive to fluctuations of its geometry [2,3].

Both in e+A scattering and UPCs, part of the process can be understood as a virtual photon interacting with the target. In UPCs, the photon is radiated from the moving projectile nucleus. Consequently, it is almost real, as $Q^2 \sim 1/R_A^2$ with R_A the nuclear radius. The fact that both nuclei can be either the photon source or the target can complicate things and interference between the two scenarios must be taken into account.

We will focus in detail on the coherent production of J/ψ vector mesons in UPCs of Pb nuclei at the LHC and discuss a variety of models and how nuclear effects are taken into account. We will point out some similarities and differences between the models, and present comparisons to experimental data. We will further discuss calculations within the Color Glass Condensate (CGC) framework in some more detail and highlight results for the energy dependence of nuclear suppression, azimuthal anisotropies caused by interference effects, and the effects of nuclear structure on diffractive vector meson production.

[a] speaker, bschenke@bnl.gov

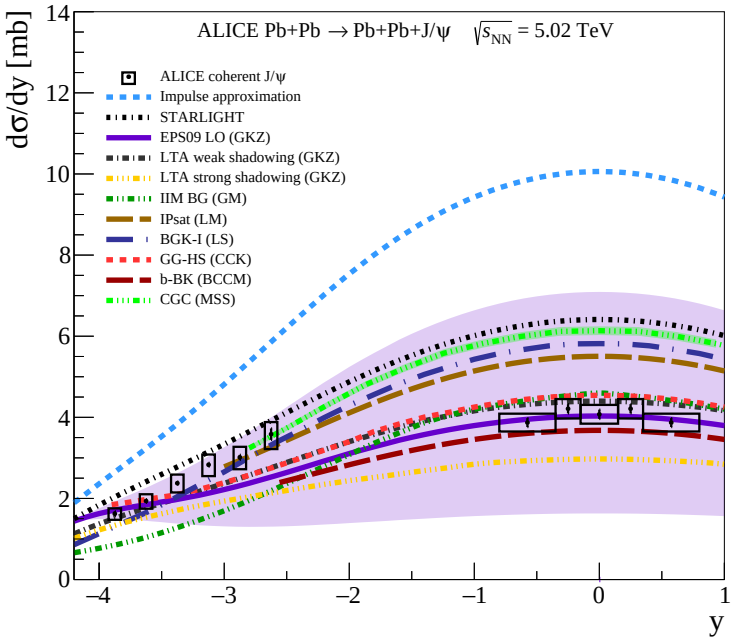

Figure 1 – Differential cross section of coherent diffractive J/ψ photoproduction in Pb+Pb UPC events. For the ALICE data[5,6], the error bars (boxes) show the statistical (systematic) uncertainties. The theoretical calculations are discussed in the text. The purple band represents the uncertainties of the EPS09 LO calculation.

2 General considerations

The photon flux is given by [4]

$$N(\omega_\pm) = \int_{|\mathbf{B}|>B_{\min}} \mathrm{d}^2\mathbf{B}\, n(\omega_\pm, \mathbf{B})\,, \tag{1}$$

where $\mathbf{B}$ is the impact parameter vector between the centers of the two nuclei, $\omega_\pm = (M_V/2)e^{\pm y}$, with M_V the vector meson mass, and

$$n(\omega, \mathbf{B}) = \frac{Z^2\alpha_{\mathrm{em}}\omega^2}{\pi^2\gamma^2} K_1^2\left(\frac{\omega|\mathbf{B}|}{\gamma}\right). \tag{2}$$

Here, $\alpha_{\mathrm{em}} = 1/137$ the fine-structure constant, Z is the ion charge and $\gamma = A\sqrt{s}/(2M_A)$, with M_A the mass of the nucleus. $B_{\min}$ is the minimal impact parameter to not have a hadronic interaction. It has to be on the order of $2\,R_A$, with R_A the nuclear radius.

At midrapidity, the cross section for the process $A_1 + A_2 \to V + A_1 + A_2$ is given by

$$\left.\frac{\mathrm{d}\sigma^{A_1+A_2\to V+A_1+A_2}}{\mathrm{d}|t|dy}\right|_{y=0} = 2\int \mathrm{d}^2\mathbf{B}\, n(\omega, |\mathbf{B}|)\frac{\mathrm{d}\sigma^{\gamma+A\to V+A}}{\mathrm{d}|t|}[1-\cos(\boldsymbol{\Delta}\cdot\mathbf{B})]\,\theta(|\mathbf{B}|-2R_A)\,, \tag{3}$$

where $\boldsymbol{\Delta}^2 = -t$. This shows that at midrapidity interference leads to a vanishing differential cross section at $t = 0$.

This simplified expression neglects photon $\mathbf{k}$, which is a good approximation except around diffractive minima in the coherent cross section, because $\mathbf{k}^2 \lesssim Q^2 \sim 1/R_A^2$. In coordinate space it is realized by assuming $|\mathbf{B}| \gg |\mathbf{b}|$, with $\mathbf{b}$ the impact parameter vector of the quasi-real photon relative to the center of the target nucleus. Further neglecting interference one obtains for the rapidity-dependent result

$$\frac{\mathrm{d}\sigma^{A_1+A_2\to V+A_1+A_2}}{\mathrm{d}y} = N(\omega_+)\sigma_+^{\gamma^*+A\to V+A} + N(\omega_-)\sigma_-^{\gamma^*+A\to V+A}\,. \tag{4}$$

Here, $\sigma_+^{\gamma^*+A\to V+A}$ and $\sigma_-^{\gamma^*+A\to V+A}$ refer to the photon-nucleus cross sections where the target structure is probed at different longitudinal momentum fractions $x_{\mathbb{P}} = (M_V/\sqrt{s})e^{\mp y}$.

3 Model comparisons

The difference between the theoretical models shown in Fig. 1 lies mainly in how the cross section $\sigma_{\pm}^{\gamma^*+A\to V+A}$ is determined. We separate the models into two classes, the leading order (LO) pQCD description following Ryskin [7] and the dipole picture, first proposed in [8].

3.1 LO pQCD framework

In the LO pQCD framework, the cross section takes on the form [9]

$$\sigma^{\gamma^*+A\to V+A} = \frac{C_A(\mu^2)}{C_p(\mu^2)} \frac{d\sigma^{\gamma^*+p\to V+p}(W_{\gamma p}, t=0)}{dt} \left[\frac{xg_A(x,\mu^2)}{Axg_p(x,\mu^2)}\right]^2 \Phi_A(t_{\min})\,, \tag{5}$$

where xg_p and xg_A are the gluon distributions in the proton and nucleus, respectively, and μ is a hard scale on the order of the charm quark mass (for J/ψ production). The cross section at $t=0$ for a proton target is given by

$$\frac{\mathrm{d}\sigma^{\gamma^*+p\to V+p}(W_{\gamma p}, t=0)}{\mathrm{d}t} = \frac{1}{16\pi}|A^{\gamma^*+p\to V+p}|^2\,, \tag{6}$$

where

$$A^{\gamma^*+p\to V+p} = i4\pi^2\sqrt{\frac{M_V^3\Gamma_{ee}}{48\alpha\mu^8}}\alpha_s(\mu^2)xg_p(x,\mu^2)F(\mu^2)\sqrt{1+\eta^2}R_g\,. \tag{7}$$

The function $\Phi_A(t_{\min}) = \int_{-\infty}^{t_{\min}} \mathrm{d}t|F_A(t)|^2$, with the nuclear form factor F_A and $t_{\min} = -M_V^4 m_N^2/W_{\gamma p}^4$ is the minimal squared momentum transfer to the nucleus. The function $F(\mu^2)$, that lies between 0 and 1, contains effects that go beyond the leading order collinear factorization used, for example next-to-leading order corrections, corrections associated with the charmonium wave function, and power-suppressed corrections in the overlap of the photon and J/ψ wave functions. [9] The factor $C_A/C_p = (1+\eta_A^2)\bar{R}_{g,A}^2/[(1+\eta^2)\bar{R}_g^2]$. Here, η_A and η are the ratios of the real to imaginary part of the $\gamma+A\to V+A$ and $\gamma+p\to V+p$ scattering amplitude, respectively, and $R_{g,A}$ and R_g are "skewness factors" that correct for the fact that we are not using generalized parton distributions (GPDs) but the usual ones. One determines η_A and $\bar{R}_{g,A}$ using the asymptotic small-x dependence of the nuclear gluon distribution. [9] This factor introduces some nuclear modification, as $R_{g,A}$ differs from R_g, but the main shadowing effect is governed by the ratio of gluon distributions

$$R = \frac{xg_A(x,\mu^2)}{Axg_p(x,\mu^2)}\,. \tag{8}$$

The "impulse approximation" in Fig. 1 is obtained using Eq. (5) with $R=1$ and $C_A/C_p = 1$. [9] It clearly overshoots the data at all rapidities. In the leading twist approximation (LTA), R is obtained from the nuclear gluon distribution in leading twist shadowing (and so is $C_A/C_p \approx 0.9$) [10]

$$g_A(x,\mu^2) = Ag_p(x,\mu^2) - 8\pi\,\mathrm{Re}\left[\frac{(1-i\eta)^2}{1+\eta^2}\int \mathrm{d}^2\mathbf{b}\int_{-\infty}^{\infty}\mathrm{d}z_1\int_{-\infty}^{\infty}\mathrm{d}z_2\int_x^{x_{\mathbb{P}}^0}\mathrm{d}x_{\mathbb{P}}\, g_N^D(x/x_{\mathbb{P}}, x_{\mathbb{P}}, \mu^2, t_{\min})\right.$$
$$\left.\rho_A(\boldsymbol{b},z_1)\rho_A(\boldsymbol{b},z_2)e^{ix_{\mathbb{P}}m_N(z_1-z_2)}e^{-\frac{1}{2}\sigma_{\mathrm{eff}}(x,\mu^2)(1-i\eta_A)\int_{z_1}^{z_2}\mathrm{d}z\rho_A(\boldsymbol{b},z)}\right]\,, \tag{9}$$

where $g_N^D(x/x_{\mathbb{P}}, x_{\mathbb{P}}, \mu^2, t_{\min})$ is the diffractive gluon density of the nucleon, $x_{\mathbb{P}}$ is the pomeron momentum fraction, and $x_{\mathbb{P}}^0 = 0.03$ a cutoff parameter. This includes the interaction with two nucleons at longitudinal positions z_1 and z_2, and the interaction with three or more nucleons is absorbed into the attenuation factor, the exponential including σ_{eff}, which is the effective cross section for the elastic rescattering of the produced diffractive state. The uncertainty in σ_{eff} leads to the variation between 'LTA weak shadowing' and 'LTA string shadowing' in Fig. 1. The factor $e^{ix_{\mathbb{P}}m_N(z_1-z_2)}$ takes into account longitudinal momentum transfer, or a finite coherence length. In the EPS09 LO curve, the factor R is obtained from the nuclear PDFs obtained using global fits of available data on lepton-nucleus DIS and hard scattering with nuclei at the Tevatron and LHC. [11]

The STARLIGHT result shown in Fig. 1 includes Glauber-like rescattering. Here, we have similar to the impulse approximation

$$\sigma^{\gamma^*+A\to V+A} = \left.\frac{\mathrm{d}\sigma^{\gamma^*+A\to V+A}}{\mathrm{d}|t|}\right|_{t=0}\Phi_A(t_{\min})\,. \tag{10}$$

Using the optical theorem and vector meson dominance [12] one can write

$$\left.\frac{\mathrm{d}\sigma^{\gamma^*+A\to V+A}}{\mathrm{d}|t|}\right|_{t=0} = \frac{4\pi\alpha}{f_v^2}\left.\frac{\mathrm{d}\sigma^{V+A\to V+A}}{\mathrm{d}|t|}\right|_{t=0} = \frac{\alpha\sigma_{\mathrm{tot}}^2(VA)}{4f_v^2}\,, \tag{11}$$

where α is the electromagnetic coupling constant, $e^2/\hbar c$, and f_v is the vector meson-photon coupling. [13] The total $V+A\to V+A$ cross section follows from a Glauber calculation

$$\sigma_{\mathrm{tot}}(VA) = 2\int \mathrm{d}^2\mathbf{b}\left(1-e^{\sigma_{\mathrm{tot}}(Vp)T_A(\boldsymbol{b})/2}\right)\,, \tag{12}$$

where $T_A(\boldsymbol{b}) = \int \mathrm{d}z\rho_A(\boldsymbol{b},z)$ is the nuclear thickness function.[b] Throughout this text we assume $\int \mathrm{d}^2\mathbf{b}\; T_A(\boldsymbol{b}) = A$, which may differ from some of the references below. Just like for nuclei above, we have

$$\sigma_{\mathrm{tot}}^2(Vp) = \frac{4f_v^2}{\alpha}\left.\frac{\mathrm{d}\sigma^{\gamma^*+p\to V+p}}{\mathrm{d}|t|}\right|_{t=0}\,, \tag{13}$$

and $\mathrm{d}\sigma^{\gamma+p\to V+p}/\mathrm{d}t|_{t=0}$ is determined from experimental data. [13]

3.2 Dipole models

Next, we move on to the various dipole models shown in Fig. 1. Here, the picture is that we are at high energy and the virtual photon first splits into a quark anti-quark dipole, which subsequently interacts with the target. A measure of whether the dipole picture is appropriate is the coherence time $l_c = 2\nu/(Q^2+M_{q\bar{q}}^2)$, compared to the nuclear size scale (ν is photon energy in the target rest frame, and $M_{q\bar{q}}^2 = (m_q^2+k_T^2)/z(1-z)$). In the limit of very small $x = Q^2/2m_N\nu$ the coherence length is longer than the nuclear size and the "frozen" dipole picture is appropriate. If the coherence time is smaller than the nuclear size scale one should correct for dipole size fluctuations during the propagation in the nucleus, which corresponds to inclusion of the phase shifts between DIS amplitudes on different nucleons, as they are included in Eq. (9). [15] For $x\le 10^{-2}$, the factor $e^{i(z_1-z_2)m_N x_{\mathbb{P}}}$ can be safely set to unity. [16]

For the coherent process that we are discussing here, the cross section is given by [17]

$$\frac{\mathrm{d}\sigma^{\gamma^*+A\to V+A}}{\mathrm{d}|t|} = \frac{1}{16\pi}|A(x,Q^2,\boldsymbol{\Delta})|^2\,, \tag{14}$$

where the dipole amplitude is

$$A(x,Q^2,\boldsymbol{\Delta}) = i\int \mathrm{d}^2\mathbf{r}\int \mathrm{d}^2\mathbf{b}\int \frac{\mathrm{d}z}{4\pi}(\psi^*\psi_V)(Q^2,\boldsymbol{r},z)e^{-i(\boldsymbol{b}-(1/2-z)\boldsymbol{r})\cdot\boldsymbol{\Delta}}\frac{\mathrm{d}\sigma_{\mathrm{dip}}}{\mathrm{d}^2\mathbf{b}}(\mathbf{b},\mathbf{r},x)\,. \tag{15}$$

Here, $(\psi^*\psi_V)(Q^2,\boldsymbol{r},z)$ represents the wave function overlap of the photon and vector meson wave functions, and $\frac{\mathrm{d}\sigma_{\mathrm{dip}}}{\mathrm{d}^2\mathbf{b}}(\mathbf{b},\mathbf{r},x)$ is the average dipole cross section (an average over configurations is performed for models that include explicit fluctuations).

Considering the proton target, we note that the dipole model amplitude (15) can be brought into the form Eq. (7) without the real part and skewness corrections, by taking the hard scattering (small r) and non-relativistic (for which $z=0.5$) limits. [15,18] In that case, one should take

$$\frac{\mathrm{d}\sigma_{\mathrm{dip}}}{\mathrm{d}^2\mathbf{b}} = \frac{\pi^2}{N_c}r^2\alpha_s(\mu^2)xg(x,\mu^2)T(\mathbf{b})\,, \tag{16}$$

essentially the small r limit of the BGK or IPSat model, which are discussed for nuclei below.

For the first dipole model shown in Fig. 1, IIM BG (GM) [19], the dipole cross section for a nuclear target is

$$\frac{\mathrm{d}\sigma_{\mathrm{dip}}}{\mathrm{d}^2\mathbf{b}} = 2(1-e^{-\frac{1}{2}\sigma_{\mathrm{dip}}^{\mathrm{IIM\,BG}}(x,\mathbf{r})T_A(\mathbf{b})})\,, \tag{17}$$

and $\sigma^{\mathrm{IIM\,BG}}$ is a parametrization fit to HERA data from Iancu, Itakura, and Munier (IIM) [20,21]

$$\sigma_{\mathrm{dip}}^{\mathrm{IIM\,BG}}(x,r) = \sigma_0\begin{cases}0.7\left(\frac{\bar{\tau}^2}{4}\right)^{\gamma_{\mathrm{eff}}(x,r)}, \text{for } \bar{\tau}\le 2,\\ 1-\exp\left[-a\ln^2(b\bar{\tau})\right], \text{for } \bar{\tau}>2\,,\end{cases} \tag{18}$$

[b] In practice, STARLIGHT used the inelastic cross section $\sigma_{\mathrm{inel}}(VA) = \int \mathrm{d}^2\mathbf{b}\left(1-e^{\sigma_{\mathrm{tot}}(Vp)T_A(\boldsymbol{b})}\right)$ instead of (12).[14]

where $\bar{\tau} = rQ_s(x)$, with the saturation scale $Q_s = (x_0/x)^{\lambda/2}$, and $\sigma_0 = 2\pi R_p^2$, with R_p the proton radius. Here, $\gamma_{\rm eff}(x,r) = \gamma_{\rm sat} + \ln(2/\bar{\tau})/(\kappa\lambda y)$ with $\kappa = 9.9$. For the vector meson wave function a boosted Gaussian (BG) is used. The structure of Eq. (17) for a nuclear target follows from the Glauber-Gribov methodology proposed in [22] and is common to almost all dipole models discussed here, except the b-BK model.

In the next dipole model, BGK-I (LS), Eq. (17) is replaced with an expression that takes the real part of the dipole-nucleon amplitude into account and uses for the dipole cross section [23]

$$\sigma_{\rm dip}^{\rm BGK-I}(x,r) = \tilde{\sigma}_0 \left(1 - \exp\left[-\frac{\pi^2 r^2 \alpha_s(\mu^2) x g(x,\mu^2)}{3\tilde{\sigma}_0}\right]\right), \tag{19}$$

where $xg(x,\mu^2)$ is obtained from DGLAP evolution of the initial condition $xg(x,\mu_0^2) = A_g x^{-\lambda_g}(1-x)^{C_g}$. Here, the free parameters are $\tilde{\sigma}_0$, μ_0^2, A_g, λ_g, and C_g.

In the IPSat (LM) model [24] calculation shown, the authors assumed a large and smooth nucleus, leading to an expression that corresponds to replacing $\sigma_{\rm dip}^{\rm IIM\,BG}(x,\boldsymbol{r})$ in (17) by

$$\sigma_{\rm dip}^{\rm IPSat} = 4\pi B_p[1 - \exp\bigl(-r^2 F(x,r)\bigr)], \tag{20}$$

with

$$F(x,r) = \frac{1}{2\pi B_p}\frac{\pi^2}{2N_c}\alpha_s \left(\mu_0^2 + \frac{C}{r^2}\right) xg\left(x, \mu_0^2 + \frac{C}{r^2}\right). \tag{21}$$

Here, C is chosen to be 4 and $\mu_0^2 = 1.17\,{\rm GeV}^2$ is the result of a fit to HERA data. [25] The r dependence of the gluon distribution is obtained from DGLAP evolution of the initial condition given by the same $xg(x,\mu_0^2)$ as in the BGK-I model above.

The next dipole model, GG-HS [26], has a similar structure as IPSat above, but is based on a Golec-Biernat - Wüsthoff (GBW) dipole amplitude. [27]

So, once again we start from Eq. (17) (hence the GG = Glauber-Gribov in the name of this model) but this time replace $\sigma_{\rm dip}^{\rm IIM\,BG}(x,\boldsymbol{r})$ by

$$\sigma_{\rm dip}(x,r) = \sigma_0[1 - \exp\bigl(-r^2 Q_s^2(x)/4\bigr)], \tag{22}$$

where $Q_s^2 = Q_{s0}^2(x_0/x)^\lambda$. This model implements subnucleonic hot spots (HS), $N_{\rm hs}$ of them per nucleon, each with a Gaussian density distribution of width $B_{\rm hs}$. Hot spots have no direct effect on the coherent cross section as that is sensitive to the average structure of the target. The incoherent cross section, in particular at large $|t|$ is sensitive to hot spots. [26,28]

Finally, in the b-BK (BCCM) model [29] uses expression (15) with

$$\frac{{\rm d}\sigma_{\rm dip}}{{\rm d}^2\mathbf{b}} = 2N(\mathbf{r},\mathbf{b},x), \tag{23}$$

where N is evolved with impact parameter dependent Balitsky-Kovchegov (BK) evolution [30,31], starting from an initial condition for the nucleus with the impact parameter dependence given by the Woods-Saxon distribution for Pb. [32] An alternative approach that employs the BK evolved dipole cross section for the proton embedded in a Glauber-Gribov expression as used above was also studied [29]. It leads to less suppression than the evolution of the nuclear dipole cross section, as the latter leads to stronger saturation effects.

It is noteworthy that none of the models achieves a good simultaneous description of the experimental data at forward and mid-rapidities.

3.3 Color Glass Condensate

The Color Glass Condensate (CGC) calculation is also based on the dipole picture, so we employ expression (15) with

$$\frac{{\rm d}\sigma_{\rm dip}}{{\rm d}^2\mathbf{b}} = \langle N(\boldsymbol{r},\boldsymbol{b},x)\rangle_\Omega = \langle 2N(\boldsymbol{x}-\boldsymbol{y},(\boldsymbol{x}+\boldsymbol{y})/2,x)\rangle_\Omega = 1 - \langle {\rm Tr}(V(\boldsymbol{x})V^\dagger(\boldsymbol{y}))/N_c\rangle_\Omega, \tag{24}$$

with the light-like Wilson line

$$V(\mathbf{x}) = {\rm P}_- \left\{\exp\left(-ig\int_{-\infty}^{\infty} {\rm d}x^- \frac{\rho^a(x^-,\mathbf{x})t^a}{\boldsymbol{\nabla}^2 - m^2}\right)\right\}. \tag{25}$$

P_- represents path ordering in the x^- direction, and m regulates unphysical Coulomb tails. Color charges ρ^a (with color index a) are sampled from a distribution whose width is given by the average squared color charge density, which can be obtained from its relation to the local saturation scale extracted from the IPSat amplitude above [33,34]. This corresponds to employing a modified McLerran-Venugopalan (MV) model [35,36] that includes the geometry of the target. Note that we included an explicit average over configurations Ω.

As can be seen from Eq. (17) (along with (20) for σ_{dip}), in the IPsat model the local saturation scale $Q_s^2(\mathbf{x})$ is proportional to the local transverse density $T_p(\mathbf{x})$. For nuclei, one first samples nucleon positions from a Woods-Saxon distribution, and then calculates the total density by summing the nucleon density profiles [33]. When constraining the geometry at an initial x_0, the evolution to smaller x via the JIMWLK equations [37] should be included [38]. This is done for the CGC (MSS) curve shown in Fig. 1, which also includes subnucleon fluctuations. The details of the implementation are described in the corresponding publication [39].

Incoherent diffraction, which we have not discussed in detail so far, is the diffractive process in which the target breaks up. Its cross section has the form of a variance of the scattering amplitude and is thus sensitive to fluctuations. [2] As the CGC framework includes fluctuations of color charges and nuclear geometry, including nucleon and subnucleon fluctuations, it is well suited to address incoherent diffraction. The differential cross section for incoherent diffractive vector meson production is given by

$$\frac{\mathrm{d}\sigma^{\gamma^*+A\to V+A^*}}{\mathrm{d}t} = \frac{1}{16\pi}\left(\left\langle\left|A\left(x,Q^2,\boldsymbol{\Delta}\right)\right|^2\right\rangle_\Omega - \left|\left\langle A\left(x,Q^2,\boldsymbol{\Delta}\right)\right\rangle_\Omega\right|^2\right), \tag{26}$$

with A from Eq. (15) but with the modification that we do not include the averages $\langle\cdot\rangle_\Omega$ in (24). Instead, we have included the averages over configurations in this expression, to allow for the computation of the variance of A.

4 Nuclear suppression

To quantify the magnitude of saturation effects in J/ψ photoproduction, one can compute nuclear suppression factors separately for the coherent and incoherent channels. We define the suppression factor for the coherent production as

$$S_{\mathrm{coh}} = \frac{\sigma^{\gamma+A\to V+A}}{\sigma^{\mathrm{IA}}}, \tag{27}$$

where σ^{IA} is given by Eq. (10), the $\gamma+p$ result scaled to the $\gamma+\mathrm{Pb}$ case by only taking into account the nuclear form factor $F(t)$ and neglecting all other potential nuclear effects. For LHC kinematics, one can set $t_{\mathrm{min}}=0$. Note that in some studies S_{coh} is defined with a square root. [40,41]

For the incoherent cross section, one can define the suppression factor: [42,43]

$$S_{\mathrm{incoh}} = \frac{\sigma^{\gamma+A\to V+A^*}}{A(\sigma^{\gamma+p\to V+p^*}+\sigma^{\gamma+p\to V+p})}. \tag{28}$$

We present results for the energy dependence of S_{coh} and S_{incoh} in Fig. 2, comparing to results from ALICE and CMS for S_{coh} [40 41] and from STAR for S_{incoh}. [42,43]

The LHC data for the coherent suppression factor seems to have a steeper W dependence than the model calculation. A slower evolution in heavy nuclei compared to the proton reference could improve agreement. One way to achieve this would be a Q_s dependent running coupling in the evolution kernel. We note, however, that in our current setup the JIMWLK evolution includes the running coupling which depends on the daughter dipole sizes, and thus should indirectly depend on the saturation scale Q_s. We compare to STAR results for Au targets, where the kinematics leads to larger x than the validity range of the framework. It will be interesting to compare to data for S_{incoh} at higher W to test the prediction in Fig. 2.

5 Azimuthal Anisotropies from Interference

In UPCs there is interference between the contributions where one nucleus is the photon source and the other is the target and the one where the roles are flipped. This can lead to interesting interference patterns. In fact, because the emitted photon is linearly polarized, the interference leads to characteristic azimuthal modulations in the angle between the decay products of a produced vector meson. This was measured for example in diffractive ρ production and its decay into pions at STAR [44].

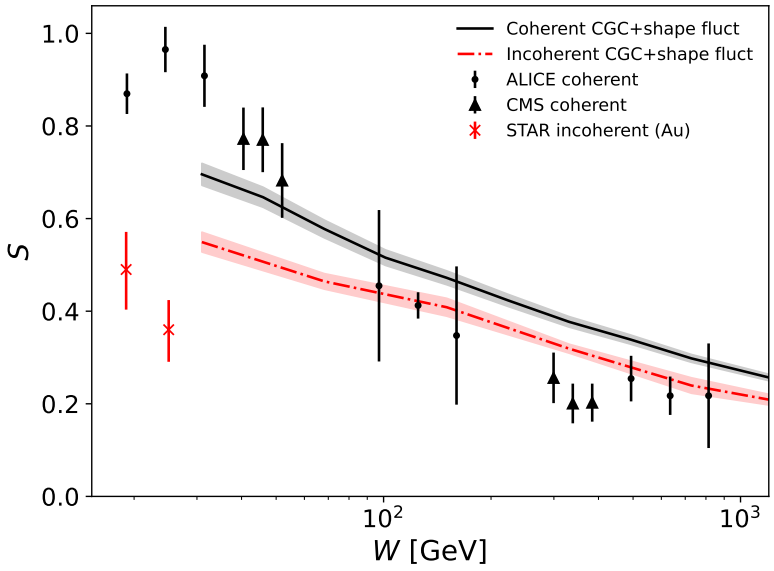

Figure 2 – Suppression factors for coherent and incoherent production for Pb targets computed in the CGC framework with nucleon shape fluctuations [38] and compared to the ALICE [40], CMS [41], and STAR [42 43] data (STAR data for Au targets).

The cross section for this process can be computed in the CGC framework using a joint impact parameter and transverse momentum-dependent formulation [45,46]. Here, the differential cross-section for the diffractive ρ (or ϕ) production, and the subsequent decay into pions or kaons, respectively, is given by [47]

$$\frac{\mathrm{d}\sigma^{\rho\to\pi^+\pi^-(\phi\to K^+K^-)}}{\mathrm{d}^2\mathbf{P}_\perp \mathrm{d}^2\mathbf{q}\mathrm{d}y_1\mathrm{d}y_2} = \frac{1}{4(2\pi)^3}\frac{P_\perp^2 f^2}{(Q^2-M_V^2)^2+M_V^2\Gamma^2}\left\{C_0(x_1,x_2,|\mathbf{q}|)+C_2(x_1,x_2,|\mathbf{q}|)\cos(2(\phi_{\mathbf{P}_\perp}-\phi_{\mathbf{q}}))\right\}, \tag{29}$$

where $\mathbf{P}_\perp = (\mathbf{p}_{1\perp}-\mathbf{p}_{2\perp})/2$ and $\mathbf{q} = \mathbf{p}_{1\perp}+\mathbf{p}_{2\perp}$ with $\mathbf{p}_{1\perp}$ and $\mathbf{p}_{2\perp}$ being the transverse momenta of the measured decay particles. Further, Q is the invariant mass of the daughter particle system, and y_1 and y_2 are the daughter particles' rapidities. The decay width is Γ and f are effective couplings. Here, we have already separated the cross section into an isotropic piece and a $\cos(2\phi)$ modulation. The coefficients of the two components are

$$C_0(x_1,x_2,|\mathbf{q}|) = \left\langle \int \mathrm{d}^2\mathbf{B}\mathcal{M}^i(x_1,x_2,\mathbf{q},\mathbf{B})\mathcal{M}^{\dagger,i}(x_1,x_2,\mathbf{q},\mathbf{B})\Theta(|\mathbf{B}|-B_{\min})\right\rangle_\Omega, \text{ and} \tag{30}$$

$$C_2(x_1,x_2,|\mathbf{q}|) = \left(\frac{2\mathbf{q}^i\mathbf{q}^j}{\mathbf{q}^2}-\delta^{ij}\right)\left\langle \int \mathrm{d}^2\mathbf{B}\mathcal{M}^i(x_1,x_2,\mathbf{q},\mathbf{B})\mathcal{M}^{\dagger,j}(x_1,x_2,\mathbf{q},\mathbf{B})\Theta(|\mathbf{B}|-B_{\min})\right\rangle_\Omega. \tag{31}$$

The amplitudes $\mathcal{M}^i(x_1,x_2,\mathbf{q},\mathbf{B})$ are expressed as the convolution of the photon field $\mathcal{F}^i_{A_k}(x_k,\mathbf{b})$ with the vector meson production amplitude $\mathcal{A}_{A_k}(x_k,\mathbf{b})$ in coordinate space [39]

$$\mathcal{M}^i(x_1,x_2,\mathbf{q},\mathbf{B}) = \int \mathrm{d}^2\mathbf{b}e^{-i\mathbf{q}\cdot\mathbf{b}}\left[\mathcal{A}_{A_1}(x_1,\mathbf{b})\mathcal{F}^i_{A_2}(x_2,\mathbf{b}-\mathbf{B})+\mathcal{A}_{A_2}(x_2,\mathbf{b}-\mathbf{B})\mathcal{F}^i_{A_1}(x_1,\mathbf{b})\right]. \tag{32}$$

The vector meson production amplitude is computed in the CGC framework using Eqs. (15) and (24), and the photon field is given by

$$\mathcal{F}^j_A(x,\mathbf{B}) = \frac{1}{2\pi}\frac{Z\alpha_{\mathrm{em}}^{1/2}\omega}{\pi\gamma}\frac{\mathbf{B}^j}{|\mathbf{B}|}K_1\left(\frac{\omega|\mathbf{B}|}{\gamma}\right). \tag{33}$$

Note that we recover the photon flux in Eq. (2) from

$$n(\omega,|\mathbf{B}|) = (2\pi)^2\left|\mathcal{F}_A(x,|\mathbf{B}|)\right|^2. \tag{34}$$

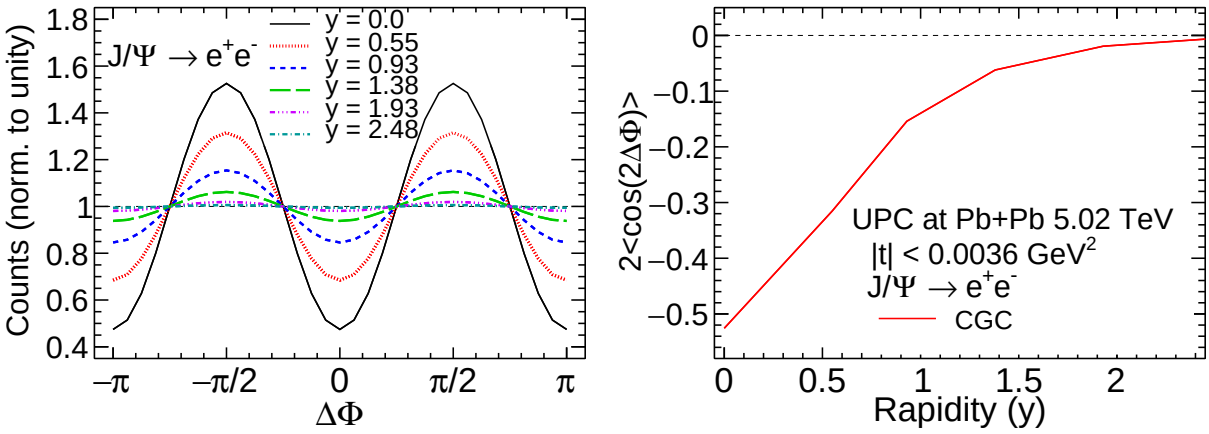

Figure 3 – Left: The modulation in the azimuthal angle difference $\Delta\Phi = \phi_{\mathbf{P}_\perp} - \phi_{\mathbf{q}}$ in J/ψ production in UPCs at the LHC for different J/ψ rapidities y. Right: The elliptic anisotropy coefficient as a function of rapidity extracted from the left plot.

For J/ψ production and its decay in to dileptons, the cross section takes the form [47,48]

$$\frac{\mathrm{d}\sigma^{\mathrm{J}/\psi\to l^+l^-}}{\mathrm{d}^2\mathbf{P}_\perp \mathrm{d}^2\mathbf{q}\mathrm{d}y_1\mathrm{d}y_2} = \frac{24\alpha_{\mathrm{em}}^2 e_q^2}{(Q^2-M_V^2)^2+M_V^2\Gamma^2}\frac{|\phi_{\mathrm{J}/\psi}(0)|^2}{\pi M_V}\left\{\left[1-\frac{2\mathbf{P}_\perp^2}{M_V^2}\right]C_0(x_1,x_2,|\mathbf{q}|) - \frac{2\mathbf{P}_\perp^2}{M_V^2}C_2(x_1,x_2,|\mathbf{q}|)\cos(2(\phi_{\mathbf{P}_\perp}-\phi_{\mathbf{q}}))\right\}, \tag{35}$$

where $|\phi_{\mathrm{J}/\psi}(0)|^2 = 0.0447$ GeV^3 [49] is the value of the modulus squared of the radial wave function of the J/ψ at the origin. The J/ψ EM decay width into two leptons is related to this via $\Gamma = 16\pi\alpha_{\mathrm{em}}^2 e_q^2 \frac{|\phi_{\mathrm{J}/\psi}(0)|^2}{M_V^2}$ [49], with $e_q = 2/3$ the charm quark charge in units of e.

Many results for azimuthal anisotropies computed in the CGC framework and compared to data from the STAR Collaboration have been published. [45,46,48,47] Here we concentrate on the rapidity dependence of the interference effect, presented in Fig. 3. The figure shows results for the azimuthal anisotropy in $\phi_{\mathbf{P}_\perp} - \phi_{\mathbf{q}}$ of the leptonic decay products in J/ψ production in $\sqrt{s_{NN}} = 5.02$ TeV Pb+Pb UPCs. Plotting counts as a funciton of $\Delta\Phi = \phi_{\mathbf{P}_\perp} - \phi_{\mathbf{q}}$ for different J/ψ rapidities y, one can see that with increasing rapidity the modulation becomes weaker, because the interference decreases as the two interfering processes become increasingly distinguishable. The right panel shows the extracted elliptic anisotropy coefficient $2\langle\cos(2\Delta\Phi)\rangle$ as a function of rapidity. We note that especially in the case of light decay products such as e^+ and e^-, corrections from soft photon radiation are expected. They were shown to predominantly affect results at $q_\perp > 0.12$ GeV/c [48].

6 Nuclear structure effects

As diffractive vector meson production is sensitive to the geometry of the target, and via incoherent production also its fluctuations, important information on nuclear deformation, clustering and subnucleonic structure can be extracted by measuring the t-differential cross sections in $\gamma + A$ collisions.

For example, the deformation of a nucleus can be incorporated via the Woods-Saxon parametrization

$$\rho(r,\theta) = \frac{\rho}{1+\exp[(r-R'(\theta))/a_{\mathrm{WS}}]}, \tag{36}$$

with $R'(\theta) = R_{\mathrm{WS}}[1+\beta_2 Y_2^0(\theta)+\beta_3 Y_3^0(\theta)+\beta_4 Y_4^0(\theta)]$, and ρ is the nuclear density at the center of the nucleus. Here R_{WS} is the radius parameter, a_{WS} is the skin diffuseness, and θ is the polar angle. The spherical harmonic functions $Y_l^m(\theta)$ and the parameters β_i account for possible deformations.

Some effects of deformation and subnucleonic structure are summarized in Fig. 4, where the incoherent cross section for J/ψ production at $Q^2 = 0$ in γ+U collisions is shown. Including subnucleon fluctuations, we show the result for the default quadrupole deformation $\beta_2 = 0.28$ along with results for a fictional uranium nucleus with $\beta_2 = 0$ and $\beta_2 = 0.5$. We also present the result for the default uranium target

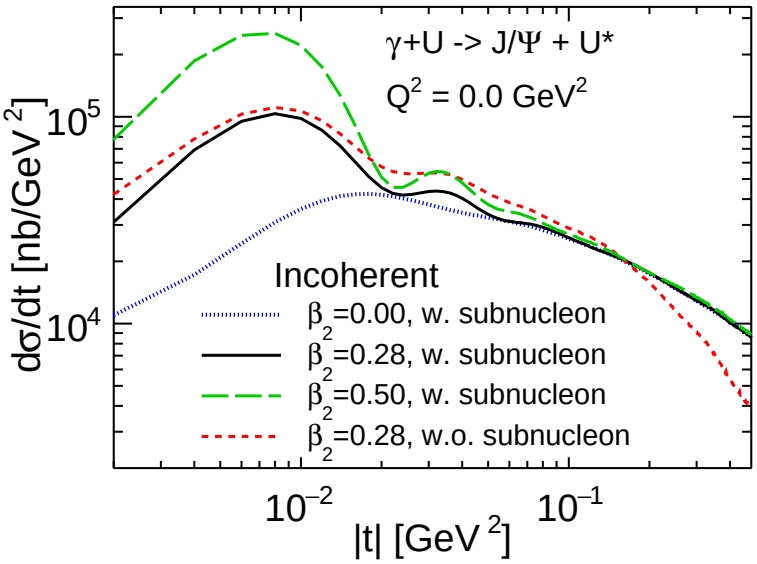

Figure 4 – Differential incoherent J/ψ photoproduction cross sections at $x = 1.7 \times 10^{-3}$ for different β_2 values and with or without subnucleonic fluctuations.

without subnucleonic fluctuations. The effects of varying β_2 is significant at $|t| < 2 \times 10^{-2}\,\mathrm{GeV}$, while subnucleon fluctuations affect the cross section at $|t| > 0.2\,\mathrm{GeV}$. It has been shown that varying β_i for increasing i affects the cross section at increasing $|t|$, showing that such measurement has sensitivity to nuclear structure over a large range of length scales. [50] This could be explored at a future Electron Ion Collider (EIC), but also in UPCs with a variety of nuclei.

Nuclear structure also affects the azimuthal modulations driven by interference that were discussed in the previous section. Here, it was shown that in particular the modification of B_{min} by nuclear radius and deformation affects the amplitude of the modulation [47].

7 Conclusions and Outlook

Vector meson production in ultraperipheral heavy ion collisions is an excellent tool to study effects of nuclear shadowing and saturation. It further provides important information on nuclear geometry, including radii, deformations, and substructure. We compared many different models that have been employed to describe experimental data on coherent vector meson production in UPCs, and laid out some similarities and differences. We delved into some details of the Color Glass Condensate calculations and highlighted the energy dependence of nuclear suppression from QCD evolution, azimuthal anisotropies from interference effects in UPCs, and the effects of nuclear structure.

All results presented here are leading order (LO) calculations. The field is moving towards higher precision with next-to-leading order (NLO) calculations, both in the perturbative QCD (pQCD) collinear factorization framework [51], and the dipole picture [52,53,54]. In the collinear factorization approach, an interesting observation at NLO was that whike the LO and NLO gluon amplitudes dominate over the NLO quark contribution, they cancel to a large degree, increasing the importance of the NLO quark contribution.

With increasingly precise calculations and more experimental data from RHIC and LHC, UPCs will play a significant role in our endeavor to pin down gluon saturation and explore the regime of non-linear QCD. This is not least due to the fact that in UPCs we can reach very low x values and study a variety of nuclear targets. Besides exclusive dijet and more inclusive observables, diffractive vector meson production is an excellent tool to address exciting physics questions already now, before the EIC will go online.

Acknowledgments

We thank Vadim Guzey for helpful comments on the manuscript. We thank Dagmar Bendová, Michal Broz, Jan Čepila, Vadim Guzey, Spencer Klein, Agnieszka Luszczak, and Wolfgang Schafer for providing

data and help with generating Figure 1. This material is based upon work supported by the U.S. Department of Energy, Office of Science, Office of Nuclear Physics, under DOE Contract No. DE-SC0012704 (B.P.S.) and Award No. DE-SC0021969 (C.S.), and within the framework of the Saturated Glue (SURGE) Topical Theory Collaboration. C.S. acknowledges a DOE Office of Science Early Career Award. H.M. is supported by the Research Council of Finland, the Centre of Excellence in Quark Matter, and projects 338263 and 346567, and under the European Union's Horizon 2020 research and innovation programme by the European Research Council (ERC, grant agreement No. ERC-2018-ADG-835105 YoctoLHC) and by the STRONG-2020 project (grant agreement No 824093). F.S. is supported by the U.S. DOE Office of Nuclear Physics under Grant No. DE-FG02-00ER41132. W.B.Z. is supported by DOE under Contract No. DE-AC02-05CH11231, by NSF under Grant No. OAC-2004571 within the X-SCAPE Collaboration, and within the framework of the SURGE Topical Theory Collaboration. The content of this article does not reflect the official opinion of the European Union and responsibility for the information and views expressed therein lies entirely with the authors. This research was done using resources provided by the Open Science Grid (OSG) [55,56], which is supported by the National Science Foundation award #2030508.

References

1. Astrid Morreale and Farid Salazar. Mining for Gluon Saturation at Colliders. *Universe*, 7(8):312, 2021.
2. Hannu I. Miettinen and Jon Pumplin. Diffraction Scattering and the Parton Structure of Hadrons. *Phys. Rev. D*, 18:1696, 1978.
3. Heikki Mäntysaari. Review of proton and nuclear shape fluctuations at high energy. *Rept. Prog. Phys.*, 83(8):082201, 2020.
4. Carlos A. Bertulani, Spencer R. Klein, and Joakim Nystrand. Physics of ultra-peripheral nuclear collisions. *Ann. Rev. Nucl. Part. Sci.*, 55:271–310, 2005.
5. Shreyasi Acharya et al. Coherent J/ψ photoproduction at forward rapidity in ultra-peripheral Pb-Pb collisions at $\sqrt{s_{\rm NN}} = 5.02$ TeV. *Phys. Lett. B*, 798:134926, 2019.
6. Shreyasi Acharya et al. Coherent J/ψ and ψ' photoproduction at midrapidity in ultra-peripheral Pb-Pb collisions at $\sqrt{s_{\rm NN}} = 5.02$ TeV. *Eur. Phys. J. C*, 81(8):712, 2021.
7. M. G. Ryskin. Diffractive J/ψ electroproduction in LLA QCD. *Z. Phys. C*, 57:89–92, 1993.
8. B. Z. Kopeliovich, L. I. Lapidus, and A. B. Zamolodchikov. Dynamics of Color in Hadron Diffraction on Nuclei. *JETP Lett.*, 33:595–597, 1981.
9. V. Guzey and M. Zhalov. Exclusive J/ψ production in ultraperipheral collisions at the LHC: constrains on the gluon distributions in the proton and nuclei. *JHEP*, 10:207, 2013.
10. L. Frankfurt, V. Guzey, M. Strikman, and M. Zhalov. Onset of perturbative color opacity at small x and upsilon coherent photoproduction off heavy nuclei at LHC. *JHEP*, 08:043, 2003.
11. K. J. Eskola, H. Paukkunen, and C. A. Salgado. EPS09: A New Generation of NLO and LO Nuclear Parton Distribution Functions. *JHEP*, 04:065, 2009.
12. T. H. Bauer, R. D. Spital, D. R. Yennie, and F. M. Pipkin. The Hadronic Properties of the Photon in High-Energy Interactions. *Rev. Mod. Phys.*, 50:261, 1978. [Erratum: Rev.Mod.Phys. 51, 407 (1979)].
13. Spencer Klein and Joakim Nystrand. Exclusive vector meson production in relativistic heavy ion collisions. *Phys. Rev. C*, 60:014903, 1999.
14. L. Frankfurt, V. Guzey, M. Strikman, and M. Zhalov. Nuclear shadowing in photoproduction of ρ mesons in ultraperipheral nucleus collisions at RHIC and the LHC. *Phys. Lett. B*, 752:51–58, 2016.
15. B. Z. Kopeliovich. Gribov inelastic shadowing in the dipole representation. *Int. J. Mod. Phys. A*, 31(28n29):1645021, 2016.
16. L. Frankfurt, V. Guzey, and M. Strikman. Leading Twist Nuclear Shadowing Phenomena in Hard Processes with Nuclei. *Phys. Rept.*, 512:255–393, 2012.
17. B. Z. Kopeliovich and B. G. Zakharov. Quantum effects and color transparency in charmonium photoproduction on nuclei. *Phys. Rev. D*, 44:3466–3472, 1991.
18. Shashank Anand and Tobias Toll. Exclusive diffractive vector meson production: A comparison between the dipole model and the leading twist shadowing approach. *Phys. Rev. C*, 100(2):024901, 2019.
19. G. Sampaio dos Santos and M. V. T. Machado. On theoretical uncertainty of color dipole phenomenology in the J/ψ and Υ photoproduction in pA and AA collisions at the CERN Large Hadron Collider. *J. Phys. G*, 42(10):105001, 2015.

20. E. Iancu, K. Itakura, and S. Munier. Saturation and BFKL dynamics in the HERA data at small x. *Phys. Lett. B*, 590:199–208, 2004.
21. Amir H. Rezaeian and Ivan Schmidt. Impact-parameter dependent Color Glass Condensate dipole model and new combined HERA data. *Phys. Rev. D*, 88:074016, 2013.
22. N. Armesto. A Simple model for nuclear structure functions at small x in the dipole picture. *Eur. Phys. J. C*, 26:35–43, 2002.
23. Agnieszka Łuszczak and Wolfgang Schäfer. Coherent photoproduction of J/ψ in nucleus-nucleus collisions in the color dipole approach. *Phys. Rev. C*, 99(4):044905, 2019.
24. T. Lappi and H. Mantysaari. J/ψ production in ultraperipheral Pb+Pb and p+Pb collisions at energies available at the CERN Large Hadron Collider. *Phys. Rev. C*, 87(3):032201, 2013.
25. H. Kowalski, L. Motyka, and G. Watt. Exclusive diffractive processes at HERA within the dipole picture. *Phys. Rev. D*, 74:074016, 2006.
26. Jan Cepila, Jesus Guillermo Contreras, and Michal Krelina. Coherent and incoherent J/ψ photonuclear production in an energy-dependent hot-spot model. *Phys. Rev. C*, 97(2):024901, 2018.
27. Krzysztof J. Golec-Biernat and M. Wusthoff. Saturation effects in deep inelastic scattering at low Q^2 and its implications on diffraction. *Phys. Rev. D*, 59:014017, 1998.
28. Heikki Mäntysaari and Björn Schenke. Probing subnucleon scale fluctuations in ultraperipheral heavy ion collisions. *Phys. Lett. B*, 772:832–838, 2017.
29. D. Bendova, J. Cepila, J. G. Contreras, and M. Matas. Photonuclear J/ψ production at the LHC: Proton-based versus nuclear dipole scattering amplitudes. *Phys. Lett. B*, 817:136306, 2021.
30. I. Balitsky. Operator expansion for high-energy scattering. *Nucl. Phys. B*, 463:99–160, 1996.
31. Yuri V. Kovchegov. Small x F_2 structure function of a nucleus including multiple pomeron exchanges. *Phys. Rev. D*, 60:034008, 1999.
32. J. Cepila, J. G. Contreras, and M. Matas. Predictions for nuclear structure functions from the impact-parameter dependent Balitsky-Kovchegov equation. *Phys. Rev. C*, 102(4):044318, 2020.
33. Bjoern Schenke, Prithwish Tribedy, and Raju Venugopalan. Fluctuating Glasma initial conditions and flow in heavy ion collisions. *Phys. Rev. Lett.*, 108:252301, 2012.
34. Bjoern Schenke, Prithwish Tribedy, and Raju Venugopalan. Event-by-event gluon multiplicity, energy density, and eccentricities in ultrarelativistic heavy-ion collisions. *Phys. Rev. C*, 86:034908, 2012.
35. Larry D. McLerran and Raju Venugopalan. Computing quark and gluon distribution functions for very large nuclei. *Phys. Rev. D*, 49:2233–2241, 1994.
36. Larry D. McLerran and Raju Venugopalan. Gluon distribution functions for very large nuclei at small transverse momentum. *Phys. Rev. D*, 49:3352–3355, 1994.
37. Alfred H. Mueller. A Simple derivation of the JIMWLK equation. *Phys. Lett. B*, 523:243–248, 2001.
38. Heikki Mäntysaari, Farid Salazar, and Björn Schenke. Energy dependent nuclear suppression from gluon saturation in exclusive vector meson production. 12 2023.
39. Heikki Mäntysaari, Farid Salazar, and Björn Schenke. Nuclear geometry at high energy from exclusive vector meson production. *Phys. Rev. D*, 106(7):074019, 2022.
40. Shreyasi Acharya et al. Energy dependence of coherent photonuclear production of J/ψ mesons in ultra-peripheral Pb-Pb collisions at $\sqrt{\mathrm{s_{NN}}} = 5.02$ TeV. *JHEP*, 10:119, 2023.
41. Armen Tumasyan et al. Probing Small Bjorken-x Nuclear Gluonic Structure via Coherent J/ψ Photoproduction in Ultraperipheral Pb-Pb Collisions at $\sqrt{s_{NN}} = 5.02$ TeV. *Phys. Rev. Lett.*, 131(26):262301, 2023.
42. Exclusive J/ψ, $\psi(2s)$, and e^+e^- pair production in Au+Au ultra-peripheral collisions at RHIC. 11 2023.
43. Observation of strong nuclear suppression in exclusive J/ψ photoproduction in Au+Au ultra-peripheral collisions at RHIC. 11 2023.
44. Mohamed Abdallah et al. Tomography of ultrarelativistic nuclei with polarized photon-gluon collisions. *Sci. Adv.*, 9(1):eabq3903, 2023.
45. Hongxi Xing, Cheng Zhang, Jian Zhou, and Ya-Jin Zhou. The cos 2ϕ azimuthal asymmetry in ρ^0 meson production in ultraperipheral heavy ion collisions. *JHEP*, 10:064, 2020.
46. Yoshikazu Hagiwara, Cheng Zhang, Jian Zhou, and Ya-Jin Zhou. Coulomb nuclear interference effect in dipion production in ultraperipheral heavy ion collisions. *Phys. Rev. D*, 103(7):074013, 2021.
47. Heikki Mäntysaari, Farid Salazar, Björn Schenke, Chun Shen, and Wenbin Zhao. Effects of nuclear structure and quantum interference on diffractive vector meson production in ultraperipheral

nuclear collisions. *Phys. Rev. C*, 109(2):024908, 2024.
48. James Daniel Brandenburg, Zhangbu Xu, Wangmei Zha, Cheng Zhang, Jian Zhou, and Yajin Zhou. Exploring gluon tomography with polarization dependent diffractive J/ψ production. *Phys. Rev. D*, 106(7):074008, 2022.
49. M. Tanabashi et al. Review of Particle Physics. *Phys. Rev. D*, 98(3):030001, 2018.
50. Heikki Mäntysaari, Björn Schenke, Chun Shen, and Wenbin Zhao. Multiscale Imaging of Nuclear Deformation at the Electron-Ion Collider. *Phys. Rev. Lett.*, 131(6):062301, 2023.
51. Kari J. Eskola, Christopher A. Flett, Vadim Guzey, Topi Löytäinen, and Hannu Paukkunen. Exclusive J/ψ photoproduction in ultraperipheral Pb+Pb collisions at the CERN Large Hadron Collider calculated at next-to-leading order perturbative QCD. *Phys. Rev. C*, 106(3):035202, 2022.
52. Miguel Ángel Escobedo and Tuomas Lappi. Dipole picture and the nonrelativistic expansion. *Phys. Rev. D*, 101(3):034030, 2020.
53. Heikki Mäntysaari and Jani Penttala. Exclusive heavy vector meson production at next-to-leading order in the dipole picture. *Phys. Lett. B*, 823:136723, 2021.
54. Heikki Mäntysaari and Jani Penttala. Complete calculation of exclusive heavy vector meson production at next-to-leading order in the dipole picture. *JHEP*, 08:247, 2022.
55. Ruth Pordes et al. The Open Science Grid. *J. Phys. Conf. Ser.*, 78:012057, 2007.
56. Igor Sfiligoi, Daniel C. Bradley, Burt Holzman, Parag Mhashilkar, Sanjay Padhi, and Frank Wurthwrin. The pilot way to Grid resources using glideinWMS. *WRI World Congress*, 2:428–432, 2009.

Vector meson production using the Balitsky-Kovchegov equation including the dipole orientation

J. Cepila, J. G. Contreras, M. Vaculciak
Faculty of Nuclear Sciences and Physical Engineering, Czech Technical University in Prague. Brehova 7, Prague, 112519 Czech Republic

In this proceedings a solution of the target-rapidity Balitsky-Kovchegov (BK) equation is presented considering the complete impact-parameter dependence, including the orientation of the dipole with respect to the impact-parameter vector. The target-rapidity formulation of the BK equation introduces non-locality in rapidity. Three different prescriptions are considered to take into account the rapidities that precede the initial condition. The solutions are used to compute the structure functions of the proton and the diffractive photo- and electro-production of J/ψ off protons. The predictions agree well with HERA data, confirming that the target-rapidity Balitsky-Kovchegov equation with the full impact parameter dependence is a viable tool to study the small Bjorken-x limit of perturbative QCD at current facilities like RHIC and LHC as well as in future colliders like the EIC.

DOI: https://doi.org/10.17161/t7r4bv27
Keywords: Balitsky-Kovchegov equation, parton saturation, vector meson production, structure functions

1 Introduction

The high-energy limit of perturbative quantum chromodynamics (pQCD) has been intensively studied in the past years. This was possible due to precise measurements from HERA experiments [1] and LHC experiments [2]. This limit is equivalent to the low Bjorken-x behavior of the gluon density in the target. Experimental data on the structure functions from DIS process [3] suggest that the gluon distribution rises rapidly for gluons carrying a small Bjorken-x. The growth of the gluon distribution is driven by splitting processes which increase the number of gluons in the proton. This mechanism was described successfully by the BFKL evolution equation [4,5]. However, when the gluon occupancy becomes large enough, recombination processes activate [6,7] until a dynamical balance between both processes, called gluon saturation, is reached.

One of the tools to describe the evolution of the proton structure at high energies within pQCD including gluon saturation is the Balitsky-Kovchegov (BK) equation [8,9,10], which describes the evolution in rapidity of the interaction between a color dipole and a hadronic target. It can be interpreted as a dressing of the original color dipole under the evolution towards higher energies by emitting additional gluons. In the limit of large number of colors the emitted gluon can be interpreted as a new dipole which effectively splits the parent dipole into two daughter dipoles. However, the BK equation also introduces a non-linear term that accounts for the possibility that two dipoles recombine.

The original BK equation used the projectile rapidity (Y) as the evolution variable. Recently, it was proposed to use the target rapidity ($\eta = \ln(x_0/x)$) as the evolution variable [11] in order to improve the stability of the equation by ensuring the correct time ordering of gluon emissions. Here, x_0 is the Bjorken-x at which the BK evolution starts. However, this change of evolution variable also introduced non-local terms in the equation.

The solution of the BK equation is the dipole scattering amplitude $N(\vec{r}, \vec{b}, \eta)$ which depends on two two-dimensional vectors defined in the transverse plane of the dipole. They can be decomposed into four scalar variables: $r = |\vec{r}|$ corresponding to the dipole size, $b = |\vec{b}|$ corresponding to the distance between the dipole and the target, θ corresponding to the angle between $\vec{r}$ and $\vec{b}$ and ϕ corresponding to the angle between $\vec{b}$ and a fixed axis. Most of the solutions of the BK equation to date assumed a large and homogeneous target and, hence, only a dependence on r was considered.

Later on, the inclusion of the impact-parameter dependence in the solutions of the BK equation evolved with the projectile rapidity has been studied in [12], where large Coulomb-like tails at large b were reported. However, it was shown that with some ad-hoc modifications to account for confinement, HERA data could be described [13,14,15].

Soon thereafter, the kernel of the BK equation improved with resummation of some of the next-to-leading order diagrams has been published [16,17,18] and, afterwards, it has been demonstrated, that this

version of the BK equation can be solved including the r and b dependence without the appearance of Coulomb tails, at least for energies relevant for currently available data [19,20,21,22].

The suppression of Coulomb tails, which allowed for phenomenological applications of the impact-parameter dependent BK equation, was mainly due to two factors: the collinearly improved kernel and choosing an appropriate initial condition. However, the kernel of the BK equation formulated in target rapidity is missing the part that supressed the Coulomb tails when evolving with the projectile rapidity. This raises the question if the new version of the BK equation is usable for phenomenological applications.

Another natural step in the study of the solution of the BK equation is to include a non-trivial dependence on θ and, hence, allow for inhomogeneous targets. This effect has been studied partially in different frameworks, e.g. Refs. [23,24,25,26,27].

In these proceedings, a numerical solutions to the target-rapidity Balitsky-Kovchegov equation including the impact-parameter dependence as well as the dependence on the angle between the dipole size and the impact-parameter vectors is presented. The major observation is that the treatment of the non-local term for rapidities earlier than the point where the BK evolution starts influences the behavior of the Coulomb tails and offers a way to tame them.

2 Balitsky-Kovchegov equation in target rapidity

The BK equation in target rapidity has a form [11]

$$\frac{\mathrm{d}N(\vec{r},\vec{b},\eta)}{\mathrm{d}\eta} = \int \mathrm{d}\vec{r}_1 K(r,r_1,r_2)\Big[N(\vec{r}_1,\vec{b}_1,\eta_1)+N(\vec{r}_2,\vec{b}_2,\eta_2)-N(\vec{r},\vec{b},\eta)-N(\vec{r}_1,\vec{b}_1,\eta_1)N(\vec{r}_2,\vec{b}_2,\eta_2)\Big]. \quad (1)$$

The first three terms with N on the right-hand-side of the equation take into account the splitting of a dipole at $(\vec{r},\vec{b})$ into two dipoles at $(\vec{r}_1,\vec{b}_1)$ and $(\vec{r}_2,\vec{b}_2)$, while the last term represents the recombination of two dipoles. The vectors introduced above are linked through the kinematic formulas

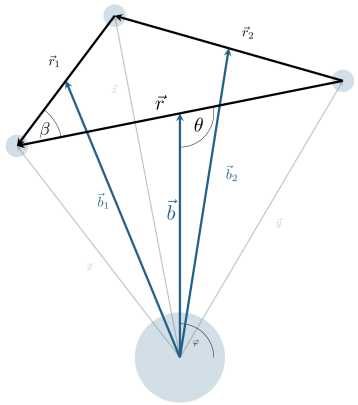

Figure 1 – Kinematics of the parent and daughter dipoles during the BK equation evolution considering non-trivial dependence of the solution on the angle θ.

$$\vec{r}_2 = \vec{r} - \vec{r}_1 \qquad \vec{b}_1 = \vec{b}_{q1} - \frac{\vec{r}_1}{2} \qquad \vec{b}_{q1} = \vec{b} + \frac{\vec{r}}{2} \qquad \vec{b}_2 = \vec{b}_{q2} - \frac{\vec{r}_2}{2} \qquad \vec{b}_{q2} = \vec{b} - \frac{\vec{r}}{2}. \quad (2)$$

The rapidities η_1 and η_2 introduce the non-local variables defined as

$$\eta_j = \eta - \max\{0, \ln(r^2/r_j^2)\}. \quad (3)$$

The collinearly improved kernel in the target rapidity is given by

$$K(\vec{r},\vec{r}_1,\vec{r}_2) = \frac{\bar{\alpha}_s}{2\pi}\frac{r^2}{r_1^2 r_2^2}\left[\frac{r^2}{\min\{r_1^2,r_2^2\}}\right]^{\pm\bar{\alpha}_s A_1}, \quad (4)$$

where the constant $A_1 = \frac{11}{12}$ and $\bar{\alpha}_s = \frac{N_C}{\pi}\alpha_s$ with the number of colors $N_C = 3$ and $\alpha_s = \alpha_s(\min\{r, r_1, r_2\})$ being the running strong coupling constant

$$\alpha_{s,n_f}(r^2) = \frac{4\pi}{\beta_{n_f}\ln\left(\frac{4C^2}{r^2\Lambda^2_{n_f}}\right)}, \quad (5)$$

where n_f corresponds to the number of flavors, $\beta_{n_f} = (11N_C - 2n_f)/3$, C^2 is an infrared regulator adjusted to describe data and $\Lambda^2_{n_f}$ is a evaluated in the variable-number-of-flavors scheme [28]. In this work, the coupling is frozen at $\alpha_s^{\rm sat} = 1$ as in [17].
The initial condition for the start of the evolution is given by

$$N(\vec{r}, \vec{b}, \eta = 0) = 1 - \exp\left(-\frac{1}{4}(Q_{s0}^2\, r^2)^\gamma\, T(b, r)\, \{1 + c\cos(2\theta)\}\right), \tag{6}$$

with

$$T(r, b) = \exp\left(-\frac{b^2 + (r/2)^2}{2B}\right). \tag{7}$$

The parameter Q_{s0}^2 is related to the onset of the saturation, $T(r, b)$ corresponds to the transverse profile of the target, the parameter B is related to the size of the target and γ is the so-called anomalous dimension (see Ref. [29]). The parameter c controls the amount of the expected asymmetry on the θ dependence.

Three different variants how to deal with shifts η_1, η_2 being negative, see Eq. (3), were considered:

A: No extrapolation bellow $\eta = 0$, namely, $N(\vec{r}, \vec{b}, \eta < 0) = 0$.

B: Smooth suppression in the range $\eta = \ln(x_0/1)$ and $\eta = 0$ according to the GBW model [30]

$$N(\vec{r}, \vec{b}, \eta < 0) = 1 - \exp\left(-\frac{1}{4}\left[(x_0/x)^\lambda\, Q_{s0}^2\, r^2\right]^\gamma\, T(b, r)\, \{1 + c\cos(2\theta)\}\right), \tag{8}$$

and then $N(\vec{r}, \vec{b}, \eta < \ln(x_0/1)) = 0$.

C: Flat extrapolation to initial conditions: $N(\vec{r}, \vec{b}, \eta < 0) = N(\vec{r}, \vec{b}, 0)$.

The BK equation is solved numerically in a logarithmic grid in r and b and a linear grid in θ using the Runge–Kutta method with the integrals performed with Simpson's method. The step in rapidity is 0.1. The parameter values that we have used for the solution of the BK equation are $x_0 = 0.01$, $Q_{s0}^2 = 0.496$ GeV^2, $B = 3.8$ GeV^{-2}, $\gamma = 1.25$, $\lambda = 0.288$, $c = 1$ and $C = 30$. The masses of the light quarks were taken to be 0.1 GeV/c^2 and the mass of the charm quark was taken to be 1.3 GeV/c^2.

3 Results

The solution of the collinearly improved BK equation in target rapidity dependent explicitly on the three kinematic variables r, b, θ has been successfully found [31]. It shows that only one of the approaches to non-locality strongly suppresses Coulomb tails, see the left plot of Fig. 2. It means that only the solution with option A is suitable for phenomenological predictions.

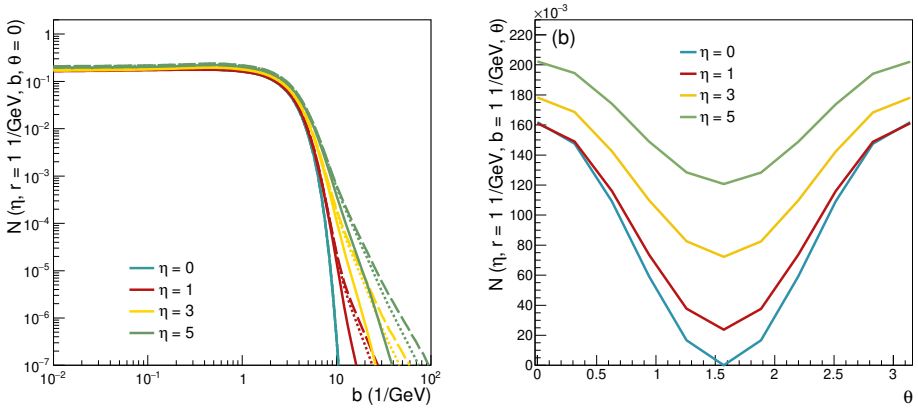

Figure 2 – Left: Dependence of the dipole amplitude on b for fixed dipole of size $r = 1$ GeV^{-1} and fixed angle $\theta = 0$ for three different approaches to non-locality. Solid line corresponds to the approach A, dotted line to the approach B and dashed line to the approach C. Right: Dependence of the dipole amplitude on θ for a dipole of size $r = 1$ GeV^{-1} at impact parameter $b = 1$ GeV^{-1}. Solutions are shown at different rapidities for the approach A to non-locality.

The dependence on θ, the angle between the dipole-size and the impact-parameter vectors, of the solutions of the BK equation is shown in the right plot of Fig. 2 for different rapidities. The range of rapidities roughly corresponds to the region that can be covered by existing experimental results or by those expected in the near and medium term. The figure presents solutions obtained with approach A to non-locality.

The r dependence of solutions of the BK equations are shown in the left plot of Fig. 3. The dipole amplitudes are shown at different rapidities at one impact parameter for approach A. At large values of r a wave front develops, in addition to the traditional wave front towards small values of r. However, the large-r region is usually suppressed by the wave function of particular process and so the development of tails at large r does not spoil the usability of the solution for phenomenology. Moreover, the emergence of the tails is a direct consequence of having a target that is finite in the impact-parameter plane [31]. The

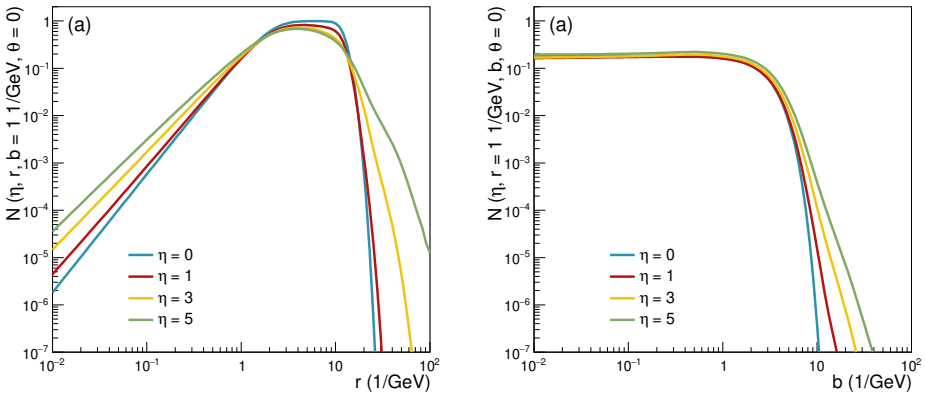

Figure 3 – Dependence of the dipole amplitude (left) on dipole size r at an impact parameter $b = 1$ GeV^{-1} and (right) on impact parameter b for a dipole size $r = 1$ GeV^{-1}. The angle between the dipole-size and the impact-parameter vectors is $\theta = 0$. Solutions are shown at different rapidities for the approach A.

dependence on impact parameter b of the solutions of the BK equation at fixed $\theta = 0$ is shown in the right plot of Fig. 3 at different rapidities for the approach A. The figure shows a flat behavior at small and medium impact parameters, while the dipole amplitude starts to decrease rapidly at large impact parameters because the initial condition represents a finite target. The evolution increases the range in impact parameter where the dipole amplitude is sizable, but it also changes the shape of the amplitude at large impact parameters. However, the speed with which the dipole amplitude rises towards large b is not so steep that it would result in unphysical predictions of e.g. structure functions of DIS towards low Bjorken-x [31].

The new observation brought up by the non-locality present in the BK equation evolved in target rapidity is that the shape and size of the large-r and of the large-b wavefront depend on the treatment of the region of rapidities earlier than the initial rapidity of the evolution.

4 Inclusive and exclusive observables

The use of the solution to the collinearly improved BK equation in target rapidity is shown using the inclusive DIS process and exclusive vector meson production. The structure function F_2 calculated using the dipole amplitude N can be written as [31]

$$F_2(x,Q^2) = \frac{Q^2}{4\pi^2\alpha_{\rm em}} \sum_f \left[\sigma_{L,f}^{\gamma^* p}\left(Q^2, x_f(x,Q^2)\right) + \sigma_{T,f}^{\gamma^* p}\left(Q^2, x_f(x,Q^2)\right)\right], \tag{9}$$

where f denotes the flavour of a quark, Q^2 is the virtuality of the exchanged photon, $\alpha_{\rm em}$ is the electromagnetic coupling constant,

$$x_f = \frac{x_0 e^{-\eta}}{1 + 4\frac{m_f^2}{Q^2}} \tag{10}$$

and

$$\sigma_{L,T,f}^{\gamma^* p}(Q^2, x_f) = 4\pi \int {\rm d}r r \int {\rm d}z |\psi_{L,T,f}(r,z,Q^2)|^2 \int {\rm d}b b \int_0^\pi {\rm d}\theta 2N(r,b,\theta,\eta(x_f)), \tag{11}$$

with the longitudinal (L) and transverse (T) light-cone wave functions

$$\left|\psi_{L,f}(r,z,Q^2)\right|^2 = \frac{N_C\alpha_{em}}{2\pi^2}e_f^2 4Q^2z^2(1-z)^2K_0^2\left(r\epsilon\right) \tag{12}$$

and

$$\left|\psi_{T,f}(r,z,Q^2)\right|^2 = \frac{N_C\alpha_{em}}{2\pi^2}e_f^2\left[(z^2+(1-z)^2)\epsilon^2K_1^2\left(r\epsilon\right)+m_f^2K_0^2\left(r\epsilon\right)\right]. \tag{13}$$

where $\epsilon = \sqrt{z(1-z)Q^2+m_f^2}$, and $K_{0,1}$ are Bessel functions.

Diffractive exclusive vector meson production calculated using the dipole amplitude N is given by the sum of the transverse and longitudinal contributions:

$$\frac{\mathrm{d}\sigma_{T,L}}{\mathrm{d}|t|}(t,Q^2,W) = \frac{1}{16\pi}(1+\beta_{T,L}^2)R_{L,T}^2\left|\mathcal{A}_{T,L}\right|^2, \tag{14}$$

where

$$\mathcal{A}(t,Q^2,W) = i2\pi\int \mathrm{d}r r\int_0^1\frac{\mathrm{d}z}{4\pi}\left(\Psi_V^\dagger\Psi\right)_{T,L}\int \mathrm{d}^2\vec{b}\,e^{-i[\vec{b}-(\frac{1}{2}-z)\vec{r}]\vec{\Delta}}2N\left(r,b,\theta,\eta\right)) \tag{15}$$

with $x = (Q^2+M^2)/(W^2+Q^2)$, M the mass of the vector meson, W the center-of-mass energy of the photon–proton system, $\vec{\Delta}^2 = -t$, and the wave function of the vector mesons given by the boosted Gaussian model with the values of all parameters as in Ref. [32]. The corrections to the real part of the amplitude and to the skewedness effect are

$$\beta_{T,L} = \tan(\pi\lambda_{T,L}/2), \qquad R_{T,L} = \frac{2^{2\lambda_{T,L}+3}}{\sqrt{\pi}}\frac{\Gamma(\lambda_{T,L}+5/2)}{\Gamma(\lambda_{T,L}+4)}, \qquad \lambda_{T,L} = \frac{\partial\ln\mathcal{A}_{T,L}(t=0)}{\partial\ln(1/x)}. \tag{16}$$

5 Predictions of observables

We have compared in [31] the solutions to the collinearly improved BK equation evolved in target rapidity to HERA measurements of structure functions obtained in deep-inelastic scattering [33] and the t-distribution of the diffractive exclusive J/ψ vector meson photo- and electro-production [34]. The comparison of the

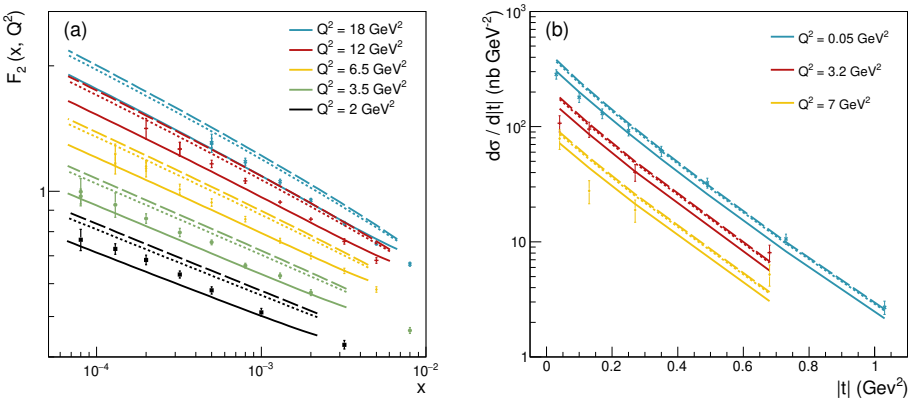

Figure 4 – Predictions of inclusive and exclusive observables using the target rapidity BK equations solved with the inclusion of angular correlations between the dipole orientation and the impact parameter. The three approaches to deal with the non-localities for early rapidities are shown with solid (A), dotted (B) and dashed (C) lines. Left plot shows the F_2 structure function as measured at HERA and right plot shows the cross section for diffractive exclusive J/ψ vector meson photo- and electro-production.

predictions of the three approaches to deal with the non-locality of the BK equation in target rapidity for early rapidities with data from HERA is shown in Fig. 4. In all cases shown in the figure, approaches B and C predict a larger cross section than approach A. The F_2 data is reasonably well described by approach A. The emergence of Coulomb tails for approaches B and C is not that fast to spoil the usability of the BK equation solution for the description of current data for F_2. However, at lower Bjorken-x the

use of the approach B and C would be more and more problematic. The same can be said about the comparison to the vector meson data. This demonstrates that the BK equation in target rapidity with the A approach can be used for phenomenological applications without adding ad-hoc prescriptions to deal with the influence of Coulomb tails.

6 Summary and outlook

In these proceedings a new solutions of the BK equation evolved in the target rapidity including the dependence on the size of the dipole r, the magnitude of the impact-parameter b and the angle between those two vectors θ is presented. A new form of initial conditions have been proposed that are inspired by the GBW model in r-dependence and respects the b- and θ-dependence from recent models. The kernel of the target rapidity BK equation lacks the Coulomb-tails suppressing term. However, we have shown that the presence of non-local terms in the evolution together with the particular choice of the approach to the contributions from terms evaluated at rapidities before the evolution starts effectively suppresses the Coulomb tails. Also, the solutions have been used to obtain predictions for physical observables for inclusive process, namely the F_2 structure function of protons, and for exclusive process, namely the cross section for diffractive exclusive photo- and electro-production of J/ψ vector mesons off protons. Both sets of predictions are compared to existing data from HERA and a reasonable agreement is found without any ad-hoc corrections. This opens the possibility to use solutions of this equation to explore other observables that are to be measured at current facilities, like RHIC and the LHC, or those that will enter operation in the near future, like the EIC.

Acknowledgments

This work was partially funded by the Czech Science Foundation (GAČR), project No. 22-27262S.

References

1. Paul R. Newman and Matthew Wing. The hadronic final state at hera. *Reviews of Modern Physics*, 86(3):1037–1092, August 2014.
2. K Akiba et al. Lhc forward physics. *Journal of Physics G: Nuclear and Particle Physics*, 43(11):110201, October 2016.
3. H. Abramowicz et al. Combination of measurements of inclusive deep inelastic $e^{\pm}p$ scattering cross sections and QCD analysis of HERA data. *Eur. Phys. J.*, C75(12):580, 2015.
4. Eh A Kuraev, LN Lipatov, and Victor S Fadin. Pomeranchuk singularity in nonabelian gauge theories. *Sov. Phys.-JETP (Engl. Transl.);(United States)*, 45(2), 1977.
5. II Balitsky and LN Lipatov. The pomeranchuk singularity, process, theory. *Soviet Journal of Nuclear Physics*, 28:822–822, 1978.
6. L. V. Gribov, E. M. Levin, and M. G. Ryskin. Semihard Processes in QCD. *Phys. Rept.*, 100:1–150, 1983.
7. Alfred H. Mueller and Jian-wei Qiu. Gluon Recombination and Shadowing at Small Values of x. *Nucl. Phys. B*, 268:427–452, 1986.
8. I. Balitsky. Operator expansion for high-energy scattering. *Nucl. Phys. B*, 463:99–160, 1996.
9. Yuri V. Kovchegov. Small x F(2) structure function of a nucleus including multiple pomeron exchanges. *Phys. Rev. D*, 60:034008, 1999.
10. Yuri V. Kovchegov. Unitarization of the BFKL pomeron on a nucleus. *Phys. Rev. D*, 61:074018, 2000.
11. B. Ducloué, E. Iancu, A. H. Mueller, G. Soyez, and D. N. Triantafyllopoulos. Non-linear evolution in QCD at high-energy beyond leading order. *JHEP*, 04:081, 2019.
12. Krzysztof J. Golec-Biernat and A. M. Stasto. On solutions of the Balitsky-Kovchegov equation with impact parameter. *Nucl. Phys. B*, 668:345–363, 2003.
13. Jeffrey Berger and Anna Stasto. Numerical solution of the nonlinear evolution equation at small x with impact parameter and beyond the LL approximation. *Phys. Rev. D*, 83:034015, 2011.
14. Jeffrey Berger and Anna M. Stasto. Small x nonlinear evolution with impact parameter and the structure function data. *Phys. Rev. D*, 84:094022, 2011.
15. Jeffrey Berger and Anna M. Stasto. Exclusive vector meson production and small-x evolution. *JHEP*, 1301:001, 2013.

16. Guillaume Beuf. Improving the kinematics for low-x QCD evolution equations in coordinate space. *Phys. Rev. D*, 89(7):074039, 2014.
17. E. Iancu, J. D. Madrigal, A. H. Mueller, G. Soyez, and D. N. Triantafyllopoulos. Resumming double logarithms in the QCD evolution of color dipoles. *Phys. Lett. B*, 744:293–302, 2015.
18. E. Iancu, J. D. Madrigal, A. H. Mueller, G. Soyez, and D. N. Triantafyllopoulos. Collinearly-improved BK evolution meets the HERA data. *Phys. Lett. B*, 750:643–652, 2015.
19. J. Cepila, J. G. Contreras, and M. Matas. Collinearly improved kernel suppresses Coulomb tails in the impact-parameter dependent Balitsky-Kovchegov evolution. *Phys. Rev. D*, 99(5):051502, 2019.
20. D. Bendova, J. Cepila, J. G. Contreras, and M. Matas. Solution to the Balitsky-Kovchegov equation with the collinearly improved kernel including impact-parameter dependence. *Phys. Rev. D*, 100(5):054015, 2019.
21. J. Cepila, J. G. Contreras, and M. Matas. Predictions for nuclear structure functions from the impact-parameter dependent Balitsky-Kovchegov equation. *Phys. Rev. C*, 102(4):044318, 2020.
22. D. Bendova, J. Cepila, J. G. Contreras, and M. Matas. Photonuclear J/ψ production at the LHC: Proton-based versus nuclear dipole scattering amplitudes. *Phys. Lett. B*, 817:136306, 2021.
23. Yoshitaka Hatta, Bo-Wen Xiao, and Feng Yuan. Gluon Tomography from Deeply Virtual Compton Scattering at Small-x. *Phys. Rev. D*, 95(11):114026, 2017.
24. Edmond Iancu and Amir H. Rezaeian. Elliptic flow from color-dipole orientation in pp and pA collisions. *Phys. Rev. D*, 95(9):094003, 2017.
25. Heikki Mäntysaari, Kaushik Roy, Farid Salazar, and Björn Schenke. Gluon imaging using azimuthal correlations in diffractive scattering at the Electron-Ion Collider. *Phys. Rev. D*, 103(9):094026, 2021.
26. Adrian Dumitru, Heikki Mäntysaari, and Risto Paatelainen. Color charge correlations in the proton at NLO: Beyond geometry based intuition. *Phys. Lett. B*, 820:136560, 2021.
27. B. Z. Kopeliovich, M. Krelina, and J. Nemchik. Electroproduction of heavy quarkonia: significance of dipole orientation. *Phys. Rev. D*, 103(9):094027, 2021.
28. Javier L. Albacete, Nestor Armesto, Jose Guilherme Milhano, Paloma Quiroga-Arias, and Carlos A. Salgado. AAMQS: A non-linear QCD analysis of new HERA data at small-x including heavy quarks. *Eur. Phys. J. C*, 71:1705, 2011.
29. J. L. Albacete, N. Armesto, J. G. Milhano, C. A. Salgado, and U. A. Wiedemann. Numerical analysis of the Balitsky-Kovchegov equation with running coupling: Dependence of the saturation scale on nuclear size and rapidity. *Phys. Rev. D*, 71:014003, 2005.
30. Krzysztof J. Golec-Biernat and M. Wusthoff. Saturation effects in deep inelastic scattering at low Q**2 and its implications on diffraction. *Phys. Rev. D*, 59:014017, 1998.
31. J. Cepila, J. G. Contreras, and M. Vaculciak. Solutions to the Balitsky-Kovchegov equation including the dipole orientation. *Phys. Lett. B*, 848:138360, 2024.
32. D. Bendova, J. Cepila, and J. G. Contreras. Dissociative production of vector mesons at electron-ion colliders. *Phys. Rev. D*, 99(3):034025, 2019.
33. F. D. Aaron et al. Combined Measurement and QCD Analysis of the Inclusive e+- p Scattering Cross Sections at HERA. *JHEP*, 01:109, 2010.
34. A. Aktas et al. Elastic J/psi production at HERA. *Eur. Phys. J. C*, 46:585–603, 2006.

Recent results on ultra-peripheral collisions with the ALICE experiment

David Grund (for the ALICE Collaboration)
Faculty of Nuclear Sciences and Physical Engineering, Czech Technical University in Prague
Prague, Czech Republic

Recent measurements of J/ψ photoproduction based on data from ultra-peripheral Pb–Pb and p–Pb collisions recorded by the ALICE experiment during Run 2 of the LHC are presented. Photoproduction as a photon-induced process is sensitive to the structure of hadrons and the results are of great importance for a better understanding of how gluon saturation and nuclear shadowing work in high-energy quantum chromodynamics. The energy evolution of coherent J/ψ photoproduction has been measured, indicating a strong suppression of nuclear gluon densities at high energies. The energy dependence has also been measured for exclusive and dissociative J/ψ production off the proton. The average distribution of the nuclear gluon matter in transverse plane, and fluctuations thereof, have been studied for the first time using the measurements of the dependence of coherent and incoherent J/ψ photoproduction on the transferred momentum $|t|$. Lastly, the data from coherent photoproduction of J/ψ in Pb–Pb ultra-peripheral collisions have been found to be compatible with a transverse polarization.

DOI: https://doi.org/10.17161/4s080j68
Keywords: ALICE experiment, heavy-ion collisions, ultra-peripheral collisions, J/ψ photoproduction

1 Introduction

When the hadronic structure is studied using a high-energy probe, corresponding to low values of Bjorken-x of the colliding parton, the gluon density becomes so large that the regime of gluon saturation [1]—a dynamic equilibrium between gluon splitting and recombination—is predicted to be reached. Additionally, when nuclei at high energies are considered, the parton distribution functions of constituent nucleons are modified with respect to free nucleons by the presence of the nuclear environment; this phenomenon is referred to as nuclear shadowing [2]. Ultra-peripheral collisions (UPCs) allow to shed light on these high-energy quantum chromodynamics (QCD) effects using photon-induced processes with large cross sections that are sensitive to the gluon distribution in the target proton or nucleus.

In UPCs, the nuclei collide at an impact parameter b larger than the sum of their radii, $b > R_1 + R_2$, so that short-range hadronic interactions are suppressed. The interactions are thus induced by quasireal photons (with low virtuality) emitted by one of the nuclei. The intensity of the photon flux scales with the nuclear charge squared, Z^2, while the photon energy increases with the beam energy (the Lorentz boost). Lead nuclei collided at the LHC thus deliver very strong electromagnetic fields.

Diffractive production of vector mesons is one of the prominent UPC processes. The J/ψ is an ideal candidate since it can be reconstructed with high precision using detectors of the ALICE experiment and its mass allows for application of perturbative QCD. If one focuses on the decay of J/ψ into a pair of electrons or muons, such photoproduction events have a very clear experimental signature – only two lepton tracks are present in an otherwise empty detector, except for potential products of electromagnetically dissociated nuclei in very forward rapidity regions.

The value of the momentum transferred in the interaction, the Mandelstam variable $|t|$, provides further insight into aspects of the photon-hadron interaction and can be used to classify photoproduction events. It approximately corresponds to the square of the transverse momentum of the vector meson, $|t| \approx p_{\mathrm{T}}^2$; the relation is not exact due to the non-zero photon momentum in the laboratory frame. In studies involving high-$|t|$ events, the photon contribution can usually be neglected. For Pb–Pb UPCs, the process is called either coherent if the photon couples coherently to all nucleons, which leads to $|t| \lesssim 0.01$ GeV^2, or incoherent if the photon couples to a single nucleon. In the latter case, $|t|$ is governed by the size of the nucleon and its characteristic value corresponds to 0.1 GeV^2. The incoherent interaction leaves the target nucleus excited and is, in most cases, followed by a breakup. If the photon scatters from smaller—subnucleon-sized—objects, which leads to nucleon dissociation, $|t|$ can easily reach the order of 1 GeV^2. In asymmetric p–Pb UPCs, the Pb nucleus is in most cases the photon emitter considering the Z^2 factor in the photon flux. If the photon interacts with the proton elastically, the average value of $|t|$ amounts to 0.1 GeV^2; values of the order of 1 GeV^2 are reached in the case of proton dissociation.

2 Ultra-peripheral collisions at ALICE

The ALICE experiment [3] at the LHC is well equipped to measure UPC processes. The detectors crucial for UPC studies using data from Run 2 (2015–2018) of the LHC are briefly described here. The central-barrel detectors, placed inside a large solenoid magnet creating a magnetic field of 0.5 T, cover together the central pseudorapidity region of $|\eta| < 0.9$. The central-barrel detectors detailed here have a cylindrical geometry and cover the full azimuth. The Silicon Pixel Detector (SPD) constitutes the two innermost layers of the Inner Tracking System (ITS) and is used for tracking, vertex reconstruction, and provides trigger inputs. Its inmost layer is located at a radius of only 3.9 cm from the beam axis. Reconstruction of tracks further away from the IP and their identification by measuring ionization energy losses is provided by the Time Projection Chamber (TPC), a large cylindrical gas chamber equipped with multi-wire proportional chambers mounted on end caps. The Time-Of-Flight (TOF) detector consisting of multi-gap resistive-plate chambers is placed outside the TPC. TOF is a fast detector and provides topological trigger signals in UPC measurements based on the number of azimuthal sectors registering a signal.

ALICE also uses a single-arm spectrometer detecting forward muons in the $-4 < \eta < -2.5$ pseudorapidity region. It is composed of an absorber with a thickness of 10 hadronic interaction lengths, followed by five tracking stations, each consisting of two planes of cathode-pad chambers. The middle station is housed in a dipole magnet providing an integrated magnetic field of 3 T·m. The muon trigger system is located at the rear of the spectrometer, separated by another muon filter in the form of an iron wall with a thickness of 7.2 hadronic interaction lengths.

The trigger configurations used for UPCs rely heavily on inputs from two forward systems of scintillation counters, V0 and ALICE Diffractive (AD). These detectors have two components (A and C) located near the beam pipe, one on each side of the IP, and operate as a veto. No activity above a certain threshold is thus allowed at the time of the collision to ensure that UPC processes are not contaminated by hadronic interactions or inelastic photonuclear processes. Additionally, the Zero Degree Calorimeters (ZDCs) installed 113 m away from the IP along the beam in both directions are used to detect protons and neutrons in very forward regions emitted from nuclear breakups.

3 Energy dependence of J/ψ photoproduction

Photoproduction of J/ψ in Pb–Pb UPCs is sensitive to the nuclear gluon density at Bjorken-x of $x = M^2_{\mathrm{J}/\psi}/W^2_{\gamma\mathrm{Pb,n}}$, where $M_{\mathrm{J}/\psi}$ is the J/ψ mass. The photon-nucleus center-of-mass energy per nucleon pair, $W_{\gamma\mathrm{Pb,n}}$, is related to the J/ψ rapidity y through

$$W^2_{\gamma\mathrm{Pb,n}} = \sqrt{s_{\mathrm{NN}}} M_{\mathrm{J}/\psi} e^{-y} \,, \tag{1}$$

where $\sqrt{s_{\mathrm{NN}}}$ is the center-of-mass energy of the collision system per nucleon pair. The rapidity is given in the laboratory frame and is defined with respect to the direction of the target. Since it is not known which ion emitted the photon and which was the target, a twofold ambiguity arises. The J/ψ produced at a rapidity y thus probes the gluons at two values of x,

$$x_{1,2} = \frac{M_{\mathrm{J}/\psi}}{\sqrt{s_{\mathrm{NN}}}} e^{\pm|y|} \,. \tag{2}$$

The cross section for J/ψ photoproduction also includes both contributions,

$$\frac{\mathrm{d}\sigma_{\mathrm{PbPb}}}{\mathrm{d}y} = n_\gamma(y, \{b\})\sigma_{\gamma\mathrm{Pb}}(y) + n_\gamma(-y, \{b\})\sigma_{\gamma\mathrm{Pb}}(-y) \,, \tag{3}$$

where n_γ is the photon flux, $\sigma_{\gamma\mathrm{Pb}}$ is the photonuclear cross section and $\{b\}$ denotes the impact parameter range taken into account in the measurement.

The ambiguity in the photon energy needs to be addressed in order to measure the energy (or x) dependence of J/ψ photoproduction. The issue is not present in studies of Pb–Pb UPCs at $y \approx 0$ since the two contributions can be effectively added up. The same applies to p–Pb collisions, where the term describing the photon emission from the proton can be neglected. For analyses of Pb–Pb UPC data in forward rapidity regions, the general strategy is to combine several measurements at the same rapidity but in different impact-parameter ranges, provided that the corresponding photon fluxes are calculated. This allows to determine the values of the photonuclear cross section $\sigma_{\gamma\mathrm{Pb}}(y)$ and $\sigma_{\gamma\mathrm{Pb}}(-y)$ upon solving a system of linear equations, given by Eq. (3) for the respective impact-parameter ranges.

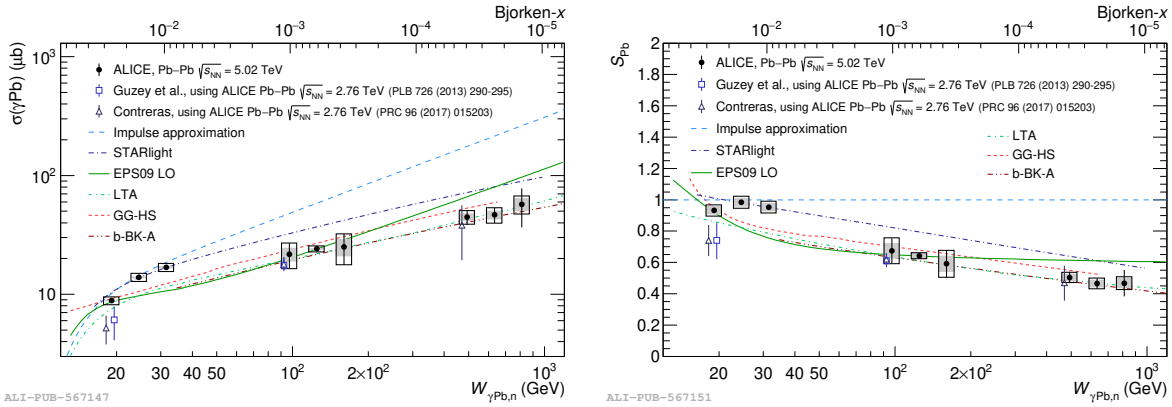

Figure 1 – The dependence of the cross section for coherent J/ψ photoproduction on photon-nucleus energy per nucleon pair, $W_{\gamma\mathrm{Pb,n}}$, or x as measured by ALICE in Pb–Pb UPCs at $\sqrt{s_{\mathrm{NN}}}$ = 5.02 TeV [7] (left). The measured energy and x dependence of the nuclear suppression factor S_{Pb} [7] (right). The vertical lines represent uncorrelated uncertainties, the empty boxes show the quadratic sum of the correlated systematic uncertainties and those coming from migration across neutron classes. The gray boxes show the theoretical uncertainty arising from the photon flux calculation. See the text for the description of the models.

Two possible implementations of this approach are based either on a combination of results from UPC and peripheral collisions ($b < R_1 + R_2$, with a partial nuclear overlap) [4] or on tagging of events using forward neutrons [5]. The latter method makes use of the fact that the electromagnetic fields of the colliding nuclei are so strong that an independent photon exchange can lead to an electromagnetic dissociation (EMD) of at least one of the nuclei, which can be accompanied by the emission of forward neutrons registered in the ZDCs. Events are then classified as 0n0n (no neutrons on either side), 0nXn or Xn0n (neutrons on one side only) or XnXn (forward neutrons on both sides). The photon spectra corresponding to these fragmentation scenarios can be calculated [6] and occupy different impact-parameter ranges.

3.1 Coherent J/ψ production

Recently, ALICE has measured the energy dependence of coherent J/ψ photonuclear production based on simultaneous analysis of Run-2 data from Pb–Pb UPCs at $\sqrt{s_{\mathrm{NN}}}$ = 5.02 TeV at central and forward rapidities [7]. Using the separation into neutron classes, the dependence of the cross section on $W_{\gamma\mathrm{Pb,n}}$, the center-of-mass energy of the γPb system per nucleon pair, was determined in the unprecedented interval of 17 to 920 GeV, corresponding to the x range spanning three orders of magnitude, from 10^{-2} down to 10^{-5}. The CMS Collaboration has performed a similar measurement in a narrower energy range [8].

The measured dependence is shown in the left panel of Figure 1 and is compared with predictions of various models. The Impulse approximation (IA) [9] describes well the low-energy data but significantly overshoots all other points at higher energies, clearly marking the onset of nuclear shadowing. STARlight [10], a hadronic model based on Glauber calculation, also describes properly only the low-energy points, implying the importance of including dynamic QCD effects as in the other models. The remaining models underestimate the cross section around 30 GeV, but provide a reasonably good description in other regions. The first model by the GSZ group [11] is based on EPS09 LO parametrization of nuclear PDFs, the latter incorporates leading twist approximation (LTA) of gluon shadowing. The GG-hs model [12] relies on a color-dipole approach and includes gluon saturation; the nucleons are pictured as a sum of hot spots, positions of which fluctuate event-by-event and their number increases with energy. The last model, b-BK-A [13], is based on a solution to the impact-parameter dependent Balitsky-Kovchegov (BK) equation and is valid only at x smaller than 10^{-2}. The new data are also compatible with Run-1 ALICE results, which were obtained by combining data from UPCs and peripheral collisions.

The results were used to calculate the nuclear suppression factor S_{Pb}, which gives a quantitative estimate of nuclear shadowing. S_{Pb} can be calculated as a square root of the ratio between the measured photonuclear cross section and the prediction given by IA, which ignores nuclear-environment effects. The measured energy dependence of S_{Pb} is depicted in the right panel of Figure 1; while S_{Pb} is approximately 0.95 around 20–40 GeV (x of 10^{-2}), it drops with increasing energy and levels off at about 0.5. Note that the value of 0.65 measured in the center point ($W_{\gamma\mathrm{Pb,n}}$ = 125 GeV) is compatible with the results

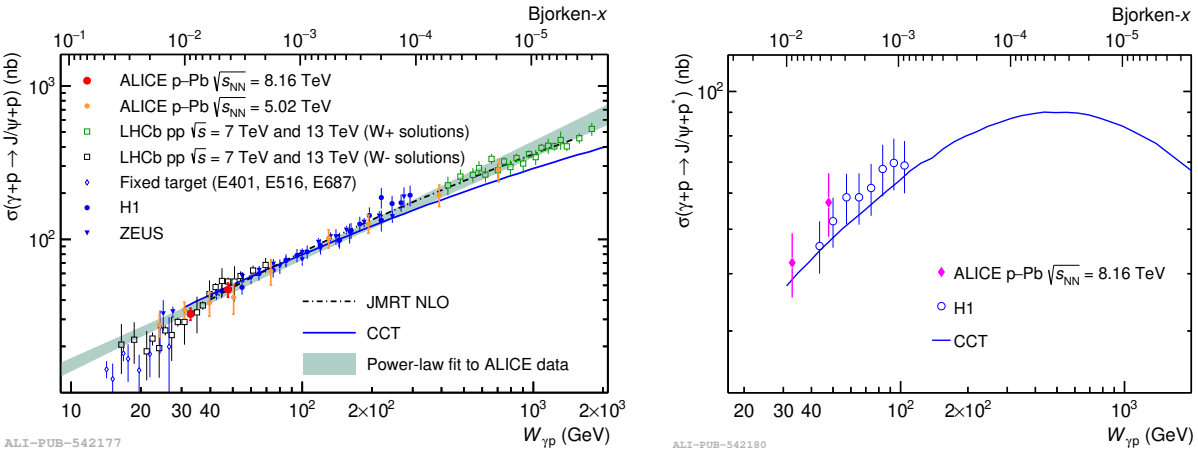

Figure 2 – The energy dependence of exclusive (left) and dissociative (right) J/ψ photoproduction measured by ALICE in p–Pb UPCs at $\sqrt{s_{\rm NN}} = 8.16$ TeV [15]. The vertical lines represent the quadratic sum of the statistical and systematic uncertainties.

derived from the previous ALICE midrapidity study of coherent J/ψ production [14].

3.2 Exclusive and dissociative J/ψ production

The energy dependence of the cross section for J/ψ photoproduction off protons has been studied by ALICE using p–Pb UPCs at $\sqrt{s_{\rm NN}} = 8.16$ TeV [15]. Events with J/ψ decaying into a pair of forward muons were registered with the muon spectrometer. The beam configuration corresponded to a low-energy photon emitted from the nucleus. Splitting the spectrometer acceptance into two rapidity bins, the cross section was determined at two values of $W_{\gamma \rm p}$, 27 and 57 GeV. The measured dependence of the exclusive J/ψ cross section is shown in the left panel of Figure 2; the new data are compatible with the previous results from ALICE, LHCb, HERA and fixed-target experiments and, in addition, are consistent with a power-law behavior, $\sigma = N(W_{\gamma \rm p}/W_0)^{\delta}$, where $W_0 = 90$ GeV. The values of $\delta = 0.70 \pm 0.04$ and $N = 71.6 \pm 3.7$ nb were obtained by fitting the data.

The ALICE measurement of the energy dependence of J/ψ photoproduction off protons accompanied by proton dissociation, shown in the right panel of Figure 2, is the first of its kind at a hadron collider. The observed energy evolution is in good agreement with previous H1 measurements and also with the CCT model [16], where the proton substructure is again represented as a superposition of hot spots with fluctuating positions. The number of hot spots increases with the energy $W_{\gamma \rm p}$. Within the framework of the CCT model, the dissociative cross section is sensitive to fluctuations of subnucleon structures inside the proton [17]. The model expects the cross section to reach a maximum at $W_{\gamma \rm p} \approx 500$ GeV, followed by a decrease. This is due to the hot spots effectively saturating the transverse area of the proton.

4 Distribution of nuclear matter in the transverse plane

Important insights into the structure of nuclei at high energies can be obtained by measuring the gluon distribution in the transverse plane. The dependence of the photonuclear cross section on Mandelstam $|t|$ is related through a two-dimensional Fourier transform to the transverse-plane distribution of the matter in the target. In the Good-Walker approach [18], coherent and incoherent photoproduction can be used to study the average and variance [17] (quantum fluctuations) of the nuclear structure, respectively. Note that there may be caveats to the applicability of this approach, as discussed in Ref. [19]. Since the value of $|t|$ is inversely proportional to the size of the scattering center, gluon density fluctuations at the subfemtometer scale can be probed at $|t| \sim 1$ GeV^2. Should such fluctuations be significant, they would be reflected in an enhancement of the incoherent cross-section in the relevant region.

The ALICE Collaboration has recently performed the first measurement of the $|t|$-dependence of incoherent J/ψ photoproduction in Pb–Pb UPCs at $\sqrt{s_{\rm NN}} = 5.02$ TeV [20], which complements the earlier ALICE study dedicated to the $|t|$-dependence of coherent J/ψ production [21]. Together, three orders of magnitude in $|t|$ are covered by ALICE with an accuracy compatible with that at HERA. Both analyses are based on the same midrapidity data sample, sensitive to the x interval of $(0.3, 1.4) \times 10^{-3}$. The analysis of coherent production focuses on the J/ψ kinematic range of $p_{\rm T} < 0.11$ GeV/c and unfolding

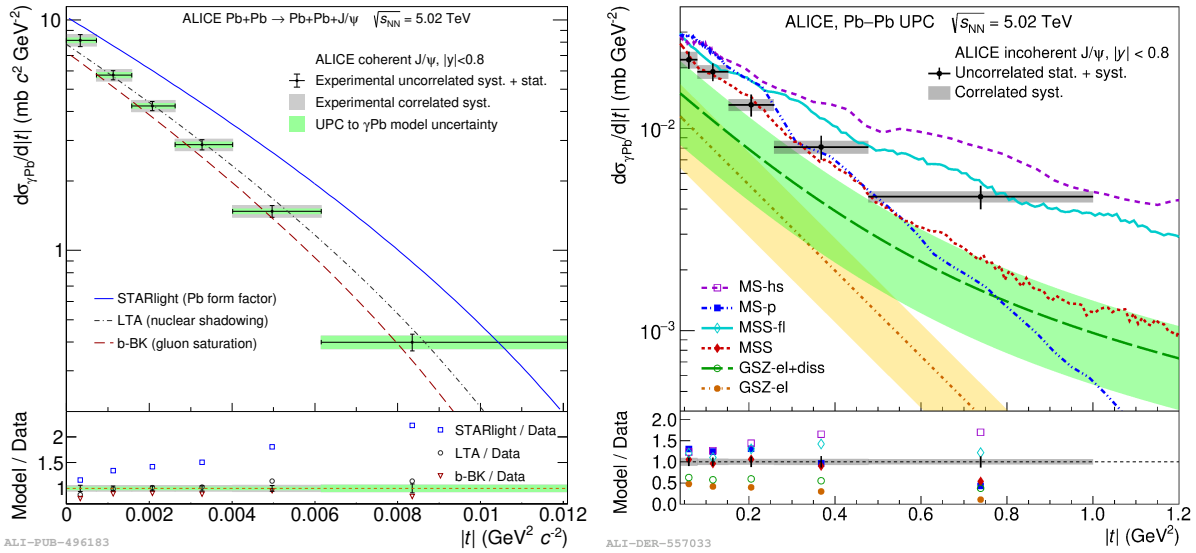

Figure 3 – The measured dependence of coherent (left) and incoherent (right) J/ψ photoproduction on the transferred momentum $|t|$ [21, 20] and the comparison with the models (see the text for details). The various uncertainties are depicted as explained in the top panels. The left bottom panel shows the model-to-data ratio in each measured point. The right bottom panel shows the ratio of the integral of the predicted to that of the measured cross section in each interval of $|t|$.

is employed to account for p_{T} migration and to correct for the photon transverse momentum. In the study of incoherent production, events with $0.2 < p_{\mathrm{T}} < 1$ GeV/c are selected, p_{T} resolution effects are negligible due to the widths of the considered intervals in $|t|$, and $|t| = p_{\mathrm{T}}^2$ owing to large transferred momenta.

The left panel of Figure 3 displays the measured $|t|$-dependence of the coherent cross section and the comparison with three phenomenological models. STARlight [10], where the p_{T} spectrum is determined from the nuclear form factor, gives a too high cross section and a slope clearly deviating from the measurement. Dynamic QCD effects are included in the two other models; either through a leading twist approximation of nuclear shadowing [22], or via solving the b-dependent BK equation, where gluon saturation effects are taken into consideration [13]. These two models describe the measurement reasonably well. With the new ALICE data from Run 3 and improved detector performance, it should soon be possible to distinguish which of the perturbative QCD calculations provides the better picture.

The measured evolution of the cross section for incoherent J/ψ production with $|t|$ is presented in the right panel of Figure 3 and compared with the predictions of three groups, MS, MSS, and GSZ [23, 24, 25], each offering two scenarios. The slope of the incoherent cross section is sensitive to fluctuations of the transverse profile of the target. The scenarios from the first group (MS-p, MSS, GSZ-el) consider elastic scattering of the photon on a full nucleon; these models generally predict steeper slopes than seen in the data. In the second scenario, subnucleon degrees of freedom are included. MS-hs includes saturation through the IPsat model [26], the nucleon is depicted as the sum of three hot spots with variable positions and fluctuations in the saturation scale are considered. The MSS-fl model incorporates perturbative small-x evolution through the solution to the JIMWLK equation. GSZ-el+diss expresses the total incoherent cross section as the sum of the elastic and dissociative parts; both are parameterized based on HERA data and multiplied by a common factor representing nuclear gluon shadowing in the LTA. At high $|t|$, the data favor the predictions from the second group, where the trend is softened by the inclusion of subnucleon degrees of freedom. Note that the models generally fail to describe the normalization of the cross section, which is mainly linked to scaling from proton to nuclear targets.

5 Polarization of coherently photoproduced J/ψ

The first measurement of the polarization of coherently photoproduced J/ψ has been performed by ALICE using Pb–Pb UPCs at $\sqrt{s_{\mathrm{NN}}} = 5.02$ TeV [27]. J/ψ mesons decaying into muon pairs were detected using the forward muon spectrometer and the polarization parameters λ_θ, λ_ϕ, and $\lambda_{\theta\phi}$ were extracted from fits to polar and azimuthal angular distributions of J/ψ yields. The angular distributions were studied

in the helicity frame, where the z axis is parallel with the J/ψ momentum in the Pb–Pb center-of-mass frame. The results are compatible with the transverse polarization, $(\lambda_\theta, \lambda_\phi, \lambda_{\theta\phi}) = (1, 0, 0)$, and constitute the first experimental evidence for the s-channel helicity conservation (SCHC) hypothesis in J/ψ photoproduction off Pb nuclei. For comparison with previous measurements in electron-proton collisions at HERA, elements of the spin density matrix were extracted; the results were found to be consistent with those from H1 but lower than those from ZEUS, where an electroproduction sample (with higher photon virtuality) was used.

6 Conclusion and outlook

This paper presents a summary of recent measurements performed by the ALICE Collaboration based on data from Pb–Pb and p–Pb ultra-peripheral collisions obtained during Run 2 of the LHC, focusing on J/ψ photoproduction. ALICE has successfully performed comprehensive studies that are crucial to improve the current understanding of the structure of protons and nuclei at high energies. The structure is characterized by the dominance of the gluon component, which is expected to saturate. For nucleons bound in nuclei, the high-energy structure is further modified by the nuclear environment, leading to nuclear shadowing. The new ALICE data provide an important benchmark for refining the predictions of current phenomenological models. The study of the energy dependence of coherent photonuclear production of J/ψ in Pb–Pb UPCs indicates a strong gluon depletion below $x \sim 10^{-2}$ due to nuclear shadowing. The first analysis of the energy dependence of dissociative photoproduction of J/ψ off protons at a hadron collider shows agreement with H1 results and represents the first experimental step in the study of fluctuations of the proton substructure. In the first measurements of the dependence of coherent and incoherent J/ψ photoproduction in Pb–Pb UPCs on Mandelstam $|t|$, the average and variation of the nuclear gluon density have been investigated, respectively. The results of the latter study suggest that quantum fluctuations of the gluon fields need to be taken into account in the available models in order to describe the data.

In Run 3 (2022–2025) and 4 (2029–2032), ALICE shall be able to perform even more detailed UPC studies and improve the accuracy of the current measurements thanks to the estimated size of data samples [28] and the upgrades on the detectors. Since Run 3, most ALICE detectors operate in continuous readout mode, which reduces the luminosity losses related to the limited efficiency of the trigger systems. ALICE performance in Run 3 particularly benefits from the upgrade to the ITS system; the new design fully relies on monolithic active pixel sensors (MAPS) with a spatial resolution of about 5 µm and significantly reduces the material budget in the vicinity of the interaction point [29]. The tracking and vertex resolution of the muon spectrometer were also considerably improved thanks to the installation of the Muon Forward Tracker (MFT) based on the same MAPS technology. In Run 4, the scheduled Forward Calorimeter (FoCal) upgrade [30] will allow to measure gluon distribution functions in the unprecedented Bjorken-x range down to 10^{-6} [31].

References

[1] A. Morreale and F. Salazar. "Mining for Gluon Saturation at Colliders". In: *Universe* 7.8 (2021), p. 312. DOI: 10.3390/universe7080312. arXiv: 2108.08254 [hep-ph].

[2] N. Armesto. "Nuclear shadowing". In: *J. Phys. G* 32 (2006), R367–R394. DOI: 10.1088/0954-3899/32/11/R01. arXiv: hep-ph/0604108.

[3] K. Aamodt et al. "The ALICE experiment at the CERN LHC". In: *JINST* 3 (2008), S08002. DOI: 10.1088/1748-0221/3/08/S08002.

[4] J. G. Contreras. "Gluon shadowing at small x from coherent J/ψ photoproduction data at energies available at the CERN Large Hadron Collider". In: *Phys. Rev. C* 96.1 (2017), p. 015203. DOI: 10.1103/PhysRevC.96.015203. arXiv: 1610.03350 [nucl-ex].

[5] V. Guzey, M. Strikman, and M. Zhalov. "Disentangling coherent and incoherent quasielastic J/ψ photoproduction on nuclei by neutron tagging in ultraperipheral ion collisions at the LHC". In: *Eur. Phys. J. C* 74.7 (2014), p. 2942. DOI: 10.1140/epjc/s10052-014-2942-z. arXiv: 1312.6486 [hep-ph].

[6] A. J. Baltz, S. R. Klein, and J. Nystrand. "Coherent vector meson photoproduction with nuclear breakup in relativistic heavy ion collisions". In: *Phys. Rev. Lett.* 89 (2002), p. 012301. DOI: 10.1103/PhysRevLett.89.012301. arXiv: nucl-th/0205031.

[7] S. Acharya et al. "Energy dependence of coherent photonuclear production of J/ψ mesons in ultra-peripheral Pb-Pb collisions at $\sqrt{s_{\mathrm{NN}}}$ = 5.02 TeV". In: *JHEP* 10 (2023), p. 119. DOI: 10.1007/JHEP10(2023)119. arXiv: 2305.19060 [nucl-ex].

[8] A. Tumasyan et al. "Probing Small Bjorken-x Nuclear Gluonic Structure via Coherent J/ψ Photoproduction in Ultraperipheral Pb-Pb Collisions at $\sqrt{s_{\mathrm{NN}}}$ = 5.02 TeV". In: *Phys. Rev. Lett.* 131.26 (2023), p. 262301. DOI: 10.1103/PhysRevLett.131.262301. arXiv: 2303.16984 [nucl-ex].

[9] G. F. Chew and G. C. Wick. "The Impulse Approximation". In: *Phys. Rev.* 85.4 (1952), p. 636. DOI: 10.1103/PhysRev.85.636.

[10] S. R. Klein et al. "STARlight: A Monte Carlo simulation program for ultra-peripheral collisions of relativistic ions". In: *Comput. Phys. Commun.* 212 (2017), pp. 258–268. DOI: 10.1016/j.cpc.2016.10.016. arXiv: 1607.03838 [hep-ph].

[11] V. Guzey, E. Kryshen, and M. Zhalov. "Coherent photoproduction of vector mesons in ultraperipheral heavy ion collisions: Update for run 2 at the CERN Large Hadron Collider". In: *Phys. Rev. C* 93.5 (2016), p. 055206. DOI: 10.1103/PhysRevC.93.055206. arXiv: 1602.01456 [nucl-th].

[12] J. Cepila, J. G. Contreras, and M. Krelina. "Coherent and incoherent J/ψ photonuclear production in an energy-dependent hot-spot model". In: *Phys. Rev. C* 97.2 (2018), p. 024901. DOI: 10.1103/PhysRevC.97.024901. arXiv: 1711.01855 [hep-ph].

[13] D. Bendova et al. "Photonuclear J/ψ production at the LHC: Proton-based versus nuclear dipole scattering amplitudes". In: *Phys. Lett. B* 817 (2021), p. 136306. DOI: 10.1016/j.physletb.2021.136306. arXiv: 2006.12980 [hep-ph].

[14] S. Acharya et al. "Coherent J/ψ and ψ' photoproduction at midrapidity in ultra-peripheral Pb-Pb collisions at $\sqrt{s_{\mathrm{NN}}}$ = 5.02 TeV". In: *Eur. Phys. J. C* 81.8 (2021), p. 712. DOI: 10.1140/epjc/s10052-021-09437-6. arXiv: 2101.04577 [nucl-ex].

[15] S. Acharya et al. "Exclusive and dissociative J/ψ photoproduction, and exclusive dimuon production, in p–Pb collisions at $\sqrt{s_{\mathrm{NN}}}$ = 8.16 TeV". In: *Phys. Rev. D* 108.11 (2023), p. 112004. DOI: 10.1103/PhysRevD.108.112004. arXiv: 2304.12403 [nucl-ex].

[16] J. Cepila, J. G. Contreras, and J. D. Tapia Takaki. "Energy dependence of dissociative J/ψ photoproduction as a signature of gluon saturation at the LHC". In: *Phys. Lett. B* 766 (2017), pp. 186–191. DOI: 10.1016/j.physletb.2016.12.063. arXiv: 1608.07559 [hep-ph].

[17] H. I. Miettinen and J. Pumplin. "Diffraction Scattering and the Parton Structure of Hadrons". In: *Phys. Rev. D* 18 (1978), p. 1696. DOI: 10.1103/PhysRevD.18.1696.

[18] M. L. Good and W. D. Walker. "Diffraction disssociation of beam particles". In: *Phys. Rev.* 120 (1960), pp. 1857–1860. DOI: 10.1103/PhysRev.120.1857.

[19] S. R. Klein. "Challenges to the Good-Walker paradigm in coherent and incoherent photoproduction". In: *Phys. Rev. C* 107.5 (2023), p. 055203. DOI: 10.1103/PhysRevC.107.055203. arXiv: 2301.01408 [hep-ph].

[20] S. Acharya et al. "First Measurement of the $|t|$ Dependence of Incoherent J/ψ Photonuclear Production". In: *Phys. Rev. Lett.* 132 (16 2024), p. 162302. DOI: 10.1103/PhysRevLett.132.162302. arXiv: 2305.06169 [nucl-ex].

[21] S. Acharya et al. "First measurement of the $|t|$-dependence of coherent J/ψ photonuclear production". In: *Phys. Lett. B* 817 (2021), p. 136280. DOI: 10.1016/j.physletb.2021.136280. arXiv: 2101.04623 [nucl-ex].

[22] V. Guzey, M. Strikman, and M. Zhalov. "Accessing transverse nucleon and gluon distributions in heavy nuclei using coherent vector meson photoproduction at high energies in ion ultraperipheral collisions". In: *Phys. Rev. C* 95.2 (2017), p. 025204. DOI: 10.1103/PhysRevC.95.025204. arXiv: 1611.05471 [hep-ph].

[23] H. Mäntysaari and B. Schenke. "Probing subnucleon scale fluctuations in ultraperipheral heavy ion collisions". In: *Phys. Lett. B* 772 (2017), pp. 832–838. DOI: 10.1016/j.physletb.2017.07.063. arXiv: 1703.09256 [hep-ph].

[24] H. Mäntysaari, F. Salazar, and B. Schenke. "Nuclear geometry at high energy from exclusive vector meson production". In: *Phys. Rev. D* 106.7 (2022), p. 074019. DOI: 10.1103/PhysRevD.106.074019. arXiv: 2207.03712 [hep-ph].

[25] V. Guzey, M. Strikman, and M. Zhalov. "Nucleon dissociation and incoherent J/ψ photoproduction on nuclei in ion ultraperipheral collisions at the Large Hadron Collider". In: *Phys. Rev. C* 99.1 (2019), p. 015201. DOI: 10.1103/PhysRevC.99.015201. arXiv: 1808.00740 [hep-ph].

[26] H. Kowalski and D. Teaney. "An Impact parameter dipole saturation model". In: *Phys. Rev. D* 68 (2003), p. 114005. DOI: 10.1103/PhysRevD.68.114005. arXiv: hep-ph/0304189.

[27] S. Acharya et al. "First polarisation measurement of coherently photoproduced J/ψ in ultra-peripheral Pb–Pb collisions at $\sqrt{s_{\mathrm{NN}}}$ = 5.02 TeV". 2023. arXiv: 2304.10928 [nucl-ex]. URL: https://cds.cern.ch/record/2856209.

[28] Z. Citron et al. "Report from Working Group 5: Future physics opportunities for high-density QCD at the LHC with heavy-ion and proton beams". In: *CERN Yellow Rep. Monogr.* 7 (2019). Ed. by Andrea Dainese et al., pp. 1159–1410. DOI: 10.23731/CYRM-2019-007.1159. arXiv: 1812.06772 [hep-ph].

[29] B. Abelev et al. "Technical Design Report for the Upgrade of the ALICE Inner Tracking System". In: *J. Phys. G* 41 (2014), p. 087002. DOI: 10.1088/0954-3899/41/8/087002.

[30] S. Acharya et al. "Letter of Intent: A Forward Calorimeter (FoCal) in the ALICE experiment". 2020. URL: https://cds.cern.ch/record/2719928.

[31] A. Bylinkin, J. Nystrand, and D. Tapia Takaki. "Vector meson photoproduction in UPCs with FoCal". In: *Journal of Physics G: Nuclear and Particle Physics* 50.5 (2023), p. 055105. DOI: 10.1088/1361-6471/acc419. arXiv: 2211.16107 [nucl-ex].

K^+K^- photoproduction in ultra-peripheral Pb–Pb collisions

Minjung Kim for the ALICE Collaboration
Department of Physics, University of California, Berkeley, CA, USA
Center for Frontiers in Nuclear Science, Stony Brook University, Stony Brook, NY, USA

In ultra-peripheral collisions (UPCs) of relativistic heavy ions, photoproduction occurs when a photon emitted from one nucleus interacts with the other nucleus from the opposing beam, producing particles in the final state. Measurements of K^+K^- photoproduction probe interactions and couplings between the $\phi(1020)$ and charged kaons with photons and nuclear targets. We report exclusive K^+K^- photoproduction cross section at midrapidity in Pb–Pb collisions at $\sqrt{s_{\rm NN}} = 5.02$ TeV, which is measured for the first time in UPCs.

DOI: https://doi.org/10.17161/4j009971
Keywords: photoproduction, UPC, heavy-ion collisions, K^+K^- production, ALICE

1 Introduction

In ultra-relativistic heavy-ion collisions, the electromagnetic field of a fast-moving heavy ion acts as a source of quasi-real photons [1, 2]. Those emitted photons can interact with the nucleus from the opposing beam. Ultra-peripheral collisions (UPCs) are those in which the impact parameter between the two colliding nuclei is greater than the sum of their nuclear radii. Photonuclear interactions can be effectively studied in UPCs since there are no hadron-hadron interactions present.

One of the interesting processes of photonuclear interactions is exclusive production of a vector meson. A virtual photon fluctuates into a quark-antiquark pair and elastically scatters off the nucleus, emerging as a vector meson [3]. The exclusivity of the process necessitates that there be no net colour charge transfer to the target, and therefore requires the exchange of at least two gluons with the target. Experimentally, the process can be rather easily identified by a rapidity gap between the produced vector meson and the target. Light vector mesons are typically reconstructed via their decay into oppositely charged meson pair, e.g., $\rho^0(700) \to \pi^+\pi^-$ or $\phi(1020) \to K^+K^-$.

However, oppositely charged meson pairs, $\pi^+\pi^-$ or K^+K^-, can emerge from different photonuclear interactions, where the photon fluctuates directly into a virtual meson pair [4]. One of the mesons can then scatter elastically from the target, making the pair real. Both processes contribute to the cross section measurements of $\pi^+\pi^-$ or K^+K^- pairs, making their distinction impractical. In order to further separate these two components, the production amplitude is described with two terms: the resonance with amplitude A_ϕ, and the continuum with amplitude $B_{\rm KK}$, giving [5]

$$\frac{{\rm d}\sigma}{{\rm d}M_{\rm KK}} = \left| A_\phi \frac{\sqrt{M_{\rm KK} M_\phi \Gamma_\phi}}{M_{\rm KK}^2 - M_\phi^2 + i M_\phi \Gamma_\phi} + B_{\rm KK} \right|^2 , \tag{1}$$

where $M_\phi = 1019.416 \pm 0.016$ MeV/c^2 [6] and Γ_ϕ are the $\phi(1020)$ mass and mass-dependent width, respectively, with

$$\Gamma_\phi = \Gamma_0 \frac{M_\phi}{M_{\rm KK}} \left(\frac{M_{\rm KK}^2 - 4M_{\rm K}^2}{M_\phi^2 - 4M_{\rm K}^2} \right)^{3/2} . \tag{2}$$

Here $\Gamma_0 = 4.249 \pm 0.013$ MeV/c^2 is the native $\phi(1020)$ width [6]. $M_{\rm K} = 493.677 \pm 0.016$ MeV/c^2 is the kaon mass [6]. By taking A_ϕ to be real, the relative phase between $\phi(1020) \to K^+K^-$ and direct K^+K^- continuum is encoded in $B_{\rm KK}$.

This article describes the first cross section measurement of the final state K^+K^- in exclusive photoproduction in UPCs with the ALICE detector [7]. The measurement covers the invariant mass of K^+K^- from 1.1 to 1.4 GeV/c^2, above the $\phi(1020)$ meson peak, with the lower mass limit set at about $M_\phi + 18\Gamma_0$. The results are presented as functions of $M_{\rm KK}$ and the dikaon transverse momentum ($p_{\rm T,KK}$) in the rapidity range $|y_{\rm KK}| < 0.8$. Additionally, studies regarding the significance of the resonance contribution and its interference with the direct production are also reported.

2 ALICE detector, data and analysis method

ALICE (A Large Ion Collider Experiment) is a general-purpose detector located at the LHC [8,9]. In the central barrel of ALICE, the Time Projection Chamber (TPC) [10] is used for charged particles tracking, as well as particle species identification based on the specific energy loss ($\mathrm{d}E/\mathrm{d}x$). The Inner Tracking System (ITS) [11] consisting of 6 layers of silicon detectors close to the beam pipe complements the TPC for tracking. In addition, the two innermost layers of the ITS are composed with silicon pixel detectors (SPD), contributes to the trigger decision. The data for this analysis was collected by the ALICE detector during the LHC Run 2 in 2015. The Time Of Flight (TOF) detector together with SPDs triggered events having two back-to-back tracks in the transverse plane in central barrel. At the same time, the events were vetoed by the V0 [12] and AD scintillators placed along the beam pipe, covering large pseudorapidity range [13,14] to ensure exclusivity [15]. The integrated luminosity of the data sample used in this analysis corresponds to 0.406 $\mu\mathrm{b}^{-1}$ with 2.6% uncertainty.

Two oppositely charged tracks form a pair candidate. Figure 1 shows the kinematic distributions of dikaon pairs as functions of M_{KK} and $p_{\mathrm{T,KK}}$ for opposite and same-charge pairs. By comparing the absolute yield of opposite-sign pairs to same-sign pairs, combinatorial background is found to be negligible in this data set. A rise of candidate opposite-sign pair yield at low $p_{\mathrm{T,KK}}$, similar to previously observed $\rho^0(700) \to \pi^+\pi^-$ in ALICE [15], as well as in STAR [16], indicates that pair candidates mostly originate from coherent photoproduction.

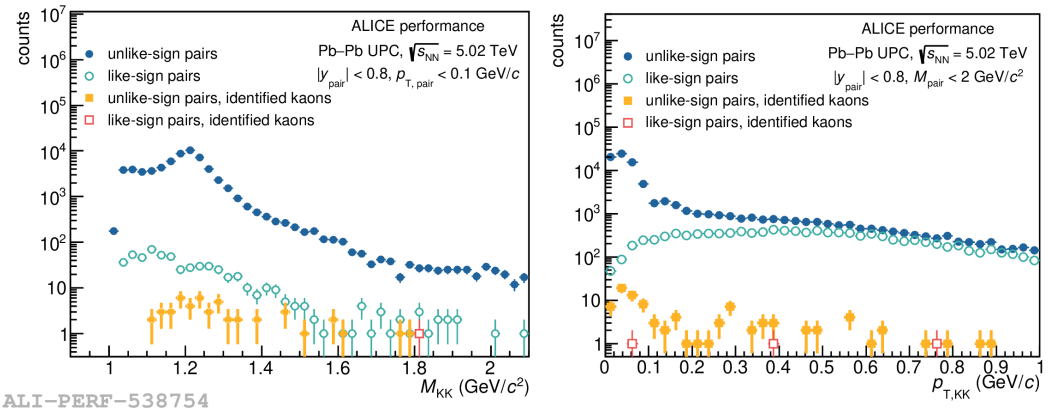

Figure 1 – Raw invariant mass (left) and transverse momentum (right) distributions for opposite-sign and same-sign pairs of inclusive charged particles and identified kaons. Identified kaons refer to satisfying kaon selection criteria based on measured TPC $\mathrm{d}E/\mathrm{d}x$ described in the text.

In order to reject the background contributions from $\pi^+\pi^-$ and dilepton pairs, stringent kaon selection criteria are required based on TPC $\mathrm{d}E/\mathrm{d}x$ information. The selection criteria are applied to the variable n_{σ_i}, the deviation of the measured signal from the expected signal in units of the $\mathrm{d}E/\mathrm{d}x$ measurement uncertainty for each particle hypothesis i, where i are π, μ, e, K. The tracks compatible within $2n_{\sigma_{\pi,\mu,e}}$ are excluded for further analysis. The TPC $\mathrm{d}E/\mathrm{d}x$ $n_{\sigma_{\mathrm{K}}}$ correlation between the two kaon candidates is presented in the left panel in Fig. 2. The remaining background is clustered around (-5,-5) while signal kaon pair candidates are centered around (0,0). Possible misidentified pair candidates within $|n_{\sigma_{\mathrm{K}}}| < 3$ are estimated using different $n_{\sigma_{\mathrm{K}}}$ boundaries shown as circular contours in the left panel in Fig. 2. The corresponding yields of signal region, $n^2_{\sigma_{\mathrm{K}}} + n^2_{\sigma_{\mathrm{K}}} < 3^2$, and background region, $4^2 < n^2_{\sigma_{\mathrm{K}}} + n^2_{\sigma_{\mathrm{K}}} < 5^2$, are projected as a function of pair invariant mass in the right panel in Fig. 2. The yield in the background region with respect to the one in the signal region is tiny in the range of 1.1 to 1.4 GeV/c^2. Thus, misidentified background is estimated to be negligible in the signal region $|n_{\sigma_{\mathrm{K}}}| < 3$ in the range of 1.1 to 1.4 GeV/c^2.

3 Cross section results

The cross section of exclusive $\mathrm{K}^+\mathrm{K}^-$ photoproduction is obtained by the number of $\mathrm{K}^+\mathrm{K}^-$ candidates, corrected by acceptance and efficiency, and the integrated luminosity. The acceptance and efficiency values are derived from Monte Carlo simulation with STARLight [17], and then complemented by a full simulation of the ALICE detector using GEANT3 [18] to model a realistic detector response.

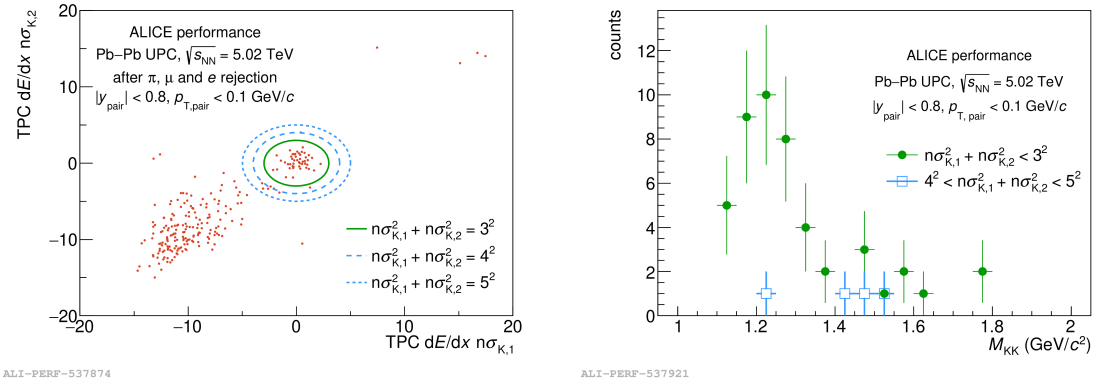

Figure 2 – Left: TPC dE/dx correlation between positive and negative charged kaon candidates in each pair represented as the deviation of the measured TPC dE/dx from the expected signal in units of the dE/dx measurement uncertainty for kaon mass hypothesis. Signal region is defined as $n^2_{\sigma_K} + n^2_{\sigma_K} < 3^2$ while the region used for background estimation is $4^2 < n^2_{\sigma_K} + n^2_{\sigma_K} < 5^2$. Circular boundaries around (0,0) with different radii are presented. Right: Raw number of kaon candidates in the signal region projected into pair invariant mass (M_{KK}) presented in green solid circle. The projection of the estimated background is shown in blue open square.

3.1 p^2_T-differential cross section for exclusive K^+K^- photoproduction

The p^2_T-differential cross section is shown in Fig. 3. The majority of the cross section is found below $p^2_{T,KK} < 0.01$ (GeV/c)^2, consistently with coherent photoproduction. The cross section for the coherent region are well described with an exponential shape $d^2\sigma/dydp^2_T = a\exp(-bp^2_T)$, where the slope parameter b is fixed to that measured for coherent ρ^0 photoproduction on Pb nuclei, $b = 428 \pm 6$ (stat.) $\pm$ 15 (syst.) (GeV/c)$^{-2}$ [19].

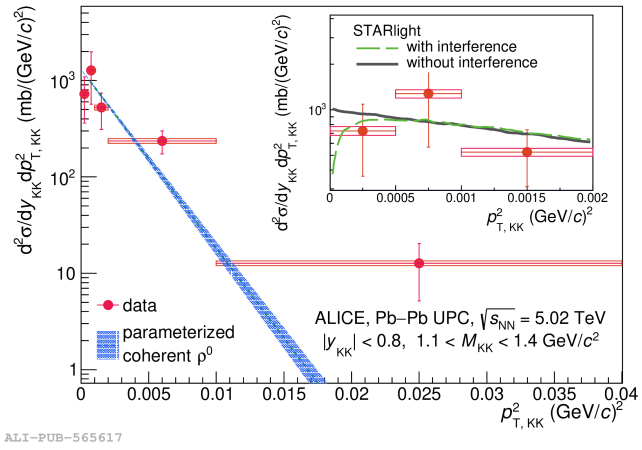

Figure 3 – p^2_T-differential cross section for exclusive K^+K^- photoproduction in $|y_{KK}| < 0.8$ in Pb–Pb UPCs at $\sqrt{s_{NN}}$= 5.02 TeV with parameterized cross section $d^2\sigma/dydp^2_T = a\exp(-bp^2_T)$, where the slope parameter b is fixed to $b = 428 \pm 6$ (stat.) $\pm$ 15 (syst.) (GeV/c)$^{-2}$, taken from previously measured coherent ρ^0 photoproduction [19]. Figure from Ref. [7].

3.2 Invariant mass distribution of coherent K^+K^- photoproduction

The left panel in Fig. 4 shows the invariant mass distribution for coherent K^+K^- photoproduction as a function of dikaon mass while rejecting most of the incoherent photoproduction contribution by requiring p^2_T >0.01 (GeV/c)^2. The spectrum is shown together with the best fit using Eq. 1 and also compared to various sets of relative fraction of direct K^+K^- contribution with respect to the amplitude of $\phi(1020) \rightarrow K^+K^-$ ($|B_{KK}/A_\phi|$) and the relative phase angle between $\phi(1020) \rightarrow K^+K^-$ and direct K^+K^- (φ). Calculations using STARLight for K^+K^- production via reactions such as $\gamma\gamma \rightarrow f_2(1270) \rightarrow K^+K^-$

(pink dashed-dotted line) show that these contributions are negligible. The black dotted line and the shaded region indicate the results under the assumption of no direct K^+K^- production. The calculations underestimate the measured cross section by about 2.1 σ in the range $1.1 < M_{K^+K^-} < 1.4$ GeV/c^2. The blue dashed line represents the prediction based on fixed values for $B_{\pi^+\pi^-}/A_\rho$ [16] and relative phase angle φ [15], determined from the measurement of the final $\pi^+\pi^-$ state system of ρ^0 meson decay and direct $\pi^+\pi^-$ production. This prediction is in agreement with the measured data points, showing slightly lower values yet still within the experimental uncertainties.

The right panel of Fig. 4 shows the confidence region for $|B_{KK}/A_\phi|$ and φ. A strong correlation between the two parameters produces a horseshoe-shaped distribution in their phase space. The solid green and dashed blue band indicate the 68% and 95% confidence level, respectively. The best-fit point shows that the results of the K^+K^- measurement is fully compatible with the prediction from the $\pi^+\pi^-$ system.

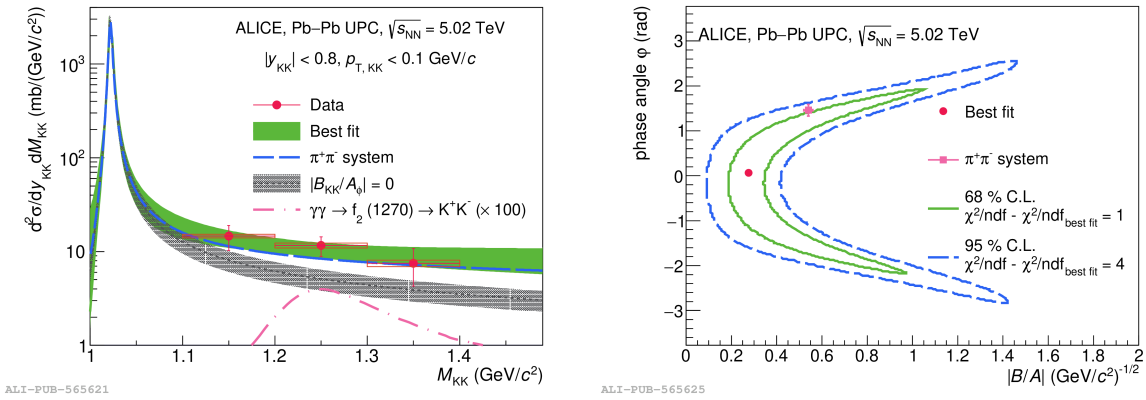

Figure 4 – Left: Differential cross section of coherent K^+K^- photoproduction as a function M_{KK} in Pb–Pb UPCs at $\sqrt{s_{NN}} = 5.02$ TeV in $|y_{KK}| < 0.8$. The lines and boxes along the data points represent statistical and systematic uncertainties, respectively. Best fit using Eq. 1 (green solid band), parameterized cross section based on ρ^0 and direct $\pi^+\pi^-$ production (blue long-dashed line) and estimated cross section without direct K^+K^- (φ) contribution (grey plaid band) are shown. $\gamma\gamma \to f_2(1270) \to K^+K^-$ (pink dashed-dotted line) is factored by 100 for better visualization. Right: Confidence regions for the relative fraction of direct K^+K^- contribution with respect to the amplitude of $\phi(1020) \to K^+K^-$ ($|B_{KK}/A_\phi|$) and the relative phase angle between $\phi(1020) \to K^+K^-$ and direct K^+K^- (φ). The green solid line and blue dashed line represent the boundary of 68% and 95% confidence regions, respectively. Figure from Ref. [7].

4 Conclusion

We report the first study of coherent K^+K^- photoproduction in ultra-peripheral collisions at the centre-of-mass energy per nucleon of the photon–nucleus15 (Pb) system $W_{\gamma Pb,n}$ from 33 to 188 GeV, in the range $1.1 < M_{KK} < 1.4$ GeV/c^2 and $|y_{KK}| < 0.8$. The measured cross section is concentrated below $p_T^2 < 0.01$ (GeV/c)^2 , consistent with coherent photoproduction. The measured cross section is about 2.1 σ larger than what is expected only from $\phi(1020)$ production, but is consistent with a mixture of $\phi(1020)$ and direct K^+K^- production. The fitted ratio of $\phi(1020)$ production to K^+K^- production is consistent with that seen for the ρ^0 and direct $\pi^+\pi^-$ production.

References

1. C. A. Bertulani, S. R. Klein and J. Nystrand, Ann. Rev. Nucl. Part. Sci. **55**, 271-310 (2005) doi:10.1146/annurev.nucl.55.090704.151526 [arXiv:nucl-ex/0502005 [nucl-ex]].
2. A. J. Baltz *et al.* Phys. Rept. **458**, 1-171 (2008) doi:10.1016/j.physrep.2007.12.001 [arXiv:0706.3356 [nucl-ex]].
3. S. R. Klein and H. Mäntysaari, Nature Rev. Phys. **1**, no.11, 662-674 (2019) doi:10.1038/s42254-019-0107-6 [arXiv:1910.10858 [hep-ex]].
4. S. R. Klein and J. Nystrand, Phys. Rev. Lett. **84**, 2330-2333 (2000) doi:10.1103/PhysRevLett.84.2330 [arXiv:hep-ph/9909237 [hep-ph]].
5. P. Soding, Phys. Lett. **19**, 702-704 (1966) doi:10.1016/0031-9163(66)90451-3

6. R. L. Workman *et al.* [Particle Data Group], PTEP **2022**, 083C01 (2022) doi:10.1093/ptep/ptac097
7. S. Acharya *et al.* [ALICE], [arXiv:2311.11792 [nucl-ex]].
8. K. Aamodt *et al.* [ALICE], JINST **3**, S08002 (2008) doi:10.1088/1748-0221/3/08/S08002
9. B. B. Abelev *et al.* [ALICE], Int. J. Mod. Phys. A **29**, 1430044 (2014) doi:10.1142/S0217751X14300440 [arXiv:1402.4476 [nucl-ex]].
10. J. Alme *et al.* Nucl. Instrum. Meth. A **622**, 316-367 (2010) doi:10.1016/j.nima.2010.04.042 [arXiv:1001.1950 [physics.ins-det]].
11. K. Aamodt *et al.* [ALICE], JINST **5**, P03003 (2010) doi:10.1088/1748-0221/5/03/P03003 [arXiv:1001.0502 [physics.ins-det]].
12. E. Abbas *et al.* [ALICE], JINST **8**, P10016 (2013) doi:10.1088/1748-0221/8/10/P10016 [arXiv:1306.3130 [nucl-ex]].
13. K. Akiba *et al.* [LHC Forward Physics Working Group], J. Phys. G **43**, 110201 (2016) doi:10.1088/0954-3899/43/11/110201 [arXiv:1611.05079 [hep-ph]].
14. M. Broz *et al.* JINST **16**, no.01, P01017 (2021) doi:10.1088/1748-0221/16/01/P01017 [arXiv:2006.14982 [physics.ins-det]].
15. S. Acharya *et al.* [ALICE], JHEP **06**, 035 (2020) doi:10.1007/JHEP06(2020)035 [arXiv:2002.10897 [nucl-ex]].
16. L. Adamczyk *et al.* [STAR], Phys. Rev. C **96**, no.5, 054904 (2017) doi:10.1103/PhysRevC.96.054904 [arXiv:1702.07705 [nucl-ex]].
17. S. R. Klein, J. Nystrand, J. Seger, Y. Gorbunov and J. Butterworth, Comput. Phys. Commun. **212**, 258-268 (2017) doi:10.1016/j.cpc.2016.10.016 [arXiv:1607.03838 [hep-ph]].
18. R. Brun, F. Bruyant, F. Carminati, S. Giani, M. Maire, A. McPherson, G. Patrick and L. Urban, doi:10.17181/CERN.MUHF.DMJ1
19. J. Adam *et al.* [ALICE], JHEP **09**, 095 (2015) doi:10.1007/JHEP09(2015)095 [arXiv:1503.09177 [nucl-ex]].

Phys. Proc. Ultra-Peripheral Collisions **1**, 006 (2024) 1-9

Quantum mechanical aspects of coherent photoproduction: the limits of coherence, and multiple vector mesons

Spencer R. Klein
Nuclear Science Division, Lawrence Berkeley National Laboratory
Berkeley CA 94720 USA

Quantum mechanics is central to coherent photoproduction in ultra-peripheral collisions (UPCs). This writeup will discuss some surprising aspects of UPCs that stem from these quantum mechanical roots. The Good-Walker (GW) paradigm, which connects coherent photoproduction with the target nucleus remaining in its ground state. This contrasts with a semi-classical picture, where coherence depends on the positions of the individual nucleons and the momentum transfer. Unlike the GW approach, the semiclassical picture is consistent with the observed data on coherent photoproduction with nuclear breakup, and with coherent photoproduction in peripheral collisions. The semiclassical approach allows for a wider variety of coherent UPC reactions, such as coherent photoproduction of charged mesons, including some non $q\bar{q}$ exotica. Quantum mechanics is also key to the coherent photoproduction of multiple vector mesons by the interactions of a single ion pair. The vector mesons share a common impact parameter, and so can exhibit richer interference patterns than single mesons. At forward rapidities, the cross sections to produce multiple identical vector mesons are enhanced due to superradiance. With enough statistics, multi-meson events may provide an opportunity to observe stimulated decays.

DOI: https://doi.org/10.17161/xdb61m86
Keywords: ultra-peripheral collisions; photoproduction; coherent interactions; interference

1 Introduction

Ultra-peripheral collisions (UPCs) are interactions where relativistic nuclei interact at impact parameters b greater than twice the nuclear radius (R_A), where there are no hadronic interactions [1,2,3,4]. Instead the ions can interact electromagnetically, via either two-photon processes or photonuclear interactions. UPCs at CERN's Large Hadron Collider (LHC) are the energy frontier for both of these classes of events. Two-photon production of lepton pairs and photon pairs (light-by-light scattering) [5] have been intensively studied, along with searches for beyond-standard-model physics [6,4]. Photonuclear interactions are an important probe of nuclear structure at low Bjorken$-x$, having been studied via photon-gluon fusion to produce dijets, and via photon-Pomeron interactions which produce vector mesons.

Exclusive production of vector mesons is of particular interest, both theoretically and experimentally. Experimentally, the final states are usually simple - two oppositely charged particles - which greatly simplifies detection. Vector meson production involves the exchange of a colorless object. At leading order, at least two gluons must be exchanged, but recent next-to-leading order calculations of J/ψ photoproduction have shown that there are significant cancellations involving the gluonic contributions to the cross sections, so the quark distributions play a large role [8]. The same calculation also found that the cross section was very sensitive to the assumed pQCD scale.

Despite these difficulties, much interest remains in using coherent vector meson production to probe nuclei because it provides access to information on the transverse positions of partons, and of their fluctuations, via the Good-Walker paradigm which links coherent production with the average nuclear configuration and incoherent production to fluctuations in the nuclear configuration, including the presence

of gluonic hot spots [7]. $d\sigma/dt$ for coherent production can be Fourier transformed to find the transverse distribution of targets (gluons) in the target.

2 Coherent and incoherent photoproduction

2.1 The Good-Walker paradigm

The total cross section for vector meson photoproduction may be written [9]

$$\frac{d\sigma_{tot}}{dt} = \frac{1}{16\pi}\langle|A(K,\Omega)|^2\rangle \tag{1}$$

where $A(K,\Omega)$ is the amplitude for producing a vector meson, where K represents the kinematic factors (vector meson momentum, momentum transfers, etc.) and Ω represents the configuration of the target, including the positions of the target nucleons and the number and positions of the partons within those nucleons. The amplitudes are squared, and then averaged over all of the possible Ω. In contrast, for coherent production, the amplitudes are added (averaged) and then squared:

$$\frac{d\sigma_{coh}}{dt} = \frac{1}{16\pi}|\langle A(K,\Omega)\rangle|^2. \tag{2}$$

Mietenlin and Pumplin pointed out [10] that the difference between these is the incoherent cross section, which is sensitive to event-by-event fluctuations in the cross section:

$$\frac{d\sigma_{incoh}}{dt} = \frac{1}{16\pi}\left(\langle|A(K,\Omega)|^2\rangle - |\langle A(K,\Omega)\rangle|^2\right). \tag{3}$$

This is the sum of squares minus the square of sums, so is directly sensitive to event-by-event fluctuations in the cross sections.

In UPCs, $|t| \approx$ pair p_T^2 (neglecting the generally small t_z). Since p_T and impact parameter (b) are conjugate variables, one can perform a 2-dimensional Fourier-Bessel transform of $d\sigma/dp_T$ to get $F(b)$, the amplitude for having an interaction at an impact parameter b [11,12]:

$$F(b) \propto \int_0^\infty p_T dp_T J_0(bp_T)\sqrt{\frac{d\sigma}{dt}}^* \tag{4}$$

where $J_0(x)$ is a Bessel function. Several caveats are associated with this transformation [13]. The asterisk is because is necessary to flip with sign of the square root when integrating across each diffractive minimum. This is to properly track the phase of the amplitude across these zeros. This is theoretically straightforward, but experimentally it can be difficult to pinpoint these zeros accurately enough. Second, the integral goes from zero to infinity, but real data has a maximum p_T. The presence of a p_T cutoff is equivalent to applying a square windowing function, and so introduces artifacts.

The STAR collaboration investigated this in a high-statistics study of ρ^0 plus direct $\pi^+\pi^-$ production[12]. They found that varying the maximum p_T cutoff affected $F(b)$ at small b, but did not change the apparent size of the target. In UPCs, the measured vector meson p_T includes contributions from the experimental resolution and from the photon p_T, although these can be removed by deconvolution [14].

2.2 Problems with the Good-Walker approach

Unfortunately, there is a significant problem with the overall Good-Walker approach [15]. Equation 2, identifies coherent production with the nucleus remaining unexcited, in the ground state. However, there is another definition of coherence - the addition of amplitudes in-phase, leading to a peak at small p_T ($p_T < \hbar/R_A$). This low p_T coherent peak has been observed in different types of reactions where the nuclear targets do not remain in the ground state.

One such class is vector meson photoproduction accompanied by mutual excitation of both nuclei. This has been seen by both STAR [16,17] and ALICE [18] collaboration. For STAR, the mutual breakup requirement is intrinsic to most of their UPC triggers. The effect of mutual breakup is calculable by assuming factorization for multi-photon exchange, whereby one photon produces the vector meson, and two additional photons each excite one of the nuclei [19], as is shown in Fig. 1 (right). The photons are emitted independently, save for their common impact parameter [20]. Factorization does a good job of predicting the cross sections for coherent production of vector mesons accompanied by neutron emission [19].

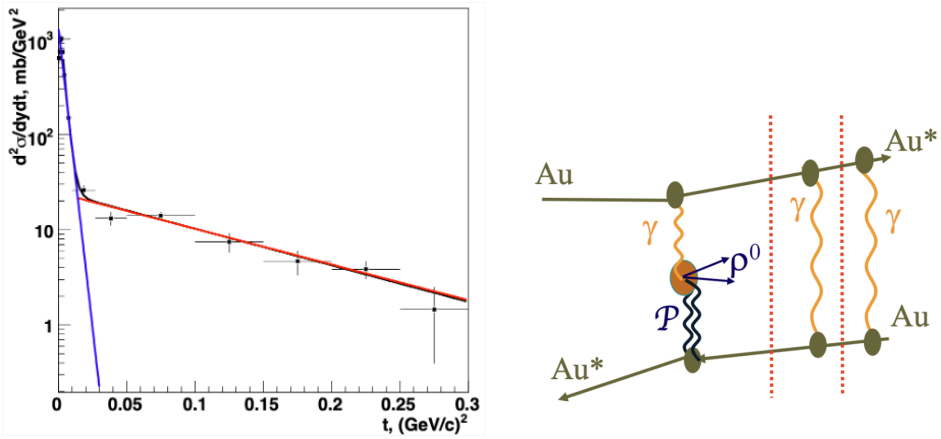

Figure 1 – (left) $d\sigma/dt$ for ρ photoproduction as measured by the STAR Collaboration. The data is well fit by two exponentials, corresponding to coherent coupling to the entire nucleus (blue) and to individual nucleons (red). This data required that both of the nuclei be excited, as evidenced by the observation of breakup neutrons in both forward zero degree calorimeters, but a coherent peak is still clearly visible. From Ref. [17]. (right) Schematic diagram showing how mutual Coulomb dissociation factorizes (decouples) from ρ photoproduction; the processes separated by the vertical red dotted lines share only a common impact parameter.

However, it does not fit into the Good-Walker approach, where the overall reaction is under scrutiny. Further, in some p_T range, incoherent photoproduction of vector mesons (one-photon exchange) and coherent photoproduction of vector mesons accompanied by the exchange of an additional photon which excites one of the nuclei will both contribute. These two channels can even interfere with each other.

One posited way out of this paradox uses time scales. Vector meson production occurs on time scales that are short compared with the nuclear excitation, so the vector meson is effectively decoupled from the nuclear breakup. However, the most common excitation, to a Giant Dipole Resonance (GDR) requires an energy of 10-20 MeV in the target rest frame. But, for a high-energy photon converting to a vector meson, the required momentum transfer from the target corresponds to considerably less energy, and therefore a longer time scale.

It is worth noting that the idea of exclusive production is slightly simplistic, in that it neglects other reactions that are likely to occur. For two ions with a relatively small b (but still with $b > 2R_A$), the probability of two-photon production of e^+e^- pairs is large - for collisions with lead nuclei at the LHC, the average number of pairs produced when $b \approx 2R_A$ is 3-4 [21]. These pairs are generally unobservable, but they are still present. And, although the cross section for bremsstrahlung emission by the ion is small, it is also infrared divergent, so some soft radiation is always expected. So, the idea of completely exclusive interactions is an unattainable theoretical ideal.

The second problematic process is vector meson production in peripheral heavy-ion collisions, where the low p_T vector meson is accompanied by hadronic interactions which can produce hundreds of particles. Coherent (again defined as exhibiting a peak at low p_T, consistent with the in-phase addition of amplitudes) photoproduction of J/ψ has been observed in gold-gold collisions by STAR [22], and in lead-lead collisions by ALICE [23] and LHCb [24]. The cross sections appear consistent with theoretical calculations that largely decouple the photoproduction from the hadronic interactions [25,26], although the precision of the data is still limited, and it is not possible to conclusively determine the size of the coherent target. It is not currently possible to reconcile this data with the underpinnings of the Good-Walker approach.

2.3 A semi-classical approach

It is possible, however, to explain all of this data in a semi-classical approach, where the cross section for vector meson production on a nucleus consisting of i nucleons at positions $\vec{x}_i$ is [15]

$$\sigma_{coh} = \Sigma_i \left| A_i \exp(i\vec{t} \cdot \vec{x}_i) \right|^2 \tag{5}$$

Here A_i is the interaction amplitude for each nucleon, and $\vec{t}$ is the 3-momentum transfer from the target. This approach is insensitive to what happens to the target, but it still reproduces the observed pp_T spectra for coherent and incoherent photoproduction. When $|\vec{t}|$ is small, the exponential is close to one, and the cross section is the square of the sum of the amplitudes; this leaves no room for incoherent

production at small $|t|$. At large $|t|$, the exponential takes on random phases, and the cross section scales as the sum of the square of the amplitudes. These regimes are visible in the STAR ρ^0 photoproduction data [17] shown in Fig. 1 (left). There, the incoherent cross section still decreases slowly with increasing p_T due to the form factor of the individual nucleons. One drawback of Eq. 5 is that it does not track the outgoing nucleus, so one cannot separate coherent and incoherent production, except via the different p_T scales - an imperfect classification.

Although the semi-classical approach makes fairly similar predictions as Good-Walker for coherent production, the interpretations for incoherent production are totally different. In Good-Walker, it depends on fluctuations, while in the semi-classical approach, it depends only on the static properties of the target.

2.4 Gold vs. lead: similar, or not?

Another issue with the Good-Walker approach appears at low $|t|$ [15]. It relates the incoherent cross section to event-by-event fluctuations in nucleon positions and subnucleonic (parton level) fluctuations. From these points of view, heavy nuclei are expected to be similar. For example, the density distributions of gold-197 and lead-208 are both well described by a Woods-Saxon distribution and they have a similar partonic structure, with similar nuclear shadowing. However, in the nuclear shell model, their structures are very different, and this their incoherent interactions must be different at low $|t|$.

Lead-208 is doubly magic, with a lowest excited state at an energy of $E_{\rm exc.} = 2.6$ MeV. No excitation (is possible at lower energy transfers, so there can be no incoherent interactions. If one assumes that the Pomeron $|t|$ is transferred to a single nucleon (as indicated by the STAR data on incoherent ρ^0 plus direct $\pi^+\pi^-$ photoproduction, taken at larger $|t|$ [12]), then the energy threshold corresponds to a minimum momentum transfer of $p = \sqrt{2m_p E_{\rm exc.}} = 71$ MeV/c. In contrast, gold-197 has a lowest excited state at an energy of 77 keV, corresponding to a minimum p of only 12 MeV/c. This indicates that incoherent photoproduction in lead is impossible for $p_T < 71$ MeV/c, while in gold the minimum is 12 MeV/c. Although Fermi motion and other factors may smooth out these cutoffs, but there should be large differences in incoherent production at small $|t|$.

2.5 Additional possibilities from the semiclassical formulation

The semi-classical formulation allows for a wider range of coherent reactions than Good-Walker. It allows for the coherent exchange of Reggeons that include non-zero quantum numbers such as spin, or even electrical charge. This permits reactions such as

$$\gamma + A \rightarrow a_2^+(1320) + (A-1) \tag{6}$$
$$\gamma + A \rightarrow a_2^-(1320) + (A+1). \tag{7}$$

The first reaction changes a proton into a neutron, while the other converts a nucleon in the other direction. In the semiclassical approach, the first reaction could be coherent over the protons in the target while the second could be coherent over the neutrons. This should lead to a well-determined production cross section ratio, based on the cross sections on protons and on the nuclear composition of the target. By measuring $d\sigma/dt$ for the two reactions, it would also be possible to determine the proton and neutron radii of the target nucleus, with a very small relative systematic error, allowing for a reliable measurement of the thickness of any neutron skin.

UPC photoproduction of the $a_2^+(1320)$ has been considered for proton targets, using parameterizations of $\sigma(\gamma p \rightarrow a_2^+(1320)p$ [27]. The photoproduction cross section is smaller than the ρ^0 cross section, but still large enough to be easily visible in pA UPCs. These reactions occur via Reggeon exchange, with the bulk of the cross section near threshold. So, as can be seen in Fig. 2, production is peaked near rapidity 2.5 at RHIC, and near 7 at the LHC. This is outside of the acceptance of most current detectors. The STAR forward upgrade [28] covers the appropriate rapidity range., so might be used to probe $a_2^+(1320)$ production if an appropriate trigger is available. UPC photoproduction in AA collisions should have similar characteristics, although with a shift toward midrapidity because of the lower target beam energy.

The $a_2^\pm(1320)$ is an example of a relatively standard 'standard candle' $q\bar{q}$ state, but other mesons can be produced, including hadronic 'exotica' like 4-quark states and other hybrids. One example is the $Z_c^+(4430)$, where the cross section is very roughly 1/400 of that of the $a_2(1320)^+$ [27]. Because of the high mass, production is somewhat shifted toward mid-rapidity.

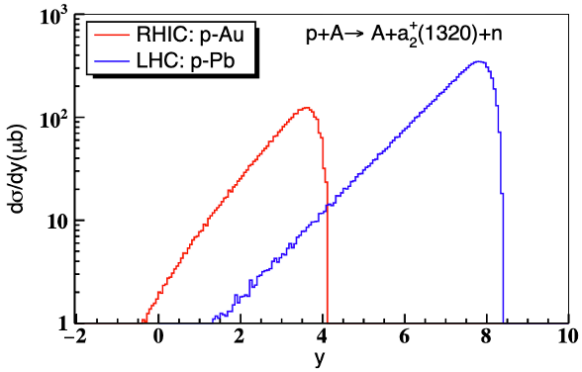

Figure 2 – Predicted $d\sigma/dy$ for photoproduction of the $a_2^+(1320)$ in pAu collisions at RHIC (red) and in pPb collisions at the LHC. From Ref. [27].

3 Multiple vector meson production and interference

The cross section for multiple vector meson production can be calculated in impact-parameter space: [19,29]:

$$\sigma(V_1, V_2) = \int d^2b P(V_1, b) P(V_2, b) \tag{8}$$

where $P(V_1, b)$ and $P(V_2, b)$ are the probabilities for producing the two vector mesons at impact parameter b. It is easy to incorporate trigger conditions (such as single of mutual Coulomb dissociation) by adding a third probability, accounting for the probability of additional photon exchange(s), leading to the desired excitation(s). Similar techniques can be used to calculate the kinematic distributions, such as the joint rapidity distribution [30,31].

Even for a single vector meson, interesting interference phenomena are observable, due to the destructive interference between photoproduction on the two ions [32,33,34]. This interference reduces production at small p_T and a given rapidity y:

$$\sigma(y, p_T) = \left| A_1(y, p_T) - A_2(y, p_T) e^{i(\vec{p}_T \cdot \vec{b})} \right|^2 \tag{9}$$

where $A_1(y, p_T)$ and $A_2(y, p_T)$ are the amplitudes for production on the two nuclei. The exponential is the propagator between the two targets. The minus sign is because vector mesons have negative parity, and swapping from production on one nucleus to production on the other is equivalent to a parity inversion. At mid-rapidity, symmetry requires $A_1(0, p_T) = A_2(0, p_T)$ and the interference is maximal; as $p_T \to 0$, production disappears [35].

Another aspect of this interference comes from the photon polarization. The photons are linearly polarized along $\vec{b}$. Since the plane formed by the decay products is preferentially oriented with respect to the electric field vector (*i. e.* to $\vec{b}$), this interference introduces an azimuthal modulation to the meson p_T distribution [36,34].

3.1 Non-identical mesons

With two vector mesons, the interference phenomenology grows richer. We first consider two non-identical mesons (*e. g.* $\rho\phi$). Four diagrams, shown in the top row of Fig. 3, contribute to two–non-identical-meson production. The joint probability (at a given b) for production of two mesons follow from these diagrams:

$$\begin{aligned} P(b) = \Big| & A_L(\vec{p_1}, b) A_L(\vec{p_2}, b) - A_L(\vec{p_1}, b) A_R(\vec{p_2}, b) e^{i(\vec{k_2} \cdot \vec{b})} \\ & - A_R(\vec{p_1}, b) A_L(\vec{p_2}, b) e^{i(\vec{k_1} \cdot \vec{b})} + A_R(\vec{p_1}, b) A_R(\vec{p_2}, b) e^{i(\vec{k_2} \cdot \vec{b})} e^{i(\vec{k_1} \cdot \vec{b})} \Big|^2 \end{aligned} \tag{10}$$

where A_L and A_R are the amplitudes for production on the left-going and right-going nuclei respectively, $\vec{p}_1$ and $\vec{p}_2$ are the vector meson momenta and $\vec{k}_1$ and $\vec{k}_2$ are the two momentum transfers from the nucleus. Equation 10 can be factorized into the product of two independent interference terms for two single mesons, and much of the phenomenology follows from that factorization: the cross section goes to zero when either one of the mesons is at mid-rapidity and has small p_T.

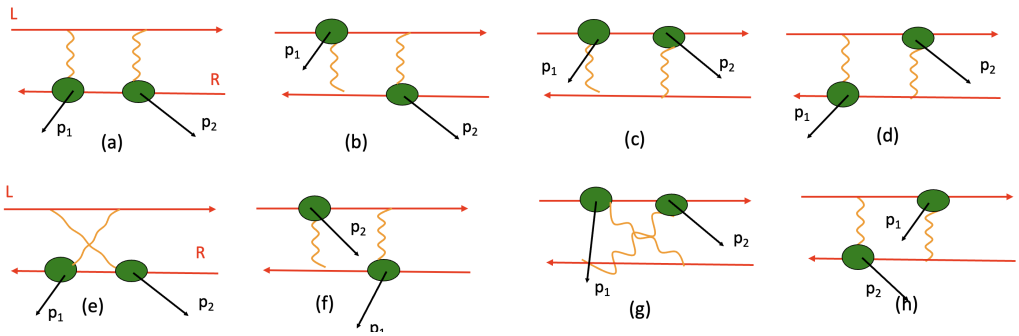

Figure 3 – (top) The four diagrams that contribute to the photoproduction of two non-identical mesons. (bottom) The four additional diagrams that contribute for the production of two identical mesons.

3.2 Identical mesons

For a pair of identical mesons, there are four additional diagrams to consider, shown on the bottom row of Fig. 3, since there are two routes to create each meson - from photon 1 or photon 2. This leads to a more complex phenomenology. One simple but interesting case involves the emission of light vector mesons at relatively forward rapidities. Light vector mesons are notable because $\sigma(\gamma A \to VA)$ increases only slowly with increasing photon energy, while the photon spectrum scales roughly as $1/k$. So, photoproduction is largest near threshold, corresponding to production at forward rapidity. In this region, the two leftmost diagrams (or, for negative rapidity, the third column of Fig. 3) are the dominant contribution, and

$$P(b) = \Big|\Sigma_i\Sigma_j A_L(\vec{p_1},b)A_L(\vec{p_2},b)\exp(i(\vec{k}_1\cdot\vec{b}_i+\vec{k}_2\cdot\vec{b}_j)) + A_L(\vec{p_2},b)A_L(\vec{p_2},a)\exp(i(\vec{k}_2\cdot\vec{b}_i+\vec{k}_1\cdot\vec{b}_j))\Big|^2. \tag{11}$$

The sums over i and j run over the target nucleons at positions $\vec{b}_i$. They exhibit the conditions for coherent emission from the nucleus. Essentially, these boil down to $|\vec{k}_1|, |\vec{k}_2| < \hbar/R_A$.

Within this low p_T constraint, Eq. 11 of the two mesons leads to two identical terms for the amplitude. If we neglect shadowing or other geometric effects then the production amplitudes are all identical. This assumption is good for heavier mesons like the J/ψ, but less accurate for lighter mesons where shadowing is large and a Glauber calculation is needed to find the total cross section. But, it simplifies the analysis, while retaining the essential physics, so we will use that assumption here. With this, at low p_T, the sums over i and j can be replaced with N (the number of nucleons in the target nucleus) times the individual amplitudes. If both vector mesons are produced at similar rapidities, so the amplitudes are similar, the cross section is

$$P(b) = |2N^2 A_L(\vec{p_1},b)^2|^2 = 4N^4 A_L(\vec{p_1},b)^4. \tag{12}$$

The cross section is double what it would be without the additional identical-particle diagrams. This is an example of superradiance.

The coherence conditions are tighter than they are for a single meson, because the exponentials in Eq. 11 sum two products of momentum and impact parameter. So, the coherence condition becomes $|\vec{k}_1|, |\vec{k}_2| < \hbar/2R_A$.

It is easy to generalize this to the emission of more than two mesons. For the emission of M mesons, there are $M!$ independent diagrams. So, the amplitude for emission, subject to all of the mesons having sufficiently low p_T is

$$P_M(b) = M!N^{M*M}A_L(\vec{p_1},b)^{M*M} = M!P_1(b)^M \tag{13}$$

The production probability is $M!$ times the probability if superradiance is neglected. For large M, $M!$ increases faster than $P_1(b)^M$. For producing ρ mesons with lead beams at the LHC, $P_1(b = 2R_A) \approx 0.03$ [29]; this might rise to ≈ 0.05 at a future higher-energy accelerator; it would also be somewhat higher with uranium or other higher$-Z$ beams.

Whatever $P_1(b)$ is, if enough vector mesons are produced, the system can reach the criteria to be considered a laser. In optical terms, "the optical gain equals the cavity loss" [37]. Here, the equivalent condition is that $P(M+1) > P(M)$. This requires M to be quite large ($M > 30$ for lead at the LHC), and it is likely that other limitations would come into play. First, the coherence conditions tighten as M

rises and the number of terms in the exponential increases, to $\vec{k} < \hbar/MR_A$. This has similarities with optical systems, where the beam divergence drops as lasing sets in. Another limitation is energetic, since the energy carried by the electromagnetic field is finite. Although the large$-M$ limit may be beyond current reach, it should be possible to observe superradiance from two or three vector mesons.

3.3 Decay correlations and stimulated decays

Correlations should also be visible in the particle decays. One effect is straightforward: the vector mesons share the same linear polarization, so there will be correlations in decay angles. Another possibility is more intriguing: if the two vector mesons are in the same quantum mechanical state, there is the possibility of stimulated decays, where the probability for decays to the identical final state is enhanced.

Stimulated decays can occur for final states particles that have integer spin (i. e. bosons). If there is already an identical particle in the same state that will result from the decay, the probability for that decay can be enhanced. Stimulated decays have previously been studied in the context of transitions between atomic states, especially the de-excitation of excited states [38]. Stimulated decay of dark matter axions has been recently considered [39]. A field of photons can stimulate the decay of axions when one of the decay photons has a momentum matching that of the field.

They are in the same state if their momentum is close enough together that they are still in-phase when the first one decays; the field of final-state particles stimulates decay to that same final state [40]. The possibility of stimulated meson decay inside nuclei (where final state mesons would already be present) has also been proposed [41]. In UPCs, stimulated decay could appear in decays like $\rho \to \pi^+\pi^-$, where the $\pi^\pm$ from multiple decays might cluster in phase space. In contrast, for decays like $J/\psi \to e^+e^-$, the fermionic statistics should preclude final state lepton clustering.

4 Conclusions

Coherence is an interesting and subtle topic, with important consequences. The Good-Walker paradigm relates coherent and incoherent photoproduction to the average nuclear configuration and configuration fluctuations respectively. In Good-Walker coherence means that the target remains in the ground state. That disagrees with some experimental observations of coherent photoproduction. An alternate approach to coherence adding amplitudes, can explain data where Good-Walker fails. The 'adding amplitudes' approach allows some new coherent UPCs channels, including coherent photoproduction of charged mesons.

UPC production of multiple vector mesons introduces several new quantum mechanical observables. When multiple mesons are produced in the forward direction, then superradiant emission may occur, increasing the probability of multiple mesons. It may even be possible to observe the stimulated decay of vector mesons.

Acknowledgments

I thank Minjung Kim for useful comments on this manuscript. This work is supported in part by the U.S. Department of Energy, Office of Science, Office of Nuclear Physics, under contract numbers DE-AC02-05CH11231.

References

1. C. A. Bertulani, S. R. Klein and J. Nystrand, Ann. Rev. Nucl. Part. Sci. **55**, 271-310 (2005) doi:10.1146/annurev.nucl.55.090704.151526 [arXiv:nucl-ex/0502005 [nucl-ex]].
2. A. J. Baltz *et al.* Phys. Rept. **458**, 1-171 (2008) doi:10.1016/j.physrep.2007.12.001 [arXiv:0706.3356 [nucl-ex]].
3. J. G. Contreras and J. D. Tapia Takaki, Int. J. Mod. Phys. A **30**, 1542012 (2015) doi:10.1142/S0217751X15420129
4. S. Klein and P. Steinberg, Ann. Rev. Nucl. Part. Sci. **70**, 323-354 (2020) doi:10.1146/annurev-nucl-030320-033923 [arXiv:2005.01872 [nucl-ex]].
5. D. d'Enterria and G. G. da Silveira, Phys. Rev. Lett. **111**, 080405 (2013) [erratum: Phys. Rev. Lett. **116**, no.12, 129901 (2016)] doi:10.1103/PhysRevLett.111.080405 [arXiv:1305.7142 [hep-ph]].
6. R. Bruce, D. d'Enterria, A. de Roeck, M. Drewes, G. R. Farrar, A. Giammanco, O. Gould, J. Hajer, L. Harland-Lang and J. Heisig, *et al.* J. Phys. G **47**, no.6, 060501 (2020) doi:10.1088/1361-6471/ab7ff7 [arXiv:1812.07688 [hep-ph]].

7. S. R. Klein and H. Mäntysaari, Nature Rev. Phys. **1**, no.11, 662-674 (2019) doi:10.1038/s42254-019-0107-6 [arXiv:1910.10858 [hep-ex]].
8. K. J. Eskola, C. A. Flett, V. Guzey, T. Löytäinen and H. Paukkunen, Phys. Rev. C **106**, no.3, 035202 (2022) doi:10.1103/PhysRevC.106.035202 [arXiv:2203.11613 [hep-ph]].
9. M. L. Good and W. D. Walker, Phys. Rev. **120**, 1857-1860 (1960) doi:10.1103/PhysRev.120.1857
10. H. I. Miettinen and J. Pumplin, Phys. Rev. D **18**, 1696 (1978) doi:10.1103/PhysRevD.18.1696
11. S. Munier, A. M. Stasto and A. H. Mueller, Nucl. Phys. B **603**, 427-445 (2001) doi:10.1016/S0550-3213(01)00168-7 [arXiv:hep-ph/0102291 [hep-ph]].
12. L. Adamczyk *et al.* [STAR], Phys. Rev. C **96**, no.5, 054904 (2017) doi:10.1103/PhysRevC.96.054904 [arXiv:1702.07705 [nucl-ex]].
13. S. R. Klein [STAR], SciPost Phys. Proc. **8**, 128 (2022) doi:10.21468/SciPostPhysProc.8.128 [arXiv:2107.10447 [nucl-ex]].
14. S. Acharya *et al.* [ALICE], Phys. Lett. B **817**, 136280 (2021) doi:10.1016/j.physletb.2021.136280 [arXiv:2101.04623 [nucl-ex]].
15. S. R. Klein, Phys. Rev. C **107**, no.5, 055203 (2023) doi:10.1103/PhysRevC.107.055203 [arXiv:2301.01408 [hep-ph]].
16. C. Adler *et al.* [STAR], Phys. Rev. Lett. **89**, 272302 (2002) doi:10.1103/PhysRevLett.89.272302 [arXiv:nucl-ex/0206004 [nucl-ex]].
17. B. I. Abelev *et al.* [STAR], Phys. Rev. C **77**, 034910 (2008) doi:10.1103/PhysRevC.77.034910 [arXiv:0712.3320 [nucl-ex]].
18. S. Acharya *et al.* [ALICE], JHEP **06**, 035 (2020) doi:10.1007/JHEP06(2020)035 [arXiv:2002.10897 [nucl-ex]].
19. A. J. Baltz, S. R. Klein and J. Nystrand, Phys. Rev. Lett. **89**, 012301 (2002) doi:10.1103/PhysRevLett.89.012301 [arXiv:nucl-th/0205031 [nucl-th]].
20. G. Baur, K. Hencken, A. Aste, D. Trautmann and S. R. Klein, Nucl. Phys. A **729**, 787-808 (2003) doi:10.1016/j.nuclphysa.2003.09.006 [arXiv:nucl-th/0307031 [nucl-th]].
21. G. Baur, K. Hencken and D. Trautmann, Phys. Rept. **453**, 1-27 (2007) doi:10.1016/j.physrep.2007.09.002 [arXiv:0706.0654 [nucl-th]].
22. J. Adam *et al.* [STAR], Phys. Rev. Lett. **123**, no.13, 132302 (2019) doi:10.1103/PhysRevLett.123.132302 [arXiv:1904.11658 [hep-ex]].
23. S. Acharya *et al.* [ALICE], Phys. Lett. B **846**, 137467 (2023) doi:10.1016/j.physletb.2022.137467 [arXiv:2204.10684 [nucl-ex]].
24. R. Aaij *et al.* [LHCb], Phys. Rev. C **105**, no.3, L032201 (2022) doi:10.1103/PhysRevC.105.L032201 [arXiv:2108.02681 [hep-ex]].
25. W. Zha, S. R. Klein, R. Ma, L. Ruan, T. Todoroki, Z. Tang, Z. Xu, C. Yang, Q. Yang and S. Yang, Phys. Rev. C **97**, no.4, 044910 (2018) doi:10.1103/PhysRevC.97.044910 [arXiv:1705.01460 [nucl-th]].
26. M. Kłusek-Gawenda and A. Szczurek, Phys. Rev. C **93**, no.4, 044912 (2016) doi:10.1103/PhysRevC.93.044912 [arXiv:1509.03173 [nucl-th]].
27. S. R. Klein and Y. P. Xie, Phys. Rev. C **100**, no.2, 024620 (2019) doi:10.1103/PhysRevC.100.024620 [arXiv:1903.02680 [nucl-th]].
28. X. Sun [STAR], Acta Phys. Polon. Supp. **16**, no.1, 1-A139 (2023) doi:10.5506/APhysPolBSupp.16.1-A139
29. S. Klein and J. Nystrand, Phys. Rev. C **60**, 014903 (1999) doi:10.1103/PhysRevC.60.014903 [arXiv:hep-ph/9902259 [hep-ph]].
30. M. Kłusek-Gawenda and A. Szczurek, Phys. Rev. C **89**, no.2, 024912 (2014) doi:10.1103/PhysRevC.89.024912 [arXiv:1309.2463 [nucl-th]].
31. C. N. Azevedo, V. P. Goncalves and B. D. Moreira, Eur. Phys. J. A **59**, no.8, 193 (2023) doi:10.1140/epja/s10050-023-01114-4 [arXiv:2306.05519 [hep-ph]].
32. S. R. Klein and J. Nystrand, Phys. Rev. Lett. **84**, 2330-2333 (2000) doi:10.1103/PhysRevLett.84.2330 [arXiv:hep-ph/9909237 [hep-ph]].
33. B. I. Abelev *et al.* [STAR], Phys. Rev. Lett. **102**, 112301 (2009) doi:10.1103/PhysRevLett.102.112301 [arXiv:0812.1063 [nucl-ex]].
34. M. Abdallah *et al.* [STAR], Sci. Adv. **9**, no.1, eabq3903 (2023) doi:10.1126/sciadv.abq3903 [arXiv:2204.01625 [nucl-ex]].
35. S. R. Klein and J. Nystrand, Phys. Lett. A **308**, 323-328 (2003) doi:10.1016/S0375-9601(03)00076-8 [arXiv:quant-ph/0206060 [quant-ph]].
36. C. Li, J. Zhou and Y. J. Zhou, Phys. Lett. B **795**, 576-580 (2019)

doi:10.1016/j.physletb.2019.07.005 [arXiv:1903.10084 [hep-ph]].
37. G. Björk, A. Karlsson and Y. Yamamoto, Phys. ReV. A **5**0, 1675 (1994).
38. F. De Martini and G. R. Jacobovitz, Phys. Rev. Lett. **60**, 1711 (1988).
39. A. Caputo, H. Liu, S. Mishra-Sharma, M. Pospelov and J. T. Ruderman, Phys. Rev. D **107**, no.12, 123033 (2023) doi:10.1103/PhysRevD.107.123033 [arXiv:2206.07713 [hep-ph]].
40. A. Caputo, M. Regis, M. Taoso and S. J. Witte, JCAP **03**, 027 (2019) doi:10.1088/1475-7516/2019/03/027 [arXiv:1811.08436 [hep-ph]].
41. W. H. Furry and J. N. Snyder, Phys. Rev. **75**, 1265 (1949).

Measurement of the impact-parameter dependent azimuthal anisotropy in coherent ρ^0 photoproduction with ALICE

A. G. Riffero (for the ALICE Collaboration)
University and INFN Torino, Italy

Coherent vector meson photoproduction in ultraperipheral heavy-ion collisions is a well-established tool to probe the gluon structure of the colliding nuclei. We will focus on the observation of quantum interference effects in the ρ^0 meson photoproduction, in the form of angular anisotropy. Such an anisotropy appears due to two different factors: first, the photons involved in the process are linearly polarized along the impact parameter, and, second, quantum interference occurs between the two amplitudes that contribute to the ρ^0 photoproduction cross section. Furthermore, the interference effect strongly depends on the impact parameter of the collision, which acts as the distance between the openings of a two-slit interferometer. We present the first measurement of this anisotropy in coherent ρ^0 photoproduction from ultraperipheral Pb–Pb collisions at a center-of-mass energy of $\sqrt{s_{\rm NN}} = 5.02$ TeV per nucleon pair, as a function of the impact parameter of the collision. The latter is estimated by classifying the events in nuclear-breakup classes defined by neutron emission. The ρ^0 mesons are detected by the ALICE experiment through their decay into a pion pair. The anisotropy occurs as a function of ϕ, defined as the azimuth angle between the two vectors formed by the sum, and the difference, of the transverse-momentum of the pions, respectively. It results in a $\cos(2\phi)$ modulation of the photoproduced ρ^0; the amplitude of the modulation is found to increase by about one order of magnitude from large to small impact parameters. This trend is compatible with the available theoretical predictions.

DOI: https://doi.org/10.17161/p17qpn24
Keywords: coherent photoproduction, ρ^0, azimuthal anisotropy, impact parameter

1 Introduction

Ultra-peripheral collisions (UPCs) occur when the impact parameter of the collision is greater than the sum of the radii of the colliding nuclei. In UPCs, due to the short range of the strong force, purely hadronic interactions are highly suppressed, allowing one to study photon-induced processes [1, 2, 3, 4]. In these interactions the electric charges of the colliding nuclei work coherently and produce an intense electromagnetic field, that can be described in terms of a flux of quasi-real photons.

Of great interest is the photoproduction of a vector meson, that is a well established tool to probe the gluon structure of the colliding nuclei. In this process one of the nuclei emits a photon that fluctuates into a quark–antiquark color dipole, which interacts strongly with the other nucleus and appears as a real vector meson. The photo-nuclear interaction can be either coherent, if the photon couples with the whole nucleus, or incoherent if it couples with only one nucleon. These processes can be disentangled using the transverse momentum of the produced vector meson, that is related to the size of the target in the impact-parameter plane, and it is of the order of 60 (500) MeV/c in the coherent (incoherent) case.

In the coherent case, it is not known which of the nuclei emits the photon and which acts as the target in the interaction, opening up the possibility to study, at femtometer scales, the fundamental quantum mechanical interference between the amplitudes [5]. At the Large Hadron Collider (LHC), the photoproduction process occurs through the exchange of a Pomeron, a color-neutral two-gluon state at lowest order. This restricts the production site within one of the two nuclei, therefore this process can be seen as a double slit experiment at fm scale, where the impact-parameter acts as the distance between the openings of the interferometer. In Ref [5] it is also shown that the interference effect involved should be

stronger at mid-rapidity, where the two amplitudes are almost the same, and at small impact parameter.

The strong electromagnetic fields in UPCs of heavy ions can cause multiple photon exchanges in a single collision. These additional photons usually lead to independent electromagnetic dissociation (EMD) processes accompanying the coherent vector meson photoproduction. These EMD processes are useful because they allow one to select different impact parameter ranges [6], always remaining ultra-peripheral, by means of neutrons emitted at beam rapidities by the excited nuclei.

Experimentally, the emitted neutrons can be detected using two zero-degree calorimeters (ZDCs) each of them covering the direction of one of the incoming colliding nuclei. UPCs can therefore be classified as: (*i*) 0n0n, if no neutrons are detected in the ZDCs, (*ii*) Xn0n + 0nXn, if at least one neutron is detected in only one of the ZDCs, and (*iii*) XnXn, if both ZDCs have neutron signal. For brevity, the Xn0n + 0nXn class will be denoted as Xn0n in the following. The intensity of the electromagnetic field decreases with increasing impact parameter. XnXn events, where at least three photons are exchanged, are dominated by relatively small impact parameters. Xn0n events select a broader impact-parameter range than XnXn, while 0n0n events cover all possible impact parameters. EMD is modeled in the RELDIS [7, 8] and $\mathbf{n^{O}_{O}n}$ [9] models, while the coherent production of vector mesons accompanied by electromagnetic dissociation is studied with $\mathbf{n^{O}_{O}n}$ and STARlight [10].

Since the electromagnetic fields of the colliding nuclei are highly Lorentz-contracted, the exchanged photons are fully linearly polarized. In Ref. [11] it has been proposed that due to this polarization the interference effect can give rise to an azimuthal anisotropy in the di-lepton production from photon-photon fusion. This effect has also been studied as a function of the impact parameter in Ref. [12], and measured, for XnXn events by the STAR Collaboration in Au–Au UPCs at $\sqrt{s_{\rm NN}} = 200$ GeV [13].

These studies were later extended to the photoproduction of a ρ^0 vector meson, where the ρ^0 inherits the linear polarization of the photon. The interference correlates momentum and polarization, ensuring that the anisotropy of the decay of a spin-1 particle into two spin-less products is preserved when averaging over events with random impact parameters. The anisotropy here is predicted to manifest as a $\cos(2\phi)$ asymmetry [14, 15], where the angle ϕ is defined as the angle between the two vectors formed by the sum and by the difference of the $p_{\rm T}$ of the pions produced in the decay $\rho^0 \to \pi^+\pi^-$.

The predicted $\cos(2\phi)$ asymmetry has been measured by the STAR Collaboration, for coherent ρ^0 photoproduction in XnXn events, in Au–Au and U–U UPCs at $\sqrt{s_{\rm NN}} = 200$ GeV and $\sqrt{s_{\rm NN}} = 193$ GeV, respectively [16]. This asymmetry has also been recently studied by the CMS Collaboration using exclusive diffractive production of jets at the LHC [17].

Here, we report the first measurement of the impact-parameter dependence of the $\cos(2\phi)$ asymmetry in Pb–Pb UPCs at $\sqrt{s_{\rm NN}} = 5.02$ TeV using the coherent photoproduction of a ρ^0 meson. The ρ^0 meson is detected through its decay into a pion pair at midrapidity. The strength of the anisotropy is measured in three different EMD classes (0n0n, Xn0n, and XnXn) that select different impact parameter ranges.

2 Experimental set-up

A full description of the ALICE apparatus and its performance is given in Refs. [18, 19]. We present in the following a brief description of the sub-detectors involved in the measurement presented in this analysis. The pion tracks are reconstructed using the Inner Tracking System (ITS) [20], a six-layer silicon tracker coaxial to the beam line, and the Time Projection Chamber (TPC) [21], a big gaseous detector that surrounds the ITS. The two innermost layers of the ITS form the Silicon Pixel Detector (SPD), that is also used for triggering. The TPC provides also particle identification, via the measurement of the specific ionization energy loss.

The V0 [22] and ALICE Diffractive (AD) [23] detectors, located at forward rapidities, are formed by scintillator arrays on both sides of the interaction point (IP) and provide a veto, suppressing hadronic interactions.

The impact parameter ranges mentioned in Sec. 1 are selected by detecting the neutrons emitted at forward rapidity, using the Zero Degree Calorimeters. There are two ZDC detectors for neutrons, one per side of the IP, that have an energy resolution good enough to be sensitive to the emission of a single neutron.

The analyzed data were collected by ALICE in 2015, during the Run 2 of the LHC, using Pb–Pb collisions at $\sqrt{s_{\rm NN}} = 5.02$ TeV, and a dedicated UPC trigger. This trigger is formed by five different signals: four of them veto any activity of the AD or V0 detector within the time window for nominal beam–beam interactions, to suppress hadronic collisions. The fifth signal is a topological trigger that selects events that have at least two track segments [24] in the SPD, with an opening angle in azimuth greater than 153 degrees. This topology was chosen since the tracks of the pions are almost back-to-

back in azimuth, due to the very small transverse momentum of coherently produced ρ^0. The integrated luminosity of the sample, determined using the V0 detectors as explained in Ref. [24], is about 485 mb^{-1}.

3 Data analysis

3.1 Event and track selection

The events selected for the analysis were required to have good-quality tracks. A track is considered good if (*i*) it has more than 50 associated TPC clusters, (*ii*) has been reconstructed in both ITS and TPC and matches the track segments in the SPD that fired the trigger, and (*iii*) has a distance of closest approach to the event primary vertex smaller than $0.0182 + 0.0350/(p_{\mathrm{T}}^{\mathrm{trk}})^{1.01}$ cm in the transverse plane and smaller than 2 cm in the longitudinal direction, where $p_{\mathrm{T}}^{\mathrm{trk}}$ is the transverse momentum, in GeV/c, associated to the track.

The passing event were required to fulfill additional selections: (*i*) have exactly two opposite-sign tracks, (*ii*) have no offline reconstructed signal in neither the V0 nor AD detectors, and (*iii*) fulfill the pion selection $\mathrm{n}_{\sigma 1}^2 + \mathrm{n}_{\sigma 2}^2 < 5^2$, where $\mathrm{n}_{\sigma 1}$ ($\mathrm{n}_{\sigma 2}$) is the difference, in units of the TPC ionization energy loss resolution, between the measured energy loss for track 1 (track 2) and the expected value for a pion with the same momentum.

Kinematic selections were also applied: (*i*) the pion pair rapidity must lie in the range $|y| < 0.8$ to avoid acceptance edge effects, (*ii*) the invariant mass of the pion pair must be inside the range $0.6\ \mathrm{GeV}/c^2 < m_{\pi\pi} < 0.95\ \mathrm{GeV}/c^2$, and (*iii*) the transverse momentum (p_{T}) of the ρ^0 candidate must be less than 0.1 GeV/c to select coherent processes with high purity. Using these selection criteria, the contamination from incoherent events is found to be lower than 4% [24]. More details about event and track selections can be found in Ref. [24].

3.2 ϕ definition

The observable used to measure the azimuthal anisotropy described in Sec. 1 is the azimuth angle ϕ, defined through the transverse momentum of the pions into which the ρ^0 decays. The ϕ angle can be defined in two different ways, indicated, respectively, as *average* and *charge*. In both cases ϕ is the angle between the transverse components of $\vec{p}_+$ and $\vec{p}_-$, where $\vec{p}_\pm = \vec{\pi}_1 \pm \vec{\pi}_2$. Using the *charge* definition, $\vec{\pi}_1$ and $\vec{\pi}_2$ are, respectively, the momentum of the positive and of the negative track. Using the *average* definition, $\vec{\pi}_{1,2}$ are randomly associated to the positive or to the negative track. The *average* definition, that by construction does not allow for a $\cos(\phi)$ component, has been used as default, while the *charge* definition has been used in the evaluation of systematic uncertainties.

3.3 Monte Carlo corrections

A Monte Carlo (MC) simulation, using the STARlight MC generator and a realistic description of the ALICE detector has been used to estimate the correction for acceptance and efficiency ($\mathrm{Acc} \times \epsilon$) to detect the pion tracks. This simulation describes the raw data kinematics well, with the exception of the transverse momentum distribution [25]. In order to improve the agreement between MC and data, a re-weighting procedure has been applied to the generated p_{T}^2 spectrum. The procedure consists of two steps: the first is to fit the inclusive pion pair p_{T}^2 distribution of the generated MC using the function:

$$\frac{\mathrm{d}N}{\mathrm{d}p_{\mathrm{T}}^2} = c \mid F(\mid t \mid,\ a_{\mathrm{Pb}},\ R_{\mathrm{Pb}}) \mid^2, \tag{1}$$

where c is a normalization constant and $F(\mid t \mid)$ is the form factor of the lead nucleus, obtained as a numerical approximation of the Fourier transform of a Wood-Saxon function [26, 27], and R_{Pb} and a_{Pb} are fit parameters. This is possible since for sufficiently high transverse momentum, p_{T}^2 can be approximated with the Mandelstam variable t. The second step is to obtain the weights using

$$\mathrm{w}(p_{\mathrm{T}}) = \frac{\mid F(\mid t \mid,\ a_{\mathrm{Pb}},\ R_{\mathrm{X}}) \mid^2}{\mid F(\mid t \mid,\ a_{\mathrm{Pb}},\ R_{\mathrm{Pb}}) \mid^2}, \tag{2}$$

where a_{Pb} is fixed to the fit result and R_{X} is chosen in such a way that, after applying the weights to each event of a given generated p_{T}, the reconstructed p_{T}^2 spectrum in the MC best reproduces the one in the data. This is achieved by minimizing the bin-by-bin difference between the p_{T} distributions of data and reconstructed MC as a function of R_{X}, using a χ^2-like variable. It was verified that the same R_{X} can

be used to reproduce the data in all ϕ bins, therefore the weights were computed using the integrated data sample.

The Acc $\times$ ϵ correction was obtained using the STARlight MC simulations by computing the ratio of reconstructed to generated number of pion pairs in each invariant mass and ϕ interval, after applying the weights discussed above at the generation level. The raw invariant mass spectra of pion pairs, for each invariant mass and ϕ interval, was then divided by Acc $\times$ ϵ, to obtain the corrected mass spectra.

3.4 Signal extraction

The corrected mass spectra, in each neutron class and in each ϕ bin, were fitted using a modified Söding model [28] to extract the different contributions to the production of pion pairs. The fitting function is

$$\frac{dN}{dm_{\pi\pi}} = \mid A \cdot BW_\rho + B \mid^2 + n_{\mu\mu}\, M(m_{\pi\pi}), \tag{3}$$

where $m_{\pi\pi}$ is the pion pair invariant mass, BW_ρ is the relativistic Breit-Wigner shape that describes the ρ^0, A is its amplitude and B is the amplitude of the continuum pion pair production. The last term models the background originating from muons produced in the $\gamma\gamma \to \mu^+\mu^-$ process that have been misidentified as pions, with a shape $M(m_{\pi\pi})$ estimated with a dedicated MC, based on the STARlight generator, and the normalization constant $n_{\mu\mu}$ as a parameter of the fit. As discussed in Ref. [24], it was verified that the contribution from the ω decay is negligible since the ρ^0 yield does not vary significantly if it is not fixed to zero.
The relativistic Breit-Wigner function describing the ρ^0 resonance is:

$$BW_\rho = \frac{\sqrt{m_{\pi\pi} \cdot m_\rho \cdot \Gamma_\rho(m_{\pi\pi})}}{m_{\pi\pi}^2 - m_\rho^2 + i \cdot m_\rho \cdot \Gamma_\rho(m_{\pi\pi})} \tag{4}$$

and its width is:

$$\Gamma_\rho(m_{\pi\pi}) = \Gamma(m_\rho) \cdot \frac{m_\rho}{m_{\pi\pi}} \cdot \left(\frac{m_{\pi\pi}^2 - 4m_\pi^2}{m_\rho^2 - 4m_\pi^2} \right)^{3/2}. \tag{5}$$

The fits were performed by fixing the pole mass m_ρ and the pole width $\Gamma(m_\rho)$ of the ρ^0 to the values reported for a ρ^0 formed in a photoproduction reaction, namely, $m_\rho = 769.2$ MeV/c^2 and $\Gamma(m_\rho) = 151.5$ MeV/c^2 [29]. A default strategy was chosen to extract the central value of the asymmetry parameter. In this strategy, the *average* definition of ϕ is used and the background contribution is fixed to zero in the invariant mass fits. Different strategies were explored and are used for the systematic uncertainty evaluation. To check the robustness of the fit procedure, the fit of the invariant mass distribution were repeated 100 times, using each time a different binning and fit ranges; the lower limit of the fit range was varied from 0.6 to 0.65 GeV/c^2, and the upper limit from 0.9 to 0.95 GeV/c^2. An example of the mass fits, performed with the default strategy for a specific ϕ interval and for the 0n0n and XnXn classes, is shown in Fig. 1. After the fit, the ρ^0 yield is obtained by integrating the signal function $|A\, BW_\rho|^2$ in the mass range $0.6 < m_{\pi\pi}$ (GeV/c^2) < 0.95. Such a range was chosen to be consistent with the STAR measurement [16] and with available theory calculations (see Sec. 4 for details).

3.5 Asymmetry extraction

The extraction of the amplitude of the modulation is affected by the migration of events between neutron classes, due to detector efficiency and pile-up effects, as discussed in Ref. [24]. To take this into account, a simultaneous fit to the ρ^0 yield as a function of ϕ in all three classes (0n0n, Xn0n, XnXn) was performed, using the following expression:

$$\begin{pmatrix} n_{\rho\,\mathrm{0n0n}(\phi)} \\ n_{\rho\,\mathrm{Xn0n}(\phi)} \\ n_{\rho\,\mathrm{XnXn}(\phi)} \end{pmatrix} = \begin{pmatrix} 1 \\ 1 \\ 1 \end{pmatrix} + \begin{pmatrix} w_{\,\mathrm{0n0n}\,\to\,\mathrm{0n0n}} & w_{\,\mathrm{Xn0n}\,\to\,\mathrm{0n0n}} & w_{\,\mathrm{XnXn}\,\to\,\mathrm{0n0n}} \\ w_{\,\mathrm{0n0n}\,\to\,\mathrm{Xn0n}} & w_{\,\mathrm{Xn0n}\,\to\,\mathrm{Xn0n}} & w_{\,\mathrm{XnXn}\,\to\,\mathrm{Xn0n}} \\ w_{\,\mathrm{0n0n}\,\to\,\mathrm{XnXn}} & w_{\,\mathrm{Xn0n}\,\to\,\mathrm{XnXn}} & w_{\,\mathrm{XnXn}\,\to\,\mathrm{XnXn}} \end{pmatrix} \begin{pmatrix} a_{2\,\mathrm{0n0n}} \\ a_{2\,\mathrm{Xn0n}} \\ a_{2\,\mathrm{XnXn}} \end{pmatrix} \cos(2\phi), \tag{6}$$

where $n_{\rho\,\mathrm{0n0n}}$ is the normalized ρ^0 yield in a given ϕ range for the 0n0n class, and similarly for other classes, and the fitting parameters $a_{2\,\mathrm{0n0n}}$, $a_{2\,\mathrm{Xn0n}}$ and $a_{2\,\mathrm{XnXn}}$ are the amplitudes of the $\cos(2\phi)$ modulation in the three classes. The coefficients $w_{\,\mathrm{Y}\,\to\,\mathrm{Z}}$ represent the contribution of the physical neutron class Y to the yield in the experimental neutron class Z, computed using the measured cross sections and migration probabilities as determined in Ref. [24]. The constant term is fixed to unity by normalization.

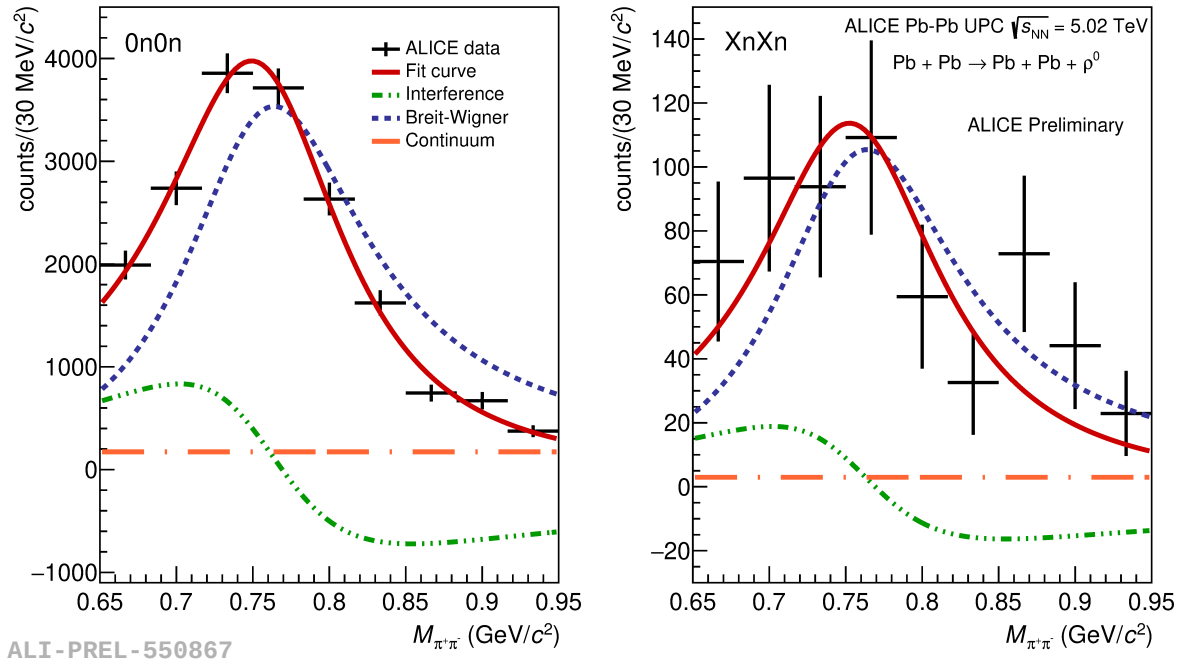

Figure 1 – Invariant-mass distribution of pion pairs, with a superimposed Söding fit, for the range $36° < \phi < 60°$, and for the default strategy discussed in the text, in the 0n0n (left) and XnXn (right) neutron classes. The different components of the pion-pair production amplitude are shown: the Breit-Wigner shape that describes the ρ^0 (dotted line), the continuum process (dash-dotted line), and the interference between the ρ^0 and the continuum (dash-dot-dot-dot line).

This simultaneous fitting procedure is repeated 100 times, on the different distributions of the ρ^0 as a function of ϕ provided by the signal extraction procedure explained in Sec. 3.4. An example of this simultaneous fit is shown in Fig. 2.

In each class, the central value of modulation has been taken as the mean value of the distribution of the amplitude, and the statistical uncertainty has been evaluated as the mean value of the distribution of the uncertainties from the fit.

3.6 Systematic uncertainties

The systematic uncertainties affecting the results presented here can be grouped in two categories: signal extraction and Acc $\times$ ϵ.

The systematic uncertainty related to the signal extraction has three contributions. The first has been evaluated as the standard deviation of the distribution of the $\cos(2\phi)$ amplitudes over the 100 trials mentioned above. The second contribution comes from using an alternative model, by Ross and Stodolsky [30], to fit the invariant mass distributions, and has been evaluated as the difference between the amplitudes obtained using the two models. The third contribution was estimated using different strategies for the measurement of the ρ^0 yield as a function of ϕ. The considered strategies include using the *charge* or *average* definition of ϕ, and setting or not the muon background to zero in the mass fits. Note that, in *charge* mode, the ρ^0 yield as a function of ϕ may have a $\cos(\phi)$ component [31], which was added to the fit function of Eq. 6. This may or may not be done for the *average* mode, resulting in six different possible strategies (including the default one). The systematic uncertainty due to the choice of a strategy has been evaluated as the difference between the result obtained with the default strategy and the mean value of results obtained with the others.

The systematic uncertainty on the Acc $\times$ ϵ mainly arises from the re-weighting procedure described in Sec. 3.3. It was obtained by using, instead of the $R_{\rm X}$ value that minimizes the χ^2, the two values of $R_{\rm X}$ for which the χ^2 increases by one unit with respect to the minimum. The systematic uncertainty is estimated as the larger difference, in each class and for the default strategy, between the results obtained with the original and with the modified sets of weights. As a consistency check, it was also verified that, when the analysis is performed in rapidity sub-ranges containing roughly half of the total number of events, the extracted amplitudes are all compatible with each other within one standard deviation.

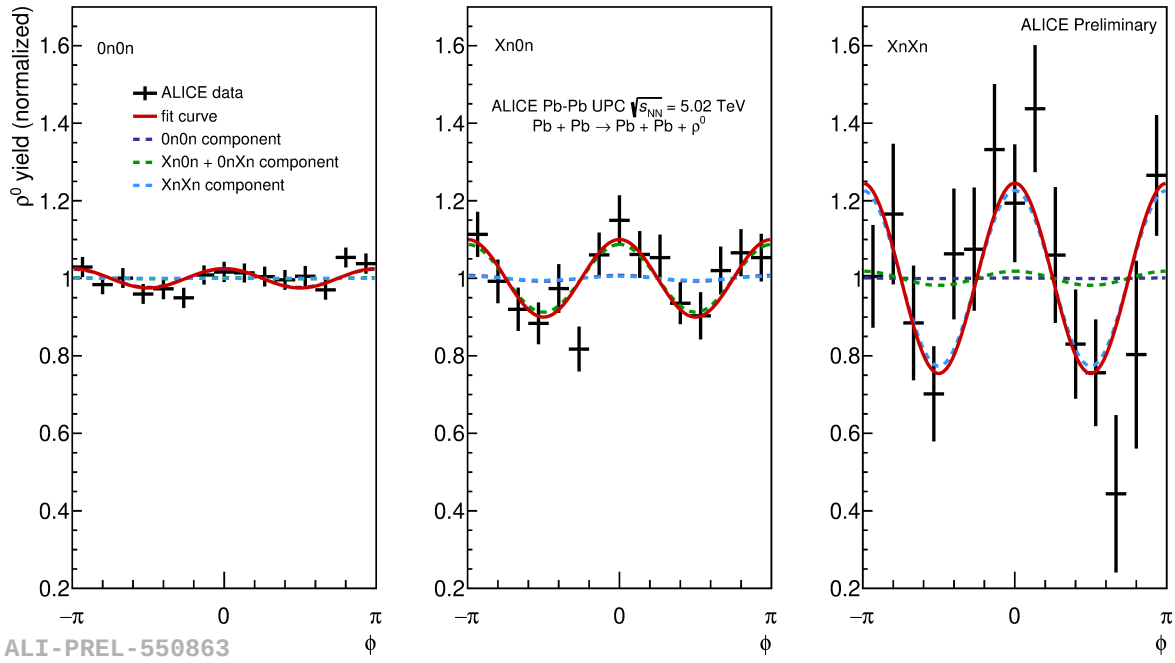

Figure 2 – Example of a simultaneous fit used to extract the amplitude of the $\cos(2\phi)$ modulation in all neutron classes. The contribution of each physical class to the yield in all experimental classes is shown.

4 Results

Figure 3 shows the extracted amplitude of the $\cos(2\phi)$ modulation as a function of the neutron class. The measured anisotropy shows a clear trend, with a significant increase, by approximately one order of magnitude, from 0n0n to XnXn, which according to $\mathbf{n^{O}_{O}n}$ corresponds to a variation of the median impact parameter between, approximately, 49 and 18 fm. Similar values can be obtained also using the analytical model presented in Ref. [32]; similar values for XnXn are also reported in Ref. [6]. We quote the median, instead of the mean, impact parameter because it is less sensitive to a tail of interactions extending to very large impact parameters [32].

As discussed in Sec. 1, the $\cos(2\phi)$ anisotropy in the model emerges from the presence of two elements: (*i*) the photon is linearly polarized along the impact parameter and this polarization is transferred to the produced vector meson, (*ii*) the two amplitudes that contribute to the cross section of the vector meson photoproduction process interfere.

The results are compared with the models by H. Xing *et al.* [14] and by W. Zhao *et al.* [33]. In the H. Xing *et al.* model, the quasi-real photon exchanged by the nuclei is treated as a color quark–antiquark dipole, that recombines to produce a ρ^0 after scattering off the color glass condensate state [34] inside the nuclei. The model from W. Zhao *et al.* uses the same formalism of the H. Xing *et al.* model, with two main differences: (*i*) the interaction of the quark–antiquark dipole with the target is implemented by computing the corresponding Wilson lines, and (*ii*) the color charge density used to obtain the Wilson lines is varied event-by-event to represent the different possible color configurations of the target.

The uncertainty of the model by H. Xing *et al.* [14] mostly comes from the probability of emitting a neutron from the scattered nucleus at a given impact parameter, where this latter has been estimated using three different parametrization from Refs. [35, 36, 37]. The model prediction is compatible with data for all neutron classes. In the model by W. Zhao *et al.* [33] the quoted uncertainty originates from the statistical precision from the finite number of sampled configurations. The predictions of this model also give a reasonable description of data, with the possible exception of the 0n0n class.

For the XnXn class, the ALICE result is also compared with the ones from the STAR Collaboration [16], for Au–Au and U–U collisions at a lower center-of-mass energy of $\sqrt{s_{\rm NN}} = 200$ GeV and $\sqrt{s_{\rm NN}} = 193$ GeV, respectively. The amplitude measured by ALICE is compatible with both STAR results. This is consistent with the models, which predict the $\cos(2\phi)$ modulation amplitude to vary with the colliding nuclei and the center-of-mass energy by less than the current experimental uncertainties.

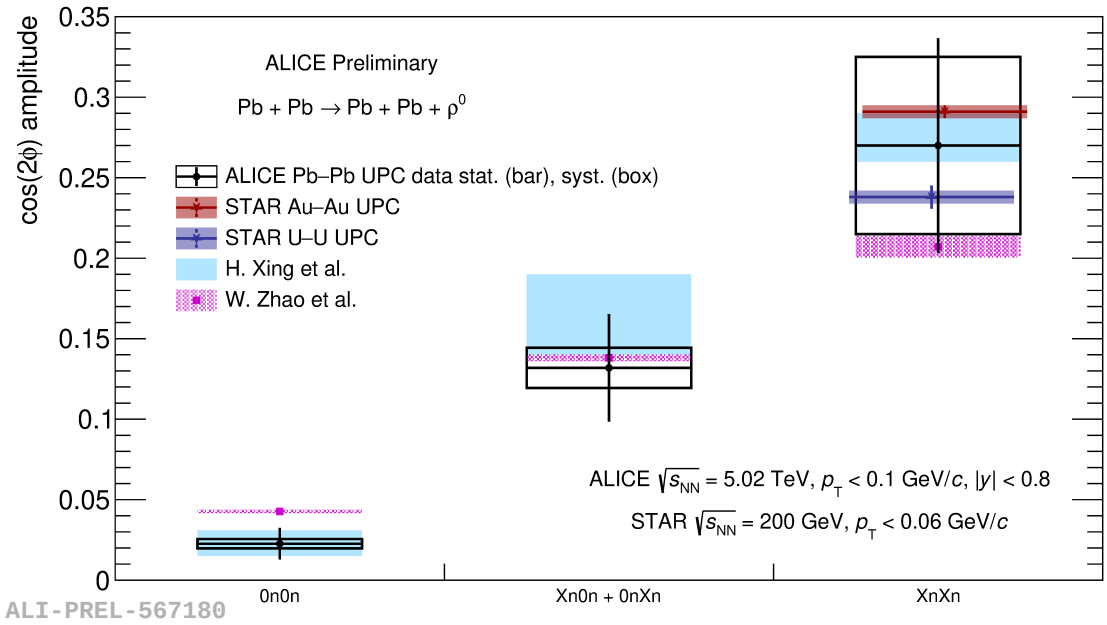

Figure 3 – Amplitudes of the $\cos(2\phi)$ modulation of the ρ^0 yield as a function of the neutron class, compared with the Xing *et al.* [14] and W. Zhao *et al.* [33] model predictions and, for XnXn, with the STAR results [16].

5 Conclusions and outlook

The first measurement of the impact-parameter dependence of the modulation of the ρ^0 yield with the ϕ angle in coherent photoproduction processes from Pb–Pb ultraperipheral collisions at a center-of-mass energy of $\sqrt{s_{\rm NN}} = 5.02$ TeV has been presented. The ρ^0 was detected using the ALICE detector through its decay into a pion pair and the observable ϕ is an azimuthal angle defined in Sec. 3.2. The impact parameter is estimated considering neutron emission at forward rapidity. A significant impact-parameter dependence of the anisotropy strength was observed, with the amplitude of the $\cos(2\phi)$ modulation increasing by about one order of magnitude from the 0n0n (no neutrons emitted, large impact parameter) to the XnXn (neutrons emitted by both colliding nuclei, relatively small impact parameter) class. This trend is well reproduced by the theoretical models [14, 33]. The results for the XnXn class are compatible with those, by the STAR Collaboration, for Au–Au and U–U collisions at RHIC.

The current experimental uncertainties do not allow the measurement to constrain the models, but this will become possible using the large data set that is being collected by ALICE during Run 3 and in the future Run 4 of the LHC. This large amount of data will also enable a more detailed characterization of the quantum interference effects, by means of more differential studies and the study of similar effects in other processes, such as the coherent photoproduction of the J/ψ, where the model predictions are expected to be more accurate.

References

[1] Gerhard Baur et al. "Coherent $\gamma\gamma$ and γA interactions in very peripheral collisions at relativistic ion colliders". In: *Phys.Rept.* 364 (2002), pp. 359–450. DOI: 10.1016/S0370-1573(01)00101-6. arXiv: hep-ph/0112211 [hep-ph].

[2] A. J. Baltz et al. "The Physics of Ultraperipheral Collisions at the LHC". In: *Phys. Rept.* 458 (2008). Ed. by G. Baur et al., pp. 1–171. DOI: 10.1016/j.physrep.2007.12.001. arXiv: 0706.3356 [nucl-ex].

[3] J. G. Contreras and J. D. Tapia Takaki. "Ultra-peripheral heavy-ion collisions at the LHC". In: *Int. J. Mod. Phys.* A30 (2015), p. 1542012. DOI: 10.1142/S0217751X15420129.

[4] Spencer R. Klein and Heikki Mäntysaari. "Imaging the nucleus with high-energy photons". In: *Nature Rev. Phys.* 1 (2019), pp. 662–674. DOI: 10.1038/s42254-019-0107-6. arXiv: 1910.10858 [hep-ex].

[5] Spencer R. Klein and Joakim Nystrand. "Interference in exclusive vector meson production in heavy ion collisions". In: *Phys. Rev. Lett.* 84 (2000), pp. 2330–2333. DOI: 10.1103/PhysRevLett.84.2330. arXiv: hep-ph/9909237.

[6] Anthony J. Baltz, Spencer R. Klein, and Joakim Nystrand. "Coherent vector meson photoproduction with nuclear breakup in relativistic heavy ion collisions". In: *Phys. Rev. Lett.* 89 (2002), p. 012301. DOI: 10.1103/PhysRevLett.89.012301. arXiv: nucl-th/0205031.

[7] I. A. Pshenichnov et al. "Mutual heavy ion dissociation in peripheral collisions at ultrarelativistic energies". In: *Phys. Rev. C* 64 (2001), p. 024903. DOI: 10.1103/PhysRevC.64.024903. arXiv: nucl-th/0101035.

[8] I. A. Pshenichnov. "Electromagnetic excitation and fragmentation of ultrarelativistic nuclei". In: *Phys. Part. Nucl.* 42 (2011), pp. 215–250. DOI: 10.1134/S1063779611020067.

[9] M. Broz, J. G. Contreras, and J. D. Tapia Takaki. "A generator of forward neutrons for ultra-peripheral collisions: $\mathbf{n}^{\mathbf{O}}_{\mathbf{O}}\mathbf{n}$". In: *Comput. Phys. Commun.* (2020), p. 107181. ISSN: 0010-4655. DOI: https://doi.org/10.1016/j.cpc.2020.107181. arXiv: 1908.08263 [nucl-th].

[10] Spencer R. Klein et al. "STARlight: A Monte Carlo simulation program for ultra-peripheral collisions of relativistic ions". In: *Comput. Phys. Commun.* 212 (2017), pp. 258–268. DOI: 10.1016/j.cpc.2016.10.016. arXiv: 1607.03838 [hep-ph].

[11] Cong Li, Jian Zhou, and Ya-Jin Zhou. "Probing the linear polarization of photons in ultraperipheral heavy ion collisions". In: *Phys. Lett. B* 795 (2019), pp. 576–580. DOI: 10.1016/j.physletb.2019.07.005. arXiv: 1903.10084 [hep-ph].

[12] Cong Li, Jian Zhou, and Ya-Jin Zhou. "Impact parameter dependence of the azimuthal asymmetry in lepton pair production in heavy ion collisions". In: *Phys. Rev. D* 101 (2020), p. 034015. DOI: 10.1103/PhysRevD.101.034015. arXiv: 1911.00237 [hep-ph].

[13] Jaroslav Adam et al. "Measurement of e^+e^- Momentum and Angular Distributions from Linearly Polarized Photon Collisions". In: *Phys. Rev. Lett.* 127 (2021), p. 052302. DOI: 10.1103/PhysRevLett.127.052302. arXiv: 1910.12400 [nucl-ex].

[14] Hongxi Xing et al. "The cos 2ϕ azimuthal asymmetry in ρ^0 meson production in ultraperipheral heavy ion collisions". In: *JHEP* 10 (2020), p. 064. DOI: 10.1007/JHEP10(2020)064. arXiv: 2006.06206 [hep-ph].

[15] Wangmei Zha et al. "Exploring the double-slit interference with linearly polarized photons". In: *Phys. Rev. D* 103 (2021), p. 033007. DOI: 10.1103/PhysRevD.103.033007. arXiv: 2006.12099 [hep-ph].

[16] Mohamed Abdallah et al. "Tomography of ultrarelativistic nuclei with polarized photon-gluon collisions". In: *Sci. Adv.* 9 (2023), eabq3903. DOI: 10.1126/sciadv.abq3903. arXiv: 2204.01625 [nucl-ex].

[17] "Azimuthal Correlations within Exclusive Dijets with Large Momentum Transfer in Photon-Lead Collisions". In: *Phys. Rev. Lett.* 131 (5 Aug. 2023), p. 051901. DOI: 10.1103/PhysRevLett.131.051901. arXiv: 2205.00045 [hep-ex].

[18] K. Aamodt et al. "The ALICE experiment at the CERN LHC". In: *JINST* 3 (2008), S08002. DOI: 10.1088/1748-0221/3/08/S08002.

[19] Betty Abelev et al. "Performance of the ALICE Experiment at the CERN LHC". In: *Int. J. Mod. Phys.* A29 (2014), p. 1430044. DOI: 10.1142/S0217751X14300440. arXiv: 1402.4476 [nucl-ex].

[20] K Aamodt et al. "Alignment of the ALICE Inner Tracking System with cosmic-ray tracks". In: *JINST* 5 (2010), P03003. DOI: 10.1088/1748-0221/5/03/P03003. arXiv: 1001.0502 [physics.ins-det].

[21] J. Alme et al. "The ALICE TPC, a large 3-dimensional tracking device with fast readout for ultra-high multiplicity events". In: *Nucl. Instrum. Meth.* A622 (2010), pp. 316–367. DOI: 10.1016/j.nima.2010.04.042. arXiv: 1001.1950 [physics.ins-det].

[22] E. Abbas et al. "Performance of the ALICE VZERO system". In: *JINST* 8 (2013), P10016. DOI: 10.1088/1748-0221/8/10/P10016. arXiv: 1306.3130 [nucl-ex].

[23] K Akiba et al. "LHC forward physics". In: *Journal of Physics G: Nuclear and Particle Physics* 43.11 (Oct. 2016), p. 110201. DOI: 10.1088/0954-3899/43/11/110201. URL: https://dx.doi.org/10.1088/0954-3899/43/11/110201.

[24] Shreyasi Acharya et al. "Coherent photoproduction of ρ^0 vector mesons in ultra-peripheral Pb–Pb collisions at $\sqrt{s_{\rm NN}}$ = 5.02 TeV". In: *JHEP* 06 (2020), p. 035. DOI: 10.1007/JHEP06(2020)035. arXiv: 2002.10897 [nucl-ex].

[25] J. Adam et al. "Coherent ρ^0 photoproduction in ultra-peripheral Pb–Pb collisions at $\sqrt{s_{\rm NN}}$ = 2.76 TeV". In: *Journal of High Energy Physics* 9 (2015). ISSN: 1029-8479. URL: http://dx.doi.org/10.1007/JHEP09(2015)095.

[26] Spencer R. Klein and Joakim Nystrand. "Exclusive vector meson production in relativistic heavy ion collisions". In: *Phys. Rev.* C60 (1999), p. 014903. DOI: 10.1103/PhysRevC.60.014903. arXiv: hep-ph/9902259 [hep-ph].

[27] L. C. Maximon and R. A. Schrack. "The form factor of the Fermi model spatial distribution". In: *J. Res. Natl. Bur. Stand. B* 70.1 (1966), pp. 85–94. DOI: 10.6028/jres.070b.007.

[28] Allan S. Krass. "Interference Effects in Photoproduction of ϱ^0 Mesons". In: *Phys. Rev.* 159 (5 1967), pp. 1496–1500. DOI: 10.1103/PhysRev.159.1496.

[29] R. L. Workman et al. "Review of Particle Physics". In: *PTEP* 2022 (2022), p. 083C01. DOI: 10.1093/ptep/ptac097.

[30] Marc Ross and Leo Stodolsky. "Photon Dissociation Model for Vector-Meson Photoproduction". In: *Phys. Rev.* 149 (4 1966), pp. 1172–1181. DOI: 10.1103/PhysRev.149.1172.

[31] Yoshikazu Hagiwara et al. "Coulomb nuclear interference effect in dipion production in ultraperipheral heavy ion collisions". In: *Phys. Rev. D* 103 (2021), p. 074013. DOI: 10.1103/PhysRevD.103.074013. arXiv: 2011.13151 [hep-ph].

[32] Gerhard Baur et al. "Multiphoton exchange processes in ultraperipheral relativistic heavy ion collisions". In: *Nucl. Phys. A* 729 (2003), pp. 787–808. DOI: 10.1016/j.nuclphysa.2003.09.006. arXiv: nucl-th/0307031.

[33] Heikki Mäntysaari et al. *Effects of nuclear structure and quantum interference on diffractive vector meson production in ultra-peripheral nuclear collisions*. 2023. arXiv: 2310.15300 [nucl-th]. URL: https://arxiv.org/abs/2310.15300.

[34] Francois Gelis et al. "The Color Glass Condensate". In: *Ann. Rev. Nucl. Part. Sci.* 60 (2010), pp. 463–489. DOI: 10.1146/annurev.nucl.010909.083629. arXiv: 1002.0333 [hep-ph].

[35] Carlos A. Bertulani and Gerhard Baur. "Electromagnetic processes in relativistic heavy ion collisions". In: *Physics Reports* 163.5 (1988), pp. 299–408. ISSN: 0370-1573. DOI: https://doi.org/10.1016/0370-1573(88)90142-1.

[36] A. J. Baltz, M. J. Rhoades-Brown, and J. Weneser. "Heavy-ion partial beam lifetimes due to Coulomb induced processes". In: *Phys. Rev. E* 54 (4 1996), pp. 4233–4239. DOI: 10.1103/PhysRevE.54.4233.

[37] A. J. Baltz and Mark Strikman. "Suppression of heavy ion $\gamma\gamma$ production of the Higgs particle by Coulomb dissociation". In: *Phys. Rev. D* 57 (1 1998), pp. 548–549. DOI: 10.1103/PhysRevD.57.548.

Coherent photoproduction of J/ψ mesons in ultraperipheral PbPb collisions at CMS

L. F. Alcerro (on behalf of the CMS Collaboration)
Department of Physics and Astronomy, The University of Kansas.
Lawrence, Kansas, 66045 USA

In this contribution we briefly describe the CMS results on J/ψ photoproduction in PbPb collisions in which the coherent J/ψ photoproduction cross section as a function of the photon-nucleus center-of-mass energy ($W_{\gamma N}^{\rm Pb}$) was measured up to 400 GeV. The cross section is observed to plateau above $W_{\gamma N}^{\rm Pb} \approx 40$ GeV and up to 400 GeV, accessing very small Bjorken-x values of $\approx 6 \times 10^{-5}$.

DOI: https://doi.org/10.17161/50bk6n12
Keywords: vector meson, ultraperipheral collisions, gluon distribution

1 Introduction

The extreme limit of an off-center collision is one in which a nucleus miss each other, so that the impact parameter is greater than sum of the nuclear radii. In these ultraperipheral collisions (UPCs), the strong electromagnetic fields surrounding the relativistic nuclei enhance photon-photon and photon-nucleus interactions over hadronic processes. Indeed these photo-induced processes dominate the total nucleus-nucleus cross section.

The photoproduction of vector mesons, where the sub process is $\gamma A \to VA$ with $V = J/\psi, \Upsilon(nS), \rho^0$ etc., represents a powerful probe of the nuclear structure, particularly at very small Bjorken-x region, where the gluon saturation is expected to be found. These interactions are usually classified depending on whether the projectile photon interacts with the target ion as a whole (coherent) or if it interacts with a single nucleon inside the ion (incoherent). The coherent production is of particular interest since at LO in pQCD, the photo-nuclear cross section is proportional to the square of the gluon distribution of the target nucleus.

In symmetric collisions, such as PbPb, one of the main difficulties to access small Bjorken-x values is the two-energy photon ambiguity which comes from the fact that either nucleus could serve as the photon emitter or the target. A novel solution to this problem was proposed in [1,2] in which the main idea is to control the collision impact parameter by detecting forward neutrons emitted via electromagnetic dissociation and classifying events in forward neutron multiplicity categories.

The CMS Collaboration exploited the above mentioned strategy to access the small-x region in J//ψ photoproduction in PbPb collisions at $\sqrt{s_{\rm NN}} = 5.02$ TeV [3]. The zero-degree calorimeters (ZDCs) [4] were used to tag forward neutrons and disentangle the low and high energy photon contributions.

2 Dataset and event selection

This analysis used PbPb UPCs collisions collected at the CMS experiment at the LHC in 2018. The data correspond to an integrated luminosity of 1.52 nb^{-1}. The event candidates are online selected with a trigger that requires at least one muon candidate coincident with a Pb-Pb bunch crossing. For the off-line analysis, events are required to have a primary vertex formed by using two or more tracks. In addition, in order to suppress hadronic interactions, the selected events are required to have energy depositions less than 7.3 and 7.6 GeV in forward calorimeters with positive and negative rapidities, respectively.

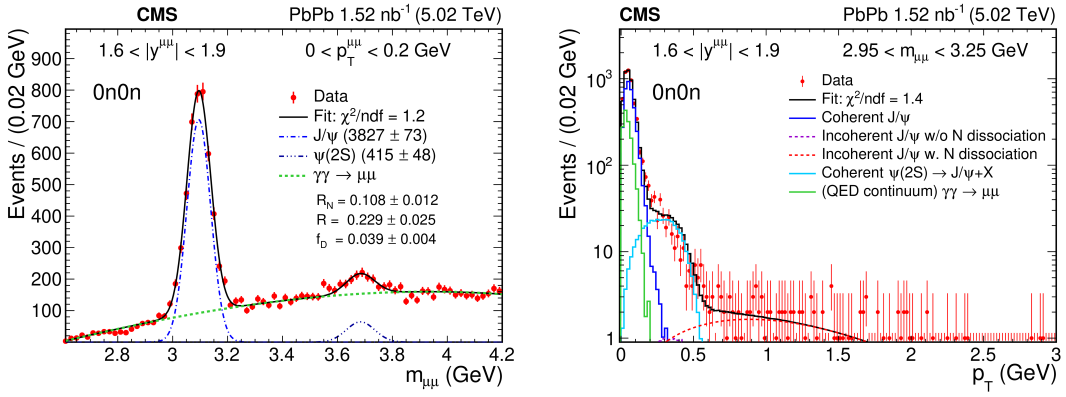

Figure 1 – Invariant mass (left) and transverse momentum distribution (right) of $\mu^+\mu^-$ pairs in the 0n0n neutron class.

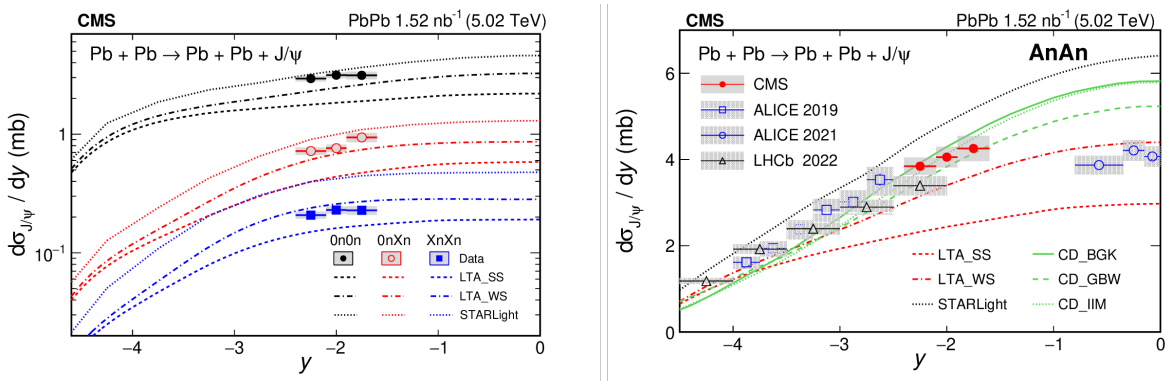

Figure 2 – Differential coherent J/ψ photoproduction cross section as a function of rapidity in different forward neutron multiplicity categories.

Pairs of high-quality muons of opposite sign within an invariant mass in the range $2.6 < m_{\mu\mu} < 4.2$ GeV are selected as J/ψ and ψ(2S) candidates.

3 Signal extraction

The signal extraction strategy relies on studying the dimuon mass and transverse momentum distributions. By looking at the invariant mass spectrum one can separate the raw number of J/ψ signal events from the main background process coming from QED $\gamma\gamma \to \mu\mu$ events, as it is shown in Fig. 1 (left). These raw J/ψ yields are a combination of different physics processes, namely coherent, incoherent (with and without nuclear breakup) and J/ψ mesons obtained from the decay of ψ(2S) (referred as "feed-down"). In order to extract the coherent J/ψ yields, multiple template fits are performed to the transverse momentum spectrum, as it is shown in Fig. 1 (right).

4 Coherent J/ψ cross section

The coherent J/ψ photoproduction differential cross section is obtained as

$$\frac{d\sigma^{\rm coh}_{\rm J/\psi}}{dy} = \frac{N_{\rm J/\psi}}{\epsilon_{\rm J/\psi}\mathcal{B}_{\rm J/\psi\to\mu\mu}\mathcal{L}\epsilon_{\rm evtsel}\Delta y}, \quad (1)$$

where $\epsilon_{\rm J/\psi}$ and $\epsilon_{\rm evtsel}$ are the reconstruction and event selection and reconstruction efficiencies, $\mathcal{B}_{\rm J/\psi\to\mu\mu}$ the J/ψ dimuon branching fraction, $\mathcal{L}$ the integrated luminosity and Δy is the rapidity bin. This is performed in different forward neutron multiplicity categories, namely, 0n0n (no neutron selection), 0nXn (zero neutrons on one side and at least one neutron on the other side), and XnXn (at least one neutron on both sides). Predictions from theoretical calculations are also shown for comparison. The results are shown in Fig. 2.

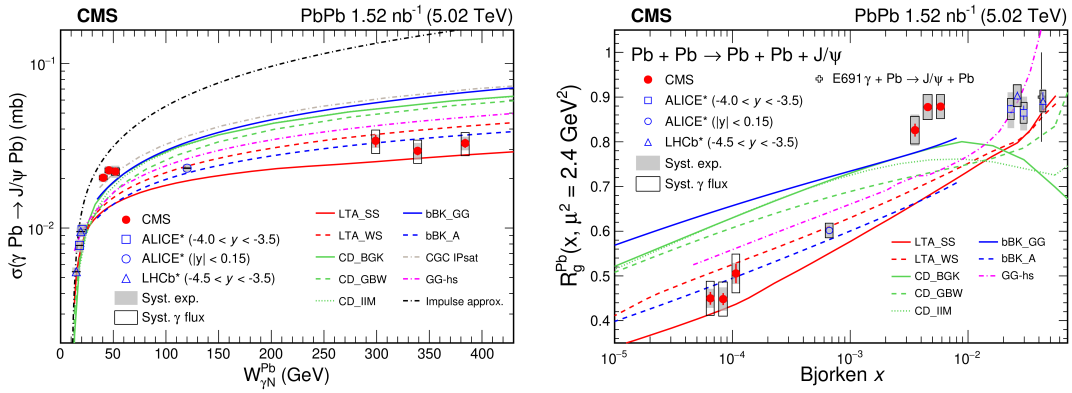

Figure 3 – Left: Coherent J/ψ photoproduction cross section as a function of $W^{\rm Pb}_{\gamma \rm N}$. The prediction from several theoretical models are also shown. Right: Nuclear suppression factor $R^{\rm Pb}_g$ as a function of Bjorken-x.

5 Energy dependence of the photo-nuclear cross section

The measured differential cross sections, shown in Fig. 2, for each neutron multiplicity class contains contributions from both low and high energy photons, $\omega = M_{\rm J/\psi}\exp(\pm y)$. The separation of the cross section in different neutron multiplicities classes allows us to disentangle both contributions and obtain the coherent photo-nuclear J/ψ cross section as a function of the center-of-mass energy of the photon-lead system ($W^{\rm Pb}_{\gamma \rm N}$). This measurement, as it is shown in Fig. 3 (left), is obtained up to energies of $W^{\rm Pb}_{\gamma \rm N} \approx 400$ GeV. At low $W^{\rm Pb}_{\gamma \rm N}$ values from 15 to 40 GeV, we observe a rapid growing energy dependence, consistent with the picture of a fast-growing gluon density at small x. This trend vanishes for $W^{\rm Pb}_{\gamma \rm N} > 40$ GeV, and the cross section begins a slow linear increase. This could imply the onset of novel physics, for example the gluon saturation of the Pb nucleus at the corresponding Bjorken-x value.

The nuclear gluon suppression factor $R^{\rm Pb}_g(x, \mu^2 = 2.4{\rm GeV}^2)$ as a function of x is also obtained. This is defined as defined as $R^{\rm Pb}_g = \sqrt{\sigma^{\rm Meas}/\sigma^{\rm IA}}$, where $\sigma^{\rm Meas}$ is the measured cross section and $\sigma^{\rm IA}$ is the prediction from the impulse approximation model. As it is shown in Fig. 3 (right), the suppression in the high-x (low $W^{\rm Pb}_{\gamma \rm N}$) region is around 0.8-0.9. As we go to small-x values, the suppression factor starts dropping rapidly to 0.4-0.5 for $x \approx 6 \times 10^{-5}$.

6 Summary

The coherent J/ψ photoproduction cross section in PbPb collisions has been presented in different forward neutron multiplicity classes. This allowed us to solve the two-way ambiguity of high and low energy photons, hence, to measure the photo-nuclear cross section as a function of the photon-nucleus center-of-mass energy $W^{\rm Pb}_{\gamma \rm N}$ over a wide range from 40 up to 400 GeV. The data show a slow linear rising trend above 40 GeV. This can be interpreted either as the first direct evidence of gluon saturation in Pb nucleus or that the scattering cross section is near the black-disc limit.

Acknowledgments

Supported by the U.S. Department of Energy, Office of Science, Nuclear Physics.

References

1. V. Guzey, M. Strikman, and M. Zhalov. Disentangling coherent and incoherent quasielastic J/ψ photoproduction on nuclei by neutron tagging in ultraperipheral ion collisions at the LHC. *Eur. Phys. J. C*, 74(7):2942, 2014.
2. V. Guzey, E. Kryshen, and M. Zhalov. Coherent photoproduction of vector mesons in ultraperipheral heavy ion collisions: Update for run 2 at the CERN Large Hadron Collider. *Phys. Rev. C*, 93(5):055206, 2016.
3. Armen Tumasyan et al. Probing small bjorken-x nuclear gluonic structure via coherent j/ψ photoproduction in ultraperipheral pbpb collisions at $\sqrt{s_{\rm NN}} = 5.02$ tev. 3 2023.

4. O. Surányi et al. Performance of the CMS Zero Degree Calorimeters in pPb collisions at the LHC. *JINST*, 16(05):P05008, 2021.

Impact parameter dependence of dilepton production: Wigner function approach and the role of photon polarizations

Wolfgang Schäfer
Institute of Nuclear Physics, Polish Academy of Sciences,
ul. Radzikowskiego 152, PL-31-342 Kraków, Poland

We revisit the Wigner function approach to the impact parameter dependent dilepton pair production developed in [M. Klusek-Gawenda, WS, A. Szczurek Phys.Lett.B 814 (2021) 136114]. We study the distribution of the angle between difference and sum of lepton transverse momenta, and show how it relates to the orbital angular momentum of leptons. The dependence on impact paramter is discussed, and we also present the different components of the Wigner function in the t-channel. A brief comparison to similar angular distributions in diffractive quark pair production will be presented.

DOI: https://doi.org/10.17161/werm5m52
Keywords: UPC, dileptons, Wigner function

1 Introduction

The uses of Weizsäcker-Williams (WW) photons in ultraperipheral collisions of heavy ions [1,2,3,4] need no introduction at this conference. Here, we will concentrate on the role of WW-photons in peripheral to semi-central processes, where nuclei overlap in impact parameter space and interact strongly. This can include the production of quark-gluon plasma in the nuclear overlap region. For our purposes the additional strong interactions create an "underlying event" to the $\gamma\gamma$-process induced by the WW-photons. The possibility of extending the WW approach to such inelastic collisions has been realized already in the 1990s [5], but has become topical after the measurements by the STAR collaboration at RHIC of J/ψ [6] and dielectrons [7] at very low transverse momenta of the produced system. Below, we concentrate on lepton pair production. In fact it is straightforward to write the relevant cross section in impact parameter space, involving a convolution of the $\boldsymbol{b}$–dependent photon fluxes:

$$\frac{d\sigma_{ll}}{d\xi d^2\boldsymbol{b}} = \int d^2\boldsymbol{b}_1 d^2\boldsymbol{b}_2\, \delta^{(2)}(\boldsymbol{b}-\boldsymbol{b}_1-\boldsymbol{b}_2) N(\omega_1,b_1) N(\omega_2,b_2) \frac{d\sigma(\gamma\gamma\to l^+l^-;\hat{s})}{d(-\hat{t})} \ , \tag{1}$$

where the phase space element is $d\xi = dy_+ dy_- dp_T^2$ with $y_\pm$, p_T and m_l the *single-lepton* rapidities, transverse momentum and mass, respectively, and

$$\omega_1 = \frac{\sqrt{p_T^2+m_l^2}}{2}\left(e^{y_+}+e^{y_-}\right) \ , \ \omega_2 = \frac{\sqrt{p_T^2+m_l^2}}{2}\left(e^{-y_+}+e^{-y_-}\right) \ , \ \hat{s} = 4\omega_1\omega_2 \ . \tag{2}$$

It is then straightforward to evaluate the cross sections/yields for different centrality classes $\mathcal{C}$, which are slices in impact parameter space $[b_{\rm min}, b_{\rm max}]$ that contain a fraction $f_{\mathcal{C}}$ of the total inelastic cross section $\sigma_{\rm AA}^{\rm in}$. For example

$$\frac{dN_{ll}[\mathcal{C}]}{dM} = \frac{1}{f_{\mathcal{C}}\cdot\sigma_{\rm AA}^{\rm in}} \int_{b_{\rm min}}^{b_{\rm max}} db \int d\xi\, \delta(M-2\sqrt{\omega_1\omega_2})\, \frac{d\sigma_{ll}}{d\xi db}\Big|_{\rm cuts} . \tag{3}$$

Up to now we have treated WW photons as purely collinear partons of the ions, in particular the dilepton pair is produced back–to–back with a delta-function distribution of the pair transverse momentum. An excellent agreement with the invariant mass distributions of dileptons with $P_T < 150\,\text{MeV}$ for the most

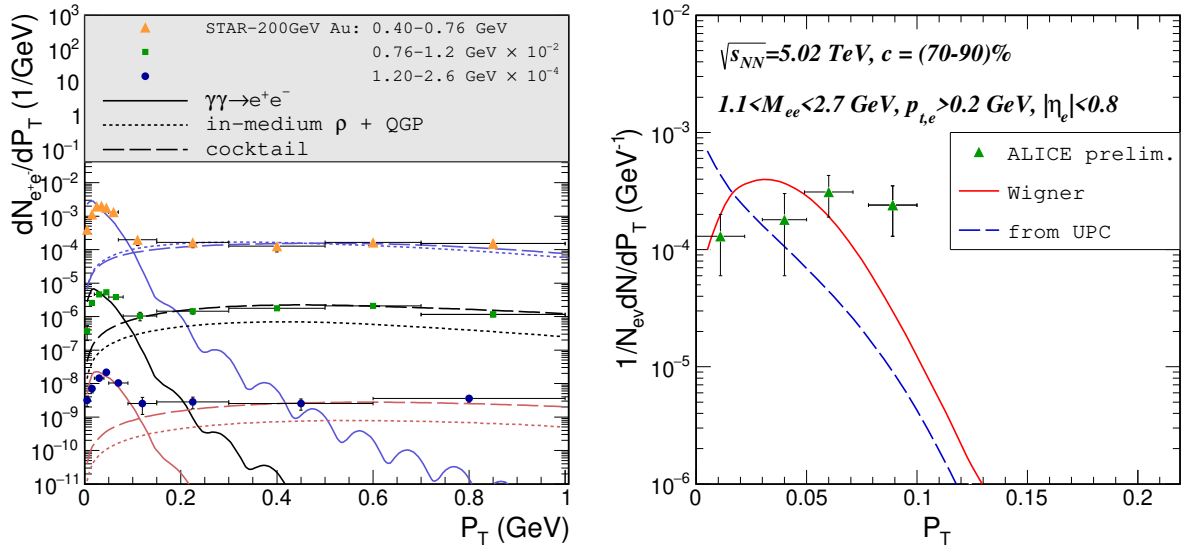

Figure 1 – Left panel: P_T spectra of the individual contributions in 3 different mass bins for 60-80% central Au+Au collisions ($\sqrt{s_{NN}}$=200 GeV), compared to STAR data [7]. Right panel: P_T distribution of the pair against old preliminary ALICE data [8].

peripheral STAR data is achieved in such an approach [9]. For more central collisions also thermal emissions and the cocktail of hadronic Dalitz as described in Ref.[10] decays plays a role.

The proof for the presence of the photon fusion mechanism however lies in the pair-transverse momentum distribution. One can easily obtain the transverse momentum dependent WW-flux of photons, which reads

$$\frac{dN(\omega,\boldsymbol{q})}{d^2\boldsymbol{q}} = \frac{Z^2\alpha_{\rm em}}{\pi^2}\frac{\boldsymbol{q}^2}{[\boldsymbol{q}^2+\frac{\omega^2}{\gamma^2}]^2}F^2_{\rm em}(\boldsymbol{q}^2+\frac{\omega^2}{\gamma^2}). \tag{4}$$

Here the electromagnetic formfactor of the nucleus restricts transverse momenta to $\boldsymbol{q}^2 \lesssim 6/R_A^2$, while the maximum of the distribution is at $\boldsymbol{q}^2 \sim \omega^2/\gamma^2$, which takes smaller values with increasing Lorentz factor γ. The dilepton cross section is then written as

$$\frac{d\sigma_{ll}}{d^2\boldsymbol{P}} = \int \frac{d\omega_1}{\omega_1}\frac{d\omega_2}{\omega_2}d^2\boldsymbol{q}_1 d^2\boldsymbol{q}_2 \frac{dN(\omega_1,\boldsymbol{q}_1^2)}{d^2\boldsymbol{q}_1}\frac{dN(\omega_2,\boldsymbol{q}_2^2)}{d^2\boldsymbol{q}_2}\delta^{(2)}(\boldsymbol{q}_1+\boldsymbol{q}_2-\boldsymbol{P})\hat{\sigma}(\gamma\gamma\to l^+l^-)\Big|_{\rm cuts}, \tag{5}$$

so that the transverse momentum distribution of the dilepton $p$air is essentially obtained by a convolution of WW-fluxes. This of course closely reminds the TMD (transverse momentum dependent) factorization formulas used in inclusive hadronic processes. The similarity would be even more obvious by using momentum fractions $x_i = 2\omega_i/\sqrt{s_{\rm NN}}$ instead of photon energies. A similar procedure is taken in the Monte-Carlo code Starlight [11]. In the left panel of Fig.1 we show the comparison of a calculation based on eq.5 with STAR data. Closer inspection shows, that the peak however is predicted at smaller P_T than what data show. This disagreement becomes rather dramatic at LHC energies, see the right panel of Fig.1. Here the blue dashed line reflects the ever smaller transverse momenta of photons at higher energies.

2 Wigner function approach

2.1 Wigner function & factorization

As it turns out it is crucial to include simultaneously the dependence on centrality/impact parameter of the collision and the pair transverse momentum [12].

$$N_{ij}(\omega,\boldsymbol{b},\boldsymbol{q}) = \int \frac{d^2\boldsymbol{Q}}{(2\pi)^2}\exp[-i\boldsymbol{bQ}]\,E_i\Big(\omega,\boldsymbol{q}+\frac{\boldsymbol{Q}}{2}\Big)E_j^*\Big(\omega,\boldsymbol{q}-\frac{\boldsymbol{Q}}{2}\Big). \tag{6}$$

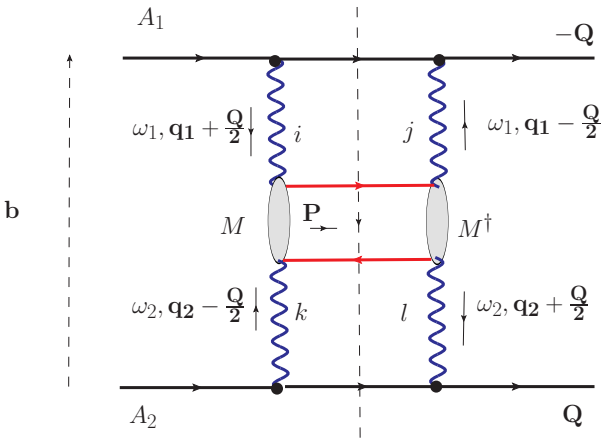

Figure 2 – Diagrammatic representation of the factorization formula for the cross section at fixed impact parameter of the colliding particles. It is related to the cut of a non-forward elastic amplitude.

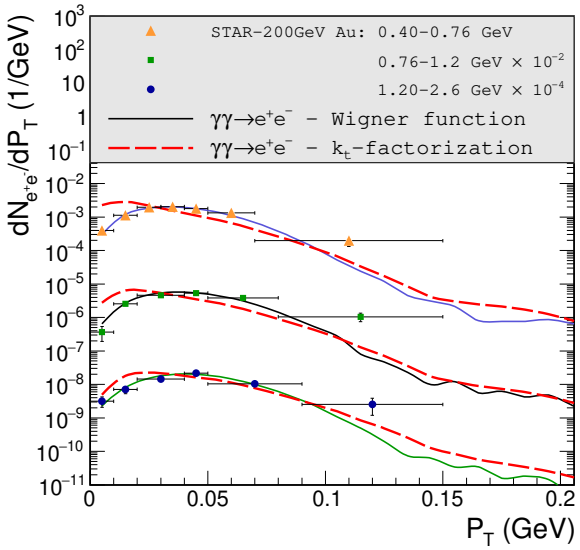

Figure 3 – P_T spectra for 60-80% central Au+Au collisions ($\sqrt{s_{\rm NN}}$=200 GeV) Calculations from Ref.[12].

Above, we introduced the electric field strength vector

$$\boldsymbol{E}(\omega, \boldsymbol{q}) \propto \frac{\boldsymbol{q} F_{\rm em}(\boldsymbol{q}^2 + \frac{\omega^2}{\gamma^2})}{\boldsymbol{q}^2 + \frac{\omega^2}{\gamma^2}}. \tag{7}$$

The Wigner function depends at the same time on impact parameter and transverse momentum, and will reproduce the above mention WW fluxes in impact parameter and transverse momentum space after being integrated over the respective other set of variables. It is also a density matrix in photon polarizations – above indices i, j correspond to cartesian (linear) polarizations of WW photons. The relation to the operator matrix element definition is shown in Ref.[13]. For earlier approaches to the impact parameter dependence, see e.g. Ref.[14] (which does not discuss the pair P_T-spectrum and photon polarizations) and Ref.[15], which is based on a numerical Fourier transform of Feynman-diagram amplitudes. For an equivalent approach to ours and a discussion of soft-photon resummation [16], see the presentation by Ya-Jin Zhou at this workshop. For the analogous QCD Wigner function of gluons with applications to mainly exclusive processes we refer to the recent review [17]. The factorization formula differs from the standard expressions in several aspects, the most important being the fact that here it is not the hard cross section averaged over incoming parton polarizations that enters, but rather a mixture of incoming

polarizations is prepared dependent on $\boldsymbol{b}$.

$$\begin{aligned}\frac{d\sigma}{d^2\boldsymbol{b}d^2\boldsymbol{P}} &= \int d^2\boldsymbol{b}_1 d^2\boldsymbol{b}_2\,\delta^{(2)}(\boldsymbol{b}-\boldsymbol{b}_1+\boldsymbol{b}_2)\int\frac{d\omega_1}{\omega_1}\frac{d\omega_2}{\omega_2}d^2\boldsymbol{q}_1 d^2\boldsymbol{q}_2\,\delta^{(2)}(\boldsymbol{P}-\boldsymbol{q}_1-\boldsymbol{q}_2)\\ &\times\; N_{ij}(\omega_1,\boldsymbol{b}_1,\boldsymbol{q}_1)N_{kl}(\omega_2,\boldsymbol{b}_2,\boldsymbol{q}_2)\;\frac{1}{2\hat{s}}M_{ik}M^{\dagger}_{jl}\,d\Phi(l^+l^-).\end{aligned}\tag{8}$$

For a diagrammatic representation, see Fig.2. For practical calculations it is useful to start from the more explicit form

$$\begin{aligned}\frac{d\sigma}{d^2\boldsymbol{b}d^2\boldsymbol{P}} &= \int\frac{d^2\boldsymbol{Q}}{(2\pi)^2}\exp[-i\boldsymbol{b}\boldsymbol{Q}]\int\frac{d\omega_1}{\omega_1}\frac{d\omega_2}{\omega_2}\int\frac{d^2\boldsymbol{q}_1}{\pi}\frac{d^2\boldsymbol{q}_2}{\pi}\,\delta^{(2)}(\boldsymbol{P}-\boldsymbol{q}_1-\boldsymbol{q}_2)\\ &\times\; E_i\Big(\omega_1,\boldsymbol{q}_1+\frac{\boldsymbol{Q}}{2}\Big)E^*_j\Big(\omega_1,\boldsymbol{q}_1-\frac{\boldsymbol{Q}}{2}\Big)E_k\Big(\omega_2,\boldsymbol{q}_2-\frac{\boldsymbol{Q}}{2}\Big)E^*_l\Big(\omega_2,\boldsymbol{q}_2+\frac{\boldsymbol{Q}}{2}\Big)\\ &\times\; \frac{1}{2\hat{s}}\sum_{\lambda\bar{\lambda}}M^{\lambda\bar{\lambda}}_{ik}M^{\lambda\bar{\lambda}\dagger}_{jl}\,d\Phi(l^+l^-).\end{aligned}$$

with

$$\begin{aligned}\sum_{\lambda\bar{\lambda}}M^{\lambda\bar{\lambda}}_{ik}M^{\lambda\bar{\lambda}\dagger}_{jl} &= \delta_{ik}\delta_{jl}\sum_{\lambda\bar{\lambda}}\Big|M^{(0,+)}_{\lambda\bar{\lambda}}\Big|^2+\epsilon_{ik}\epsilon_{jl}\sum_{\lambda\bar{\lambda}}\Big|M^{(0,-)}_{\lambda\bar{\lambda}}\Big|^2\\ &+\; P^{\parallel}_{ik}P^{\parallel}_{jl}\sum_{\lambda\bar{\lambda}}\Big|M^{(2,-)}_{\lambda\bar{\lambda}}\Big|^2+P^{\perp}_{ik}P^{\perp}_{jl}\sum_{\lambda\bar{\lambda}}\Big|M^{(2,+)}_{\lambda\bar{\lambda}}\Big|^2+\text{interferences}\,.\end{aligned}\tag{9}$$

Here, the mutually orthogonal $O(2)$-tensors

$$\delta_{ik} = \hat{x}_i\hat{x}_k+\hat{y}_i\hat{y}_k,\;\; \epsilon_{ik}=\hat{x}_i\hat{y}_k-\hat{y}_i\hat{x}_k,\;\; P^{\parallel}_{ik}=\hat{x}_i\hat{x}_k-\hat{y}_i\hat{y}_k,\;\; P^{\perp}_{ik}=\hat{x}_i\hat{y}_k+\hat{y}_i\hat{x}_k\tag{10}$$

project the incoming (s-channel) photon polarization states into definite $J_z=0,\pm2$ and parity. In Fig.3 we see that the inclusion of the impact parameter dependence within the Wigner function approach gives an improved description of STAR data with no new parameters introduced. Other successes[12] include a good description of the evolution of azimuthal decaorrelation of dileptons with centrality, as measured by the ATLAS Collaboration [18].

2.2 Positivity

The form of the cross section given in eq.9 also gives straightforward insight into positivity issues. Namely the Wigner function is not necessarily a non-negative function. One may therefore doubt, whether our cross section is manifestly positive, i.e. well-defined. To this end, we can introduce:

$$G_{ik}(\omega_1,\omega_2,\boldsymbol{P};\boldsymbol{b})\equiv\int\frac{d^2\boldsymbol{k}}{2\pi^2}\exp[-i\boldsymbol{b}\boldsymbol{k}]\,E_i(\omega_1,\boldsymbol{k})E_k(\omega_2,\boldsymbol{P}-\boldsymbol{k})\,,\tag{11}$$

so that our cross section takes the form

$$\frac{d\sigma}{d^2\boldsymbol{b}d^2\boldsymbol{P}} = \int\frac{d\omega_1}{\omega_1}\frac{d\omega_2}{\omega_2}G_{ik}(\omega_1,\omega_2,\boldsymbol{P};\boldsymbol{b})G^*_{jl}(\omega_1,\omega_2,\boldsymbol{P};\boldsymbol{b})\,\frac{1}{2\hat{s}}\sum_{\lambda\bar{\lambda}}M^{\lambda\bar{\lambda}}_{ik}M^{\lambda\bar{\lambda}\dagger}_{jl}\,d\Phi(l^+l^-)\,.\tag{12}$$

from which we obtain the cross section as a sum of squares which is manifestly positive:

$$\begin{aligned}\frac{d\sigma}{d^2\boldsymbol{b}d^2\boldsymbol{P}} &= \int\frac{d\omega_1}{\omega_1}\frac{d\omega_2}{\omega_2}\Big\{|G_{xx}+G_{yy}|^2\sum_{\lambda\bar{\lambda}}\Big|M^{(0,+)}_{\lambda\bar{\lambda}}\Big|^2+|G_{xy}-G_{yx}|^2\sum_{\lambda\bar{\lambda}}\Big|M^{(0,-)}_{\lambda\bar{\lambda}}\Big|^2\\ &+\; |G_{xx}-G_{yy}|^2\sum_{\lambda\bar{\lambda}}\Big|M^{(2,+)}_{\lambda\bar{\lambda}}\Big|^2+|G_{xy}+G_{yx}|^2\sum_{\lambda\bar{\lambda}}\Big|M^{(2,-)}_{\lambda\bar{\lambda}}\Big|^2\Big\}\frac{d\Phi(l^+l^-)}{2\hat{s}}\,.\end{aligned}\tag{13}$$

2.3 Fierz transformation & t-channel viewpoint

While positivity is easiest proven from the s-channel point of view, it is of interest to analyze which components of the spin-density matrix *of* the beam/target nuclei are being probed by the "hard process"

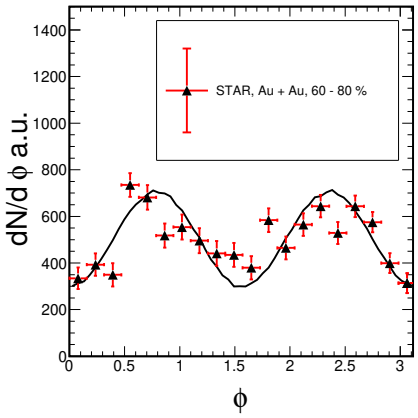

Figure 4 – Data from STAR [20],experimental cuts: $0.45 < M < 0.76$ GeV, $P_T < 0.1$ GeV.

under discussion. Here one often uses the generalized transverse momentum distribitions (GTMDs), which are derived from the Wigner distributions by another Fourier transform (see the e.g. the review[17]):

$$\mathcal{G}_{ij}(x,\boldsymbol{q},\boldsymbol{Q}) \propto \int d^2\boldsymbol{b}\, \exp[i\boldsymbol{b}\boldsymbol{Q}]\, N_{ij}(x,\boldsymbol{b},\boldsymbol{q})\,. \tag{14}$$

While it would be perhaps most convenient to decompose the GTMD/density matrix in terms of the orthogonal $O(2)$ tensors given above, popular parametrizations (see e.g.[19]) use decompositions like

$$\begin{aligned}\mathcal{G}_{ij}(x,\boldsymbol{q},\boldsymbol{Q}) &= \delta_{ij}\mathcal{G}_1(x,\boldsymbol{q},\boldsymbol{Q}) + (2q_iq_j - \boldsymbol{q}^2\delta_{ij})\mathcal{G}_2(x,\boldsymbol{q},\boldsymbol{Q}) \\ &+ (2Q_iQ_j - \boldsymbol{Q}^2\delta_{ij})\mathcal{G}_3(x,\boldsymbol{q},\boldsymbol{Q}) + (q_iQ_j - Q_iq_j)\mathcal{G}_4(x,\boldsymbol{q},\boldsymbol{Q}),\end{aligned} \tag{15}$$

where in fact for small-x photons all the GTMDs are proportional to each other. In the forward limit $\boldsymbol{Q} \to 0$, which corresponds to the integration over impact parameters in the Wigner function, we have the TMD limits $\mathcal{G}_1 \to f_1(x,\boldsymbol{q})$, $\mathcal{G}_2 \to h_1^\perp(x,\boldsymbol{q})$, where f_1 and $h_1^\perp$ are the TMD for unpolarized and linearly polarized photons repsectively.. To convert the sums over polarizations in Eq.9, one may use a "Fierz transformation" which swaps contractions $P_{ik}P_{jl}$ to $P_{ij}P_{kl}$:

$$\begin{pmatrix} \mathbb{I}\otimes\mathbb{I} \\ \varepsilon\otimes\varepsilon \\ P^\parallel\otimes P^\parallel \\ P^\perp\otimes P^\perp \end{pmatrix}\Big|_{s-\text{channel}} = \frac{1}{2}\begin{pmatrix} 1 & 1 & 1 & 1 \\ 1 & 1 & -1 & -1 \\ 1 & -1 & 1 & -1 \\ 1 & -1 & -1 & 1 \end{pmatrix}\begin{pmatrix} \mathbb{I}\otimes\mathbb{I} \\ \varepsilon\otimes\varepsilon \\ P^\parallel\otimes P^\parallel \\ P^\perp\otimes P^\perp \end{pmatrix}\Big|_{t-\text{channel}} \tag{16}$$

2.4 Polarization structure & angular dependence

Before we come to the angular dependence of the cross section, let us briefly look at helicity amplitudes of leptons in states of definite J_z and parity. As it turns out, all amplitudes with $J_z = 0$ vanish in the limit of massless fermions. We work in terms of light-front momentum fractions $z, 1-z$ of one of the photons carried by the (anti-)lepton and the relative transverse momentum

$$\boldsymbol{k} = z\boldsymbol{p}_- - (1-z)\boldsymbol{p}_+\,. \tag{17}$$

As the total angular momentum is decomposed into spin and orbital angular momentum $J_z = S_z + L_z$, amplitudes will have dependences on the azimuthal angle ϕ of $\boldsymbol{k}$ which involve

$$\exp(\pm iL_z\phi) = \exp(\pm i(J_z - S_z)\phi). \tag{18}$$

For example, the positive parity, $J_z = 0, S_z = 1$ amplitude has the form

$$M^{(0,+)}_{\uparrow\uparrow} \propto \frac{mk_\perp e^{-i\phi}}{k_\perp^2 + m^2}\,, \tag{19}$$

while for $J_z = 2, S_z = 0, P = +1$, we have

$$M^{(2,+)}_{\uparrow\downarrow} \propto \frac{-k_\perp^2 (z e^{i2\phi} - (1-z) e^{-i2\phi})}{k_\perp^2 + m^2}\,, \tag{20}$$

which does not vanish as $m \to 0$. Indeed, in the massless case only amplitudes for $J_z = \pm 2, S_z = 0$ with $L_z = \pm 2$ contribute. The amplitudes in this case enter the cross section as

$$\begin{aligned}\sum_{\lambda\bar\lambda} M^{\lambda\bar\lambda}_{ik} M^{\lambda\bar\lambda\dagger}_{jl} \quad \Longrightarrow \quad & P^{\parallel}_{ik} P^{\parallel}_{jl} \sum_{\lambda=-\bar\lambda} \left| M^{(2,-)}_{\lambda\bar\lambda} \right|^2 + P^{\perp}_{ik} P^{\perp}_{jl} \sum_{\lambda=-\bar\lambda} \left| M^{(2,+)}_{\lambda\bar\lambda} \right|^2 \\ = \quad & \frac{2}{k_\perp^2} \Big\{ \frac{z^2 + (1-z)^2}{z(1-z)} \Big(P^{\parallel}_{ik} P^{\parallel}_{jl} + P^{\perp}_{ik} P^{\perp}_{jl} \Big) \\ + \quad & 2\cos(4\phi) \Big(P^{\parallel}_{ik} P^{\parallel}_{jl} - P^{\perp}_{ik} P^{\perp}_{jl} \Big) \Big\}\end{aligned}$$

We observe, that at the cross section level, the $L_z = \pm 2$ amplitudes give rise to a $\cos(4\phi)$ modulation. It gives rise to a difference between $\parallel$ and $\perp$ linear polarizations of "s-channel" photons. As the cross section is the absorptive part of a forward amplitude, which in turn can be related to an index of refraction, one can indeed relate this to a "birefringence" of the vacuum, see the discussion in Ref. [21]. Furthermore, from the Fierz transformation

$$\begin{aligned}\Big(P^{\parallel} \otimes P^{\parallel} + P^{\perp} \otimes P^{\perp} \Big)\Big|_{s-\text{channel}} \quad &= \quad \Big(\mathbb{I} \otimes \mathbb{I} - \varepsilon \otimes \varepsilon \Big)\Big|_{t-\text{channel}} \\ \Big(P^{\parallel} \otimes P^{\parallel} - P^{\perp} \otimes P^{\perp} \Big)\Big|_{s-\text{channel}} \quad &= \quad \Big(P^{\parallel} \otimes P^{\parallel} - P^{\perp} \otimes P^{\perp} \Big)\Big|_{t-\text{channel}},\end{aligned} \tag{21}$$

one can derive, that in the $\boldsymbol{b}$-integrated cross section, the $\cos(4\phi)$ modulation stems from the linearly polarized TMD $h_1^\perp(x, q_\perp^2)$ as previously shown in Ref.[22]. In the massive case, relevant to invariant masses close to the threshold, **interferences** between $J_z = 0$ and $J_z = \pm 2$ amplitudes of equal parity can induce a $\cos(2\phi)$ modulation.

$$\begin{aligned}\sum_{\lambda\bar\lambda} M^{\lambda\bar\lambda}_{ik} M^{\lambda\bar\lambda\dagger}_{jl} \quad \supset \quad & \delta_{ik} P^{\parallel}_{jl} \sum_{\lambda\bar\lambda} M^{(0,+)}_{\lambda\bar\lambda} M^{(2,+)\dagger}_{\lambda\bar\lambda} + P^{\parallel}_{ik} \delta_{jl} \sum_{\lambda\bar\lambda} M^{(2,+)}_{\lambda\bar\lambda} M^{(0,+)\dagger}_{\lambda\bar\lambda} \\ + \quad & \epsilon_{ik} P^{\perp}_{jl} \sum_{\lambda\bar\lambda} M^{(0,-)}_{\lambda\bar\lambda} M^{(2,-)\dagger}_{\lambda\bar\lambda} + P^{\perp}_{ik} \epsilon_{jl} \sum_{\lambda\bar\lambda} M^{(2,-)}_{\lambda\bar\lambda} M^{(0,-)\dagger}_{\lambda\bar\lambda}\end{aligned} \tag{22}$$

We can expect a different dependence on centrality the $\cos 2\phi$ and $\cos 4\phi$ contributions. In the $\boldsymbol{b}$–integrated cross section the $\cos 2\phi$ stems from the product of unpolarized & linearly polarized TMD's: $f_1(x_1, q_{1\perp}^2) h_1^\perp(x_2, q_{2\perp}^2) + (x_1, q_{1\perp} \leftrightarrow x_2, q_{2\perp})$, in agreement with the analysis in Ref.[22].

2.5 Comparison with STAR data

$\sqrt{s_{NN}} = 200$ GeV	Wigner	Wigner	STAR	STAR
centrality	A_4	$\sqrt{\langle P_T^2 \rangle}$ MeV	$\lvert A_4 \rvert$	$\sqrt{\langle P_T^2 \rangle}$ MeV
60-80 %	-0.39	47.7	0.27 ± 6	50.9 ± 2.5
40-60 %	-0.49	51.0	–	–
20-40 %	-0.62	54.8	-	-
0-20%	-0.77	59.6	-	-

Table 1: Centrality dependence of angular coefficient and mean P_T of e^+e^--pair.

Let us now go to the comparison with experimental data. Here we define, event by event, the x-axis in the transverse plane to be along $\boldsymbol{P} = \boldsymbol{p}_+ + \boldsymbol{p}_-$, so that the internal orbital angular momenta of leptons reflect themselves in a modulation in the angle:

$$\cos\phi = \frac{\boldsymbol{P} \cdot (\boldsymbol{p}_- - \boldsymbol{p}_+)}{|\boldsymbol{P}||\boldsymbol{p}_- - \boldsymbol{p}_+|} \approx \frac{\boldsymbol{P} \cdot \boldsymbol{k}}{|\boldsymbol{P}||\boldsymbol{k}|},. \tag{23}$$

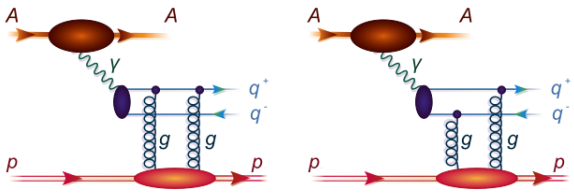

Figure 5 – Feynman diagrams for the diffractive photoproduction of $q\bar{q}$ pairs in nucleus-proton collisions, discussed in the present paper.

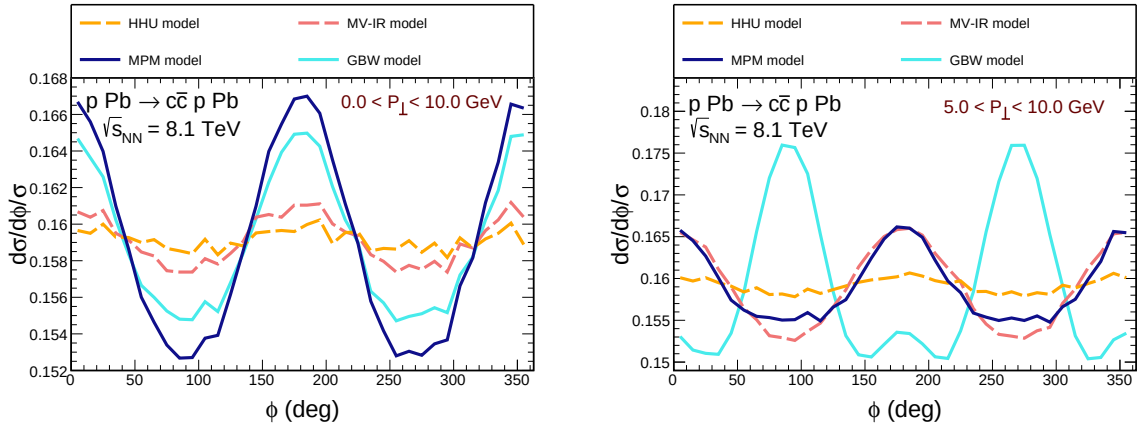

Figure 6 – Distributions in the azimuthal angle ϕ between $\vec{P}_\perp$ and $\vec{\Delta}_\perp$ normalised to the total cross section for $0.01 < P_\perp < 10.0\,\text{GeV}$ on the left and for $5.0 < P_\perp < 10.0\,\text{GeV}$ on the right.

A comparison with STAR[20] data in the $60-80\%$ centrality class, which show a sizable, negative $\cos(4\phi)$ modulation, is seen in Fig.4. The angular modulation clearly reflects the orbital angular momentum $L_z = \pm 2$ of leptons. The agreement with data is good, we stress that no new parameters enter the calculation. In Table 1 we show the A_4 correlation coefficient in

$$\frac{dN}{d\phi} \propto 1 + A_2 \cos 2\phi + A_4 \cos 4\phi + \dots . \tag{24}$$

In particular we predict its evolution with centrality: an increasing in size, and negative azimuthal correlation A_4.

3 Diffractive photoproduction of $c\bar{c}$ pairs

Finally, let us return to the gluon Wigner distribution/GTMD. Here, also ultraperipheral collisions have been proposed as a means to gain access to the latter [23,24]. We briefly summarize the main results of our recent paper[25] regarding the azimuthal correlations of diffractively produced $c\bar{c}$-pairs. Here we have in mind UPC in proton-nucleus collisions, where the nucleus provides the photon flux and the diffractive photoproduction process proceeds on the proton (see Fig.5). The photoproduction amplitude in the dipole picture is expresed as

$$\frac{d\sigma(\gamma p \to Q\bar{Q}p; s_{\gamma p})}{dz d^2\boldsymbol{P} d^2\boldsymbol{\Delta}} = \overline{\sum_{\lambda_\gamma,\lambda,\bar{\lambda}} \Big| \int \frac{d^2\boldsymbol{b} d^2\boldsymbol{r}}{(2\pi)^2} e^{-i\boldsymbol{\Delta}\cdot\boldsymbol{b}} e^{-i\boldsymbol{P}\cdot\boldsymbol{r}} N(Y,\boldsymbol{r},\boldsymbol{b})\, \Psi^{\lambda_\gamma}_{\lambda\bar{\lambda}}(z,\boldsymbol{r}) \Big|^2} . \tag{25}$$

Now, one is interested in the azimuthal correlation in the angle

$$\cos\phi = \frac{\boldsymbol{P}\cdot\boldsymbol{\Delta}}{P_\perp \Delta_\perp} \tag{26}$$

Indeed, a possible correlation between dipole size $\boldsymbol{r}$ and impact parameter $\boldsymbol{b}$ reflects itself in an angular correlation in the GTMD (the so-called "elliptic GTMD".

$$f\Big(Y, \frac{\boldsymbol{q}}{2}+\boldsymbol{\kappa}, \frac{\boldsymbol{q}}{2}-\boldsymbol{\kappa}\Big) = f_0(Y,\kappa_\perp,q_\perp) + 2\cos(2\phi_{q\kappa})\, f_2(Y,\kappa_\perp,q_\perp)\,. \tag{27}$$

Here Y is the rapidity gap between diffractive system and proton, and the gluon GTMD relates to the dipole amplitude as

$$\begin{aligned} N(Y,\boldsymbol{r},\boldsymbol{b}) &= \int d^2\boldsymbol{q} d^2\boldsymbol{\kappa}\, f\Big(Y, \frac{\boldsymbol{q}}{2}+\boldsymbol{\kappa}, \frac{\boldsymbol{q}}{2}-\boldsymbol{\kappa}\Big) \exp[i\vec{q}_\perp\cdot\vec{b}_\perp] \\ &\times \Big\{\exp\Big[i\frac{1}{2}\boldsymbol{q}\cdot\boldsymbol{r}\Big] + \exp\Big[-i\frac{1}{2}\boldsymbol{q}\cdot\boldsymbol{r}\Big] - \exp[i\boldsymbol{\kappa}\cdot\boldsymbol{r}] - \exp[-i\boldsymbol{\kappa}\cdot\boldsymbol{r}]\Big\}\,. \end{aligned} \tag{28}$$

In this case, the dominant correlation turns out to be $\cos 2\phi$, and it inded stems from the "elliptic glue". The size of the effect shown in Fig.6 however is much smaller than the one in photon-photon fusion production for the dilepton.

4 Summary

We have reviewed our studies of low-P_T dilepton production in ultrarelativistic heavy-ion collisions. We first performed a comparison of dilepton production via thermal radiation and photon-photon fusion within the coherent fields of the incoming nuclei. Coherent emission dominates for the two peripheral samples, and is comparable to the cocktail and thermal radiation yields in semi-central collisions. The impact-parameter dependent dilepton P_T distribution is described by a Wigner function density matrix generalization of the Weizsäcker-Williams fluxes. Here the $J_z = 0, \pm 2$ channels of the $\gamma\gamma$-system enter with different $\boldsymbol{b}$-dependent weights. For e^+e^- pairs the $J_z = \pm 2$ channels dominate. Comparison to recent STAR data shows a good description of low-P_T dilepton data in Au-Au($\sqrt{s_{NN}}$=200 GeV) collisions in three centrality classes, for invariant masses from threshold to $\sim$4 GeV. Proper account for the b-dependence turns out to be crucial at LHC energies. We obtain a very good description of ATLAS azimuthal decorrelations, our predictions agree well with recent ALICE data.

Also the azimuthal $\cos 4\phi$ correlation measured by STAR is well reproduced, and can be traced to orbital angular momentum of leptons. Here the linear photon polarizations play an important role. The angular coefficient rises for more central collisions.

In contrast, in diffractive heavy quark production, the parton-level $\cos 2\phi$ azimuthal correlations induced by the elliptic Wigner function are much smaller than the ones in the QED process.

Acknowledgments

It is a pleasure to thank the organizers for the invitation to this topical workshop, which brought back fond memories of Gerhard Baur's kindness and encouragement. I hope he would have liked the results presented here. This work was partially supported by the Polish National Science Center grant UMO-2018/31/B/ST2/03537.

References

1. Carlos A. Bertulani and Gerhard Baur. Electromagnetic Processes in Relativistic Heavy Ion Collisions. *Phys. Rept.*, 163:299, 1988.
2. Carlos A. Bertulani, Spencer R. Klein, and Joakim Nystrand. Physics of ultra-peripheral nuclear collisions. *Ann. Rev. Nucl. Part. Sci.*, 55:271–310, 2005.
3. J.G. Contreras and J.D. Tapia Takaki. Ultra-peripheral heavy-ion collisions at the LHC. *Int. J. Mod. Phys. A*, 30:1542012, 2015.
4. Wolfgang Schäfer. Photon induced processes: from ultraperipheral to semicentral heavy ion collisions. *Eur. Phys. J. A*, 56(9):231, 2020.
5. N. Baron and G. Baur. Unraveling gamma gamma dileptons in central relativistic heavy ion collisions. *Z. Phys. C*, 60:95–100, 1993.
6. Jaroslav Adam et al. Measurement of an excess in the yield of J/ψ at very low $p_{\rm T}$ in Pb-Pb collisions at $\sqrt{s_{\rm NN}} = 2.76$ TeV. *Phys. Rev. Lett.*, 116(22):222301, 2016.
7. Jaroslav Adam et al. Low-p_T e^+e^- pair production in Au+Au collisions at $\sqrt{s_{NN}} = 200$ GeV and U+U collisions at $\sqrt{s_{NN}} = 193$ GeV at STAR. *Phys. Rev. Lett.*, 121(13):132301, 2018.

8. Sebastian Lehner. Dielectron production at low transverse momentum in Pb-Pb collisions at $\sqrt{s_{\rm NN}} = 5.02$ TeV with ALICE. *PoS*, LHCP2019:164, 2019.
9. Mariola Kłusek-Gawenda, Ralf Rapp, Wolfgang Schäfer, and Antoni Szczurek. Dilepton Radiation in Heavy-Ion Collisions at Small Transverse Momentum. *Phys. Lett. B*, 790:339–344, 2019.
10. Ralf Rapp. Dilepton Spectroscopy of QCD Matter at Collider Energies. *Adv. High Energy Phys.*, 2013:148253, 2013.
11. Spencer R. Klein, Joakim Nystrand, Janet Seger, Yuri Gorbunov, and Joey Butterworth. STARlight: A Monte Carlo simulation program for ultra-peripheral collisions of relativistic ions. *Comput. Phys. Commun.*, 212:258–268, 2017.
12. Mariola Kłusek-Gawenda, Wolfgang Schäfer, and Antoni Szczurek. Centrality dependence of dilepton production via $\gamma\gamma$ processes from Wigner distributions of photons in nuclei. *Phys. Lett. B*, 814:136114, 2021.
13. Spencer Klein, A. H. Mueller, Bo-Wen Xiao, and Feng Yuan. Lepton Pair Production Through Two Photon Process in Heavy Ion Collisions. *Phys. Rev. D*, 102(9):094013, 2020.
14. M. Vidovic, M. Greiner, C. Best, and G. Soff. Impact parameter dependence of the electromagnetic particle production in ultrarelativistic heavy ion collisions. *Phys. Rev. C*, 47:2308–2319, 1993.
15. Kai Hencken, Gerhard Baur, and Dirk Trautmann. Production of QED pairs at small impact parameter in relativistic heavy ion collisions. *Phys. Rev. C*, 69:054902, 2004.
16. Cong Li, Jian Zhou, and Ya-Jin Zhou. Impact parameter dependence of the azimuthal asymmetry in lepton pair production in heavy ion collisions. *Phys. Rev. D*, 101(3):034015, 2020.
17. Roman Pasechnik and Marek Taševský. Multi-dimensional hadron structure through the lens of gluon Wigner distribution, hep-ph2310.10793. 10 2023.
18. Georges Aad et al. Measurement of muon pairs produced via $\gamma\gamma$ scattering in nonultraperipheral Pb+Pb collisions at sNN=5.02 TeV with the ATLAS detector. *Phys. Rev. C*, 107(5):054907, 2023.
19. Daniël Boer, Tom Van Daal, Piet J. Mulders, and Elena Petreska. Directed flow from C-odd gluon correlations at small x. *JHEP*, 07:140, 2018.
20. Jaroslav Adam et al. Measurement of e^+e^- Momentum and Angular Distributions from Linearly Polarized Photon Collisions. *Phys. Rev. Lett.*, 127(5):052302, 2021.
21. James Daniel Brandenburg, Janet Seger, Zhangbu Xu, and Wangmei Zha. Report on progress in physics: observation of the Breit–Wheeler process and vacuum birefringence in heavy-ion collisions. *Rept. Prog. Phys.*, 86(8):083901, 2023.
22. Cong Li, Jian Zhou, and Ya-Jin Zhou. Probing the linear polarization of photons in ultraperipheral heavy ion collisions. *Phys. Lett. B*, 795:576–580, 2019.
23. Yoshikazu Hagiwara, Yoshitaka Hatta, Roman Pasechnik, Marek Tasevsky, and Oleg Teryaev. Accessing the gluon Wigner distribution in ultraperipheral pA collisions. *Phys. Rev. D*, 96(3):034009, 2017.
24. Mateus Reinke Pelicer, Emmanuel Gräve De Oliveira, and Roman Pasechnik. Exclusive heavy quark-pair production in ultraperipheral collisions. *Phys. Rev. D*, 99(3):034016, 2019.
25. Barbara Linek, Agnieszka Łuszczak, Marta Łuszczak, Roman Pasechnik, Wolfgang Schäfer, and Antoni Szczurek. Probing proton structure with $c\bar{c}$ correlations in ultraperipheral pA collisions. *JHEP*, 10:179, 2023.

Measurement of dilepton production from photon fusion processes in Pb+Pb UPC with the ATLAS detector

I. Grabowska-Bold (for the ATLAS Collaboration)
Faculty of Physics and Applied Computer Science, AGH University of Krakow.
Al. Mickiewicza 30, 30-059 Kraków, Poland

Relativistic heavy-ion beams at the LHC are accompanied by a large flux of equivalent photons, leading to multiple photon-induced processes. This report presents a series of measurements of dilepton production from photon fusion performed by the ATLAS Collaboration. Recent measurements of exclusive dielectron production in ultra-peripheral collisions (UPC) are presented. These processes provide strong constraints on the nuclear photon flux and its dependence on the impact parameter and photon energy. Comparisons of the measured cross sections to QED predictions from the STARLIGHT and SUPERCHIC models are also presented. Tau-pair production measurements can constrain the tau lepton's anomalous magnetic dipole moment (g-2), and a recent ATLAS measurement using muonic decays of tau leptons in association with electrons and tracks provides one of the most stringent limits available to date. Furthermore, measurements of muon pairs produced via two-photon scattering processes in hadronic (i.e. non-UPC) Pb+Pb collisions are discussed. These non-UPC measurements provide a novel test of strong-field QED and may be a potentially sensitive electromagnetic probe of the quark-gluon plasma. These measurements include the dependence of the cross section and angular correlation on the mean-p_{T} of the dimuon pair, the rapidity separation between the muons, and the angle of the pair relative to the second-order event-plane, all measured differentially as a function of the Pb+Pb collision centrality.

DOI: https://doi.org/10.17161/jyr73a92
Keywords: ultra-peripheral collisions, photon-induced processes, exclusive production of lepton pairs, tau anomalous magnetic moment, non-UPC dimuons

1 Introduction

Heavy-ion collisions at ultra-relativistic energies are typically examined in processes in which nuclear beams interact hadronically at impact parameters less than twice the nuclear radius. In the overlap region of two colliding nuclei a dense quark–gluon plasma is expected to be produced. On the other hand, the strong electromagnetic (EM) fields associated with the nuclei can also lead to interactions in ultra-peripheral collisions (UPC), events with impact parameters well beyond twice the nuclear radius, where any contributions from strong processes are suppressed.

At high energies of the Large Hadron Collider (LHC), UPC can induce a wide variety of exclusive final states – dileptons, dijets, and diphotons being the most commonly studied – for which no other activity in the detectors is observed, except for nucleons emitted at very small angles relative to the beam direction. The photons are also characterized by small transverse momenta, such that high-energy decay products in these exclusive final states are almost perfectly balanced in the transverse direction. UPC processes have also been proposed to be utilized as a competitive tool to search for beyond Standard Model (BSM) physics [1].

In this report the most recent results on photon-photon ($\gamma\gamma$) induced processes in UPC physics from the ATLAS experiment [2] are reviewed. Furthermore, a measurement of the $\gamma\gamma \to \mu^+\mu^-$ process occurring simultaneously to hadronic Pb+Pb collisions is studied. Prospects for the 2023 Pb+Pb data are also discussed.

2 Exclusive dimuon and dielectron production

ATLAS measured exclusive $\gamma\gamma \to \mu^+\mu^-$ production [3] in UPC Pb+Pb collisions at $\sqrt{s_{\rm NN}} = 5.02$ TeV collisions in the data set with an integrated luminosity of 0.48 nb^{-1}. The fiducial region of the measurement is defined by single muon $p_{\rm T} > 4$ GeV and $|\eta| < 2.4$. Furthermore, requirements on invariant mass of the dimuon system, $m_{\mu\mu} > 10$ GeV, and its transverse momentum, $p_{\rm T}^{\mu\mu} < 2$ GeV, are imposed. The event selection allows exactly two opposite-charge muons per event with no other activity in the detector. It results in about 12k event candidates from the $\gamma\gamma \to \mu^+\mu^-$ process. After the evaluation and subtraction of dissociative background, which amounts to 3%, differential cross sections are measured in $m_{\mu\mu}$, dimuon rapidity $y_{\mu\mu}$, scattering angle in the dimuon rest frame $\cos\theta^*$, initial-photon momenta $k_{\rm min}$, $k_{\rm max}$ and acoplanarity, $\alpha = 1 - |\Delta\phi|/\pi$ as well as the integrated cross section. The latter quantifies how two muons are aligned in the azimuthal angle.

The left panel of Figure 1 presents differential cross sections for exclusive $\gamma\gamma \to \mu^+\mu^-$ production as a function of α. STARLIGHT [4] fails in describing a tail of this differential cross section. For $\alpha > 5 \times 10^{-3}$

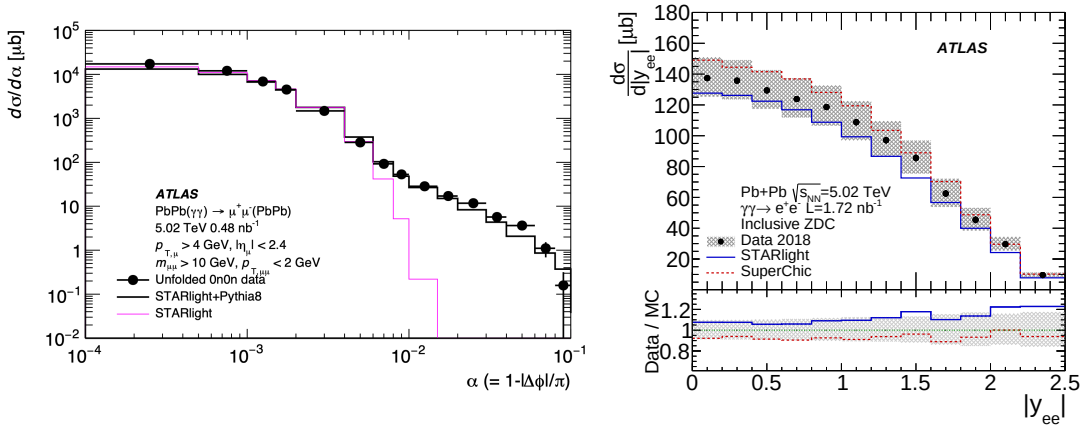

Figure 1 – (Left) Differential cross section as a function of acoplanarity (right) for exclusive $\gamma\gamma \to \mu^+\mu^-$ production in UPC Pb+Pb collisions [3]. Data points are compared with predictions from STARLIGHT or STARLIGHT+PYTHIA to account for the FSR contribution. (Right) Differential cross section as a function of $|y_{ee}|$ for exclusive $\gamma\gamma \to e^+e^-$ production in UPC Pb+Pb collisions [6]. In the bottom panel, data-to-prediction ratio is shown for STARLIGHT and SUPERCHIC.

an expected contribution of signal events is suppressed and the excess of data is visible. It is caused by a contribution from the final state radiation (FSR) which is not accounted for in the STARLIGHT calculation. A better description of the full α distribution is obtained by interfacing STARLIGHT with PYTHIA which accounts for the FSR contribution. This result demonstrates need for FSR modeling to get a good description of the data by the calculation for exclusive dilepton production.

A measurement of exclusive $\gamma\gamma \to e^+e^-$ production was performed [6] by ATLAS in the Pb+Pb data set with an integrated luminosity of 1.72 nb^{-1}. The fiducial region of the measurement is defined by single electron $p_{\rm T} > 2.5$ GeV and $|\eta| < 2.5$. Furthermore, requirements on invariant mass of the dielectron system, $m_{ee} > 5$ GeV, and its transverse momentum, $p_{\rm T}^{ee} < 2$ GeV, are imposed. The event selection requires exactly two opposite-charge electrons per event and no other activity in the detector. In comparison to the $\gamma\gamma \to \mu^+\mu^-$ measurement, the dielectron analysis features three times larger statistics, the extended fiducial coverage at low electron $p_{\rm T}$ and m_{ee}, and advancement in the background evaluation techniques.

The right panel of Figure 1 shows differential cross sections for exclusive $\gamma\gamma \to e^+e^-$ production as a function of $|y_{ee}|$, where y_{ee} stands for rapidity of the dielectron system. The data is corrected to the Born level i.e. before the FSR. The measurement precision is dominated by systematic uncertainties. The data is compared with two Monte Carlo (MC) predictions for the $\gamma\gamma \to e^+e^-$ process: STARLIGHT v3.13 and SUPERCHIC v3.05 [5], which are systematically about 10% lower and higher than the data, respectively. SUPERCHIC tends to better describe the shape of the distribution.

3 Forward neutron activity in $\gamma\gamma \to \ell^+\ell^-$ events

An inclusive sample of $\gamma\gamma \to \ell^+\ell^-$ events with $\ell^\pm = \mu^\pm, e^\pm$ can be inspected using information from the Zero Degree Calorimeters (ZDC) which are located in the forward region ± 140 m away from the ATLAS interaction point (IP). The ZDC detectors are designed to detect neutral particles originating from IP. In particular in hadronic Pb+Pb collisions they detect spectator neutrons. On the other hand, in UPC events the probability of exchanging one or more photons between the two incoming ions is sizable. These additional photons may dissociate one or both nuclei and cause emission of single neutrons in ZDC. Because of the radial dependence of the photon flux [7], the presence of these additional photons can preferentially select certain impact parameter ranges, and so can influence the photon spectrum of the other photons.

ATLAS measured forward neutron activity in exclusive $\gamma\gamma \to \mu^+\mu^-$ [3] and $\gamma\gamma \to e^+e^-$ [6] processes. In both cases, all $\gamma\gamma \to \ell^+\ell^-$ event candidates are divided into three categories.

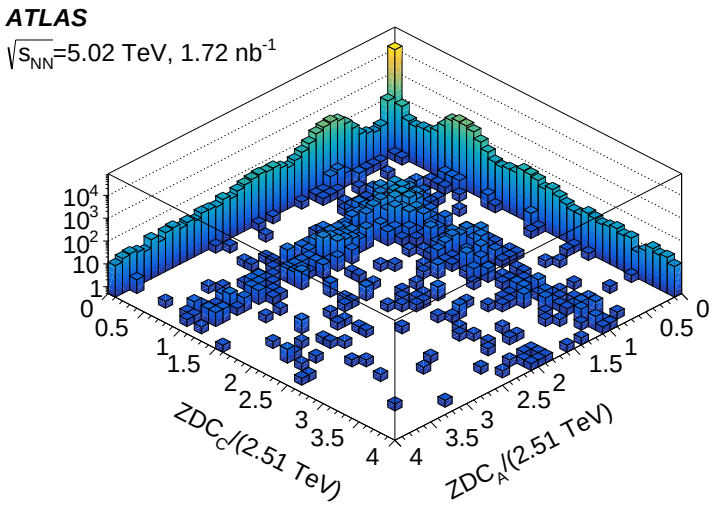

Figure 2 – Correlation of energy deposited in each of the ZDC arms, normalized to the per-nucleon beam energy, in a sample of $\gamma\gamma \to e^+e^-$ events [6].

Figure 2 shows the correlation of energies normalized to the per-nucleon beam energy in both ZDC sides. It illustrates the three primary topologies available for these events: 1) the most probable configuration is no activity in either ZDC ("0n0n"), 2) the next mostly likely configuration is observing one or more forward neutrons in one ZDC, and none in the other ("Xn0n"), and 3) finally, the rarest configuration is observing one or more forward neutrons in both ZDC arms ("XnXn").

After subtracting the dissociative background contribution and accounting for simultaneous EM interactions in the same bunch crossing, fractions of events falling into each category are measured.

The left panel of Figure 3 shows corrected fractions of events in the 0n0n category measured in $\gamma\gamma \to e^+e^-$ data as a function of m_{ee} in three bins of $|y_{ee}|$. These fractions drop from about 80% at low m_{ee} to 60% at high m_{ee} and $|y_{ee}| < 0.8$, and in general are larger for higher $|y_{ee}|$ values. These observations are consistent with the conclusions for forward neutron activity measured in the $\gamma\gamma \to \mu^+\mu^-$ process [3].

The right panel of Figure 3 presents the differential cross section as a function of $|y_{ee}|$ for the 0n0n category of the $\gamma\gamma \to e^+e^-$ process. It is compared with the MC predictions from STARLIGHT and SUPERCHIC. Both simulated samples were produced inclusively and reweighted to the 0n0n category using the measured fractions. Each theory prediction is represented by two curves reflecting the systematic variations of the measured 0n0n fractions. STARLIGHT can also generate a prediction conditional on the presence of neutron emission in one or both directions. These dedicated predictions from STARLIGHT for the 0n0n category are shown in the same plots. That prediction agrees well with the shape of the inclusive STARLIGHT calculation corrected for the measured 0n0n fractions, but is systematically lower by 2%–3% for $|y_{ee}| < 1.4$. The general conclusions from this comparison between MC predictions and data are consistent with the inclusive case presented in Section 2.

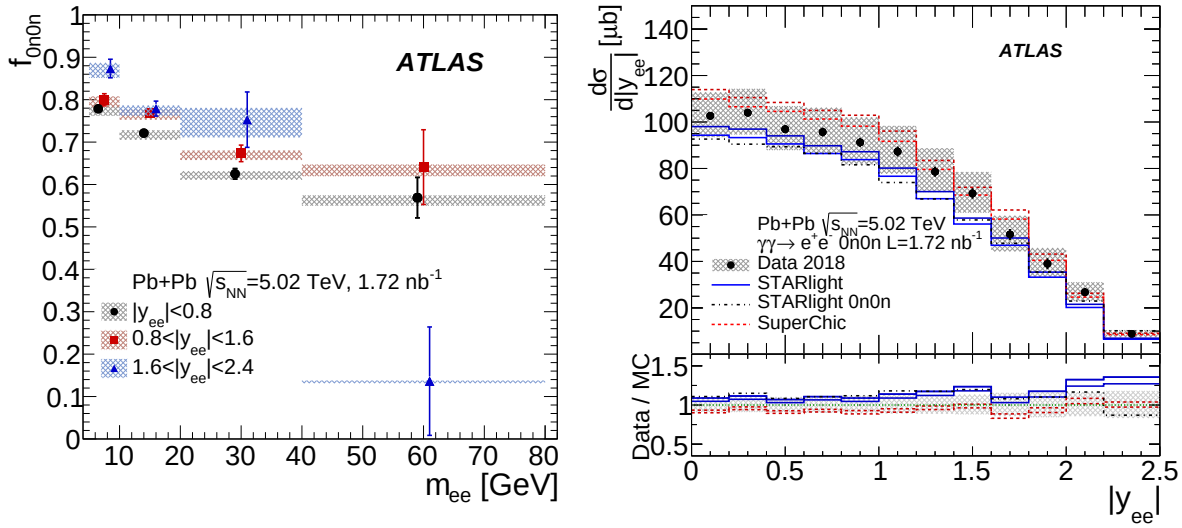

Figure 3 – (Left) Fractions of events in the 0n0n category evaluated from $\gamma\gamma \to e^+e^-$ data in three ranges of the dielectron rapidity, $|y_{ee}|$, corrected for the presence of additional neutrons [6]. Error bars represent statistical uncertainties, while shaded boxes represent systematic uncertainties. Points for $|y_{ee}| < 0.8$ and $1.6 < |y_{ee}| < 2.4$ are displaced horizontally for better visibility. (Right) Differential cross section measured for the 0n0n category for exclusive dielectron production as a function of $|y_{ee}|$ [6]. The cross section is compared with MC predictions from STARLIGHT (solid blue) and SUPERCHIC v3.05 (dashed red), each represented by two lines reflecting systematic variations. Also, a dedicated prediction from STARLIGHT for the 0n0n category (dashed-dotted black) is shown. The bottom panels show the ratios of data to predictions. The shaded area represents the total uncertainty of the data, excluding the 2% luminosity uncertainty.

4 Exclusive $\gamma\gamma \to \tau^+\tau^-$ production and tau anomalous magnetic moment

The ATLAS Collaboration made the observation of exclusive $\gamma\gamma \to \tau^+\tau^-$ production [8] in 2018 Pb+Pb collisions with an integrated luminosity of 1.44 nb^{-1}. Selected events contain one muon from a τ-lepton decay, an electron or charged-particle track(s) from the other τ-lepton decay, little additional central-detector activity, and no forward neutrons (0n0n category). After applying the full event selection, a total of 656 data events are observed in three signal regions (SR) in which the analysis is conducted. Figure 4 presents pre-fit control plots for muon-track invariant mass in the SR with one muon and one track (labeled μ1T-SR), three-track invariant mass in the SR with one muon and three tracks (labeled μ3T-SR), and muon-electron invariant mass in the SR with one muon and one electron (labeled μe-SR). A total of 532, 85, and 39 data events are observed in the μ1T-SR, μ3T-SR, and μe-SR, respectively. The most dominant background contributions in the SRs originate from exclusive $\gamma\gamma \to \mu^+\mu^-$ followed by FSR and dissociative photo-nuclear processes. Overall background is expected to contribute 84 ± 19, 9 ± 3, and 2.8 ± 0.7 events in the μ1T-SR, μ3T-SR, and μe-SR, respectively.

The $\gamma\gamma \to \tau^+\tau^-$ process is observed with a significance exceeding 5 standard deviations, and a signal strength of $\mu_{\tau\tau} = 1.03^{+0.06}_{-0.05}$ assuming the Standard Model value for the anomalous magnetic moment of the τ lepton, a_τ. The left panel of Figure 5 shows $\mu_{\tau\tau}$ extracted from the fit, based on the individual SRs. The combined $\mu_{\tau\tau}$ is also shown which is in agreement with the prediction from the Standard Model.

The measurement of $\gamma\gamma \to \tau^+\tau^-$ production from ATLAS provides also constraints on a_τ [8]. To measure a_τ, a profile-likelihood fit to the muon p_{T} distribution is performed in the three SRs with a_τ being the only free parameter. Also a control region with events from the $\gamma\gamma \to \mu^+\mu^-$ process is used in the fit to constrain initial-photon fluxes. The right panel of Figure 5 depicts the a_τ measurement alongside previous results obtained at LEP. The precision of this measurement is similar to the most precise single-experiment measurement by the DELPHI Collaboration [9].

5 Non-UPC dimuon production

Dimuon production induced by $\gamma\gamma$ fusion was also measured by ATLAS using non-UPC Pb+Pb collisions [10] spanning all centralities with an integrated luminosity of 1.94 nb^{-1}. The $\gamma\gamma \to \mu^+\mu^-$ pairs are identified using selections on pair momentum asymmetry, $A = (|p_{\mathrm{T},1} - p_{\mathrm{T},2}|/(p_{\mathrm{T},1} + p_{\mathrm{T},2}))$, and acopla-

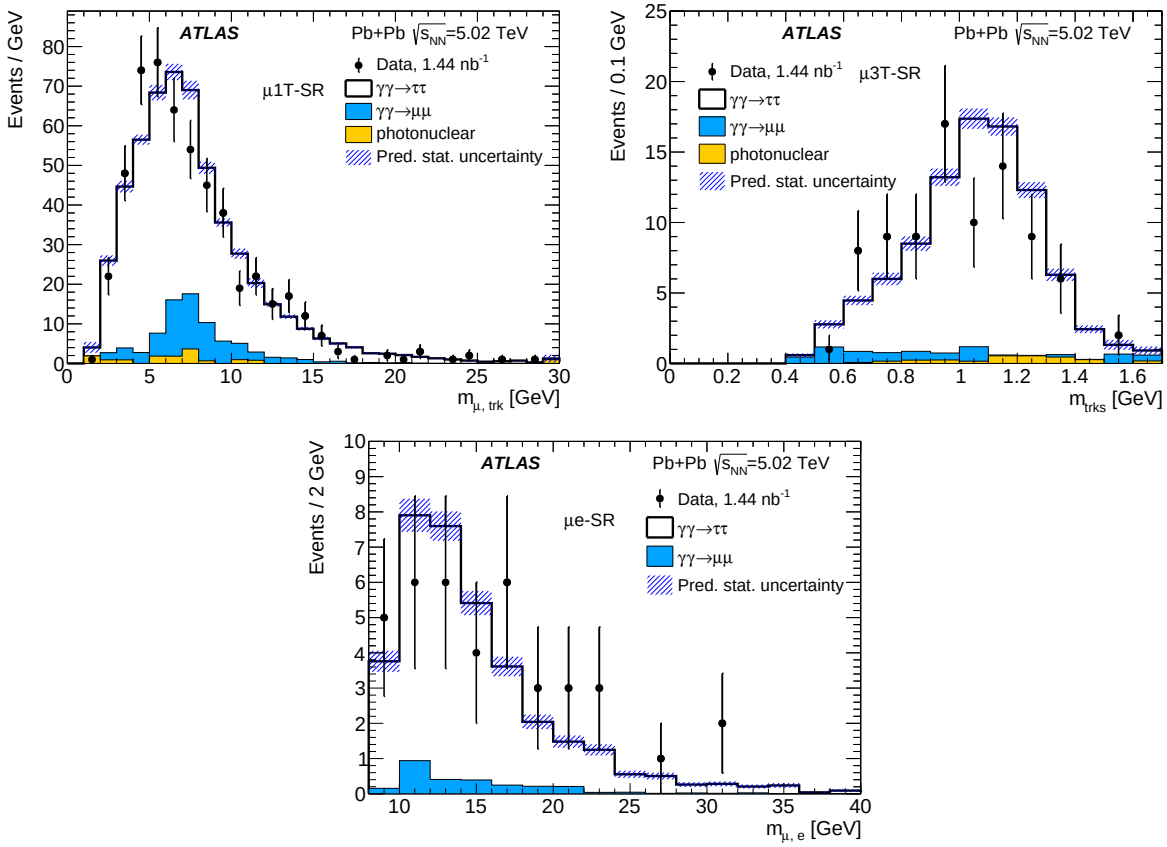

Figure 4 – Pre-fit control plots for (top-left) muon-track invariant mass in the μ1T-SR, (top-right) 3-track invariant mass in the μ3T-SR, (bottom) muon–electron invariant mass in the μe-SR [8]. Statistical uncertainties on the predictions are shown as hatched bands.

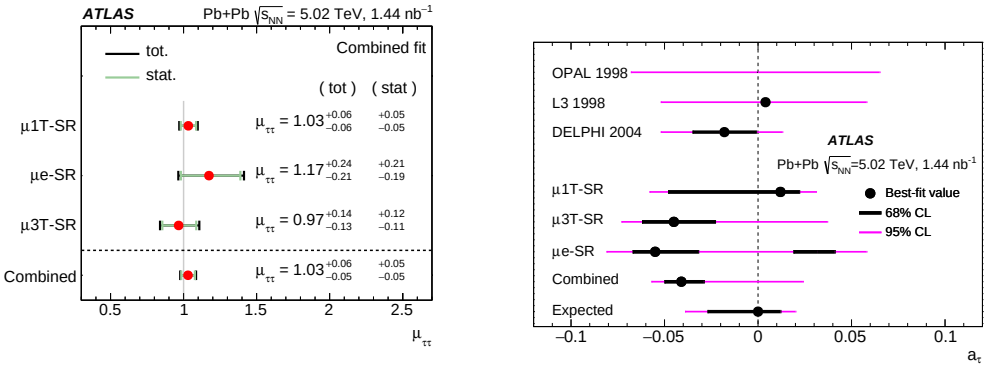

Figure 5 – (Left) Best-fit values of the signal strength parameter, $\mu_{\tau\tau}$, under the Standard Model a_τ value assumption, extracted from the fit based on the individual SRs [8]. (Right) Anomalous magnetic moment of tau a_τ from fits to individual SRs, and from the combined fit [8]. These are compared with existing measurements from the OPAL, L3 and DELPHI experiments at LEP.

narity of the dimuon system, α. Backgrounds, dominated by heavy-flavor decays, are evaluated using template fits to the distribution of muon-pair transverse impact parameter.

The STARLIGHT model, which was recently augmented to allow evaluation of cross sections for $\gamma\gamma \to \mu^+\mu^-$ production within restricted impact parameter intervals, is found to substantially underestimate the measured cross sections. Measurements of α and the associated transverse momentum scale, $k_\perp = \pi\alpha\bar{p_T}$, distributions ($\bar{p_T}$ stands for an average p_T of the two muons) confirm a significant centrality dependence in mean, RMS and standard deviations which are shown for α in Figure 6. The moments calculated for the initial-state QED [11] and PWF [12] predictions are in excellent agreement with each other except for the most central collisions where the QED results are slightly higher. Both calculations show systematic differences from the data in all centrality intervals including more peripheral collisions. Especially in the 60–70% and 70–80% intervals they are significant.

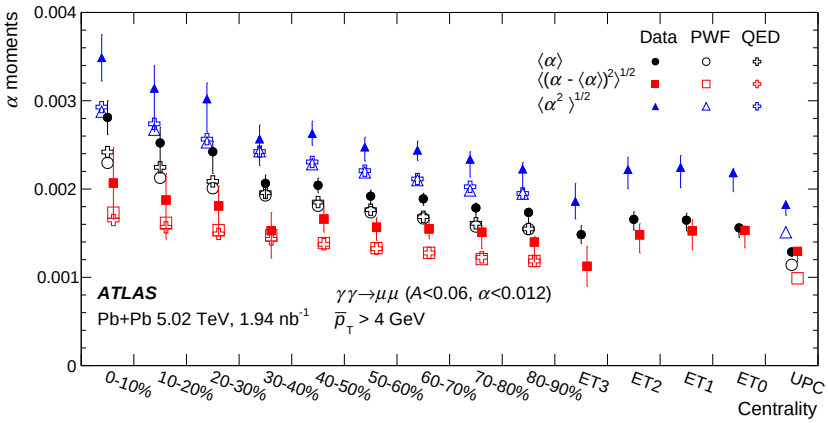

Figure 6 – Moments of the $\gamma\gamma \to \mu^+\mu^-$ acoplanarity distributions as a function of centrality compared with the QED and PWF predictions [10]. The error bars on the data points indicate combined statistical and systematic uncertainties.

With the improved statistical precision of this measurement, an additional depletion is observed in the α and $k_\perp$ distributions near zero values of the corresponding quantities. In more peripheral collisions, both calculations show weaker suppression near $\alpha = 0$ than is observed in the data. This is demonstrated in Figure 7 which shows the evolution of the α distribution as a function of centrality.

Moreover, the predicted trends associated with effects of magnetic fields on the dimuons are not observed in the ATLAS data.

6 Prospects for 2023 Pb+Pb measurements

In fall of 2023, a first high-luminosity data-taking campaign for heavy ions took place as part of Run-3 operations. Pb+Pb collisions were provided at the record center-of-mass energy of 5.36 TeV per nucleon pair. In preparation to the data-taking new triggering techniques were developed and optimized to provide better performance. Also the offline reconstruction for some objects was tuned. Last but not least the ZDC detectors were refurbished what resulted in a new functionality.

The left panel of Figure 8 shows a comparison of the average p_T for electrons from the $\gamma\gamma \to e^+e^-$ process between 2023 (markers) and 2018 (solid histogram) Pb+Pb data from UPC. The excess of electrons in the region of $2 < p_T < 5$ GeV results from the dedicated electron/photon reconstruction optimization for Run 3 and also dedicated trigger developments [14]. This improvement will extend future measurements involving electrons in UPC to cover this new kinematic regime. The reduction of systematic uncertainties originating from the limited statistics of electron/photon candidates in the Run-2 data is also anticipated. Improvements to photon reconstruction at low-p_T will open an opportunity for a new series of measurements involving photons from light-by-light scattering [16].

The right panel of Figure 8 depicts two-track invariant mass in the J/ψ window for events selected online using a novel approach with the Transition Radiation Tracker (TRT) trigger [15]. A clear excess of J/ψ event candidates can be identified at $m_{2\text{trk}} = 3.1$ GeV. Also large statistics of dimuon candidates contributing to the continuum region is visible. This development paves a way for dimuon measurements with low p_T muons in UPC Pb+Pb by ATLAS for the first time.

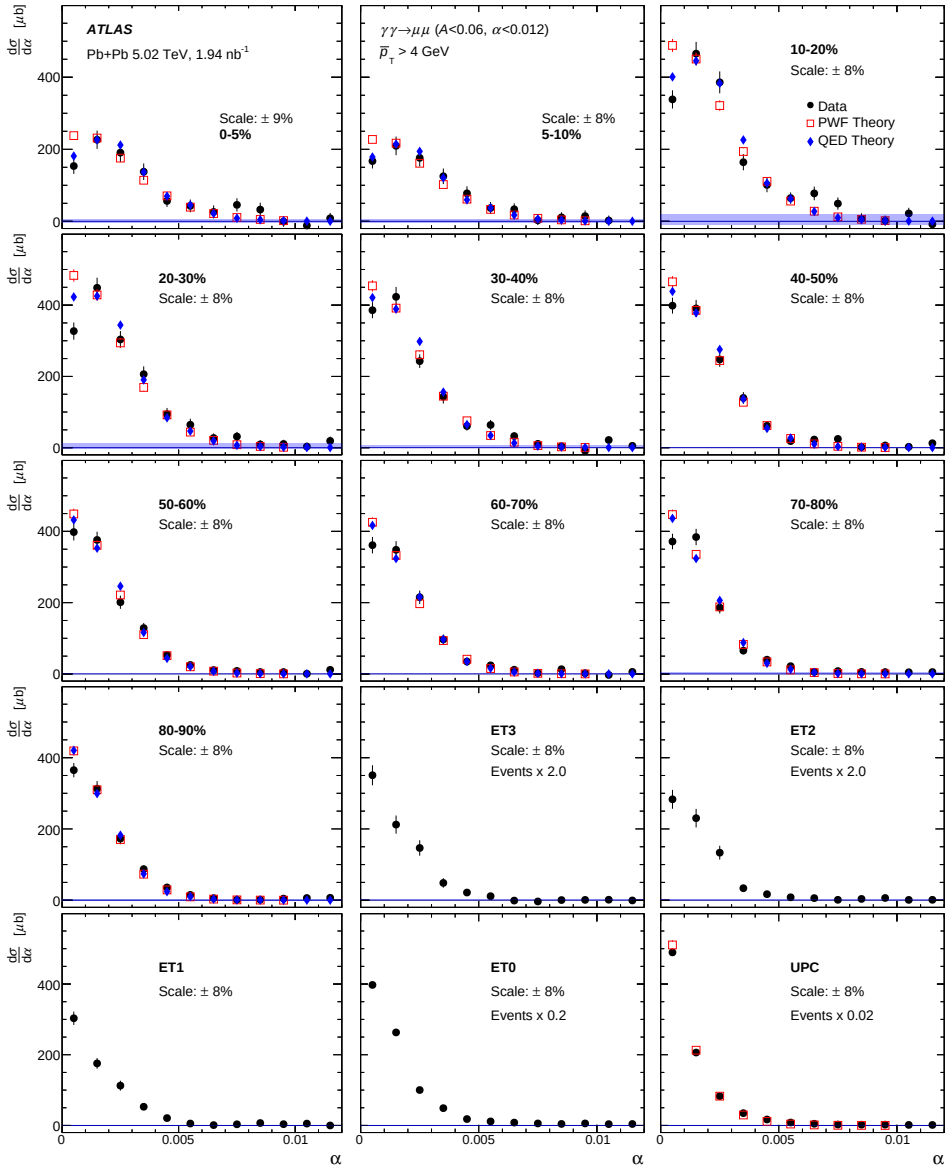

Figure 7 – Differential cross sections as a function of α for $\gamma\gamma \to \mu^+\mu^-$ pairs [10]. Each panel represents a different centrality interval, with the last panel representing the UPC events. The error bars indicate combined statistical and systematic uncertainties, excluding the background subtraction uncertainties, which are indicated by a shaded band at $d\sigma/d\alpha = 0$, and overall normalization uncertainties, which are quoted on each panel as "Scale". Also shown are the results of the QED and PWF theoretical calculations.

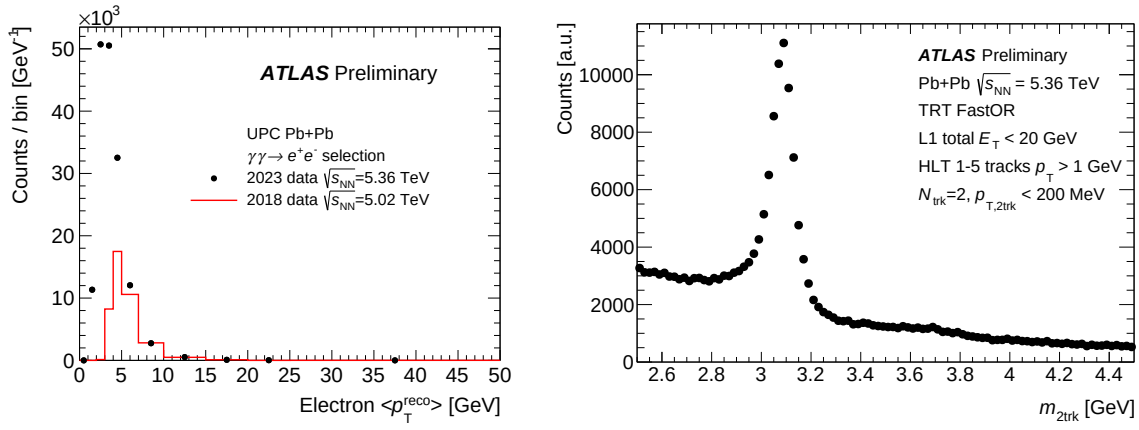

Figure 8 – (Left) Comparison of the average electron p_T between 2023 (markers) and 2018 (solid histogram) Pb+Pb data from UPC [13]. (Right) Two-track invariant mass in the J/ψ region for events selected by the level-1 TRT trigger.

7 Summary and outlook

In this report, the latest results for $\gamma\gamma$ fusion processes from the ATLAS Collaboration were discussed. The UPC physics program focused on precise measurements of exclusive $\gamma\gamma \to \mu^+\mu^-$ and $\gamma\gamma \to e^+e^-$ production including also forward neutron emission. Thanks to a large integrated luminosity of Pb+Pb collisions collected by ATLAS, low-rate processes such as $\gamma\gamma \to \tau^+\tau^-$ could be measured at the LHC for the first time. Also UPC proved to be a competitive tool for BSM searches. In particular, they provided constraints on τ anomalous magnetic moment with the precision comparable to the best world-limits from the LEP experiments. The latest precision results for $\gamma\gamma \to \mu^+\mu^-$ measured in non-UPC Pb+Pb collisions in all centralities revealed new features and made progress on the interpretation using the latest initial-state calculations. With a new sample of Pb+Pb data collected at the record center-of-mass energy of 5.36 TeV with about 1.7 nb^{-1} at the end of 2023, the ATLAS UPC physics program has a bright future.

Acknowledgments

This work was partly supported by the National Science Center of Poland under grant number UMO-2020/37/B/ST2/01043 and by PL-GRID infrastructure.

References

1. D. d'Enterria et al., J. Phys. G: Nucl. Part. Phys. **50**, 050501 (2023), doi:10.1088/1361-6471/
2. ATLAS Collaboration, JINST **3**, S08003 (2008), doi:10.1088/1748-0221/3/08/S08003
3. ATLAS Collaboration, Phys. Rev. **C 104**, 024906 (2021), https://doi.org/10.1103/PhysRevC.104.024906
4. S.R. Klein et al., Comp. Phys. Comm. **212**, 258 (2017), https://doi.org/10.1016/j.cpc.2016.10.016
5. L. A. Harland-Lang et al., Eur. Phys. J. C **76**, 1-9 (2016), https://doi.org/10.1140/epjc/s10052-015-3832-8
6. ATLAS Collaboration, J. High Energy Phys. **06**, 182 (2023), https://doi.org/10.1007/JHEP06(2023)182
7. S.R. Klein, P. Steinberg, Ann. Rev. Nucl. Part. Sci. **70**, 323-354 (2020), https://doi.org/10.1146/annurev-nucl-030320-033923
8. ATLAS Collaboration, Phys. Rev. Lett. **131**, 151802 (2023), https://doi.org/10.1103/PhysRevLett.131.151802
9. DELPHI Collaboration, Eur. Phys. J. **C 35**, 159 (2004), doi:10.1140/epjc/s2004-01852-y
10. ATLAS Collaboration, Phys. Rev. **C 107**, 054907 (2023), https://doi.org/10.1103/PhysRevC.107.054907

11. S. Klein, A. H. Mueller, B.-W. Xiao, and F. Yuan, Phys. Rev. **D 102**, 094013 (2020), https://doi.org/10.1103/PhysRevD.102.094013
12. W. Zha, J. D. Brandenburg, Z. Tang, and Z. Xu, Phys. Lett. **B 800**, 135089 (2020), https://doi.org/10.1016/j.physletb.2019.135089
13. ATLAS Collaboration, https://atlas.web.cern.ch/Atlas/GROUPS/PHYSICS/PLOTS/HION-2023-001/
14. Karolina Domijan (for the ATLAS Collaboration), https://cds.cern.ch/record/2881824, https://doi.org/10.22323/1.450.0265
15. Pawel Rybczynski (for the ATLAS Collaboration), https://cds.cern.ch/record/2891399
16. ATLAS Collaboration, J. High Energy Phys. **03**, 243 (2021), https://doi.org/10.1007/JHEP03(2021)243

Phys. Proc. Ultra-Peripheral Collisions **1**, 011 (2024) 1-8

Four-pion state in UPC

Mariola Kłusek-Gawenda
Institute of Nuclear Physics Polish Academy of Sciences,
Radzikowskiego 152, PL-31-342 Kraków, Poland

The production of $2\pi^+2\pi^-$ in ultraperipheral heavy-ion collisions at RHIC and LHC energies is studied. Preliminary H1 data is used to enhance the understanding of the poorly known process. Predictions for photon-nucleus interactions are calculated for various excited states of mesons. Agreement between theoretical predictions and available STAR data at RHIC is presented. The comparison of the $2\pi^+2\pi^-$ invariant mass spectrum and nuclear total cross section indicates that $\rho(1570)$ plays a crucial role in accurately describing existing experimental data. Nuclear predictions for LHC energy in the central region of rapidity are also provided.

DOI: https://doi.org/10.17161/bc489f93
Keywords: Heavy ion ultraperipheral collisions, rho meson, four-pion production

1 Motivation

The exclusive production of four charged pions is an area of growing interest within the field of particle physics. This process, particularly in the context of ultraperipheral heavy-ion collisions and photoproduction, provides a unique opportunity to explore a variety of fundamental aspects of the underlying physics. These include resonance production, and searches for exotic resonances. In recent studies, the H1 collaboration at HERA [1] has presented preliminary data on exclusive four-pion production, marking a significant step forward in our understanding of this complex process. This data, along with earlier findings from the STAR Collaboration [2], highlights the potential of studying this decay mode to uncover the characteristics of various resonances that contribute to the process. Furthermore, the exclusive production of four charged pions at low photon virtualities ($Q^2 < 2$ GeV^2) and in ultraperipheral heavy-ion collisions offers an opportunity to observe coherent photoproduction and the behavior of vector mesons such as $\rho(1450)$, $\rho(1570)$, $\rho^0(1700)$. The invariant mass spectrum associated with this production often reveals broad peaks, providing crucial insights into the properties of mesonic states.

The motivation for this study stems from findings presented by the H1 collaboration, which suggest intriguing avenues for further investigation. By studying four charged pion photoproduction at LHC energies, we aim to make predictions and contribute valuable insights to this evolving field [3].

2 Meson photonuclear production

Vector meson photoproduction is a key area of study in particle physics, particularly for understanding the interactions between photons and protons. One commonly used theoretical framework for this process is the vector meson dominance model (VDM) [4,5]. The photon is treated as fluctuating into a hadronic state that can interact with a proton through Pomeron or Reggeon exchange. The VDM provides a way to describe the behavior of the photon in terms of vector mesons, which mediate the interaction with the proton. This approach has been successful in explaining various aspects of photoproduction and scattering processes. For instance, the proton, meson, or photon ($X = p, V, \gamma$ respectively) cross sections can be modeled using the Donnachie and Landshoff model [6], which accounts for exchanges through Pomeron and Reggeon trajectories. Through VDM, the total cross section dependence can be analyzed, allowing researchers to gain insights into the underlying dynamics of vector meson photoproduction. The

dependence of the total cross section on the two main trajectories can be expressed as follows

$$\sigma_{tot}(Xp) = \alpha_1 W_{\gamma p}^{-\delta_1} + \alpha_2 W_{\gamma p}^{\delta_2} \,. \tag{1}$$

The component with a negative power corresponds to the Reggeon exchange, specifically involving the exchange of mesons such as ρ, ω, f and a. The second term in Eq. 1 arises from the Pomeron exchange, which becomes dominant at sufficiently high energies. By analogy with the Reggeon and Pomeron exchange, the cross section for exclusive vector meson production can be determined. The CMS Collaboration measured exclusive $\rho^0(770)$ meson photoproduction in ultraperipheral $p-Pb$ collisions at a center-of-mass energy of 5.02 TeV [7]. Their measurements of δ_1 and δ_2 are utilized in this analysis.

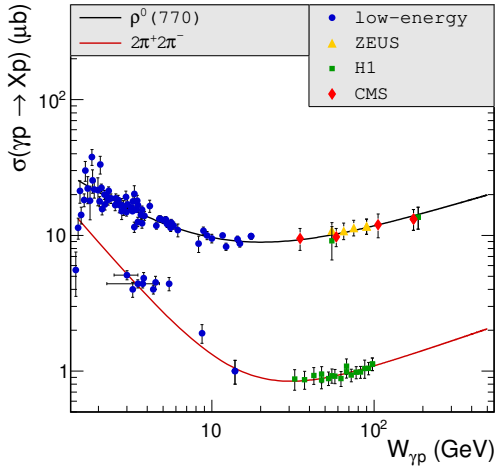

Figure 1 – Total cross section for the exclusive production of $\rho^0(770)$ vector meson (upper line) and $2\pi^+2\pi^-$ production (lower line). The parametrization of low-energy [8,9,10,11] and high-energy $\rho^0(770)$ data [12,13,7] as well as low-energy [14,15,16,17,18] and preliminary H1 four-charged-pion data [1] are presented.

Fig. 1 shows the total cross section for exclusive photoproduction of $\rho^0(770)$ vector meson and the $2\pi^+2\pi^-$ state. The low-energy data (blue circular points), with $W_{\gamma p} < 20$ GeV, were obtained using fixed-target experiments. The cross section for the $\sigma(\gamma p \to \rho^0(770)p)$ process was measured at an average energy of $< W_{\gamma p} >= 92.6$ GeV by the CMS Collaboration and found to be 11.2 ± 1.4 (stat) ± 1.0 (syst.) μb. The CMS measurement aligns with the previous data [8,9,10]. The data show good agreement with our calculations, particularly at HERA and LHC energies

Due to the limited experimental data on four-pion production, there is no consensus on which resonance states play the most significant role. At low $W_{\gamma p}$ energies (less than 3 GeV), the non-resonant signal dominates, while excited states of the ρ meson become important for $W_{\gamma p} > 4$ GeV. Such resonances should be considered in the context of $\pi^+\pi^-\pi^+\pi^-$ production at HERA, RHIC, and LHC energies. A simple fit to H1 data [1] demonstrated that a combination of the Breit-Wigner $\rho(1570)$ resonant, non-resonant four-pion state, and complex phase ($\rho(1570) - 4\pi$ interference) adequately describes the experimental points. From the four-pion invariant mass distribution ($M_{4\pi}$), it can be inferred that a single broad $\rho(1570)$ resonance is the most significant in the photoproduction of exclusive $2\pi^+2\pi^-$ final states. Additionally, data reveals a correlation in the four-pion invariant mass of oppositely charged pions, suggesting an enhancement of the four-pion signal around $M_{4\pi} = 1450$ and 1700 MeV. These correspond to the $\rho(1450) \equiv \rho'$ and $\rho(1700) \equiv \rho''$ states. Unfortunately, the branching rates of these resonances to four-pion states remain uncertain, limiting our ability to accurately determine these factors. Similarly, the branching ratio for $\rho \to e^+e^-$ is another value lacking precision. Table 1 shows the mass and width of resonances [19] as well as estimated values of $\Gamma(V \to e^+e^-)$ used in this analysis.

In the VDM-Regge approach, the photon state $|\gamma>$ is considered aquantum mechanical superposition of the quantum electrodynamics photon state $|\gamma_{QED}>$ and a hadronic state $|h>$:

$$|\gamma >= \mathcal{N}|\gamma_{QED} > + |h> \text{ , where } |h >= \sum_h \frac{e}{f_V}|V> \ . \tag{2}$$

The vector meson-photon coupling , represented by $f_V^2 = \frac{e^2 \alpha_{em} m_V}{3\Gamma(V \to e^+e^-)}$, is derived from the e^+e^- decay width of the vector meson with m_V mass. The constant factor f_V is independent of Q^2 and represents

Table 1: Characteristic of the ρ', $\rho(1570)$ and ρ'' mesons.

Resonance	m [GeV]	Γ [GeV]	$\Gamma_{e^+e^-}$ [keV]
$\rho(1450)$	1.465 ± 0.025	0.4 ± 0.05	$4.30 - 10$
$\rho(1570)$	1.570 ± 0.070	0.144 ± 0.09	$0.35 - 0.5$
$\rho(1700)$	1.720 ± 0.020	0.25 ± 0.01	$6.30 - 8.9$

the probability of the photon transitioning into a vector meson. The normalization factor $\mathcal{N}$ in Eq. (2) ensured the proper balance of the superposition. The hadronic state $|h>$ is expected to have the same additive quantum numbers as the photon, with $J^{PC} = 1^{--}$, and $Q = B = S = 0$ for vector meson. The QED component on its own does not interact with hadrons [20]. Notably, the primary contributions to the hadronic component $|V>$ come from the light vector mesons (ρ^0, ω and ϕ), which forms the central hypothesis of the VDM approach. The straightforward VDM-Regge approach enables the description of the photon-to-vector meson transition using the relation of the photon-proton cross section. Given that H1 data does not provide differential cross sections in the square of the momentum transfer for the $\gamma p \to 2\pi^+2\pi^- p$ process, we have used $\sigma(\gamma p \to 2\pi^+2\pi^- p)$ as the baseline for this analysis. In the VMD-Regge model, the total cross section for Vp photoproduction can be calculated through the optical theorem considering the forward $\gamma p \to Vp$ cross section:

$$\sigma_{tot}(Vp) = \frac{f_V^2}{e^2}\sigma(\gamma p \to Vp) \, . \tag{3}$$

Our simple calculation effectively models the experimental data for $\sigma(\gamma p \to 2\pi^+2\pi^- p)$ (see Fig. 1), particularly at the energy levels relevant to H1.

Photoproduction of vector mesons on the nucleus can be considered by integrating the VDM-Regge model with the Glauber theory of multiple scattering [21]. The total cross section for light vector meson–nucleus interaction is computed using the nuclear optical density normalized to unity ($T_A(\vec{b}) = \int_{-\infty}^{+\infty} \rho(\vec{b}, z)\mathrm{d}z$) in the following equation [22]:

$$\sigma_{tot}(VA) = \int \left[1 - \exp\left(-\sigma_{tot}\,(Vp)\, T_A(\vec{b})\right)\right] \mathrm{d}^2 b \tag{4}$$

The two-parameter Fermi model is employed to represent the densities of gold and lead nuclei [23]. The charge distribution within the nucleus is adjusted to match the mass number using the relation: $\int \mathrm{d}^2 b \rho(b, z)\mathrm{d}z = A$. Eq. (4) is framed within the "classical mechanics" context. It's important to mention that the "quantum expression" is also frequently referenced in literature. Nonetheless, as detailed in Ref. [26], for coherent J/ψ photoproduction in ultraperipheral collisions, there is approximately a 15% deviation between these two different rescattering approaches. Additionally, the discrepancy between the methods increases when considering $\rho^0(770)$ photoproduction [27]. The formula for coherent vector meson photoproduction on nuclei is as follows:

$$\sigma\left(\gamma A \to VA\right) = \frac{1}{16\pi}\frac{e^2}{f_V^2}\sigma_{tot}^2\left(VA\right)\int |F(t)|^2 \, \mathrm{d}t \, . \tag{5}$$

The nuclear form factor is expressed through charge distribution in the nucleus. Here we use the so-called realistic form factor. See *e.g.* Ref. [24] for more details.

Fig. 2(a) illustrates the cross section for the photoproduction of two- and four-pion state, particularly for the lead nucleus. The highest cross section is observed when the $\rho^0(770)$ meson decays into the $\pi^+\pi^-$ channel. The theoretical model, which includes the classical approach of ρ^0 photoproduction (Eq. (4)), aligns well with the LHC experimental data. We present two datasets from the STAR collaboration at RHIC. The first dataset (represented by green triangular points) has been utilized in numerous theoretical and phenomenological studies on $\rho^0(770)$ photoproduction, such as Ref. [32]. Our parametrization agrees with these calculations, while Ref. [33] identifies a slight discrepancy with other approaches. The new data points provide an estimation of STAR data for $Au - Au$ collision energies of 62.4, 130, and 200 GeV. The mid-rapidity cross section is as follows:

$$\sigma(\gamma A \to VA; y = 0) = \frac{1}{N_{\gamma A}(y = 0)}\frac{\mathrm{d}\sigma(AA \to AAV; y = 0)}{\mathrm{d}y} \, . \tag{6}$$

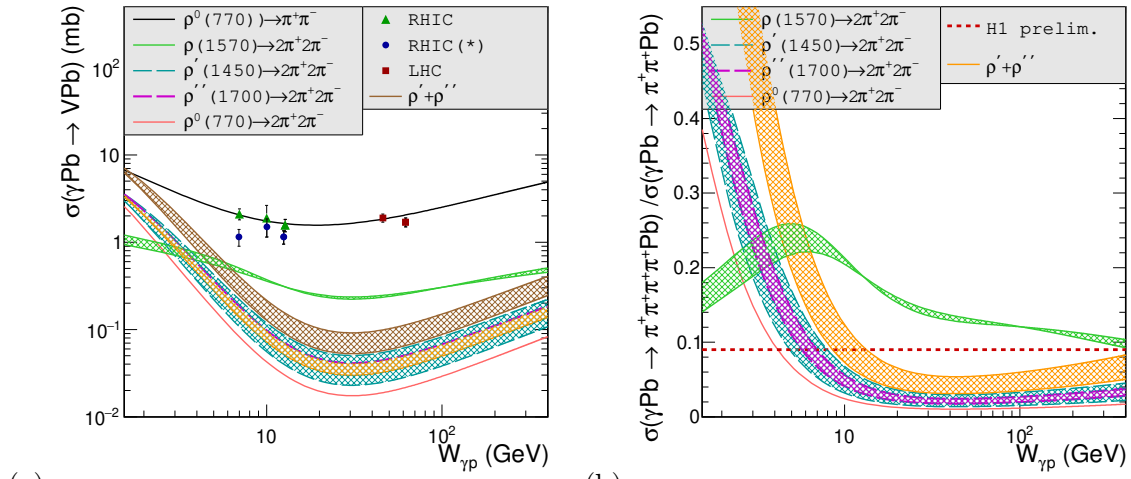

Figure 2 – (a) Cross section for the $\gamma Pb \to VPb$ process. The upper black line shows the results for $V = \rho^0(770)$ that decays into two charged pions. Lowers curves correspond to $2\pi^+2\pi^-$ production. Results for $\gamma Pb \to \pi^+\pi^- Pb$ are compared with existing experimental data [28,35,30,31]. (b) Ratio of four to two charged pions photoproduction. The theoretical results are compared with the recent H1 preliminary data [1].

Results set has been calculated using so-called realistic form factor. The flux of equivalent photons is heavily dependent on the charge distribution within the nucleus, especially at small impact parameters. This subject requires further detailed investigation in subsequent studies.

The branching ratios of excited ρ states are not well established. The final result of the photonuclear section depends on this limit. Fig. 2 shows band of uncertainty correspond to the decay of $\rho', \rho'', \rho(1570)$ into 4 charged pions. At low photon-nucleus energies, the combined contribution of ρ' and ρ'' surpasses the impact of the $\rho(1570) \to 4\pi$ decay. The $\gamma Pb \to \rho(1570)Pb$ cross section starts to dominate over other excited states only when $W_{\gamma p}$ is above 8 GeV. The lowest curve is associated with the $\rho^0(770)$ meson, which decays into a four-charged-pion channel. The difference in distribution between two- and four-pion states from ρ^0 decay can vary by as much as two orders of magnitude. Fig. 2(b) illustrates the ratio of $\pi^+\pi^-\pi^+\pi^-$ to $\pi^+\pi^-$ photoproduction. Theoretical results are compared with preliminary H1 data, which is around 9% [1]. The range of $W_{\gamma p}$ energy used for photoproduction at LHC energy is approximately 10 GeV for $y = -4$ and 650 GeV for $y = 4$. For the decay of $\rho(1570) \to 2\pi^+2\pi^-$ at mid-rapidity, the energy is around 90 GeV. While our results do not perfectly match the H1 value, they are close to it. The results for $\rho(1570)$ tend to overestimate the data, whereas the combined sum of ρ' and ρ'' is less than the preliminary H1 point in the energy range that aligns with LHC measurements

3 Cross sections for nuclear four-pion production

Nuclear photoproduction of a vector meson V can be expressed as the combination of the photonuclear cross section Eq. (5) and equivalent photons fluxes:

$$\frac{\mathrm{d}\sigma(AA \to AAV)}{\mathrm{d}^2b\mathrm{d}y} = \omega_1 N(\omega_1, b)\sigma(\gamma A_2 \to VA_2) + \omega_2 N(\omega_2, b)\sigma(\gamma A_1 \to VA_1)\ , \tag{7}$$

In the equation, $\omega_i = m_V/2exp(\pm y)$ represents the energy of emitted photon, while b stands for the impact parameter. We focus on ultraperipheral collisions, implying that transverse distance between the centers of the nuclei is larger than the sum of the radii of nuclei [25]. The photon flux depends on the form factor, specially on the charge distribution within the nucleus. For a detailed analysis of the model for vector meson photoproduction, refer to [26,34]. Eq. (7) allows the calculation of both total and differentail cross section as a function of the rapidity of outgoing photon or impact parameter. A comprehensive analysis should also account for the kinematics of the decay products. In the study of four-pion production, the rapidity of each outgoing pion must be considered, achieved by accounting for the smearing of ρ mesons. The widths of ρ', ρ'', and $\rho(1570)$ are knows, see Table 1. The primary part of the vector meson's spectral shape is derived from the Breit-Wigner formula:

$$\mathcal{A} = \mathcal{A}_{BW}\frac{\sqrt{mm_V\Gamma(m)}}{m^2 - m_V^2 + im_V\Gamma(m)} + \mathcal{A}_{bkg}\ . \tag{8}$$

The mass-dependent width is expressed using the following formula:

$$\Gamma(m) = \Gamma_V \frac{m_V}{m} \left(\frac{m^2 - 4m_V^2}{m_V^2 - 4m_\pi^2} \right)^{\frac{3}{2}} . \tag{9}$$

A term $\mathcal{A}_{bkg}$ is understood to represent the background contribution from $\pi^+\pi^-$ production. This factor accounts for the enhancement on the left side of the resonance term and some blurring on the right side. Ideally, data including the rapidity of each decay particle would allow for a thorough kinematic study of the $1 \to 4$ process. For simplicity, we consider the $1 \to 4$ state as a two-step process: $1 \to 2 \to 4$:

$$\sigma(AA \to AAV \to AA\pi^+\pi^-\pi^+\pi^-, y_V) = \mathcal{C} \times \tag{10}$$
$$\left[\sigma(AA \to AAV \to AA\pi^+\pi^-\pi^+\pi^-; y_{\pi_1} y_{\pi_2}) \times \right. \tag{11}$$
$$\left. \sigma(AA \to AAV \to AA\pi^+\pi^-\pi^+\pi^-; y_{\pi_3} y_{\pi_4}) \right] .$$

The normalization constant $\mathcal{C}$ varies for each excited state of the ρ meson and is computed as follows:

$$\begin{aligned} \mathcal{C} \;=\; & 2\pi \frac{|\mathcal{A}|^2}{\int |\mathcal{A}|^2 dm_V} \frac{\mathrm{d}\sigma(AA \to AAV \to AA\pi^+\pi^-\pi^+\pi^-)}{\mathrm{d}^2 b \mathrm{d}y_V} \mathrm{d}m_V \mathrm{d}y_V \mathrm{d}b \\ / \; & \left[\frac{\mathrm{d}\sigma(AA \to AAV \to AA\pi^+\pi^-\pi^+\pi^-; y_{\pi_1} y_{\pi_2})}{\mathrm{d}y_{V_1} \mathrm{d}m_{V_1}} (1 - z_{\pi_1}^2) \mathrm{d}y_{V_1} \mathrm{d}m_{V_1} \right] \\ / \; & \left[\frac{\mathrm{d}\sigma(AA \to AAV \to AA\pi^+\pi^-\pi^+\pi^-; y_{\pi_3} y_{\pi_4})}{\mathrm{d}y_{V_2} \mathrm{d}m_{V_2}} (1 - z_{\pi_3}^2) \mathrm{d}y_{V_2} \mathrm{d}m_{V_2} \right] . \end{aligned} \tag{12}$$

The normalization takes into account the so-called a weight, which depends on the angle of vertical dispersion, $\sin^2(\theta)$. The normalization factor is equal to 1 for the case when pions are measured in full range. Then the total cross section for the production of four pions is equal to the total cross section for the production of a meson that decays into the four-pion state under study.

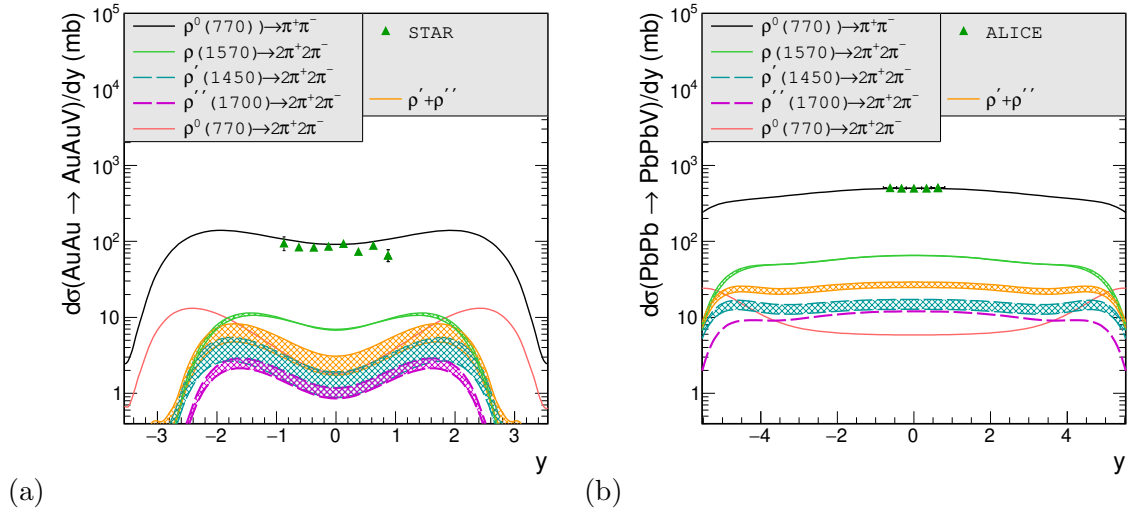

Figure 3 – Differential cross section as a function of rapidity of vector meson that decays into two or four charged pions. Results for $\pi^+\pi^-$ production are compared to the STAR data [35] (a) and the ALICE data [36] (b).

Fig. 3 presents the results for ultraperipheral $Au - Au$ collisions at $\sqrt{s_{NN}} = 200$ GeV (a) and Pb–Pb collisions at $\sqrt{s_{NN}} = 5.02$ TeV (b). the photoproduction of the $\rho(770)$ meson, which decays into two charged pions (represented by the upper black line), as well as the photoproduction of other vector meson ($\rho(1570)$ - solid green line, $\rho(1450)$ - dashed blue line, $\rho(1700)$ - dashed purple line, $\rho^0(770)$ - solid red line) are shown. As with the results in Fig. 2, uncertainties related to $V - \gamma$ coupling constant are indicated. The combined contribution from the ρ' and ρ'' is also highlighted (orange band). It is evident that the contribution for $\rho^0(770) \to \pi^+\pi^-\pi^+\pi^-$ state plays a significant role across a wide range of the meson rapidity at STAR, but it becomes less prominent at forward rapidities. The cross section for the production of four-charged-pion is largest in the case of $\rho(1570)$ meson decay.

The STAR Collaboration reported on the photoproduction of four pions in ultraperipheral $Au - Au$ collisions at $\sqrt{s_{NN}} = 200$ GeV [2], measuring pions at mid-rapidity, $|y_\pi| < 1$. Fig. 4 shows the four-pion invariant mass distribution, comparing the STAR data with our calculation. It also illustrated the

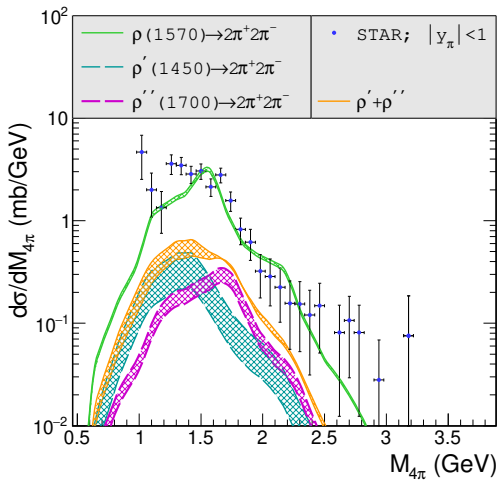

Figure 4 – Differential cross section as a function of four pion invariant mass.

contribution from the double-scattering ρ^0 mechanism discussed in Ref. [34], which accounts for approximately 20% of the measured cross section. Four-pion production can be also attributed to the subprocess $\gamma\gamma \to \rho^0\rho^0$, Ref. [37]. However, the cross section for the reaction $AuAu \to AuAu\rho^0\rho^0 \to AuAu2\pi^+2\pi^-$ is approximately two orders of magnitude smaller than the cross section measured by STAR. Fig. 4 also shows distributions for ρ', ρ'', their combined sum, and $\rho(1570)$. A correction for the acceptance function described in [34] has been applied. We find good agreement with the experimental data, particularly in terms of the decay of the $\rho(1570)$ resonance, which closely matches the STAR data. The shape of the four-pion invariant mass is strongly influenced by the Breit-Wigner description. In other words, the profile of the resonance smearing depends on the background correction factor, although the normalization of the smearing mass function remains consistent regardless of this factor. Although the H1 has also reported the four-pion invariant mass distribution, additional data is needed for direct comparison with our calculation. The sum of incoherent $\rho^{'}$ and $\rho^{''}$ mesons results in a cross section range of $0.41-0.74$ mb. The coherent sum of the mesons includes two $e^{i\varphi}$ factors in the Breit-Wigner formula. The first phase corresponds to the ρ' resonance, while the second phase φ_2 pertains to ρ''. The shape of the invariant mass is heavily dependent on the phase. The experimental cross section within $|y| < 1$ is measured at $\sigma = 2.4 \pm 0.2 \pm 0.8$ mb. The theoretical result for the $AuAu \to AuAu\rho(1570)(\to \pi^+\pi^-\pi^+\pi^-)$ process gives a range between $(2.16 - 2.31)$ mb.

Table 2: Ratio of the total cross section for the production of exclusive $\pi^+\pi^-\pi^+\pi^-$ to exclusive $\pi^+\pi^-$ in ultra-peripheral heavy ion collisions at $\sqrt{s_{NN}} = 200$ GeV and $\sqrt{s_{NN}} = 5.5$ TeV.

	$Au-Au$ at $\sqrt{s_{NN}} = 200$ GeV		$Pb-Pb$ at $\sqrt{s_{NN}} = 5.5$ TeV	
Resonance	$\lvert y_\pi\rvert < 10$	$\lvert y_\pi\rvert < 1$	$\lvert y_\pi\rvert < 10$	$\lvert y_\pi\rvert < 1$
$\rho(1450)$	$(2.1-2.8)\%$	$(1.9-2.5)\%$	3.7%	3%
$\rho(1570)$	$(5.8-6.2)\%$	8.2%	11.6%	13%
$\rho(1700)$	1.2%	1.3%	2.3%	2.4%
experimental data	$(13.4 \pm 4.5)\%$	$(16.4 \pm 5.3)\%$		

Given the strong agreement between the STAR data and our calculations, we now discuss predictions for LHC energies. Table 2 shows the ratio of total cross sections for the photoproduction of exclusive four-charged-pion to two-charged-pion states. The collision energies correspond to RHIC and LHC energies, with results provided for two intervals of pion rapidity: mid-rapidity in the range $(-1, 1)$ and $(-10, 10)$. Our predictions are compared with those from RHIC [2]. The cross sections are calculated using the decay width ranges specified in Table 1.

4 Summary and conclusions

We have presented the results from a simple model for the photoproduction of vector mesons that decay into the pion states. By incorporating a parametrization of recent preliminary data from the H1 Collaboration, this work enhances our understanding of the role of the ρ' and ρ'' resonances, as well as the $\rho(1570)$ meson, in exclusive four-pion production. Our study reveals that the $\rho(1570) \to \pi^+\pi^-\pi^+\pi^-$ process is dominant in the ultraperipheral heavy-ion collisions. A single ρ' or ρ'' resonances appears sufficient to describe the data. This work also highlights the significance of the broad $\rho(1570)$ resonance into the $AuAu \to AuAu\pi^+\pi^-\pi^+\pi^-$ process. The primary objective of this analysis was to offer specific predictions for LHC energies.

Recently, the ALICE Collaboration measured the cross section of exclusive four-pion photoproduction in ultraperipheral $Pb-Pb$ collisions at $\sqrt{s_{NN}} = 5.02$ TeV, Ref. [38]. The integrated four-pion cross section over the invariant mass range (0.8–2.5) GeV was found to be $d\sigma/dy = 47.8 \pm 2.3$ (stat.) ± 7.7 (syst.) mb at midrapidity $|y| < 0.5$. The peak around the invariant mass 1.5 GeV aligns with results reported by the STAR Collaboration. ALICE's data showes a better agreement with the two-resonance scenario than with the $\rho(1570)$. However, the data diverged by 2.1σ from our calculations based on a single resonance, as suggested by the H1 Collaboration. The ratio of the cross sections of ρ to ρ^0 is lower than measured by STAR in the events with mutual nuclear excitation.

Acknowledgments

I would like to thank Daniel Tapia-Takaki and Gerardo Herrera, co-chairs of the conference, for making the idea of organizing the first international workshop on the physics of Ultra Peripheral Collisions. This work has been supported by the Polish National Science Center grant DEC-2021/42/E/ST2/00350.

References

1. H1 Collaboration, S. Schmitt, 26th International Workshop on Deep Inelastic Scattering and Related Subjects (DIS 2018): Port Island, Kobe, Japan, April 16-20, 2018.
2. STAR Collaboration, B.I. Abelev et al., Phys. Rev. **C81** (2010) 044901 doi:10.1103/PhysRevC.81.044901
3. M. Klusek-Gawenda and J.D. Tapia Takaki, Acta Phys. Polon. **B51** (2020) 6, 1393 doi:10.5506/APhysPolB.51.1393
4. J.J. Sakurai, Annals Phys. 11 (1960) 1 doi:10.1016/0003-4916(60)90126-3
5. M. Gell-Mann and F. Zachariasen, Phys. Rev. **124** (1961) 953 doi:10.1103/PhysRev.124.953
6. A. Donnachie, P.V. Landshoff, Phys. Lett. **B296** (1992) 227 doi:10.1016/0370-2693(92)90832-O
7. CMS Collaboration, A. M. Sirunyan et al., Eur. Phys. J. **C79** (2019) 8 doi:10.1140/epjc/s10052-019-7202-9",
8. D. G. Cassel et al., Phys. Rev. **D24** (1981) 2787 doi:10.1103/PhysRevD.24.2787
9. E665 Collaboration, M. R. Adams et al., Z. Phys. **C74** (1997) 237 doi:E665:1997qph
10. CLAS Collaboration, C. Hadjidakis et al., Phys. Lett. **B605** (2005) 256 doi:10.1016/j.physletb.2004.11.019
11. CLAS Collaboration, S. A. Morrow et al., Eur. Phys. J. **A39** (2009) 5 doi:10.1140/epja/i2008-10683-5
12. H1 Collaboration, S. Aid et al., Nucl. Phys. **B463** (1996) 3 doi:10.1016/0550-3213(96)00045-4",
13. ZEUS Collaboration, J. Breitweg et al., Eur. Phys. J. **C2** (1998) 247 doi:10.1007/s100520050136
14. H. H. Bingham et al., Phys. Lett. **41B** (1972) 635 doi:10.1016/0370-2693(72)90653-3
15. M. Davier, et al., Nucl. Phys. **B58** (1973) 31 doi:10.1016/0550-3213(73)90545-2
16. P. Schacht, et al., Nucl. Phys. **B81** (1974) 205 doi;10.1016/0550-3213(74)90164-3
17. M. S. Atiya, et al., Phys. Rev. Lett. **43** (1979) 1691 doi:10.1103/PhysRevLett.43.1691
18. D. Aston, et al., Nucl. Phys. **B189** (1981) 15 doi:10.1016/0550-3213(81)90079-1
19. Particle Data Group, M. Tanabashi et al., Phys. Rev. **D98** (2018) 030001 doi:10.1103/PhysRevD.98.030001
20. T. H. Bauer, et al., Rev. Mod. Phys. **50** (1978) 261. [Erratum: Rev. Mod. Phys.51,407(1979)] doi:10.1103/RevModPhys.50.261
21. R. Glauber, *Lectures in theoretical physics*, vol.1. W.e. brittin, l.g. dunham (eds.), Interscience Publisher Inc., New-York.
22. S. Klein and J. Nystrand, Phys. Rev. **C60** (1999) 014903 doi:10.1103/PhysRevC.60.014903

23. H. De Vries, C. W. De Jager, and C. De Vries, Atom. Data Nucl. Data Tabl. **36** (1987) 495 doi:10.1016/0092-640X(87)90013-1
24. M. Kłusek-Gawenda and A. Szczurek, Phys. Rev. **C82** (2010) 014904 doi:10.1103/PhysRevC.82.014904
25. J. Contreras and J.D. Tapia Takaki, Int. J. Mod. Phys. A **30** (2015), 1542012 doi:10.1142/S0217751X15420129
26. M. Kłusek-Gawenda and A. Szczurek, Phys.Rev. **C93** (2016) 044912 doi:10.1103/PhysRevC.93.044912
27. M. Kłusek-Gawenda, PhD thesis, *Production of pairs of mesons, leptons and quarks in ultraperipheral ultrarelativistic heavy ion collisions*, Kraków, 2015.
28. STAR Collaboration, C. Adler et al., Phys.Rev.Lett. 89 (2002) 272302 doi:10.1103/PhysRevLett.89.272302
29. STAR Collaboration, B. I. Abelev et al., Phys. Rev. **C77** (2008) 034910.
30. STAR Collaboration, G. Agakishiev et al., Phys. Rev. **C85** (2012) 014910 doi:10.1103/PhysRevC.77.034910
31. ALICE Collaboration, J. Adam et al., JHEP 09 (2015) 095 doi:10.1007/JHEP09(2015)095
32. L. Frankfurt,V. Guzey, M. Strikman and M. Zhalov, Phys. Lett. **B752** (2016) 51 doi:10.1016/j.physletb.2015.11.012
33. J. Cepila, J.G. Contreras, M. Krelina and J.D. Tapia Takaki, Nucl. Phys. **B934** (2018) 330 doi:10.1016/j.nuclphysb.2018.07.010
34. M. Kłusek-Gawenda and A. Szczurek, Phys. Rev. **C89** (2014) 024912 doi:10.1103/PhysRevC.89.024912
35. STAR Collaboration, B.I. Abelev, Phys.Rev. **C77** (2008) 034910 doi:10.1103/PhysRevC.77.034910
36. ALICE Collaboration, S. Acharya et al., JHEP 06 (2020) 035 doi: 10.1007/JHEP06(2020)035
37. M. Kłusek and A. Szczurek, Phys.Lett.B 674 (2009) 92 doi:10.1016/j.physletb.2009.03.006
38. ALICE Collaboration, S. Acharya et al., arXiv: 2404.07542 [nucl-ex]

Two-body densities as a framework for dynamical imaging and their connection to ultra-peripheral collisions

Zaki Panjsheeri, Joshua Bautista, and Simonetta Liuti
University of Virginia Physics Department,
382 McCormick Rd, Charlottesville, Virginia

We present results on two-parton densities in coordinate space which capture a fuller dynamical picture of the proton's internal structure, including information on the relative position between quarks and gluons in the transverse plane. The connection of such two-body densities to observables, proceeds in QCD, via the definition of double generalized parton distributions (DGPDs) that can be accessed in the production of two vector mesons, or two dimuon systems in ultraperipheral collisions (UPCs) through a double scattering process.

DOI: https://doi.org/10.17161/r71z8v22
Keywords: generalized parton distributions, GPD, ultra-peripheral collisions, UPC

1 Introduction

The exclusive process of deeply virtual Compton scattering (DVCS) allows us to access generalized parton distributions (GPDs) [1,2,3] (We refer the reader to Refs.[4,5,6] for reviews on the subject). In turn, GPDs, through Fourier transformation, give spatial information on the charge and matter distributions of the quarks and gluons inside the nucleon [7]. The physical properties derived from the Fourier transforms of GPDs include the spatial distributions of each partonic component of the nucleon in the transverse plane with respect to the proton's motion, as well as the orbital component of angular momentum. Notwithstanding the wealth of information that one could obtain from these Fourier transformed quantities, to capture a fuller dynamical picture of the proton's internal structure, it is fundamental to be able to determine the *relative* position between partons. In order to access information on the relative position of quarks and gluons in a QCD-motivated picture, one needs to define the correlation functions yielding the two-body density distribution in the transverse plane. Connecting the two-body densities to observables, we found that the latter can be defined in QCD through generalized double parton distributions (GDPDs), namely generalized parton distibutions characterized by two hard parton scatterings occurring during the electron-proton or electron-nucleus collision. Using GDPDs, we can define additional observables to describe quark and gluon dynamics, including their overlap probabilities. Such quantities can be extracted from experimental measurements of deeply virtual exclusive processes characterized by multi-particle final states.

2 From one body to two body density

We focus our description on the unpolarized quark inside an unpolarized nucleon described by the GPD, $H^q(X, \zeta = 0, t)$, where x is the quark longitudinal momentum fraction, $t = \Delta^2$ is the four-momentum transfer squared between the initial and final proton, and ζ, the skewness parameter is set to zero. Through Fourier transformation, one obtains the impact parameter-dependent parton distribution function (IPPDF) $\rho(X, \mathbf{b}_T)$, in terms of $\mathbf{b}_T$, the Fourier conjugate to the transverse momentum transfer, $\mathbf{\Delta}_T$ [7,8]. The spatial variables relevant for this problem are described in the left diagram in Figure 1, giving a partonic picture in coordinate space, as first observed using Light Cone (LC) kinematics in Ref.[9].

From the figure, one can see that two relevant variables describe the spatial configuration in a parton-spectator system, namely, $b = b_T$, the relevant transverse distance of the parton from the Center

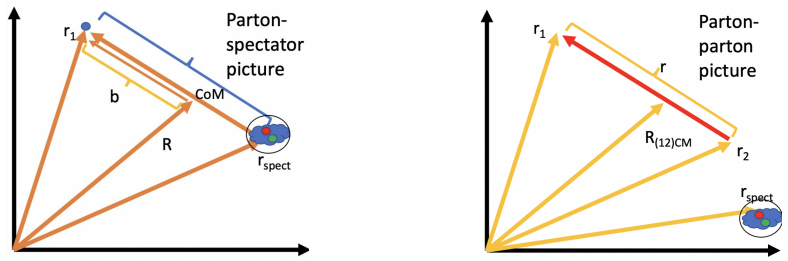

Figure 1 – Spatial coordinates in the transverse plane for one-body distributions (left) and two-body distributions (right).

of Momentum (CoM), and R, the position of the nucleon's CoM. To obtain such a picture through GPDs, we take the correlation function represented in momentum space by Fig. 2,

$$W^{\Gamma}_{\Lambda,\Lambda'} = \int \frac{dz^-_{in}}{(2\pi)} \int \frac{dz^-_{out}}{(2\pi)^2}\, e^{i(k_{in} z_{in})}\, e^{-i(k_{out} z_{out})}\, \langle p', \Lambda' | \overline{\psi}(z_{out})\, \Gamma\, \mathcal{U}(z_{in}, z_{out}) \psi(z_{in}) | p, \Lambda \rangle \Big|_{\substack{z^+_{in(out)}=0 \\ \mathbf{z}_{T,in(out)}=0}} , \quad (1)$$

We represent the four-vectors in LC notation, $v \equiv (v^+, v^-, \mathbf{v}_T)$, $v^{\pm} = (v^o \pm v^3)/\sqrt{2}$, $d^4z = dz^- dz^+ d^2\mathbf{z}_T$;

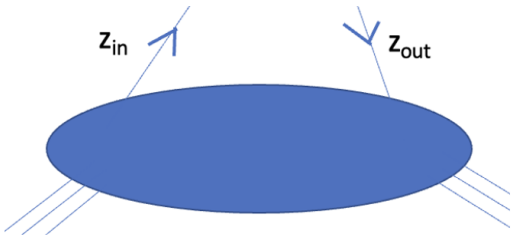

Figure 2 – Correlation function for the GPD in momentum space

we evaluate the fields at equal LC time, $z^+ = 0$. $\psi(z_{in})$, $\bar{\psi}_{out}(z)$ are the quark fields; Γ is an operator between quark fields, *i.e.* either a specific gamma matrix, or a combination of gamma matrices; finally, $\mathcal{U}(z_{in}, z_{out})$, is the link ensuring gauge invariance. In what follows we choose the LC gauge for which $\mathcal{U}(z_{in}, z_{out})$ can be taken equal to one. The field operators product in Eq.(1) is evaluated between an incoming proton state, $|\, p, \Lambda\rangle$, of definite momentum, p, and helicity, Λ, and an outgoing proton state, $|\, p', \Lambda'\rangle$, with momentum, $p' = p - \Delta$, and helicity, Λ'. Taking $\Gamma = \gamma^+$, and Fourier transforming, one obtains [a]

$$\begin{aligned} W^{\gamma^+}_{\Lambda,\Lambda'} &= \int \frac{dz^-}{(2\pi)}\, e^{i(X-\zeta/2)p^+ z^-}\, \langle p' = p - \Delta, \Lambda' | \overline{\psi}\,(0)\, \gamma^+\, \psi\,(z^-)\, | p, \Lambda \rangle, \\ &= \frac{1}{2P^+} \left\{ H_q(X,\zeta,t) \bar{u}(p-\Delta,\Lambda') \gamma^+ u(p,\Lambda) + E_q(X,\zeta,t) \bar{u}(p-\Delta,\Lambda') \frac{\sigma^{i+} \Delta_i}{2M} u(p,\Lambda) \right\}. \quad (2) \end{aligned}$$

Isolating the GPD H for an unpolarized quark inside an unpolarized proton at skewness ζ equal to 0, in momentum space the $H_q(X,0,t)$ is off-diagonal in momentum,

$$H_q(X,0,t) = \int d^2\mathbf{k}_{T,in}\, \phi^*(X, \mathbf{k}_{T,in} - \boldsymbol{\Delta}) \phi(X, \mathbf{k}_{T,in}), \quad (3)$$

and with Fourier transformations of the vertex functions,

$$\phi(X, \mathbf{k}_{in}) = \frac{1}{(2\pi)^2} \int d^2\mathbf{z}_{in}\, e^{i\mathbf{k}_{in}\cdot\mathbf{z}_{in}}\, \tilde{\phi}(X, \mathbf{z}_{in}), \quad (4a)$$

$$\phi^*(X, \mathbf{k}_{out}) = \frac{1}{(2\pi)^2} \int d^2\mathbf{z}_{out}\, e^{-i\mathbf{k}_{out}\cdot\mathbf{z}_{out}}\, \tilde{\phi}^*(X, \mathbf{z}_{out}). \quad (4b)$$

[a] The correlation function's parametrization in terms of GPDs also depends on the QCD evolution scale for the process, and Q^2, that is omitted in these formulae for ease of presentation.

the relationship between the GPD and the IPPDF emerges:

$$H_q(X,0,t) = \int d^2\mathbf{b}\, e^{i\mathbf{b}\cdot\boldsymbol{\Delta}}\, \tilde{\phi}^*(X,\mathbf{b})\, \tilde{\phi}(X,\mathbf{b}) = \int d^2\mathbf{b}\, e^{i\mathbf{b}\cdot\boldsymbol{\Delta}}\, \rho_q(X,\mathbf{b}) \tag{5a}$$

$$\rho_q(X,\mathbf{b}) = \int \frac{d^2\boldsymbol{\Delta}}{(2\pi)^2} e^{-i\mathbf{b}\cdot\boldsymbol{\Delta}} H_q(X,0,t), \tag{5b}$$

where we have defined the transverse space one-body diagonal density distribution. The index q refers to the quark flavor. A similar distribution is ibtained for gluons.

In Figure 3 we show an example of a one-body density distribution, $\rho_g(X,b)$, evaluated for the gluon GPD parametrization from Refs.[10,11], where H_g was constrained by its first moment in X evaluated in lattice QCD [12,13]. Notice that in this case, the gluon distribution depends rather strongly on the scale for the process, Q^2.

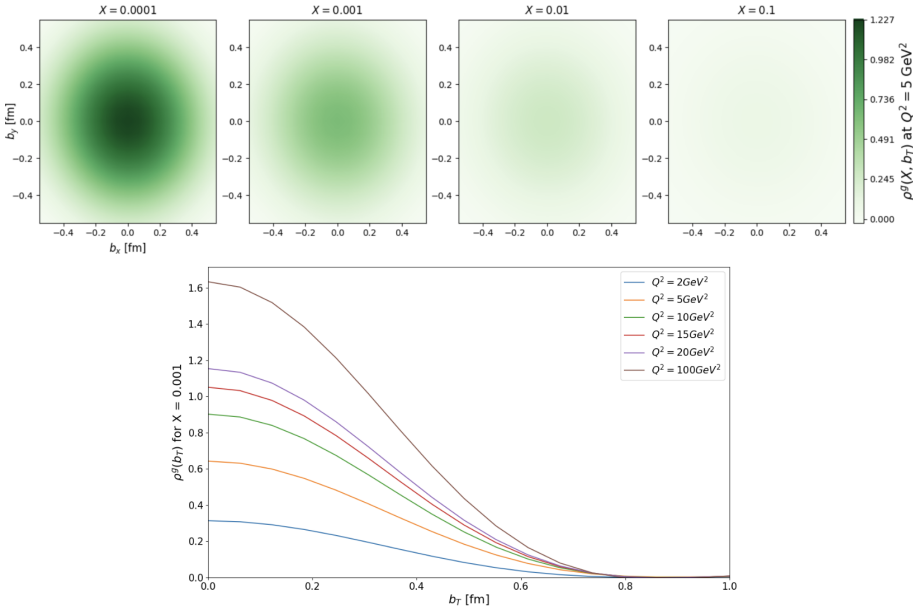

Figure 3 – The Fourier transform $\rho_g(x,b)$ of the unpolarized gluon GPD H_g calculated as a function of x and Q^2.

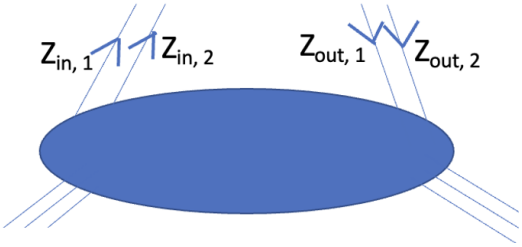

Figure 4 – Two-body correlation function

Although the one-body density distributions already give rich spatial information about the proton's internal structure, as we show in Section 3, in order to study the dynamics of the proton's constituents, we must move from a single-body to a two-body picture, studying now double-parton correlations. We thus introduce the two-body correlation function, as in Figure 4, defined through the following bilinear expression,

$$\begin{aligned} W^{\Gamma}_{\Lambda,\Lambda'} &= \int \frac{dz^-_{1,in}d\mathbf{z}_{1,T,in}}{(2\pi)^3}\frac{dz^-_{2,in}d\mathbf{z}_{2,T,in}}{(2\pi)^3}\int \frac{dz^-_{1,out}d\mathbf{z}_{1,T,out}}{(2\pi)^3}\frac{dz^-_{2out}d\mathbf{z}_{2,T,out}}{(2\pi)^3} \\ &\times\ e^{i(k_{1,in}z_{1,in}+k_{2,in}z_{2,in})}\, e^{-i(k_{1,out}z_{1,out}+k_{2,out}z_{2,out})} \\ &\times\ \langle p',\Lambda'|\overline{\psi}(z_{1,out})\,\Gamma\psi(z_{1,in})\,\overline{\psi}(z_{2,out})\,\Gamma\psi(z_{2,in})|p,\Lambda\rangle\Big|_{z_1^+=z_2^+=0} \end{aligned} \tag{6}$$

This definition involving quark fields is similar to the double parton distribution function (DPDF) introduced in [14], but with the initial and final proton states being different, ($p' \neq p$). Proceeding similarly to

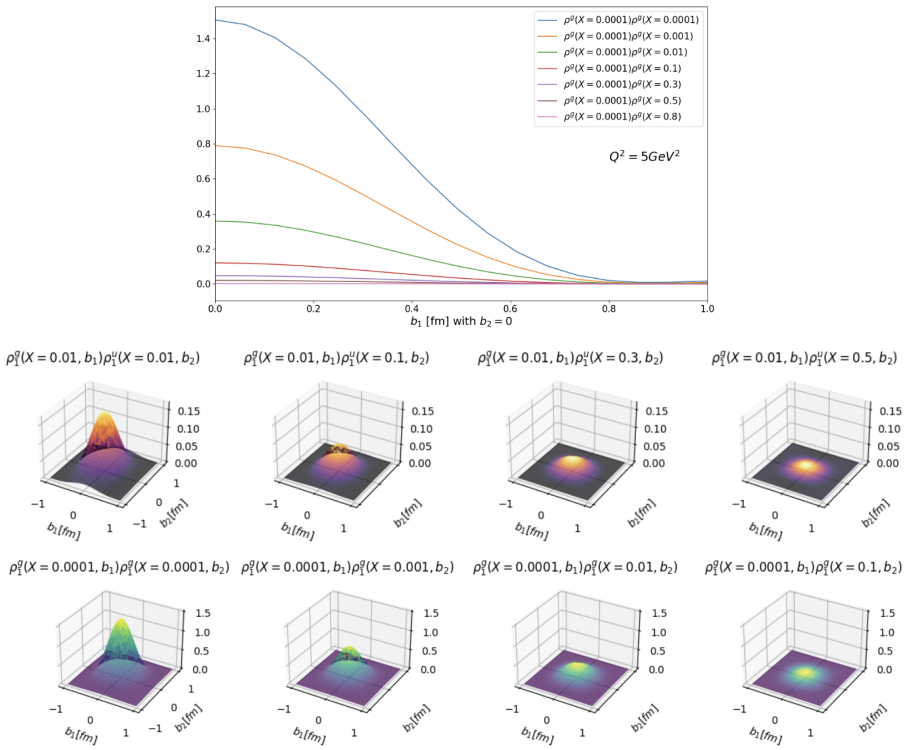

Figure 5 – Visualizing the two-body density as a function of b_1 and b_2 (Eq.9), for different values of x_2, while keeping x_1 fixed.

the one-body case, we can now form the following combinations of the two different quark fields locations, $z_{i,in}$ and $z_{i,out}$, $(i = 1, 2)$, respectively given by,

$$\begin{cases} z_i & = z_{i,in} - z_{i,out} \\ b_i & = \dfrac{1}{2}(z_{i,in} + z_{i,out}) \end{cases} \Rightarrow \begin{cases} z_{i,in} & = b_i + \dfrac{z_i}{2} \\ z_{out} & = b_i - \dfrac{z_i}{2} \end{cases}, \tag{7}$$

as well as the conjugate momenta to b_i and z_i,

$$\begin{cases} \Delta_i & = k_{i,in} - k_{i,out} & \leftrightarrow & b_i \\ k_i & = \dfrac{1}{2}(k_{i,in} + k_{i,out}) & \leftrightarrow & z_i \end{cases} \tag{8}$$

Following a procedure similar to the one-body case, we derived a formulation for the Fourier transform of the four-point correlation function (6), showing that it can be cast in a two-body density form, $\rho_2^{qq}(x_1, \mathbf{b}_1; x_2, \mathbf{b}_2)$, describing the probability of simultaneously finding quark 1 carrying a momentum fraction x_1 at location $\mathbf{b}_1$ and quark 2 carrying a momentum fraction x_2 at location $\mathbf{b}_2$ with respect to the center of momentum of the system. In the absence of correlations in the relative motion of the two quarks, the two-body transverse spatial distribution is described by,

$$\rho_2^{qq}(X_1, \mathbf{b}_1; X_2, \mathbf{b}_2) = \rho_q(X_1, \mathbf{b}_1)\rho_q(X_2, \mathbf{b}_2) \tag{9}$$

where ρ is the diagonal one-body density defined in Eq.(5). Distributions with parton configurations other than qq, *e.g.* qg, or gg, can be written in a similar way, starting from the appropriate two-body correlation function definition.

A visualization of the two-body density distribution, is provided in Fig. 5 where in the upper panel we show a 2D rendition of the gluon-gluon distribution obtained by plotting the quantity, $\rho_2^{gg}(X_1, \mathbf{b}_1; X_2, \mathbf{b}_2)$ at the scale, $Q^2 = 5$ GeV ^{2}, for $X_1 = 10^{-3}$, and fixed $\mathbf{b}_2$, varying X_2 and $\mathbf{b}_1$; in the lower panels, we show 3D versions obtained at $x_1 = 0.01$ (top) and $X_1 = 10^{-3}$, plotted in the $\mathbf{b}_1$, $\mathbf{b}_2$ for various values of X_2.

3 Observables

The average radii described in the previous Section in terms of the Fourier transform of the GPD H for zero skewness are described through the impact parameter dependent PDF (IPPDF), in Figure 6; on the *lhs* we plotted the valence u and we d quark geometric radii compared to the gluon one, at $Q^2 = 5$ GeV^2; on the *rhs* the behavior of the gluon radius with Q^2 is shown. All calculations were performed using the parametrization from Refs.[10,11]. One can see that the gluon radius is much smaller than the quark one, consistent with the geometric representation of baryon junctions, as proposed in Ref.[15] and recently investigated in, *e.g.*, Ref.[16]. Furthermore, we find that, while the radii for all q and g components show a small variation with Q^2 at larger values of $X > 0.01$, at small X, this dependence is substantial, and it should, therefore be more easily detectable in experiment.

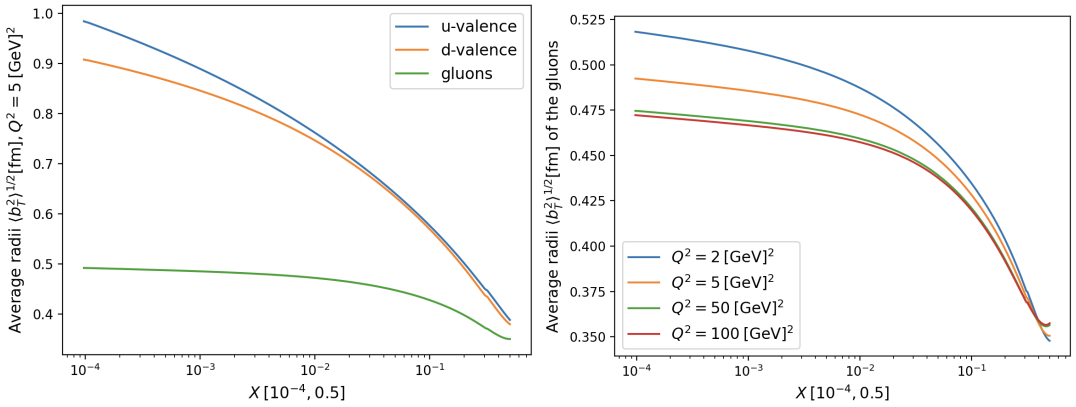

Figure 6 – The average radii for u, d (valence) and g (gluon) distributions (left) provide a quantitative method for extracting spatial information through even the one-body density. We can also study the Q^2-dependence of these average radii through perturbative evolution, as shown for the gluons (right).

From the vectors locating the partons 1 and 2 positions in the transverse plane, $\mathbf{b}_1$ and $\mathbf{b}_2$, respectively, we define the relative distance between them, $\mathbf{r}$, and the distance of the center of mass of the two partons from the origin, $\mathbf{R}_{12}$,

$$\mathbf{r} = \mathbf{b}_1 - \mathbf{b}_2 \tag{10}$$

$$\mathbf{R}_{12} = \frac{\mathbf{b}_1 + \mathbf{b}_2}{2} \tag{11}$$

Defining the root mean squared of their expectation values, one obtains the square average relative distance and average center of mass of the two partons,

$$\langle \mathbf{r}^2 \rangle (X_1, X_2) = \frac{1}{\mathcal{N}} \int\int d^2\mathbf{r}\, d^2\mathbf{R}_{12}\, \left|\mathbf{r}^2\right|\, \rho_2 \left(X_1, \mathbf{R}_{12} + \frac{\mathbf{r}}{2}; X_2, \mathbf{R}_{12} - \frac{\mathbf{r}}{2}\right) \tag{12}$$

$$\langle \mathbf{R}_{12}^2 \rangle (X_1, X_2) = \frac{1}{\mathcal{N}} \int\int d^2\mathbf{r}\, r^2 \mathbf{R}_{12}\, \left|\mathbf{R}_{12}^2\right|\, \rho_2 \left(X_1, \mathbf{R}_{12} + \frac{\mathbf{r}}{2}; X_2, \mathbf{R}_{12} - \frac{\mathbf{r}}{2}\right) \tag{13}$$

$$\mathcal{N} = \int\int d^2\mathbf{r}\, r^2 \mathbf{R}_{12}\, \rho_2 \left(X_1, \mathbf{R}_{12} + \frac{\mathbf{r}}{2}; X_2, \mathbf{R}_{12} - \frac{\mathbf{r}}{2}\right) \tag{14}$$

The numerical results obtained using our parametrization for the average relative distance, given in Fig. 7, for the specific case of $X_1 = X_2$, correlate with the results for the single parton distributions, in that the distance between a quark of flavor u, d and a gluon field is always larger than the distance of two gluon fields, revealing that gluonic configurations tend to be more compact.

Through the two-body densities we can now address quantitatively the question of whether the u, quarks and gluons will overlap forming localized "hot spots," as suggested in an event-by-event analysis in Refs. [17,18], or whether the gluon field surrounds uniformly the valence quarks.

The geometric average two-parton overlap probability in the transverse plane can be defined as,

$$\langle A(X_1, X_2) \rangle = \frac{1}{\mathcal{N}} \int d^2\mathbf{b}_1 d^2\mathbf{b}_2\, \rho_2^{ij}(X_1, \mathbf{b}_1; X_2, \mathbf{b}_2) A(|\, \mathbf{b}_1 - \mathbf{b}_2\, |),$$

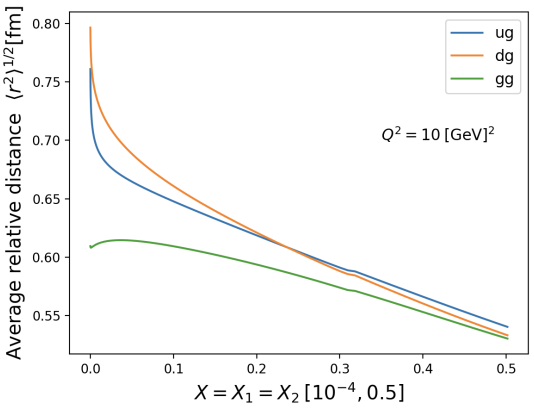

Figure 7 – Average relative distance between the u quark and gluon, the d quark and gluon, and two gluon fields inside the proton plotted vs. $X = X_1 = X_2$, at $Q^2 = 10$ GeV^2.

where $A(r =\mid \mathbf{b}_1 - \mathbf{b}_2 \mid)$ is taken as the geometric area overlap of the two azimuthally symmetric single parton distributions measured in units of an average radius $a = (\langle b_1 \rangle^2 + \langle b_2 \rangle^2)^{1/2}/\sqrt{2}$,

$$A(r) \quad = \quad a^2\pi - \frac{r-\delta}{2}\,(\alpha_1 + \alpha_2) - a_1^2 \arctan\frac{r-\delta}{2\alpha_1} - a_2^2 \arctan\frac{r-\delta}{2\alpha_2} \tag{15}$$

with,

$$\alpha_i = \sqrt{a_i^2 - \frac{(r-\delta)^2}{4}}, \qquad i = 1, 2 \tag{16}$$

and $\delta = a_1 - a_2$.
Performing a change of variables, the average two-parton overlap probability is given as,

$$\langle A(X_1, X_2) \rangle \quad = \quad \frac{1}{\mathcal{N}} \int\int d^2\mathbf{r}\, d^2\mathbf{R}_{12}\, A(r)\, \rho_2^{gg}\left(X_1, \mathbf{R}_{12} + \frac{\mathbf{r}}{2}; X_2, \mathbf{R}_{12} - \frac{\mathbf{r}}{2}\right). \tag{17}$$

Numerical results for the overlap probability are given in Figure 8 for the u quark and gluon case. The figure shows $A(X_1, X_2)$, Eq.(17), plotted vs. X, with $X = X_1 = X_2$, and $Q^2 = 10$ GeV^2, divided by the maximum overlap surface. Putting together results from Figs.6, 7, and 8, we can see that while all parton types tend to be more broadly distributed at low X (Fig.6), thus also spanning broadly distributed relative distances, their overlap probability also increase (Fig.8).

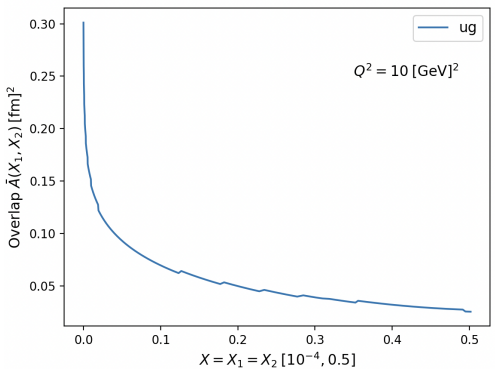

Figure 8 – The overlap probability of the u quark and gluon distributions in the proton plotted vs $X = X_1 = X_2$ for $Q^2 = 10$ GeV^2.

This picture complements the recent BNL approach [19,17,18,20], describing geometrical fluctuations, or event-by-event fluctuations in the proton wave function where the three constituent quarks emit small$-x$ gluons around them, which form "hot-spots" at random locations in the transverse plane.

As first pointed out in Ref.[21] (See also Ref.[22]) in ultraperipheral collisions (UPCs) where, a proton and a nucleus or a proton and a proton collide at impact parameters larger than the sum of the particles'

radii, time-like Compton scattering (TCS), an exclusive process from which one can extract GPDs, may be observed (Fig. 9). We seek to extract GDPDs in double TCS through UPC processes, proposing to use, for example, double vector meson or double dimuon production.

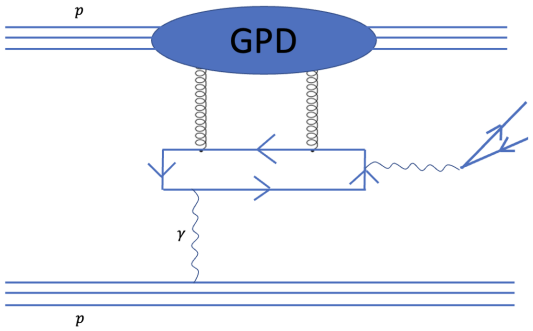

Figure 9 – Connection between UPCs and GPDs

4 Conclusions

We presented results on our study of two-body parton distributions as a means of obtaining information on the relative positions of quarks and gluons inside the proton. While one-body distributions are limited to capturing average static properties of the proton's internal structure, such as the radius covered by various parton distributions, the proton is a complex, multi-body environment, and it is, therefore, more properly imaged through multi-body distributions. As a first step towards the general problem of imaging this multi-body system, and to provide tools to address multiparton correlations beyond the one-body formalism, we studied the geometric correlations between the u and d quark distributions and gluons.

In Refs.[17,18] a connection was provided between the two approaches, "GPDs" on one side, and "geometrical fluctuations" on the other. In particular, the dipole-based description of *coherent* diffractive J/ψ production off a proton was connected to the correlation functions for GPDs, within the collinear framework of QCD. However, the more interesting channel of *incoherent* diffraction, described in terms of double dipole diffraction and leading to small$-x$ gluon fluctuations, or event-by-event, color density geometry driven fluctuations has remained a puzzle in that it could not be rendered, so far, within standard QCD approaches. By introducing two-body correlations functions, we provide a framework to investigate these scenarios and to allow us to study relative spatial configurations of quarks and gluons inside the proton and the atomic nuclei.

Acknowledgments

This research is funded by DOE grant DE-SC0016286.

References

1. Xiang-Dong Ji. Gauge-Invariant Decomposition of Nucleon Spin. *Phys. Rev. Lett.*, 78:610–613, 1997.
2. Xiang-Dong Ji. Deeply virtual Compton scattering. *Phys. Rev.*, D55:7114–7125, 1997.
3. A. V. Radyushkin. Nonforward parton distributions. *Phys. Rev.*, D56:5524–5557, 1997.
4. M. Diehl. Generalized parton distributions with helicity flip. *Eur.Phys.J.*, C19:485–492, 2001.
5. A.V. Belitsky and A.V. Radyushkin. Unraveling hadron structure with generalized parton distributions. *Phys.Rept.*, 418:1–387, 2005.
6. Kresimir Kumericki, Simonetta Liuti, and Herve Moutarde. GPD phenomenology and DVCS fitting - Entering the high-precision era. 2016.
7. Matthias Burkardt. Impact parameter dependent parton distributions and off forward parton distributions for zeta —¿ 0. *Phys. Rev. D*, 62:071503, 2000. [Erratum: Phys.Rev.D 66, 119903 (2002)].
8. M. Diehl. Generalized parton distributions in impact parameter space. *Eur. Phys. J. C*, 25:223–232, 2002. [Erratum: Eur.Phys.J.C 31, 277–278 (2003)].

9. Davison E. Soper. The Parton Model and the Bethe-Salpeter Wave Function. *Phys. Rev.*, D15:1141, 1977.
10. Brandon Kriesten, Philip Velie, Emma Yeats, Fernanda Yepez Lopez, and Simonetta Liuti. Parametrization of quark and gluon generalized parton distributions in a dynamical framework. *Phys. Rev. D*, 105(5):056022, 2022.
11. Gary R. Goldstein, J. OsvaldoGonzalez Hernandez, and Simonetta Liuti. Flexible Parametrization of Generalized Parton Distributions from Deeply Virtual Compton Scattering Observables. *Phys.Rev.*, D84:034007, 2011.
12. P. E. Shanahan and W. Detmold. Gluon gravitational form factors of the nucleon and the pion from lattice QCD. *Phys. Rev. D*, 99(1):014511, 2019.
13. Dimitra A. Pefkou, Daniel C. Hackett, and Phiala E. Shanahan. Gluon gravitational structure of hadrons of different spin. *Phys. Rev. D*, 105(5):054509, 2022.
14. Markus Diehl, Daniel Ostermeier, and Andreas Schafer. Elements of a theory for multiparton interactions in QCD. *JHEP*, 03:089, 2012. [Erratum: JHEP 03, 001 (2016)].
15. D. Kharzeev. Can gluons trace baryon number? *Physics Letters B*, 378(1–4):238–246, June 1996.
16. R. Terra and F. S. Navarra. Charmonium production in high multiplicity *pp* collisions and the structure of the proton. *Phys. Rev. D*, 108:054002, Sep 2023.
17. Heikki Mäntysaari. Review of proton and nuclear shape fluctuations at high energy. *Rept. Prog. Phys.*, 83(8):082201, 2020.
18. Heikki Mäntysaari, Kaushik Roy, Farid Salazar, and Björn Schenke. Gluon imaging using azimuthal correlations in diffractive scattering at the Electron-Ion Collider. *Phys. Rev. D*, 103(9):094026, 2021.
19. Heikki Mäntysaari and Björn Schenke. Accessing the gluonic structure of light nuclei at a future electron-ion collider. *Phys. Rev. C*, 101(1):015203, 2020.
20. Adrian Dumitru, Heikki Mäntysaari, and Risto Paatelainen. Color charge correlations in the proton at NLO: Beyond geometry based intuition. *Phys. Lett. B*, 820:136560, 2021.
21. J. P. Lansberg, L. Szymanowski, and J. Wagner. Lepton-pair production in ultraperipheral collisions at AFTER@LHC. *JHEP*, 09:087, 2015.
22. Ya-Ping Xie and V.P. Gonçalves. Timelike compton scattering in ultraperipheral ppb collisions. *Physics Letters B*, 839:137762, April 2023.

The ratio of $\Psi(2s)$ and J/Ψ exclusive photoproduction cross-sections as a tool to detect non-linear QCD evolution

Marco Antonio Alcazar Peredo[1] and Martin Hentschinski[2]
[1] *Instituto de Física Teórica, Universidad Autónoma de Madrid, 28049 Madrid, Spain*
[2] *Departamento de Actuaria, Física y Matemáticas, Universidad de las Americas Puebla, Santa Catarina Martir, 72820 Puebla, Mexico*

We study the proposal that the rise with energy of the ratio of $\Psi(2s)$ and J/Ψ exclusive photoproduction cross-sections might serve as an indicator of the presence of non-linear QCD evolution, related to the presence of high and potentially saturated gluon densities in both the proton and a lead nucleus. Our study employs recent fits of the GBW and BGK dipole models and provides predictions for both exclusive photoproduction on a proton and on a lead nucleus. While the cross-sections for photoproduction on a proton depend only weakly on non-linear low x corrections, we find an increased sensitivity for the cross-section ratio, which is directly related to the node in the $\Psi(2s)$ wave function. We further give a description of recent ALICE data for exclusive J/Ψ photoproduction on a lead nucleus and provide predictions for $\Psi(2s)$ photoproduction on a lead nucleus as well as for the corresponding cross-section ratio.

DOI: https://doi.org/10.17161/8cyw5q54
Keywords: Diffractive production, QCD phenomenology, Quantum chromodynamics, Strong interaction

1 Introduction

Exclusive photoproduction of charmonium in ultra-peripheral collisions at the Large Hadron Collider (LHC) provides a unique opportunity to examine Quantum Chromodynamics (QCD) at very low values of x. With $x = M_V^2/W^2$, where M_V is the mass of the vector meson, and W the center-of-mass energy of the photon-proton or photon-nucleus collision, this corresponds to the high-energy limit of perturbative strong interactions. Examining this low x limit is of interest, since it allows us to investigate an important open question in the exploration of strongly interacting matter: In the above-described interaction of a photon with a proton (or an entire nucleus), we explore the gluon distribution of the proton (or nucleus), if the reaction occurs in the presence of hard scale; the latter allows for the identification of partonic degrees of freedom. Such a scenario is realized for charmonium production, where the mass of the charm quark provides the hard mass scale. In the region of phase space where the variable x takes small values – roughly speaking values smaller than 0.01 – BFKL evolution predicts for the inclusive gluon distribution a powerlike rise with x. While such a rise has been clearly seen in data, there are strong theoretical arguments that suggest that such a rise must at some value of x slow down and eventually come to hold[1,2]. The growth of the gluon density will therefore saturate at some value of x. While there are strong arguments for gluon saturation, the determination of the value of x, where this new phenomena should manifest itself in data, is still an open task.

Reactions that involve charmed final states are in this context particularly interesting[3,4], since they sit on the boundary between perturbative and non-perturbative QCD dynamics. While the presence of a hard scale is essential for a description based on microscopic degrees of freedom, a large hard scale will select regions of the phase space, where non-linear terms in QCD evolution equations are suppressed. These

non-linear terms occur in extensions of the BFKL evolution equation, such as the BK equation, where they lead to a slowdown of the growth of the gluon distribution. Previously, a description of the energy dependence of the photoproduction cross-sections of charmonium[5,6,7,8,9,10,11] has been provided through comparing fits of unintegrated gluon distributions subject to next-to-leading order (NLO) BFKL evolution [12,13,14] (Hentschinski-Salas-Sabio-Vera; HSS) and DGLAP-modified BK evolution [15] (Kutak-Sapeta; KS). This approach allows for direct evaluation of linear and non-linear low-x frameworks and attempts to search for features which distinguish between them, if compared to experimental data. Although unintegrated gluon distributions subject to linear and non-linear QCD evolution start to diverge at values of $x < 10^{-4} - 10^{-5}$, uncertainties prevent drawing firm conclusions whether signs of non-linear QCD dynamics are present in data. However, it was noted[8,5] that the ratio of photoproduction cross-sections of $\Psi(2s)$ and J/Ψ vector mesons shows distinct energy dependence for linear (BFKL) and non-linear (BK) evolution equations: The ratio rises with energy under full non-linear QCD evolution, while it stays relatively constant with linear evolution. Although the rise in the ratio of $\Psi(2s)$ and J/Ψ photoproduction cross-sections with energy has been previously documented for unitarized dipole models[16 17], the constant ratio with linear QCD evolution has not been thoroughly studied, to the best of our knowledge.

An interesting question in this context is whether the observed features are a coincidence related to the specific form of the HSS and KS distributions or whether they constitute a general characteristic of dipole cross-sections and/or gluon distributions with or without non-linear QCD dynamics. We therefore repeat the previous analysis[5], using two dipole models to represent the gluon density: the Golec-Biernat Wusthoff[18] (GBW) and the Bartels Golec-Biernat Kowalski[7] (BGK) model. While these are models which themselves are not subject to low x QCD evolution equations, they allow for direct manipulation of non-linear corrections and therefore for an exploration of their relevance for the photoproduction cross-section. We work with both models in their linearized and complete exponentiated (unitarized) versions, offering detailed definitions further down. While our primary focus is on the ratio of $\Psi(2s)$ to J/Ψ photoproduction in photon-proton collisions, we also discuss recent data from the ALICE experiment on J/Ψ photoproduction in photon-lead collisions [19,20], using these models for our analysis. Additionally, we provide predictions for $\Psi(2s)$ photoproduction in photonuclear reactions and the ratio of $\Psi(2s)$ to J/Ψ.

In this contribution, we summarize essential recent results[21,22], to which refer the interested reader for more details.

2 Photoproduction cross-sections

We study the process,

$$\gamma(q) + H(p) \to V(q') + p(p'), \qquad V = J/\Psi, \psi(2S)\,, \tag{1}$$

where γ denotes a quasi-real photon with virtuality $Q \simeq 0$, which stems from an electron (HERA) or a proton/lead nucleus in the case of LHC data; H is the proton or lead nucleus respectively. $W^2 = (q+p)^2$ the squared center-of-mass energy of the $\gamma(q) + H(p)$ reaction. With $t = (q - q')^2$, the differential cross-section for the exclusive photo-production of a vector meson can be written as,

$$\frac{d\sigma}{dt}\left(\gamma p \to V p\right) = \frac{1}{16\pi}\left|\mathcal{A}_T^{\gamma p \to V p}(x,t)\right|^2, \qquad V = J/\Psi, \psi(2S)\,. \tag{2}$$

Here $\mathcal{A}_T(W^2, t)$ denotes the scattering amplitude for a transverse polarized real photon with color singlet exchange in the t-channel, with an overall factor W^2 already extracted. $x = M_V^2/W^2$ with M_V the mass of the vector meson[7]. We finally have for the photoproduction cross-section

$$\sigma^{\gamma p \to V p}(W^2) = \frac{1}{B_D(W)}\frac{d\sigma}{dt}\left(\gamma p \to V p\right)\Big|_{t=0}, \tag{3}$$

where B_D is diffractive slope parameter[21]. For the proton, we use[17]

$$B_{D,p}(W) = \left[b_{0,p} + 4\alpha'_p \ln\frac{W}{W_0}\right] \mathrm{GeV}^{-2}, \tag{4}$$

with $b_{0,p}^{J/\Psi} = 4.62$, $b_{0,p}^{\Psi(2s)} = 4.86$, $\alpha_p^{'J/\Psi} = 0.171$ and $\alpha_p^{'\Psi(2s)} = 0.151$. For the lead nucleus we have $B_D = (4.01 \pm 0.15) \cdot 10^2/\mathrm{GeV}^2$, which we determined from a fit to the $|t|$ dependence of the coherent J/Ψ photonuclear production by the ALICE collaboration[23].

2.1 Wavefunction overlap

Within high energy factorization, the imaginary part of the scattering amplitude at $t = 0$ is obtained as a convolution of the light-front wave function – which describes the formation of a color dipole and its subsequent transition into a vector meson – and the dipole cross-section. In the following, we use a simple Gaussian model for the vector meson wave function,

$$\Im\mathrm{m}\,\mathcal{A}_T^{\gamma p\to Vp}(x,t=0) = \int d^2\mathbf{r}\Sigma(r)\,\sigma_{q\bar{q}}\,(x,r)\ , \tag{5}$$

where $r = |\mathbf{r}|$ denotes the transverse separation of the dipole and

$$\begin{aligned}\Sigma(r) &= \int_0^1 \frac{dz}{4\pi}\ \left(\Psi_V^*\Psi_T\right)(r,z)\\ &= \int_0^1 \frac{dz}{4\pi}\ \frac{\hat{e}_f e N_c}{\pi z(1-z)}\Big\{m_f^2 K_0(m_c r)\phi_T(r,z) - \left[z^2+(1-z)^2\right]\epsilon K_1(m_c r)\partial_r\phi_T(r,z)\Big\}.\end{aligned} \tag{6}$$

Although previously[5] a more refined description of the wave function overlap[24,17] has been used, the effects are minimal for our current study. Thus, we opted for the simpler boosted Gaussian model following the Brodsky-Huang-Lepage prescription[25,?,?]:

$$\phi_T^{1s}(r,z) = \mathcal{N}_{T,1s}z(1-z)\exp\left(-\frac{m_f^2\mathcal{R}_{1s}^2}{8z(1-z)} - \frac{2z(1-z)r^2}{\mathcal{R}_{1s}^2} + \frac{m_f^2\mathcal{R}_{1s}^2}{2}\right)\ , \tag{7}$$

$$\begin{aligned}\phi_{T,L}^{2s}(r,z) = \mathcal{N}_{T,2s}z(1-z)\exp&\left(-\frac{m_f^2\mathcal{R}_{2s}^2}{8z(1-z)} - \frac{2z(1-z)r^2}{\mathcal{R}_{2s}^2} + \frac{m_f^2\mathcal{R}_{2s}^2}{2}\right)\\ &\cdot\left[1+\alpha_{2s}\left(2+\frac{m_f^2\mathcal{R}_{2s}^2}{4z(1-z)} - \frac{4z(1-z)r^2}{\mathcal{R}_{2s}^2} - m_f^2\mathcal{R}_{2s}^2\right)\right]\ .\end{aligned} \tag{8}$$

The free parameters of this parametrization have been determined in various studies from the normalization and orthogonality of the wave functions as well as the decay width of the vector mesons. Here we use[26] $\mathcal{N}_{T,1s} = 0.57, \mathcal{N}_{T,2s} = 0.67, m_c = 1.4$ GeV, $\mathcal{R}_{1s}^2 = 2.45$ GeV^{-2}, $\mathcal{R}_{2s}^2 = 3.72$ GeV^{-2}, $\alpha_{2s} = -0.61$ and $m_c = 1.4$ GeV.

2.2 Dipole cross-sections

Within collinear factorization, one finds to leading order for the dipole cross-section[27 28]

$$\sigma_{q\bar{q}}^{\mathrm{collinear}}(x,r) = \frac{\pi^2}{3}r^2\alpha_s(\mu^2)xg(x,\mu^2). \tag{9}$$

The renormalization scale μ is usually identified with the factorization scale and taken to depend on the dipole size with $\mu^2 \sim 1/r^2$ for small dipole sizes; $xg(x,\mu^2)$ denotes the collinear gluon distribution subject to leading order DGLAP evolution. A simple way to estimate corrections that yield unitarization of this dipole cross-section in the limit of large dipole separations r and/or large gluon densities is to exponentiate the collinear cross-section, which yields the Bartels–Golec-Biernat–Kowalski (BGK) model,

$$\sigma_{q\bar{q}}^{\mathrm{BGK}}(x,r) = \sigma_0^{\mathrm{BGK}}\left[1-\exp\left(-\frac{r^2\pi^2\alpha_s(\mu_r^2)xg(x,\mu_r^2)}{3\sigma_0^{\mathrm{BGK}}}\right)\right]. \tag{10}$$

The above exponentation introduces a new parameter, σ_0, which yields the value of the dipole cross-section in the black disk limit, corresponding to the transverse size of the target. An even simpler model is provided by the Golec-Biernat, Wüsthoff (GBW) model,

$$\sigma_{q\bar{q}}^{\mathrm{GBW}}(x,r) = \sigma_0^{\mathrm{GBW}}\left[1-\exp\left(-\frac{r^2Q_s^2(x)}{4}\right)\right], \qquad Q_s^2(x) = Q_0^2\left(\frac{x_0}{x}\right)^\lambda, \tag{11}$$

where Q_s denotes the saturation scale within the model and gathers various elements of the collinear cross-section into a single factor. Both models have been recently refitted for dipole scattering on a proton to combined HERA data in [29] where free parameters are obtained as $\sigma_0^{\mathrm{GBW}} = (27.43 \pm 0.35)$ mb,

$\lambda = 0.248 \pm 0.002$, $x_0 = (0.40 \pm 0.04) \cdot 10^{-4}$, while $Q_0 = 1$ GeV for the GBW model. For the BGK model, $g(x, \mu^2)$ is subject to leading order DGLAP evolution equation without quarks,

$$\frac{d}{d\mu^2} g(x, \mu^2) = \frac{\alpha_s}{2\pi} \int_x^1 \frac{dz}{z} P_{gg}(z) g(x/z, \mu^2), \qquad xg(x, Q_0^2) = A_g x^{-\lambda_g} (1-x)^{5.6}, \tag{12}$$

where $xg(x, Q_0^2)$ denotes the gluon distribution at the initial scale $Q_0 = 1$ GeV. Following the recent fit[29] of this model, we evaluate the gluon distribution and the QCD running coupling at the dipole size dependent scale

$$\mu_r^2 = \frac{\mu_0^2}{1 - \exp\left(-\mu_0^2 r^2 / C\right)}. \tag{13}$$

The remaining parameters of the model have been obtained as $\sigma_0^{\rm BGK} = (22.93 \pm 0.27)$ mb, $A_g = 1.07 \pm 0.13$, $\lambda_g = 0.11 \pm 0.03$, $C = 0.27 \pm 0.04$, $\mu_0^2 = (1.74 \pm 0.16)$ GeV^2. The exponentiated terms allow us within these simple models to explore the relevance of non-linear QCD dynamics for the description of data.

2.3 Modified Dipole Cross-sections and nuclear effects

To explore the relevance of the exponentiated terms, which simulate non-linear QCD evolution, we will compare for the following numerical study both complete and linearized models. In addition, we introduce in the following a parameter 'k' which allows for a smooth transition between both scenarios, i.e., which allows to vary the 'density' of gluons by hand. We introduce this parameter k through a rescaling $Q_s^2(x) \to k \cdot Q_s^2(x)$, while we keep the linearized dipole cross-sections fixed. For the GBW model, this leads to

$$\begin{aligned} \sigma_{q\bar{q}}^{\rm GBW}(x, r, k) &= \sigma_0^{\rm GBW} Q_s^2(x) \left(\frac{r^2}{4}\right) \left[1 + \sum_{n=1}^{\infty} \frac{1}{(n+1)!} \left(-k \cdot \frac{r^2 Q_s^2(x)}{4}\right)^n\right] \\ &= \frac{\sigma_0^{\rm GBW}}{k} \left[1 - \exp\left(-k \cdot \frac{r^2 Q_s^2(x)}{4}\right)\right]. \end{aligned} \tag{14}$$

With this modification, $k = 0$ corresponds to the linear case, whereas $k = 1$ yields the current HERA fit of the model; finally, $k > 1$ implies an additional enhancement of non-linear effects. Within this simple approach, k can be understood as a parameter that controls the strength of the triple Pomeron vertex and, therefore, the relevance of non-linear dynamics. We also apply an identical modification to the BGK model,

$$\sigma_{q\bar{q}}^{\rm BGK}(x, r, k) = \frac{\sigma_0^{\rm BGK}}{k} \left[1 - \exp\left(-k \cdot \frac{r^2 \pi^2 \alpha_s(\mu_r^2) x g(x, \mu_r^2)}{3\sigma_0^{\rm BGK}}\right)\right]. \tag{15}$$

If the color dipole scatters on a large nucleus instead of a single proton, one expects an increase in the saturation scale due to the nuclear "oomph factor",

$$Q_{s,A}^2(x) \simeq A^{\frac{1}{3}} Q_s^2(x), \tag{16}$$

where A denotes the number of nucleons in the nucleus, and $Q_{s,A}^2(x)$ is the saturation scale for the nuclear target, while $Q_s^2(x)$ denotes the saturation scale for a single proton, as obtained from the fit to HERA data. With the transverse size of the dipole cross-section scaling as $\sim A^{2/3}$, we finally obtain

$$\sigma_{q\bar{q},A}(x, r) = A^{\frac{2}{3}} \sigma_{q\bar{q}}(x, r, k = A^{\frac{1}{3}}). \tag{17}$$

3 Non-linear corrections and the $\Psi(2s)$ over J/Ψ ratio

Having set up the theoretical framework, we ask ourselves the question whether one can expect a manifestation of non-linear QCD dynamics in the photoproduction of J/Ψ and $\Psi(2s)$ vector mesons. Taking a first look at the predictions for the production cross-section, Fig. 1, we observe a clear difference between linearized and complete dipole models. Compared to the results based on BFKL/BK evolution[5], one observes that the difference between linear and non-linear cases is more pronounced in the case of dipole models. This is not a surprise: while both HSS (linear) and KS (non-linear) gluon distributions

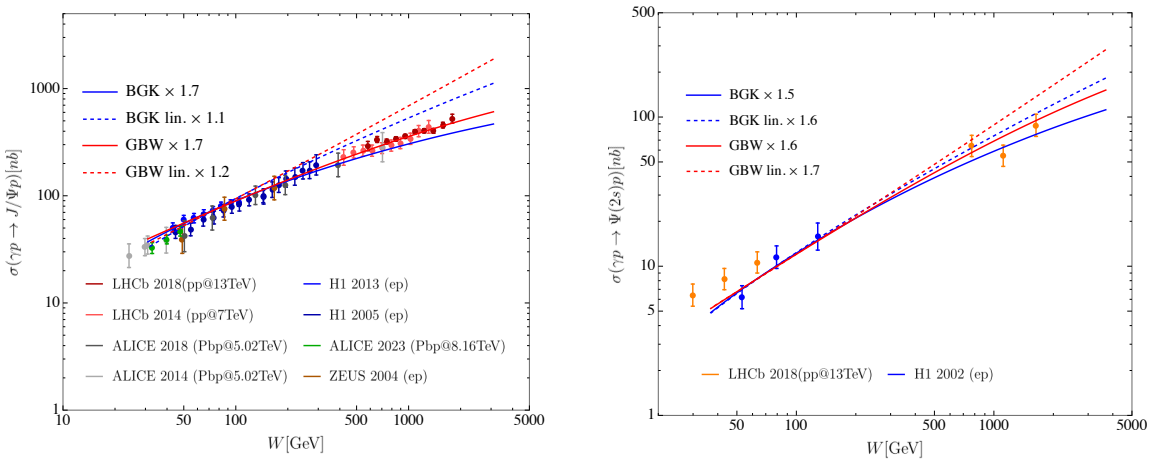

Figure 1 – Energy dependence of the total cross-sections for exclusive photoproduction of J/Ψ (left) and $\Psi(2s)$(right) as obtained within the dipole models discussed in the text. We further display photo-production data measured at HERA by ZEUS[30] and H1[31,32] collaborations as well as LHC data obtained from ALICE[33,34,35] and LHCb[36,37] for J/Ψ production as well as H1[38,39] and LHCb data[37] for the $\Psi(2s)$ photoproduction cross-section.

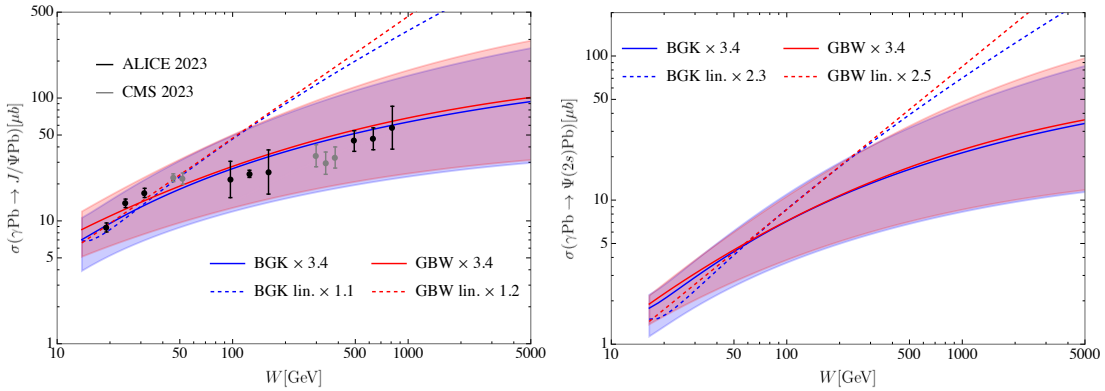

Figure 2 – Predictions of the photonuclear production of J/Ψ and $\Psi(2s)$. We further show ALICE [19] and CMS [40] data.

have been fit to HERA data, for the dipole models such a fit has been only performed for the complete (non-linear) models. This is also the reason why we require different K-factors for linearized and complete models. Fig. 2 provides the corresponding predictions for the photonuclear reaction, where charmonium is produced through the scattering of a photon on a lead nucleus. In comparison to the proton case, the energy dependence of the complete dipole models shows now a clear saturation effect in the sense that there is a clear difference between the powerlike rise with the energy of the linearized models and the energy dependence of the complete models. We however note that the energy dependence of the linearized model is identical to the energy dependence of the proton cross-section; nuclear shadowing effects absent in this case. As discussed in [19], the data set can be described with a similar accuracy if one employs a powerlike growth, with a reduced Pomeron intercept. We believe that a closer investigation of this aspect would be a very interesting research task for the future.

3.1 Charmonium production and the scaling region

In the following, we would like to reinvestigate the potential relevance of non-linear corrections based on general estimates of the size of such corrections for different regions of phase space of the dipole cross-section. With

$$Q_s^{\mathrm{GBW}}(x = 10^{-6}) \simeq 1.58 \text{ GeV}, \tag{18}$$

the numerical value of the saturation scale in the proton is close to the hard scale of the charmonium production cross-section, $m_c \simeq 1.4$ GeV. One therefore does not enter a region of phase space where $Q_s^2 \gg m_c^2$ and where therefore an expansion of the cross-section in powers of Q_s^2/m_c^2 is clearly breaking

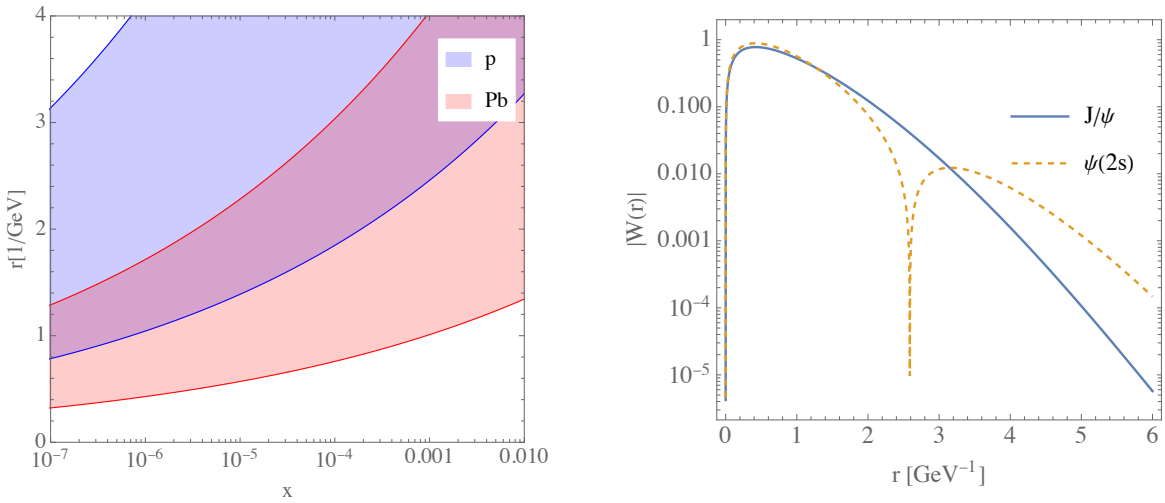

Figure 3 – Left: Estimated geometric scaling region, based on the GBW saturation scale for both proton and lead. Right: Integrated Gaussian wave function overlap for photo-production of vector mesons J/Ψ and $\Psi(2s)$

down. We are therefore not sensitive to the saturated region of the dipole cross-section, but at most to the so-called (geometric) scaling region[41]. In this region of phase space, the dimensionless dipole cross-section $\sigma_{q\bar{q}}(x,r)/\sigma_0$ is still weak, $\sigma_{q\bar{q}}(x,r)/\sigma_0 \ll 1$, but the existence of a region of saturated dipole cross-section[42] $\sigma_{q\bar{q}}(x,r)/\sigma_0 \sim 1$ reflects itself already in the dynamics of the dipole cross-section. Seen from a different perspective, the geometric scaling region can be defined as the range in dipole size r, where the dipole cross-section $\sigma_{q\bar{q}}(x,r)$ turns into a function of a single variable, $\sigma_{q\bar{q}}(x,r) \to \sigma_{q\bar{q}}(r^2 Q_s^2(x))$; the saturation scale therefore turns in this region of phase space into the relevant mass scale of the dipole cross-section. Note that such a dependence is generally assumed in the employed dipole models.

Using properties of solutions to the BK equations, this scaling region can be estimated using the following inequality[43,44,45]:

$$1 < \left|\ln\left(r^2 Q_s^2(x)\right)\right| \leq \sqrt{\overline{\alpha}_s \chi_0''(\gamma_0)}, \tag{19}$$

with $\chi_0(\gamma) = 2\Psi(1) - \Psi(\gamma) - \Psi(1-\gamma)$ the leading order BFKL eigenvalue and γ_0 implicitly defined through $\chi_0(\gamma_0)/\gamma_0 = \chi_0'(\gamma_0)$ with $\gamma_0 \simeq 0.627549$. The resulting scaling region is illustrated in Fig. 3 (left) using the GBW saturation scale and $\overline{\alpha}_s(m_c) \simeq 0.29$, for both the proton and a lead nucleus. For the proton, even at the lowest accessible values of x, one enters the scaling region only for $r > 1/\text{GeV}$; one is therefore in a region of phase space which is dominated by non-perturbative dynamics. This is in general one of the reasons why one searches for events on the boundary between perturbative and non-perburative QCD dynamics, since it is this region of phase space where non-linear effects are enhanced. For a lead nucleus, the scaling region starts already at $r > 0.4/\text{GeV}$, since the gluon density is enhanced through the overlap of various nucleons. To compare the scaling region to the region in dipole sizes probed for J/Ψ and $\Psi(2s)$ production, we introduce the normalized wave function overlap

$$W_V(r) = \frac{r\int_0^1 dz (\Psi_V^* \Psi_T)(r,z)}{\int dr r \int_0^1 dz (\Psi_V^* \Psi_T)(r,z)}, \qquad \int_0^\infty dr W(r) = 1, \tag{20}$$

see Fig. 3, right; note that $W_{\Psi(2s)}(r) < 0$ for $r > 2.59/\text{GeV}$. To access the relevance of the different regions in dipole size r for the complete cross-section, we further provide in Tab. 1 the integrated $W_V(r)$ function for different regions. For the photonuclear production cross-section, the bulk of the dipole sizes probed in the reaction – approximately three quarters – lies within the geometric scaling region; this

Table 1: Percentage of $w_V = \int_{r_{min}}^{r_{max}} dr W_{J/\Psi}$ for different regions of dipole size r. Note that the $W_{\Psi(2s)} < 0$ for $r > 2.59/\text{GeV}$.

	$0 < r < 0.4/\text{GeV}$	$0.4 < r < 1/\text{GeV}$	$1 < r < 3/\text{GeV}$	$r > 3/\text{GeV}$
$w_{J/\Psi}(\%)$	23.6	40.8	34.9	0.7
$w_{\Psi(2s)}(\%)$	26.7	45.7	30.0	- 1.4

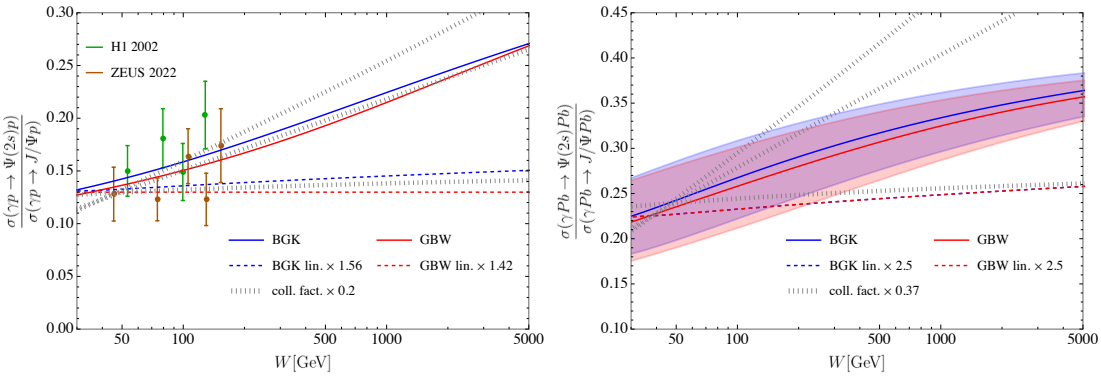

Figure 4 – Ratio of photoproduction cross-sections both for the proton (left) and lead (right). For the proton we further depict ZEUS[46] and H1[47] data

explains the clear imprint of a non-linear energy dependence in the photoproduction cross-section shown in Fig. 2. For photoproduction on a proton, this contribution is however reduced to approximately a third, which explains the relatively weak non-linear dynamics in Fig. 1.

3.2 The ratio of the photo-production cross-sections

To have access to the geometrical scaling region in the proton, it is necessary to probe observables that are somehow sensitive to dipole sizes $1 < r < 3/\text{GeV}$. In this region, both wave function overlaps are still sizeable, while they differ significantly in shape due to the node of $W_{\psi(2s)}$ at $r = 2.59/\text{GeV}$. A possibility to gain sensitivity to this region is given by observables which attempt to probe the difference in this wave function shape. An obvious candidate is obviously the ratio of both photo-production cross-sections. To understand the behavior of this ratio, it is best to study it first for the scenario where non-linear dynamics are absent. For the linearized GBW model,

$$\sigma_{q\bar{q}}^{\text{GBW, lin.}}(x,r) = \sigma_0^{\text{GBW}} r^2 Q_s^2(x)/4, \tag{21}$$

Eq. (5) turns into

$$\Im\text{m}\mathcal{A}_T^{\gamma p \to Vp}(x) = Q_s^2(x) \cdot \sigma_0^{\text{GBW}} \int d^2\mathbf{r} \Sigma(r) r^2/4, \qquad V = J/\Psi, \Psi(2s). \tag{22}$$

For the ratio of both photoproduction cross-sections, the energy dependence therefore cancels and one is left with a ratio constant with energy. This differs for the complete dipole model, where x and r-dependence do not factorizae. For the BGK model, one finds a dipole size dependent saturation scale or gluon distribution. The x-dependence does therefore not cancel in the ratio. Nevertheless, in the region of interest corresponding to dipole sizes $r > 1/\text{GeV}$, the factorization scale approaches rapidly $\mu_0 \simeq 1.32$ GeV and one deals again with a dipole size independent saturation scale. For $r > 1/\text{GeV}$, the x-dependence of the collinear leading order dipole cross-section Eq. (9) turns r-independent and one finds again a ratio which is approximately x independent, if one sticks to the linear dipole cross-section. For $r < 1/\text{GeV}$, there is clearly a dependence on the dipole size, while in this region the shape of both wave functions is very similar; the difference will therefore not manifest itself at the cross-section level.

4 Predictions for the ratio of photoproduction cross-sections

We finally present our numerical results at the level of cross-sections measured in experiment in Fig. 4. As expected we find for the photoproduction on a proton an approximately linear growth of the cross-section ratio, if non-linear effects are fully included; the regarding linearized versions lead on the other hand to a cross-section ratio constant with energy W. The scenario is similar for photoproduction on a lead nucleus, with the important difference that for the largest center of mass energies we can already observe a slowdown of the growth of the ratio. This is in a certain sense a deviation from a possible growth of the ratio within collinear factorization, which can accommodate, but not predict a growing ratio. In that case, a growing or constant ratio is obtained due to different choices for the collinear factorization scale; for a detailed discussion we refer to the paper[21].

5 Conclusions

We examined the proposal[5], suggesting that an increasing ratio of photoproduction cross-sections for $\Psi(2s)$ and J/Ψ can be an indicater for non-linear low x dynamics in protons or nuclei. Our analysis utilized dipole cross-sections from the GBW and BGK models, which essentially exponentiate linear cross-sections to investigate the effects of non-linear low x dynamics. As an initial outcome, we confirmed that the observation[5] holds if gluon distributions under linear NLO BFKL and non-linear BK evolutions are replaced by linearized and unitarized dipole models: without non-linear low x dynamics, the ratio of the two cross-sections remains nearly constant, but it rises when using the fully exponentiated dipole model. This behavior can be explained by the convolution of the dipole cross-section and the wave function overlap: if the dipole cross-section's shape changes with x in regions where wave function overlaps for the transition from photon to $\Psi(2s)$ and J/Ψ differ, the ratio increases. In linearized models, this phenomenon is absent because only the normalization changes with x while the shape in dipole size remains approximately constant, apart from minor adjustments from DGLAP evolution.

Acknowledgments

We acknowledge support by Consejo Nacional de Ciencia y Tecnología grant number A1 S-43940 (CONACYT-SEP Ciencias Básicas). We would like to thank Heikki Mäntysaari for pointing out to us the incorrect use of incoherent instead of coherent photonuclear ALICE data for the determination of the nuclear diffractive slope in our initial manuscript.

References

1. L.V. Gribov, E.M. Levin, and M.G. Ryskin. Semihard Processes in QCD. *Phys. Rept.*, 100:1–150, 1983.
2. Martin Hentschinski et al. White Paper on Forward Physics, BFKL, Saturation Physics and Diffraction. *Acta Phys. Polon. B*, 54(3):3–A2, 2023.
3. Francesco Giovanni Celiberto. Vector Quarkonia at the LHC with Jethad: A High-Energy Viewpoint. *Universe*, 9(7):324, 2023.
4. Emilien Chapon et al. Prospects for quarkonium studies at the high-luminosity LHC. *Prog. Part. Nucl. Phys.*, 122:103906, 2022.
5. Martin Hentschinski and Emilio Padrón Molina. Exclusive J/Ψ and $\Psi(2s)$ photo-production as a probe of QCD low x evolution equations. *Phys. Rev. D*, 103(7):074008, 2021.
6. A. Arroyo Garcia, M. Hentschinski, and K. Kutak. QCD evolution based evidence for the onset of gluon saturation in exclusive photo-production of vector mesons. *Phys. Lett. B*, 795:569–575, 2019.
7. I. Bautista, A. Fernandez Tellez, and Martin Hentschinski. BFKL evolution and the growth with energy of exclusive J/ψ and Υ photoproduction cross sections. *Phys. Rev. D*, 94(5):054002, 2016.
8. Martin Hentschinski. The use of QCD evolution to detect gluon saturation in exclusive photo-production of vector mesons. In *Workshop of QCD and Forward Physics at the the LHC, the future Electron Ion Collider and Cosmic Ray Physics*, pages 187–192, Lawrence, 2020. University of Kansas Libraries.
9. Martin Hentschinski. QCD evolution based evidence for the onset of gluon saturation in exclusive photo-production of vector mesons. *PoS*, EPS-HEP2019:528, 2020.
10. Martin Hentschinski and Krzysztof Kutak. Signs for the onset of gluon saturation in exclusive photo-production of vector mesons. *PoS*, LHCP2019:039, 2019.
11. Martin Hentschinski. The growth with energy of vector meson photo-production cross-sections and low x evolution. *PoS*, DIS2017:054, 2018.
12. Martin Hentschinski, Agustín Sabio Vera, and Clara Salas. Hard to Soft Pomeron Transition in Small-x Deep Inelastic Scattering Data Using Optimal Renormalization. *Phys. Rev. Lett.*, 110(4):041601, 2013.
13. Martin Hentschinski, Agustin Sabio Vera, and Clara Salas. F_2 and F_L at small x using a collinearly improved BFKL resummation. *Phys. Rev. D*, 87(7):076005, 2013.
14. Grigorios Chachamis, Michal Deák, Martin Hentschinski, Germán Rodrigo, and Agustín Sabio Vera. Single bottom quark production in k-factorisation. *Journal of High Energy Physics*, 2015(9):1–17, 2015.

15. Krzysztof Kutak and Sebastian Sapeta. Gluon saturation in dijet production in p-Pb collisions at Large Hadron Collider. *Phys. Rev. D*, 86:094043, 2012.
16. J. Nemchik, Nikolai N. Nikolaev, E. Predazzi, B. G. Zakharov, and V. R. Zoller. The Diffraction cone for exclusive vector meson production in deep inelastic scattering. *J. Exp. Theor. Phys.*, 86:1054–1073, 1998.
17. Jan Cepila, Jan Nemchik, Michal Krelina, and Roman Pasechnik. Theoretical uncertainties in exclusive electroproduction of s-wave heavy quarkonia. *The European Physical Journal C*, 79:1–29, 2019.
18. Krzysztof J. Golec-Biernat and M. Wusthoff. Saturation effects in deep inelastic scattering at low Q**2 and its implications on diffraction. *Phys. Rev. D*, 59:014017, 1998.
19. Shreyasi Acharya et al. Energy dependence of coherent photonuclear production of J/ψ mesons in ultra-peripheral Pb-Pb collisions at $\sqrt{s_{\rm NN}}$=5.02 TeV. 5 2023.
20. Shreyasi Acharya et al. First measurement of the $|t|$-dependence of incoherent J/ψ photonuclear production. 5 2023.
21. Marco Alcazar Peredo and Martin Hentschinski. Ratio of J/Ψ and Ψ(2s) exclusive photoproduction cross sections as an indicator for the presence of nonlinear QCD evolution. *Phys. Rev. D*, 109(1):014032, 2024.
22. Marco Antonio Alcazar Peredo and Martin Hentschinski. Exclusive Photo-production of J/Ψ and Ψ(2s) as a tool to explore the transition to high and saturated gluon densities at the LHC. *Rev. Mex. Fis. Suppl.*, 4(2):021121, 2023.
23. S. Acharya, D. Adamová, et al. First measurement of the —t—-dependence of coherent j/ photonuclear production. *Physics Letters B*, 817:136280, 2021.
24. Michal Krelina, Jan Nemchik, Roman Pasechnik, and Jan Cepila. Spin rotation effects in diffractive electroproduction of heavy quarkonia. *Eur. Phys. J. C*, 79(2):154, 2019.
25. Stanley J. Brodsky, Tao Huang, and G.Peter Lepage. The Hadronic Wave Function in Quantum Chromodynamics. 6 1980.
26. Néstor Armesto and Amir H. Rezaeian. Exclusive vector meson production at high energies and gluon saturation. *Phys. Rev. D*, 90(5):054003, 2014.
27. L. Frankfurt, A. Radyushkin, and M. Strikman. Interaction of small size wave packet with hadron target. *Phys. Rev. D*, 55:98–104, 1997.
28. J. Bartels, K. Golec-Biernat, and H. Kowalski. Modification of the saturation model: Dokshitzer-gribov-lipatov-altarelli-parisi evolution. *Phys. Rev. D*, 66:014001, Jun 2002.
29. Krzysztof Golec-Biernat and Sebastian Sapeta. Saturation model of DIS : an update. *JHEP*, 03:102, 2018.
30. S. Chekanov et al. Exclusive electroproduction of J/psi mesons at HERA. *Nucl. Phys. B*, 695:3–37, 2004.
31. C. Alexa et al. Elastic and Proton-Dissociative Photoproduction of J/psi Mesons at HERA. *Eur. Phys. J. C*, 73(6):2466, 2013.
32. A. Aktas et al. Elastic J/psi production at HERA. *Eur. Phys. J. C*, 46:585–603, 2006.
33. Betty Bezverkhny Abelev et al. Exclusive J/ψ photoproduction off protons in ultra-peripheral p-Pb collisions at $\sqrt{s_{\rm NN}} = 5.02$ TeV. *Phys. Rev. Lett.*, 113(23):232504, 2014.
34. Shreyasi Acharya et al. Energy dependence of exclusive J/ψ photoproduction off protons in ultra-peripheral p–Pb collisions at $\sqrt{s_{\rm NN}} = 5.02$ TeV. *Eur. Phys. J. C*, 79(5):402, 2019.
35. Exclusive and dissociative J/ψ photoproduction, and exclusive dimuon production, in p$-$Pb collisions at $\sqrt{s_{\rm NN}} = 8.16$ TeV. 4 2023.
36. R Aaij et al. Exclusive J/ψ and ψ(2S) production in pp collisions at $\sqrt{s} = 7$ TeV. *J. Phys. G*, 40:045001, 2013.
37. Roel Aaij et al. Central exclusive production of J/ψ and $\psi(2S)$ mesons in pp collisions at $\sqrt{s} = 13$ TeV. *JHEP*, 10:167, 2018.
38. D. Schmidt. *Diffractive photoproduction of charmonium in the H1 detector at HERA*. PhD thesis, Hamburg U., 2001.
39. C. Adloff et al. Diffractive photoproduction of psi(2S) mesons at HERA. *Phys. Lett. B*, 541:251–264, 2002.
40. Armen Tumasyan et al. Probing Small Bjorken-x Nuclear Gluonic Structure via Coherent J/ψ Photoproduction in Ultraperipheral Pb-Pb Collisions at sNN=5.02 TeV. *Phys. Rev. Lett.*, 131(26):262301, 2023.
41. A. M. Stasto, Krzysztof J. Golec-Biernat, and J. Kwiecinski. Geometric scaling for the total gamma* p cross-section in the low x region. *Phys. Rev. Lett.*, 86:596–599, 2001.

42. A. H. Mueller and S. Munier. Rapidity gap distribution in diffractive deep-inelastic scattering and parton genealogy. *Phys. Rev. D*, 98(3):034021, 2018.
43. A. H. Mueller and D. N. Triantafyllopoulos. The Energy dependence of the saturation momentum. *Nucl. Phys. B*, 640:331–350, 2002.
44. S. Munier and Robert B. Peschanski. Traveling wave fronts and the transition to saturation. *Phys. Rev. D*, 69:034008, 2004.
45. S. Munier and Robert B. Peschanski. Geometric scaling as traveling waves. *Phys. Rev. Lett.*, 91:232001, 2003.
46. I. Abt et al. Measurement of the cross-section ratio $\sigma_{(2S)}/\sigma_{J/(1S)}$ in exclusive photoproduction at HERA. *JHEP*, 12:164, 2022.
47. C. Adloff et al. Diffractive photoproduction of psi(2S) mesons at HERA. *Phys. Lett. B*, 541:251–264, 2002.

Nuclear Shadowing in Inelastic Photon-Nucleus Scattering in UPCs with Forward Neutrons

M. ALVIOLI [1,2], V. GUZEY [3], M. STRIKMAN [4]

[1] *Consiglio Nazionale delle Ricerche, Istituto di Ricerca per la Protezione Idrogeologica, via Madonna Alta 126, I-06128, Perugia, Italy*

[2] *Istituto Nazionale di Fisica Nucleare, Sezione di Perugia, via Pascoli 23c, I-06123, Perugia, Italy*

[3] *University of Jyvaskyla, Department of Physics, P.O. Box 35, FI-40014 University of Jyvaskyla, Finland and Helsinki Institute of Physics, P.O. Box 64, FI-00014 University of Helsinki, Finland*

[4] *Pennsylvania State University, University Park, PA, 16802, USA*

We argue that measurements of forward neutrons from nuclear breakup in inclusive high energy photon-nucleus (γA) scattering provide a novel complementary way to study small-x dynamics of QCD in heavy-ion ultraperipheral collisions (UPCs). Using the leading twist approach to nuclear shadowing, we calculate the distribution over the number of evaporation neutrons produced in γPb collisions at the LHC. We demonstrate that it allows one to determine the distribution over the number of wounded nucleons (inelastic collisions), which constrains the mechanism of nuclear shadowing of nuclear parton distributions and gives an access to their impact parameter dependence.

DOI: https://doi.org/10.17161/fnzwt563

Keywords: Heavy-ion scattering, ultraperipheral collisions, nuclear shadowing

1 Introduction

One of the main directions of modern high-energy nuclear physics is understanding of the dynamics of strong interactions and the structure of nuclei and nucleons in terms of quantum chromodynamics (QCD). Among many open questions, the limit of very high energies (small momentum fractions x) is of particular interest since it is predicted that the linear Dokshitzer-Gribov-Lipatov-Altarelli-Parisi (DGLAP) approximation for parton distributions (PDFs) will eventually break down [1,2] and a new, non-linear regime of high parton densities characterized by their saturation will set it [3,4]. Experimental studies of this and other open QCD questions are carried out at the Large Hadron Collider (LHC) [5,6] and the Relativistic Heavy Ion Collider (RHIC) and are planned at the future Electron-Ion Collider (EIC) at Brookhaven National Laboratory [7,8]. Note that heavy-ion scattering at the LHC and electron-nucleus collisions at the EIC present two complementary options for studying small-x QCD: while at the LHC practically all data are collected for the nucleus of lead (Pb), and the large collision energy and detector geometry allow one to probe down to $x \sim 10^{-5} - 10^{-4}$, the EIC will employ a wide array of light and heavy nuclei and will reach $x \sim 10^{-3}$ for momentum transfers of a few GeV.

An important part of the heavy-ion program at the LHC is related to ultraperipheral collisions (UPCs), where a photon emitted by one of the nuclei interacts with the other nucleus [9]. The focus of such measurements has so far been coherent and incoherent production of light and heavy vector mesons. In particular, over the last decade the data discovered a significant nuclear suppression of coherent J/ψ photoproduction in Pb-Pb UPCs compared to the impulse approximation prediction, see [10] for references. When interpreted in terms of the gluon distribution [11], it amounts to strong gluon nuclear shadowing [12,13], $R_{\rm Pb}^g(x,Q^2) = g_A(x,Q^2)/[Ag_N(x,Q^2)] \approx 0.6$ at $x = 10^{-3}$ and $R_{\rm Pb}^g(x,Q^2) \approx 0.5$ for $x = 10^{-5} - 10^{-4}$ at $Q^2 = 3$ GeV^2, where $g_A(x,Q^2)$ and $g_N(x,Q^2)$ are the nucleus and nucleon gluon densities, respectively. These values of $R_{\rm Pb}^g$ agree very well with the predictions of the leading twist approximation (LTA) for nuclear shadowing made more than 10 years ago [14]. The recent STAR data [15] indicate that the nuclear

suppression persists also for larger x, $R^g_{\rm Pb}(x,Q^2)=\sqrt{S^{\rm Au}_{\rm coh}}=0.84\pm0.05$ at $\langle x\rangle=0.015$.

Note that this interpretation of the J/ψ UPC data in terms of the gluon nuclear shadowing is complicated at the next-to-leading order (NLO) of the perturbative expansion in powers of $\log Q^2$ (perturbative QCD) by large cancellations between the leading-order (LO) and NLO gluon coefficient functions, which leaves a numerically important quark contribution [16,17]. A method to stabilize the perturbation series and restore the gluon dominance in this process on the proton target was suggested in [18,19].

Other hard UPC processes considered in the literature are inclusive [20,21] and diffractive [22,23] dijet photoproduction (there is preliminary ATLAS data for this process [24,25]), timelike Compton scattering [26,27,28], and heavy quark photoproduction [29,30,31].

In this contribution, we would like to outline several new directions of future UPC studies, which were not discussed in the review [9]. We explore for the first time the possibility to probe small-x nuclear shadowing by measuring the rates of forward neutron production from nuclear breakup in the zero degree calorimeters (ZDCs) at the LHC. Our numerical studies demonstrate that the number of produced neutrons is correlated with the number of wounded nucleons (inelastic photon-nucleon interactions), which presents a complementary way to study the mechanism of nuclear shadowing of nuclear PDFs. Importantly, it allows one to effectively access the centrality (impact parameter) dependence of nuclear PDFs.

This contribution is organized as follows. In Sec. 2 we summarize expectations based on applications of the Abramovski-Gribov-Kancheli (AGK) theorem to photon-nucleus scattering, model the distribution over the number of wounded nucleons and estimate its average value in the current UPC kinematics. Section 3 presents our predictions for the distributions over the number of emitted forward neutrons from nuclear breakup in inelastic photon-nucleus scattering and its connection to parameters of the leading twist approximation of nuclear shadowing. Our conclusions and outlook are given Sec. 4.

2 Abramovski-Gribov-Kancheli (AGK) cutting rules, nuclear shadowing and the number of wounded nucleons in γA scattering

It was demonstrated by Abramovski, Gribov and Kancheli in 1973 [32] that different unitary cuts of the diagrams corresponding to multi-Pomeron (color singlet) exchanges result in different multiplicities of produced particles in the central rapidity region and that the absorptive part of the amplitude can be expressed in terms of a small number of cut diagrams, which are related by combinatorial factors; these are the so-called Abramovski-Gribov-Kancheli (AGK) cutting rules or the AGK cancellation. For the interpretation of the AGK rules in QCD and other effective field theories, see Refs. [33,34,35,36,37].

In our analysis, we employ the following two applications of the AGK cutting rules to real photon-nucleus scattering. First, they allow one to express the nuclear shadowing correction to the total nuclear cross section $\sigma^{\gamma A}_{\rm tot}$ in terms of the diffractive cross section on individual nucleons. Further, using the QCD factorization theorem for hard diffraction [38], the connection between nuclear shadowing and diffraction can be established at the level of leading twist nuclear PDFs of individual flavors (quarks and gluons) [14,39].

Second, defining the total photon-nucleus inelastic cross section $\sigma^{\gamma A}_{\rm inel}$ as the difference between the total and total elastic (coherent plus incoherent) cross sections, it can be presented in the following form [40,41]

$$\sigma^{\gamma A}_{\rm inel}=\sum_{\nu=1}^{A}\sigma_\nu\,, \tag{1}$$

where

$$\sigma_\nu=\frac{A!}{(A-\nu)!\nu!}\int d^2\vec{b}\int d\sigma P_\gamma(\sigma)(\sigma_{\rm inel}T_A(\vec{b}))^\nu(1-\sigma_{\rm inel}T_A(\vec{b}))^{A-\nu}\,. \tag{2}$$

Equation (2) generalizes the expression for σ_ν in hadron-nucleus scattering to the case of photon-nucleus scattering, where the photon is represented by its hadronic fluctuations with the distribution $P_\gamma(\sigma)$. In Eq. (2), $\vec{b}$ is the impact parameter (transverse coordinate) of the interacting nucleon, $T_A(\vec{b})=\int dz\rho_A(\vec{b},z)$, where $\rho_A(\vec{b},z)$ is the nuclear density normalized to unity, and $\sigma_{\rm inel}=0.85\,\sigma$ is the inelastic cross section for the interaction of a hadronic fluctuation of the photon with a target nucleon, which is based on the estimate that the ρ meson-nucleon elastic cross section constitutes approximately 15% of the total one. The cross sections σ_ν are positive and represent the physical process, where ν nucleons undergo inelastic scattering, while the remaining $A-\nu$ nucleons provide absorption. In the literature, one uses the term "wounded nucleons" [42] and the notation $\nu=N_{\rm coll}$.

The distribution $P_\gamma(\sigma)$ gives the probability density for hadronic fluctuations of the real photon to interact with nucleons with the cross section σ [41,43]. The shape of $P_\gamma(\sigma)$ cannot be calculated from the

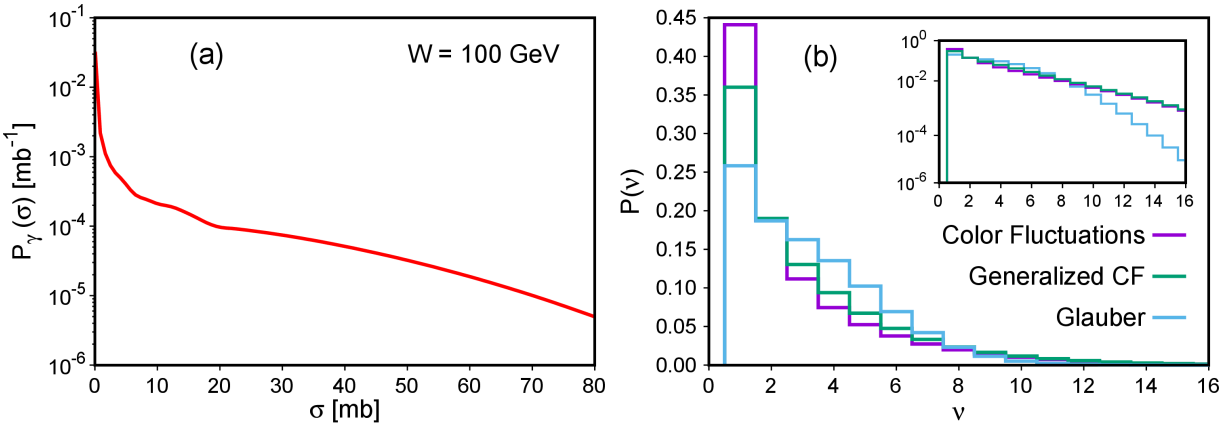

Figure 1 – (a) The distribution $P_\gamma(\sigma)$ as a function of σ at $W = 100$ GeV. (b) The distribution $P(\nu)$ for inelastic photon-nucleus (Pb) scattering as a function of the number of wounded nucleons ν. The three curves correspond to three models for $P_\gamma(\sigma)$, see text for details. The insert emphasizes the region of large ν.

first principles, but one can model it using its first moments and the small-σ and large-σ limits. Indeed, the total photon-proton cross section $\sigma_{\gamma p}(W)$ and the cross section of photon diffractive dissociation on the proton $d\sigma_{\gamma p\to Xp}(W, t=0)/dt$ constrain the first two moments of $P_\gamma(\sigma)$,

$$\begin{aligned} \sigma_{\gamma p}(W) &= \int d\sigma P_\gamma(\sigma)\sigma\,, \\ \frac{d\sigma_{\gamma p}(W,t=0)}{dt} &= \frac{1}{16\pi}\int d\sigma P_\gamma(\sigma)\sigma^2\,, \end{aligned} \tag{3}$$

where W is the invariant photon-nucleon center-of-mass-energy. Further, in the small-σ limit, one can express $P_\gamma(\sigma)$ in terms of the quark-antiquark component of the photon light-cone wave function and the color dipole cross section, which leads to $P_\gamma(\sigma) \propto 1/\sigma$. In the opposite limit of large σ, the photon behaves as a superposition of the ρ, ω and ϕ vector mesons in the spirit of the vector meson dominance model and, hence, $P_\gamma(\sigma)$ can be modeled using hadronic (cross section) fluctuations in ρ mesons, which in turn are related to those for pions. Finally, the small-σ and large-σ limits can be smoothly interpolated. Note that this matching is achieved best, when the light quark masses m_q are taken to be those of the constituent quarks, $m_q \sim 300$ MeV. For details, see [41,43].

The left panel of Fig. 1 presents the distribution $P_\gamma(\sigma)$ as a function of σ at $W = 100$ GeV. Since the W dependence of $P_\gamma(\sigma)$ is weak, the presented distribution is applicable in a wide range of energies probed in heavy-ion UPCs at the LHC. Note that the distribution $P_\gamma(\sigma)$ parametrizes the so-called resolved photon contribution to photon-induced scattering and does contain the direct photon contribution.

Using Eqs. (1) and (2), one can readily define the probability distribution over the number of wounded nucleons ν in inelastic photon-nucleus scattering, $P(\nu)$, as follows [41],

$$P(\nu) = \frac{\sigma_\nu}{\sum_{\nu=1}^{A}\sigma_\nu}\,, \tag{4}$$

where σ_ν are given by Eq. (2).

In our numerical analysis of Eq. (4), we use the Monte Carlo generator for nucleon configurations in complex nuclei [44], which also includes nucleon-nucleon correlations in the nucleus wave function [45,46]. The resulting distribution $P(\nu)$ as a function of ν for lead (^{208}Pb) is shown by the curve labeled "Color Fluctuations" in the right panel of Fig. 1.

The small-σ behavior of $P_\gamma(\sigma)$ is derived using the quark-antiquark component of the photon wave function, which does not capture the observed strong gluon nuclear shadowing discussed in Introduction. To take it into account, we model the nuclear suppression of the dipoles with $\sigma \le \sigma_0 = 20$ mb by the factor of R_A^g, which leads to the modified distribution $\tilde{P}_\gamma(\sigma)$,

$$\tilde{P}_\gamma(\sigma) = \left[R_A^g(x,Q^2)\theta(\sigma_0-\sigma) + \theta(\sigma-\sigma_0)\right] P_\gamma(\sigma)\,, \tag{5}$$

where $x = Q^2/W^2$ and $Q^2 = 3$ GeV^2. The distribution $P(\nu)$ corresponding to σ_ν, which is calculated using $\tilde{P}_\gamma(\sigma)$, is given by the curve "Generalized CF" in the right panel of Fig. 1.

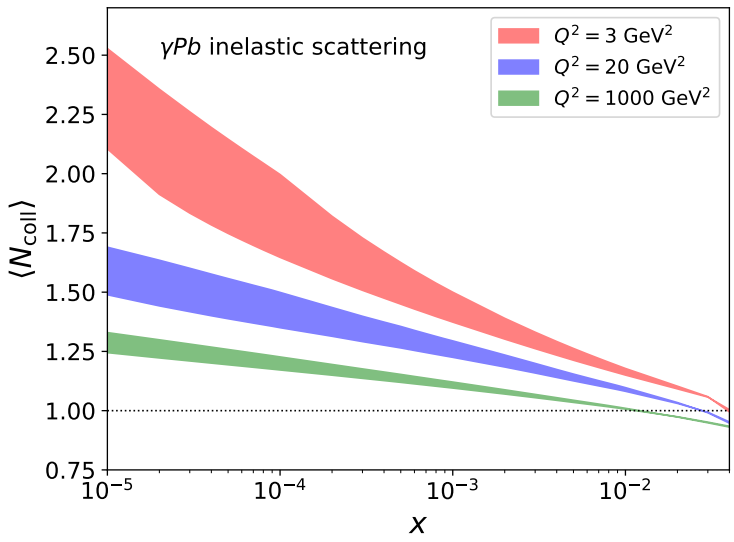

Figure 2 – The LTA predictions for the average number of wounded nucleons $\langle N_{\rm coll}\rangle$ in inelastic photon-nucleus (Pb) scattering as a function of x at $Q^2 = 3$, 20, and 1000 GeV^2.

Finally, to test the importance of cross section fluctuations in the real photon, we calculated $P(\nu)$ neglecting these fluctuations and using

$$P_\gamma(\sigma) = \delta(\sigma - 25\,{\rm mb})\,. \tag{6}$$

The result is given by the curve "Glauber" in Fig. 1. One can see from this figure that cross section (color) fluctuations in the real photon significantly increase the distribution $P(\nu)$ at small and large ν; the latter is emphasized in the insert.

In the total inelastic photon-nucleus cross section $\sigma_{\rm inel}^{\gamma A}$, the AGK cancellations manifest themselves as the observation that the average number of wounded nucleons $\langle N_{\rm coll}\rangle$ is inversely proportional to the nuclear shadowing factor. Generalizing the result of [40] for hadron-nucleus scattering to the case of photon-induced scattering, one obtains

$$\langle N_{\rm coll}\rangle \equiv \sum_{\nu=1}^{A} P(\nu)\nu = \frac{\sum_{\nu=1}^{A}\nu\sigma_\nu}{\sum_{\nu=1}^{A}\sigma_\nu} = \frac{A\sigma_{\rm inel}^{\gamma N}}{\sigma_{\rm inel}^{\gamma A}}\,, \tag{7}$$

where $\sigma_{\rm inel}^{\gamma N}$ is the photon-nucleon inelastic cross section. Considering a particular hard process in inelastic photon-nucleus scattering that probes the nuclear gluon distribution, e.g., inclusive charmonium (bottomonium) production $\gamma + A \to J/\psi(\Upsilon) + X$ or inclusive heavy-quark dijet production $\gamma + A \to Q\bar{Q} + X$, one obtains using Eq. (7),

$$\langle N_{\rm coll}\rangle \approx \frac{1}{R_{\rm Pb}^g(x,Q^2)} \lesssim 2\,. \tag{8}$$

In this estimate we used the numerical values for $R_{\rm Pb}^g(x,Q^2)$ discussed in Introduction and the observation that within LTA theoretical uncertainties, the effects of nuclear shadowing in the total and inelastic photon-nucleus cross sections are approximately equal.

Figure 2 shows LTA predictions for the average number of wounded nucleons $\langle N_{\rm coll}\rangle = 1/R_{\rm Pb}^g(x,Q^2)$ in inelastic photon-nucleus (Pb) scattering as a function of x at $Q^2 = 3$, 20, and 1000 GeV^2. These values of Q^2 correspond to photoproduction of J/ψ, Υ, and high-p_T dijets, respectively. One can see from the figure that in the discussed kinematics, the average number of wounded nucleons is modest and the series in Eq. (7) converges rather rapidly. In particular, we have checked that it is saturated by first six terms with a 5% precision. Note, however, that the convergence slows down in the limit of small x.

Measurements of $\langle N_{\rm coll}\rangle$ present a new method to study nuclear shadowing in inelastic photon-nucleus scattering. Unlike the observables used so far, the constraint of Eq. (8) indicates that one can perform a "Pomeron surgery" of nuclear shadowing by cutting a small number of Pomeron exchanges controlling the number of inelastic interactions with target nucleons. As a result, it gives an opportunity for an experimental determination of a small number of parameters quantifying nuclear shadowing, which leads to a systematic improvement of its theoretical description.

3 The distributions over the number of wounded nucleons and forward neutrons from nuclear breakup

While the average number of inelastic interactions $\langle N_{\rm coll}\rangle$ encodes information on the energy and scale dependence of nuclear shadowing, its dependence on the impact parameter of the collision is averaged over. To obtain a more microscopic description of nuclear shadowing and access the impact parameter dependence of nuclear PDFs, one needs to determine not only $\langle N_{\rm coll}\rangle$, but also the entire distribution over the number of wounded nucleons. This can be done using experimental data on the neutron emission resulting from nucleus fragmentation in a given UPC process, e.g., in inclusive quarkonium or dijet photoproduction in heavy-ion UPCs with an additional condition of Xn neutrons in the zero degree calorimeter (ZDC) on the nuclear target side [24,25].

Experimental information on neutron emission in high energy scattering off heavy nuclei is sparse and comes essentially from the following two sources. The ALICE collaboration measured the distribution over $\langle N_{\rm coll}\rangle$ in proton-nucleus scattering, where it was determined by the energy release (E_T) at central rapidities [47]. It was observed that $\langle N_{\rm coll}(E_T)\rangle$ is linearly proportional to the number of evaporation neutrons $\langle M_n(E_T)\rangle$ for the same E_T bins at least up to $\langle N_{\rm coll}\rangle \sim 10$. Note that in our case, $\langle N_{\rm coll}\rangle$ is much lower, see Eq. (8).

Another important observation is the E665 experiment at Fermilab on muon-nucleus deep inelastic scattering (DIS) in coincidence with detection of slow neutrons, $\mu^- + A \to n + X$, which showed that the average neutron multiplicity $\langle M_n\rangle$ for the lead target is [48]

$$\langle M_n\rangle \approx 5\,. \tag{9}$$

This result has been understood in the framework of cascade models of nuclear DIS [49,50], where soft neutrons are produced either directly in DIS on a bound nucleon or through statistical decay (de-excitation) of the excited residual nucleus, leading to neutron evaporation. A similar conclusion was reached using the BeAGLE Monte Carlo generator [51].

It suggests the following space-time picture of forward neutron production in high energy photon-nucleus scattering. The incoming photon fluctuates into hadronic components, which pass through the nucleus and interact inelastically with several nucleons. This leads to the creation of holes in the nucleus (particle-hole excitations in terminology of a nuclear shell model), which de-excite and cool the nucleus by evaporating neutrons. It also produces a number of soft particles with the momenta less than 1 GeV/c, which in turn generate more neutrons.

The nucleon fragmentation weakly depends on the incident energy due to Feynman scaling and, hence, the energy transfer used to heat the residual nuclear system is proportional to $\langle N_{\rm coll}\rangle$. Since the Fermilab data [48] corresponds to the average momentum fraction $\langle x\rangle = 0.015$, where the nuclear shadowing effect is small, one finds that $\langle N_{\rm coll}\rangle \approx 1$, see Eq. (7). Thus, every inelastic photon-nucleon interaction results on average in 5 forward neutrons.

To test this hypothesis, we perform two numerical studies. First, we consider a simple model, which assumes that the probability density of neutron emission is given by the Poisson distribution and that each hole created in the target nucleus generates independently on average $\langle M_n\rangle$ neutrons. Therefore, the neutron probability distribution for $\nu = \langle N_{\rm coll}\rangle$ wounded nucleons is

$$P_{\rm Poisson}(N;\lambda=\nu\langle M_n\rangle) = \frac{(\nu\langle M_n\rangle)^N e^{-\nu\langle M_n\rangle}}{N!}\,, \tag{10}$$

where N is the number of produced neutrons (neutron multiplicity).

The resulting probability density (frequency) for ^{208}Pb as a function of N is shown in the left panel of Fig. 3. In this estimate, we used $\langle M_n\rangle = 5$, see Eq. (9), and $\nu = \langle N_{\rm coll}\rangle = 1, 2, 3$ independent neutron emissions. One can see from the figure that since the distributions for different ν are peaked at different values of N and do not significantly overlap, the measurement of the forward neutron multiplicity can be used to reliably separate contributions of different $\langle N_{\rm coll}\rangle$. Our analysis also shows that this separation becomes even cleaner with an increase of $\langle M_n\rangle$ (not shown here).

In the second study, we combine the distribution over the number of wounded nucleons $P(\nu)$ that we discussed in Sec. 2 with the Poisson distribution of produced neutrons. The resulting probability distribution of forward neutrons is given by the following convolution,

$$P_{\rm comb}(N) = \sum_{\nu=1}^{A} P(\nu) P_{\rm Poisson}(N;\nu\langle M_n\rangle)\,. \tag{11}$$

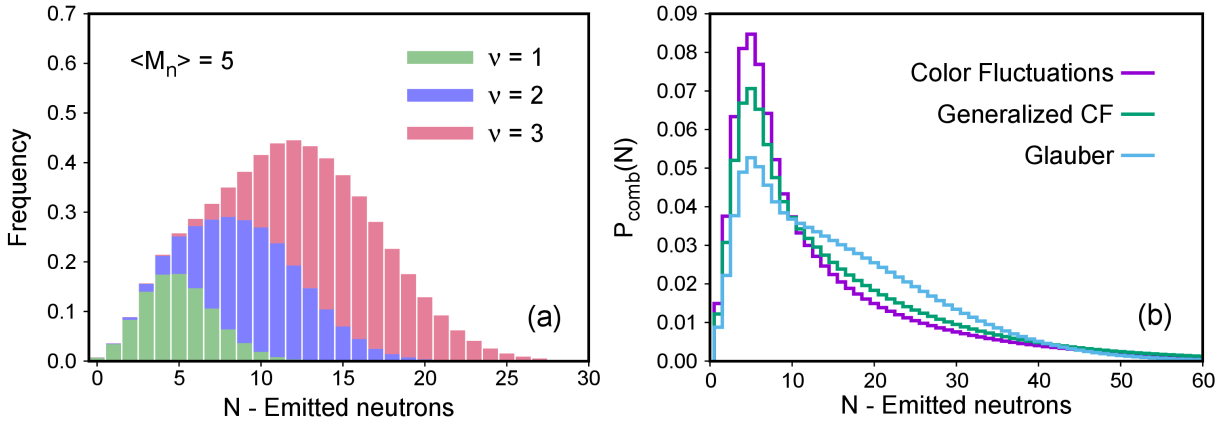

Figure 3 – (a) The probability distribution (frequency) for ^{208}Pb to produce N forward neutrons assuming their Poisson distribution with $\nu = \langle N_{\rm coll}\rangle = 1, 2, 3$ independent emissions and the average multiplicity for a single inelastic scattering $\langle M_n\rangle = 5$. (b) The probability distribution of forward neutron emission $P_{\rm comb}(N)$ (11) in the model combining the distribution over the number of wounded nucleons, which is calculated using three models for hadronic fluctuations in the photon (see Fig. 1), with the Poisson distribution of produced neutrons.

The right panel of Fig. 3 presents $P_{\rm comb}(N)$ as a function of forward neutrons N for $\langle M_n\rangle = 5$. The three curves correspond to the three models for $P_\gamma(\sigma)$, see the right panel of Fig. 1. One can see from the figure that cross section fluctuations in the real photon noticeably affect the shape of the neutron distribution: its maximum around $N = 5 - 7$ becomes higher and narrower compared to the "Glauber" result and is also somewhat suppressed by the leading twist shadowing in the "Generalized CF" case.

Our numerical studies suggest that one can examine details of the theoretical description of small-x nuclear shadowing in QCD using the distribution of forward neutrons from nuclear breakup emitted in a given hard UPC process, which is directly correlated with the number of inelastic interactions (wounded nucleons). By studying the dispersion of this distribution, one can single out the individual contributions of $\nu = 1$, 2, 3, ... wounded nucleons. In particular, using Eq. (2) in the approximation that the series in Eq. (7) is saturated by first few terms, which corresponds to the limit of small-to-modest nuclear shadowing, one obtains [41,52]

$$\sigma_2(x,Q^2) \equiv \frac{\langle\sigma^2_{\rm inel}\rangle}{\langle\sigma_{\rm inel}\rangle} = \frac{\langle N_{\rm coll}-1\rangle}{\frac{(A-1)}{2}\int d^2\vec{b}\,T_A^2(\vec{b})}\,, \tag{12}$$

and

$$\sigma_3(x,Q^2) \equiv \frac{\langle\sigma^3_{\rm inel}\rangle}{\langle\sigma^2_{\rm inel}\rangle} = \frac{\langle\sigma^3_{\rm inel}\rangle}{\langle\sigma_{\rm inel}\rangle}\frac{\langle\sigma^2_{\rm inel}\rangle}{\langle\sigma^2_{\rm inel}\rangle} = \frac{(\langle N_{\rm coll}-2\rangle)(\langle N_{\rm coll}-1\rangle)}{\langle N_{\rm coll}-1\rangle}\frac{\frac{(A-1)}{2}\int d^2\vec{b}\,T_A^2(\vec{b})}{\frac{(A-2)(A-1)}{2}\int d^2\vec{b}\,T_A^3(\vec{b})}\,, \tag{13}$$

where $\langle\sigma^n_{\rm inel}\rangle = \int d\sigma P_\gamma(\sigma)\sigma^n_{\rm inel}$. The cross sections $\sigma_2(x,Q^2)$ and $\sigma_3(x,Q^2)$ are essential ingredients of the LTA approach [14]. While $\sigma_2(x,Q^2)$ is determined using the HERA data on inclusive diffraction in lepton-proton DIS, $\sigma_3(x,Q^2)$ is model-dependent and its variation leads to LTA theoretical uncertainties. Thus, an independent determination $\sigma_2(x,Q^2)$ and $\sigma_3(x,Q^2)$ using UPCs with forward neutrons will supply new constraints on these quantities.

Note that to reach a high accuracy in such an analysis, one needs to calibrate the theoretical description against the kinematics, where only one target nucleon is struck in $\gamma + A \to 2$ jets $+ X$ or quasi-elastic J/ψ production for $x_A \geq 0.01$, where the effect of nuclear shadowing is small and $\langle N_{\rm coll}\rangle \approx 1$.

4 Conclusions and outlook

In this contribution, we advertise measurements of forward neutrons from nuclear breakup in inclusive high energy photon-nucleus scattering in heavy-ion UPCs, e.g., charmonium (bottomonium) production $\gamma + A \to J/\psi(\Upsilon) + X$ or heavy-quark dijet production $\gamma + A \to Q\bar{Q} + X$, as a novel way to study the QCD dynamics at small x. The key quantity is the number of inelastic photon-nucleon interactions (the number of wounded nucleons): its average value $\langle N_{\rm coll}\rangle$ is proportional to inverse of the gluon nuclear shadowing factor and its first moments are sensitive to details of the leading twist mechanism of nuclear shadowing.

Our numerical analysis has demonstrated that the number of forward neutrons from nuclear breakup detected in the ZDC on the nuclear target side is rather unambiguously proportional to the number of wounded nucleons, which provides a practical opportunity for novel studies of nuclear shadowing.

On top of providing stringent tests of the dynamics of leading twist shadowing of gluon PDFs, it would be possible to explore effects related to proximity to the black disk limit of the strong interaction. For example, one can study fragmentation of leading hadrons in γA scattering and look for suppression of their multiplicity as a function of Feynman x_F and W as well as for broadening of their transverse momentum distribution [53]. These effects should be more pronounced for central collisions characterized by an enhanced activity in the ZDC. It should be possible to construct from the data an analog of the R_{CP} ratio, which would probe the density dependence of fragmentation. It would also be useful to construct similar quantities for low p_T charm production.

Another interesting application is for multiparton interactions in proton-nucleus (pA) scattering. It was argued in [54] that the single and double scattering can be separated using their dependence on the impact parameter: the former is proportional to A, while the latter $\propto A^{4/3}$. However, since both hard interactions are typically detected in a limited range of rapidities $|y| \leq 3-4$, centrality is difficult to determine from the transverse energy E_T signal because multiparton interactions also contribute to E_T. The use of forward neutrons in ZDCs would alleviate this problem.

One should point out that the neutrons detected in ZDCs can be a promising complementary way to determine centrality of various photon-nucleus and proton-nucleus inelastic collisions expanding the use of ZDCs beyond their current use in vector meson diffractive production and for determining of centrality of the heavy-ion collisions. The main advantage of using forward neutrons rather than the transverse energy E_T for the determination of centrality is a much larger distance in rapidity between the rapidity of the hard process and that of the process used for determination of the centrality.

One of the principal problems of using UPCs for studies of small-x phenomena is a lack of the nucleon reference data at similar energies with the precision necessary to observe nuclear effects with a better than 10% accuracy (J/ψ exclusive photoproduction is a notable exception). Here we outline a possible strategy for overcoming this problem. Note that we are not aiming to optimize cuts or to account for the energy resolution of ZDCs since this would require a dedicated Monte Carlo study.

One can separate events into two classes: peripheral events corresponding to $\langle N_{\rm coll}\rangle \leq 2$ (we call it class "L") and more central events corresponding to $\langle N_{\rm coll}\rangle \geq 1.5-2$ and $\langle M_n\rangle \sim 7-10$ (class "H"). If statistics is sufficient, the lower limit for class "H" can be gradually increased, which will push up the average number of wounded nucleons. Then, the ratio of the number of events in the two classes, $\hat{R} =$ Yield(H)/Yield(L), should quantify the effect of nuclear shadowing at small and large impact parameters, which in principle probes the dependence of nuclear shadowing on the thickness of nuclear matter. The promising channels for such an analysis include inclusive charm production with the transverse momentum in the range $p_T = 5-20$ GeV/c and production of soft particles with small $p_T < 0.5$ GeV/c. A comparison of the rates of these processes will allow one to study the transition between the soft and hard regimes and will serve as a consistency check of the description of small-x dynamics in the current models.

The methods presented in this paper can be readily generalized to the case of virtual photons and allow one to predict the distribution over the number of forward neutrons in inelastic (virtual) photon-nucleus scattering at the EIC.

Acknowledgments

The research of V.G. was funded by the Academy of Finland project 330448, the Center of Excellence in Quark Matter of the Academy of Finland (projects 346325 and 346326), and the European Research Council project ERC-2018-ADG-835105 YoctoLHC. The research of M.S. was supported by the US Department of Energy Office of Science, Office of Nuclear Physics under Award No. DE- FG02-93ER40771.

References

1. Y. L. Dokshitzer, D. Diakonov and S. I. Troian, Phys. Rept. **58**, 269-395 (1980)
2. L. V. Gribov, E. M. Levin and M. G. Ryskin, Phys. Rept. **100**, 1-150 (1983)
3. F. Gelis, E. Iancu, J. Jalilian-Marian and R. Venugopalan, Ann. Rev. Nucl. Part. Sci. **60**, 463-489 (2010) [arXiv:1002.0333 [hep-ph]].
4. A. Morreale and F. Salazar, Universe **7**, no.8, 312 (2021) [arXiv:2108.08254 [hep-ph]].
5. C. A. Salgado, J. Alvarez-Muniz, F. Arleo, N. Armesto, M. Botje, M. Cacciari, J. Campbell,

C. Carli, B. Cole and D. D'Enterria, *et al.* J. Phys. G **39**, 015010 (2012) [arXiv:1105.3919 [hep-ph]].
6. Z. Citron, A. Dainese, J. F. Grosse-Oetringhaus, J. M. Jowett, Y. J. Lee, U. A. Wiedemann, M. Winn, A. Andronic, F. Bellini and E. Bruna, *et al.* CERN Yellow Rep. Monogr. **7**, 1159-1410 (2019) [arXiv:1812.06772 [hep-ph]].
7. A. Accardi, J. L. Albacete, M. Anselmino, N. Armesto, E. C. Aschenauer, A. Bacchetta, D. Boer, W. K. Brooks, T. Burton and N. B. Chang, *et al.* Eur. Phys. J. A **52**, no.9, 268 (2016) [arXiv:1212.1701 [nucl-ex]].
8. R. Abdul Khalek, A. Accardi, J. Adam, D. Adamiak, W. Akers, M. Albaladejo, A. Al-bataineh, M. G. Alexeev, F. Ameli and P. Antonioli, *et al.* Nucl. Phys. A **1026**, 122447 (2022) [arXiv:2103.05419 [physics.ins-det]].
9. A. J. Baltz, G. Baur, D. d'Enterria, L. Frankfurt, F. Gelis, V. Guzey, K. Hencken, Y. Kharlov, M. Klasen and S. R. Klein, *et al.* Phys. Rept. **458**, 1-171 (2008)
10. M. Alvioli, V. Guzey and M. Strikman, [arXiv:2402.19060 [hep-ph]].
11. M. G. Ryskin, Z. Phys. C **57**, 89-92 (1993)
12. V. Guzey, E. Kryshen, M. Strikman and M. Zhalov, Phys. Lett. B **726**, 290-295 (2013) [arXiv:1305.1724 [hep-ph]].
13. V. Guzey and M. Zhalov, JHEP **10**, 207 (2013) [arXiv:1307.4526 [hep-ph]].
14. L. Frankfurt, V. Guzey and M. Strikman, Phys. Rept. **512**, 255-393 (2012) [arXiv:1106.2091 [hep-ph]].
15. [STAR], [arXiv:2311.13632 [nucl-ex]].
16. K. J. Eskola, C. A. Flett, V. Guzey, T. Löytäinen and H. Paukkunen, Phys. Rev. C **106**, no.3, 035202 (2022) [arXiv:2203.11613 [hep-ph]].
17. K. J. Eskola, C. A. Flett, V. Guzey, T. Löytäinen and H. Paukkunen, Phys. Rev. C **107**, no.4, 044912 (2023) [arXiv:2210.16048 [hep-ph]].
18. S. P. Jones, A. D. Martin, M. G. Ryskin and T. Teubner, J. Phys. G **43**, no.3, 035002 (2016) [arXiv:1507.06942 [hep-ph]].
19. S. P. Jones, A. D. Martin, M. G. Ryskin and T. Teubner, Eur. Phys. J. C **76**, no.11, 633 (2016) [arXiv:1610.02272 [hep-ph]].
20. M. Strikman, R. Vogt and S. N. White, Phys. Rev. Lett. **96**, 082001 (2006) [arXiv:hep-ph/0508296 [hep-ph]].
21. V. Guzey and M. Klasen, Phys. Rev. C **99**, no.6, 065202 (2019) [arXiv:1811.10236 [hep-ph]].
22. V. Guzey and M. Klasen, JHEP **04**, 158 (2016) [arXiv:1603.06055 [hep-ph]].
23. I. Helenius, SciPost Phys. Proc. **8**, 145 (2022) [arXiv:2107.07389 [hep-ph]].
24. [ATLAS], "Photo-nuclear dijet production in ultra-peripheral Pb+Pb collisions," ATLAS-CONF-2017-011.
25. [ATLAS], "Photo-nuclear jet production in ultra-peripheral Pb+Pb collisions at $\sqrt{s}_{\mathrm{NN}} = 5.02$ TeV with the ATLAS detector," ATLAS-CONF-2022-021.
26. B. Pire, L. Szymanowski and J. Wagner, Phys. Rev. D **79**, 014010 (2009) [arXiv:0811.0321 [hep-ph]].
27. W. Schafer, G. Slipek and A. Szczurek, Phys. Lett. B **688**, 185-191 (2010) [arXiv:1003.0610 [hep-ph]].
28. G. M. Peccini, L. S. Moriggi and M. V. T. Machado, Phys. Rev. D **103**, no.5, 054009 (2021) [arXiv:2101.08338 [hep-ph]].
29. S. R. Klein, J. Nystrand and R. Vogt, Phys. Rev. C **66**, 044906 (2002) [arXiv:hep-ph/0206220 [hep-ph]].
30. V. P. Goncalves, M. V. T. Machado and A. R. Meneses, Phys. Rev. D **80**, 034021 (2009) [arXiv:0905.2067 [hep-ph]].
31. V. P. Gonçalves, G. Sampaio dos Santos and C. R. Sena, Nucl. Phys. A **976**, 33-45 (2018) [arXiv:1711.04497 [hep-ph]].
32. V. A. Abramovsky, V. N. Gribov and O. V. Kancheli, Yad. Fiz. **18**, 595-616 (1973), Sov. J. Nucl. Phys. 18, 308-317 (1974).
33. D. Treleani, Int. J. Mod. Phys. A **11**, 613-654 (1996)
34. J. Jalilian-Marian and Y. V. Kovchegov, Phys. Rev. D **70**, 114017 (2004) [erratum: Phys. Rev. D **71**, 079901 (2005)] [arXiv:hep-ph/0405266 [hep-ph]].
35. F. Gelis and R. Venugopalan, Nucl. Phys. A **776**, 135-171 (2006) [arXiv:hep-ph/0601209 [hep-ph]].
36. A. Kovner and M. Lublinsky, JHEP **11**, 083 (2006) [arXiv:hep-ph/0609227 [hep-ph]].
37. N. N. Nikolaev and W. Schafer, Phys. Rev. D **74**, 074021 (2006) [arXiv:hep-ph/0607307 [hep-ph]].

38. J. C. Collins, Phys. Rev. D **57**, 3051-3056 (1998) [erratum: Phys. Rev. D **61**, 019902 (2000)] [arXiv:hep-ph/9709499 [hep-ph]].
39. L. Frankfurt and M. Strikman, Eur. Phys. J. A **5**, 293-306 (1999) [arXiv:hep-ph/9812322 [hep-ph]].
40. L. Bertocchi and D. Treleani, J. Phys. G **3**, 147 (1977)
41. M. Alvioli, L. Frankfurt, V. Guzey, M. Strikman and M. Zhalov, Phys. Lett. B **767**, 450-457 (2017) [arXiv:1605.06606 [hep-ph]].
42. A. Bialas, M. Bleszynski and W. Czyz, Nucl. Phys. B **111**, 461-476 (1976)
43. L. Frankfurt, V. Guzey, A. Stasto and M. Strikman, Rept. Prog. Phys. **85**, no.12, 126301 (2022) [arXiv:2203.12289 [hep-ph]].
44. M. Alvioli, H. J. Drescher and M. Strikman, Phys. Lett. B **680**, 225-230 (2009) [arXiv:0905.2670 [nucl-th]].
45. M. Alvioli, C. Ciofi degli Atti, I. Marchino, V. Palli and H. Morita, Phys. Rev. C **78**, 031601 (2008) [arXiv:0807.0873 [nucl-th]].
46. M. Alvioli, C. Ciofi degli Atti and H. Morita, Phys. Rev. Lett. **100**, 162503 (2008)
47. S. Acharya *et al.* [ALICE], JHEP **08**, 086 (2022) [arXiv:2107.10757 [nucl-ex]].
48. M. R. Adams *et al.* [E665], Phys. Rev. Lett. **74**, 5198-5201 (1995) [erratum: Phys. Rev. Lett. **80**, 2020-2021 (1998)]
49. M. Strikman, M. G. Tverskoii and M. B. Zhalov, Phys. Lett. B **459**, 37-42 (1999) [arXiv:nucl-th/9806099 [nucl-th]].
50. A. B. Larionov and M. Strikman, Phys. Rev. C **101**, no.1, 014617 (2020) [arXiv:1812.08231 [hep-ph]].
51. W. Chang, E. C. Aschenauer, M. D. Baker, A. Jentsch, J. H. Lee, Z. Tu, Z. Yin and L. Zheng, Phys. Rev. D **106**, no.1, 012007 (2022) [arXiv:2204.11998 [physics.comp-ph]].
52. M. Alvioli, L. Frankfurt, V. Guzey and M. Strikman, Phys. Rev. C **90**, 034914 (2014) [arXiv:1402.2868 [hep-ph]].
53. L. Frankfurt, V. Guzey, M. McDermott and M. Strikman, Phys. Rev. Lett. **87**, 192301 (2001) [arXiv:hep-ph/0104154 [hep-ph]].
54. M. Alvioli, M. Azarkin, B. Blok and M. Strikman, Eur. Phys. J. C **79**, no.6, 482 (2019) [arXiv:1901.11266 [hep-ph]].

Inclusive and Diffractive Dijet Photoproduction in Ultraperipheral Pb-Pb Collisions at the LHC

V. GUZEY
University of Jyvaskyla, Department of Physics, P.O. Box 35, FI-40014 University of Jyvaskyla, Finland and Helsinki Institute of Physics, P.O. Box 64, FI-00014 University of Helsinki, Finland

In this contribution, we summarize NLO pQCD predictions for inclusive and diffractive dijet photoproduction in Pb-Pb UPCs at the LHC. We demonstrate that the theory describes well the preliminary ATLAS data on the inclusive cross section, which probes nuclear parton distributions (PDFs) down to $x_A \approx 0.005$ and which can reduce current uncertainties of the small-x nuclear gluon distribution by approximately a factor of 2. Employing predictions of the leading twist approach to nuclear shadowing for nuclear diffractive PDFs, we calculate the cross section of diffractive dijet photoproduction and show that its x_γ dependence is sensitive to the effect of nuclear shadowing and the mechanism of QCD factorization breaking in hard diffraction. We also find that due to large leading twist nuclear shadowing and restricted kinematics, the diffractive contribution to the inclusive cross section of dijet photoproduction does not exceed $5-10\%$, which helps with an ambiguous interpretation of the ATLAS data.

DOI: https://doi.org/10.17161/w85e0h13
Keywords: Heavy-ion scattering, ultraperipheral collisions, dijet photoproduction, perturbative QCD, nuclear parton distributions, diffraction, nuclear shadowing

1 Introduction

Jets are collimated sprays of hadrons (π, K, ...) produced in high-energy e^+e^-, lepton-hadron, and hadron-hadron collisions. Jets have been instrumental in establishing quantum chromodynamics (QCD) as the correct theory of the strong interactions and, in particular, its concepts of asymptotic freedom and confinement [1,2,3]. A classic example of it is 3-jet events observed in e^+e^- annihilation, which has proved the existence of gluons. In perturbative QCD (pQCD), measurements of jets are commonly used to test validity of the QCD collinear factorization theorem, determine the strong coupling constant α_s [4,5], and provide complementary information on parton distribution functions (PDFs) [6,7].

In particular, since in electron-proton (ep) deep-inelastic scattering (DIS) and hard hadron scattering, jet cross sections are sensitive to quark and gluon distributions of the target at the same order of the perturbation series in powers of α_s, jet data provide additional constraints on the gluon distribution, which complement those from the total DIS cross section. Global QCD fits of proton PDFs take advantage of it by including data on jet production in ep DIS at HERA, proton-antiproton scattering at Tevatron and proton-proton (pp) scattering at the Large Hadron Collider (LHC) [8,9,10]. Extending this to nuclear targets, essential constraints on the nuclear gluon distribution have been obtained by employing data on dijet production in proton-nucleus scattering at the LHC [11]. Similarly, HERA data on dijet photoproduction on the proton enables one to determine the gluon distribution in the real photon more reliably compared to the case, when one only uses the data on the $F_2^\gamma(x,Q^2)$ structure function measured in e^+e^- annihilation [12].

In addition, it has been discussed in the literature that measurements of forward dijet production may aid in searching for small-x Balitsky-Fadin-Kuraev-Lipatov (BFKL) and saturation physics at the LHC [13,14] and the planned Electron-Ion Collider (EIC) in USA [15]. Finally, jets present a Standard Model background for many new physics processes.

Focusing on production of jets by real photons, we notice that while all experimental information on jet photoproduction comes from ep scattering at HERA [6,7,16], there is preliminary ATLAS data on dijet

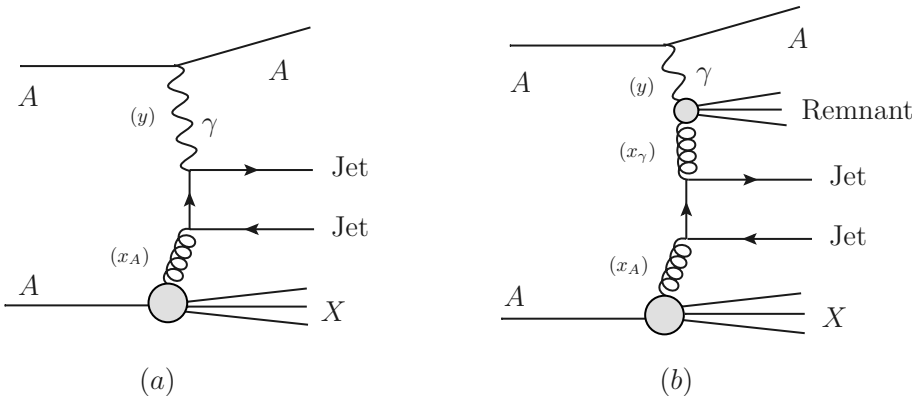

Figure 1 – Typical LO pQCD diagrams for inclusive dijet photoproduction in AA UPCs: (a) direct and (b) resolved photon contributions. The corresponding momentum fractions are given in parenthesis.

photoproduction in Pb-Pb ultraperipheral collisions (UPCs) at the LHC [17,18]. In UPCs, colliding ions pass each other at large impact parameters and interact via emission of quasi-real photons, which effectively makes the LHC a high-energy and high-intensity photon-nucleus collider [19]. So far the emphasis of UPC measurements has been coherent and incoherent production of light and heavy vector mesons. Notably, it has been argued that exclusive photoproduction of charmonium J/ψ mesons in pp UPCs allows one to probe and constrain the gluon density in the proton down to $x_p \approx 3 \times 10^{-6}$ at the resolution scale of the order of the charm quark mass [20]. In the nucleus case, the data on coherent J/ψ photoproduction in Pb-Pb UPCs have discovered a large nuclear suppression, which can be interpreted in terms of strong gluon nuclear shadowing [21,22] at $x_A \approx 10^{-3}$ and all the way down to $x_A \approx 10^{-5}$. These findings have nicely confirmed predictions of the leading twist approach (LTA) to nuclear shadowing [23].

Measurements of inclusive and diffractive dijet photoproduction in Pb-Pb UPCs at the LHC allow one to expand the scope of the UPC physics program. Compared to J/ψ production, the theoretical description of the dijet cross section in perturbative QCD is cleaner since it does not involve the charmonium wave function and complications associated with the kinematics of exclusive reactions and generalized parton distributions. In the case of inclusive dijet production, $A + A \to A + 2\text{jets} + X$, where X denotes the hadronic final state resulting from nucleus dissociation, the dijet cross section probes nuclear and real photon PDFs at large energy scales, which are determined by the jet transverse momentum and, thus, explores the kinematic region complementary to the one in vector meson photoproduction. Requiring that the target nucleus is intact, one can study diffractive dijet photoproduction, $A + A \to A + 2\text{jets} + X' + A$, which gives an access to novel nuclear diffractive PDFs and which may also shed new light on the mechanism of QCD factorization breaking in hard diffraction.

Pioneering leading-order (LO) pQCD calculations of photoproduction of heavy flavor (bottom) jets [24] and heavy quarks [25] (see also [26,27]) in UPCs have demonstrated feasibility and large rates of such measurements in the LHC kinematics..

The rest of this contribution is organized as follows. Section 2 summarizes NLO pQCD predictions for the cross section of inclusive dijet photoproduction in Pb-Pb UPCs at 5.02 TeV, their comparison to the ATLAS data and the magnitude of nuclear modifications as well as the potential of this process to provide additional constraints on nuclear PDFs at small x. In Sec. 3, we present NLO pQCD predictions for diffractive dijet photoproduction in Pb-Pb UPCs at the LHC and discuss sensitivity of the x_γ dependence to the mechanism of the QCD factorization breaking in hard diffraction. We also quantify the diffractive contribution to the cross section of inclusive dijet photoproduction in UPCs. We draw conclusions in Sec. 4.

2 Inclusive dijet photoproduction in Pb-Pb UPCs at the LHC

In the framework of collinear factorization of pQCD, the formalism for calculation of the cross section of inclusive dijet photoproduction is well-established, and results of calculations performed at next-to-leading order (NLO) accuracy successfully describe the available HERA data [28,29,30,31]. Applying it to UPCs, one can write the cross section of inclusive dijet photoproduction in Pb-Pb UPCs, $A + A \to A + 2\text{jets} + X$,

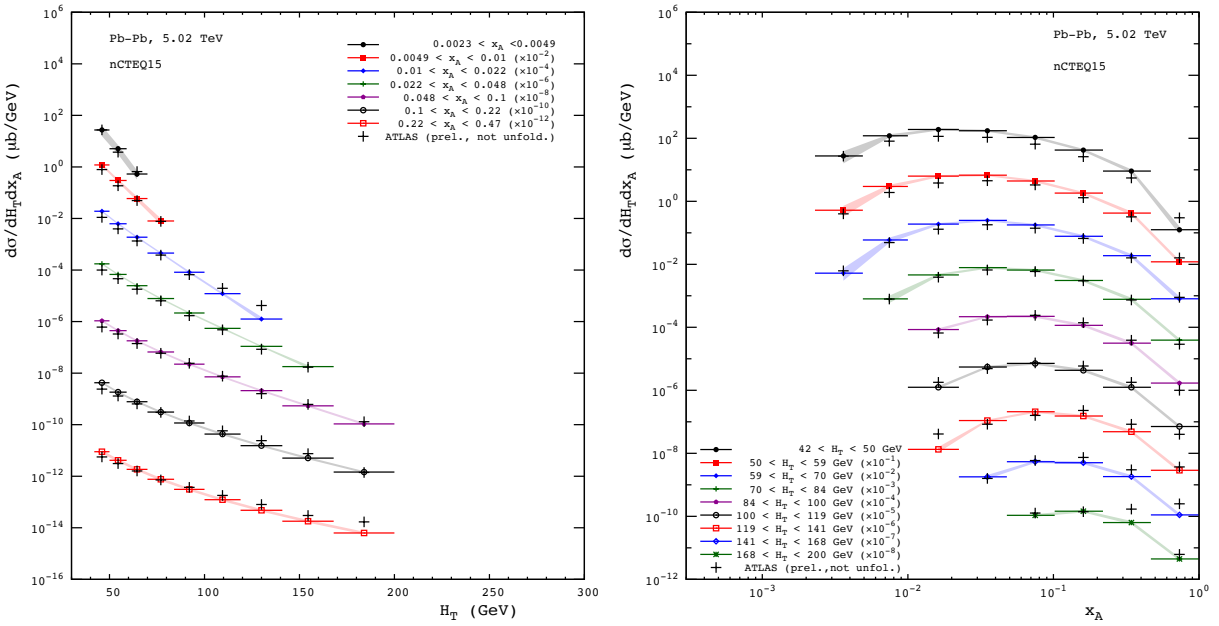

Figure 2 – The cross section of inclusive dijet photoproduction in Pb-Pb UPCs at $\sqrt{s_{NN}} = 5.02$ TeV as a function of $H_T = p_{T,1} + p_{T,2}$ in different bins of x_A (left) and as a function of x_A in bins of H_T (right). The NLO pQCD predictions with the nCTEQ15 nuclear PDFs are compared with the ATLAS preliminary data, see text for details.

as the following convolution [32],

$$d\sigma(AA \to A + 2\text{jets} + X) = \sum_{a,b} \int dy \int dx_\gamma \int dx_A f_{\gamma/A}(y) f_{a/\gamma}(x_\gamma, \mu) f_{b/A}(x_A, \mu) d\hat{\sigma}_{ab\to\text{jets}} \,, \qquad (1)$$

where $f_{\gamma/A}(y)$ is the flux of equivalent photons, $f_{a/\gamma}(x_\gamma, \mu)$ are photon PDFs, $f_{b/A}(x_A, \mu)$ are nuclear PDFs, and $d\hat{\sigma}_{ab\to\text{jets}}$ is the elementary cross section to produce jets in hard scattering of partons a and b. The longitudinal momentum fractions are y for the photon, x_γ for parton a in the photon, and x_A for parton b in a target nucleus. The PDFs are evaluated at the resolution scale μ, which is usually identified with the jet transverse momentum p_T.

Figure 1 illustrates Eq. (1) by showing typical LO pQCD diagrams for the direct contribution (graph a), where the photon as a whole takes part in the hard reaction, and the resolved contribution (graph b), where a parton of a hadronic fluctuation of the photon (photon PDFs) participates in the hard scattering reaction. The corresponding momentum fractions are given in parenthesis. Separation of the direct and resolved contributions is unambiguous only at LO, where $f_{a/\gamma}(x_\gamma, \mu) = \delta(1 - x_\gamma)$ for the direct term. At NLO, due to renormalization of standard collinear divergences of pQCD, the definition of the direct and resolved terms begins to depend on a choice of the factorization scheme and scale. Nevertheless, the notion of the direct and resolved contributions remains useful.

The photon flux $N_{\gamma/A}(y)$ is usually calculated using the Weizsäcker-Williams equivalent photon approximation combined with the probability for the nuclei not to interact strongly at small impact parameters. However, for purposes of the present analysis, the exact expression can be approximated by the photon flux produced by a relativistic point-like charge Z passing a target at the minimum impact parameter $b_{\min}$,

$$N_{\gamma/A}(y) = \frac{2\alpha_{\text{e.m.}} Z^2}{\pi} \frac{1}{y} \left[\zeta K_0(\zeta) K_1(\zeta) - \frac{\zeta^2}{2} (K_0^2(\zeta) - K_1^2(\zeta)) \right] , \qquad (2)$$

where $\alpha_{\text{e.m.}}$ is the fine-structure constant, $K_{0,1}$ are modified Bessel functions of the second kind, and $\zeta = y m_p b_{\min}$ with m_p the proton mass and $b_{\min} = 14.2$ fm for Pb-Pb UPCs [33].

The momentum fractions x_γ and x_A in Eq. (1) can be estimated using the measured jet rapidities and transverse momenta. In particular, one can use the following relations

$$x_\gamma = \frac{m_{\text{jets}}}{\sqrt{s_{NN}}} e^{y_{\text{jets}}} \,, \qquad x_A = \frac{m_{\text{jets}}}{\sqrt{s_{NN}}} e^{-y_{\text{jets}}} \,, \qquad (3)$$

where m_{jets} is the invariant mass of the jet system and y_{jets} its rapidity [17].

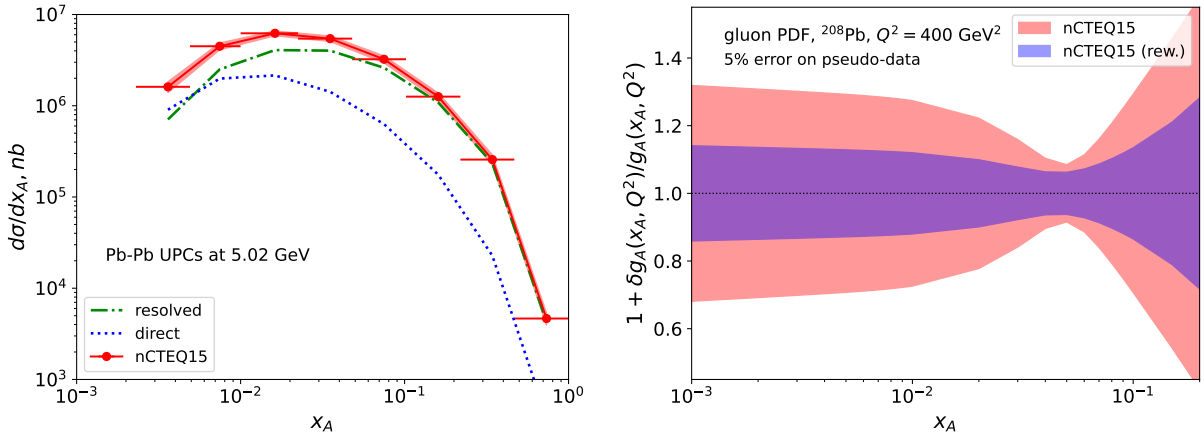

Figure 3 – (Left) NLO pQCD predictions for the cross section of dijet photoproduction in Pb-Pb UPCs at 5.02 TeV as a function of x_A using the nCTEQ15 nuclear PDFs and ATLAS experimental cuts. The curves show separately the direct (dashed) and resolved (dot-dashed) photon contributions as well as their sum (solid). (Right) Relative uncertainties of the nCTEQ15 gluon distribution in ^{208}Pb as a function of x_A at $Q^2 = 400$ GeV^2 before (outer pink shaded band) and after (inner blue band) the reweighting using pseudo-data on dijet photoproduction in Pb-Pb UPCs at 5.02 TeV.

Note that Eq. (1) gives the cross section at the level of massless partons and for a comparison with data needs to be supplemented with hadronization corrections. They are usually estimated using Monte Carlo generators, which involve LO matrix elements and include the effects of parton showers [34,35].

Figure 2 presents a comparison of the NLO pQCD predictions [32] for the cross section of inclusive dijet photoproduction in Pb-Pb UPCs at $\sqrt{s_{NN}} = 5.02$ TeV with the preliminary ATLAS data [17]. The calculation used the nCTEQ15 nuclear PDFs [36], whose uncertainty propagation is shown by the shaded bands, GRVHO photon PDFs [37], and the ATLAS experimental cuts, importantly, $p_{T,1} > 20$ GeV for the leading jet and $p_{T,2} > 15$ GeV for other jets. The left panel shows the distribution in $H_T = p_{T,1} + p_{T,2}$ in different bins of x_A; the right panel shows the distribution in x_A in bins of H_T. One can see from the figure that the NLO pQCD results correctly reproduce the shape and normalization of the data, which have not been corrected for detector response. Note that in the considered kinematics, the coverage in x_A extends down to $x_A \approx 5 \times 10^{-3}$ at $\mu^2 = (H_T/2)^2$, which provides a certain sensitivity to nuclear PDFs at small x and large μ, see the discussion below.

It is instructive to examine an interplay of the direct and resolved photon contributions to the dijet cross section. The left panel of Fig. 3 shows separately the direct and resolved terms as well as their sum as a function of x_A. One can see from the figure that the resolved contribution dominates for $x_A > 0.01$, while the two contributions are compatible in size for $x_A < 0.01$. This trend is generally expected because the direct photon contribution increases in the $x_\gamma \to 1$ limit (the values of x_γ and x_A are anti-correlated, see Eq. (3)) and agrees with the expectations based on PYTHIA 8 Monte Carlo framework [34,35].

The cross section of dijet photoproduction in Pb-Pb UPCs in Fig. 3 is sensitive to nuclear modifications of nuclear PDFs: its $\approx 10\%$ suppression for $x_A < 0.01$ compared to the impulse approximation estimate is caused by nuclear shadowing and $\approx 20\%$ enhancement around $x_A < 0.1$ by antishadowing of the gluon distribution; it is followed by a $5 - 10\%$ suppression for $x_A > 0.05$ due to the EMC effect, which is built in most of nuclear PDFs.

One can turn this around and quantitatively investigate the potential of this process to further constrain nuclear PDFs using the technique of Bayesian reweighting [38]. In short, using $N_{\rm rep} = 10,000$ random replicas of nCTEQ15 error PDFs, $f^k_{i/A}(x, Q^2)$ with i the parton flavor, one can calculate the dijet cross section for each replica $k = 1, 2, \ldots, N_{\rm rep}$ and then determine the statistical weights ω_k for replicas to reproduce observables. The latter was taken to be the dijet cross section calculated using the central nCTEQ15 PDFs, which was assigned a $5-15\%$ uncertainty playing the role of experimental errors. After this procedure, the new reweighted central values $\langle f_{i/A}(x, Q^2)\rangle_{\rm new}$ and uncertainties $\delta\langle f_{i/A}(x, Q^2)\rangle_{\rm new}$ of

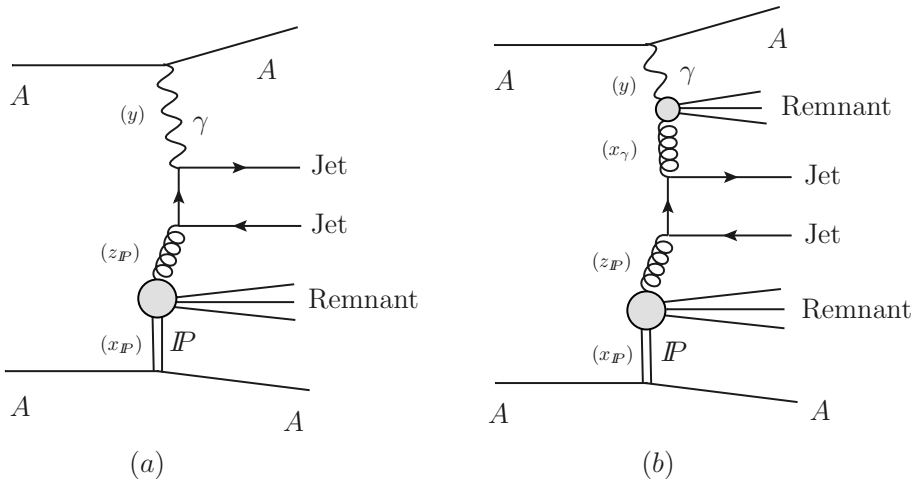

Figure 4 – Typical LO pQCD diagrams for diffractive dijet photoproduction in AA UPCs: (a) direct and (b) resolved photon contributions. The diffractive exchange is denoted by the Pomeron contribution. The corresponding momentum fractions are given in parenthesis.

nuclear PDFs become

$$\begin{aligned} \langle f_{i/A}(x,Q^2)\rangle_{\rm new} &= \frac{1}{N_{\rm rep}}\sum_{k=1}^{N_{\rm rep}} \omega_k f^k_{i/A}(x,Q^2)\,, \\ \delta\langle f_{i/A}(x,Q^2)\rangle_{\rm new} &= \sqrt{\frac{1}{N_{\rm rep}}\sum_{k=1}^{N_{\rm rep}} \omega_k \left(f^k_{i/A}(x,Q^2) - \langle f_{i/A}(x,Q^2)\rangle_{\rm new}\right)^2}\,. \end{aligned} \tag{4}$$

The right panel of Fig. 3 illustrates the result of the Bayesian reweighting of the nCTEQ15 gluon distribution in ^{208}Pb at $Q^2 = 400$ GeV^2 using the procedure outlined above. It presents the relative uncertainty of the gluon nPDF, $1 + \delta g_A(x_A, Q^2)/g_A(x_A, Q^2)$, as a function of x_A before (outer pink shaded band) and after (inner blue band) the reweighting. One can see from the figure that assigning a 5% uncertainty to the pseudo-data leads to a reduction of uncertainties in the gluon distribution for $x_A < 0.005$ by approximately a factor of 2.

3 Diffractive dijet photoproduction in Pb-Pb UPCs at the LHC

The considerations of the previous section can be extended to diffractive jet photoproduction in heavy-ion UPCs, where one imposes the additional condition that the target nucleus remains intact and recoils elastically. Figure 4 shows typical LO pQCD diagrams for the direct (graph a) and resolved (graph b) photon contributions, where the vertical double lines denote the diffractive exchange (Pomeron flux) labeled "$I\!P$".

Unlike the inclusive case, UPC cross sections corresponding to coherent underlying photon-nucleus scattering receive contributions from both left-moving and right-moving colliding ions, which introduces a well-known two-fold ambiguity between the photon energy and rapidity of the final dijet system. Generalizing Eq. (1), the contribution of the right-moving photon source to the cross section of diffractive dijet photoproduction in Pb-Pb UPCs, $A + A \to A + 2\text{jets} + X' + A$, where X' includes hadronic debris of the "Pomeron" and photon, can be written in the following form [39]

$$\begin{aligned} d\sigma(AA \to A + 2\text{jets} + X' + A)^{(+)} &= \sum_{a,b}\int dt \int dx_{I\!P} \int dz_{I\!P} \int dy \int dx_\gamma \\ &\times\ f_{\gamma/A}(y) f_{a/\gamma}(x_\gamma,\mu) f^{D(4)}_{b/A}(x_{I\!P}, z_{I\!P}, t, \mu) d\hat{\sigma}_{ab\to\text{jets}}\,. \end{aligned} \tag{5}$$

The contribution of the left-moving photon source is obtained from Eq. (5) by inverting signs of the jet rapidities. In Eq. (5), $f^{D(4)}_{b/A}(x_{I\!P}, z_{I\!P}, t, \mu)$ denote the nuclear diffractive PDFs, which represent the conditional probability to find parton b with the momentum fraction $z_{I\!P}$ with respect to the diffractive exchange (Pomeron) carrying the momentum fraction $x_{I\!P}$, provided that the nucleus remains intact and

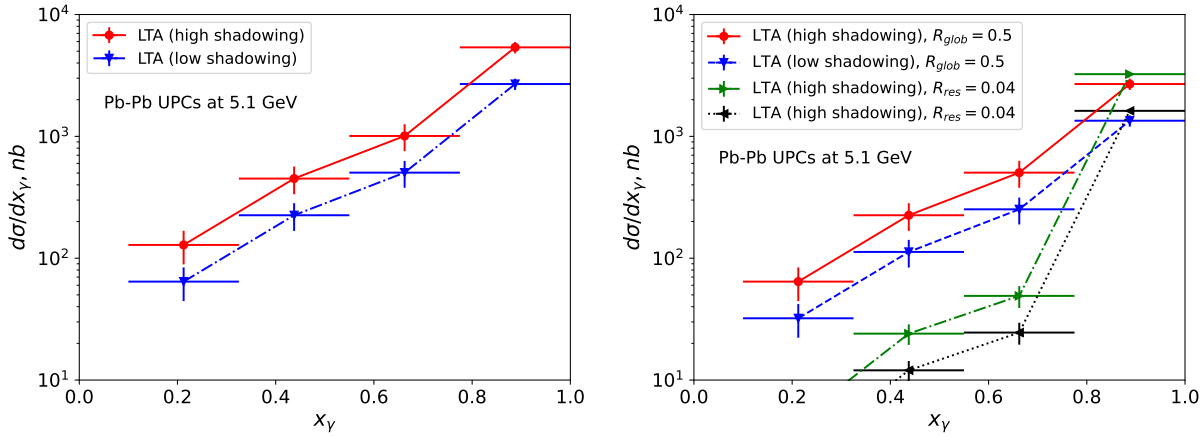

Figure 5 – NLO pQCD predictions for the cross section of diffractive dijet photoproduction in Pb-Pb UPCs at 5.1 TeV as a function of x_γ. The results are obtained using LTA predictions for nuclear diffractive PDFs ("high shadowing" and "low shadowing" versions) and assuming either no QCD factorization breaking in hard diffraction (left) or two scenarios of it realized through the suppression factors $R_{\rm glob}$ and $R_{\rm res}$ (right), see text for details.

recoils elastically with the momentum transfer t. The momentum fractions involved in Eq. (5) are shown in parenthesis in Fig. 4.

Similarly to usual nuclear PDFs, nuclear diffractive PDFs are subject to nuclear modifications, notably, due to nuclear shadowing. The leading twist approach to nuclear shadowing [23] makes definite predictions for $f_{b/A}^{D(4)}$, which are characterized by their strong suppression at small x. It can be quantified by introducing the suppression factor R_b with respect to $f_{b/A}^{D(4)}$ evaluated in the impulse approximation,

$$f_{b/A}^{D(4)}(x_{I\!P}, z_{I\!P}, t, \mu) = R_b(x_{I\!P}, z_{I\!P}, \mu) A^2 F_A^2(t) f_{b/p}^{D(4)}(x_{I\!P}, z_{I\!P}, t=0, \mu)\,, \tag{6}$$

where $F_A(t)$ is the nucleus form factor and $f_{b/p}^{D(4)}$ is the diffractive PDFs of the proton. An examination of R_b shows that it rather weakly depends on flavor b, the light-cone momentum fractions $x_{I\!P}$ and $z_{I\!P}$ (provided that $x_{I\!P}$ is sufficiently small), and the resolution scale μ. Hence, for the purpose of estimating yields of this process, one can approximate R_b by a single number [39,40]

$$R_b(x_{I\!P}, z_{I\!P}, \mu) \approx 0.08 - 0.16\,, \tag{7}$$

where the upper and lower values correspond to the "high shadowing" and "low shadowing" scenarios, respectively. This spread in the values for R_b reflects a significant theoretical uncertainty of LTA predictions for nuclear diffractive PDFs, for a detailed discussion, see [40].

The left panel of Fig. 5 presents NLO pQCD predictions for the cross section of diffractive dijet photoproduction in Pb-Pb UPCs at 5.1 TeV as a function of x_γ using the LTA results for nuclear diffractive PDFs, see Eqs. (6) and (7), $p_{T,1} > 20$ GeV for the leading jet and $p_{T,2} > 18$ GeV for subleading jets and other otherwise generic cuts specified in [39]. The upper and lower curves corresponds to the "high shadowing" and "low shadowing" LTA predictions, respectively. The horizontal lines show the width of bins in x_γ, and the vertical bars quantify the effect of the variation of the hard scale of the process in the $p_{T,1}/2 < \mu < 2p_{T,1}$ interval. One can see from the figure that the uncertainty due to the scale variation is smaller than the uncertainty in the value of R_b. Overall, the figure shows that the predicted yields are significant demonstrating feasibility of such measurements.

Analyses of diffractive dijet photoproduction in ep scattering at HERA have shown that the QCD factorization theorem for hard diffraction [41] is violated and NLO pQCD calculations overestimate the cross sections measured by the ZEUS and H1 collaborations at HERA by a approximately a factor of 2, see details in [42]. The pattern of this factorization breaking is yet unknown since a good description of the data can be achieved by introducing a global suppression factor $R_{\rm glob} = 0.5$ or the suppression factor $R_{\rm res} = 0.34$ for the resolved photon contribution only, or the flavor-dependent and x_γ-dependent suppression factor interpolating between $R_{\rm glob}$ and $R_{\rm res}$, see [43].

As a consequence, one of the most sensitive observables to various scenarios of factorization breaking is the distribution in the momentum fraction x_γ. Thus, it has been argued in [39] that measurements of

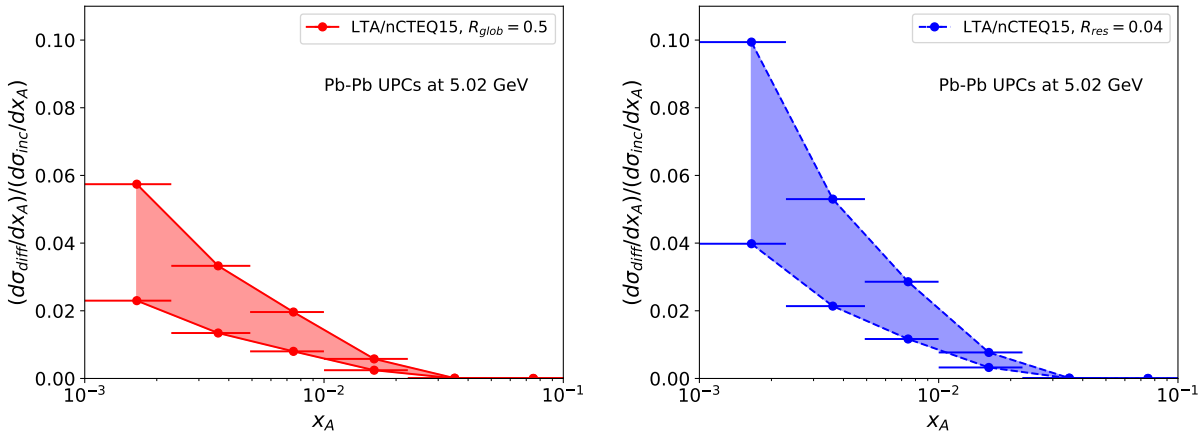

Figure 6 – NLO pQCD predictions for the ratio of the cross sections of diffractive to inclusive dijet photoproduction in Pb-Pb UPCs at 5.02 TeV as a function of x_A. The calculation uses LTA predictions for nuclear diffractive PDFs (the shaded bands represent the theoretical uncertainty), the nCTEQ15 nuclear PDFs, and two scenarios of the QCD factorization breaking in hard diffraction realized through the global suppression factor $R_{\rm glob} = 0.5$ (left panel) and the direct photon suppression factor $R_{\rm res} = 0.04$ (right panel).

the x_γ dependence of the cross section of diffractive dijet photoproduction in UPCs at the LHC may help to shed new light on this phenomenon.

The right panel of Fig. 5 illustrates the effect of the QCD factorization breaking for hard diffraction on NLO pQCD predictions for the cross section of diffractive dijet photoproduction in Pb-Pb UPCs at 5.1 TeV as a function of x_γ. These predictions are obtained by rescaling the result of Eq. (5) either by the global suppression factor of $R_{\rm glob} = 0.5$ or by suppressing only the resolved photon term by the factor of $R_{\rm res} = 0.04$. The latter value is estimated using the Glauber model for ρ meson-nucleus scattering, see details in [43]. One can see from the figure that the two prescriptions for factorization breaking result in rather distinct shapes of the x_γ distribution, which supports its potential to discriminate between these two scenarios.

The ATLAS measurement of inclusive dijet photoproduction in Pb-Pb UPCs was performed in the so-called "0nXn" event topology, which required a particular number of forward neutrons in zero degree calorimeters (ZDCs), namely, no neutrons in one direction and one or more neutrons in the opposite direction. This condition has totally eliminated the contribution of coherent nuclear diffraction, which is part of nuclear PDFs. It raises the practical question of the magnitude of the diffractive contribution to inclusive dijet photoproduction in UPCs.

The analysis [44] has shown that the diffractive contribution to inclusive dijet photoproduction in Pb-Pb UPCs in the ATLAS kinematics does not exceed $5-10\%$ at small x_A. It is illustrated in Fig. 6 showing the ratio of the cross sections of diffractive to inclusive dijet photoproduction in Pb-Pb UPCs at 5.02 TeV, $(d\sigma_{\rm diff}/dx_A)/(d\sigma_{\rm inc}/dx_A)$, as a a function of x_A. The calculation uses the LTA predictions for nuclear diffractive PDFs entering the diffractive cross section (the shaded bands quantity the theoretical uncertainty, see Fig. 5) and the nCTEQ15 nuclear PDFs for the inclusive cross section. The effect of the QCD factorization breaking for hard diffraction (see the discussion above) is included through either the global suppression factor $R_{\rm glob} = 0.5$ (left panel) or the direct photon suppression factor $R_{\rm res} = 0.04$ (right panel). The two scenarios of the factorization breaking lead to different magnitudes and shapes of the dependence of $(d\sigma_{\rm diff}/dx_A)/(d\sigma_{\rm inc}/dx_A)$ on x_A.

The small value of the $(d\sigma_{\rm diff}/dx_A)/(d\sigma_{\rm inc}/dx_A)$ ratio is predominantly an effect of the restricted kinematics with large $p_{T,1} > 20$ GeV and not-sufficiently small $x_A > 0.001$ and large relative suppression of nuclear diffractive PDFs by leading twist nuclear shadowing [40]. Thus, the diffractive contribution and the ensuing ambiguity in the determination of the photon-emitting nucleus (ambiguity in the invariant photon-nucleon energy $W_{\gamma p}$) can be safely neglected in the kinematics of the ATLAS measurement.

To enhance the diffractive signal, one needs to expand the kinematic coverage by primarily lowering p_T of jets. For instance, using $p_{T,1} > 10$ GeV and $p_{T,2} > 5{-}7$ GeV, one can reach $(d\sigma_{\rm diff}/dx_A)/(d\sigma_{\rm inc}/dx_A)) = 10-20\%$ at $x_A \approx 5\times10^{-4}$. In the case of pp UPCs at 13 TeV, where the collision energy is larger and there is no nuclear suppression of diffractive PDFs by nuclear shadowing, the ratio of the diffractive and inclusive cross sections of dijet production is sizable, $(d\sigma_{\rm diff}/dx_p)/(d\sigma_{\rm inc}/dx_p) \approx 10{-}15\%$ at $x_p \approx 5{\times}10^{-4}$.

4 Summary and outlook

Photoproduction of jets is a standard tool of perturbative QCD, which provides important information on parton distributions of the proton, the real photon, and nuclei. Within the framework of collinear factorization of pQCD, NLO calculations describe well the available data on dijet photoproduction in ep scattering at HERA. Application of this framework to photon-nucleus scattering in heavy-ion UPCs at the LHC can be used to obtain complementary constraints on nuclear PDFs, measure for the first time nuclear diffractive PDFs and shed new light on the mechanism of QCD factorization breaking in hard diffraction.

Using NLO pQCD, we calculate the cross section of inclusive dijet photoproduction in Pb-Pb UPCs at 5.02 TeV at the LHC and demonstrate that it describes well the preliminary ATLAS data. We show that this cross section probes nuclear PDFs down to $x_A \approx 0.005$ and, when used in the form of pseudo-data in a Bayesian analysis, can reduce the current small-x uncertainties of the state-of-art nuclear PDFs by approximately a factor of 2.

Considering coherent nuclear scattering and using predictions of the leading twist approach (LTA) to nuclear shadowing for nuclear diffractive PDFs, we make NLO pQCD predictions for the cross section of diffractive dijet photoproduction in Pb-Pb UPCs at 5.1 TeV. We show that its distribution in the photon momentum fraction x_γ is sensitive to both the effect of nuclear shadowing in nuclear diffractive PDFs and the mechanism of QCD factorization breaking in hard diffraction. In particular, it allows one to discriminate between the two scenarios of factorization breaking, where its effect is introducing either through the global suppression factor $R_{\rm glob} = 0.5$ or the resolved photon suppression factor $R_{\rm res} = 0.04$. We also show that due to large leading twist nuclear shadowing and restricted ATLAS kinematics (large jet transverse momentum p_T and not sufficiently small x_A), the diffractive contribution to the inclusive cross section of dijet photoproduction does not exceed $5 - 10\%$. It means that one can expect only small corrections of the ATLAS (and other similar) data for the excluded diffractive contribution, which simplifies their interpretation in terms of usual nuclear PDFs.

Both inclusive and diffractive dijet photoproduction in Pb-Pb UPCs at the LHC can be viewed as precursors of analogous measurement in photon-nucleus scattering at the planned Electron-Ion Collider (EIC) [45,46].

Acknowledgments

The research of V.G. was funded by the Academy of Finland project 330448, the Center of Excellence in Quark Matter of the Academy of Finland (projects 346325 and 346326), and the European Research Council project ERC-2018-ADG-835105 YoctoLHC. The research of M.S. was supported by the US Department of Energy Office of Science, Office of Nuclear Physics under Award No. DE- FG02-93ER40771.

References

1. G. P. Salam, [arXiv:1011.5131 [hep-ph]].
2. S. Sapeta, Prog. Part. Nucl. Phys. **89**, 1-55 (2016) [arXiv:1511.09336 [hep-ph]].
3. E. Laenen, [arXiv:1708.00770 [hep-ph]].
4. H. Abramowicz *et al.* [ZEUS], Nucl. Phys. B **864**, 1-37 (2012) [arXiv:1205.6153 [hep-ex]].
5. V. Andreev *et al.* [H1], Eur. Phys. J. C **75**, no.2, 65 (2015) [arXiv:1406.4709 [hep-ex]].
6. M. Klein and R. Yoshida, Prog. Part. Nucl. Phys. **61**, 343-393 (2008) [arXiv:0805.3334 [hep-ex]].
7. P. Newman and M. Wing, Rev. Mod. Phys. **86**, no.3, 1037 (2014) [arXiv:1308.3368 [hep-ex]].
8. S. Chekanov *et al.* [ZEUS], Eur. Phys. J. C **42**, 1-16 (2005) [arXiv:hep-ph/0503274 [hep-ph]].
9. R. D. Ball *et al.* [NNPDF], Eur. Phys. J. C **82**, no.5, 428 (2022) [arXiv:2109.02653 [hep-ph]].
10. T. J. Hou, J. Gao, T. J. Hobbs, K. Xie, S. Dulat, M. Guzzi, J. Huston, P. Nadolsky, J. Pumplin and C. Schmidt, *et al.* Phys. Rev. D **103**, no.1, 014013 (2021) [arXiv:1912.10053 [hep-ph]].
11. K. J. Eskola, P. Paakkinen, H. Paukkunen and C. A. Salgado, Eur. Phys. J. C **82**, no.5, 413 (2022) [arXiv:2112.12462 [hep-ph]].
12. W. Slominski, H. Abramowicz and A. Levy, Eur. Phys. J. C **45**, 633-641 (2006) [arXiv:hep-ph/0504003 [hep-ph]].
13. M. Hentschinski, C. Royon, M. A. Peredo, C. Baldenegro, A. Bellora, R. Boussarie, F. G. Celiberto, S. Cerci, G. Chachamis and J. G. Contreras, *et al.* Acta Phys. Polon. B **54**, no.3, 3-A2 (2023) [arXiv:2203.08129 [hep-ph]].

14. E. Iancu, A. H. Mueller, D. N. Triantafyllopoulos and S. Y. Wei, Eur. Phys. J. C **83**, no.11, 1078 (2023) [arXiv:2304.12401 [hep-ph]].
15. R. Boussarie, H. Mäntysaari, F. Salazar and B. Schenke, JHEP **09**, 178 (2021) [arXiv:2106.11301 [hep-ph]].
16. J. M. Butterworth and M. Wing, Rept. Prog. Phys. **68**, 2773-2828 (2005) [arXiv:hep-ex/0509018 [hep-ex]].
17. [ATLAS], "Photo-nuclear dijet production in ultra-peripheral Pb+Pb collisions," ATLAS-CONF-2017-011.
18. [ATLAS], "Photo-nuclear jet production in ultra-peripheral Pb+Pb collisions at $\sqrt{s}_{\rm NN} = 5.02$ TeV with the ATLAS detector," ATLAS-CONF-2022-021.
19. A. J. Baltz, G. Baur, D. d'Enterria, L. Frankfurt, F. Gelis, V. Guzey, K. Hencken, Y. Kharlov, M. Klasen and S. R. Klein, *et al.* Phys. Rept. **458**, 1-171 (2008)
20. C. A. Flett, A. D. Martin, M. G. Ryskin and T. Teubner, Phys. Rev. D **102**, 114021 (2020) [arXiv:2006.13857 [hep-ph]].
21. V. Guzey, E. Kryshen, M. Strikman and M. Zhalov, Phys. Lett. B **726**, 290-295 (2013) [arXiv:1305.1724 [hep-ph]].
22. V. Guzey and M. Zhalov, JHEP **10**, 207 (2013) [arXiv:1307.4526 [hep-ph]].
23. L. Frankfurt, V. Guzey and M. Strikman, Phys. Rept. **512**, 255-393 (2012) [arXiv:1106.2091 [hep-ph]].
24. M. Strikman, R. Vogt and S. N. White, Phys. Rev. Lett. **96**, 082001 (2006) [arXiv:hep-ph/0508296 [hep-ph]].
25. S. R. Klein, J. Nystrand and R. Vogt, Phys. Rev. C **66**, 044906 (2002) [arXiv:hep-ph/0206220 [hep-ph]].
26. V. P. Goncalves, M. V. T. Machado and A. R. Meneses, Phys. Rev. D **80**, 034021 (2009) [arXiv:0905.2067 [hep-ph]].
27. V. P. Gonçalves, G. Sampaio dos Santos and C. R. Sena, Nucl. Phys. A **976**, 33-45 (2018) [arXiv:1711.04497 [hep-ph]].
28. S. Frixione and G. Ridolfi, Nucl. Phys. B **507**, 315-333 (1997) [arXiv:hep-ph/9707345 [hep-ph]].
29. M. Klasen and G. Kramer, Z. Phys. C **76**, 67-74 (1997) [arXiv:hep-ph/9611450 [hep-ph]].
30. P. Aurenche, L. Bourhis, M. Fontannaz and J. P. Guillet, Eur. Phys. J. C **17**, 413-421 (2000) [arXiv:hep-ph/0006011 [hep-ph]].
31. M. Klasen, Rev. Mod. Phys. **74**, 1221-1282 (2002) [arXiv:hep-ph/0206169 [hep-ph]].
32. V. Guzey and M. Klasen, Phys. Rev. C **99**, no.6, 065202 (2019) [arXiv:1811.10236 [hep-ph]].
33. J. Nystrand, Nucl. Phys. A **752**, 470-479 (2005) [arXiv:hep-ph/0412096 [hep-ph]].
34. I. Helenius, PoS **HardProbes2018**, 118 (2018) [arXiv:1811.10931 [hep-ph]].
35. I. Helenius and C. O. Rasmussen, Eur. Phys. J. C **79**, no.5, 413 (2019) [arXiv:1901.05261 [hep-ph]].
36. K. Kovarik, A. Kusina, T. Jezo, D. B. Clark, C. Keppel, F. Lyonnet, J. G. Morfin, F. I. Olness, J. F. Owens and I. Schienbein, *et al.* Phys. Rev. D **93**, no.8, 085037 (2016) [arXiv:1509.00792 [hep-ph]].
37. M. Gluck, E. Reya and A. Vogt, Phys. Rev. D **46**, 1973-1979 (1992)
38. V. Guzey and M. Klasen, Eur. Phys. J. C **79**, no.5, 396 (2019) [arXiv:1902.05126 [hep-ph]].
39. V. Guzey and M. Klasen, JHEP **04**, 158 (2016) [arXiv:1603.06055 [hep-ph]].
40. V. Guzey and M. Strikman, [arXiv:2403.08342 [hep-ph]].
41. J. C. Collins, Phys. Rev. D **57**, 3051-3056 (1998) [erratum: Phys. Rev. D **61**, 019902 (2000)] [arXiv:hep-ph/9709499 [hep-ph]].
42. M. Klasen and G. Kramer, Eur. Phys. J. C **70**, 91-106 (2010) [arXiv:1006.4964 [hep-ph]].
43. V. Guzey and M. Klasen, Eur. Phys. J. C **76**, no.8, 467 (2016) [arXiv:1606.01350 [hep-ph]].
44. V. Guzey and M. Klasen, Phys. Rev. D **104**, no.11, 114013 (2021) [arXiv:2012.13277 [hep-ph]].
45. V. Guzey and M. Klasen, Phys. Rev. C **102**, no.6, 065201 (2020) [arXiv:2003.09129 [hep-ph]].
46. V. Guzey and M. Klasen, JHEP **05**, 074 (2020) [arXiv:2004.06972 [hep-ph]].

Collision geometry in UPC dijet production

Kari J. Eskola, Vadim Guzey, Ilkka Helenius, Petja Paakkinen and Hannu Paukkunen
University of Jyväskylä, Department of Physics, P.O. Box 35, FI-40014 University of Jyväskylä, Finland and Helsinki Institute of Physics, P.O. Box 64, FI-00014 University of Helsinki, Finland

We present a comprehensive NLO pQCD study on inclusive dijet photoproduction in ultra-peripheral nucleus-nucleus collisions (UPCs). Our analysis takes into account the finite size of both the photon-emitting and the target nucleus, estimated using the Wood-Saxon nuclear density profile. We show that a significant part of the measured dijets at large z_γ in UPC Pb+Pb collisions at 5.02 TeV come from events with relatively small impact parameters of the order of a few nuclear radii, and the cross section predictions thus become sensitive to the modelling of the collision geometry and photon flux near the source nucleus. In addition, we include the modelling of electromagnetic breakup survival factor needed for a direct comparison with the experimental data and study the resolution power of this process in terms of the impact-parameter dependent nuclear parton distribution functions.

DOI: https://doi.org/10.17161/qcs5kh43
Keywords: inclusive photonuclear processes, jet photoproduction, perturbative QCD, impact-parameter dependence, neutron-class event selection

1 Introduction

In ultraperipheral nucleus-nucleus collisions (UPCs), inclusive dijet photoproduction has been proposed as a valuable probe for studying nuclear parton distribution functions (nPDFs).[1,2,3] Compared to e.g. jet production in proton-nucleus collisions this offers an arguably cleaner probe with considerably smaller underlying event activity. However, the unique condition of UPCs—specifically, the absence of nuclear overlap—imposes restrictions on the impact parameter space. This limitation becomes particularly relevant in dijet production, where the requirement for high-transverse-momentum jets necessitates an energetic photon in the initial state. Such photons are more likely to originate from close to the source nucleus, and, consequently, the cross section predictions for dijet production become sensitive to the modeling of nuclear geometry and the photon flux near the source nucleus.

Here, we present a study on the inclusive UPC dijet photoproduction using next-to-leading order (NLO) perturbative QCD (pQCD) and the impact-parameter dependent equivalent photon approximation (EPA).[4,5,6] The study considers the finite size of both the photon-emitting and the target nucleus, revealing a sensitivity to the transverse-plane geometry of the UPC events.[7] We discuss also the role of the forward-neutron event-class selection in isolating the photonuclear cross section and include the associated probability for no electromagnetic (e.m.) breakup of the photon-emitting nucleus in the predictions. We show that the geometrical effects survive even after including this additional suppression factor. Full details of this work can be found in Ref. 7.

2 Dijet production in impact-parameter dependent EPA

We work here in terms of the impact-parameter dependent EPA,[4,5,6] where the UPC dijet cross section may be written as

$$\mathrm{d}\sigma^{AB\to A+\mathrm{dijet}+X} = \sum_{i,j,X'} \int \mathrm{d}^2\mathbf{b}\,\Gamma_{AB}(\mathbf{b}) \int \mathrm{d}^2\mathbf{r}\, f_{\gamma/A}(y,\mathbf{r}) \otimes f_{i/\gamma}(x_\gamma,Q^2) \otimes \int \mathrm{d}^2\mathbf{s}\, f_{j/B}(x,Q^2,\mathbf{s}) \otimes \mathrm{d}\hat{\sigma}^{ij\to\mathrm{dijet}+X'}(x_\gamma y p_A, x p_B, Q^2) \times \delta^{(2)}(\mathbf{r}-\mathbf{s}-\mathbf{b}). \quad (1)$$

Here, $f_{\gamma/A}(y,\mathbf{r})$ is the flux of photons from a source A carrying a fraction y of the per nucleon beam momentum p_A, evaluated at a transverse distance $|\mathbf{r}|$ from the center of A. A photon represented by this flux interacts with a parton j from the target B at a distance $|\mathbf{s}|$ from its center, with the associated impact-parameter dependent nPDF denoted as $f_{j/B}(x,Q^2,\mathbf{s})$ for a parton with a fraction x of the per nucleon beam momentum p_B. This interaction, characterised by the partonic cross section $\hat{\sigma}^{ij\to\mathrm{dijet}+X'}(x_\gamma y p_A, x p_B, Q^2)$ with a hard scale Q^2, can happen either directly, where $i=\gamma$ and $f_{\gamma/\gamma}(x_\gamma,Q^2)=\delta(1-x_\gamma)$, or through a resolved contribution, with $i=q,\bar{q},g$ and $f_{i/\gamma}(x_\gamma,Q^2)$ being

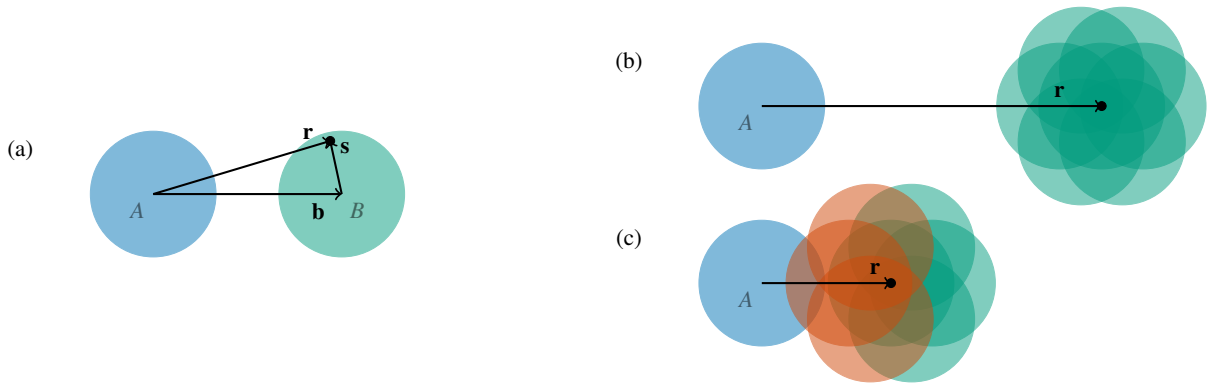

Figure 1 – (a) An illustration of the transverse-plane vectors $\mathbf{r}$, $\mathbf{b}$ and $\mathbf{s}$. (b) A 'far-passing', large $|\mathbf{r}|$ scenario. (c) A 'near-encounter', small $|\mathbf{r}|$ scenario. Figure from Ref. 7.

the corresponding photon parton distribution for a parton carrying a fraction x_γ of the photon energy. Finally, the survival probability $\Gamma_{AB}(\mathbf{b})$ requires that there is no hadronic interaction between the nuclei A and B at the impact parameter $\mathbf{b} = \mathbf{r} - \mathbf{s}$.

The collision geometry is illustrated in Fig. 1, panel (a). The phase space can be split into two regions, cf. the discussion in the following section: For large $|\mathbf{r}| \sim |\mathbf{b}| \gg |\mathbf{s}|$, Fig. 1, panel (b), the two nuclei never overlap, and thus any value of $|\mathbf{s}| < R_B$ is allowed in this 'far-passing' region and the spatial dependence effectively integrates out. For $|\mathbf{r}| \sim |\mathbf{b}| \sim |\mathbf{s}|$ instead, Fig. 1, panel (c), some configurations lead to nuclear overlap and are thus excluded from the UPC cross section. As we will show, this restriction in the transverse phase space for these 'near-encounter' events leads to a sensitivity on the transverse-space geometry of the colliding nuclei in the UPC dijet cross section.

3 Effective photon flux

Using a simple assumption that the transverse and longitudinal degrees of freedom factorize for the impact-parameter dependent nPDFs, $f_{j/B}(x, Q^2, \mathbf{s}) = \frac{1}{B}\, T_B(\mathbf{s}) \times f_{j/B}(x, Q^2)$, where $T_B(\mathbf{s})$ is the nuclear thickness function, $B = \int \mathrm{d}^2\mathbf{s}\, T_B(\mathbf{s})$ is the number of nucleons in the target nucleus and $f_{j/B}(x, Q^2)$ the ordinary (spatially averaged) nPDF, one can reorganise Eq. (1) to the form

$$\mathrm{d}\sigma^{AB\to A+\mathrm{dijet}+X} = \sum_{i,j,X'} f^{\mathrm{eff}}_{\gamma/A}(y) \otimes f_{i/\gamma}(x_\gamma, Q^2) \otimes f_{j/B}(x, Q^2) \otimes \mathrm{d}\hat{\sigma}^{ij\to\mathrm{dijet}+X'}(x_\gamma y p_A, x p_B, Q^2) \qquad (2)$$

where

$$f^{\mathrm{eff}}_{\gamma/A}(y) = \frac{1}{B} \int \mathrm{d}^2\mathbf{r} \int \mathrm{d}^2\mathbf{s}\, f_{\gamma/A}(y, \mathbf{r})\, T_B(\mathbf{s})\, \Gamma_{AB}(\mathbf{r}-\mathbf{s}) \qquad (3)$$

is an effective photon flux encoding all the spatial dependence. Various approximations can be used for calculating this effective flux. We consider here the following options in order to demonstrate the importance of the geometrical effects:

PL refers to the pointlike approximation, where the finite size of the colliding nuclei is accounted for only in requiring the impact parameter to be larger than twice the nuclear hard-sphere radius, $R_{\mathrm{PL}} = 7.1$ fm for a lead nucleus of $A = 208$, i.e. $\Gamma^{\mathrm{PL}}_{AB}(\mathbf{b}) = \theta(|\mathbf{b}| - 2R_{\mathrm{PL}})$. Other than that, the nuclei are treated as pointlike objects with

$$f^{\mathrm{PL}}_{\gamma/A}(y, \mathbf{r}) = \frac{Z^2\alpha_{\mathrm{e.m.}}}{\pi^2} m_p^2 y [K_1^2(\xi) + \frac{1}{\gamma_L} K_0^2(\xi)], \quad \xi = y m_p |\mathbf{r}|, \qquad (4)$$

as the bare photon flux,[8] where Z is the nuclear charge, $\alpha_{\mathrm{e.m.}}$ the fine-structure constant, m_p the proton mass, γ_L the nucleus Lorentz factor and $K_{0,1}$ are modified Bessel functions of the second kind, and the target parton spatial distribution is taken as $T^{\mathrm{PL}}_B(\mathbf{s}) = B\delta^{(2)}(\mathbf{s})$.

WS$_{\delta(\mathbf{s})}$ refers to the approximation where the survival factor is obtained through the optical Glauber-model $\Gamma^{\mathrm{WS}}_{AB}(\mathbf{b}) = \exp[-\sigma_{\mathrm{NN}} T^{\mathrm{WS}}_{AB}(\mathbf{b})]$ with the nuclear overlap function T^{WS}_{AB} calculated from the Woods-Saxon distribution and σ_{NN} taken as the total (elastic+inelastic) nucleon-nucleon cross

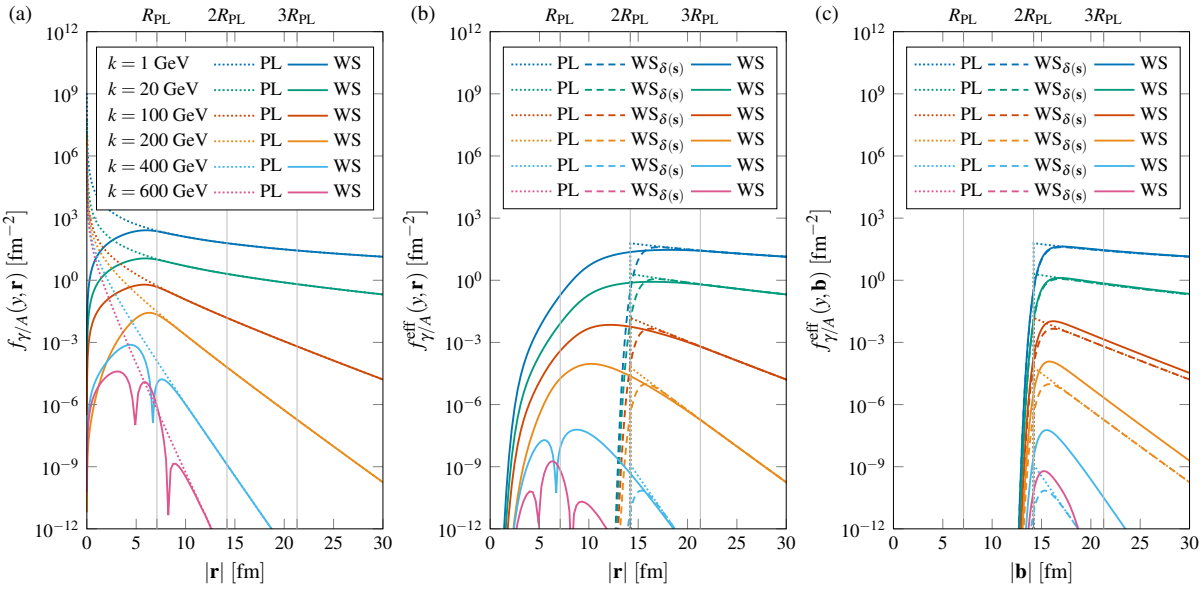

Figure 2 – (a) A comparison of the bare flux from the pointlike, Eq. (4), and Woods-Saxon, Eq. (5), sources. (b) The effective $|\mathbf{r}|$-dependent flux calculated through Eq. (6). (c) The effective $|\mathbf{b}|$-dependent flux calculated through Eq. (7). Figure from Ref. 7.

section. Likewise, the bare photon flux is taken as the one of an extended charge distribution[6]

$$f^{\rm WS}_{\gamma/A}(y,\mathbf{r}) = \frac{Z^2\alpha_{\rm e.m.}}{\pi^2}\frac{1}{y}\left|\int_0^\infty \frac{\mathrm{d}k_\perp k_\perp^2}{k_\perp^2+(ym_p)^2}F_A^{\rm WS}(k_\perp^2+(ym_p)^2)J_1(|\mathbf{r}|k_\perp)\right|^2, \tag{5}$$

where the form factor $F_A^{\rm WS}$ is again obtained from the Woods-Saxon distribution and J_1 is the cylindrical modified Bessel function of the first kind. For this intermediate result, we still keep $T_B^{\rm PL}(\mathbf{s}) = B\delta^{(2)}(\mathbf{s})$, thus neglecting the spatial distribution of partons in the target nucleus.

WS is finally the full Woods-Saxon approximation, where in addition to the survival factor and the bare flux as in the previous case, also the nuclear thickness function for the target parton distribution is calculated from the Woods-Saxon distribution, $T_B^{\rm WS}(\mathbf{s}) = \int_{-\infty}^{\infty}\mathrm{d}z\,\rho_B^{\rm WS}\left(\sqrt{z^2+\mathbf{s}^2}\right)$.

In Fig. 2, panel (a), we compare the bare fluxes from the pointlike, Eq. (4), and Woods-Saxon, Eq. (5), sources. As expected, differences appear only for small values of $|\mathbf{r}|$. Panels (b) and (c) then show the effective flux as a function of $|\mathbf{r}|$ and $|\mathbf{b}|$, respectively, with

$$f^{\rm eff}_{\gamma/A}(y,\mathbf{r}) = f_{\gamma/A}(y,\mathbf{r}) \times \frac{1}{B}\int \mathrm{d}^2\mathbf{s}\,T_B(\mathbf{s})\,\Gamma_{AB}(\mathbf{r}-\mathbf{s}) \tag{6}$$

$$f^{\rm eff}_{\gamma/A}(y,\mathbf{b}) = \Gamma_{AB}(\mathbf{b}) \times \frac{1}{B}\int \mathrm{d}^2\mathbf{s}\,f_{\gamma/A}(y,\mathbf{b}+\mathbf{s})\,T_B(\mathbf{s}) \tag{7}$$

satisfying $f^{\rm eff}_{\gamma/A}(y) = \int \mathrm{d}^2\mathbf{r}\,f^{\rm eff}_{\gamma/A}(y,\mathbf{r}) = \int \mathrm{d}^2\mathbf{b}\,f^{\rm eff}_{\gamma/A}(y,\mathbf{b})$. For the $|\mathbf{r}|$-dependent effective flux, we see that when $|\mathbf{r}| > 3R_{\rm PL}$, i.e. for 'far-passing' nuclei, the three approximations described above yield an identical flux. That is, viewed from afar, any source appears as pointlike, and since in this region the probability for hadronic interaction between the nuclei is practically zero (i.e. $\Gamma_{AB} \approx 1$), the dependence on the target spatial distribution also integrates out in Eq. (6). For $|\mathbf{r}| < 3R_{\rm PL}$, i.e. 'near-encounter' events, the three approximations differ due to a finite probability for nuclear overlap, and the full WS effective flux has a non-negligible contribution in the region $|\mathbf{r}| < 2R_{\rm PL}$ due to the integration over the full target width that is not taken into account by the other approximations. This becomes particularly important for high-energy photons, where the flux drops very fast as a function of $|\mathbf{r}|$. Note that if considered as a function of $|\mathbf{b}|$, Eq. (7), the integration over the target width causes always an enhancement in the WS flux over the $\mathrm{WS}_{\delta(\mathbf{s})}$ approximation and one cannot easily find a limit where the different fluxes would resolve to the PL approximation. See Ref. 7 for more details.

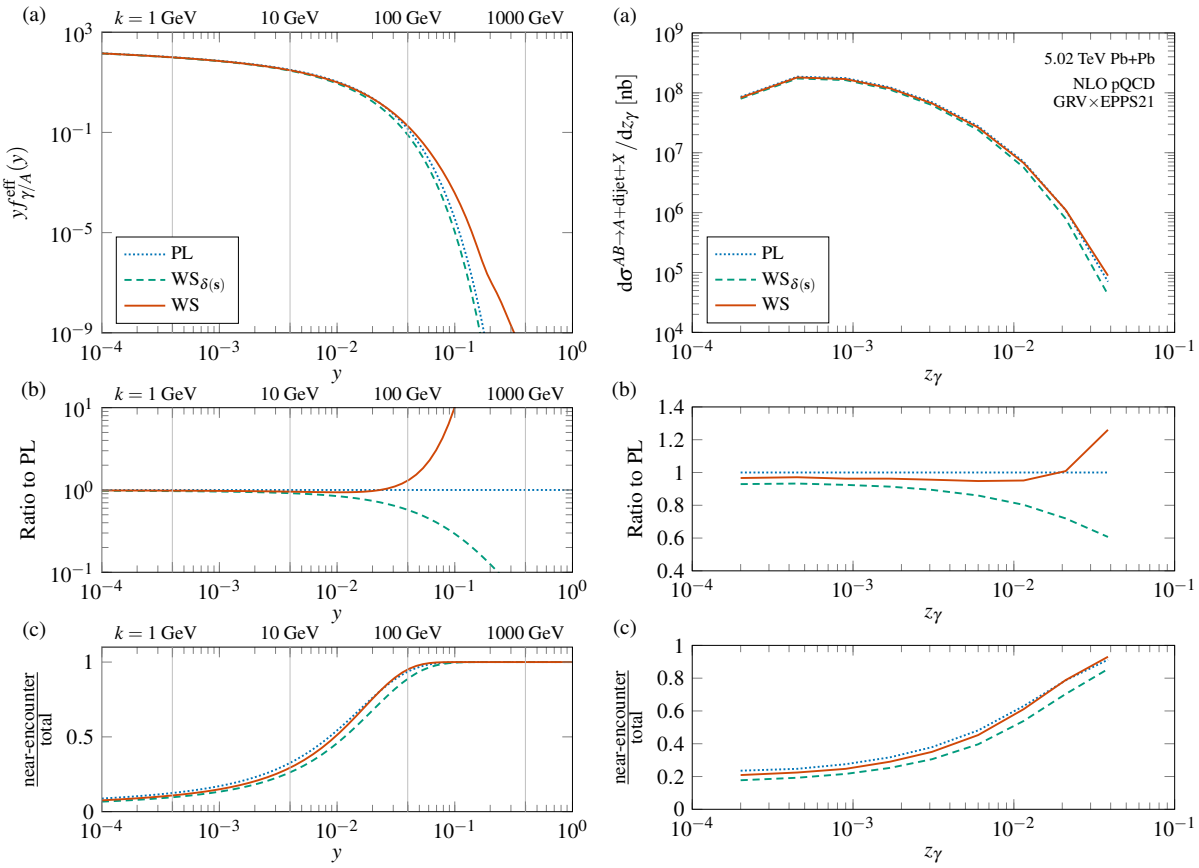

Figure 3 – Comparison of the effective photon flux (left) and UPC dijet cross section (right) in Pb+Pb collisions at $\sqrt{s_{\rm NN}} = 5.02$ TeV. (a) Absolute quantities. (b) Ratios of the different flux approximations with respect to the pointlike one. (c) Fraction of $|\mathbf{r}| < 3R_{\rm PL}$ 'near-encounter' versus total number of events. Figures from Ref. 7.

4 UPC dijets in Pb+Pb at 5.02 TeV

We compare the effective flux $f^{\rm eff}_{\gamma/A}(y)$ and the inclusive UPC dijet cross section for Pb+Pb collisions at $\sqrt{s_{\rm NN}} = 5.02$ TeV in Fig. 3. For the latter, we show the single-differential distribution as a function of $z_\gamma = M_{\rm jets}\exp(y_{\rm jets})/\sqrt{s_{\rm NN}}$, where $M_{\rm jets}$, $y_{\rm jets}$ are the invariant mass and rapidity of the anti-$k_{\rm T}$ ($R = 0.4$) jets passing the kinematical cuts. For these cuts we use the ones from the ATLAS analysis,[9] where the jets are required to be confined in rapidity to $|\eta_{\rm jet}| < 4.4$ and have a transverse momentum of at least $p_{\rm T,jet} > 15$ GeV with $M_{\rm jets} > 35$ GeV. At leading order, one would have $z_\gamma = x_\gamma y$ and thus this observable can be used as an experimental proxy for the cross section dependence on the photon flux. Here, we perform the calculations in NLO with the Frixione & Ridolfi jet photoproduction code.[10]

As can be seen from the figure, the effective photon flux as a function of y (Fig. 3, left) and the UPC dijet cross section as a function of z_γ (Fig. 3, right) exhibit rather common behaviour due to their intertwined nature. For low photon energies (i.e. small y or z_γ), the three approximations discussed in the previous section agree nicely. This is due to the fact that only a small fraction of events in these kinematics come from the near-encounter configurations where the geometrical effects become significant. As the photon energy is increased, so does the fraction of events from the near-encounter configurations, and eventually the predictions from the three predictions begin to diverge. In the bin of highest z_γ this results in a 20% enhancement in the WS compared to the PL approximation and, quite strikingly, a factor of two difference between the WS and WS$_{\delta(\mathbf{s})}$ approximations. The latter clearly indicates that taking into account the spatial extent of the target nucleus is truly needed for an accurate interpretation of this observable.

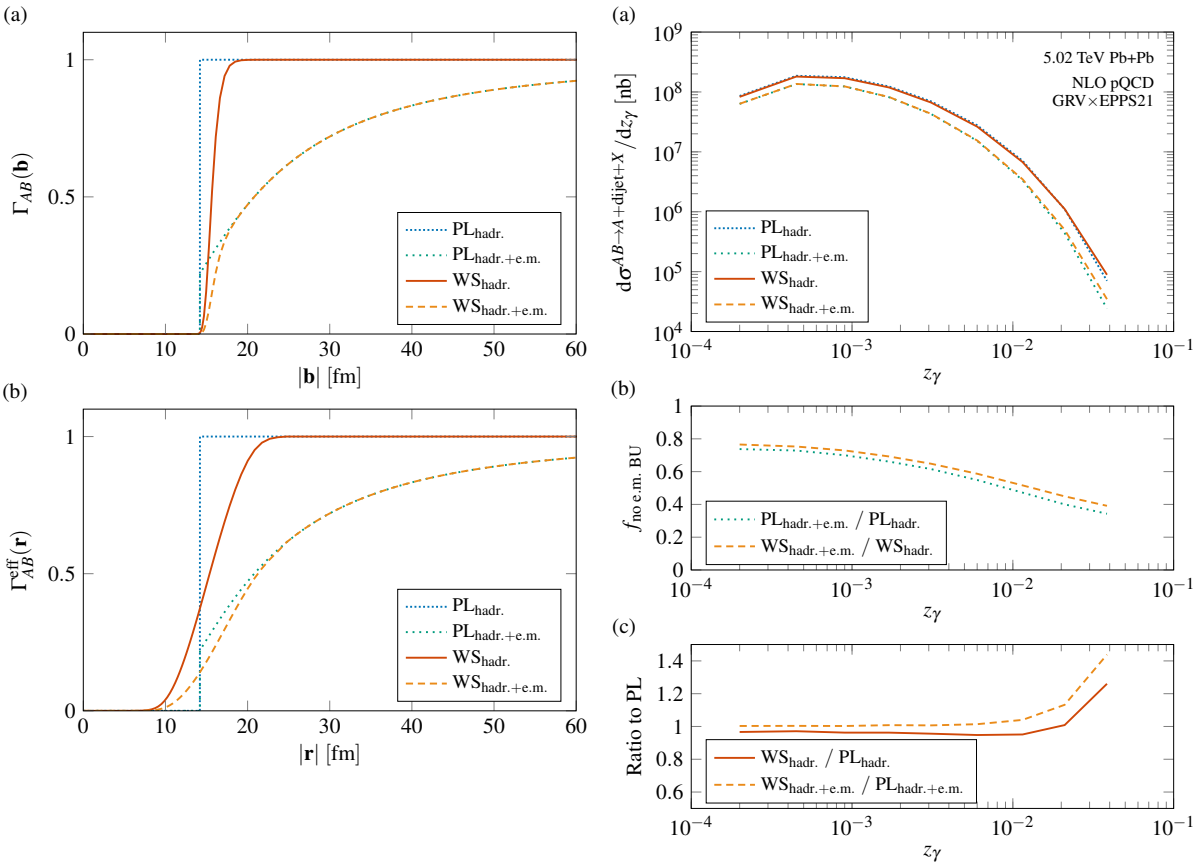

Figure 4 – Left: (a) The survival factor in pointlike and Wood-Saxon approximations, without and with the e.m. breakup factor. (b) Same, but for the effective $|\mathbf{r}|$-dependent survival factor. Right: The impact of the e.m. breakup correction on the dijet production. (a) Absolute cross section. (b) The size of the e.m. breakup correction. (c) The ratio between the predictions in pointlike and Wood-Saxon approximations, without and with the e.m. breakup factor. Figures from Ref. 7.

5 Modelling the e.m. breakup for the neutron-class selection

Our treatment of the UPC dijet production in the previous section was fully inclusive, apart from requiring no direct hadronic interaction between the incoming nuclei. The experimental measurement however uses a 0nXn forward-neutron event-class selection and associated rapidity cuts for isolating the photonuclear events from generic nucleus-nucleus collisions.[9] To account for the requirement of zero neutrons in the photon-going direction, we employ the Poissonian probability for no electromagnetic breakup of nucleus A through Coulomb excitations [11]

$$\Gamma^{\text{e.m.}}_{AB}(\mathbf{b}) = \exp\left[-\int_0^1 \mathrm{d}y f_{\gamma/B}(y,\mathbf{b})\sigma_{\gamma A\to A^*}(\sqrt{y\,s_{\text{NN}}})\right] \tag{8}$$

which we take from the Starlight event generator.[12] The total (hadr.+e.m.) survival probability then reads

$$\Gamma^{\text{hadr.+e.m.}}_{AB}(\mathbf{b}) = \Gamma^{\text{e.m.}}_{AB}(\mathbf{b})\Gamma^{\text{hadr.}}_{AB}(\mathbf{b}), \qquad \Gamma^{\text{hadr.+e.m.}}_{AB,\text{eff}}(\mathbf{r}) = \frac{1}{B}\int \mathrm{d}^2\mathbf{s}\, T_B(\mathbf{s})\,\Gamma^{\text{hadr.+e.m.}}_{AB}(\mathbf{r}-\mathbf{s}), \tag{9}$$

where the latter form is the effective suppression factor multiplying the bare flux in Eq. (6). These are presented in Fig. 4 left, panels (a) and (b), respectively, without and with the e.m. breakup factor, for the PL and WS approximations. Requiring no e.m. breakup causes a clear, impact-parameter dependent reduction in the survival probability.

The impact on the dijet production is shown in Fig. 4 right, panels (a) and (b), where we see that taking into account the e.m. breakup yields a substantial suppression in the cross section. The impact-parameter dependence manifests itself here as a dependence in z_γ, and the suppression varies from 20% at the lowest to 60% at the highest z_γ. Noteworthily, this additional suppression does not reduce the

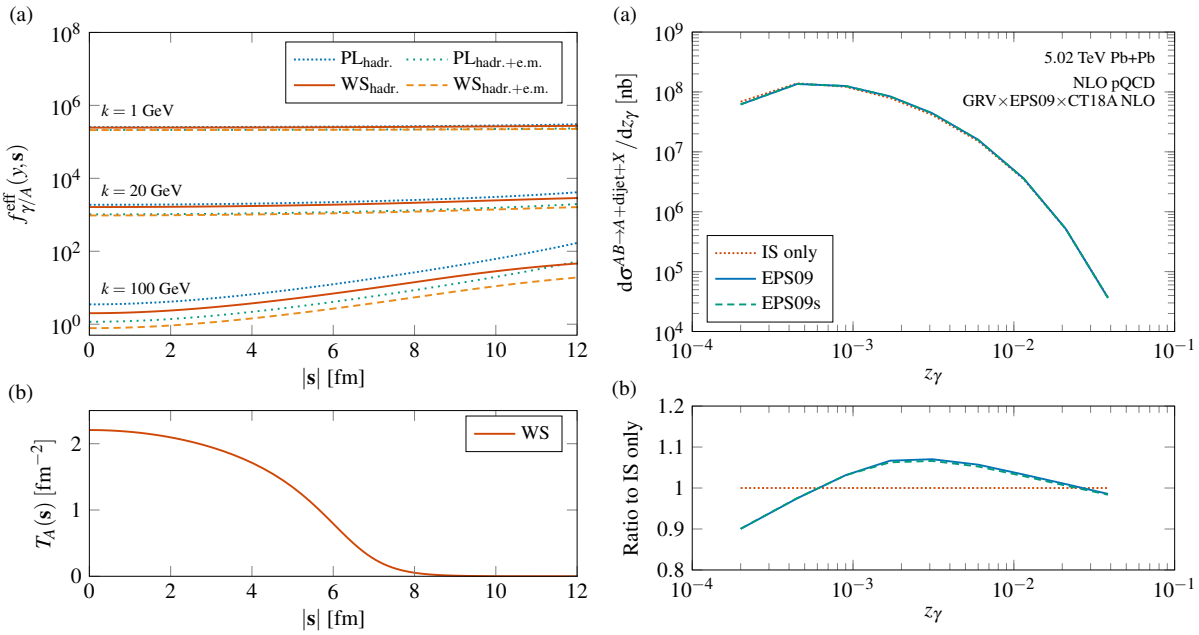

Figure 5 – Left: (a) The **s**-dependent effective flux. (b) The nuclear thickness function. Right: (a) The UPC dijet cross section with predictions using either no nuclear modifications (IS only), spatially independent nuclear modifications (EPS09) or spatially dependent nuclear modifications (EPS09s). (b) Ratios to the IS only prediction. Figures from Ref. 7.

difference between the PL and WS approximations of the effective flux, but rather enhances it and results in a 40% difference in the highest z_γ bin, as shown in Fig. 4 right, panel (c). Note that in order to match with the $X \geq 1$ neutron condition in the target-going direction, we should still subtract a diffractive contribution from our inclusive results, but we expect this to be a small correction in most of the phase-space.[7,13]

6 Spatial dependence in the nuclear modifications

In above, we have treated the nPDFs under the factorization assumption $f_{j/B}(x,Q^2,\mathbf{s}) = \frac{1}{B}\,T_B(\mathbf{s}) \times f_{j/B}(x,Q^2)$. This is of course just a simplification, and one should use proper impact-parameter dependent nPDFs instead.[14,15] To study this, we begin by rewriting Eq. (1) as

$$\mathrm{d}\sigma^{AB\to A+\text{dijet}+X} = \sum_{i,j,X'} \int \mathrm{d}^2\mathbf{s}\, f^{\text{eff}}_{\gamma/A}(y,\mathbf{s}) \otimes f_{i/\gamma}(x_\gamma,Q^2) \otimes f_{j/B}(x,Q^2,\mathbf{s}) \otimes \mathrm{d}\hat{\sigma}^{ij\to\text{dijet}+X'}(x_\gamma y p_A, x p_B, Q^2), \tag{10}$$

thus making no assumption on the form of $f_{j/B}(x,Q^2,\mathbf{s})$, and where

$$f^{\text{eff}}_{\gamma/A}(y,\mathbf{s}) = \int \mathrm{d}^2\mathbf{r}\,\Gamma_{AB}(\mathbf{r}-\mathbf{s})\, f_{\gamma/A}(y,\mathbf{r}) \tag{11}$$

is an **s**-dependent effective photon flux. Should the spatial dependence integrate out, as happens in the far-passing region, this function would be constant in |**s**|, whereas any sensitivity to the spatial dependence of the target nPDF would appear as a non-constant behaviour. This function is shown in Fig. 5 left, panel (a), and compared with the target thickness function shown in Fig. 5 left, panel (b). We see that, as could be expected from the discussion above, the **s**-dependent effective flux is almost constant for low-energy photons where most of the contribution come from far-passing events, but for high-energy photons an enhancement towards the edge of the target appears due to an increasing contribution from the near-encounter region.

To test whether this |**s**|-dependence of the flux at high photon energies can be used to probe the spatial dependence of nuclear modification, we employ the phenomenological EPS09s parametrization.[15]

The cross section can then be written as

$$\mathrm{d}\sigma^{AB\to A+\mathrm{dijet}+X} = \sum_{i,j,X'}\sum_{m=0}^{4} f_{\gamma/A}^{\mathrm{eff},m}(y)\otimes f_{i/\gamma}(x_\gamma,Q^2)\otimes f_{j/B}^{m}(x,Q^2)\otimes \mathrm{d}\hat{\sigma}^{ij\to\mathrm{dijet}+X'}(x_\gamma y p_A, x p_B, Q^2), \tag{12}$$

where

$$f_{\gamma/A}^{\mathrm{eff},m}(y) = \frac{1}{B}\int \mathrm{d}^2\mathbf{s}\, f_{\gamma/A}^{\mathrm{eff}}(y,\mathbf{s})\,[T_B(\mathbf{s})]^m, \qquad f_{j/B}^{m}(x,Q^2) = \sum_N c_m^{j/N}(x,Q^2) f_{j/N}(x,Q^2) \tag{13}$$

are a generalised effective flux for different powers of the nuclear thickness function and the nuclear PDFs with EPS09s nuclear modification coefficients $c_m^{j/N}$ (where the sum goes over the nucleons N in the nucleus B), respectively. The resulting dijet cross section is shown in Fig. 5 right, panels (a) and (b), comparing the prediction with spatially dependent nuclear modifications (EPS09s) to a version of the same nPDFs with no spatial dependence in the nuclear modifications (EPS09)[16] and a prediction with no nuclear modifications in the PDFs but taking into account the trivial isospin dependence (IS only). As we can see, the nuclear modifications result in an order of 10% effect in the cross section (EPS09 vs. IS only), while the spatial dependence in them gives only a small correction to that (EPS09s vs. EPS09). Hence, even though the spatial resolution at high z_γ caused by the dominance of near-encounter events was able to distinguish the overall shape of the target nucleus (cf. the large difference between WS and $\mathrm{WS}_{\delta(\mathbf{s})}$ predictions), it is not strong enough to probe the spatial dependence of the nuclear modifications in impact-parameter dependent nPDFs.

7 Conclusions

In summary, the inclusive dijet photoproduction in UPCs provides valuable insights into nPDFs, but a careful consideration of the collision geometry and photon flux is essential for robust predictions and meaningful constraints. Even though we found that the spatial dependence in the nuclear modifications as encoded in the EPS09s nPDFs gave only a very small correction compared to the spatially independent EPS09 nuclear modifications, one should note that there is still a significant 40% correction at large z_γ from using a full WS calculation for the effective photon flux compared to the simple PL approximation, in the case when the e.m. breakup probability is properly taken into account. This e.m. survival factor was needed in order to match with the experimental 0nXn event selection.[9] We also note that further measurements in the XnXn and 0n0n event classes will be helpful for experimentally quantifying the size of this e.m. survival factor and the diffractive contribution, and guide the reader to Ref. 7 for further discussion.

Acknowledgments

This research was funded through the Research Council of Finland project No. 330448, as a part of the Center of Excellence in Quark Matter of the Research Council of Finland (projects No. 346325 and No. 346326) and as a part of the European Research Council project ERC-2018-ADG-835105 YoctoLHC. We acknowledge computing resources from the Finnish IT Center for Science (CSC), utilised under the project jyy2580.

References

1. M. Strikman, R. Vogt and S. N. White, "Probing small x parton densities in ultraperipheral AA and pA collisions at the LHC," Phys. Rev. Lett. **96**, 082001 (2006), doi:10.1103/PhysRevLett.96.082001
2. V. Guzey and M. Klasen, "Inclusive dijet photoproduction in ultraperipheral heavy ion collisions at the CERN Large Hadron Collider in next-to-leading order QCD," Phys. Rev. C **99**, no.6, 065202 (2019), doi:10.1103/PhysRevC.99.065202
3. V. Guzey and M. Klasen, "Constraints on nuclear parton distributions from dijet photoproduction at the LHC," Eur. Phys. J. C **79**, no.5, 396 (2019), doi:10.1140/epjc/s10052-019-6905-2
4. N. Baron and G. Baur, "Photon - hadron interactions in relativistic heavy ion collisions," Phys. Rev. C **48**, 1999-2010 (1993), doi:10.1103/PhysRevC.48.1999

5. M. Greiner, M. Vidovic, C. Hofmann, A. Schafer and G. Soff, "Deduction of the in-medium gluon distribution from photon - gluon fusion processes in peripheral ultrarelativistic heavy ion collisions," Phys. Rev. C **51**, 911-921 (1995), doi:10.1103/PhysRevC.51.911
6. F. Krauss, M. Greiner and G. Soff, "Photon and gluon induced processes in relativistic heavy ion collisions," Prog. Part. Nucl. Phys. **39**, 503-564 (1997), doi:10.1016/S0146-6410(97)00049-5
7. K. J. Eskola, V. Guzey, I. Helenius, P. Paakkinen and H. Paukkunen, "Nuclear spatial resolution in near-encounter UPC dijet photoproduction," arXiv:2404.09731 [hep-ph]
8. C. A. Bertulani and G. Baur, "Electromagnetic Processes in Relativistic Heavy Ion Collisions," Phys. Rept. **163**, 299 (1988), doi:10.1016/0370-1573(88)90142-1
9. ATLAS collaboration, "Photo-nuclear jet production in ultra-peripheral Pb+Pb collisions at $\sqrt{s}_{\mathrm{NN}} = 5.02$ TeV with the ATLAS detector," ATLAS-CONF-2022-021
10. S. Frixione and G. Ridolfi, "Jet photoproduction at HERA," Nucl. Phys. B **507**, 315-333 (1997), doi:10.1016/S0550-3213(97)00575-0
11. A. J. Baltz, S. R. Klein and J. Nystrand, "Coherent vector meson photoproduction with nuclear breakup in relativistic heavy ion collisions," Phys. Rev. Lett. **89**, 012301 (2002), doi:10.1103/PhysRevLett.89.012301
12. S. R. Klein, J. Nystrand, J. Seger, Y. Gorbunov and J. Butterworth, "STARlight: A Monte Carlo simulation program for ultra-peripheral collisions of relativistic ions," Comput. Phys. Commun. **212**, 258-268 (2017), doi:10.1016/j.cpc.2016.10.016
13. V. Guzey and M. Klasen, "How large is the diffractive contribution to inclusive dijet photoproduction in ultraperipheral collisions at the LHC?," Phys. Rev. D **104**, no.11, 114013 (2021), doi:10.1103/PhysRevD.104.114013
14. L. Frankfurt, V. Guzey and M. Strikman, "Leading Twist Nuclear Shadowing Phenomena in Hard Processes with Nuclei," Phys. Rept. **512**, 255-393 (2012), doi:10.1016/j.physrep.2011.12.002
15. I. Helenius, K. J. Eskola, H. Honkanen and C. A. Salgado, "Impact-Parameter Dependent Nuclear Parton Distribution Functions: EPS09s and EKS98s and Their Applications in Nuclear Hard Processes," JHEP **07**, 073 (2012), doi:10.1007/JHEP07(2012)073
16. K. J. Eskola, H. Paukkunen and C. A. Salgado, "EPS09: A New Generation of NLO and LO Nuclear Parton Distribution Functions," JHEP **04**, 065 (2009), doi:10.1088/1126-6708/2009/04/065

Axion Physics in UPC and LbyL Scattering

C. O. Ramírez-Álvarez[1], A. Fernández-Téllez[1] and A. I. Hernández-Juárez[2]
[1] *Facultad de Ciencias Físico Matemáticas, Benemérita Universidad Autónoma de Puebla. H. Puebla de Zaragoza, Puebla, 72000 México.*
[2] *Facultad de Estudios Superiores Cuautitlán, Universidad Nacional Autónoma de México. Cuautilán Izcalli, Edo. de México, 54740 México.*

In this work, we revisited the light-by-light scattering physics in ultraperipheral collisions. Furthermore, an extension model with axion-like particles is also studied. We used MadGraph5_aMC@NLO+gamma-UPC event generator for our analysis and the proposed kinematic cuts for the ALICE 3 experiment were considered. Different distribution functions for both light-by-light and axion-like particles are analyzed and we find that the transverse momentum is a good channel to observe the production of axions in ultraperipheral collisions.

DOI: https://doi.org/10.17161/fzbrwb17
Keywords: photon, LbyL, ALP, MonteCarlo

1 Introduction

A novel way to study BSM theories is with ultraperipheral collisions (UPC) of PbPb, which relies on EPA (Equivalent Photon Approximation) [1,2,3,4], a method that considers the electromagnetic fields generated by a moving charged particle as a flow of virtual photons with small virtuality, given by $Q^2 < 1/R^2$, and proportional to Z^4. This results is an enormous improvement, which can be used to search for new physics that couples to photons.

Light-by-light (LbyL) scattering $\gamma\gamma \to \gamma\gamma$, is a rare Standard Model (SM) process and it is not allowed by classical electrodynamics, therefore the reaction $\gamma\gamma \to \gamma\gamma$ arise at the one-loop level, where the Feynman diagrams involve fermions and W bosons running into the loop. The LbyL was first discussed in Ref. [5]. Recently, the detection of this interaction through UPC of heavy ions at the LHC has been pointed out [6,7,8,9,10], whereas both ATLAS and CMS experiments measured this process [11,12,13]. The data obtained can be explained with theoretical and simulation studies, considering only box diagrams with fermions in the loop, since the W boson contributions are relevant energies of the order of $M_{\gamma\gamma} > M_W$.

Experimental and theoretical observations indicate that the SM is an incomplete theory, as it not explain the neutrino mass, hierarchy problem, or CP violation. This has motivated multiple physics communities to propose solutions by introducing new particles or sectors that go beyond the SM (BSM), such as the Axion-Like Particles (ALP), which are pseudoscalar bosons with independent couplings and masses and can have masses up to the TeV scale [14].

In this work, we analyze the SM and Axion-Like Particles phenomenological implications under the context of the physics of the ALICE 3 experiment [15]. MonteCarlo studies are presented using MadGraph5_aMC@NLO+gamma-UPC [16,17] generators to model di-photon invariant mass distributions of two different scenarios, LbyL scattering and ALP-$\gamma\gamma$, the latter we consider different couplings and ALP masses.

2 Light by Light Scattering

In the SM, the $\gamma\gamma \to \gamma\gamma$ scattering is induced through one-loop level diagrams with charged particles (fermions and W boson) running into the loop. For this study, the Feynman-'t Hooft gauge is used, hence

scalar particles related to the W boson appear in the loop. The corresponding Feynman diagrams are shown in Fig. 1.

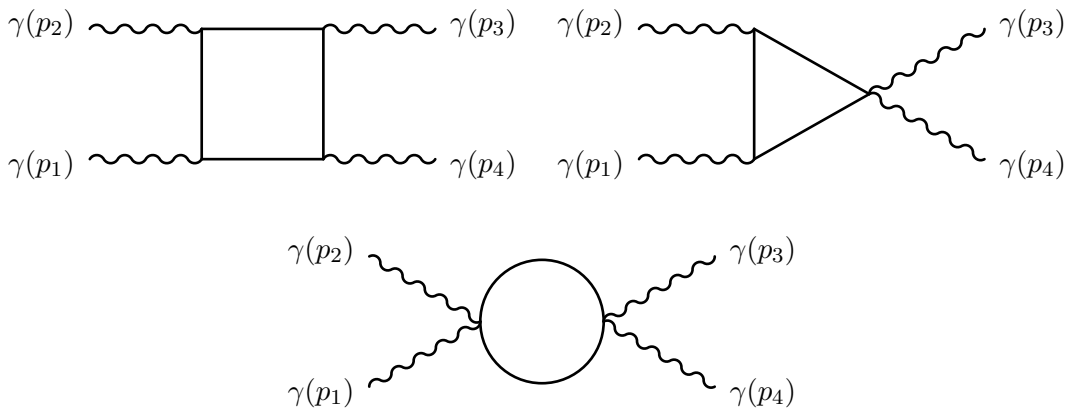

Figure 1: Contributing Feynman diagrams to the LbyL scattering process. The fermions only appear in box diagrams, while the W boson and its associated particles (charged scalars $\varphi^{\pm}$ and ghosts $u^{\pm}$) contribute in the remaining diagrams.

In order to test gamma-UPC library, we reproduce some results obtained for LbyL in [7,9,10]. The MonteCarlo event simulations were performed in MadGraph5_aMC@NLO using the gamma-UPC library that calculates the photon flux for unique $\gamma\gamma$ processes in PbPb UPC, such a formalism is discussed in Ref. [17]. The event selection is according to the proposed ALICE 3 experiment upgrade [15]. We also consider the ECal detector. The kinematic cuts are $p_T > 50$ MeV and $-4 < \eta < 4$. The distribution of the differential cross section with respect to the invariant mass obtained from our simulation is shown in Fig. 2 for 3 cases: only fermions, only W bosons and the total SM. We observe that the fermions contribution dominates at low values in the invariant mass, whereas the W boson contribution becomes relevant at high values $M_{\gamma\gamma}$ and its maximum values are reached at $M_{\gamma\gamma} > 2M_W$. The Fig. 2 is consistent with the reported one in Ref. [18], where proton beams are considered.

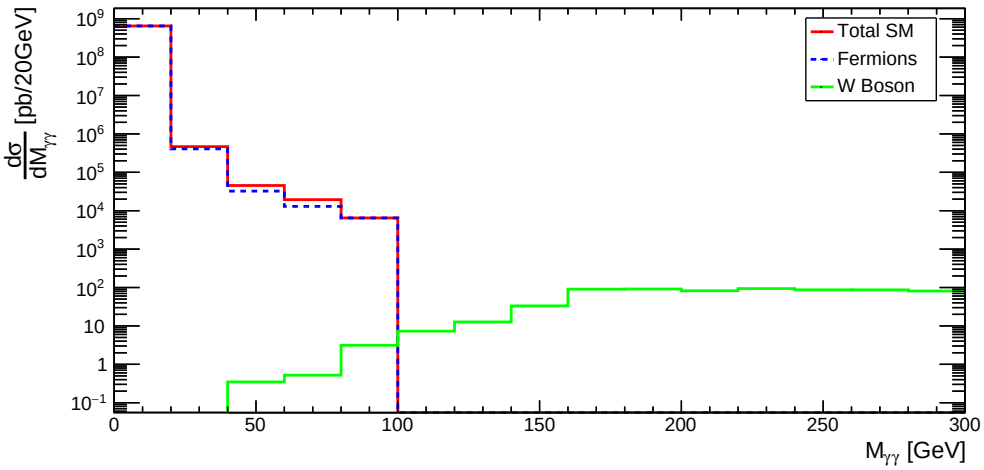

Figure 2: Differential cross section with respect to the invariant mass of di-photons in PbPb UPC at 5.02 TeV. The blue dotted and green line lines corresponds to the diagrams including only fermions and W bosons, respectively, whereas the red line corresponds to the total SM contribution considering all diagrams.

Now, since the experimental measurement obtained by ATLAS and CMS was on a scale of $p_T > 2$ GeV, ALICE 3 will provide the opportunity to perform measurements for low p_T, which implies more precision at low invariant masses. In this sense, it is possible to study LbyL scattering with fermion box and background generated at these scales. In Fig. 3, we show the differential cross section of LbyL scattering with respect to three kinematic variables: invariant mass, rapidity and transverse momentum, where only the contribution with fermions in the loop are considered. Our results agree with those

reported in Ref. [9,10].

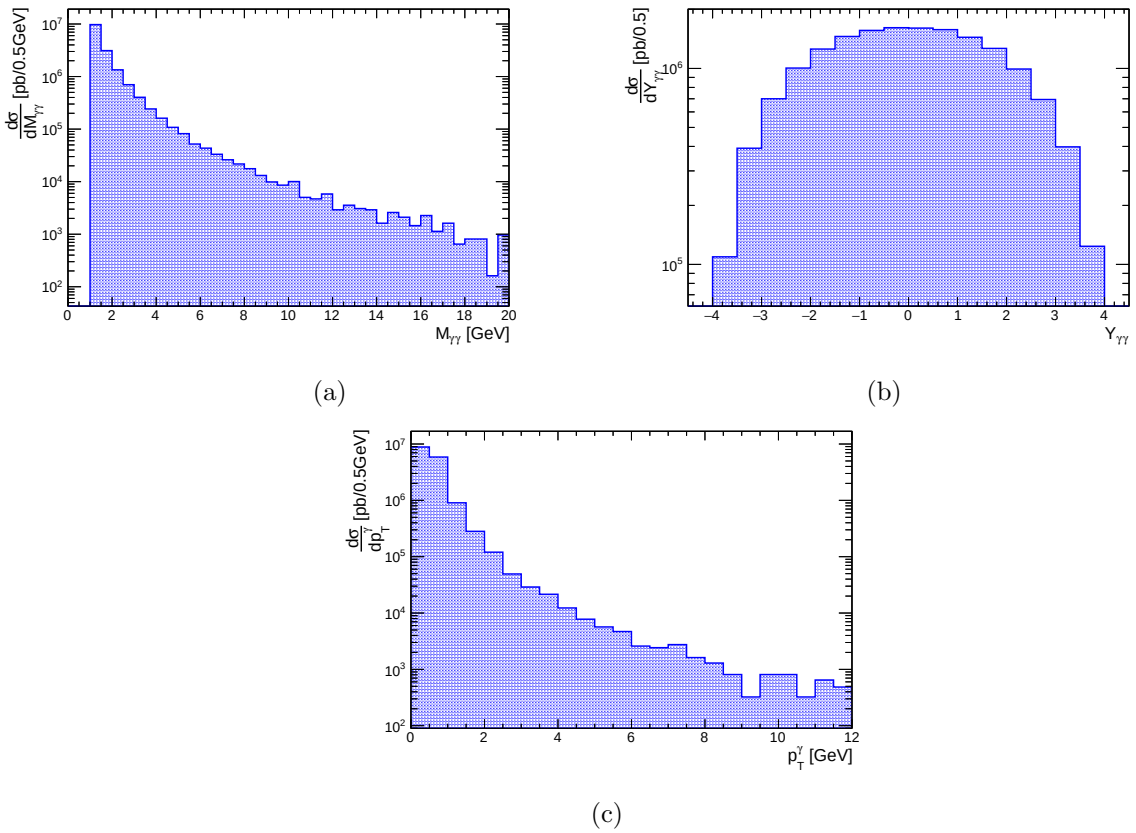

Figure 3: Differential cross section with respect to: (a) the invariant mass of di-photons, (b) the rapidity of di-photons and (c) the transverse momentum of a photon generated with MadGraph5_aMC@NLO+gamma-UPC in PbPb at 5.02 TeV.

3 Axion-Like Particles

Axions were proposed by Pecci-Quinn in 1977 to solve a strong CP Problem in QCD [19,20]. They are Nambu-Goldstone pseudo-bosons related to the spontaneous breaking of a new global symmetry $U(1)_{\rm PQ}$.

In particular, Axion-Like Particles (ALP) are pseudoscalar bosons with independent couplings and masses, which can be the TeVs [14]. These particles are coupled to the electromagnetic sector via the Lagrangian:

$$\mathscr{L}_{a\gamma\gamma} = \frac{1}{2}\left(\partial a\right)^2 - \frac{1}{2}M_a^2 a^2 - \frac{1}{4}\frac{k}{\Lambda} a F^{\mu\nu}\tilde{F}_{\mu\nu}, \tag{1}$$

where a is the ALP, M_a its mass, $\frac{k}{\Lambda}$ the coupling constant, $F^{\mu\nu}$ the electromagnetic field tensor, and the dual tenso $\tilde{F}_{\mu\nu}$ is defined as $\tilde{F}_{\mu\nu} \equiv \frac{1}{2}\epsilon_{\mu\nu\alpha\beta}F^{\alpha\beta}$. One can rewrite the ALP-$\gamma\gamma$ coupling in terms of the electric $\mathbf{E}$ and magnetic $\mathbf{B}$ fields as:

$$\mathscr{L}_{\rm int} = \frac{k}{\Lambda} a \mathbf{E}\cdot\mathbf{B}, \tag{2}$$

which implies that photons can mix with ALP in the presence of electromagnetic fields. The LbyL scattering is a clean channel for the search of ALPs as they can be considered as a background to the $\gamma\gamma \to \gamma\gamma$ process. The ALP physics has been revisited in Refs.[14,21,22,23,24,25,26].

The ALPs can be produced in LbyL sacttering through s-channel, as in Fig. 4. For this study, a model with a ALP-$\gamma\gamma$ coupling in the Eq. (1) was generated in the UFO format [27] with the help of the FeynRules package [28]. Then, the model was loaded into MadGraph5_aMC@NLO+gamma-UPC. To observe the ALP resonances, PbPb UPC events at 5.02 TeV were simulated following the same event selection as LbyL, setting $\Lambda = 1$ TeV and varying k. Results are shown for two different ALP masses in Fig. 5 for masses $M_a = 7$ GeV and $M_a = 12$ GeV. We have considered $M_{\gamma\gamma}$ larger than 5 GeV to avoid

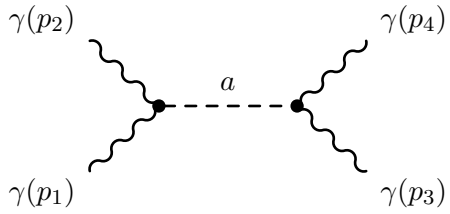

Figure 4: Feynman diagram of the ALP-$\gamma\gamma$ coupling for the s-channel.

the pion background [10] and the light meson resonances [9]. It is observed that the ALP resonances dominate as the value of k increases, whereas for $k < 1.5$ the LbyL signal is the relevant one.

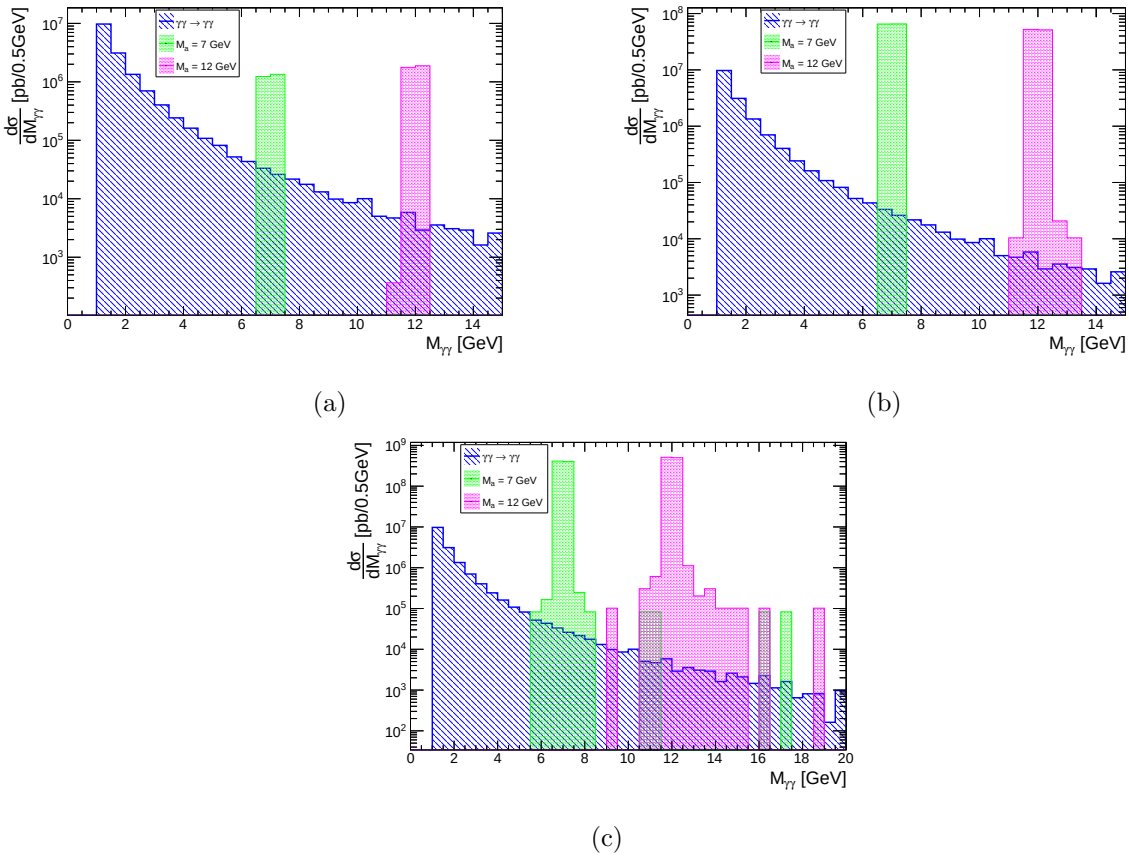

Figure 5: Differential cross section with respect to the di-photon invariant mass in UPC of PbPb at 5.02 TeV with $\Lambda = 1$ TeV for (a) $k = 1.5$ (b) $k = 8$ and (c) $k = 25$. The green histogram for $M_a = 7$ GeV and the pink histogram for $M_a = 12$ GeV. The histogram for LbyL is included.

Now, to confirm the behavior of the resonances according to the values of k, three other cases are presented with the same ALP masses in Fig. 6 and $k = 0.1, 50, 100$. We note that for $k = 0.1$ the signal dominance correspond to LbyL. On the other hand, for large values of k (50 and 100) the ALP resonances dominate over the LbyL signal. Moreover, an overlap between ALP distributions for the different M_a, which is more visible at $k = 100$.

The differential cross section as function of the rapidity and transverse momentum are shown in Fig. 7 and 8, respectively. We have considered $k = 8$ for different values of ALP masses. In Fig. 7, a similar behavior to the observed in the LbyL case is found. Nevertheless, the differential cross section decreases for large ALP masses.

In contrast, for the distribution functions of the transverse momentum (Fig. 8) the behavior with respect to the LbyL scattering totally different. For the ALP-$\gamma\gamma$ model the signal grows until it reaches its maximum and then it decreases, whereas in the LbyL case the signal is always decreasing until it disappears. This result is interesting as the ALP signal can be distinguished from the LbyL one. Therefore, the transverse momentum is a good channel to observe new physics from ALP. A similar

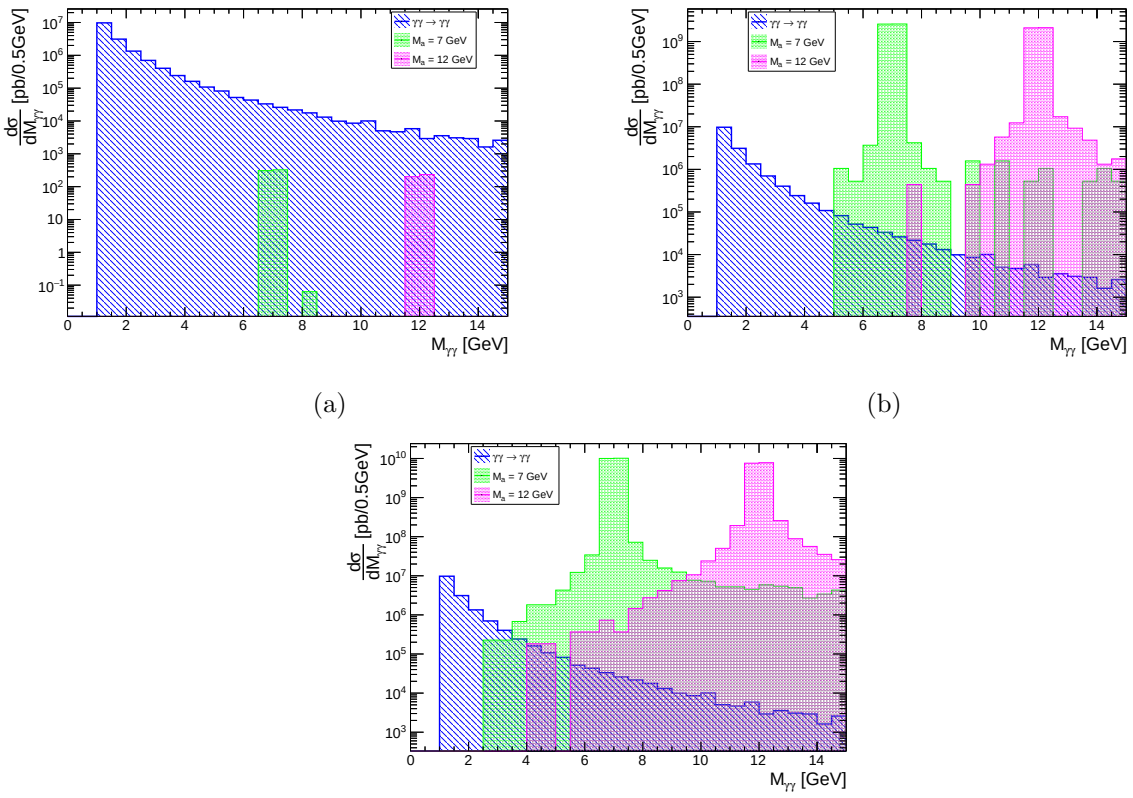

Figure 6: Differential cross section with respect to the di-photon invariant mass in UPC of PbPb at 5.02 TeV with $\Lambda = 1$ TeV for (a) $k = 0.1$ (b) $k = 50$ and (c) $k = 100$. The green histogram for $M_a = 7$ GeV and the pink histogram for $M_a = 12$ GeV. The histogram for LbyL is included.

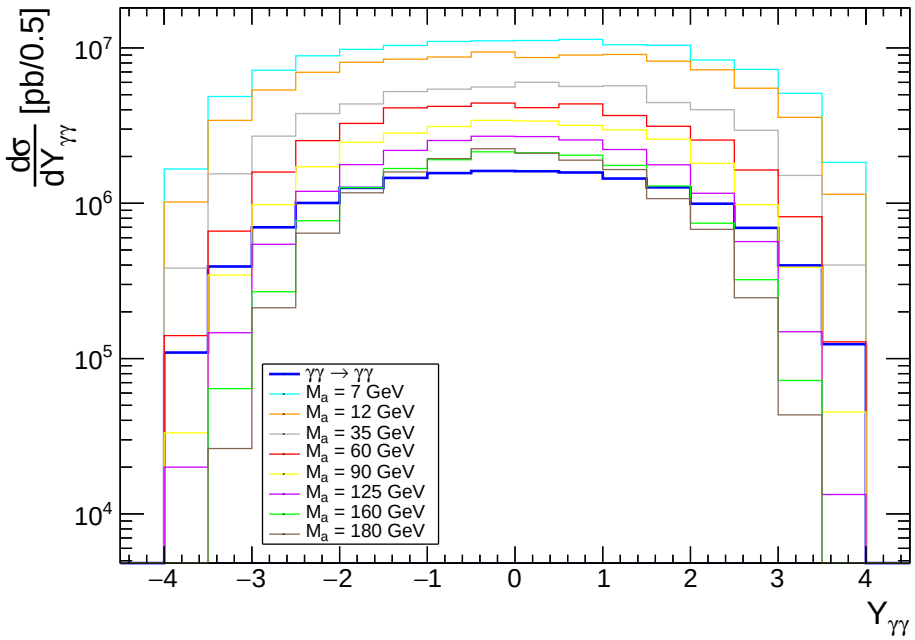

Figure 7: Differential cross section as a function of rapidity with $k = 8$ and different values of M_a setting $\Lambda = 1$ GeV in UPC of PbPb at 5.02 TeV. The LbyL distribution is included.

distribution has been reported in Ref. [25], however, the ALPs arise from $e\gamma$ collisions.

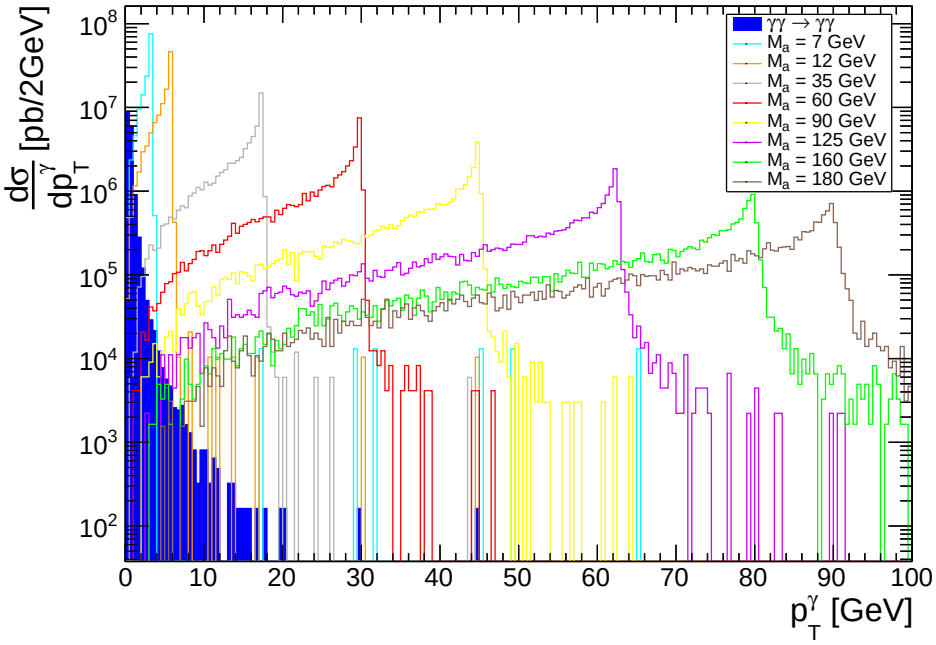

Figure 8: Differential cross section as a function of transverse momentum with $k = 8$ and different values of M_a setting $\Lambda = 1$ GeV in UPC of PbPb at 5.02 TeV. The LbyL distribution is included.

4 Conclusions

In this work, we have presented MonteCarlo simulations, which were performed at the partonic level for the $\gamma\gamma \to \gamma\gamma$ scattering at the one-loop level in the SM. The MadGraph5_aMC@NLO+gamma-UPC MonteCarlo generator was used. Furthermore, the ALP-$\gamma\gamma$ model (BSM) was also implemented. The simulations were carried out in PbPb UPC at 5.02 TeV with a selection of events similar to the proposed for the ALICE 3 experiment.

For LbyL, differential cross section distributions were obtained. They agree with results previously reported in the literature. On the other hand, for the ALP-$\gamma\gamma$ model it was observed that in the inavariant mass distributions functions the ALP resonances dominates for $k > 25$. In the case of rapidity, the ALP distributions are almost indentical to the LbyL signal.

Finally, for the differential cross section with respect to the transverse momentum in the ALP-$\gamma\gamma$ model, we find that the distribution functions are distinguishable from the LbyL case. Thus, this kinematic variable is a good channel for observing ALP production.

References

[1] E. Fermi, WORLD SCIENTIFIC (2003) doi:10.1142/9789812704214_0026
[2] E. J. Williams. Phys. Rev. **45**, 729-730 (1934) doi:10.1103/PhysRev.45.729
[3] C. von Weizsacker, Z. Phys. **88**, 612-625 (1934) doi:10.1007/BF01333110
[4] C. A. Bertulani and G. Baur, Phys. Rept. **163**, 299 (1988) doi:10.1016/0370-1573(88)90142-1
[5] H. Euler and B. Kockel, Naturwissenschaften. **23**, 246-247 (1935) doi:10.1007/BF01493898
[6] D. d'Enterria and G. G. Silveira, Phys. Rev. Lett. **111**, (2013) doi:10.1103/PhysRevLett.111.080405 [Erratum: Phys. Rev. Lett. **116**, 129901 (2016)].
[7] M. Klusek-Gawenda, P. Lebiedowicz and A. Szczurek, Phys. Rev. C **93**, 044907 (2016) doi:10.1103/PhysRevC.93.044907
[8] M. Klusek-Gawenda, W. Schäfer and A. Szczurek, Phys. Lett. B 761, 399-407 (2016) doi:10.1016/j.physletb.2016.08.059
[9] M. Klusek-Gawenda, R. McNulty, R. Schicker and A. Szczurek, Phys. Rev. D **99**, 093013 (2019) doi:10.1103/PhysRevD.99.093013
[10] P. Jucha, M. Klusek-Gawenda and A. Szczurek, Phys. Rev. D **109**, 014004 (2024) doi:10.1103/PhysRevD.109.014004
[11] M. Aaboud, et al. (ATLAS Collaboration), Nature Phys. **13**, 852–858 (2017)

doi:10.1038/nphys4208
[12] A. M. Sirunyan, et al. (CMS Collaboration), Phys. Lett. B **797**, 134826 (2019) doi:10.1016/j.physletb.2019.134826
[13] G. Aad, et al. (ATLAS Collaboration), Phys. Rev. Lett. **123**, 052001 (2019) doi:10.1103/PhysRevLett.123.052001
[14] S. Knapen, T. Lin, H. Keong and T. Melia, Phys. Rev. Lett. **118**, 171801 (2017) doi:10.1103/PhysRevLett.118.171801
[15] L. Musa and W Riegler. (ALICE collaboration), CERN-LHCC-2022-009 (2022) doi:10.48550/arXiv.2211.02491
[16] J. Alwall, R. Frederix, S. Frixione, et al., J. High Energ. Phys. **07**, 79 (2014) doi:10.1007/JHEP07(2014)079
[17] H. S. Shao and D. d'Enterria, J. High Energ. Phys. **09**, 248 (2022) doi:10.1007/JHEP09(2022)248
[18] S. Fichet, G. von Gersdorff, B. Lenzi, et al., J. High Energ. Phys. **2015**, 165 (2015) doi:10.1007/JHEP02(2015)165
[19] R. D. Peccei and H. R. Quinn, Phys. Rev. Lett. **38**, 1440-1443 (1977) doi:10.1103/PhysRevLett.38.1440
[20] S. Weinberg, Phys. Rev. Lett. **40**, 223-226 (1978) doi:10.1103/PhysRevLett.40.223
[21] C. Baldenegro, S. Fichet, G. von Gersdorff et al., J. High Energ. Phys. **2018**, 131 (2018) doi:10.1007/JHEP06(2018)131
[22] K. Mimasu, V. Sanz, J. High Energ. Phys. **2015**, 173 (2015) doi:10.1007/JHEP06(2015)173
[23] M. Bauer, M. Heiles, M. Neubert, et al., Eur. Phys. J. C **79**, 74 (2019) doi:10.1140/epjc/s10052-019-6587-9
[24] I. Brivio, M. B. Gavela, L. Merlo, et al., Eur. Phys. J. C **77**, 572 (2017) doi:10.1140/epjc/s10052-017-5111-3
[25] Y. Chong-Xing, L. Ming-Ze and G. Yu-Chen, Phys. Rev. D **100**, 015020 (2019) doi:10.1103/PhysRevD.100.015020
[26] I. Brevik, M. Chaichian and M. Oksanen, Eur. Phys. J. C **81**, 926 (2021) doi:10.1140/epjc/s10052-021-09707-3
[27] C. Degrande, C. Duhr, B. Fuks. et al., Comput. Phys. Commun. **183**, 121-1214 (2012) doi:10.1016/j.cpc.2012.01.022
[28] A. Alloul, N. D. Christensen, C. Degrande, et al., Comput. Phys. Commun. **185**, 2250-2300 (2014) doi:10.1016/j.cpc.2014.04.012

Photoproduction of J/ψ and dileptons in Pb–Pb collisions with nuclear overlap

N. Bizé (for the ALICE Collaboration)
SUBATECH, Nantes Université, IMT-Atlantique, CNRS.
Nantes, France

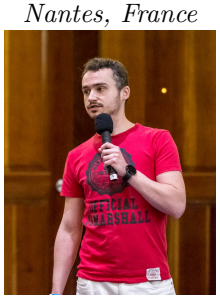

Photon-photon reactions and the production of J/ψ meson through photonuclear reactions have been extensively studied in ultra-peripheral heavy-ion collisions, in which the impact parameter is larger than twice the nuclear radius. In recent years, coherently photoproduced J/ψ and dilepton production via photon-photon interactions have also been observed in nucleus-nucleus (A–A) collisions with nuclear overlap. The former can help to constrain the nuclear gluon distributions at low Bjorken-x and high energy, while the latter could be used to further map the electromagnetic fields produced in heavy-ion collisions. In addition, these measurements can shed light on the theory behind photon-induced reactions in A–A collisions with nuclear overlap, including possible interactions of the measured probes with the formed and fast expanding quark-gluon plasma. Since the produced quarkonium is expected to keep the polarization of the incoming photon due to s-channel helicity conservation, the photoproduction origin of the J/ψ yield excess at very low transverse momentum, p_{T}, can be confirmed by the measurement of the J/ψ polarization. The ALICE detector can perform quarkonium production measurements at both mid ($|y| < 0.9$) and forward ($2.5 < y < 4$) rapidities down to $p_{\mathrm{T}} = 0$. In the following, the new ALICE measurements of the J/ψ y-differential cross section and the first polarization results of coherently photoproduced J/ψ via the dimuon decay channel at forward rapidity in Pb–Pb collisions at $\sqrt{s_{\mathrm{NN}}} = 5.02$ TeV are reported. Additionally, the measurement of an excess with respect to expectations from hadronic production in the dielectron yield, at low mass and p_{T}, at midrapidity in Pb–Pb collisions at $\sqrt{s_{\mathrm{NN}}} = 5.02$ TeV, is presented. The results are compared with available theoretical models.

DOI: https://doi.org/10.17161/8vtpsj90
Keywords: vector mesons, dileptons, photoproduction, nuclear overlap

1 Introduction

Strong electromagnetic fields are generated in ultra-peripheral collisions (UPC), where the impact parameter is larger than the sum of the radii of the two colliding nucleus. In such collisions, hadronic interactions are strongly suppressed. UPC provide therefore a clean environment to study vector meson and dilepton photoproduction and extensive measurements have been carried out. Recently, the aforementioned probes have also been studied in events with nuclear overlap, where hadronic interactions become dominant. In such events, the vector meson photoproduction can help to probe the gluon distribution in the nuclei for different Bjorken-x regions. In addition, it allows to test the survival of the coherence process while the nuclei are broken during the hadronic collision. The dilepton photoproduction can provide constraints on the mapping of the electromagnetic fields that are generated by the fast moving charges around the nuclei. Both processes could be useful to look for possible final-state medium effects. Previous measurements of dielectron photoproduction with nuclear overlap have been performed at STAR [1] and ATLAS [2], including an excess found at low p_{T} with respect to expectations from known hadronic sources. Furthermore, a J/ψ yield excess has been observed at very low p_{T}, for $p_{\mathrm{T}} < 0.3$ GeV/c and forward rapidity in peripheral Pb–Pb collisions at $\sqrt{s_{\mathrm{NN}}} = 2.76$ TeV [3] and 5.02 TeV [4]. The coherently photoproduced J/ψ cross section as a function of centrality in this p_{T} region has been measured in Pb–Pb collisions with nuclear overlap [4]. The theoretical models [5] predict a strong ra-

pidity dependence of the vector meson cross section, in particular at forward rapidity. Finally, previous measurements in UPC [6] indicate a transverse polarization of the coherently photoproduced J/ψ. While the latter is expected to keep the polarization of the incoming photon due to s-channel helicity conservation, such measurement in events with nuclear overlap is important to confirm the photoproduction origin of the very low-p_{T} J/ψ excess. In the following, new ALICE measurements of the y–differential cross section of the coherently photoproduced J/ψ and the inclusive J/ψ polarization at forward rapidity in Pb–Pb collisions at $\sqrt{s_{\mathrm{NN}}} = 5.02$ TeV with nuclear overlap are presented. In addition, an excess of the photoproduced dielectron yield with respect to the expectations from the hadronic production, at low mass and p_{T}, at midrapidity in Pb–Pb collisions at $\sqrt{s_{\mathrm{NN}}} = 5.02$ TeV, is reported.

2 Experimental apparatus

A detailed description of the ALICE experiment can be found in [7]. In the following results, dielectron measurements are performed at midrapidity ($|y| < 0.9$) with the ALICE central barrel. The main detectors used for tracking and electron identification are the Inner Tracking System (ITS), the Time Projection Chamber (TPC) and the Time-Of-Flight (TOF) system. All three detectors cover at least the pseudorapidity acceptance $|\eta| < 0.9$. The ITS is composed of six concentric cylindrical layers of silicon detectors. It is designed to locate the primary collision vertex with a spatial resolution of the order of 100 μm. In addition, it allows tracking and particle identification (PID) for very low p_{T}, $p_{\mathrm{T}} < 0.2$ GeV/c. The TPC is a cylindrical detector filled with a gas mixture ($\mathrm{Ne/CO_2/N_2}$) containing a central cathode and two end plates each composed of 18 Multiple Wired Proportional Chambers (MWPC). The primary electrons drift into the gas mixture on either side of the cathode to the end plates. TPC is used for PID by measuring specific energy loss $\mathrm{d}E/\mathrm{d}x$, tracking and vertex reconstruction in a large p_{T} interval ranging from 0.1 to 100 GeV/c. The TOF is a cylindrical detector composed of Multiple Resistive Plate Chambers (MRPCs). The use of MRPCs technology allows one to reach the required time resolution of less than 100 ps to identify particles using their time-of-flight for $p_{\mathrm{T}} < 2.5$ GeV/c. The J/ψ is studied via the dimuon decay channel at forward rapidity ($2.5 < y < 4$) with the ALICE muon spectrometer. The latter is composed of a tracking system, the Muon Chambers (MCH) and a trigger system, the Muon Trigger (MTR). MCH is made of five tracking stations, each one formed of two chambers based on the technology of the MWPCs. The detector is designed to reach a spatial resolution of the order of 100 μm to obtain the required invariant mass resolution for quarkonium analysis (~ 100 MeV/c^2 for the Υ). MTR is composed of four Resistive Plate Chambers (RPCs), which are allocated in two stations. The purpose of this trigger system is to reduce the probability to keep an event containing only muons coming from π or K. It is performed by applying a configurable p_{T}–threshold ranging from 0.5 to 4.2 GeV/c. A front absorber is placed upstream from MCH to suppress the background coming from hadrons and secondary muons. An iron wall is installed between MCH and MTR to filter out the muons originating from the remaining hadrons while a rear absorber is placed downstream from MTR to protect the spectrometer from beam-background interactions.

3 Results

3.1 Dielectron photoproduction measurement at midrapidity

ALICE measured dielectron photoproduction with nuclear overlap at midrapidity within the ALICE central barrel acceptance ($|\eta_e| < 0.8$). The details of the analysis can be found in [8]. The efficiency-corrected e^+e^- invariant mass spectra at low p_{T}, $p_{\mathrm{T,ee}} < 0.1$ GeV/c in peripheral (70–90% centrality class) and semi-peripheral (50–70% centrality class) Pb–Pb collisions at $\sqrt{s_{NN}} = 5.02$ TeV is shown in Fig. 1. Data are compared to the expected dielectron yield from known hadron decays produced in Pb–Pb collisions, called the hadronic cocktail. It is calculated with a fast simulation of the ALICE central barrel. An excess compared to known hadronic expectation is observed for both centrality classes. A larger significance is found for the most peripheral Pb–Pb collisions (70–90%) with a factor of about 20.

The e^+e^- invariant mass distributions where the hadronic cocktail contribution is subtracted to the data are shown in Fig. 2 for $p_{\mathrm{T,ee}} < 0.1$ GeV/c. The excess yield is compared with different calculations for dielectron photoproduction which are lowest-order QED calculations [9, 10], Wigner formalism [11] and the STARlight MC generator using the equivalent photon approach [12, 13]. On one hand, the STARlight model uses the k_{T}-factorisation method, where the single-photon distribution is integrated over all transverse distances to obtain the shape of the k_{T}–distribution. On the other hand the models based on QED calculations and Wigner formalism include the impact parameter dependence of the photon k_{T}–distribution. The expected contributions from the thermal dielectrons, estimated with an expanding

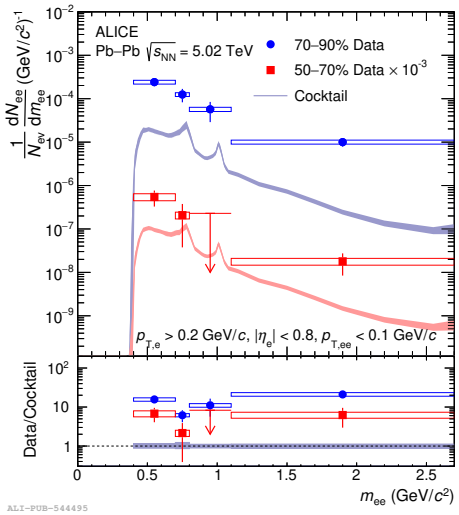

Figure 1: e^+e^- invariant mass spectra in peripheral (70–90%) and semi-peripheral (50–70%) Pb–Pb collisions at $\sqrt{s_{NN}} = 5.02$ TeV. Data are compared with the expected e^+e^- from known hadronic contributions. Vertical bars and boxes represent the data statistic and systematic uncertainties, respectively. Bands show the uncertainties of the hadronic cocktail. Arrows indicate upper limits at 90% confidence level.

fireball model including in-medium broadened ρ spectral function [14–16] are also shown. The latter is expected to be at least one order of magnitude smaller than the measured excess.

The inclusive dielectron $p_{\mathrm{T,ee}}$ spectra are shown for three different mass ranges in peripheral Pb–Pb collisions at $\sqrt{s_{NN}} = 5.02$ TeV in Fig. 3. While the data are well described by the hadronic cocktail for higher $p_{\mathrm{T,ee}} \geq 0.1$ GeV/c, a clear peak is observed for $p_{\mathrm{T,ee}} < 0.1$ GeV/c in all m_{ee} ranges. The latter is reproduced by the lowest-order QED calculations and the Wigner formalism, where both models include the impact parameter dependence of the photon k_{T}–distribution. However, the STARlight model is rising down to $p_{\mathrm{T,ee}} = 0$ and fails to reproduce the excess.

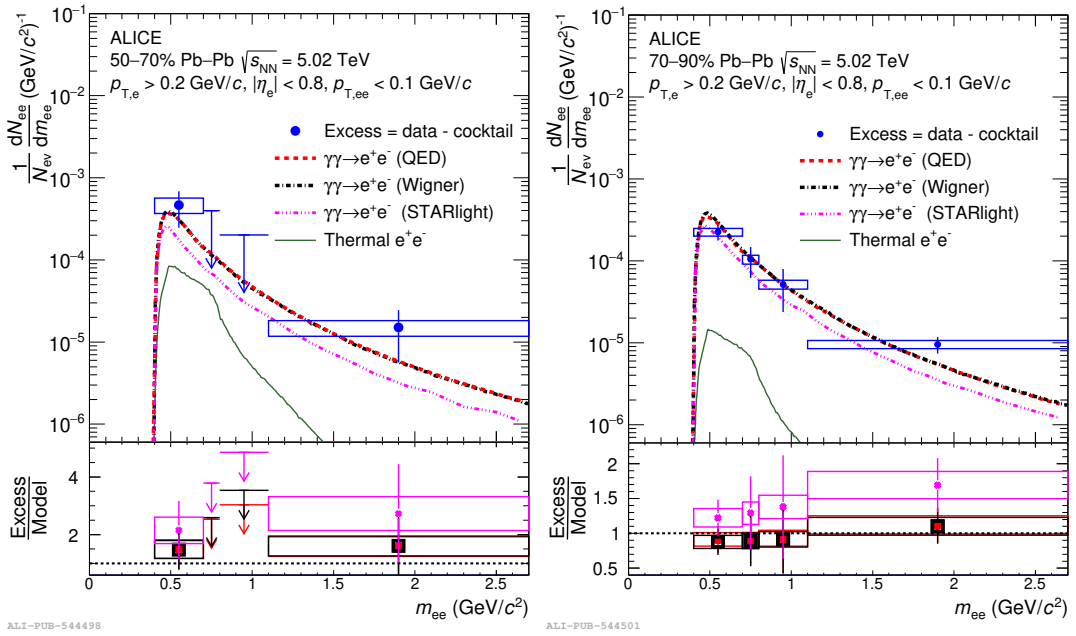

Figure 2: e^+e^- invariant mass spectra of excess yield after subtraction of the hadronic cocktail to the data in semi-peripheral (left panel) and peripheral (right panel) Pb–Pb collisions at $\sqrt{s_{\rm NN}}$ = 5.02 TeV. The excess is compared with several calculations for photoproduction of electron pairs. Vertical bars and boxes represent the data statistic and systematic uncertainties, respectively. Arrows indicate upper limits at 90% confidence level.

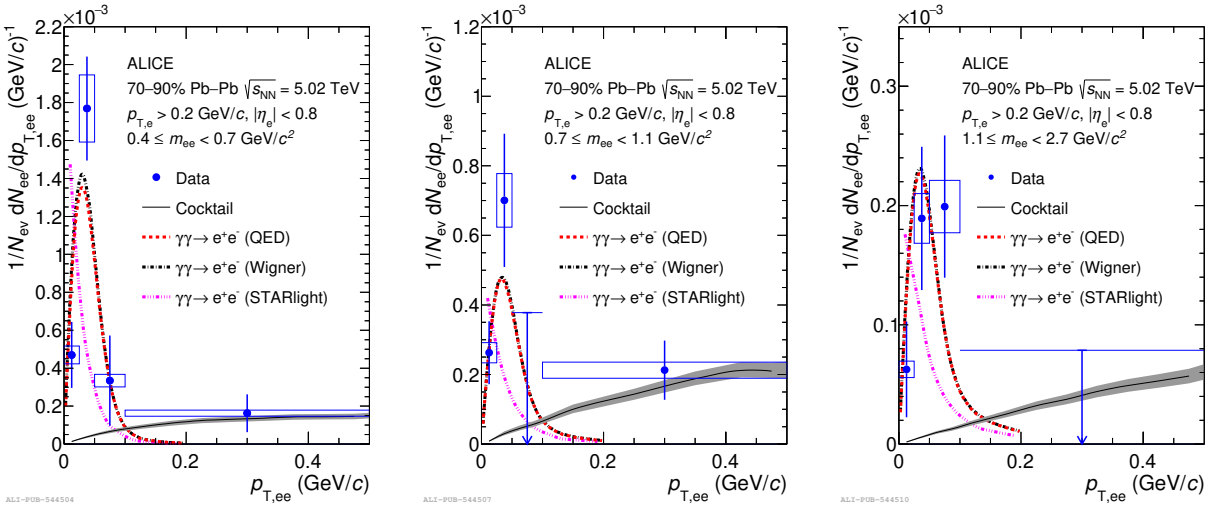

(a) (b) (c)

Figure 3: e^+e^- $p_{\rm T}$ spectra. The data are compared with a cocktail of e^+e^- coming from known hadronic contributions and with several calculations for photoproduction of electron pairs. Vertical bars and boxes represent the data statistic and systematic uncertainties, respectively. Arrows indicate upper limits at 90% confidence level.

3.2 J/ψ photoproduction measurements at forward rapidity

The first measurement of the coherently photoproduced J/ψ y–differential cross section in the dimuon decay channel is now described. The J/ψ raw yield is extracted at forward rapidity in Pb–Pb collisions at $\sqrt{s_{\rm NN}}$ = 5.02 TeV in the centrality class 70–90 % in six different rapidity intervals within the muon spectrometer acceptance $2.5 < y < 4$ as shown in the left panel of Fig. 4. An excess is observed for $p_{\rm T} < 0.3$ GeV/c in all the rapidity intervals. The nuclear modification factor (R_{AA}), used to quantify nuclear effects in heavy-ion collisions with respect to pp collisions, is defined as

$$R_{AA}^{\rm J/\psi} = \frac{Y_{AA}^{\rm J/\psi}}{\langle T_{AA} \rangle \cdot \sigma_{pp}^{\rm J/\psi}}, \tag{1}$$

where $Y_{AA}^{\rm J/\psi}$ is the measured yield of J/ψ in A–A collisions, $\langle T_{AA} \rangle$ the average nuclear overlap function and $\sigma_{pp}^{\rm J/\psi}$ the J/ψ cross section in pp collisions. On the right panel of Fig. 4 the R_{AA} of the J/ψ is displayed. For all rapidity intervals, a strong increase of the R_{AA} for $p_{\rm T} < 0.3$ GeV/c is observed.

The excess yield is estimated by subtracting the hadronic J/ψ yield to the raw J/ψ yield. The estimation of the hadronic yield is data driven and is performed using the J/ψ R_{AA}, the J/ψ cross section in pp collisions at the same center-of-mass energy and the hadronic J/ψ Acceptance-Efficiency ($\mathcal{A} \times \mathcal{E}$) in Pb–Pb collisions. The coherent J/ψ yield is then obtained by correcting the excess from the fraction of incoherently photoproduced J/ψ (f_I) and the fraction of coherent J/ψ from coherently photoproduced ψ(2S) feed-down (f_D). Both f_I and f_D are taken from UPC measurements [17]. The cross section of the coherently photoproduced J/ψ is described as

$$\frac{{\rm d}\sigma_{coh}^{\rm J/\psi}}{{\rm d}y} = \frac{Y_{coh}^{\rm J/\psi}}{{\rm BR}({\rm J/\psi} \to \mu^+\mu^-) \times (\mathcal{A} \times \mathcal{E})_{AA}^{coh{\rm J/\psi}} \times \mathcal{L}_{int} \times \Delta y}, \tag{2}$$

where $Y_{coh}^{\rm J/\psi}$ is the obtained coherently photoproduced J/ψ yield, BR(J/$\psi \to \mu^+\mu^-$) is the branching ratio for the J/ψ to dimuon decay with BR = 5.961 $\pm$ 0.033 %, $(\mathcal{A} \times \mathcal{E})_{AA}^{coh{\rm J/\psi}}$ is the Acceptance-Efficiency of the coherently photoproduced J/ψ in Pb–Pb collisions and $\mathcal{L}_{int}$ = 755.7 $\pm$ 18.9 $\mu{\rm b}^{-1}$ is the integrated luminosity on the Pb–Pb data sample used.

The coherently photoproduced J/ψ y-differential cross section is shown in Fig. 5. The measurement shows a strong rapidity dependence and is compared to several models of J/ψ photoproduction in UPC, adapted to take into account the nuclear overlap. The hot-spot model (GG-hs) [18] proposes that the photon flux is constrained by the impact parameter range for a given class of centrality. In the model suggested by Zha [19], an emitted photon from one nucleus interacts with a pomeron emitted from the spectator region of the other one. The GBW/IIM [5] models offer three scenarios. The first scenario has no relevant modifications with respect to UPC calculations. In the second one, only the photon reaching the spectator nucleon region is considered and the photonuclear cross section remains unmodified. The third scenario includes the same effective photon flux as the second one but the nuclear overlap region is excluded from the calculation of the photonuclear cross section. The three scenarios are displayed on the right panel of Fig. 5. They are all able to qualitatively describe the cross section.

The last ALICE measurement reported in these proceedings is the inclusive J/ψ polarization measured at forward rapidity, $2.5 < y < 4$, in Pb–Pb collisions at $\sqrt{s_{\rm NN}}$ = 5.02 TeV in the 70–90% centrality class. The J/ψ signal is extracted in the dimuon decay channel in six different $\cos\theta$ intervals at low $p_{\rm T}$, $p_{\rm T} < 0.3$ GeV/c as shown in the left panel of Fig. 6. θ is the angle between the muon direction in the J/ψ rest frame and the flight direction of the J/ψ in the Pb–Pb center-of-mass frame. The $\cos\theta$ distribution is fitted with the dimuon angular distribution expressed as

$$W(\cos\theta, \phi) \propto \frac{1}{3 + \lambda_\theta} \left[1 + \lambda_\theta \cos^2\theta + \lambda_\phi \sin^2\theta \cos 2\phi + \lambda_{\theta\phi} \sin 2\theta \cos\phi\right], \tag{3}$$

where λ_ϕ and $\lambda_{\theta\phi}$ are set to zero. The polarization of the J/ψ is transverse when $\lambda_\theta = 1$ and longitudinal when λ_θ = -1. A λ_θ value equal to zero indicates no polarization. The measured angular distribution suggests a transverse polarization of the inclusive J/ψ for $p_{\rm T} < 0.3$ GeV/c as expected for photoproduced J/ψ and from s–channel helicity conservation. As shown on the right panel of Fig. 6, the λ_θ value obtained with the present measurement is close to unity and compatible with the one obtained for coherently photoproduced J/ψ as described in [6].

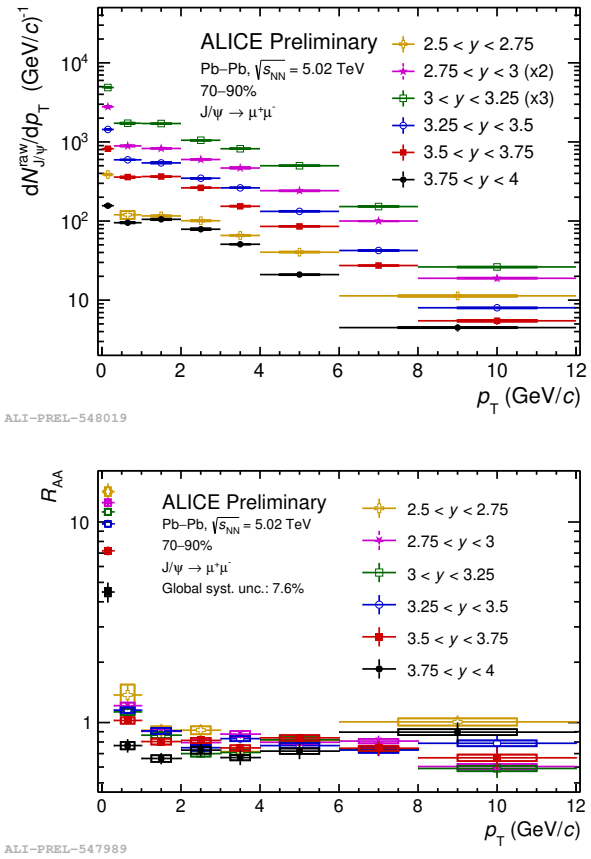

Figure 4: p_{T}–differential raw J/ψ yield (left panel) and J/ψ R_{AA} (right panel) in six different rapidity intervals in Pb–Pb collisions at $\sqrt{s_{\mathrm{NN}}} = 5.02$ TeV in the centrality class 70–90 %. Vertical bars and boxes represent the data statistic and systematic uncertainties, respectively.

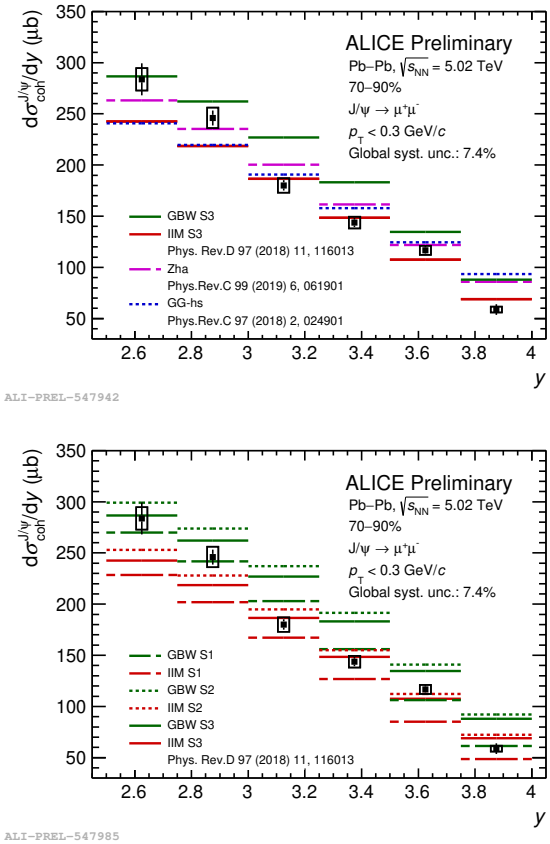

Figure 5: Coherently photoproduced J/ψ cross section as a function of rapidity in Pb–Pb collisions at $\sqrt{s_{\rm NN}} = 5.02$ TeV in the centrality class 70–90 %. Data are compared to several UPC models adapted for Pb–Pb collisions with nuclear overlap. Vertical bars and boxes represent the data statistic and systematic uncertainties, respectively.

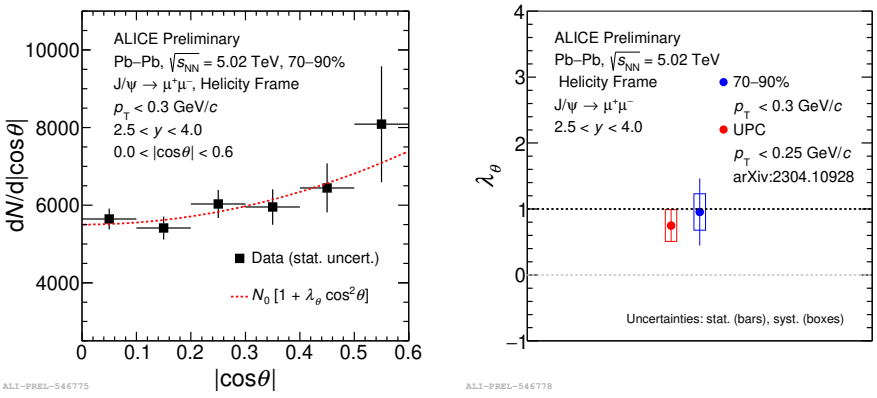

Figure 6: Dimuon angular distribution in semi-peripheral (left panel) and peripheral (right panel) Pb–Pb collisions at $\sqrt{s_{\rm NN}} = 5.02$ TeV and λ_θ value compared to UPC measurements [6]. Vertical bars and boxes represent the data statistic and systematic uncertainties, respectively.

4 Conclusion

An excess of dielectron photoproduction measurement at low p_{T} in the 50–70% and 70–90% centrality classes in Pb–Pb collisions at $\sqrt{s_{\mathrm{NN}}} = 5.02$ TeV was presented. The two-photons models that include the impact parameter dependence of the photon k_{T}–distribution are able to describe the data. In addition, the first y–differential cross section of the coherent J/ψ photoproduction and the first inclusive J/ψ polarization measurements for $p_{\mathrm{T}} < 0.3$ GeV/c in the 70–90% centrality class in Pb–Pb collisions at $\sqrt{s_{\mathrm{NN}}} = 5.02$ TeV have been discussed. Several models developed for UPC and adapted to consider the nuclear overlap are able to qualitatively reproduce the y–differential cross section. The inclusive J/ψ polarization measurement is consistent with a transverse polarization as expected for photoproduced J/ψ and from the s-channel helicity conservation. The measured polarization is in agreement with previous measurements in UPC. The ALICE Run 3 and Run 4 will provide a larger Pb–Pb data sample. The increased statistics will allow one to study the dileptons and J/ψ photoproduction in more central events both at mid and forward rapidities. A better precision on the cross section and the polarization measurements is also expected. Such improvement will be useful to provide further constraints on the theoretical models. Finally, this will help to access other coherently photoproduced excited states like the ψ(2S) and to look for possible final-state medium effects on the photoproduced vector mesons.

Acknowledgments

I would like to thanks the organizers for giving me the opportunity to present ALICE collaboration results at the first edition of the UPC workshop that took place in such a marvelous place as Playa Del Carmen, Mexico.

References

[1] STAR Collaboration, J. Adam, et al. In: *Phys. Rev. Lett.* **121**, 132301 (2018). DOI: 10.1103/PhysRevLett.121.132301.
[2] ATLAS Collaboration, M. Aaboud, et al. In: *Phys. Rev. Lett.* **121**, 212301 (2018). DOI: 10.1103/PhysRevLett.121.212301.
[3] ALICE Collaboration, J. Adam, et al. In: *Phys. Rev. Lett.* 116.22 (2016), p. 222301. DOI: 10.1103/PhysRevLett.116.222301.
[4] ALICE Collaboration, S. Acharya, et al. In: *Phys. Lett. B* 846 (2023), p. 137467. DOI: 10.1016/j.physletb.2022.137467.
[5] M. B. Gay Ducati and S. Martins. In: *Phys. Rev. D* 97.11 (2018), p. 116013. DOI: 10.1103/PhysRevD.97.116013.
[6] ALICE Collaboration, S. Acharya, et al. In: (2023). arXiv: 2304.10928 [nucl-ex].
[7] ALICE Collaboration, K. Aamodt, et al. In: *JINST* 3 (2008), S08002. DOI: {10.1088/1748-0221/3/08/S08002}.
[8] ALICE Collaboration, S. Acharya, et al. In: *J. High Energ. Phys.* 2023, 24 (2023). DOI: 10.1007/JHEP06(2023)024.
[9] W. Zha et al. In: *Phys. Lett. B* 800 (2020), p. 135089. DOI: 10.1016/j.physletb.2019.135089.
[10] J. D. Brandenburg, W. Zha, and Z. Xu. In: *Eur. Phys. J. A* 57.10 (2021), p. 299. DOI: 10.1140/epja/s10050-021-00595-5.
[11] M. Kłusek-Gawenda, W. Schäfer, and A. Szczurek. In: *Phys. Lett. B* 814 (2021), p. 136114. DOI: 10.1016/j.physletb.2021.136114.
[12] S. R. Klein et al. In: *Comput. Phys. Commun.* 212 (2017), pp. 258–268. DOI: 10.1016/j.cpc.2016.10.016.
[13] S. R. Klein. In: *Phys. Rev. C* 97.5 (2018), p. 054903. DOI: 10.1103/PhysRevC.97.054903.
[14] R. Rapp and J. Wambach. In: *Eur. Phys. J. A* 6 (1999), pp. 415–420. DOI: 10.1007/s100500050364.
[15] H. van Hees and R. Rapp. In: *Nucl. Phys. A* 806 (2008), pp. 339–387. DOI: 10.1016/j.nuclphysa.2008.03.009.

[16] R. Rapp. In: *Adv. High Energy Phys.* 2013 (2013), p. 148253. DOI: 10.1155/2013/148253.
[17] ALICE Collaboration, S. Acharya, et al. In: *Phys. Lett. B* 798 (2019), p. 134926. DOI: 10.1016/j.physletb.2019.134926.
[18] J. Cepila, J. G. Contreras, and M. Krelina. In: *Phys. Rev. C* 97.2 (2018), p. 024901. DOI: 10.1103/PhysRevC.97.024901.
[19] W. Zha et al. In: *Phys. Rev. C* 99.6 (2019), p. 061901. DOI: 10.1103/PhysRevC.99.061901.

Novel aspects of particle production in ultra-peripheral collisions

F.C. Sobrinho[1], L.M. Abreu[1,2], C.A. Bertulani[3,4], I. Danhoni[4], F.S. Navarra[1]

[1]Instituto de Física, Universidade de São Paulo, Rua do Matão 1371, Cidade Universitária, - 05508-090, São Paulo, SP, Brazil
[2]Instituto de Física, Universidade Federal da Bahia, Campus Ondina - 40170-115, Salvador, Bahia, Brazil
[3]Department of Physics and Astronomy, Texas A&M University-Commerce, Commerce, Texas 75429, USA
[4]Institut für Kernphysik, Technische Universität Darmstadt, 64289 Darmstadt, Germany

One of the hot topics in hadron physics is the study of the new exotic charmonium states and the determination of their internal struture. Another important topic is the study of the magnetic field produced in relativistic heavy ion collisions and its effects on observables. In this note we show that we can use ultra-peripheral collisions to address both topics. We compute the cross section for the production of the D^+D^- molecular bound state in photon-photon collisions and also the cross section for π^0 production in the target induced by the magnetic field of the projectile. Both cross sections are sizeable and their measurement would be very useful to elucidate the above mentioned questions.

DOI: https://doi.org/10.17161/d02wbn61
Keywords: ultra-peripheral collisions,exotic charmonium,strong magnetic field

1 Introduction

In ultra-peripheral collisions (UPCs) target and projectile do not overlap and stay intact. As a consequence only few particles are produced, the background is reduced and we can study more carefully specific particle production processes, such as those addressed here. These features have been explored at the large hadron collider (LHC) at CERN and at the relativistic heavy ion collider (RHIC) at Brookhaven. In UPCs the elementary processes which contribute to particle production are photon-photon, photon-Pomeron and Pomeron-Pomeron fusion. They are a good environment to search for particles which are more difficult to identify in central collisions [1].

In this work we discuss two processes of particle production, which may be studied in UPCs: production of D^+D^- meson molecules and production of forward pions. In the first we can gain some insight on the nature of these exotic charmonium states and in the second we can measure the magnetic field produced by relativistic heavy ions. In the next section we briefly describe the formalism employed to study the production of charm molecules, in the following section we address forward pion production and at the end we present some conclusions.

2 Production of charm meson molecules

One important research topic in modern hadron physics is the study of the exotic charmonium states [2]. These new mesonic states are not conventional $c\bar{c}$ configurations and their minimum quark content is $c\bar{c}q\bar{q}$. The main question in the field is: are these multiquark states compact tetraquarks or are they large and loosely bound meson molecules? Perhaps the largest fraction of the community tends to believe that they are molecules. One of the frequently invoked arguments is that the masses of almost all these states are very close to thresholds, i.e. to the sum of the masses of two well known meson states [2,3,4]. A genuine tetraquark state could in principle have any mass, including masses far from thresholds. Besides, some problems have been detected in the calculation of tetraquark masses with QCD sum rules [5,6]. Nevertheless, so far there is no conclusive answer.

The production of hadron molecules has been discussed in the context of B decays [3], in e^+e^- collisions, in proton-proton [4,7,8], in proton-nucleus, in central nucleus-nucleus collisions [9] and also in UPCs [10]. In

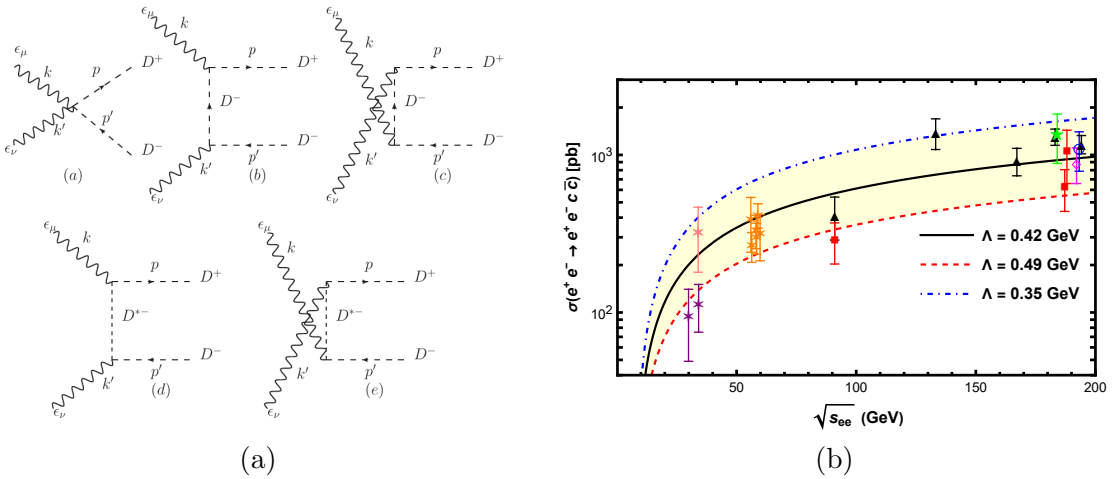

Figure 1 – a) Feynman diagrams for the process $\gamma\gamma \to D^+D^-$. b) Cross sections of the process $e^+e^- \to e^+e^-c\bar{c}$ as a function of the energy $\sqrt{s}$. Points are a compilation of LEP data published in arXiv:hep-ex/0010060 [hep-ex]. Lines represent the results obtained with Eq.(15) adapted to $e^+e^- \to e^+e^-D^+D^-$.

this section we focus on the D^+D^- molecule production in UPCs, but the method employed here is applicable to all molecular states.

The D^+D^- pair is produced from two photons. This process can be described by well known hadronic effective Lagrangians, from which we obtain the pair production amplitude. This amplitude is subsequently projected onto the amplitude for bound state formation. If the properties of the bound state are known, the only unknown in this formalism is the form factor, which must be attached to the vertices to account for the finite size of the hadrons.

We will study the process $\gamma\gamma \to D^+D^-$ with the Lagrangian densities [11]

$$\mathcal{L} = (D_\mu\phi)^*(D^\mu\phi) - m_D^2\phi^*\phi - \frac{1}{4}F_{\mu\nu}F^{\mu\nu}\,, \tag{1}$$

and

$$\mathcal{L} = -ig_{\gamma D^+D^{*-}}F_{\mu\nu}\epsilon^{\mu\nu\alpha\beta}(D^{*-}_\alpha\partial_\beta D^+ - \partial_\beta D^{*-}_\alpha D^+ + D^-\partial_\beta D^{*+}_\alpha - \partial_\beta D^- D^{*+}_\alpha)\,, \tag{2}$$

where

$$D_\mu\phi = \partial_\mu\phi + ieA_\mu\phi\,, \qquad F_{\mu\nu} = \partial_\mu A_\nu - \partial_\nu A_\mu\,, \tag{3}$$

and ϕ, D^* and A_μ represent the pseudoscalar charm meson (with mass m_D), the vector charm meson (with mass m_D^*) and the photon field, respectively. The Feynman rules can be derived from the interaction terms and they yield the Feynman diagrams for the process $\gamma\gamma \to D^+D^-$ shown in Fig. 1a. In the figure we also show the quadrimomenta of the incoming photons $k^\mu = (E_p, 0, 0, \mathbf{k})$, $k'^\mu = (E_{k'}, 0, 0, \mathbf{k}')$ and of the outgoing mesons $p^\mu = (E_p, 0, 0, \mathbf{p})$, $p'^\mu = (E_{p'}, 0, 0, \mathbf{p}')$. The scattering amplitude can be derived from the Feynman rules.

As usual, we include form factors, $F(q)$, in the vertices of the amplitudes. We shall follow [12] and use the monopole form factor given by

$$F(q^2) = \frac{\Lambda^2 - m_{D^{(*)}}^2}{\Lambda^2 - q^2}\,, \tag{4}$$

where q is the 4-momentum of the exchanged meson and Λ is a cut-off parameter. This choice has the advantage of yielding automatically $F(m_D^2) = 1$ and $F(m_{D^*}^2) = 1$ when the exchanged meson is on-shell. The above form is arbitrary but there is hope to improve this ingredient of the calculation using QCD sum rules to calculate the form factor, as done in [13], thereby reducing the uncertainties. Taking the square of the amplitude and the average over the photon polarizations it is straigthforward to calculate the cross section:

$$\sigma = \frac{1}{64\pi^2}\frac{1}{\hat{s}}\sqrt{1 - \frac{4m_D^2}{\hat{s}}}\int |M(\gamma\gamma \to D^+D^-)|^2 d\Omega\,. \tag{5}$$

where $\hat{s} = (k+k')^2$. We emphasize that the only unknown in our calculation is the cut-off parameter Λ. In what follows, we will determine it fitting our cross section to the LEP data on the process $e^+e^- \to e^+e^-c\bar{c}$.

From the D^+D^- pair we can construct a bound state (denoted B). As in [4], we impose phase space constraints on the mesons, forcing them to be "close together". Here we do this through the prescription discussed in [14]. The bound state $|B\rangle$ is defined as

$$\frac{|B\rangle}{\sqrt{2E_B}} \equiv \int \frac{d^3q}{(2\pi)^3}\tilde{\psi}^*(\mathbf{q})\frac{1}{\sqrt{2E_q}}\frac{1}{\sqrt{2E_{-q}}}|\mathbf{q},-\mathbf{q}\rangle, \tag{6}$$

where E_B is the bound state energy, $\mathbf{q}$ is the relative three momentum between D^+ and D^- in the state B, $E_{\pm q}$ are the energies of D^+ and D^- and $\tilde{\psi}(\mathbf{q})$ is the bound state wave function in momentum space. From Eq. (6), we can write the following relation between the amplitudes:

$$\frac{M(\gamma\gamma\to B)}{\sqrt{2E_B}} = \int \frac{d^3q}{(2\pi)^3}\tilde{\psi}^*(\mathbf{q})\frac{1}{\sqrt{2E_{D^+}}}\frac{1}{\sqrt{2E_{D^-}}}M(\gamma\gamma\to D^+D^-), \tag{7}$$

We assume that the $\mathbf{p}\simeq\mathbf{p}'$ and hence $E_{D^+}\simeq E_{D^-}=E_D$. Consequently, the relative momentum $\mathbf{q}=\mathbf{p}-\mathbf{p}'$ is close to zero. Therefore the energy E_D and the amplitude $M(\gamma\gamma\to D^+D^-)$ depend only weakly on $\mathbf{q}$ and can be taken out of the integral. Moreover, since the binding energy is small we have $E_B\simeq 2E_D$ and hence

$$M(\gamma\gamma\to B) = \psi^*(0)\sqrt{\frac{2}{E_B}}M(\gamma\gamma\to D^+D^-)\,. \tag{8}$$

With the amplitude above we calculate the cross section for bound state production:

$$d\sigma = \frac{1}{H}\frac{d^3p_B}{(2\pi)^3}\frac{1}{2E_B}(2\pi)^4\delta^{(4)}(k+k'-p_B)|M(\gamma\gamma\to B)|^2, \tag{9}$$

where p_B is the momentum of the produced bound state and H is the flux factor. In the center of mass frame of the $AA\to AAB$ collision, we have

$$k=(\omega_1,0,0,\omega_1)\,,\qquad k'=(\omega_2,0,0,-\omega_2)\,,\qquad p_B\equiv p+p'=(E_B,0,0,\omega_1-\omega_2)\,, \tag{10}$$

where $E_B=\sqrt{(\omega_1-\omega_2)^2+m_B^2}$ and ω_1 and ω_2 are the energies of the colliding photons. The flux factor is then given by $H=8\omega_1\omega_2$. The integrated cross section reads:

$$\sigma(\omega_1,\omega_2) = \frac{2\pi}{2(4\omega_1\omega_2)}\int\frac{d^3p_B}{2E_B}\delta(E_{CM}-E_B)\delta^{(3)}(\mathbf{k}+\mathbf{k}'-\mathbf{p}_B)\left[\frac{2}{E_B}|\psi(0)|^2|M(\gamma\gamma\to D^+D^-)|^2\right] \tag{11}$$

where $E_{CM}^2=4\omega_1\omega_2$. To complete the calculation we need the bound state wave function at the origin $|\psi(0)|^2$. In [15] a similar bound state of open charm mesons was studied with the Bethe-Salpeter equation and an expression for the wave function was derived. Here we will just quote the final expression needed to calculate $\psi(0)$, which is given by:

$$\psi(0) = \frac{-8\mu\pi g}{(2\pi)^{3/2}}\left(\Lambda_0-\sqrt{2\mu E_b}\arctan\left(\frac{\Lambda_0}{\sqrt{2\mu E_b}}\right)\right)\,,\qquad g^2=\frac{\sqrt{2\mu E_b}}{8\pi\mu^2(\arctan(\frac{\Lambda_0}{\sqrt{2\mu E_b}})-\frac{\sqrt{2\mu E_b}\Lambda_0}{2\mu E_b+\Lambda_0^2})}. \tag{12}$$

In the above expressions μ is the reduced mass ($\mu=m_D/2$), Λ_0 is a cut-off parameter and E_b is the binding energy. We shall follow [16] and assume that $\Lambda_0=1$ GeV. From [16] we see that one can compute the (dynamically generated) mass of a bound state and then determine its binding energy. Knowing μ, E_b and fixing Λ_0, we can use (12) to calculate $\psi(0)$. In what follows our reference value will be obtained using $m_D=1870$ MeV and the mass of the bound state equal to $M_B=3723$ MeV, as found in [16]. With these numbers we get $E_b=17$ MeV and $|\psi(0)|^2=0.008$ GeV^3.

The equivalent photon approximation is well known and it is described in several papers [17]. In general, when the photon source is a nucleus one has to use form factors and the calculation becomes somewhat complicated. Here we will follow [18] and define an UPC in momentum space. The distribution of equivalent photons generated by a moving particle with the charge Ze is [18]:

$$n(\mathbf{q})d^3q = \frac{Z^2\alpha}{\pi^2}\frac{(\mathbf{q}_\perp)^2}{\omega\,q^4}d^3q = \frac{Z^2\alpha}{\pi^2\omega}\frac{(\mathbf{q}_\perp)^2}{\left((\mathbf{q}_\perp)^2+(\omega/\gamma)^2\right)^2}d^3q \tag{13}$$

where q is the photon 4-momentum, $\mathbf{q}_\perp$ is its transverse component, ω is the photon energy and γ is the Lorentz factor of the photon source ($\gamma=\sqrt{s}/2m_p$ where m_p is the proton mass). To obtain the equivalent

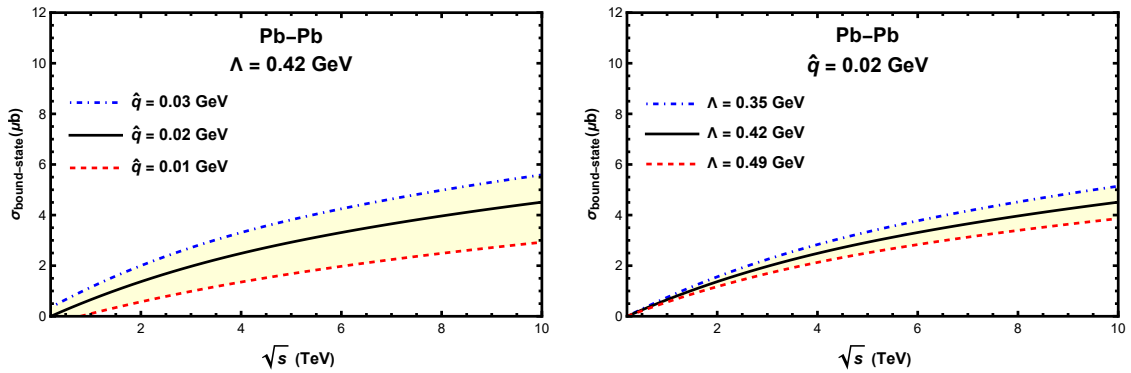

(a) (b)

Figure 2 – Cross sections for D^+D^- bound state production as a function of the energy $\sqrt{s}$. a) Dependence on $\hat{q}$ for fixed Λ. b) Dependence on Λ for fixed $\hat{q}$.

photon spectrum, one has to integrate this expression over the transverse momentum up to some value $\hat{q}$. The value of $\hat{q}$ is given by $\hat{q} = \hbar c/2R$, where R is the radius of the projetile. For Pb, $R \approx 7$ fm and hence $\hat{q} \approx 0.014$ GeV. After the integration over the photon transverse momentum the equivalent photon energy spectrum is given by:

$$n(\omega)d\omega = \frac{2Z^2\alpha}{\pi} \ln\left(\frac{\hat{q}\gamma}{\omega}\right) \frac{d\omega}{\omega}, \tag{14}$$

Because of the approximations [18] the above distribution is valid when the condition $\omega \ll \hat{q}\gamma$ is fullfiled. Using Eq. (14) we can compute the cross sections of free pair production, σ_P, and of bound state production, σ_B. They are given by:

$$\sigma_P(A\,A \to A\,A\,D^+D^-) = \int\limits_{m_D^2/\hat{q}\gamma}^{\hat{q}\gamma} d\omega_1 \int\limits_{m_D^2/\omega_1}^{\hat{q}\gamma} d\omega_2\, \sigma_P(\omega_1,\omega_2)\, n(\omega_1)\, n(\omega_2), \tag{15}$$

$$\sigma_B(A\,A \to A\,A\,B) = \int\limits_{m_D^2/\hat{q}\gamma}^{\hat{q}\gamma} d\omega_1 \int\limits_{m_D^2/\omega_1}^{\hat{q}\gamma} d\omega_2\, \sigma_B(\omega_1,\omega_2)\, n(\omega_1)\, n(\omega_2), \tag{16}$$

where $\sigma_P(\omega_1,\omega_2)$ and $\sigma_B(\omega_1,\omega_2)$ are given by Eqs. (5) (with $\hat{s} = 4\omega_1\omega_2$) and (11) respectively.

In Fig. 1b we show the cross sections for free pair production and compare it to the existing experimental data from LEP [19]. In fact, the LEP data are for $e^+\,e^- \to e^+\,e^-\,c\,\bar{c}$, i.e., the measured final states are D^+D^- and $D^0\bar{D}^0$. We assume that these two final states have the same cross section and, in order to compare with the data, we multiply our cross section $\sigma(e^+\,e^- \to e^+\,e^-\,D^+\,D^-)$ by a factor two. In order to fit these data we will adapt expression (15) to electron-positron collisions. The $\gamma\gamma \to D^+D^-$ cross section is the same but the photon flux from the electron (and also from the positron) and the integration limits are different [1,17,18]. Comparing our formula with these data, we determine the only parameter in the calculation, which is the cut-off Λ. In the figure, the curves are obtained substituting Eqs. (5) and (14) into (15). In the latter $\hat{q} = m_e$. The band is defined by the choice of two limiting values of Λ. In what follows we will use these values to estimate the uncertainty of our results.

In Fig. 2 we present the cross section for bound state production and study its dependence on $\hat{q}$ (Fig. 2a)) and on Λ (Fig. 2b)). It is encouraging to see that at $\sqrt{s_{NN}} \approx 5.02$ TeV we have:

$$\sigma(Pb\,Pb \to Pb\,Pb\,B) = 3.0^{+0.8}_{-1.2}\ \mu b \tag{17}$$

This number should be compared with results found in [10] and in [20]. In those papers, the production cross section of scalar states $X(3940)$ and $X(3915)$ in Pb Pb ultra-peripheral collisions at $\sqrt{s_{NN}} = 5.02$ TeV were calculated and the results were in the range

$$5 \leq \sigma(Pb\,Pb \to Pb\,Pb\,R) \leq 11\ \mu b \tag{18}$$

where R stands for $X(3940)$ or $X(3915)$. These states are heavier than the one considered here but in both papers the X states were treated as meson molecules, as in the present work. It is reassuring to see that, in spite of the differences, the obtained cross sections are of the same order of magnitude.

3 Production of very forward pions

The magnetic field produced in relativistic heavy ion collisions is extremely strong [21,22]. A natural place to study the effects of this field is in ultra-peripheral relativistic heavy ion collisions [1]. Since there is no superposition of hadronic matter, the collision becomes essentially a very clean electromagnetic process.

In [23] it was argued that forward pions are very likely to be produced by magnetic excitation (ME) of the nucleons in the nuclei. The strong classical magnetic field produced by one nucleus induces magnetic transitions, such as $N \to \Delta$ (where N is a proton or a neutron), in the nucleons of the other nucleus. The produced Δ keeps moving together with the nucleus (or very close to it) and then decays almost exclusively through the reaction $\Delta \to N + \pi$. The produced pion has a very large longitudinal momentum and very large rapidity. Since there is no other competing mechanism for forward pion production in UPCs, the observation of these pions would be a signature of the magnetic excitation of the nucleons and also an indirect measurement of the magnetic field. In [23] it was shown that ME has a very large cross section. In [24] we proposed a way to test the classical approximation for the magnetic field. The process discussed in [23], $N \to \Delta \to N'\pi$, was recalculated. In the quantum formalism the transition was induced by photons and not by the classical magnetic field. We computed the same process using a different formalism where the quanta of the field play the important role. We then compared the results obtained with the two formalisms. In this contribution we review the content of [23] and [24] and expand the discussion.

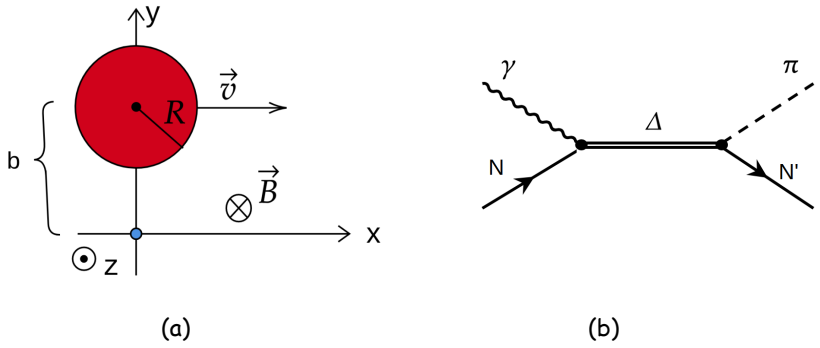

Figure 3 – a) Classical magnetic transition: a moving projectile creates a magnetic field $\vec{B}$ which acts on the target at rest (at the origin of coordinates) flipping its spin. b) Quantum version of the same transition.

A strong magnetic field can convert a hadron into another one with a different spin, by "flipping the constituent quark spins". Let us consider an ultra-peripheral $Pb - p$ collision, where the proton is at rest, as shown in Fig. 3a. Under the influence of the strong magnetic field generated by the moving nucleus, the nucleon is converted into a Δ. For the sake of definiteness let us consider the transition $|p\uparrow\rangle \to |\Delta^+\uparrow\rangle$. The amplitude for this process is given by [23]:

$$a_{fi} = -i \int_{-\infty}^{\infty} e^{iE_{fi}t'} \langle \Delta^+ \uparrow | H_{int}(t') | p \uparrow \rangle \, dt' \tag{19}$$

where $\hbar = 1$ and $E_{fi} = (m_\Delta^2 - m_n^2)/2m_n$, where m_Δ and m_n are the Δ and nucleon masses respectively. The interaction Hamiltonian is given by:

$$H_{int}(t) = -\vec{\mu}.\vec{B}(t) \qquad \text{with} \qquad \vec{\mu} = \sum_{i=u,d} \vec{\mu}_i = \sum_{i=u,d} \frac{q_i}{m_i} \vec{S}_i \tag{20}$$

The magnetic dipole moment of the nucleon is given by the sum of the magnetic dipole moments of the corresponding constituent quarks, q_i and m_i are the charge and constituent mass of the quark of type i and $\vec{S}_i$ is the spin operator acting on the spin state of this quark.

In Fig. 3a we show the system of coordinates, the moving projectile nucleus and target proton at the origin of the coordinates. We assume that the projectile-generated field is the same produced by a point charge. The field is given by [23]:

$$B_z(t) = \frac{1}{4\pi} \frac{qv\gamma(b-y)}{((\gamma(x-vt))^2 + (y-b)^2 + z^2)^{3/2}} \tag{21}$$

In the above expression γ is the Lorentz factor, b is the impact parameter along the y direction, $v \simeq 1$ is the projectile velocity and the projectile electric charge is $q = Ze$. The interaction Hamiltonian acts on spin states. The relevant ones are:

$$|p\uparrow\rangle = \frac{1}{3\sqrt{2}}[udu(\downarrow\uparrow\uparrow + \uparrow\uparrow\downarrow - 2\uparrow\downarrow\uparrow) + duu(\uparrow\downarrow\uparrow + \uparrow\uparrow\downarrow - 2\downarrow\uparrow\uparrow) + uud(\uparrow\downarrow\uparrow + \downarrow\uparrow\uparrow - 2\uparrow\uparrow\downarrow)] \tag{22}$$

$$|\Delta^+\uparrow\rangle = \frac{1}{3}(uud + udu + duu)(\uparrow\uparrow\downarrow + \uparrow\downarrow\uparrow + \downarrow\uparrow\uparrow) \tag{23}$$

With these ingredients we can compute the matrix element $\langle\Delta^+\uparrow|H_{int}|p\uparrow\rangle$. It can be obtained by substituting Eq. (21) into Eq. (20) and then calculating the sandwiches of H_{int} with the spin states given above. The cross section for a single $N \to \Delta$ transition is given by:

$$\sigma = \int |a_{fi}|^2\, d^2b = 2\pi \int |a_{fi}|^2\, b\, db \tag{24}$$

Inserting the matrix elements into (19) and using it in the above expression we find:

$$\sigma = \frac{Z^2e^4}{9\pi m^2}\left(\frac{E_{fi}}{v\gamma}\right)^2 \int_R^\infty \left[K_1\Big(\frac{E_{fi}b}{v\gamma}\Big)\right]^2 b\, db \tag{25}$$

where K_1 is the modified Bessel function. This is the result obtained with the semi-classical approach. For the purpose of comparison it is enough to consider a nucleon as a target. In [23] we computed the cross section for a nucleus-nucleus collision.

In the quantum formalism, the electromagnetic field produced by an ultra-relativistic electric charge is replaced by a flux of photons Now, in a high energy UPC, the projectile becomes a source of almost real photons and we replace the classical field by a collection of quanta. Thus, the cross section of the process shown in Fig. 3b can be written in a factorized form in terms of the photon flux produced by the projectile and the photon-nucleon cross section [1]:

$$\sigma = \int \frac{d\omega}{\omega}\, n(\omega)\, \sigma_{\gamma N\to N\pi}(\omega) \tag{26}$$

In the above expression $n(\omega)$ represents the photon spectrum generated by the source [1]:

$$n(\omega) = \frac{Z^2\alpha}{\pi}\left[2\xi K_0(\xi)K_1(\xi) - \xi^2[K_1^2(\xi) - K_0^2(\xi)]\right], \qquad \xi = \frac{\omega(R_1+R_2)}{\gamma} \tag{27}$$

where ω is the photon energy, R_1 and R_2 are the radii of the projectile and the target, parametrized as $R_A = 1.2\, A^{1/3} fm$, and γ the Lorentz boost in the target frame. From the above expression it is clear that the average energy carried by an emitted photon increases with γ and hence with the collision energy $\sqrt{s}$. In the LHC energy region $\gamma \simeq 1000$ and the photon average energy $\bar{\omega}$ may reach large values, such as $\bar{\omega} \simeq 10$ GeV.

In order to perform the calculation of the total cross section, it is necessary to know the cross section of the process $\gamma N \to N\pi$. In a first approximation $\sigma_{\gamma N\to N\pi}$ can be calculated evaluating the Feynman diagram shown in Fig. 3b. We need a formula which correctly reproduces the behavior of the cross section in the Δ resonance region and which can be extrapolated to higher energies. This is the most important source of uncertainty in the evaluation of (26). A simple parametrization of the π^0 photoproduction cross section can be taken from Jones and Scadron [24]. Knowing $\sigma_{\gamma N\to N\pi}$, we insert it into (26) and evaluate the cross section of the quantum process. The results are then compared with the results obtained with the semi-classical approach (given by (25)) and presented in Fig. 4. The cross sections are plotted as a function of the energy per nucleon (of the projectile) in the laboratory frame $E_{Lab} = \gamma\, m_n$. We compare the curves obtained with (25) (dashed line) and with (26) (solid lines). The band in the lower curve represents the different choices of the decay width Γ. The difference between the curves obtained with (25) and with (26) is small and reaches 9 % at the highest energies. These results suggest that the classical approximation of the magnetic field reproduces most of the photon interaction in photoproduction in high energies.

The produced charged pions will be deviated by the dipole magnets which bend the colliding beams into the two separate beam pipes. However the neutral pions will not be bended by the magnetic field and will fly away following a tangent trajectory and reaching the zero degree calorimeters (ZDC's) which

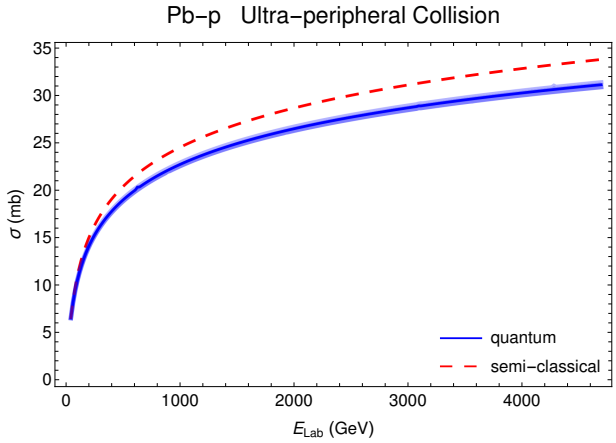

Figure 4 – Cross sections for pion production obtained with the semi-classical formalism, Eq.(25), dashed line, and with the quantum formalism, Eq. (26), solid line.

are part of both the ALICE and the ATLAS set up. They will be measured exactly in the same way as the ultra-forward neutrons produced in the electromagnetic dissociation processes already measured by the ALICE collaboration [25]. In fact, ultra-forward neutral pions have already been measured in proton-proton collisions at $\sqrt{s} = 7$ TeV and in p-Pb collisions at $\sqrt{s} = 5.02$ TeV by the LHCf collaboration [26] but no attempt was made to separate central from peripheral collisions. This might be done in the future.

4 Conclusion

We have calculated the cross section for the production of a D^+D^- molecule in ultra-peripheral collisions. It is $\sigma_B(AA \to AAB) = 3.0^{+0.8}_{-1.2}\ \mu b$ for $\sqrt{s_{NN}} = 5.02$ TeV. This number is consistent with the results obtained for other scalar exotic charmonium molecules in Ref. [10] and in Ref. [20]. The parameters of the calculation are the hadronic form factor cut-off, the maximum transverse momentum of an emitted photon and the binding energy. All these parameters can be constrained by experimental information and/or by calculations and hence the precision of our calculation can be increased. The method used here can be easily applied to other exotic states.

We have also calculated the cross section for the production of very forward pions. We have used two methods, one with a classical magnetic field and the other with equivalent photons. Both methods yield a similar result: a quite large cross section for forward pion production. The neutral pions can in principle be measured. This would improve our knowledge about the validity of the classical approximation and about the strength of the magnetic field created in these collisions.

Acknowledgments

We are deeply indebted to K. Khemchandani and A. Martinez Torres for instructive discussions. This work was partially financed by the Brazilian funding agencies CNPq, CAPES, FAPESP, FAPERGS and INCT-FNA (process number 464898/2014-5). F.S.N. gratefully acknowledges the support from the Fundação de Amparo à Pesquisa do Estado de São Paulo (FAPESP).

References

1. C. A. Bertulani, S. R. Klein and J. Nystrand, Ann. Rev. Nucl. Part. Sci. **55**, 271 (2005).
2. N. Brambilla, S. Eidelman, C. Hanhart, A. Nefediev, C.-P. Shen, C. E. Thomas, A. Vairo, and C.-Z. Yuan, Phys. Rept. **873**, 1 (2020); R. M. Albuquerque, J. M. Dias, K. P. Khemchandani, A. Martinez Torres, F. S. Navarra, M. Nielsen and C. M. Zanetti, J. Phys. G **46**, 093002 (2019).
3. T. W. Wu, Y. W. Pan, M. Z. Liu and L. S. Geng, Sci. Bull. **67**, 1735 (2022); [arXiv:2208.00882 [hep-ph]]; D. Marietti, A. Pilloni and U. Tamponi, Phys. Rev. D **106**, 094040 (2022). Pioneering studies were presented in S. J. Brodsky and F. S. Navarra, Phys. Lett. B **411**, 152 (1997).
4. P. Artoisenet and E. Braaten, Phys. Rev. D **83**, 014019 (2011); Phys. Rev. D **81**, 114018 (2010).
5. W. Lucha, D. Melikhov and H. Sazdjian, Phys. Rev. D **100**, 014010 (2019); Phys. Rev. D **98**, 094011 (2018).
6. R. D. Matheus, F. S. Navarra, M. Nielsen and R. Rodrigues da Silva, Phys. Rev. D **76**, 056005 (2007).
7. A. Esposito, E. G. Ferreiro, A. Pilloni, A. D. Polosa and C. A. Salgado, Eur. Phys. J. C **81**, 669 (2021).
8. C. Bignamini, B. Grinstein, F. Piccinini, A. D. Polosa and C. Sabelli, Phys. Rev. Lett. **103**, 162001 (2009).
9. H. Zhang, J. Liao, E. Wang, Q. Wang and H. Xing, Phys. Rev. Lett. **126**, 012301 (2021); B. Wu, X. Du, M. Sibila and R. Rapp, Eur. Phys. J. A **57**, 122 (2021).
10. B. D. Moreira, C. A. Bertulani, V. P. Goncalves and F. S. Navarra, Phys. Rev. D **94**, 094024 (2016).
11. X. H. Cao, M. L. Du and F. K. Guo, [arXiv:2401.16112 [hep-ph]] and references therein.
12. P. Lebiedowicz, O. Nachtmann and A. Szczurek, Phys. Rev. D **98**, 014001 (2018).
13. M. E. Bracco, M. Chiapparini, F. S. Navarra and M. Nielsen, Prog. Part. Nucl. Phys. **67**, 1019 (2012).
14. An introduction to quantum field theory, M. Peskin and M. Schroeder, Addison-Wesley (1996), p. 150.
15. D. Gamermann, J. Nieves, E. Oset and E. Ruiz Arriola, Phys. Rev. D **81**, 014029 (2010).
16. C. W. Xiao and E. Oset, Eur. Phys. J. A **49**, 52 (2013).
17. G. Baur, K. Hencken, D. Trautmann, S. Sadovsky and Y. Kharlov, Phys. Rept. **364**, 359 (2002).
18. M. I. Vysotskii and E. Zhemchugov, Phys. Usp. **62**, 910 (2019); [arXiv:1806.07238 [hep-ph]].
19. W. Da Silva [DELPHI], Nucl. Phys. B Proc. Suppl. **126**, 185 (2004); A. Csilling [OPAL], AIP Conf. Proc. **571**, 276 (2001). [arXiv:hep-ex/0010060 [hep-ex]].
20. R. Fariello, D. Bhandari, C. A. Bertulani and F. S. Navarra, Phys. Rev. C **108**, 044901 (2023).
21. V. Skokov, A. Y. Illarionov and V. Toneev, Int. J. Mod. Phys. A **24**, 5925 (2009).
22. V. Voronyuk et al., Phys. Rev. C **83**, 054911 (2011); C. S. Machado, F. S. Navarra, E. G. de Oliveira, J. Noronha and M. Strickland, Phys. Rev. D **88**, 034009 (2013).
23. I. Danhoni and F. S. Navarra, Phys. Lett. B **805**, 135463 (2020).
24. I. Danhoni and F. S. Navarra, Phys. Rev. C **103**, 024902 (2021).
25. B. Abelev, et al., ALICE Collaboration, Phys. Rev. Lett. **109**, 252302 (2012).
26. O. Adriani et al., LHCf Collaboration, Phys. Rev. D **94**, 032007 (2016).

Azimuthal angular correlations in lepton pair production in ultra-peripheral heavy ion collisions

Ya-jin Zhou
Key Laboratory of Particle Physics and Particle Irradiation (MOE), Institute of Frontier and Interdisciplinary Science, Shandong University, QingDao, China

The coherent photons induced by relativistic heavy ions are highly linearly polarized, in close analogy to the linear polarization of gluons in a large nucleus. We proposed to measure the photon polarization through azimuthal asymmetries in dilepton production in ultra-peripheral collisions. Our prediction for the asymmetries were soon confirmed by the STAR experiment with high precision. We refined our analysis recently by including the final state soft photon radiation effect beyond the double leading logarithm approximation. The azimuthal asymmetries and acoplanarity at relatively high transverse momentum provide unique opportunities to test the resummation formalism thanks to the extremely high photon flux in UPCs. Our results clearly show the feasibility to access the sub-leading resummation effects in UPCs at the RHIC and LHC.

DOI: https://doi.org/10.17161/z8ryf568
Keywords: linearly polarized photon, resummation, ultra-peripheral collisions

1 Linearly polarized gluons and photons

In high-energy hadron colliders, the partons carry longitudinal momenta as well as transverse momenta, as shown in the left panel of Fig.1, which made it necessary to describe the parton distributions in the framework of transverse momentum dependent (TMD) factorization. Take the gluon TMD as an

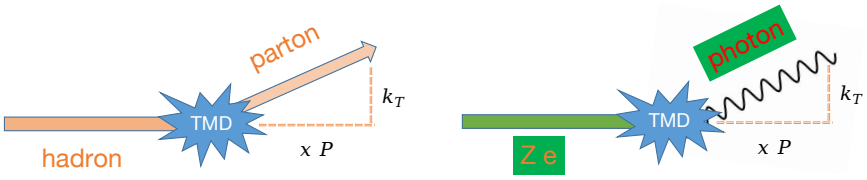

Figure 1 – Illustration diagrams of the longitudinal and transverse momenta of a parton from a hadron (left) and a photon from a heavy ion (right).

example, the leading twist gluon correlator of an unpolarzied hadron can be defined and be parametrized in terms of leading twist TMDs [1]:

$$\int \frac{2dy^- d^2y_\perp}{xP^+(2\pi)^3} e^{ik\cdot y}\langle P|F_+^i(0)U_{[0,y]}F_+^j(y)U'_{[y,0]}|P\rangle\big|_{y^+=0} = \delta_\perp^{ij} f_1(x,\boldsymbol{k}_\perp^2) + \left(\frac{2k_\perp^i k_\perp^j}{\boldsymbol{k}_\perp^2} - \delta_\perp^{ij}\right) h_1^\perp(x,\boldsymbol{k}_\perp^2), \quad (1)$$

where $f_1(x,\boldsymbol{k}_\perp^2)$ and $h_1^\perp(x,\boldsymbol{k}_\perp^2)$ are the unpolarized and linearly polarized gluon TMDs, respectively, and the Wilson lines $U_{[0,y]}$ and $U'_{[y,0]}$ guarantee color gauge invariance. For a hadron moves relativistically along P^+ direction, A^+ component dominant the gauge potential components due to the Lorentz boost effect, so the field tensor reads $F_+^i = \partial_+ A^i - \partial^i A_+$. For a gluon with momentum k, the field tensor $F_+^i \propto k_+ A^i - k^i A_+$. Usually the transverse momentum of the photon $k_\perp$ is much smaller than its longitudinal momentum $k^+ = xP^+$, so it's hard to tell which component is more important in the field

tensor. But at small-x limit $k_\perp^i A^+$ is obviously dominant, so $F_+^i \propto k_\perp^i A^+$ approximately. Compare both sides of Eq.(1), one can conclude that $f_1(x, \boldsymbol{k}_\perp^2) = h_1^\perp(x, \boldsymbol{k}_\perp^2)$, which means that the gluons are totally linearly polarized [2].

On the other hand, it's well known that relativistically moving ions will introduce electromagnetic field, which can be described by equivalent photon approximation (EPA) developed by Fermi [3], Weizäscker and Williams [4,5]. These EPA photons will also carry transverse momenta, as shown in the right panel of Fig.1, and analogy to gluons, they can also be formulated in the context of TMD factorization using Eq.(1). The only difference is that the Wilson lines guaranteeing gauge invariance in the QCD case are not necessary here, since photons carry no charge and are gauge invariant by themselves. In the typical kinematic region of the heavy-ion colliders, e.g., RHIC and LHC, the EPA photons carry small longitudinal momentum fraction x, so based on the analysis in the previous paragraph, it is natural to conclude that the EPA photons are also highly linearly polarized [6].

Linearly polarized gluons can be probed through azimuthal asymmetry effects, so as the linearly polarized photons. Due to the huge QCD background in the central collision area on heavy ion colliders, ultra-peripheral collision (UPC) physics where two heavy ions pass by each other has attracted great interest in recent years. One of the most interesting QED processes in UPCs is $\gamma\gamma \to l^+l^-$, which has been extensively studied for unpolarized photons theoretically and experimentally, and is also an ideal process to probe linearly polarized photon through $\cos 4\phi$ or $\cos 2\phi$ azimuthal asymmetries [6,7], as well as a unique way to test the resummation formalism through the all-order resummation of the soft photon radiation effect [8,9].

2 Probing the linear polarization of photons

The di-lepton production process via photon-photon fusion at the lowest order QED can be written as

$$\gamma_1(x_1 P + \tilde{k}_{1\perp}) + \gamma_2(x_2 \bar{P} + \tilde{k}_{2\perp}) \to l^+(p_1) + l^-(p_2), \tag{2}$$

where P, $\bar{P}$, p_1 and p_2 represent the four momenta of the two nucleons and the leptons in the final state, respectively. The transverse momenta of the photons are represented by $\boldsymbol{k}_{1\perp}$ and $\boldsymbol{k}_{2\perp}$, with $\tilde{k}_{1\perp} = (0, 0, \boldsymbol{k}_{1\perp})$ and $\tilde{k}_{2\perp} = (0, 0, \boldsymbol{k}_{2\perp})$. The leptons are produced in a nearly back-to-back configuration in azimuth with $q_\perp = |\boldsymbol{q}_\perp| \ll P_\perp = |\boldsymbol{P}_\perp|$, with the total transverse momentum $\boldsymbol{q}_\perp \equiv \boldsymbol{p}_{1\perp} + \boldsymbol{p}_{2\perp} = \boldsymbol{k}_{1\perp} + \boldsymbol{k}_{2\perp}$ and $\boldsymbol{P}_\perp = (\boldsymbol{p}_{1\perp} - \boldsymbol{p}_{2\perp})/2$.

The impact-parameter-integrated cross section is written as

$$\frac{d\sigma}{d^2\boldsymbol{p}_{1\perp} d^2\boldsymbol{p}_{2\perp} dy_1 dy_2} = \frac{2\alpha_e^2}{Q^4} \left[\mathcal{A} + \mathcal{B}\cos 2\phi + \mathcal{C}\cos 4\phi\right] \tag{3}$$

where ϕ is the angle between transverse momenta $\boldsymbol{q}_\perp$ and $\boldsymbol{P}_\perp$, as shown in the left panel of Fig.2. y_1 and

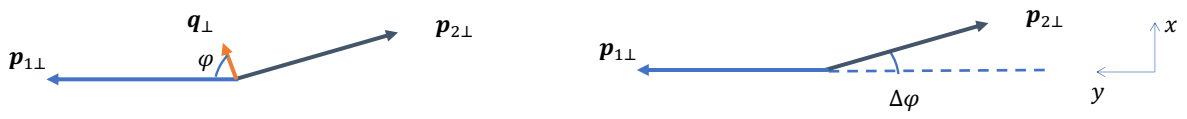

Figure 2 – Azimuthal angle definitions in the transverse plane.

y_2 are lepton rapidities, respectively. Q is the invariant mass of the lepton pair. The coefficients $\mathcal{A}$, $\mathcal{B}$

and $\mathcal{C}$ contain convolutions of photon TMDs,

$$\begin{aligned}\mathcal{A} &= \frac{(Q^2-2m^2)m^2+(Q^2-2P_\perp^2)P_\perp^2}{(m^2+P_\perp^2)^2}x_1x_2\int d^2\boldsymbol{k}_{1\perp}d^2\boldsymbol{k}_{2\perp}\delta^2(\boldsymbol{q}_\perp-\boldsymbol{k}_{1\perp}-\boldsymbol{k}_{2\perp})f_1^\gamma(x_1,\boldsymbol{k}_{1\perp}^2)f_1^\gamma(x_2,\boldsymbol{k}_{2\perp}^2)\\ &+\frac{m^4}{(m^2+P_\perp^2)^2}x_1x_2\int d^2\boldsymbol{k}_{1\perp}d^2\boldsymbol{k}_{2\perp}\delta^2(\boldsymbol{q}_\perp-\boldsymbol{k}_{1\perp}-\boldsymbol{k}_{2\perp})\left[2(\hat{\boldsymbol{k}}_{1\perp}\cdot\hat{\boldsymbol{k}}_{2\perp})^2-1\right]h_1^{\perp\gamma}(x_1,\boldsymbol{k}_{1\perp}^2)h_1^{\perp\gamma}(x_2,\boldsymbol{k}_{2\perp}^2),\end{aligned} \tag{4}$$

$$\begin{aligned}\mathcal{B} &= \frac{4m^2P_\perp^2}{(m^2+P_\perp^2)^2}x_1x_2\int d^2\boldsymbol{k}_{1\perp}d^2\boldsymbol{k}_{2\perp}\delta^2(\boldsymbol{q}_\perp-\boldsymbol{k}_{1\perp}-\boldsymbol{k}_{2\perp})\\ &\times\left\{\left[2(\hat{\boldsymbol{k}}_{2\perp}\cdot\hat{\boldsymbol{q}}_\perp)^2-1\right]f_1^\gamma(x_1,\boldsymbol{k}_{1\perp}^2)h_1^{\perp\gamma}(x_2,\boldsymbol{k}_{2\perp}^2)+\left[2(\hat{\boldsymbol{k}}_{1\perp}\cdot\hat{\boldsymbol{q}}_\perp)^2-1\right]h_1^{\perp\gamma}(x_1,\boldsymbol{k}_{1\perp}^2)f_1^\gamma(x_2,\boldsymbol{k}_{2\perp}^2)\right\},\end{aligned} \tag{5}$$

$$\begin{aligned}\mathcal{C} &= \frac{-2P_\perp^4}{(m^2+P_\perp^2)^2}x_1x_2\int d^2\boldsymbol{k}_{1\perp}d^2\boldsymbol{k}_{2\perp}\delta^2(\boldsymbol{q}_\perp-\boldsymbol{k}_{1\perp}-\boldsymbol{k}_{2\perp})\\ &\times\left[2\left(2(\hat{\boldsymbol{k}}_{2\perp}\cdot\hat{\boldsymbol{q}}_\perp)(\hat{\boldsymbol{k}}_{1\perp}\cdot\hat{\boldsymbol{q}}_\perp)-\hat{\boldsymbol{k}}_{1\perp}\cdot\hat{\boldsymbol{k}}_{2\perp}\right)^2-1\right]h_1^{\perp\gamma}(x_1,\boldsymbol{k}_{1\perp}^2)h_1^{\perp\gamma}(x_2,\boldsymbol{k}_{2\perp}^2),\end{aligned} \tag{6}$$

where a vector with a hat on it means a unit vector, and $f_1^\gamma(x,\boldsymbol{k}_\perp^2)$ and $h_1^{\perp\gamma}(x,\boldsymbol{k}_\perp^2)$ represent the unpolarized and linearly polarized photon TMDs, respectively. One can clearly see that the process has unique angular correlations induced by linearly polarized photons. The longitudinal momentum fractions of the leptons are fixed according to $x_1\simeq\sqrt{(P_\perp^2+m^2)/s}\,(e^{y_1}+e^{y_2})$, $x_2\simeq\sqrt{(P_\perp^2+m^2)/s}\,(e^{-y_1}+e^{-y_2})$, with s, m being the center of mass energy and the lepton mass, respectively.

To sort out the UPC events, we must include the dependence of the impact parameters in the cross-section, and then integrate $\boldsymbol{b}_\perp$ from $2R_{\rm WS}$ to ∞, where $\boldsymbol{b}_\perp$ is the impact parameter between the two colliding nuclei and $R_{\rm WS}$ is the nuclear radius. Once $\boldsymbol{b}_\perp$ is introduced, the incident coherent photon is no longer in the eigenstate of the transverse momentum, and accordingly the photon transverse momenta appearing in the amplitude and conjugate amplitude are no longer the same. We use $\boldsymbol{k}_{1\perp}$, $\boldsymbol{k}_{2\perp}$ and $\boldsymbol{k}'_{1\perp}$, $\boldsymbol{k}'_{2\perp}$ to denote the transverse momenta in the amplitude and in the conjugate amplitude with the constraint $\boldsymbol{k}'_{1\perp}+\boldsymbol{k}'_{2\perp}\equiv\boldsymbol{q}_\perp$. The calculation of the impact parameter dependent cross-section was first developed in Ref. 10, and we extended this calculation to the azimuthally dependent situation [7]. The joint $\boldsymbol{b}_\perp$ and $\boldsymbol{q}_\perp$ dependent di-lepton production cross section at the lowest order of QED can be written as,

$$\frac{d\sigma_0}{d^2\boldsymbol{p}_{1\perp}\boldsymbol{p}_{2\perp}dy_1dy_2d^2\boldsymbol{b}_\perp}=\frac{2\alpha_e^2}{(2\pi)^2Q^4}\left[\mathcal{A}+\mathcal{B}\cos2\phi+\mathcal{C}\cos4\phi\right] \tag{7}$$

with

$$\begin{aligned}\mathcal{A} &= \int[d\mathcal{K}_\perp]\frac{1}{(P_\perp^2+m^2)^2}\Big[-2m^4\cos\left(\phi_{\boldsymbol{k}_{1\perp}}+\phi_{\boldsymbol{k}'_{1\perp}}-\phi_{\boldsymbol{k}_{2\perp}}-\phi_{\boldsymbol{k}'_{2\perp}}\right)+m^2\left(Q^2-2m^2\right)\\ &\times\cos\left(\phi_{\boldsymbol{k}_{1\perp}}-\phi_{\boldsymbol{k}'_{1\perp}}-\phi_{\boldsymbol{k}_{2\perp}}+\phi_{\boldsymbol{k}'_{2\perp}}\right)+P_\perp^2\left(Q^2-2P_\perp^2\right)\cos\left(\phi_{\boldsymbol{k}_{1\perp}}-\phi_{\boldsymbol{k}'_{1\perp}}+\phi_{\boldsymbol{k}_{2\perp}}-\phi_{\boldsymbol{k}'_{2\perp}}\right)\Big],\end{aligned} \tag{8}$$

$$\mathcal{B} = \int[d\mathcal{K}_\perp]\frac{8m^2P_\perp^2}{\left(P_\perp^2+m^2\right)^2}\cos\left(\phi_{\boldsymbol{k}_{1\perp}}-\phi_{\boldsymbol{k}_{2\perp}}\right)\cos\left(\phi_{\boldsymbol{k}'_{1\perp}}+\phi_{\boldsymbol{k}'_{2\perp}}-2\phi\right), \tag{9}$$

$$\mathcal{C} = \int[d\mathcal{K}_\perp]\frac{-2P_\perp^4}{\left(P_\perp^2+m^2\right)^2}\cos\left(\phi_{\boldsymbol{k}_{1\perp}}+\phi_{\boldsymbol{k}'_{1\perp}}+\phi_{\boldsymbol{k}_{2\perp}}+\phi_{\boldsymbol{k}'_{2\perp}}-4\phi\right), \tag{10}$$

where $\phi_{\boldsymbol{k}_i}$ is the azimuthal angle between $\boldsymbol{P}_\perp$ and $\boldsymbol{k}_i$, and the shorthand notation represent

$$\begin{aligned}\int[d\mathcal{K}_\perp] &\equiv \int d^2\boldsymbol{k}_{1\perp}d^2\boldsymbol{k}_{2\perp}d^2\boldsymbol{k}'_{1\perp}d^2\boldsymbol{k}'_{2\perp}e^{i(\boldsymbol{k}_{1\perp}-\boldsymbol{k}'_{1\perp})\cdot\boldsymbol{b}_\perp}\delta^2(\boldsymbol{k}_{1\perp}+\boldsymbol{k}_{2\perp}-\boldsymbol{q}_\perp)\delta^2(\boldsymbol{k}'_{1\perp}+\boldsymbol{k}'_{2\perp}-\boldsymbol{q}_\perp)\\ &\times\mathcal{F}(x_1,\boldsymbol{k}_{1\perp}^2)\mathcal{F}(x_2,\boldsymbol{k}_{2\perp}^2)\mathcal{F}(x_1,\boldsymbol{k}_{1\perp}'^2)\mathcal{F}(x_2,\boldsymbol{k}_{2\perp}'^2).\end{aligned} \tag{11}$$

One notices that the $\boldsymbol{b}_\perp$ dependence enters the cross section via the phase $e^{i(\boldsymbol{k}_{1\perp}-\boldsymbol{k}'_{1\perp})\cdot\boldsymbol{b}_\perp}$. The function $\mathcal{F}(x_1,\boldsymbol{k}_\perp^2)$ describes the probability amplitude for a photon carrying a given momentum. It can be related to the normal photon TMD:

$$|\mathcal{F}(x_1,\boldsymbol{k}_\perp^2)|^2=x_1f_1^\gamma(x_1,\boldsymbol{k}_\perp^2)=\frac{Z^2\alpha_e}{\pi^2}\boldsymbol{k}_\perp^2\left[\frac{F(\boldsymbol{k}_\perp^2+x^2M_p^2)}{(\boldsymbol{k}_\perp^2+x^2M_p^2)}\right]^2, \tag{12}$$

where F is the Woods-Saxon form factor

$$F(\boldsymbol{k}^2) = \int d^3\boldsymbol{r} e^{i\boldsymbol{k}\cdot\boldsymbol{r}} \frac{\rho^0}{1+\exp\left[(r-R_{\rm WS})/d\right]}. \tag{13}$$

Considering higher-order QED contributions, the lepton pair will acquire a recoil transverse momentum through the final state soft photon radiation effect, which will cause large logarithmic terms $\alpha_e^n \ln^{2n}\frac{Q^2}{m^2}$. These large logarithms can be resumed by using the Collins-Soper formalism [11] and result in Sudakov factor in the exponential in the impact parameter space. At the one-loop order the Sudakov factor reads [12,13],

$$\mathrm{Sud}(\mu_r, r_\perp) = \frac{\alpha_e}{\pi}\ln\frac{Q^2}{m^2}\ln\frac{P_\perp^2}{\mu_r^2}, \tag{14}$$

with $\mu_r = 2e^{-\gamma_E}/r_\perp$. The cross section is then expressed as

$$\frac{d\sigma}{d^2\boldsymbol{p}_{1\perp}d^2\boldsymbol{p}_{2\perp}dy_1dy_2d^2\boldsymbol{b}_\perp} = \int \frac{d^2\boldsymbol{r}_\perp}{(2\pi)^2} e^{i\boldsymbol{r}_\perp\cdot\boldsymbol{q}_\perp} e^{-\mathrm{Sud}(r_\perp)} \int d^2\boldsymbol{q}'_\perp e^{-i\boldsymbol{r}_\perp\cdot\boldsymbol{q}'_\perp} \frac{d\sigma_0(\boldsymbol{q}'_\perp)}{d\mathcal{P}.\mathcal{S}.}, \tag{15}$$

where $d\mathcal{P}.\mathcal{S}. = d^2\boldsymbol{p}_{1\perp}d^2\boldsymbol{p}_{2\perp}dy_1dy_2d^2\boldsymbol{b}_\perp$ being the phase space factor. The azimuthal asymmetries, i.e., the average value of the $\cos(n\phi)$, is defined as

$$\langle\cos(n\phi)\rangle = \frac{\int \frac{d\sigma}{d\mathcal{P}.\mathcal{S}.}\cos(n\phi)\, d\mathcal{P}.\mathcal{S}.}{\int \frac{d\sigma}{d\mathcal{P}.\mathcal{S}.} d\mathcal{P}.\mathcal{S}.}. \tag{16}$$

Numerical results for $\langle\cos(4\phi)\rangle$ of the di-electron and di-muon production in UPCs at RHIC and LHC energy regions have been calculated in Refs. 6 and 7, where we predicted significant $\langle\cos(4\phi)\rangle$ asymmetries as shown in Fig.3. This effect was promotely verified by RHIC STAR collaboration [14]. As

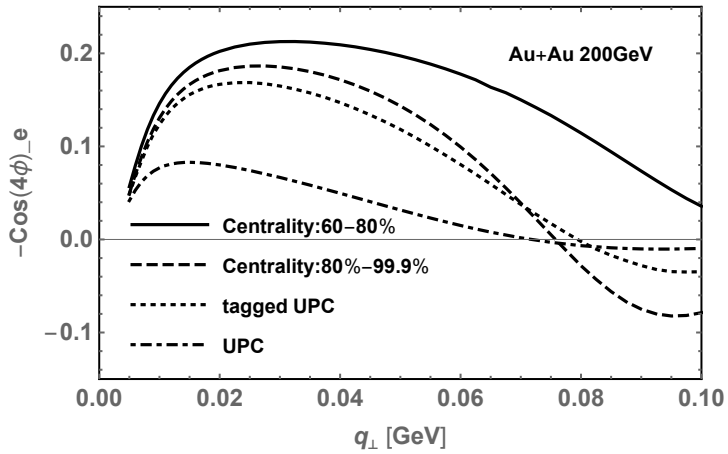

Figure 3 – Estimates of the $\cos 4\phi$ asymmetry as the function of $q_\perp$ for different centralities at $\sqrt{s} = 200$ GeV. The electron and positron rapidities and transverse momenta are integrated over the regions [-1, 1] and [0.2, 0.4] GeV, respectively.

demonstrated in Table 1, the measured $\langle\cos(4\phi)\rangle$ for the process $\gamma\gamma \to e^+e^-$ aligns excellently with the theoretical predictions. A similar theoretical outcome for the centrality of 60%-80% was obtained based on the Wigner distributions of photons [15].

3 Toward the precision test of the resummation formalism

Besides directly measuring the $q_\perp$ distribution, the azimuthal angular decorrelation of the lepton pair is often experimentally studied as well. When the lepton pair acquires finite transverse momentum, they will deviate from the exact back-to-back configuration in the transverse momentum space, and the deviation degree is measured by the so called acoplanarity with the definition being $\alpha = |\Delta\phi|/\pi$. The azimuthal angle $\Delta\phi$ is defined as $\Delta\phi = \pi - (\phi_1 - \phi_2)$ where ϕ_1 and ϕ_2 represent the azimuthal angles for the lepton and the anti-lepton, respectively, as shown in the right panel of Fig.2. We fix the direction of

	Measured $\|2\langle\cos(4\phi)\rangle\|$	QED calculated $2\langle\cos(4\phi)\rangle$
UPC	16.8%±2.5%	−16.5%
60%-80%	27%±6%	−34.5%

Table 1: Theoretical and experimental results for $\cos(4\phi)$ asymmetry in di-electron UPC production in Au+Au collisions at RHIC with $\sqrt{s} = 200$ GeV. The invariant mass Q is integrated over [0.45, 0.76] GeV, the electron and positron rapidities $y_{1,2}$ are integrated over [-1, 1], and the total transverse momentum of the dielectron $q_\perp$ is integrated over [0, 0.1] GeV. The individual electron transverse momentum is restricted to $P_\perp > 0.2$ GeV.

the electron transverse momentum $\boldsymbol{p}_{1\perp}$ to be Y-axis. The acoplanarity can then be easily reconstructed by the ratio of q_x (the component of $\boldsymbol{q}_\perp$ aligned with X-axis) and $P_\perp$.

In this section we discuss the soft photon radiation effect on both the azimuthal asymmetries and the acoplanarity. In the previous studies the soft photon contributions were resummed within double leading logarithm approximation [12,16]. In Ref. 9, we extended the resummation formalism to the next to leading logarithm accuracy and investigate its phenomenological consequence as well. We will briefly demonstrate the steps and results later.

3.1 The calculation of the azimuthal asymmetries

First we discuss the azimuthal asymmetry. It's already known that the final state soft photon radiation effect introduces modifications to the cross sections, as discussed in the preceding section, thereby influencing the magnitude of azimuthal asymmetries. While on the other hand, the photon that is emitted also induce a recoil effect on the lepton that emit it. Given that the lepton pair are nearly back-to-back in the transverse plane, the recoil effect will also cause azimuthal asymmetry [17,13]. The cross section with soft photon radiation can be written as [18,19,17,13]

$$\frac{d\sigma(q_\perp)}{d\mathcal{P}.\mathcal{S}.} = \int d^2q'_\perp \frac{d\sigma_0(q'_\perp)}{d\mathcal{P}.\mathcal{S}.} S(q_\perp - q'_\perp) \tag{17}$$

and the soft factor is expanded at the leading order as [13],

$$S(l_\perp) = \delta(l_\perp) + \frac{\alpha_e}{\pi^2 l_\perp^2} \left\{c_0 + 2\,c_2 \cos 2\phi + 2\,c_4 \cos 4\phi + ...\right\}, \tag{18}$$

with $c_0 \approx \ln\frac{Q^2}{m_\pi^2}$, $c_2 \approx \ln\frac{Q^2}{m_\pi^2} + \delta y \sinh\delta y - 2\cosh^2\frac{\delta y}{2}\ln[2(1+\cosh\delta y)]$... when the final-state particle mass is much smaller than $P_\perp$. $\delta y = y_1 - y_2$ is the difference between the two rapidities of the leptons.

The final state soft photon radiation mainly occurs in regions where the lepton transverse momentum $q_\perp$ is relatively large, for instance, when $q_\perp$ is larger than about 100 MeV. The previous section mainly focused on the small transverse momentum area, so we ignore the azimuthal asymmetry effect induced by the recoiled lepton there. In this section we will cover the [0, 200] MeV region for $q_\perp$, where both coherent photons and final state radiations can play their important roles. Considering an all-order resummation of the large logarithmic terms, the cross section is also expressed as Eq.(15) in the transverse position space, except that here we will include the subleading logarithm contributions.

We used the soft collinear effective theory (SCET) [20,21,22,23,24] and the standard Renormalization Group (RG) methods to derive the resummation formula that includes the effects of lepton mass resummation to all orders. We re-factorize the massive hard and soft functions in the small mass limit ($Q \gg q_\perp \gtrsim m$), where the massive hard function $H(Q,m,\mu)$ is factorized as the product of the massless hard function $H(Q,\mu)$ and collinear jet functions $J(m,\mu)$, and the massive soft function $S(l_\perp,\Delta y,m,\mu)$ is factorized as the product of the massless soft function $S(l_\perp,\Delta y,\mu)$ and collinear-soft functions $C_i(k_{i,\perp},p_T,m,\mu)$. The resulting differential cross section is given by

$$\begin{aligned}\frac{d\sigma(q_\perp)}{d\mathcal{P}.\mathcal{S}.} &= H(Q,\mu)J^2(m,\mu)\int d^2\boldsymbol{l}_\perp d^2\boldsymbol{k}_{1\perp} d^2\boldsymbol{k}_{2\perp} \frac{d\sigma_0(\boldsymbol{q}_\perp - \boldsymbol{l}_\perp - \boldsymbol{k}_{1\perp} - \boldsymbol{k}_{2\perp})}{d\mathcal{P}.\mathcal{S}.} \\ &\times S(l_\perp,\Delta y,\mu) C_1(k_{1\perp},P_\perp,y_1,m,\mu) C_2(k_{2\perp},P_\perp,y_2,m,\mu),\end{aligned} \tag{19}$$

where the hard function $H(Q,\mu)$ comes from the matching from QED to the low energy effective theory, and the corresponding anomalous dimension is written as

$$\Gamma_H = \frac{\alpha_e}{4\pi}\left(8\ln\frac{Q^2}{\mu^2} - 12\right). \tag{20}$$

One can calculate the next-to-leading order contributions to the collinear jet function, the massive soft function, and the collinear-soft function, respectively, and obtain the corresponding anomalous dimensions which satisfying the consistency relations for the RG evolutions. The results are:

$$\Gamma_S = \frac{\alpha_e}{4\pi}\left(8\ln\frac{\mu^2 r_\perp^2}{b_0^2} + 8\ln\cos^2\phi_r - 8\ln\frac{1+\cosh\Delta y}{2}\right), \tag{21}$$

$$\Gamma_J = \frac{\alpha_e}{4\pi}\left(4\ln\frac{\mu^2}{m^2} + 2\right), \tag{22}$$

$$\Gamma_{C_{1,2}} = \frac{\alpha_e}{4\pi}\left(-4\ln\frac{4P_\perp^2\mu^2 r_\perp^2}{b_0^2 m^2} + 4 - 4\ln\cos^2\phi_r \pm 4i\pi\right). \tag{23}$$

Then the Sudakov factor is given by

$$\mathrm{Sud}(r_\perp) = \int_{\mu_r}^{Q}\frac{d\mu}{\mu}\Gamma_H + 2\int_{\mu_r}^{m}\frac{d\mu}{\mu}\Gamma_J + \int_{\mu_r}^{\mu_r m/(2P_\perp)}\frac{d\mu}{\mu}\Gamma_{C_1} + \int_{\mu_r}^{\mu_r m/(2P_\perp)}\frac{d\mu}{\mu}\Gamma_{C_2}. \tag{24}$$

In the numerical calculation we compute both the azimuthal independent cross sections and the $\cos 2\phi$ and $\cos 4\phi$ asymmetries for the unrestricted UPC case, where the impact parameter is simply integrated over $[2R_{\mathrm{WS}}, \infty)$. The nucleus radius R_{WS} is taken as 6.4 fm for Au and 6.68 fm for Pb. We show the azimuthal independent cross section, $\langle(\cos 2\phi)\rangle$ and $\langle(\cos 4\phi)\rangle$ as a function of $q_\perp$ at RHIC energy in Fig.4 and at LHC energy in Fig.5. In these curves the blue solid lines stand for the fully resummed results from Eq.(24), and the purple dashed lines represent the results with the azimuthal dependent part being treated at the one-loop order. The results without soft photon radiation effect are shown with the dotted orange lines. It is evident that the perturbative tail, which is a result of soft photon radiation, takes precedence over the lepton pair transverse momentum spectrum, which is determined by the coherent photon primordial $k_\perp$ distribution, at relatively high $q_\perp$ values. The most remarkable contrast is the $\cos 2\phi$ asymmetry, which is ignorable at the lowest order due to the negligible mass of electron, exhibit large values at high $q_\perp$. In the current study, we resum both the azimuthally independent and dependent leading logarithms into an exponential form. In the previous works [17,13], the azimuthally independent logarithm was resummed to all orders and the azimuthally dependent component was treated at the fixed order. We make a numerical comparison of the results derived from these two resummation schemes. The difference between these two approaches becomes apparent in the large $q_\perp$ region, especially for the $\cos 4\phi$ azimuthal asymmetry. It would be intriguing to examine such a resummation effect in future experiments.

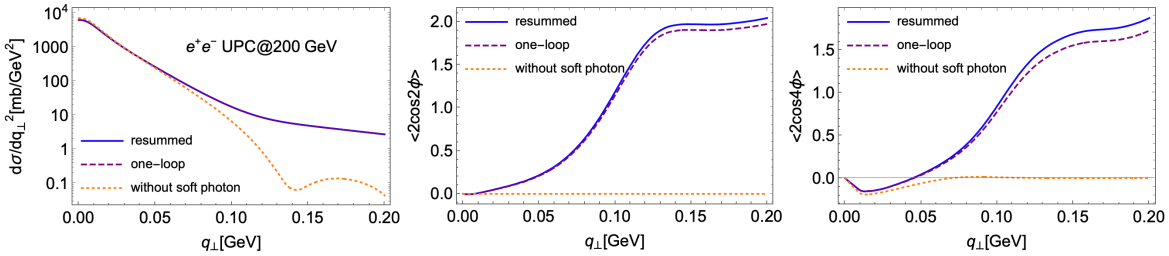

Figure 4 – Di-electron production in unrestricted UPCs in Au+Au collisions at the RHIC energy. The following kinematic cuts are imposed: the rapidities $|y_{1,2}| < 1$, transverse momentum $P_\perp > 200$ MeV, and the invariant mass of the electron pair 450 MeV $< Q <$ 760 MeV. Left panel: azimuthal averaged differential cross sections; middle panel: $\langle\cos(2\phi)\rangle$ azimuthal asymmetry; right panel: $\langle\cos(4\phi)\rangle$ azimuthal asymmetry.

3.2 The calculation of the acoplanarity

In the coordinate frame that we established at the beginning of this section, the acoplanarity can be constructed as $\alpha = q_x/P_\perp$. Integrate Eq.(15) over q_y one obtain the q_x dependent cross section,

$$\begin{aligned}\frac{d\sigma}{dq_x d^2\boldsymbol{P}_\perp dy_1 dy_2 d^2\boldsymbol{b}_\perp} &= \int dq_y \frac{dr_y dr_x}{(2\pi)^2} e^{i(r_x q_x + r_y q_y)} e^{-\mathrm{Sud_a}(r_x, r_y)} \int dq_x' dq_y' \; e^{-i(r_x q_x' + r_y q_y')} \frac{d\sigma_0(q_\perp')}{d\mathcal{P}.\mathcal{S}.} \\ &= \int \frac{dr_x}{2\pi} e^{i r_x q_x} e^{-\mathrm{Sud_a}(r_x, r_y=0)} \int dq_x' dq_y' \; e^{-i r_x q_x'} \frac{d\sigma_0(q_\perp')}{d\mathcal{P}.\mathcal{S}.},\end{aligned} \tag{25}$$

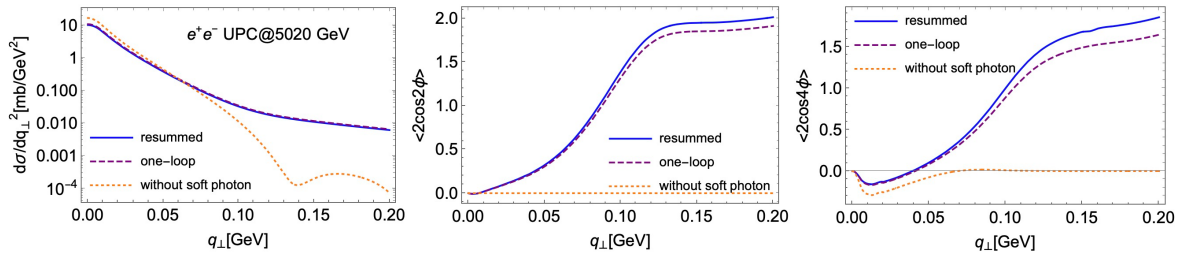

Figure 5 – Di-electron production in unrestricted UPCs in Pb+Pb collisions at the LHC energy. The following kinematic cuts are imposed: the rapidities $|y_{1,2}| < 0.8$ and the invariant mass of the di-electron 10 GeV $< Q <$ 20 GeV. Left panel: azimuthal averaged differential cross sections; middle panel: $\langle\cos(2\phi)\rangle$ azimuthal asymmetry; right panel: $\langle\cos(4\phi)\rangle$ azimuthal asymmetry.

where the leading logarithm contribution to the Sudakov factor $\mathrm{Sud_a}(r_x)$ is given by,

$$\mathrm{Sud_a}(r_x) = \frac{\alpha_e}{2\pi}\left[\ln^2\frac{Q^2}{\mu_{rx}^2} - \ln^2\frac{m^2}{\mu_{rx}^2}\theta(m-\mu_{rx})\right], \tag{26}$$

with $\mu_{rx} = 2e^{-\gamma_E}/r_x$.

A one-dimensional Fourier transform is made in Eq.(25) since the acoplanarity is a one-dimensional observable, apart from the two-dimensional $q_\perp$ distribution situation. When deriving the momentum space expression of the Sudakov factor $\mathrm{Sud_a}(l_x)$, the Y-component of the soft photon transverse momentum has to be integrated over the whole available phase-space region. Given this we need to re-derive a factorization formula instead of integrating out q_y from the resummed $q_\perp$ distribution. At the small α limit, the factorization formula is written as,

$$\begin{aligned}\frac{d\sigma(\alpha)}{d\mathcal{P}.\mathcal{S}.} =& 2P_\perp H(Q,\mu)J^2(m,\mu)\int dl_x dk_{1,x} dk_{2,x}\frac{d\sigma_0(q_x - l_x - k_{1x} - k_{2x})}{d\mathcal{P}.\mathcal{S}.} \\ &\times S(l_x,\Delta y,\mu,\nu)C_1(k_{1x},P_\perp,y_1,m,\mu,\nu)C_2(k_{2x},P_\perp,y_2,m,\mu,\nu),\end{aligned} \tag{27}$$

where the hard and jet functions are the same with those in Eq.(19) since they are independent of specific observables. Implementing the one-dimensional Fourier transformation, one can define the r_x dependent soft and soft-collinear functions, calculate them to the next-to-leading order, and finally resummed to all orders as exponential form. The Sudakov factor is expressed as

$$\begin{aligned}\mathrm{Sud}_a(r_x) &= \int_{\mu_{rx}}^{Q}\frac{d\mu}{\mu}\Gamma_H + 2\int_{\mu_{rx}}^{m}\frac{d\mu}{\mu}\Gamma_J\theta(m-\mu_{rx}) \\ &= \frac{\alpha_e}{2\pi}\left[\left(\ln^2\frac{Q^2}{\mu_{rx}^2} - 3\ln\frac{Q^2}{\mu_{rx}^2}\right) - \left(\ln^2\frac{m^2}{\mu_{rx}^2} - \ln\frac{m^2}{\mu_{rx}^2}\right)\theta(m-\mu_{rx})\right].\end{aligned} \tag{28}$$

We numerically calculated the acoplanarity distributions for di-muon production at CMS and di-electron production at ATLAS to compare with their measurements[25,26], as shown in Fig.6. We only made estimations for the 0n0n events in which no neutron emission from the excited nuclei in the forward region to avoid possible contributions from incoherent photons. In this case the impact parameter dependence of the cross section is weighted with a $b_\perp$ distribution (see the review article[27] and references therein),

$$2\pi\int_{2R}^{\infty} b_\perp db_\perp P^2(b_\perp)d\sigma(b_\perp,\ ...), \tag{29}$$

where the probability $P(b_\perp)$ for the 0n event for Pb can be parameterized as[28],

$$P(b_\perp) = \exp\left[-\frac{(17.4\ \mathrm{fm})^2}{b_\perp^2}\right]. \tag{30}$$

The theoretical results align with both ATLAS and CMS low α data. Yet, in the region of relatively high α, our numerical estimations noticeably exceed the experimental data. Compared with the results with double logarithm resummation, the inclusion of the leading single logarithm contribution into the resummation formalism somewhat reduces the discrepancy between the experimental data and the theoretical estimation, although the deviations are still apparent. The potential reason for this needs further investigation. We also reconstruct the acoplanarity using the resummed $q_\perp$ distribution as given in Eq. (15). The observed α distribution evidently does not support this approach as shown with the yellow dotted lines in Fig. 6.

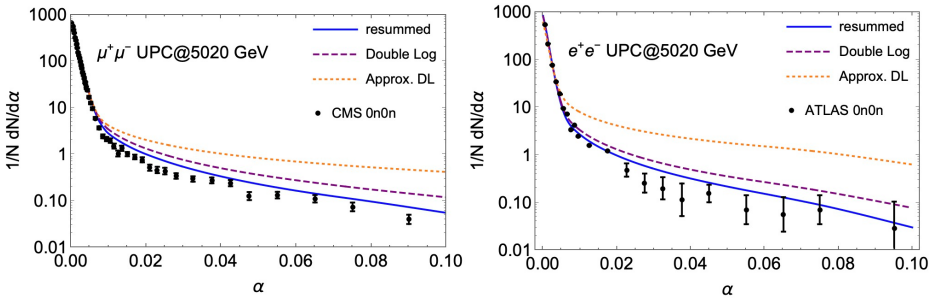

Figure 6 – The normalized cross sections of di-lepton production as a function of α. Left panel: di-muon production at CMS for the 0n0n case, with the kinematic cutoff: $|y_{1,2}| < 2.4$, $P_\perp > 3.5$ GeV and 8 GeV $< Q <$ 60 GeV. Right panel: di-electron production at ATLAS for the 0n0n case, with the kinematic cutoff: $|y_{1,2}| < 0.8$ and 10 GeV $< Q <$ 20 GeV. The blue solid lines stand for the fully resummed results from Eq.(28), and the purple dashed lines represent the leading double logarithm resummed results obtained using Eq.(26). The acoplanarity distribution reconstructed from the resummed $q_\perp$ distribution given by Eq. (15) and Eq. (14) is shown with the dotted orange lines. The CMS data displayed in the figure is taken from Ref. 25 and the ATLAS data is taken from Ref. 26.

4 Summary

In heavy ion ultra-peripheral collisions, the photons induced by the relativistically moving ions carry small transverse momenta. In TMD physics, it's known that gluons carrying small transverse momenta in an unpolarized hadron are linearly polarized. Through the analogy of QED to QCD, we derived that coherent photons are highly linearly polarized, and further predicted that this effect can be measured through the $\cos 2\phi$ and $\cos 4\phi$ azimuthal asymmetries in di-lepton production in UPCs. We calculated the azimuthal asymmetries in the RHIC energy region, and consistent data for the $\cos 4\phi$ asymmetry in di-electron production process was soon obtained by the STAR collaboration, confirming that coherent photons are linearly polarized.

During the calculation, the contribution from high-order QED corrections cannot be ignored, especially when $q_\perp$ is relatively large. These contributions not only change the size of the cross sections so that change the magnitude of the azimuthal asymmetries, but also will induce azimuthal asymmetries by themselves due to the recoil effect. We revisited the di-lepton production process in UPCs, focusing on the final state soft photon radiation resummation effect on two observables: azimuthal asymmetry and acoplanarity. The results show that at relatively high $q_\perp$, the soft photon radiation effect is dominant, and will significantly change the shapes of azimuthal asymmetries, particularly, it will induce large $\cos 2\phi$ asymmetry which is absent at leading order due to the negligible electron mass. It is worth mentioning that the resummation of soft photon radiation has different formulas for the $q_\perp$ distribution and acoplanarity, because Fourier transforms were performed in different dimensions. Within the SCET framework, we carry out the resummation for these two observables to all orders, including the contribution of single logarithm. Our results show that the $q_\perp$-dependent azimuthal asymmetry is not very sensitive to the subleading resummation effect, while the all order one-dimensional resummation is necessary to describe the acoplanarity data of ATLAS and CMS. Although our calculation still has some deviation from the experimental data, the result after including the single logarithm is much closer to the experiment. Therefore, the di-lepton production process in UPCs provides a good opportunity to test the resummation formula through the measurement of angular correlation.

Acknowledgments

The author thanks D.Y. Shao, C. Li, C. Zhang and J. Zhou for their contributions to the papers [6,7,9] which make this presentation possible.

References

1. P. J. Mulders and J. Rodrigues, Phys. Rev. D **63**, 094021 (2001) doi:10.1103/PhysRevD.63.094021 [arXiv:hep-ph/0009343 [hep-ph]].
2. A. Metz and J. Zhou, Phys. Rev. D **84**, 051503 (2011) doi:10.1103/PhysRevD.84.051503 [arXiv:1105.1991 [hep-ph]].

3. E. Fermi, Z. Phys. **29**, 315-327 (1924) doi:10.1007/BF03184853
4. C. F. von Weizsacker, Z. Phys. **88**, 612-625 (1934) doi:10.1007/BF01333110
5. E. J. Williams, Phys. Rev. **45**, 729-730 (1934) doi:10.1103/PhysRev.45.729
6. C. Li, J. Zhou and Y. J. Zhou, Phys. Lett. B **795**, 576-580 (2019) doi:10.1016/j.physletb.2019.07.005 [arXiv:1903.10084 [hep-ph]].
7. C. Li, J. Zhou and Y. J. Zhou, Phys. Rev. D **101**, no.3, 034015 (2020) doi:10.1103/PhysRevD.101.034015 [arXiv:1911.00237 [hep-ph]].
8. D. Y. Shao, C. Zhang, J. Zhou and Y. J. Zhou, Phys. Rev. D **107**, no.3, 036020 (2023) doi:10.1103/PhysRevD.107.036020 [arXiv:2212.05775 [hep-ph]].
9. D. Y. Shao, C. Zhang, J. Zhou and Y. j. Zhou, Phys. Rev. D **108**, no.11, 116015 (2023) doi:10.1103/PhysRevD.108.116015 [arXiv:2306.02337 [hep-ph]].
10. M. Vidovic, M. Greiner, C. Best and G. Soff, Phys. Rev. C **47**, 2308-2319 (1993) doi:10.1103/PhysRevC.47.2308
11. J. C. Collins, D. E. Soper and G. F. Sterman, Nucl. Phys. B **250**, 199-224 (1985) doi:10.1016/0550-3213(85)90479-1
12. S. Klein, A. H. Mueller, B. W. Xiao and F. Yuan, Phys. Rev. Lett. **122**, no.13, 132301 (2019) doi:10.1103/PhysRevLett.122.132301 [arXiv:1811.05519 [hep-ph]].
13. Y. Hatta, B. W. Xiao, F. Yuan and J. Zhou, Phys. Rev. D **104**, no.5, 054037 (2021) doi:10.1103/PhysRevD.104.054037 [arXiv:2106.05307 [hep-ph]].
14. J. Adam *et al.* [STAR], Phys. Rev. Lett. **127**, no.5, 052302 (2021) doi:10.1103/PhysRevLett.127.052302 [arXiv:1910.12400 [nucl-ex]].
15. M. Kłusek-Gawenda, W. Schäfer and A. Szczurek, Phys. Lett. B **814**, 136114 (2021) doi:10.1016/j.physletb.2021.136114 [arXiv:2012.11973 [hep-ph]].
16. S. Klein, A. H. Mueller, B. W. Xiao and F. Yuan, Phys. Rev. D **102**, no.9, 094013 (2020) doi:10.1103/PhysRevD.102.094013 [arXiv:2003.02947 [hep-ph]].
17. Y. Hatta, B. W. Xiao, F. Yuan and J. Zhou, Phys. Rev. Lett. **126**, no.14, 142001 (2021) doi:10.1103/PhysRevLett.126.142001 [arXiv:2010.10774 [hep-ph]].
18. S. Catani, M. Grazzini and A. Torre, Nucl. Phys. B **890**, 518-538 (2014) doi:10.1016/j.nuclphysb.2014.11.019 [arXiv:1408.4564 [hep-ph]].
19. S. Catani, M. Grazzini and H. Sargsyan, JHEP **06**, 017 (2017) doi:10.1007/JHEP06(2017)017 [arXiv:1703.08468 [hep-ph]].
20. C. W. Bauer, S. Fleming, D. Pirjol and I. W. Stewart, Phys. Rev. D **63**, 114020 (2001) doi:10.1103/PhysRevD.63.114020 [arXiv:hep-ph/0011336 [hep-ph]].
21. C. W. Bauer and I. W. Stewart, Phys. Lett. B **516**, 134-142 (2001) doi:10.1016/S0370-2693(01)00902-9 [arXiv:hep-ph/0107001 [hep-ph]].
22. C. W. Bauer, D. Pirjol and I. W. Stewart, Phys. Rev. D **65**, 054022 (2002) doi:10.1103/PhysRevD.65.054022 [arXiv:hep-ph/0109045 [hep-ph]].
23. C. W. Bauer, S. Fleming, D. Pirjol, I. Z. Rothstein and I. W. Stewart, Phys. Rev. D **66**, 014017 (2002) doi:10.1103/PhysRevD.66.014017 [arXiv:hep-ph/0202088 [hep-ph]].
24. M. Beneke, A. P. Chapovsky, M. Diehl and T. Feldmann, Nucl. Phys. B **643**, 431-476 (2002) doi:10.1016/S0550-3213(02)00687-9 [arXiv:hep-ph/0206152 [hep-ph]].
25. A. M. Sirunyan *et al.* [CMS], Phys. Rev. Lett. **127**, no.12, 122001 (2021) doi:10.1103/PhysRevLett.127.122001 [arXiv:2011.05239 [hep-ex]].
26. G. Aad *et al.* [ATLAS], JHEP **2306**, 182 (2023) doi:10.1007/JHEP06(2023)182 [arXiv:2207.12781 [nucl-ex]].
27. M. L. Miller, K. Reygers, S. J. Sanders and P. Steinberg, Ann. Rev. Nucl. Part. Sci. **57**, 205-243 (2007) doi:10.1146/annurev.nucl.57.090506.123020 [arXiv:nucl-ex/0701025 [nucl-ex]].
28. A. J. Baltz and M. Strikman, Phys. Rev. D **57**, 548-549 (1998) doi:10.1103/PhysRevD.57.548 [arXiv:hep-ph/9705220 [hep-ph]].

Light-by-light scattering in ultraperipheral collisions of heavy ions with future FoCal and ALICE 3 detectors

Antoni Szczurek
Institute of Nuclear Physics, PAN, Kraków
ul Radzikowskiego 152, PL-31-342 Kraków, Poland and
Rzeszów University
ul. Pigonia 1, PL-35-310 Rzeszów, Poland

I present possible future studies of light-by-light scattering using FoCal@ALICE and ALICE 3 detectors. Different mechanisms are discussed. The PbPb→PbPb$\gamma\gamma$ cross section is calculated within equivalent photon approximation in the impact parameter space. Several differential distributions are presented and discussed. We predict cross section in the (mb-b) range for typical ALICE 3 cuts, a few orders of magnitude larger than for the current ATLAS or CMS experiments. We also consider the two-π^0 background which can, in principle, be eliminated at the new kinematical range for the ALICE 3 measurements by imposing dedicated cuts on diphoton transverse momentum and/or so-called vector asymmetry.

DOI: https://doi.org/10.17161/758g5k69
Keywords: photon-photon scattering, ultrarelativistic heavy-ion processes, equivalent photon approximation, ALICE-3

1 Introduction

Photon-photon scattering is purely quantal effect (does not happen in classical physics). It was studied experimentally only recently in ultrarelativistic heavy ion collisions by the ATLAS [1] and CMS [2] collaborations. The ATLAS and CMS kinematics implies that box diagrams are the dominant reaction mechanism and other mechanisms are practically negligible. In [3] we studied whether this process could be sudied at lower photon-photon energies using ALICE and LHCb infrastructures. The experimental analysis using ALICE data is in progress. At the lower energies one should worry about background due to $\gamma\gamma \to \pi^0\pi^0$ process. We have worked out there techniques how to reduce the unwanted background [3].

The $\gamma\gamma \to \gamma\gamma$ is also interesting in the context of searching for effects beyond Standard Model [7].

Recently we explored what future FoCal [8] and ALICE 3 [9] detectors could do in this respect [4]. A forward electromagnetic calorimeter is planned as an upgrade to the ALICE experiment for data-taking in 2027-2029 at the LHC. The FoCal will cover pseudorapidities range of $3.4 < \eta < 5.8$. Runs 5 and 6 will measure more than five times the present Pb-Pb luminosity. This increase of luminosity, in combination with improved detector capabilities, will enable the success of the physical program planned for ALICE 3. A significant feature of FoCal and ALICE 3 programs is the ability to measure photons in relatively low transverse momenta.

In our recent paper we have taken into account different mechanisms for photon-photon scattering: boxes, VDM-Regge, two-gluon exchanges, meson (resonance) contributions, see Fig.1.

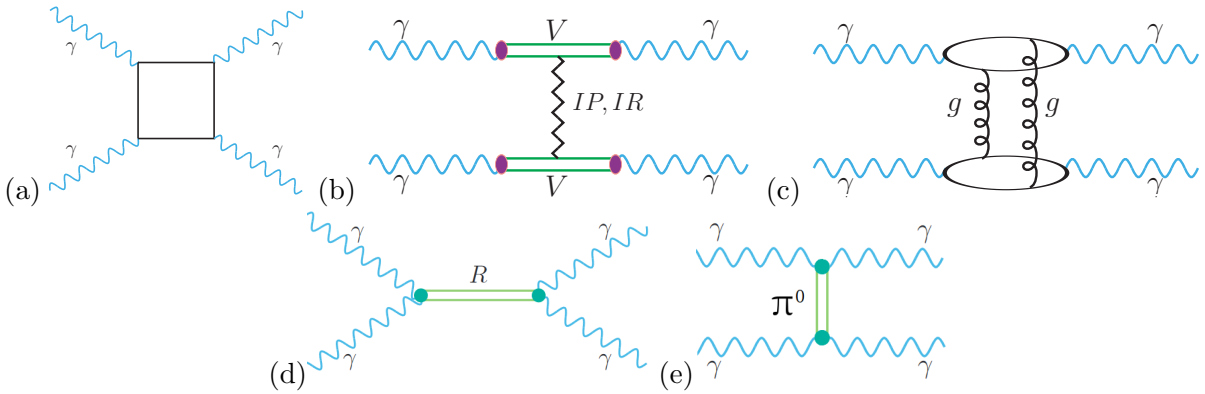

Figure 1 – Feynman diagrams representing different mechanisms: a) fermionic loops, b) VDM-Regge, c) 2-gluon exchange, d) low mass resonances in s-channel, e) π^0-exchange in t-channel.

Here, in this presentation, I will present the main results from [4].

2 Sketch of the formalism

Here we briefly discuss only some selected problems discussed in detail in [4].

2.1 Double-photon hadronic fluctuations

This component was calculated for the first time in [6] assuming vector dominance model. In this approach, the amplitude for the process is given as:

$$\begin{aligned}\mathcal{M} &= \Sigma_{i,j} C_i^2 C_j^2 \left(C_{I\!P} \left(\frac{s}{s_0}\right)^{\alpha_{I\!P}(t)-1} F(t) + C_{I\!R} \left(\frac{s}{s_0}\right)^{\alpha_{I\!R}(t)-1} F(t) \right) , \\ &+ \Sigma_{i,j} C_i^2 C_j^2 \left(C_{I\!P} \left(\frac{s}{s_0}\right)^{\alpha_{I\!P}(u)-1} F(u) + C_{I\!R} \left(\frac{s}{s_0}\right)^{\alpha_{I\!R}(u)-1} F(u) \right) . \end{aligned} \tag{1}$$

In the simplest version of the model $i,j = \rho^0, \omega, \phi$ (only light vector mesons are included). The couplings C_i, C_j describe the $\gamma \to V_{i/j}$ transitions that are calculated based on vector meson dilepton width. $C_{I\!P}$ and $C_{I\!R}$ are extracted from the Regge factorization hypothesis.

It was shown in [6] that the component is concentrated mainly at small photon transverse momenta which at not too small subsystem energies corresponds to $z \approx \pm 1$. The Regge trajectories are usually written in a linear form:

$$\begin{aligned}\alpha_{I\!P}(t/u) &= \alpha_{I\!P}(0) + \alpha'_{I\!P} t/u , \\ \alpha_{I\!R}(t/u) &= \alpha_{I\!R}(0) + \alpha'_{I\!R} t/u . \end{aligned} \tag{2}$$

These linear forms are valid at not too large $|t|$ or $|u|$. At large $|t|$ or $|u|$ the energy dependent factors are artificially small. In [4] we proposed to smoothly switch off the t/u dependent terms in (2) at $t, u \sim$ -0.5 GeV^2. The actual place where it should be done is not known precisely. Another option would be to use $\sqrt{t/u}$ trajectories [11,10].

We also analyzed in [4] whether more heavy vector mesons such as J/ψ can give a sizeable contribution.

For the double J/ψ fluctuations (both photons fluctuate into virtual J/ψ mesons) we took the following Ansatz for the helicity conserving amplitude:

$$\begin{aligned}\mathcal{M}^{J/\psi J/\psi}_{VDM} &= g^2_{J/\psi} C^{J/\psi}_{I\!P} \left(\frac{s}{s_0}\right)^{\alpha^{J/\psi J/\psi}_{I\!P}(t)-1} F^H_{J/\psi J/\psi I\!P}(t) F^H_{J/\psi J/\psi I\!P}(t) \\ &+ g^2_{J/\psi} C^{J/\psi}_{I\!P} \left(\frac{s}{s_0}\right)^{\alpha^{J/\psi J/\psi}_{I\!P}(u)-1} F^H_{J/\psi J/\psi I\!P}(u) F^H_{J/\psi J/\psi I\!P}(u) . \end{aligned} \tag{3}$$

In this case (double J/ψ fluctuations) only pomeron can be exchanged (no subleading reggeons are possible due to the pure $c\bar{c}$ structure of J/ψ). In this case, for simplicity, we took the simplified trajectories as

$$\alpha^{J/\psi J/\psi}_{I\!P}(t) = \alpha^{J/\psi J/\psi}_{I\!P}(u) = \alpha^{J/\psi J/\psi}_{I\!P}(0) . \tag{4}$$

Here the t/u dependencies of the trajectories are totally ignored. In numerical calculations we take $\alpha^{J/\psi J/\psi}_{I\!P}(0) = 1.3 - 1.4$ (typical hard pomeron). Since the J/ψ mesons are far off-mass-shell and more compact than light vector mesons the form factors are different than those for light vector mesons. In [4] we took them in the following form:

$$F^H_{J/\psi J/\psi I\!P}(t) = \exp\left(\frac{t - m^2_{J/\psi}}{\Lambda^2_{J/\psi}}\right) , \tag{5}$$

$$F^H_{J/\psi J/\Psi I\!P}(u) = \exp\left(\frac{u - m^2_{J/\psi}}{\Lambda^2_{J/\psi}}\right) . \tag{6}$$

These form factors are normalized to 1 on the meson (J/ψ) mass shell. One could also use monopole form factors in this context. The form factors reduce the $J/\psi J/\psi$ component of the amplitude in comparison

to light vector meson components. However, due to compactness of J/ψ we expect $\Lambda_{J/\psi}$ to be large. In [4]we took $\Lambda_{J/\psi} = 2$ GeV for illustration, the actual value is not precisely known. Also, the normalization parameter $C_{I\!P}^{J/\psi}$ is not well known. It is expected to be smaller than for light vector mesons.

In a similar fashion, one could include one J/ψ fluctuation and one light vector meson fluctuation. However, there the choice of trajectories is not clear. We will leave the discussion of these components for future studies.

In [4] we assumed the following helicity structure of the double photon hadronic fluctuation amplitude:

$$\mathcal{M}^{(t)}_{\lambda_1\lambda_2\to\lambda_3\lambda_4} = A(t)\,\delta_{\lambda_1\lambda_3}\delta_{\lambda_2\lambda_4}\,, \tag{7}$$

$$\mathcal{M}^{(u)}_{\lambda_1\lambda_2\to\lambda_3\lambda_4} = A(u)\,\delta_{\lambda_1\lambda_4}\delta_{\lambda_2\lambda_3}\,. \tag{8}$$

$A(t)$ and $A(u)$ are given explicitly in (1). Then the total double VDM amplitude, including t and u processes, reads:

$$\mathcal{M}^{VDM}_{\lambda_1\lambda_2\to\lambda_3\lambda_4} = \frac{1}{\sqrt{2}}\left(\mathcal{M}^{VDM,(t)}_{\lambda_1\lambda_2\to\lambda_3\lambda_4} + \mathcal{M}^{VDM,(u)}_{\lambda_1\lambda_2\to\lambda_3\lambda_4}\right)\,. \tag{9}$$

Now we can add amplitudes for different mechanisms:

$$\mathcal{M}_{\lambda_1\lambda_2\to\lambda_3\lambda_4} = \mathcal{M}^{boxes}_{\lambda_1\lambda_2\to\lambda_3\lambda_4} + \mathcal{M}^{VDM}_{\lambda_1\lambda_2\to\lambda_3\lambda_4} + \mathcal{M}^{\pi^0}_{\lambda_1\lambda_2\to\lambda_3\lambda_4} + \dots\,. \tag{10}$$

In the following, we shall discuss the sum of the larger two components (boxes and VDM) and quantify their interference effects.

2.2 Cross section for nuclear UPC

In [4] the nuclear cross section is calculated using equivalent photon approximation (EPA) in the b-space. In this approach, the diphoton cross section can be written as (see [6]):

$$\begin{aligned}\frac{d\sigma(PbPb\to PbPb\gamma\gamma)}{dy_{\gamma_1}dy_{\gamma_2}dp_{t,\gamma}} &= \int \frac{d\sigma_{\gamma\gamma\to\gamma\gamma}(W_{\gamma\gamma})}{dz} N(\omega_1,b_1)N(\omega_2,b_2)S^2_{abs}(b) \\ &\times\; d^2b d\bar{b_x} d\bar{b_y} \frac{W_{\gamma\gamma}}{2}\frac{dW_{\gamma\gamma}dY_{\gamma\gamma}}{dy_{\gamma_1}dy_{\gamma_2}dp_{t,\gamma}}dz\,,\end{aligned} \tag{11}$$

where $\bar{b}_x = (b_{1x}+b_{2x})/2$ and $\bar{b}_y = (b_{1y}+b_{2y})/2$. The relation between $\vec{b}_1$, $\vec{b}_2$ and impact parameter: $b = |\vec{b}| = \sqrt{|\vec{b}_1|^2 + |\vec{b}_2|^2 - 2|\vec{b}_1||\vec{b}_2|\cos\phi}$. Absorption factor $S^2_{abs}(b)$ in [4]was calculated as:

$$S^2_{abs}(b) = \Theta(b - b_{max}) \tag{12}$$

or

$$S^2_{abs}(b) = exp\left(-\sigma_{NN}T_{AA}(b)\right)\,, \tag{13}$$

where σ_{NN} is the energy-dependent nucleon-nucleon interaction cross section, and $T_{AA}(b)$ is related to the so-called nuclear thickness, $T_A(b)$,

$$T_{AA}\left(|\vec{b}|\right) = \int d^2\rho T_A\left(\vec{\rho}-\vec{b}\right)T_A\left(\rho\right), \tag{14}$$

and the nuclear thickness is obtained by integrating the nuclear density

$$T_A\left(\vec{\rho}\right) = \int \rho_A\left(\vec{r}\right)dz, \qquad \vec{r} = (\vec{\rho}, z)\,, \tag{15}$$

where ρ_A is the nuclear charge distribution. The nuclear photon fluxes $N(\omega_1, b_1)$ and $N(\omega_2, b_2)$ are calculated using realistic charge distribution.

Very often the UPC results are shown only with a sharp cut on the impact parameter, usually taken as a sum of two radii of the nuclei, i.e. $b > R_A + R_B \approx 14$ fm for Pb+Pb collisions. Due to the no homogeneous nuclear charge distribution, it seems to be more reasonable to use the absorption factor given by Eq. (13).

2.3 Background contribution

As shown in [3] the $\gamma\gamma \to \pi^0(\to 2\gamma)\pi^0(\to 2\gamma)$ reaction constitutes a background for the measurement of $\gamma\gamma \to \gamma\gamma$ process at intermediate $M_{\gamma\gamma}$.

In our approach the calculation of the background proceeds in three steps. First, the cross section for $\gamma\gamma \to \pi^0\pi^0$ is calculated (for details, see [12]). Next the cross section for $AA \to AA\pi^0\pi^0$ is computed in the equivalent photon approximation in an analogous way as described in the subsection above. In the last step the simulation of both π^0 decays is performed and joint distributions of one photon from the first π^0 and one photon from the second π^0 are constructed.

3 Selected results

3.1 Elementary cross section

In Fig. 2 we show $d\sigma/dz$ for $\gamma\gamma \to \gamma\gamma$ for (a) boxes, (b) double hadronic fluctuation calculated within the VDM-Regge approach and (c) the π^0-exchange calculated as in Ref. [5]. Results are presented for five energies in the range of $(1-50)$ GeV. At larger energies, the VDM-Regge contribution peaks at $z = \pm 1$. On the other hand, the π^0 exchange contribution has minima at $z = \pm 1$ which is due to the structure of corresponding vertices. The latter contribution is relatively small. In general, the box contributions dominate, especially for low photon-photon scattering energies. At larger scattering energies ($W_{\gamma\gamma} > 2$ GeV) the VDM-Regge contribution competes with the box contributions only at $z \sim \pm 1$. Can one expect sizeable interference effects of both mechanisms?

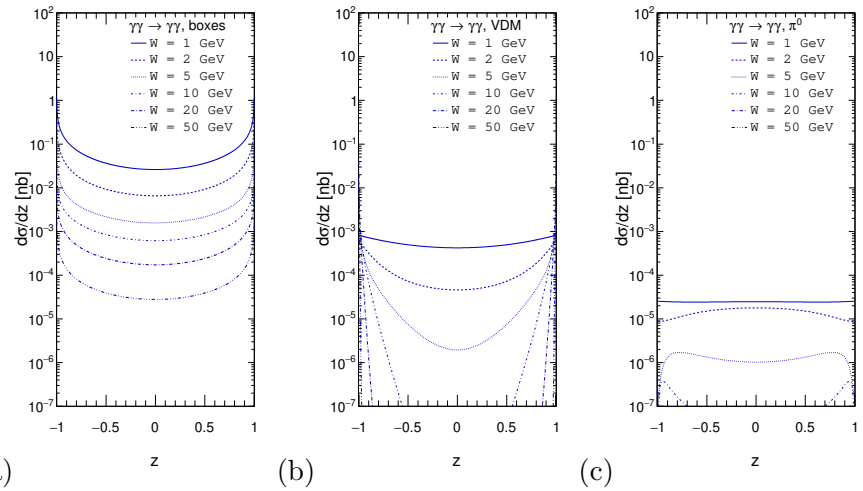

Figure 2 – $cos(\theta)$ distributions for (a) boxes, (b) double hadronic fluctuations and (c) π^0 exchange for different photon-photon collision energies $W = 1, 2, 5, 10, 20, 50$ GeV.

Now we wish to discuss briefly the second biggest contribution: double photon fluctuations. The results are shown in Fig.2. In [4] we includeed both light vector mesons ρ^0, ω, ϕ) as well as J/ψ (one or two) as described in the theoretical section. Our results, for two collision energies ($W = 2, 5$ GeV), are shown in Fig.3. The dotted line includes only light vector meson fluctuations, the dashed line in addition double J/ψ fluctuations and the solid line all combinations of photon fluctuations. The inclusion of J/ψ meson fluctuations leads to an enhancement of the cross section at -0.5 $< z <$ 0.5. The enhancement is more spectacular for larger collision energy. The corresponding cross section there is, however, much smaller than the box contribution (see Fig.2).

Now we wish to concentrate on how the elementary cross section changes when adding the box and VDM-Regge contributions. This is shown in Fig.4. The red line represents the incoherent sum, while the blue line includes also interference effects. In this calculation, the so-called "sqrt" trajectories [10,11] were used. one observes a negative interference effect. Adding the remaining contributions would lead to additional deviations.

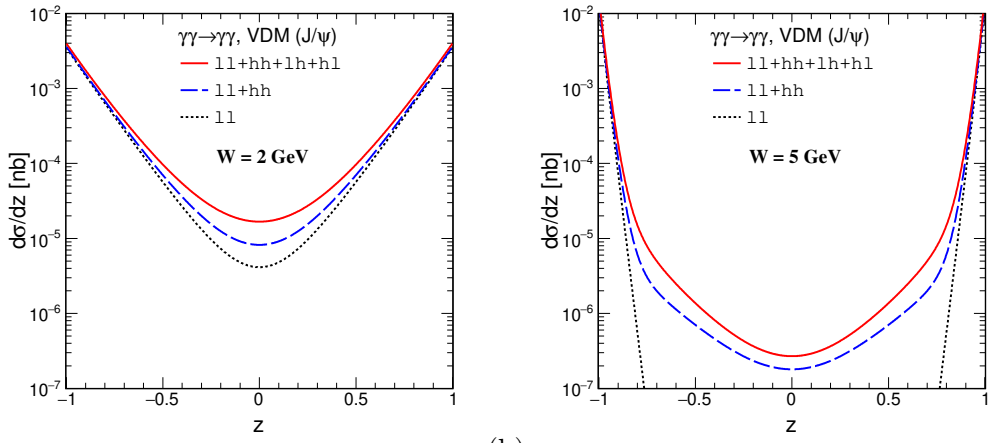

(a) (b)

Figure 3 – Modification of $d\sigma/dz$ due to inclusion of fluctuations of photons into virtual J/ψ mesons: (a) $W = 2$ GeV, (b) $W = 5$ GeV. The top solid line includes all components (light (l) and heavy (h) vector mesons), the dotted line only light vector mesons.

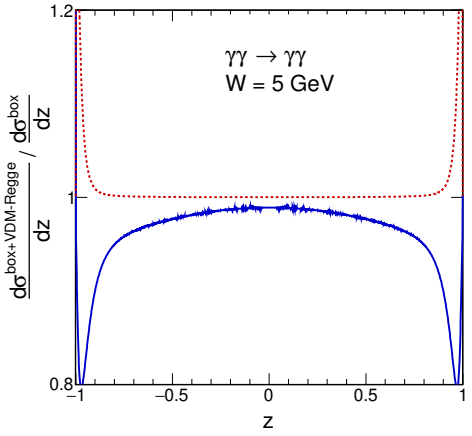

Figure 4 – The ratio of the coherent (blue) and incoherent (red) sum of the box and VDM-Regge contributions divided by the cross section for the box contribution alone for $W = 5$ GeV.

3.2 Heavy ion UPC

To summarize the present status of $\gamma\gamma \to \gamma\gamma$ scattering in Fig.3.2 we confront results of our calculation with current ATLAS data [13]. We discuss also how the results depend on the treatment of absorption corrections. The results of the two different approximations (as described in the figure caption) almost coincide. For comparison, we show also results obtained with the SuperChic generator [14]. In general, there is reasonable agreement of the Standard Model predictions with the ATLAS data. Similar agreement is achieved for the CMS data.

Many light vector mesons have large coupling to two photons. In [5] for a first time the role of resonances was discussed, for elementary cross section only. In Fig.6 we show the contributions of light mesonic photon-photon resonances for heavy ion UPC. The results shown are for a broad range of photon rapidities and transverse momenta. We show distribution in diphoton inariant mass (left) and photon transverse momentum (right). It is obvious that elimination of the resonance contributions may be difficult. But perhaps it is not necessary as the mesonic resonance contributions are a part of photon-photon scattering. The cuts used by ATLAS or CMS allowed to eliminate the contributions of light mesons. The contribution of heavy mesons is expected to be small.

The FoCal detector planned for Run 4 was described in [8]. It is a general purpose detector. It can also measure photons. We start our presentation from the results when both photons are measured by FoCal. In Fig.7 (a) we show results when both photons have energies bigger than 200 MeV. In addition, we show the contribution of the $\pi^0\pi^0$ background. In this case, only two photons are measured. Without

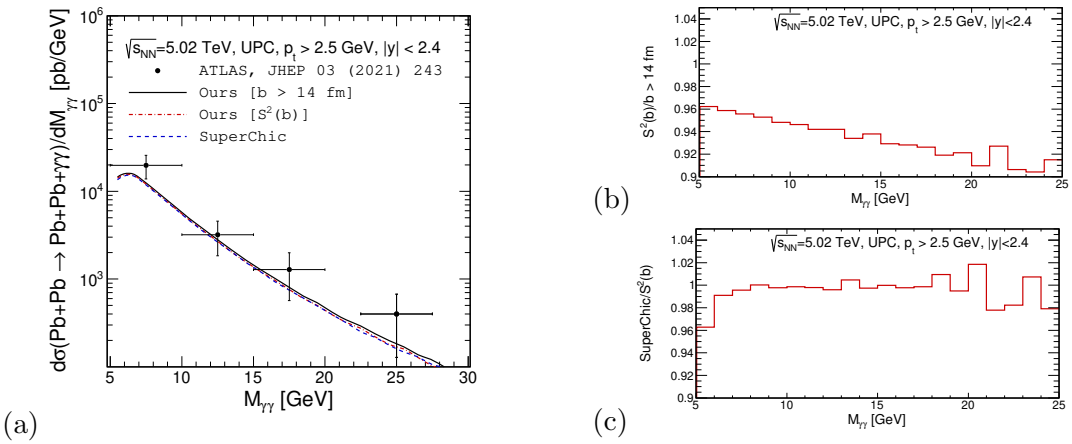

Figure 5 – Differential cross section as a function of two-photon invariant mass at $\sqrt{s_{NN}} = 5.02$ TeV. (a) The ATLAS experimental data are collected together with theoretical results including a sharp cut on impact parameter ($b > 14$ fm - solid black line) and smooth nuclear absorption factor $S^2(b)$ (dash-dotted red line). For completeness, results that are obtained with the help of Eq. (11) are compared with results from SuperChic. The right panel shows two ratios: (b) ratio of distributions calculated by us with sharp and smooth cut-off on impact parameter and (c) the ratio of SuperChic result to our result, using a smooth representation of the gap survival factor.

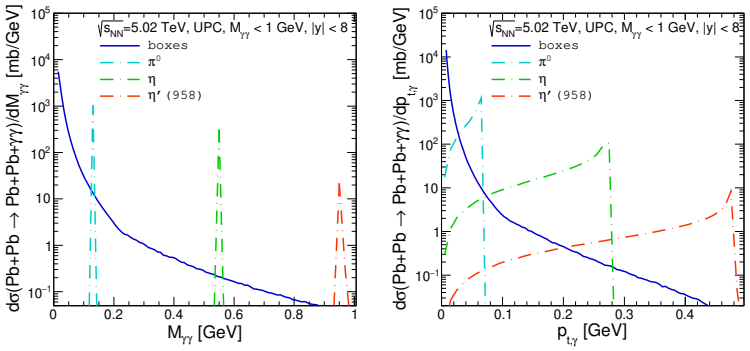

Figure 6 – Box versus resonance contributions for diphoton invariant mass (left) and photon transverse momentum (right).

additional cuts, the background is clearly bigger than the signal. However, by imposing extra conditions on vector asymmetry, we can lower the background contribution.

In Fig.8 we show similar distributions but for $p_t > 0.2$ GeV and combined ALICE and FoCal rapidity region. Here in some regions of the phase space, the VDM-Regge contribution could be seen as 10% modification of the cross section with respect to the calculations with only boxes. Here the separated VDM-Regge component is even bigger. We conclude that already at Run 4 one could indirectly observe a signature of mechanisms other than fermionic boxes.

Now we will show distributions relevant for the ALICE 3 detector.

In Fig. 9 we show distributions in diphoton invariant mass for photons $-4 < y_1, y_2 < 4$ and $E_\gamma > 50$ MeV (see Ref. [9]). We show the light-by-light box contribution (solid line) as well as the $\pi^0\pi^0$ background contribution (red lines). At diphoton invariant masses, 0.5 GeV $< M_{\gamma\gamma} <$ 1 GeV, the background contribution is almost as big as the signal contribution. As discussed in [3] it can be to some extent reduced. Although the background is smaller than fermionic boxes in the full range of diphoton invariant mass, it can be further reduced by imposing the cut on $|\vec{p_{1t}} + \vec{p_{2t}}| < 0.1$ GeV and vector asymmetry $A_V < 0.02$. Imposing a cut on the background causes that the background in the whole diphoton invariant mass range is much smaller than the signal.

In Fig. 10 we show distribution in $y_{diff} = y_1 - y_2$. Again different contributions are shown separately. The results for the double-π^0 background contribution are particularly interesting. It has a maximal contribution at $y_{diff} = 0$ and drops quickly for larger $|y_{diff}|$. An extra cut on y_{diff} could therefore considerably reduce the unwanted double-π^0 contribution. In Fig. 10 we show what happens when

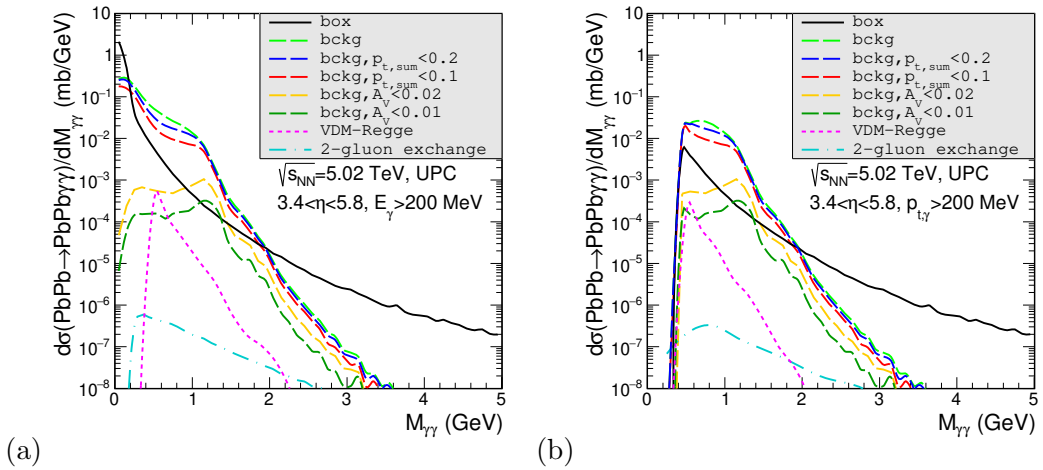

Figure 7 – Diphoton invariant mass distribution for the UPCs. Predictions are made for the future FoCal acceptance, i.e. (a) $E_{t,\gamma} > 200$ MeV and $3.4 < y_{\gamma_{1/2}} < 5.8$, (b) $p_{t,\gamma} > 200$ MeV and $3.4 < y_{\gamma_{1/2}} < 5.8$. Here, both photons are "measured" in FoCal. The background contribution is presented for different cuts.

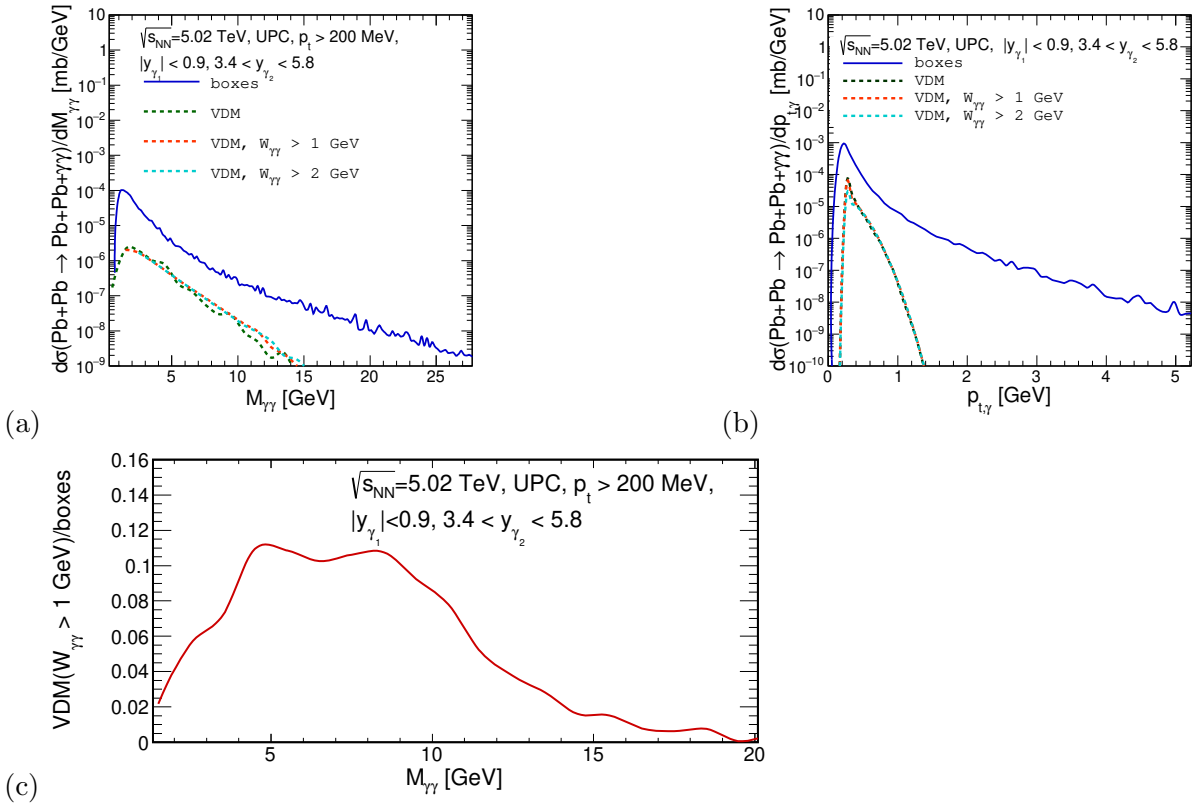

Figure 8 – Prediction for the FoCal detector in association with mid-rapidity ALICE detector for photons: $p_t > 200$ MeV, diphoton mass $M_{\gamma\gamma} > 400$ MeV and photon rapidities $|y_1| < 0.9$ and $y_2 \in (3.4, 5.8)$. The blue line corresponds to fermionic loops and the green lines to the VDM-Regge contribution. (a) Diphoton invariant mass distribution, (b) photon transverse momentum distribution, (c) ratio of the VDM-Regge ($W_{\gamma\gamma} > 1$ GeV) and box contributions as a function of di-photon invariant mass. No interference effects were included here.

imposing the cut on y_{diff}. The effect of such a cut on box contribution is relatively small but leads to a huge reduction of the $\pi^0\pi^0$ background. The effect of the cut is much larger for small $M_{\gamma\gamma}$ and therefore could be avoided if one is interested in this region of energies.

In Fig.11 we show distribution in $M_{\gamma\gamma}$ (a) and p_t (b) for a planned special photon detector in forward direction $3 < y_\gamma < 5$. Here $p_t > 5$ MeV was imposed as described in Ref. [9]. We show that at low $M_{\gamma\gamma}$ and low p_t the LbL signal by far exceeds the $\pi^0\pi^0$ background, even without including any suppression

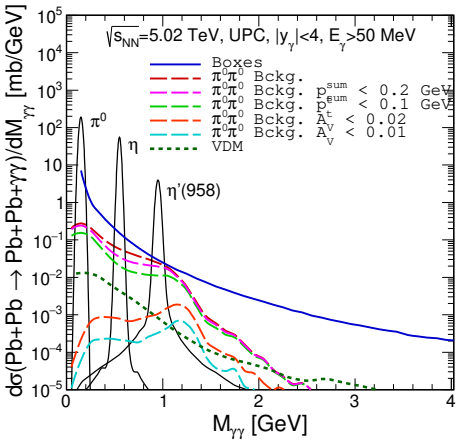

Figure 9 – Diphoton invariant mass distribution for ALICE 3, i.e. rapidity $y_{1/2} \in (-4, 4)$ and photon energy $E_\gamma >$ 50 MeV. Here the blue solid line relates to the box contribution, the dotted line to the VDM-Regge component and the dashed lines are for double-π^0 background contribution. Here we impose several extra conditions on diphoton transverse momenta and vector asymmetry.

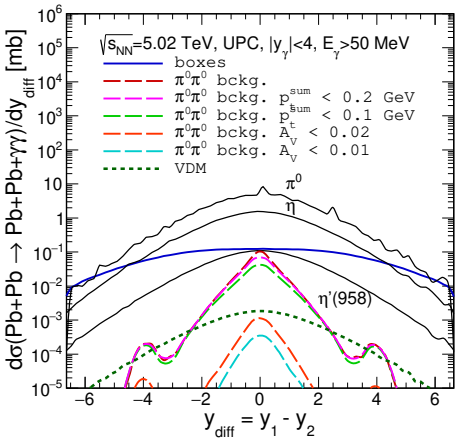

Figure 10 – Differential cross section as a function of $y_{diff} = y_1 - y_2$ for extended ALICE 3 kinematics: $|y_{1/2}| < 4$ and $E_\gamma > 50$ MeV. Results are presented for boxes, resonances, VDM-Regge and double-π^0 background.

condition for the background. Here we assumed 2 π azimuthal coverage of the planned special photon detector. The special detector having the planned very small transverse momentum coverage should allow to measure completely new, low energy, regime of photon-photon scattering. Here both background and mesonic resonance contributions should be absent.

4 Conclusions

Recently we discussed different mechanisms of $\gamma\gamma \to \gamma\gamma$ scattering such as leptonic/quarkish boxes, double hadronic fluctuations, neutral t/u-channel pion exchanges and two-gluon exchanges. Possible effects of the searched for subleading mechanisms have been discussed. The latter contributions turned out difficult to be identified in ATLAS and CMS measurements. We have discussed possible interference effect of box and double-hadronic fluctuations for $\gamma\gamma \to \gamma\gamma$ scattering for future measurements.

In the literature only the box contributions were discussed before. We have tried to identify the region where the other contributions could appear. In addition we discussed how to reduce the unwanted $\gamma\gamma \to \pi^0\pi^0$ background.

The FoCal project does not seem to allow for breakthroughs for LbL scattering. but may be used to supplement the ALICE, not yet officially presented, experimental studies.

We have also made predictions for the ALICE 3 ($-4 < y_\gamma < 4$) and for a planned special soft

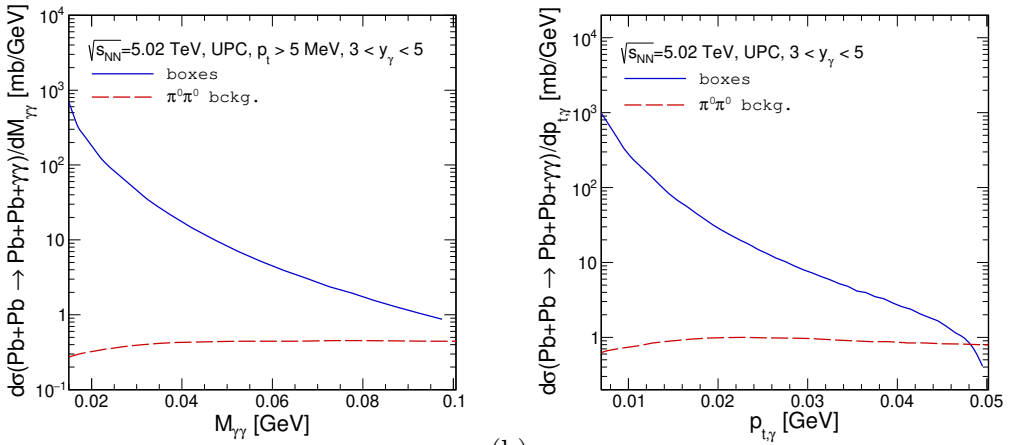

Figure 11 – Prediction for the ALICE 3 experiment for soft photons: $p_t = (5 - 50)$ MeV and photon rapidities $y_i \in (3, 5)$. The blue line corresponds to fermionic loops, the red line relates to the double-π^0 background. (a) diphoton invariant mass distribution, (b) photon transverse momentum distribution.

photon detector ($3 < y_\gamma < 5$). We have shown that by imposing a cut on $y_{diff} = y_1 - y_2$ one can efficiently eliminate the unwanted $\pi^0\pi^0$ background. The soft photon detector can be used to measure the $\gamma\gamma \to \gamma\gamma$ scattering at extremely small energies, $W_{\gamma\gamma} < 0.05$ GeV. Therefore we conclude that the ALICE 3 infrastructure will be extremely useful to study the $\gamma\gamma \to \gamma\gamma$ scattering in a new, not yet explored, domain of energies and transverse momenta. In this domain the $\pi^0\pi^0$ background can to large extent be eliminated.

In our recent calculations we used EPA in the impact parameter space. In the future one can try to use also so-called Wigner function approach used for e^+e^- production in semi-peripheral lead-lead collisions (never used for the di-photon production). This goes, however, beyond the scope of the first exploratory study.

5 Acknowledgments

This work was partially supported by the Polish National Science Center grant UMO-2018/31/B/ST2/03537 and by the Center for Innovation and Transfer of Natural Sciences and Engineering Knowledge in Rzeszów.

References

1. M. Aaboud et al. (ATLAS collaboration), Nature Phys. **13**, 852 (2017).
2. A.M. Sirunyan et al. (CMS collaboration), Phys. Lett. **B797**, 134826 (2019).
3. M. Klusek-Gawenda, R. McNulty,, R. Schicker and A. Szczurek, Phys. Rev. **D99**, 093013 (2019).
4. P. Jucha, M. Klusek-Gawenda and A. Szczurek, Phys. Rev. **D109**, 014004 (2024).
5. P. Lebiedowicz and A. Szczurek, Phys. Lett. **B772**, 330 (2017).
6. M. Klusek-Gawenda, P. Lebiedowicz and A. Szczurek, Phys. Rev. **C93**, 044907 (2016).
7. C. Baldenegro, S. Fichet, G. von Gersdorff and C. Royon, JHEP **06**, 131 (2018).
8. C. Loizides, W. Riegler et al. (ALICE collaboration), CERN Document Server (2020), 2211.024991.
9. L. Musa, W. Riegler et al. (ALICE collaboration), CERN Document Server (2022), 2211.02491.
10. M.M. Brisudova, L. Burakovsky and T. Goldman, Phys. Rev. **D61**, 054013 (2000).
11. M.M. Brisudova, L. Burakovsky, T. Goldman and A. Szczepaniak, Phys. Rev. **D67**, 094016 (2003).
12. M. Klusek-Gawenda and A. Szczurek, Phys. Rev. **C87**, 054908 (2013).
13. G. Aad et al. (ATLAS collaboration), Phys. Rev. Lett. **123**, 052001 (2019).
14. L.A. Harland-Lang, M. Tasevsky, V.A. Khoze and M.G. Ryskin, Eur. Phys.J. **C80**, 925 (2020).

Phys. Proc. Ultra-Peripheral Collisions **1**, 022 (2024) 1-8

UPC physics with ALICE in Run 3

Anisa Khatun (for the ALICE Collaboration)
Department of Physics and Astronomy, The University of Kansas.
Lawrence, Kansas, 66045 USA

The ALICE experiment has undergone a major detector upgrade for Run 3, expanding its detection capabilities for a wide variety of studies. The new continuous readout has significantly enhanced the physics potential for ultra-peripheral collision analyses. In this talk, we discussed some of the physics analyses that can be carried out in ultra-peripheral collisions using the Run 3 data and presented some of the first physics performance plots in both proton-proton and heavy-ion collisions.

DOI: https://doi.org/10.17161/5b46x852
Keywords: UPC, ALICE, Run 3, continuous readout

1 Introduction

An ultra-peripheral collision (UPC) occurs when two relativistic heavy ions interact at very high energies with an impact parameter larger than the sum of the radii of the colliding nuclei. In a UPC, the two ions approach each other closely, but due to their high electric charge, they can interact electromagnetically without colliding nucleons. This leads to phenomena such as photonuclear interactions, where one or both ions emit photons that interact with the other. The hadronic process is suppressed in UPC due to the large impact parameter interaction. Either ion can emit a quasi-real photon, that can interact with a Pomeron and produce, for example, only a vector meson in the final state. This class of UPC interactions is known as the exclusive process (left Fig. 1). The exclusive process can be divided into two sub-classes: coherent process (photon interacts with whole nucleus) and incoherent (photon interacts with some of the nucleons). In the exclusive process, both the projectile and target remain intact. The photon can also break up the target as shown in the right Fig. 1.

UPCs provide a great tool to probe the nucleus and nucleons. LHC can produce UPCs at luminosities and energies beyond what is achievable in any other collider. For example, the LHC can reach γp (photon-proton) energies ten times higher than those achieved at the Hadron-Electron Ring Accelerator (HERA). Consequently, in UPCs it is possible to probe lower Bjorken $-x$ values down to 10^{-6} for the study of nuclear shadowing (and possibly gluon saturation) region of gluon distribution in the target nucleus [1]. ALICE has provided a rich variety of UPC physics studies with the data collected in the LHC Run 1 and Run 2 [2]. In the Run 3 program, ALICE continuous readout offers unique advantages for studying UPCs, including its good acceptance for both charged particles at low transverse momentum (p_{T}) and excellent particle identification at midrapidity, which allows for precise characterization of the particles produced in UPCs [3].

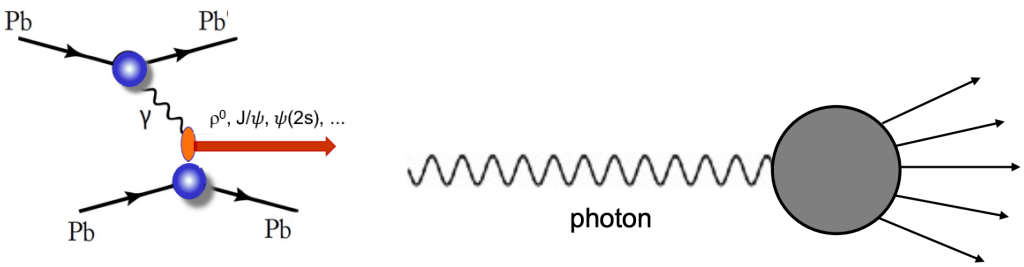

Figure 1 – Typical exclusive vector meson production in UPC (left). The photon can also break up the target (right).

2 The ALICE experiment in Run 3

In ALICE, one can study UPC physics at mid-, forward, and semi-forward (one track in the central barrel and one track in the muon arm) rapidity (see Fig. 4). At midrapidity, the track reconstruction and particle identification are done using data from the detectors: Inner Tracking System (ITS) [4], Time Projection Chamber (TPC) [5], Time of Flight (TOF) [6] and Transition Radiation Detector (TRD) [7]. At forward rapidity ALICE reconstructs muons using a muon spectrometer [8]. The interaction rate was 8 kHz for Pb–Pb and 100 kHz for pp collisions in Run 2. The ALICE experiment underwent a major upgrade to cope with an increased interaction rate of up to 50 kHz for Pb-Pb, 500 kHz for p-Pb and 1 MHz for pp collisions in continuous readout mode. A new Forward Interaction Trigger (FIT) replaced the V0 and T0 detectors and AD (used for trigger purposes in Run 2) [9]. The FIT detectors are placed on either side (A and C) of the interaction point, namely FT0A, FT0C, FV0A, FDDA, and FDDC. FIT provides veto on forward rapidity activity for UPC and diffractive physics studies and is also important for measuring the collision time and determining global collision parameters [9].

The upgraded ITS detector (ITS2) is a full silicon pixel detector and consists of 7 layers with an extended acceptance of pseudo-rapidity coverage $|\eta| < 1.22$. ITS2 provides improved tracking efficiency, particle detection, and p_{T} resolution down to low p_{T} at 500 MeV/c. ITS2 is capable of providing a standalone reconstruction of tracks along with improved reconstruction of the primary and secondary vertices (originating from heavy-flavour hadrons) [10]. TPC has been upgraded with a GEM-based readout to cope with the high interaction rate and also retains excellent particle identification [13]. Both ITS2 and upgraded TPC are very important for UPC measurements of lower momentum particles at midrapidity ($|\eta| < 0.9$). The readout for TOF, the Zero Degree Calorimeter (ZDC), and the muon arm have been improved. In particular, TOF has now an excellent time resolution of 56 *ps* and improved particle identification which can be useful for UPC measurements for particles with relatively higher momentum [14].

The MCH has been upgraded, and the muon trigger system has been replaced with the Muon Identifier (MID) [11]. A new addition to the muon arm is the Muon Forward Tracker (MFT) [12]. Especially, MFT extends tracking for charged particles to $|\eta| \sim 3.6$ and also enables secondary vertexing for heavy-flavour measurements. Not only UPC quarkonia but also open heavy-flavour measurements are possible with MFT. The upgraded muon spectrometer with MFT can also be used to measure UPC low-mass vector mesons at forward rapidity thanks to reduced combinatorial background and improved mass resolution. The ZDC is used for UPC studies associated with neutron and proton emissions [15].

2.1 New common online-offline computing system

ALICE now has a whole new software framework to process data samples more than 1000 times in pp and about 100 times in Pb-Pb collisions than the combined Run 1 and Run 2 samples at midrapidity. This software integrates online data taking using a new central trigger processor (CTP) and Data Quality Acquisition (DAQ)/Offline architecture as well as the analysis framework known as Online-Offline (O^2) software [16].

The ALICE Central Trigger Processor (CTP) was used in Run 2. The Local Trigger Unit (LTU) board for each detector has provided the detector readout using the Trigger-Timing-Control (TTC). In Run 3, the ALICE detectors are self-triggered. The new CTP provides time stamps to synchronize data from different detectors, meaning no discrete events but a continuous data stream [17]. Software trigger is applied on the analysis level. The lack of any hardware trigger is referred to as 'trigger-less mode'. The data flow in the current Run 3 setup is shown in Fig. 2.

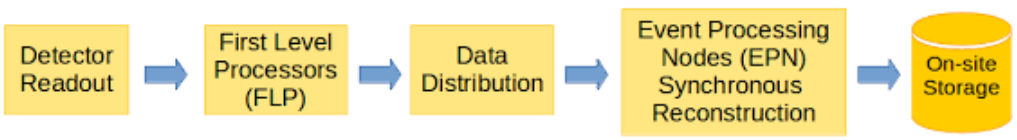

Figure 2 – Schematic view of data-taking procedure.

3 Progress on UPCs at ALICE

ALICE has come a long way with UPC physics from Run 1 to Run 2 [2]. If we take the example of coherent ρ^0 meson photoproduction, yield statistics had increased 10-fold during Run 2 at midrapidity (see Fig. 3). The collected integrated luminosity in Run 2 was 1 nb^{-1}, and the expected luminosity to reach during Run 3 and Run 4 is 13 nb^{-1} in total. A significant increase in statistics in Run 3 is possible with continuous readout [18].

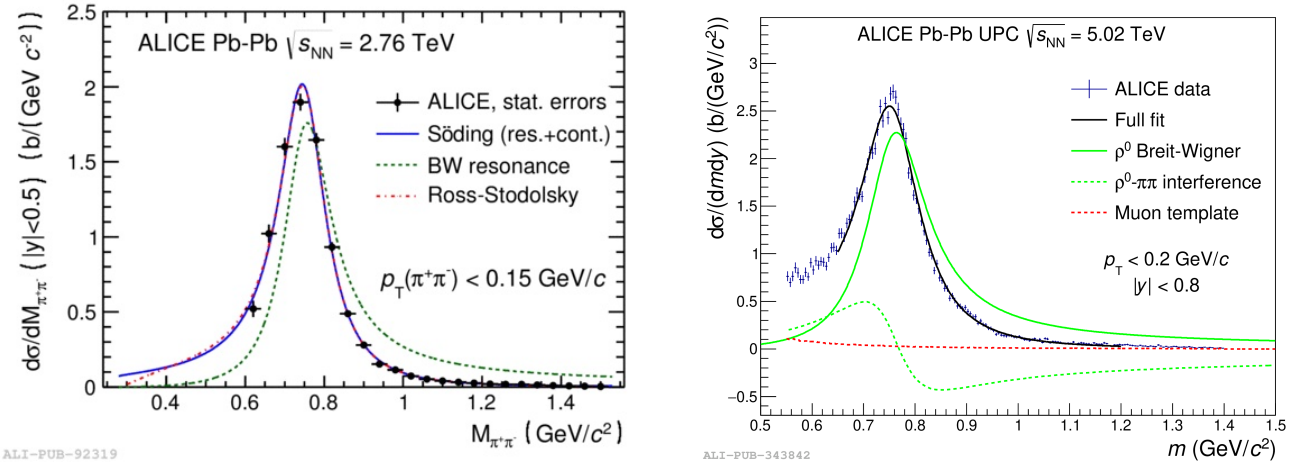

Figure 3 – a) Run 1 : $\sim$ 7k events [19]. b) Run 2 : $\sim$ 60k events [20].

3.1 Datasets available for UPC in Run 3

First Pb-Pb data taking with 2 kHz hadronic interaction rate was recorded on 26$^{\text{th}}$ September 2023. Data are taken successfully with 45 kHz Hadronic Interaction Rate. The total collected integrated luminosity in 2023 is about 1.5 nb^{-1} for UPC events. The data sample for minimum bias events collected in Run 3 at the end of 2023 is 40 times larger than Run 1 and Run 2 combined. The value 1.5 nb^{-1} is 3000 times larger than integrated luminosity used in ρ^0 analysis of Run 2 data. About 29 pb^{-1} of integrated luminosity was recorded in pp collisions at $\sqrt{s}$ = 13.6 TeV in 2022 and 2023. The collected luminosity of total triggered events was $\sim$ 8 pb^{-1} in Run 2 for pp collisions. The data in pp collisions are important for studying Central Exclusive Production (CEP), which is discussed in Section 5. In Run 2, the study of CEP events was not possible since the collected data with high multiplicity in V0 and MUON, Electromagnetic Calorimeter and TRD triggers were most likely to exclude all CEP events in pp collisions.

3.2 UPC event selection

As in Run 2, selecting an exclusive vector meson requires two opposite sign tracks with no signal in the FIT detectors (see Fig. 4). The coherent ($p_{\text{T}}^{\text{VM}} \sim 1/R_{\text{Pb}}$ = 50 MeV) and incoherent ($p_{\text{T}}^{\text{VM}} \sim 1/R_{\text{p}}$ = 400 MeV) can be separated by selecting the p_T scale of the system. Further, a veto can be applied on the ZDC signal for truly exclusive events or associated neutron emission processes can be studied using the ZDC signal. The ALICE trigger-less readout offers the possibility to veto signals coming from the individual A-side and C-side FIT subdetectors and performing a selection of inclusive and semi-inclusive UPC events.

3.3 Ongoing UPC activity in Run 3

At present, among the ongoing photoproduction analyses using Run 3 data are the coherent ρ^0 at midrapidity and coherent J/ψ at forward rapidity worth mentioning. These are chosen as Run 2 reference analyses to evaluate the performance of the ALICE reconstruction software in Run 3. The performance examples of these two analyses are shown in Fig. 5. Clear resonance peak of coherent ρ^0 in Pb-Pb UPCs at $\sqrt{s_{NN}}$ = 5.36 TeV is observed. The transverse momentum distribution of the photoproduced J/ψ in Fig. 5 shows both coherent and incoherent processes.

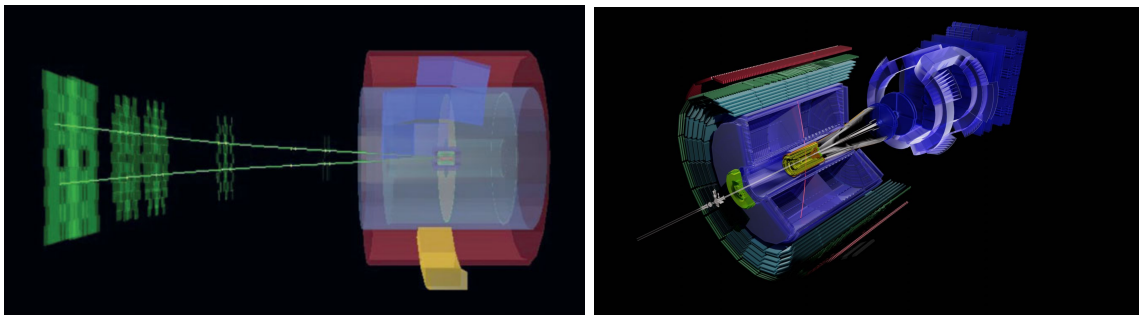

Figure 4 – UPC event in Run 2 at forward rapidity (left) and UPC event in Run 3 at midrapidity (right).

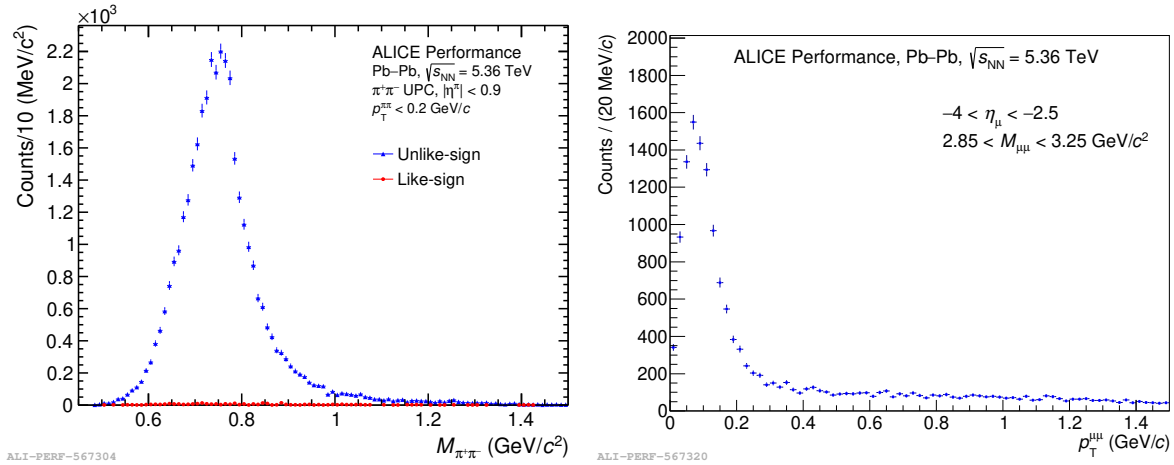

Figure 5 – Coherent ρ^0 invariant mass distribution (left) and p_{T} distribution of exclusive J/ψ (right).

4 UPC physics prospects in Run 3 and beyond

4.1 Exclusive vector meson photoproduction

As discussed in Section 3, a significant increase in integrated luminosity allows the precision study of vector meson photoproduction in UPCs with Run 3 data. For example, experimental uncertainties for nuclear suppression factor for $\gamma + Pb \rightarrow \mathrm{J}/\psi + \mathrm{Pb}$ processes are expected to be at the level of 4% [18] while in Run 2 measurements these were of the order of ~ 10 % [21]. It is also possible to analyse double vector meson photoproduction of higher quarkonium states such as $\psi(2S)$ and $\Upsilon(ns)$ with abundant exclusive UPC events [22]. In addition, the Run 3 data opens the possibility of measuring strangeness in UPC in particular $\phi(1020) \rightarrow K^+ + K^-$. Photo-production of K^+K^- pairs has been measured with Run 2 data in ALICE [23]. It will be possible to measure the exclusive photoproduction of a much wider range of particles, including excited vector mesons and searches for exotica, e.g. $X(3872)$.

4.2 Exclusive vector meson photoproduction with FoCal

The Forward Calorimeter (FoCal) is part of the ALICE upgrade for Run 4 (starting from 2029). It will be positioned 7 m from the interaction point on the A-side, covering $3.4 < \eta < 5.8$. As shown in Ref. [24], the FoCal will provide access to the kinematic region where the gluon saturation phenomena dominate. The future measurements of the energy dependence of J/ψ photoproduction will provide a direct model-independent probe for gluon saturation with large statistics and more forward acceptance in p-Pb and Pb-Pb UPC collisions. The ratio of exclusive $\psi(2S)$ to J/ψ photoproduction cross section as a function of the energy ($W_{\gamma p}$) using the muon arm data in Run 3 alone shows sensitivity to the gluon saturation as shown in Fig. 6. FoCal will enable a comprehensive study at the highest energy point (see Fig. 6). The projections are also shown for dissociative J/ψ in Run 3 with FOCAL acceptance in Run 4, which is sensitive to the gluon saturation [24].

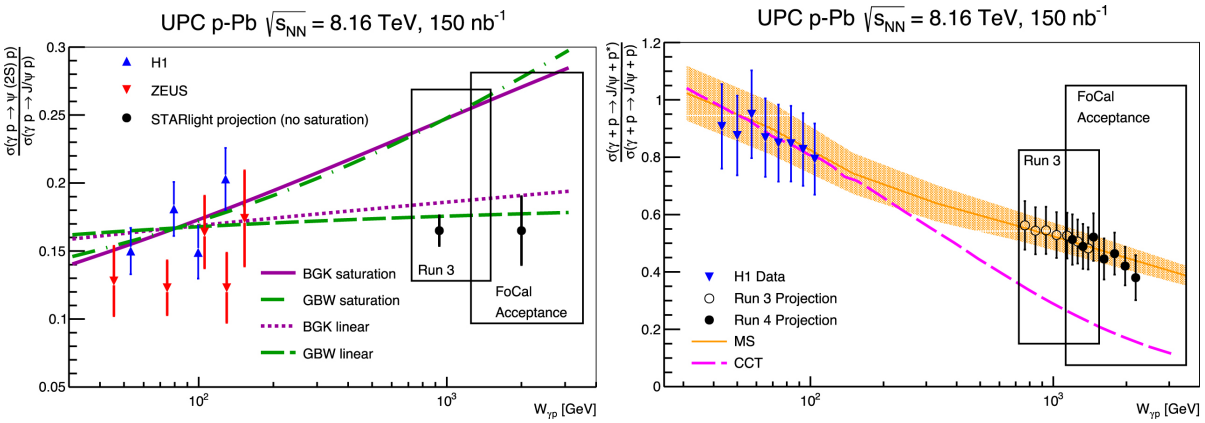

Figure 6 – Projection of ALICE Run 3 with Focal acceptance in Run 4 ratio of energy dependence: Exclusive $\psi(2S)$ to J/ψ photoproduction cross section (left) and dissociative J/ψ to exclusive J/ψ photoproduction cross sections (right).

4.3 Search for new particles and inclusive UPCs

The trigger-less data taking enables ALICE to study inclusive, inelastic photonuclear processes, e.g. inclusive J/ψ, jets in UPCs. The inclusive processes have never been studied at LHC so far; only results from HERA are available in the field of inelastic photonuclear interactions. This opens the possibility for studying open heavy flavours like D^0 in UPCs. Unlike vector meson photoproductions, a single gluon is involved, resulting in a 5 to 10 times larger cross section than for charmonia [25, 26].

The continuous readout also may enable the possibility to measure the rare fundamental QED process $\gamma\gamma \to \gamma\gamma$ interactions with ALICE, known as light-by-light scattering. The search for Axion Like Particles (ALPs) is done while measuring light-by-light scattering in Pb-Pb and looking for resonances in the invariant mass distributions as ALPs can couple to photons in the initial or final state of $\gamma\gamma \to \gamma\gamma$. Previously measured by ATLAS [27] and CMS [28] in Run 2. As discussed here [29], ALICE can potentially go down to 1 GeV to study elastic $\gamma\gamma \to \gamma\gamma$ scattering, focusing on low diphoton invariant masses below 5 GeV/c^2 (see Fig. 7). However, the considered backgrounds (e.g. direct η_c production) are underestimated as the calculation does not include soft photons coming from radiative decays of vector mesons such as γ+Pomeron− > J/ψ− > η_c+γ [30]. Measuring ALPs is very challenging with the Run 3 setup as ALICE calorimeters can not measure low momenta neutral particles with high resolutions which will be possible in the Run 5 ALICE 3 program [31].

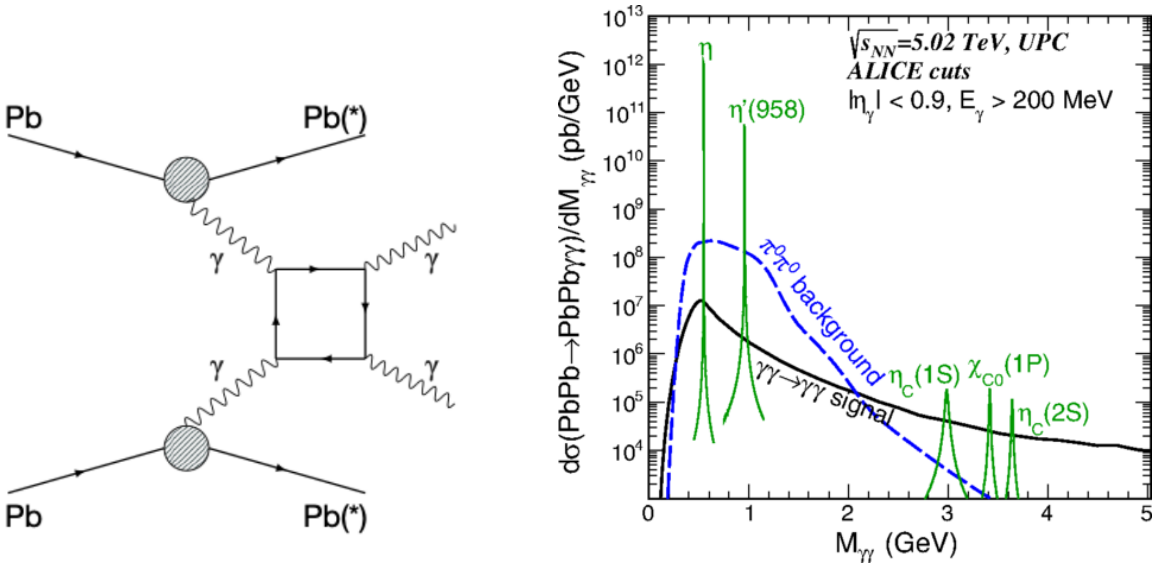

Figure 7 – The light-by-light scattering process (left) and contributions from resonances decays into two photons as a function of the invariant mass (right) [29].

Another potential scenario is the direct measurement of τ anomalous magnetic moment ($a_\tau = (g-2)/2$) in Run 3 with UPCs by studying $\gamma\gamma \to \tau^+\tau^+$ channel. The results from ATLAS [32] and CMS [33] using muon and one track ($e, \mu, hadron$), three tracks (3 hadrons) and electron topologies show precision similar to that achieved by DELPHI. This value is sensitive to many beyond-standard models (BSM) such as supersymmetry ($\delta a_\tau = m_\tau^2/M^2$). Run 3 provides luminosity to perform such studies in ALICE. The ALICE acceptance can allow us to perform these measurements down to low p_T tracks and possibly constrains the uncertainty limits twice than is measured by ATLAS (Fig. 8).

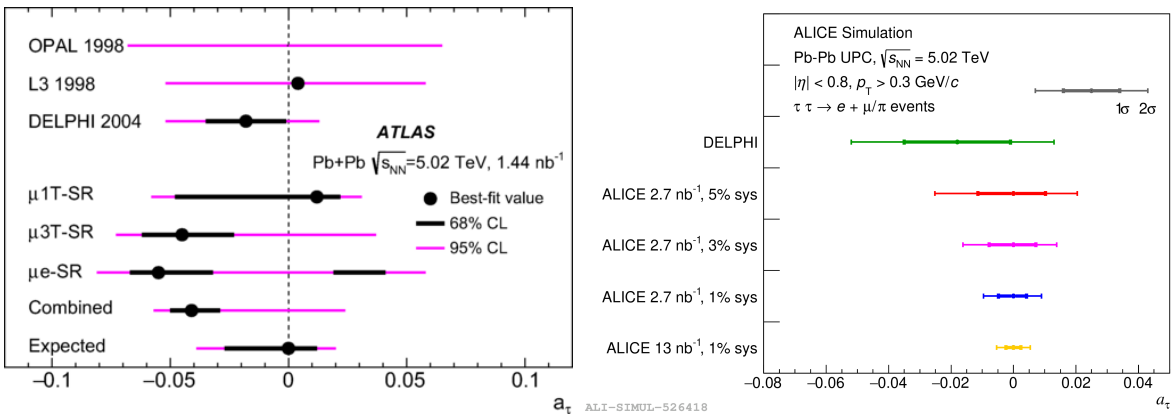

Figure 8 – The value of a_τ measured by ATLAS (left) and ALICE simulation with Run 3 acceptance for a_τ (right) [32].

In $\gamma\gamma$ interactions, it is also possible to study heavy tetra quark states $\gamma\gamma \to T_{4Q} \to 4l$ in UPC Pb-Pb collisions. Prediction for $X(6900) \to J/\psi J/\psi$ and $X(19000) \to \Upsilon\Upsilon$ within the ALICE kinematic range are discussed in Ref. [34]. An estimate of 100 events of charm tetra quark is expected before acceptance efficiency correction.

5 Central exclusive production in pp collisions

Run 3 has opened the possibility to explore Central Exclusive Production (CEP) events in pp collisions to a new extent, which was not possible during Run 1 or Run 2. CEP events are studied using double-gap topology in the ALICE central barrel at mid-rapidity. Tracks are selected within the central barrel, having no signal on the FIT detectors. Several such diffraction processes are of interest, as shown in Fig. 9.

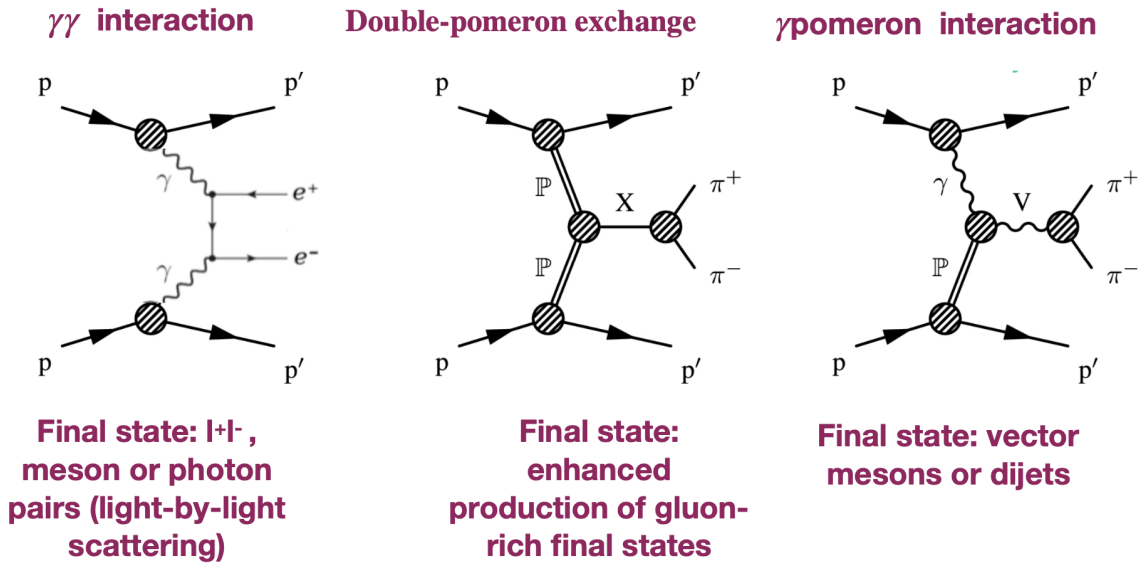

Figure 9 – Schematic diagram of various CEP events.

As mentioned in Section 3, the minimum bias data collected in pp collisions in Run 3 in 2022 and 2023 is more than 3 times than Run 2. After using the double gap topology, the events are selected with two opposite charge tracks. Then, the particle identification is carried out by TPC down to low p_T based on specific energy loss (pion, kaon hypothesis). Such analyses show visible resonances in raw invariant mass distributions of opposite-sign pions and kaons (see Fig. 10). It will be possible to study strangeness in double gap events with ϕ1020 and $f_2(1525)$ states.

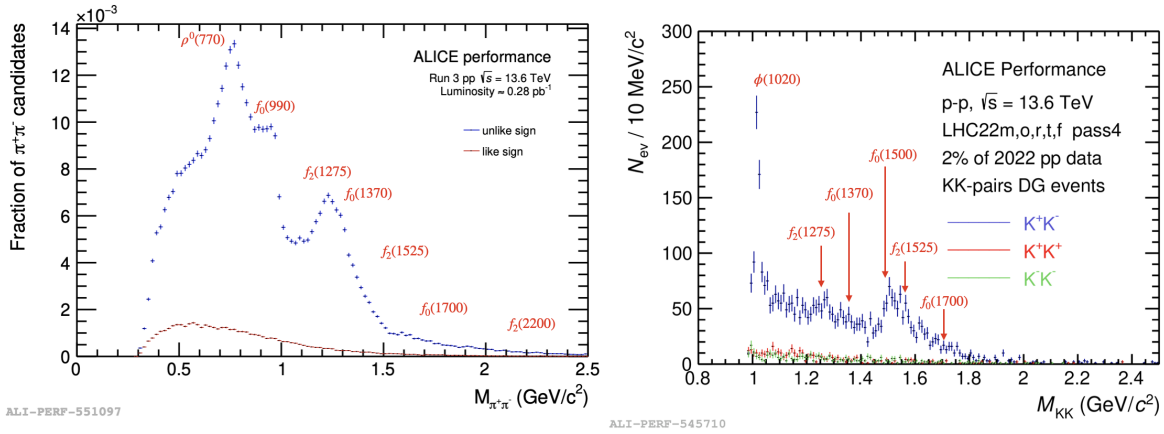

Figure 10 – Raw invariant mass distributions of two pions and two kaons candidates of CEP events in pp collisions.

6 Summary

The field of UPCs in Run 3 and Run 4 is of great scientific interest. ALICE has already collected intriguing data from both Pb-Pb and pp collisions, with upcoming prospects for p-Pb data collection. These endeavours promise precision measurements of non-linear QCD effects such as saturation, the discovery of new resonances, and the exploration of new physics phenomena such as ALPs and Tetraquarks. UPCs also offer avenues for investigating strangeness, heavy-quarkonia like Upsilon states, and open charm. The new analysis framework is equipped to manage the anticipated event rates throughout Run 3 and beyond.

Acknowledgments

This research has been supported by the U.S. Department of Energy, Office of Science, Nuclear Physics.

References

1. J. G. Contreras and J. D. Tapia Takaki, Int. J. Mod. Phys. A**30**, (2015) 1542012 doi:https://doi.org/10.1142/S0217751X15420129
2. ALICE Collaboration, arXiv:2211.04384 [nucl-ex] doi:https://doi.org/10.48550/arXiv.2211.04384
3. ALICE Collaboration, arXiv:2302.01238 [physics.ins-det] doi:https://doi.org/10.48550/arXiv.2302.01238
4. ALICE Collaboration, J. Phys. G**41** (2014) 087002 doi:10.1088/0954-3899/41/8/087002
5. ALICE Collaboration, CERN-LHCC-2015-002, ALICE-TDR-016-ADD-1, (2015) 2
6. ALICE Collaboration, CERN-LHCC-2002-016, ALICE-TDR-08, (2002) 4
7. ALICE Collaboration, Nucl. Instrum. Methods A**881** (2018) 88 doi:https://doi.org/10.1016/j.nima.2017.09.028
8. C. Finck, ALICE Collaboration, J. Phys. Conf. Series **50** (2006) 397-401 doi:10.1088/1742-6596/50/1/056
9. M. Slupecki, ALICE collaboration, Nucl. Instrum. Methods A**1039**, (2022) 167021 doi:https://doi.org/10.1016/j.nima.2022.167021
10. F. Reidt, ALICE Collaboration, Nucl. Instrum. Methods A**1032** (2022) 166632 doi:https://doi.org/10.1016/j.nima.2022.166632
11. L. Terlizzi, ALICE Collaboration, JINST **15** (2020) C10031 doi:10.1088/1748-0221/15/10/C10031
12. ALICE Collaboration, CERN-LHCC-2015-001, ALICE-TDR-018 (2015) 30

13. ALICE Collaboration, JINST **16** (2021) P03022 doi:https://doi.org/10.1088/1748-0221/16/03/p03022
14. F. Carnesecchi, ALICE Collaboration, JINST **14** (2019) C06023 doi:10.1088/1748-0221/14/06/C06023
15. P. Cortese, ALICE Collaboration, IOP Conf. Series: Journal of Physics: Conf. Series **1162** (2019) 012006 doi:10.1088/1742-6596/1162/1/012006
16. G. Eulisse, P. Konopka, M. Krzewicki, M. Richter, D. Rohr, and S. Wenzel, EPJ Web of Conferences **214**, 05010 (2019) CHEP 2018 doi:https://doi.org/10.1051/epjconf/201921405010
17. J. Kvapil and A. Bhasin, et al., EPJ Web of Conferences **251**, 04022 (2021) CHEP 2021 doi: https://doi.org/10.1051/epjconf/202125104022
18. Z. Citron et al., CERN Yellow Rep. Monogr **7**, (2019) 1159-1410 doi: https://doi.org/10.48550/arXiv.1812.06772
19. ALICE Collaboration, JHEP **09** (2015) 095 doi: https://doi.org/10.1007/JHEP09(2015)095
20. ALICE Collaboration, JHEP **06** (2020) 035 doi: https://doi.org/10.1007/JHEP06(2020)035
21. ALICE Collaboration, JHEP **10** (2023) 119 doi: https://doi.org/10.1007/JHEP10(2023)119
22. K. Eskola and C. Flett, arXiv:2303.03007 [hep-ph] doi: https://doi.org/10.48550/arXiv.2303.03007
23. ALICE Collaboration, arXiv:2311.11792 [nucl-ex] doi: https://doi.org/10.48550/arXiv.2311.11792
24. A. Bylinkin J. Nystrand and D. Tapia Takaki, J. Phys. G: Nucl. Part. Phys.**50** 055105 doi: https://doi.org/10.1088/1361-6471/acc419
25. S. R. Klein, J. Nystrand and Ramona Vogt, Phys. Rev. C**66**, 044906 (2002) doi: https://doi.org/10.1103/PhysRevC.66.044906
26. V. P. Gonçalves, G. Sampaio dos Santos and C. R. Sena, Nucl. Phys. A**976** (2018) 33-45 doi: https://doi.org/10.1016/j.nuclphysa.2018.05.002
27. ATLAS Collaboration, JHEP **03** (2021) 243 doi: https://doi.org/10.1007/JHEP11(2021)050
28. CMS Collaboration, Phys. Lett. B**797** (2019) 134826 doi: https://doi.org/10.1016/j.physletb.2019.134826
29. M. Kłusek-Gawenda, R. McNulty, R. Schicker, and A. Szczurek, Phys. Rev. D **99** (2019) 9, 093013 doi: https://doi.org/10.1103/PhysRevD.99.093013
30. S. R. Klein, Phys.Rev.D **98** (2018) 11, 118501 doi:10.1103/PhysRevD.98.118501
31. ALICE Collaboration, arXiv:2211.02491 [physics.ins-det] doi:https://doi.org/10.48550/arXiv.2211.02491
32. ATLAS Collaboration, Phys. Rev. Lett. **131** (2023) 151802 doi: https://doi.org/10.1103/PhysRevLett.131.151802
33. CMS Collaboration, Phys. Rev. Lett. **131** (2023) 151803 doi: https://doi.org/10.1103/PhysRevLett.131.151803
34. Victor P. Gonçalves and Bruno D. Moreira b, Phys. Lett. B **816** (2021) 136249 doi: https://doi.org/10.1016/j.physletb.2021.136249

Exclusive η_c production by $\gamma^*\gamma$ interactions in electron-ion collisions

I. Babiarz[a], V. P. Goncalves[b], W. Schäfer[a], A. Szczurek [a,c]
[a] *Institute of Nuclear Physics, Polish Academy of Sciences, ul. Radzikowskiego 152, PL-31-342 Kraków, Poland*
[b] *Physics and Mathematics Institute, Federal University of Pelotas, Postal Code 354, 96010-900, Pelotas, RS, Brazil*
[c] *College of Mathematics and Natural Sciences, University of Rzeszów, ul. Pigonia 1, PL-35-310 Rzeszów, Poland*

One of the main goals of future electron-ion colliders is to improve our understanding of the structure of hadrons. We study the exclusive η_c production by $\gamma\gamma^*$ interactions in eA collisions and demonstrate that future experimental analysis of this process can be used to improve the description of the transition form factor. The rapidity, transverse momentum and photon virtuality distributions are estimated considering the energy and target configurations expected to be present at the EIC, EicC and LHeC and assuming different predictions for the light-front wave function of the meson. Our results indicate that the electron-ion colliders can be considered an alternative for providing supplementary data to those obtained in colliders.

DOI: https://doi.org/10.17161/4g2x0s19
Keywords: quarkonium, exclusive production, EIC

1 Introduction

Studies of transition form factors in various processes can provide complementary information on quarkonium structure and exotic state compositions. We shortly remind the clue of the light front wave function approach (LFWF) to the photon-photon transition form factor. In Fig. 1, we depict an example of photon-photon fusion in e^+e^- collision. We consider the space-like region, where both photons are off-shell. In the LFWF approach, we assume that the dominant contribution in the light front Fock state expansion is the $\mathsf{Q}\bar{\mathsf{Q}}$ component:

$$|\eta_c; P_+, \vec{P}_\perp\rangle = \sum_{i,j,\lambda,\bar{\lambda}} \frac{\delta^i_j}{\sqrt{N_c}} \int \frac{dz d^2\vec{k}_\perp}{z(1-z)16\pi^3} \Psi_{\lambda\bar{\lambda}}(z,\vec{k}_\perp) \big|\mathsf{Q}_{i\lambda}(zP_+, \vec{p}_{\perp c})\bar{\mathsf{Q}}^j_{\bar{\lambda}}((1-z)P_+, \vec{p}_{\perp\bar{c}})\big\rangle + \dots . \tag{1}$$

Thus we consider the $\mathsf{Q}\bar{\mathsf{Q}}$ bound system in colour-singlet configuration. Here $\Psi_{\lambda\bar{\lambda}}(z,\vec{k}_\perp)$ is the corresponding light front wave function. In ref.[1,2], we describe in detail the procedure to construct the spin-orbit part of the rest frame $c\bar{c}$ wave function and the transformation to light-front via Melosh spin-rotation matrix. The radial part is the solution of the Schrödinger equation for five potential models from the literature, mapped to light-front representation. In the current analysis, we also employ a wave function obtained from the Basis Light Front Quantisation (BLFQ) approach [3,4,5].

We can define transition form factor via covariant amplitude $\mathcal{M}_{\mu\nu}$ of the photon-photon to quark-antiquark:

$$\mathcal{M}_{\mu\nu}(\gamma^*(q_1)\gamma^*(q_2) \to \eta_c) = 4\pi\alpha_{\rm em}\,(-i)\varepsilon_{\mu\nu\alpha\beta} q_1^\alpha q_2^\beta\, F(Q_1^2, Q_2^2)\,. \tag{2}$$

Above we denote photons four momenta as q_1, q_2, and $\varepsilon_{\mu\nu\alpha\beta}$ is the antisymmetric tensor. Remaining indices $\mu\nu$ refer to photon's helicties $e_1^\mu(\lambda_1)$, $e_2^\nu(\lambda_2)$, which depend on the chosen frame. In Refs. [1,6], we

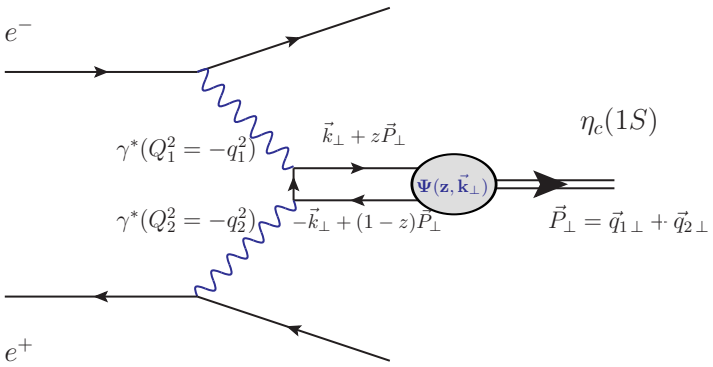

Figure 1 – The sketch of the photon-photon interaction in e^+e^- collision. Here photons are space-like, their virtualities: $Q^2_{1;2} > 0$. Quark $\mathtt{Q}$, and antiquark $\bar{\mathtt{Q}}$ carry the fraction of the meson P_+ momenta z and $(1-z)$, respectively, $\vec{k}_\perp$ is relative momentum between quark and antiquark.

put into evidence that in the limit for $Q_2^2 \to 0$, transition form factor takes the form:

$$F(Q^2, 0) = e_c^2 \sqrt{N_c}\, 4 \int \frac{dz d^2\vec{k}_\perp}{\sqrt{z(1-z)} 16\pi^3} \left\{ \frac{\tilde{\psi}_{\uparrow\downarrow}(z, k_\perp)}{\vec{k}_\perp{}^2 + \mu^2} + \frac{\vec{k}_\perp{}^2}{[\vec{k}_\perp{}^2 + \mu^2]^2} \left(\tilde{\psi}_{\uparrow\downarrow}(z, k_\perp) + \frac{m_c}{k_\perp} \tilde{\psi}_{\uparrow\uparrow}(z, k_\perp) \right) \right\}, \quad (3)$$

with $\mu^2 = z(1-z)Q^2 + m_c^2$, and the helicity components $\tilde{\psi}_{\uparrow\downarrow}(z, k_\perp), \tilde{\psi}_{\uparrow\uparrow}(z, k_\perp)$ are related to the same radial wave function $\psi(z, k_\perp)$ as:

$$\tilde{\psi}_{\uparrow\downarrow}(z, k_\perp) \to \frac{m_c}{\sqrt{z(1-z)}} \psi(z, k_\perp), \quad \text{and} \quad \tilde{\psi}_{\uparrow\uparrow}(z, k_\perp) \to \frac{-|\vec{k}_\perp|}{\sqrt{z(1-z)}} \psi(z, k_\perp), \quad (4)$$

so that there appears cancellation of the terms in the round brackets in Eq. (3) [1]. Other approaches, such as the BLFQ approach of [3,4] do not guarantee this cancellation. In particular, at the on-shell point, where two photons are real, the transition form factor is related to radiative decay width:

$$\Gamma_{\gamma\gamma\to\eta_c} = \frac{\pi}{4} \alpha_{em}^2 M_{\eta_c}^3 |F(0,0)|^2, \quad (5)$$

with α_{em} being fine-structure constant.

2 Cross-section for one virtual photon in eA collision

The contribution of η_c production associated with photon-photon interactions is similar to a proton target. It dominates when an ion is present, which is directly associated with nuclear charge squared (Z^2) enhancement present in the nuclear photon flux. This point is the main motivation for exclusive analysis of η_c production, which can occur via photon-photon fusion in an electron-ion collision.

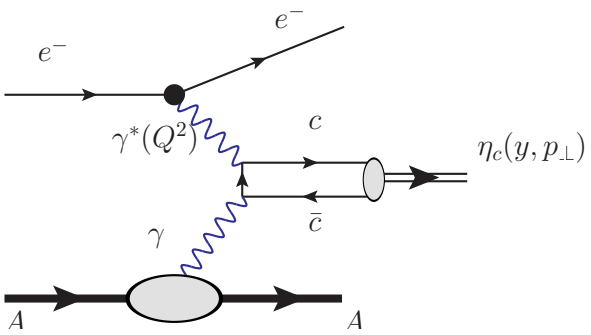

Figure 2 – Example illustration of an electron-ion collision involving one virtual photon. In particular we consider ions: ^{197}Au or ^{208}Pb.

Here we are interested in the process, where one of the photons has virtuality Q^2, and the second emitted by the ion is quasi-real, see Fig. 2. In order to describe exclusive production we can take advantage of the factorisation formula

$$\sigma(eA \to e\eta_c A) = \int d\omega_e dQ^2 \frac{d^2N_e}{d\omega_e dQ^2} \sigma(\gamma^* A \to \eta_c A)\,, \tag{6}$$

where the electron flux factor is given by [7]

$$\frac{d^2N_e}{d\omega_e dQ^2} = \frac{\alpha_{em}}{\pi\omega_e Q^2}\left[\left(1-\frac{\omega_e}{E_e}\right)\left(1-\frac{Q^2_{min}}{Q^2}\right)+\frac{\omega_e^2}{2E_e^2}\right]. \tag{7}$$

Here we denote ω_e as the energy of the photon emitted by the electron with energy E_e. Constrains by the maximum of the electron energy loss imply that $Q^2_{min} = m_e^2\omega_e^2/[E_e(E_e-\omega_e)]$ and $Q^2_{max} = 4E_e(E_e-\omega_e)$. If we assume that the production of η_c is dominated by the subprocess $\gamma^*\gamma \to \eta_c$, we can apply the equivalent photon approximation in the form:

$$\sigma(\gamma^* A \to \eta_c A) = \int d\omega_A \frac{dN}{d\omega_A}\, \sigma_{\rm TT}(\gamma^*\gamma \to \eta_c; W_{\gamma\gamma}, Q^2, 0)\,, \tag{8}$$

here the nucleus photon fluxes for a photon with energy ω_A are found to be [8,9,10,11,12]

$$\frac{dN}{d\omega_A} = \frac{2Z^2\alpha_{em}}{\pi\omega_A}\left[\xi K_0(\xi)K_1(\xi) - \frac{\xi^2}{2}(K_1^2(\xi)-K_0^2(\xi))\right]. \tag{9}$$

Here $\xi = R_A\omega_A/\gamma_L$, with $R_A = r_0 A^{1/3}$, and $r_0 = 1.1\,$fm is the nuclear radius, γ_L is the Lorentz factor. The modified Bessel functions are K_0 and K_1. We can express the photon-photon center of mass energy $W_{\gamma^*\gamma}$ by transverse momentum of the meson in the final state $p_\perp$:

$$W_{\gamma\gamma} = \sqrt{4\omega_e\omega_A - p_\perp^2}\,, \tag{10}$$

where $p_\perp^2 = \left(1-\frac{\omega_e}{E_e}\right)Q^2$. Moreover, in an electron-ion cm frame we can find the energies of the photon in terms of the rapidity of the final state:

$$\omega_e = \frac{\sqrt{M_{\eta_c}^2+p_\perp^2}}{2}e^{+y} \quad \text{and} \quad \omega_A = \frac{\sqrt{M_{\eta_c}^2+p_\perp^2}}{2}e^{-y}\,. \tag{11}$$

This brings us to the main ingredient of calculation of the exclusive production, mainly the cross-section of the subprocess $\gamma^*\gamma \to \eta_c$. The standard formulation of the cross-section in case of two virtual photons reads [7,13]:

$$\sigma_{\rm TT}(W_{\gamma\gamma}, Q_1^2, Q_2^2) = \frac{1}{4\sqrt{X}}\frac{M_{\eta_c}\Gamma_{\rm tot}}{(W_{\gamma\gamma}^2-M_{\eta_c}^2)^2+M_{\eta_c}^2\Gamma_{\rm tot}^2}\,\mathcal{M}^*(++)\mathcal{M}(++)\,, \tag{12}$$

with the kinematic factor $X = (q_1\cdot q_2)^2 - q_1^2q_2^2$, and the photon virtualities being defined by $Q_i^2 = -q_i^2$. We can use Eq. (5) and the narrow width approximation in Eq. 12, thus we obtain:

$$\sigma_{\rm TT}(W_{\gamma\gamma}, Q^2, 0) \;\approx\; 8\pi^2\,\delta(W_{\gamma\gamma}^2 - M_{\eta_c}^2)\,\frac{\Gamma_{\gamma\gamma}}{M_{\eta_c}}\left(1+\frac{Q^2}{M_{\eta_c}^2}\right)\left(\frac{F(Q^2,0)}{F(0,0)}\right)^2, \tag{13}$$

Wrapping up the formulas above, we can write the total cross-section as follows:

$$\sigma(\gamma^* A \to \eta_c A) = \left.\frac{dN}{d\omega_A}\right|_{\omega_A=(M_{\eta_c}^2+p_\perp^2)/(4\omega_e)} 8\pi^2\frac{1}{4\omega_e}\frac{\Gamma_{\gamma\gamma}}{M_{\eta_c}}\left(1+\frac{Q^2}{M_{\eta_c}^2}\right)\left(\frac{F(Q^2,0)}{F(0,0)}\right)^2. \tag{14}$$

3 Numerical analysis and conclusions

In the numerical analysis, we consider energy and target configurations expected to be available at the EIC (BNL)[14,15,16,17,18,19], EicC (China) [20] and LHeC (CERN) [21]. As the future electron-ion collider at BNL will reach luminosities in the $10^{33} - 10^{34}$ cm^{-2}s^{-1} range, in our analysis, we assume two ranges to

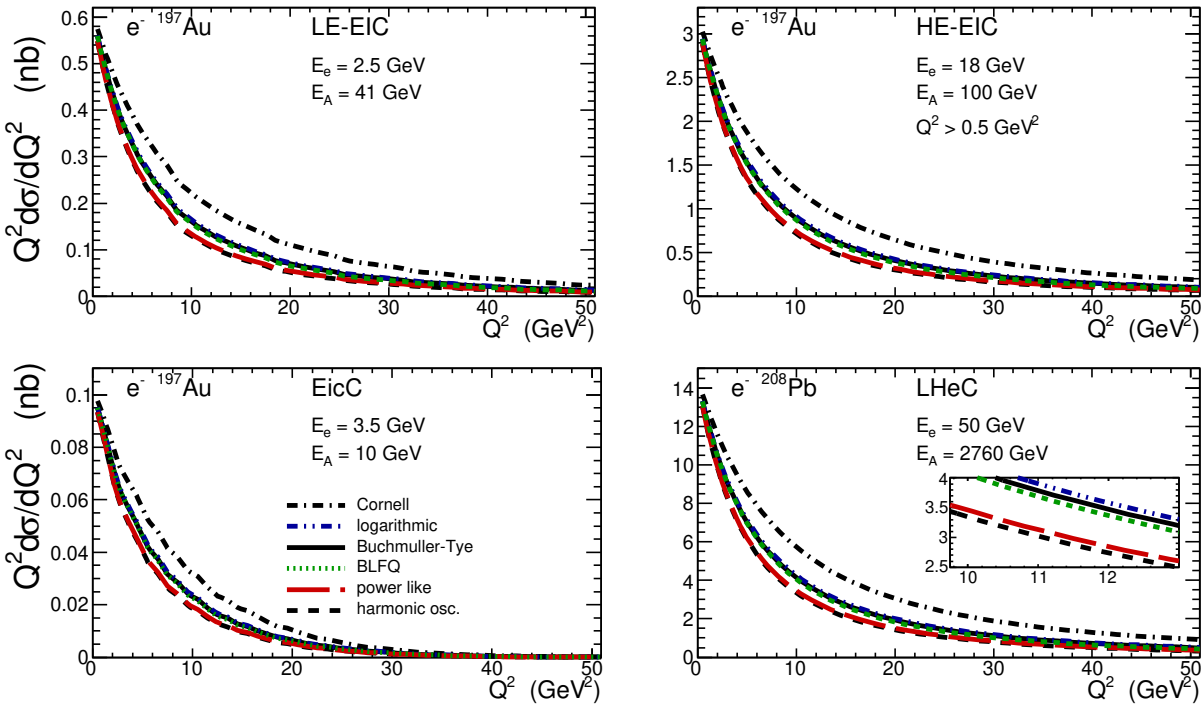

Figure 3 – Differential distribution in photon virtuality multiplied by Q^2 for four energy ranges: lower energy range EIC (LE-EIC), higher energy range (HE-EIC), electron-ion collider in China (EicC) and a large hadron-electron collider (LHeC).

be for the electron and Au - ion energies: (a) $(E_e, E_{Au}) = (2.5, 41)$ GeV and (b) $(E_e, E_{Au}) = (18, 100)$ GeV. In Fig. 3 [6], we labelled these two setups as LE - EIC, and HE - EIC, respectively. In the case of EicC predictions, we are concerned with: $E_e = 3.5$ GeV, $E_{Au} = 10$ GeV and $\mathcal{L} = 10^{33}$ cm^{-2}s^{-1}), and for LHeC: $E_e = 50$ GeV, $E_{Pb} = 2760$ GeV and $\mathcal{L} = 10^{32}$ cm^{-2}s^{-1}. The electron tagging in the final state could provide Q^2 dependence on the differential distribution $Q^2 d\sigma/dQ^2$, see Fig.3 [6]. Our model for the Cornell wave function gives generally larger values. The predictions obtained from the harmonic oscillator and power-like model of the wave function are rather similar to each other in the same manner as results for the BLFQ, Buchmüller-Tye and logarithmic models. The difference between the predictions increases with the center-of-mass energies. The results show that the distribution analysis considered in this letter can be useful for constraining the transition factor[6]. The numerical results for the total cross-section in the range of $50\,\text{GeV}^2 > Q^2 > 0.5\,\text{GeV}^2$ gives approximately 0.1-60 nb.

Our results strongly encourage a more detailed study, which includes realistic experimental limitations for the detectors proposed for installation in the BNL EIC, which we plan to perform in future studies. In principle, analysis can be extended to other final states that the $\gamma^*\gamma$ interaction can produce.

Acknowledgments

This work was partially supported by the Polish National Science Center grant UMO-2018/31/B/ST2/03537.

References

1. I. Babiarz, V. P. Goncalves, R. Pasechnik, W. Schäfer and A. Szczurek, Phys. Rev. D **100** (2019) no.5, 054018 doi:10.1103/PhysRevD.100.054018 [arXiv:1908.07802 [hep-ph]].
2. I. Babiarz, R. Pasechnik, W. Schäfer and A. Szczurek, JHEP **06** (2020), 101 doi:10.1007/JHEP06(2020)101 [arXiv:2002.09352 [hep-ph]].
3. Y. Li, P. Maris and J. P. Vary, Phys. Rev. D **96** (2017), 016022 doi:10.1103/PhysRevD.96.016022 [arXiv:1704.06968 [hep-ph]].
4. Y. Li, P. Maris and J. Vary, Phys. Rev. D **97** (2018) no.5, 054034 doi:10.1103/PhysRevD.97.054034 [arXiv:1712.03467 [hep-ph]].
5. Y. Li., Mendeley Data V2, doi: 10.17632/cjs4ykv8cv.2, (2019).

6. I. Babiarz, V. P. Goncalves, W. Schäfer and A. Szczurek, Phys. Lett. B **843** (2023), 138046 doi:10.1016/j.physletb.2023.138046 [arXiv:2306.00754 [hep-ph]].
7. V. M. Budnev, I. F. Ginzburg, G. V. Meledin and V. G. Serbo, Phys. Rept. **15** (1975), 181-281 doi:10.1016/0370-1573(75)90009-5.
8. C. A. Bertulani and G. Baur, Phys. Rept. **163** (1988), 299 doi:10.1016/0370-1573(88)90142-1.
9. C. A. Bertulani, S. R. Klein and J. Nystrand, Ann. Rev. Nucl. Part. Sci. **55** (2005), 271-310 doi:10.1146/annurev.nucl.55.090704.151526 [arXiv:nucl-ex/0502005 [nucl-ex]].
10. V. P. Goncalves and M. V. T. Machado, J. Phys. G **32** (2006), 295-308 doi:10.1088/0954-3899/32/3/005 [arXiv:hep-ph/0506331 [hep-ph]].
11. A. J. Baltz, G. Baur, D. d'Enterria, L. Frankfurt, F. Gelis, V. Guzey, K. Hencken, Y. Kharlov, M. Klasen and S. R. Klein, *et al.* Phys. Rept. **458** (2008), 1-171 doi:10.1016/j.physrep.2007.12.001 [arXiv:0706.3356 [nucl-ex]].
12. J. G. Contreras and J. D. Tapia Takaki, Int. J. Mod. Phys. A **30** (2015), 1542012 doi:10.1142/S0217751X15420129.
13. M. Poppe, Int. J. Mod. Phys. A **1** (1986), 545-668 doi:10.1142/S0217751X8600023X.
14. D. Boer, M. Diehl, R. Milner, R. Venugopalan, W. Vogelsang, D. Kaplan, H. Montgomery, S. Vigdor, A. Accardi and E. C. Aschenauer, *et al.* [arXiv:1108.1713 [nucl-th]].
15. A. Accardi, J. L. Albacete, M. Anselmino, N. Armesto, E. C. Aschenauer, A. Bacchetta, D. Boer, W. K. Brooks, T. Burton and N. B. Chang, *et al.* Eur. Phys. J. A **52** (2016) no.9, 268 doi:10.1140/epja/i2016-16268-9 [arXiv:1212.1701 [nucl-ex]].
16. E. C. Aschenauer, S. Fazio, J. H. Lee, H. Mantysaari, B. S. Page, B. Schenke, T. Ullrich, R. Venugopalan and P. Zurita, Rept. Prog. Phys. **82** (2019) no.2, 024301 doi:10.1088/1361-6633/aaf216 [arXiv:1708.01527 [nucl-ex]].
17. R. Abdul Khalek, A. Accardi, J. Adam, D. Adamiak, W. Akers, M. Albaladejo, A. Al-bataineh, M. G. Alexeev, F. Ameli and P. Antonioli, *et al.* Nucl. Phys. A **1026** (2022), 122447 doi:10.1016/j.nuclphysa.2022.122447 [arXiv:2103.05419 [physics.ins-det]].
18. V. D. Burkert, L. Elouadrhiri, A. Afanasev, J. Arrington, M. Contalbrigo, W. Cosyn, A. Deshpande, D. I. Glazier, X. Ji and S. Liuti, *et al.* Prog. Part. Nucl. Phys. **131** (2023), 104032 doi:10.1016/j.ppnp.2023.104032 [arXiv:2211.15746 [nucl-ex]].
19. R. Abir, I. Akushevich, T. Altinoluk, D. P. Anderle, F. P. Aslan, A. Bacchetta, B. Balantekin, J. Barata, M. Battaglieri and C. A. Bertulani, *et al.* [arXiv:2305.14572 [hep-ph]].
20. D. P. Anderle, V. Bertone, X. Cao, L. Chang, N. Chang, G. Chen, X. Chen, Z. Chen, Z. Cui and L. Dai, *et al.* Front. Phys. (Beijing) **16** (2021) no.6, 64701 doi:10.1007/s11467-021-1062-0 [arXiv:2102.09222 [nucl-ex]].
21. J. L. Abelleira Fernandez *et al.* [LHeC Study Group], J. Phys. G **39** (2012), 075001 doi:10.1088/0954-3899/39/7/075001 [arXiv:1206.2913 [physics.acc-ph]].

Phys. Proc. Ultra-Peripheral Collisions **1**, 024 (2024) 1-8

Photo-nuclear collisions in Pythia 8

I. Helenius and M. Utheim
University of Jyvaskyla, Department of Physics, P.O. Box 35, FI-40014 University of Jyvaskyla, Finland
Helsinki Institute of Physics, P.O. Box 64, FI-00014 University of Helsinki, Finland

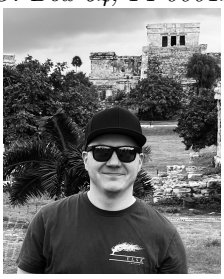

We present a new extension in Pythia Monte Carlo event generator that allows to simulate the leading contribution in collisions of a real photon and a heavy ion. The model is based on a vector meson dominance (VMD) where a real photon is modelled as a linear combination of different vector-meson states, and an extension of Angantyr, the heavy-ion model in Pythia, that allow simulations of a generic hadron colliding with an ion target. We first verify the VMD implementation by comparing simulations to HERA photoproduction data. Then we present simulated results corresponding to event selection criteria applied in a recent ATLAS analysis for ultra-peripheral Pb-Pb collisions at the LHC. We find that the simulated results are in line with the ATLAS data when accounting for the limited detector efficiency for charged-particle reconstruction. We also consider two-particle correlations and study whether the simulated events reproduce the collective behaviour seen in the ATLAS γ-Pb data.

DOI: https://doi.org/10.17161/9279nk67
Keywords: Monte Carlo event generation, Ultra-peripheral collisions, photoproduction, charged-particle production, collectivity

1 Introduction

Ultraperipheral heavy ion collisions (UPCs)[1,2] provide the first opportunity to study photo-nuclear interactions at collider energies. In addition to exclusive processes, the photon projectile emitted by the other beam nucleus may also break up the target nucleon in the interaction. Such collisions result as a complex hadronic final state. Monte Carlo event generators provide the necessary modelling to describe the collision process from the primary scattering to the long-lived hadrons measured in the detectors. The highly-virtual partons created in the hard scattering are evolved with DGLAP evolution equations to generate QCD radiation in the collinear approximation[3] and after reaching non-perturbative scales, the partons form colour-neutral hadronic states that decay into stable ones. In case of hadronic collisions additional particle production takes place from multiparton interactions (MPIs) and beam remnants[4].

In this work we present the necessary extensions to the Pythia Monte Carlo event generator[5] that allows to simulate UPCs. We model the flux of photons from heavy nuclei using equivalent photon approximation (EPA)[6]. Unlike in the case of point-like leptons, the virtuality of photons emitted by charged hadrons and nuclei are limited and thus these can be assumed as real photons. Such photons can fluctuate into a hadronic state and simulations for these events will require all the same components as any other hadronic collision including beam remnants and MPIs. Furthermore, in case of nuclear target also subsequent collisions with multiple nucleons needs to be accounted for.

The main motivation for the present extensions is provided by the recent ATLAS analysis[7] which studies the charged-particle production in UPCs at the LHC. An interesting observation in the analysis was the finite values for Fourier coefficients fitted to two-particle azimuthal correlations using a template fitting procedure. Such effects are typically connected to hydrodynamic flow in heavy-ion collisions. In this study we compare the simulated results to the measurement including multiplicity and pseudorapidity distributions and perform a similar template fitting to two-particle correlations. Such a setup is not only relevant for the UPCs at the LHC but similar γ-A processes can be studied also in future Electron-Ion Collider (EIC)[8].

2 Theoretical background

2.1 Structure of a real photon

For hard-process generation that initiates the simulation chain we apply collinear factorization. In this framework the long-distance physics describing the structure of the incoming beams can be factorized from the short-distance interactions that can be calcuated with perturbative QCD (pQCD). The structure of hadrons can be encoded into parton distribution functions (PDFs), $f_i^A(x_A, \mu^2)$, which describe the number distribution of parton i at the momentum fraction x_A inside a particle A when probed at scale μ^2. In this framework the differential cross section to produce two partons, k and l, in a photo-initiated process can be computed from

$$\mathrm{d}\sigma^{AB\to kl+X} = f_\gamma^B(x) \otimes f_j^\gamma(x_\gamma, \mu^2) \otimes f_i^A(x_A, \mu^2) \otimes \mathrm{d}\sigma^{ij\to kl}, \tag{1}$$

where $f_\gamma^B(x)$ is the photon flux from beam particle B and x the momentum fraction of the photon wrt. the beam particle. The PDFs of the photon, $f_j^\gamma(x_\gamma, \mu^2)$ can be written as a sum of different components: direct, anomalous and hadron-like

$$f_i^\gamma(x_\gamma, \mu^2) = f_i^{\gamma,\mathrm{dir}}(x_\gamma, \mu^2) + f_i^{\gamma,\mathrm{anom}}(x_\gamma, \mu^2) + f_i^{\gamma,\mathrm{hl}}(x_\gamma, \mu^2). \tag{2}$$

In case of direct contribution the incoming photon is simply the initiator of the hard process and we can replace $f_i^{\gamma,\mathrm{dir}}(x_\gamma, \mu^2) = \delta_{i\gamma}\delta(1 - x_\gamma)$. For the anomalous component, where the photon splits into quark-antiquark pair perturbatively, the PDF can be directly calculated. For the hadron-like part the scale evolution can still be derived from DGLAP equations but a non-perturbative input is needed. This can either be fitted to data or it can be modelled with a vector-meson dominance (VMD) model where this state is given by a linear combination of vector-meson states[9]. In this study we will consider both approaches for the hadron-like part. Together with the anomalous part this form the resolved-photon contribution. In case of VMD the cross section for the collision between a hadron-like photon and a nucleon n is given by

$$\sigma^{\mathrm{VMD}-n} = \sum_V \frac{4\pi\alpha_{\mathrm{em}}}{f_V^2}\sigma^{\mathrm{V}-n}, \tag{3}$$

where the couplings f_V can be obtained from data[10].

When we apply the DGLAP-evolved PDFs for resolved photons with anomalous component, we need to include a term describing the $\gamma \to q\bar{q}$ splitting into the parton-shower algorithm. Such a term is included into the default parton shower in Pythia. Sampling such splitting during the evolution will collapse the photon back to an unresolved state where no MPIs or beam remnants are needed.

2.2 Photon fluxes

The photon fluxes for different beam configurations can be calculated from EPA. In case of electron-proton collisions the photon flux becomes

$$f_\gamma^{\mathrm{e}}(x, Q^2) = \frac{\alpha_{\mathrm{em}}}{2\pi}\frac{1}{Q^2}\frac{1 + (1-x)^2}{x}, \tag{4}$$

where the upper limit for the virtuality is obtained from the experimental setup and the lower limit follows from kinematical consideration giving $Q^2_{\mathrm{min}} \approx m_{\mathrm{e}}^2 x^2/(1-x)$. Having the flux differential also in Q^2 allows for sampling of the virtuality and deriving complete kinematics of the event, including transverse momentum of the outgoing lepton and the intermediate photon. Also photon flux from protons has been implemented in Pythia where a form factor has to be included in the calculation to account for the finite size of the emitting particle and to keep it intact.

In case of heavy ions it is more convenient to work out the flux in impact-parameter space as this allows for a straightforward rejection of events where the beam particles would interact hadronically via short-range strong interaction. Assuming a point-like flux and a sharp cut-off for the allowed impact parameter values we have

$$f_\gamma^A(x) = \frac{2\alpha_{\mathrm{em}}Z^2}{x\,\pi}\left[\xi\,K_1(\xi)K_0(\xi) - \frac{\xi^2}{2}\left(K_1^2(\xi) - K_0^2(\xi)\right)\right], \tag{5}$$

where $\xi = b_{\mathrm{min}}\,x\,m$, m is the per-nucleon mass for nucleus A and K_i modified Bessel functions of the first kind. We select $b_{\mathrm{min}} = 2R_A$, where R_A is the radius of the colliding nuclei to reject the nuclear

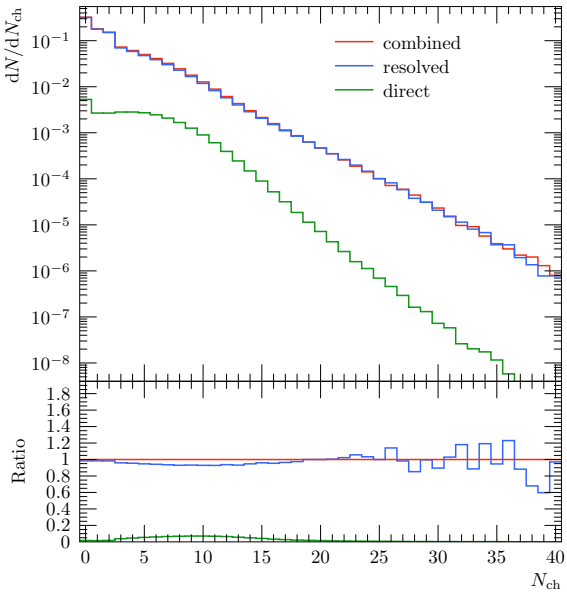

Figure 1 – Multiplicity distribution in photoproduction in electron-proton collisions corresponding to event selection criteria in the ZEUS analysis from complete simulations (red) and from resolved (blue) and direct (green) components separately.

overlap. This approximation works well in the kinematic region relevant for this study but break down for final states which require a large energy for the intermediate photons[11]. In addition to hadronic break-up probability factor it has been shown that to match the experimental event selection criteria also a rejection for subsequent electro-magnetic interactions could be significant[12].

3 Photoproduction in electron-proton collisions

Due to the low virtuality of photons emitted by charged hadrons and heavy ions, the UPC events are similar to photoproduction that has been extensively studied with proton target in HERA collider. We can therefore use these data to validate our implementation of photon structure and compare the VMD approach to the full description of quasi-real photons. Here we will apply a recent ZEUS analysis[13] which focuses on high-multiplicity events where the resolved photons are expected to dominate the cross section. As a validation for the previous statement we show the multiplicity distribution of charged particles from our simulations in figure 1. In addition to the total multiplicity also the direct and resolved contributions are shown separately. The direct contribution is at most 10% for events with around 10 charged particles. Furthermore, in the region where $N_{\mathrm{ch}} > 20$, direct photons contribution well below 1% and can be safely neglected in the following studies. We note that the definition of N_{ch} does not include all particles in the event but mathces the acceptance and particle-selection criteria applied in the ZEUS analysis.

We present comparisons with the simulated results and the data in figure 2 for charged-particle multiplicity, N_{ch}, and pseudorapidity, η distribution. In case of simulation, we show results using the full photoproduction setup as implemented in Pythia (gm-p) and by using only the VMD model (vmd-p). Furthermore, we vary the parameter $p_{\mathrm{T},0}^{\mathrm{ref}}$, that controls the probability for MPIs, for both setups within values $p_{\mathrm{T},0}^{\mathrm{ref}} = 3, 4$ GeV. In case of N_{ch} distribution we notice that the probability of large multiplicity events are sensitive to the parameter value applied for $p_{\mathrm{T},0}^{\mathrm{ref}}$. Especially in case of full photoprodution implementation we find a factor of five difference between the two applied values at the highest multplicities. With the VMD-only calculation, with the two parameter values lead somewhat reduced variation. More importantly we notice that the two applied approaches are in a good agreement with each other and the data and that these data could provide further constraints for MPI modelling in photon-hadron collisions. For the η distribution we again notice that the calculated results from both models are in a good agreement with each other and the experimental data. As a large fraction of events passing the selection criteria are from the low end of multiplicity distribution, the sensitivity to $p_{\mathrm{T},0}^{\mathrm{ref}}$ parameter is significantly reduced compared to N_{ch} distribution. We can thus conclude that, while there are some underlying theoretical uncertainty, both applied approaches, the full photoproduction model with the resolved-photon

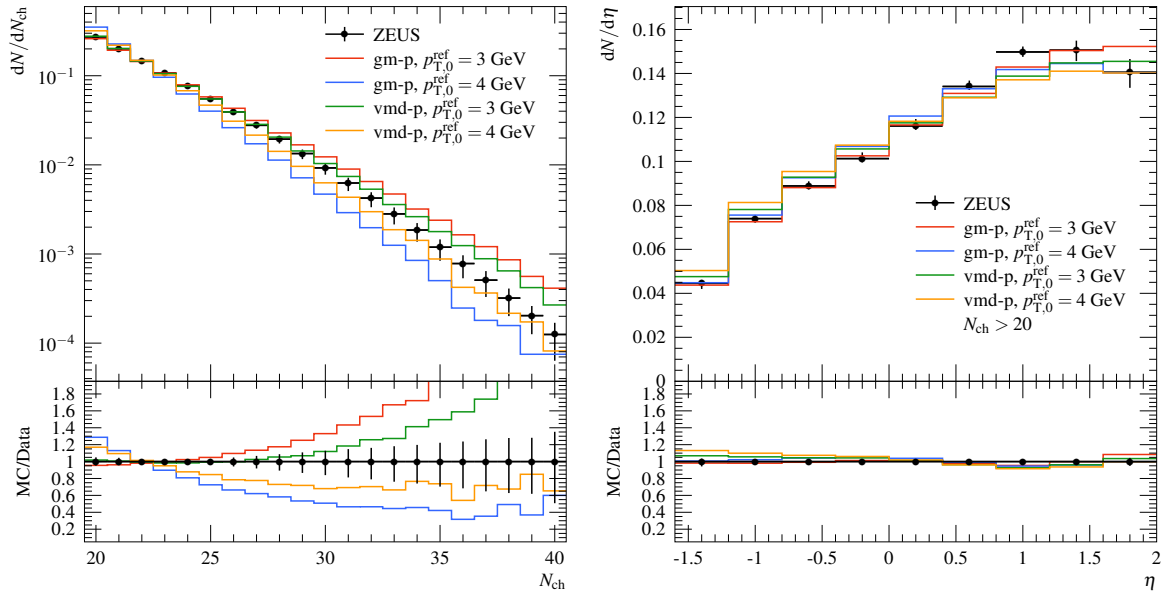

Figure 2 – Charged-particle multiplicity and rapidity distributions in photoproduction in electron-proton collisions from a ZEUS analaysis compared with the simulations from full photoproduction (gm-p) model and VMD-based implementation (vmd-p) for resolved photons with two different values for parameter $p_{T,0}^{ref}$.

PDFs and the VMD-based model, are adequate to describe the minimum bias photon-proton collisions especially in case of the high-multiplicity events.

4 Ultraperipheral collisions at the LHC

4.1 Photon-ion collisions

As a first step for full model for interactions between a real photon and a heavy nucleus in ultraperipheral heavy-ion collisions we have extended recent work that enable generation of collisions with generic hadron beams with varying energy on a proton target[14] in Pythia 8 to handle also collisions with a nuclear target. The nuclear effects are modelled with the existing Angantyr model[15] where the heavy ion collisions are generated by deriving the nucleon-nucleon collisions from a Monte Carlo Glauber model. The interaction probabilities include cross section fluctuations and sampling for the type of the primary interaction which can be non-diffractive, single diffractive, double diffractive or elastic. The secondary interactions are modelled using diffractive excitations which account for the reduced energy which the projectile particle has lost in the primary interaction. The Angatyr model builds up the nuclear collisions from a collection of nucleon-nucleon events generated with Pythia, which we have extended to handle also a generic handron as a beam particle. In particular the cross section fluctuations in the Angantyr model has been adjusted to handle also such beam configurations.

Comparison between different projectiles for the charged-particle multiplicity and rapidity distributinos in a hadron-lead nucleus collision at $\sqrt{s_{nn}} = 5.02$ TeV are shown in figure 3. The considered projectile particles include proton as a baseline and ρ, ϕ and J/Ψ to demonstrate the components of the VMD model. The multiplicity distribution has two distinct components, a peak at low multiplicity which arises from diffractive and elastic events and an another peak around 150-350 particles from non-diffractive events. The multiplicity distribution from the non-diffractive events becomes more narrow when switching the projectile from protons to vector mesons. This is due to having less secondary collisions in case of vector mesons due to lower non-diffractive cross section that determines the effective size of the projectile in the Glauber model. In the rapidity distribution we notice that the distribution of generated particles are more symmetric in case of collisions with vector-meson projectiles. This mainly follows from the same reason as above since the particles produced in the primary interactions are symmetric in rapidity and the asymmetry is mainly generated by the secondary interactions that are less frequent in case of vector mesons. Also the shape of the PDFs play some role here especially in case of J/Ψ where the heavy valence quarks carry a large fraction of the momenta of the particle that results as an almost symmetric

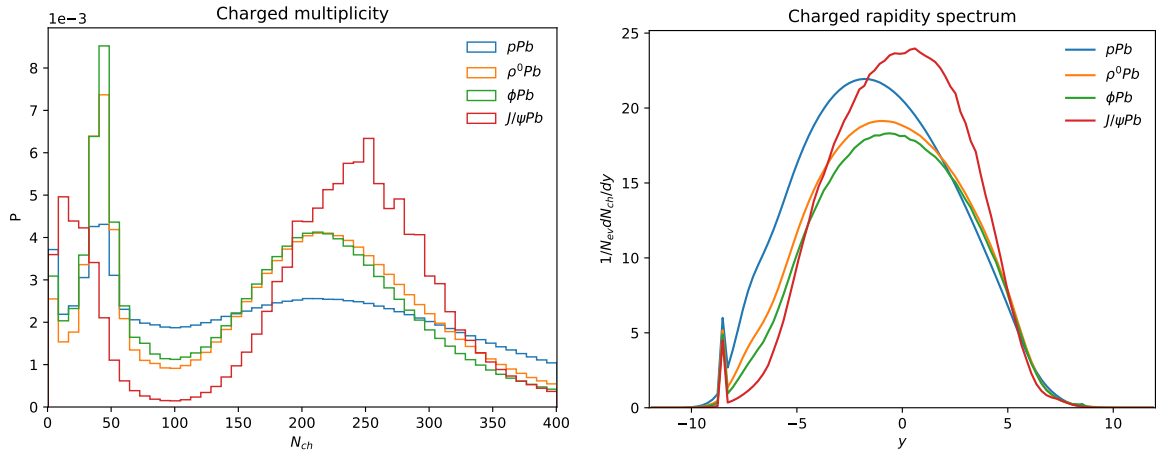

Figure 3 – Multiplicity (left) and rapidity (right) distributions of different hadron-nucleus collisions at $\sqrt{s_{\mathrm{NN}}}$ = 5.0 TeV with lead target and proton (blue), ρ^0 (orange), ϕ (green) and JΨ (red) projectiles.

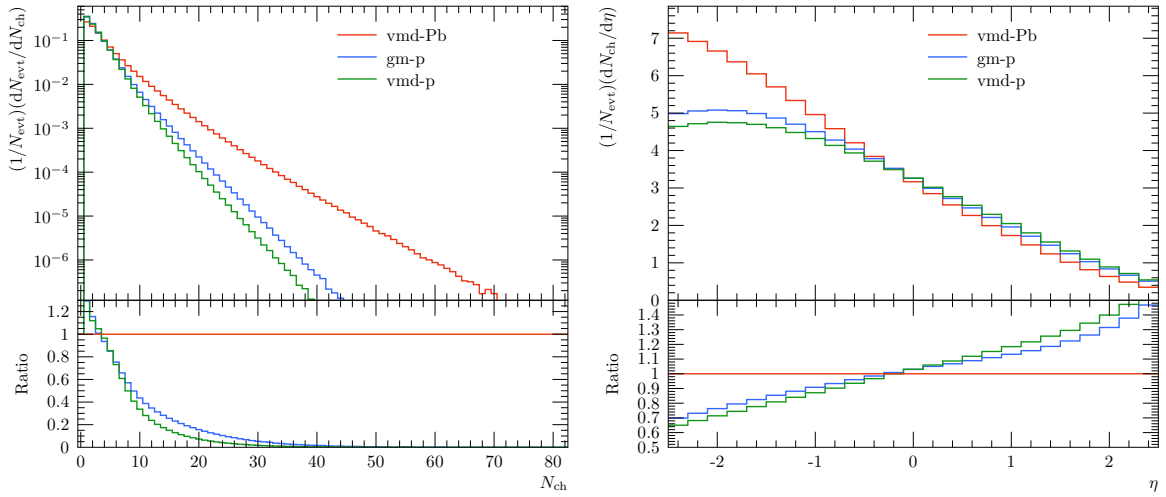

Figure 4 – Multiplicity (left) and rapidity (right) distributions for VMD-Pb simulations (red) compared to simulations with proton target applying VMD model (green) and full photoproduction (blue) at $\sqrt{s_{\mathrm{NN}}} = 5.02$ TeV.

rapidity distribution even with a nuclear target.

To account for the varying collisions energy from photon-flux sampling, the model parameters are fitted at a few fixed values in the specified energy range and then interpolated to obtain the values corresponding to the collision energy sampled according to the photon flux. Enabling this allows simulations for UPC events at the LHC with the VMD-nucleus setup based on the extended Angatyr model. We can compare these results then to the ATLAS data[7] for different observables. The main caveat with this data is, however, that the relevant distributions for charged-particle multiplicity and rapidity distributions with a multiplicity cut have not been corrected for limited particle-detection efficiency and therefore are not available for direct comparisons. Thus we only show results of our simulations with VMD model using proton and nucleus targets and compare these with the full photoproduction with proton target that was included in ATLAS results. This allows to estimate the agreement with the data by comparing the relative difference between this baseline simulation and the VMD-Pb setup to the experimental one. Again, we consider charged-particle multiplicity and pseudorapidity distributions in figure 4. We apply the same event-selection criteria as in the ATLAS study including a cut for the sum-of-rapidity-gaps measure $\Sigma_\gamma \Delta\phi$. We also adjust the multiplicity cut applied for the η distribution with an effiency correction estimated by comparing the N_{ch} from the gm-p setup in figure 4 to the one presented the ATLAS study giving an efficieny of 80% which is in line with previous ATLAS studies in different beam configurations[16]. With this corrections in place, we find that the simulated distributions are well in line with the experimental data.

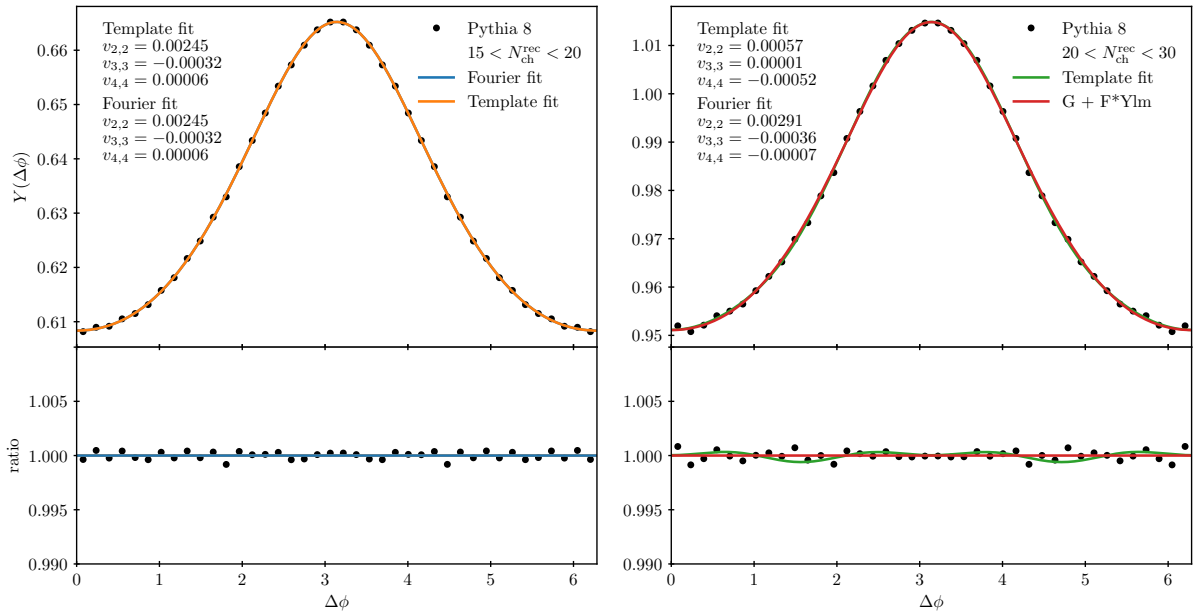

Figure 5 – An example of the template fitting procedure to the simulated data.

4.2 Correlations

Having a framework to succesfully describe the single-particle properties in high-multiplicity γ-Pb events, we can study such collisions with multiparton correlations. A particularly interesting observation in the ATLAS study was the observation of finite values for v_2 and v_3 that are typically considered as a signature of collective behaviour. While the template fitting procedure applied in the ATLAS analysis should remove the "non-flow" contribution such as jet-like correlations, it is still interesting to check whether any similar effects would arise from the MC simulations without any explicit final-state effects. The reason for this is that the binning to low- and high-multiplicity events will also bias the underlying energy distributions since higher collisions energy for the γ-Pb system will lead to higher average event multiplicity. Therefore the low-multiplicity event sample needed for the template fit might not capture all the jet-like correlations present in the high-multiplicity events at higher collision energy.

The template fitting procedure involves a simultaneous fit of two-particle correlation function $Y(\Delta\phi)$ for low- (LM) and high-multiplicity (HM) event samples which are obtained by integrating over relative pseudorapidity separation, $\Delta\eta$, with limits $2.0 < |\Delta\eta| < 5.0$ to focus on long-range η correlations. In case of low-multiplicity events, the following truncated Fourier series is applied

$$Y^{\mathrm{LM}}(\Delta\phi) = c_0 + 2 \cdot \sum_{n=1}^{4} c_n \cos(n\Delta\phi), \tag{6}$$

where c_n are free parameters that can be related to flow harmonics v_n. In case of HM event sample the $Y(\Delta\phi)$ is fitted with

$$Y^{\mathrm{HM}}(\Delta\phi) = F \cdot Y^{\mathrm{LM}}(\Delta\phi) + G \left[1 + 2 \cdot \sum_{n=2}^{4} v_{n,n} \cos(n\Delta\phi) \right], \tag{7}$$

where now a scaled $Y^{\mathrm{LM}}(\Delta\phi)$ is used as a baseline and $v_{n,n}$ allow for additional modulation for the HM sample. The scaling factors F and G are connected so in total there are 8 free parameters in the fit. An example of the fitting procedure is shown in figure 5 where $Y^{\mathrm{LM}}(\Delta\phi)$ and $Y^{\mathrm{HM}}(\Delta\phi)$ are fitted to the simulated data simultaneously. We have also performed independent Fourier fits with 4 parameters corresponding to equation (6) to both LM and HM samples. In case of the former event class this allows to check that the full template fitting does not bias the LM sample fitting and in case of latter this provide the Fourier harmonics without the "non-flow" subtraction for comparison. For the example configuration in figure 5 we have taken $15 < N_{\mathrm{ch}}^{\mathrm{rec}} < 20$ for the LM sample and $20 < N_{\mathrm{ch}}^{\mathrm{rec}} < 30$ for the HM sample. Both particles, the trigger and the associated, had a transverse momentum of $0.4 < p_{\mathrm{T}} < 2.0$ GeV.

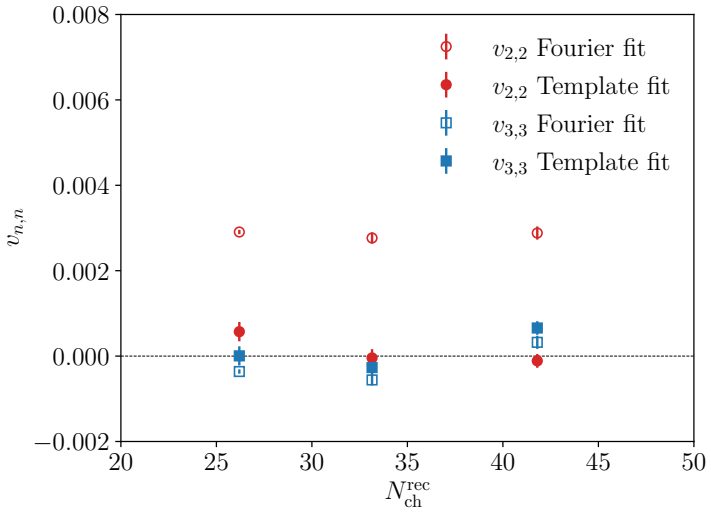

Figure 6 – Fitted values for $v_{2,2}$ (red) and $v_{3,3}$ (blue) from a direct Fourier fit, equation (6), (open markers) and a full template fit, equation (7), (closed markers) as a function of charged-particle multiplicity. Error bars quantify the fit uncertainty due to finite simulation statistics.

Similarly as in the ATLAS analysis, we have performed the fit with varying HM selection and plot the resulting $v_{n,n}$ values in figure 6. We notice that while the resulting values for $v_{2,2}$ and $v_{3,3}$ in case of a direct Fourier fit are in line with the measured ones, the values from a full template fit are consistent with zero in all considered multiplicity bins. This implies that our simulations do not reproduce the observed finite values of $v_{n,n}$ seen in the ATLAS γ-Pb data when the template fitting is applied. This confirms that the positive values for v_n in the ATLAS analysis are a result from a final-state (or initial-state) collectivity and not due to biased collision energy due to multiplicity sampling and that the template method work as expected also when applied to data with multiplicity binning in γ-Pb.

5 Summary and Outlook

We have presented a new model to simulate collisions between real photons and heavy ions based on a vector-meson dominance model within Pythia Monte Carlo event generator. In this model the photon is described as a linear combination of different vector-mesons states, ρ, ω, ϕ and J/Ψ. While this model does only account for the hadron-like part of the photon structure, such events are expected to dominate the total cross section and especially the high-multiplicity events. Unlike the direct-photon component, these resolved photons may interact with other nucleons inside a nucleus and give rise to events with large multiplicity. We have demonstarted that this contribution is indeed the dominant one in high multiplicity events and that the model is in line with the multiplicity distributions measured at HERA for γ-p collisions. Furthermore, we notice that when accounting for the limited efficiency, the model provides a good description of the charged-particle multiplicity and rapidity distributions in γ-Pb measured by ATLAS in ultra-peripheral Pb-Pb collisions.

We have also considered two-particle correlations and derived Fourier coefficients from the simulated events using a similar template fitting procedure as in the ATLAS analysis. Here the low- and high-multiplicity event samples are simultaenously fitted with truncated Fourier series which is supposed to remove possible "non-flow" jet-like contributions. While it is non-trivial that this procedure should work also in case of varying photon-energy spectrum which can lead to biased collision energy distribution when multiplicity binning is applied, we find that the resulting $v_{n,n}$ coefficients are consistent with zero. Thus we conclude that the observed collectivity in γ-Pb events is not reproduced with the default Pythia hadronization model. There have been recent studies, however, where including string interactions, such rope hadronization and string shoving, in the hadronization model have given rise to similar collective effects when applied to high-multiplicity proton-proton and proton-lead collisions. We plan to study these effects in case of γ-Pb in a future study. Also, the presented framework will serve as a starting for a more complete simulations of photon-ion collisions relevant also for the EIC.

Acknowledgments

We acknowledge the financial support from the Research Council of Finland, Project No. 331545. The work has been support also through the Centre of Excellence in Quark Matter funded by the Research Council of Finland. The reported work is associated with the European Research Council project ERC-2018-ADG-835105 YoctoLHC. We acknowledge grants of computer capacity from the Finnish Grid and Cloud Infrastructure (persistent identifier `urn:nbn:fi:research-infras-2016072533`).

References

1. C. A. Bertulani, S. R. Klein and J. Nystrand, Ann. Rev. Nucl. Part. Sci. **55** (2005), 271-310 doi:10.1146/annurev.nucl.55.090704.151526 [arXiv:nucl-ex/0502005 [nucl-ex]].
2. S. Klein and P. Steinberg, Ann. Rev. Nucl. Part. Sci. **70** (2020), 323-354 doi:10.1146/annurev-nucl-030320-033923 [arXiv:2005.01872 [nucl-ex]].
3. T. Sjöstrand and P. Z. Skands, Eur. Phys. J. C **39** (2005), 129-154 doi:10.1140/epjc/s2004-02084-y [arXiv:hep-ph/0408302 [hep-ph]].
4. T. Sjöstrand and P. Z. Skands, JHEP **03** (2004), 053 doi:10.1088/1126-6708/2004/03/053 [arXiv:hep-ph/0402078 [hep-ph]].
5. C. Bierlich, S. Chakraborty, N. Desai, L. Gellersen, I. Helenius, P. Ilten, L. Lönnblad, S. Mrenna, S. Prestel and C. T. Preuss, *et al.* SciPost Phys. Codeb. **2022** (2022), 8 doi:10.21468/SciPostPhysCodeb.8 [arXiv:2203.11601 [hep-ph]].
6. V. M. Budnev, I. F. Ginzburg, G. V. Meledin and V. G. Serbo, Phys. Rept. **15** (1975), 181-281 doi:10.1016/0370-1573(75)90009-5
7. G. Aad *et al.* [ATLAS collaboration], Phys. Rev. C **104** (2021) no.1, 014903 doi:10.1103/PhysRevC.104.014903 [arXiv:2101.10771 [nucl-ex]].
8. R. Abdul Khalek, A. Accardi, J. Adam, D. Adamiak, W. Akers, M. Albaladejo, A. Al-bataineh, M. G. Alexeev, F. Ameli and P. Antonioli, *et al.* Nucl. Phys. A **1026** (2022), 122447 doi:10.1016/j.nuclphysa.2022.122447 [arXiv:2103.05419 [physics.ins-det]].
9. M. Gluck, E. Reya and A. Vogt, Phys. Rev. D **46** (1992), 1973-1979 doi:10.1103/PhysRevD.46.1973
10. T. H. Bauer, R. D. Spital, D. R. Yennie and F. M. Pipkin, Rev. Mod. Phys. **50** (1978), 261 [erratum: Rev. Mod. Phys. **51** (1979) no.2, 407] doi:10.1103/RevModPhys.50.261
11. K. J. Eskola, V. Guzey, I. Helenius, P. Paakkinen and H. Paukkunen, [arXiv:2404.09731 [hep-ph]].
12. [ATLAS collaboration], ATLAS-CONF-2022-021.
13. I. Abt *et al.* [ZEUS collaboration], JHEP **12** (2021), 102 doi:10.1007/JHEP12(2021)102 [arXiv:2106.12377 [hep-ex]].
14. T. Sjöstrand and M. Utheim, Eur. Phys. J. C **82** (2022) no.1, 21 doi:10.1140/epjc/s10052-021-09953-5 [arXiv:2108.03481 [hep-ph]].
15. C. Bierlich, G. Gustafson, L. Lönnblad and H. Shah, JHEP **10** (2018), 134 doi:10.1007/JHEP10(2018)134 [arXiv:1806.10820 [hep-ph]].
16. M. Aaboud *et al.* [ATLAS collaboration], Phys. Rev. C **96** (2017) no.2, 024908 doi:10.1103/PhysRevC.96.024908 [arXiv:1609.06213 [nucl-ex]].

Recent results from ultra-peripheral lead-lead collisions with ATLAS

K. Maj, on behalf of the ATLAS Collaboration
AGH University of Kraków
al. Mickiewicza 30, 30-059 Kraków, Poland

Relativistic heavy-ion beams at the LHC are accompanied by a large flux of equivalent photons, leading to multiple photon-induced processes. This report presents a series of measurements of such processes performed by the ATLAS Collaboration. Measurements of exclusive dilepton production (electron, muon, and tau pairs) are discussed. These processes provide strong constraints on the nuclear photon flux and its dependence on the impact parameter and photon energy. In particular, measurements of the cross-sections in the presence of forward neutrons provide an additional experimental handle on the impact parameter range sampled in the observed events. Furthermore, the tau-pair production measurements can constrain the anomalous magnetic dipole moment of the tau lepton. High statistics measurements of light-by-light scattering shown in this talk provide a precise and unique opportunity to investigate extensions of the Standard Model, such as the presence of axion-like particles. The measurement of charged hadron in photonuclear collisions using 5.02 TeV Pb+Pb data collected in 2018 by ATLAS is also discussed. The charged hadron particle yields are presented as a functions of pseudorapidity and transverse momentum in different categories of event multiplicity. Measurement of jet production in ultra-peripheral collisions performed with the ATLAS detector using high-statistics 2018 Pb+Pb data is presented.

DOI: https://doi.org/10.17161/m9njk524

Keywords: ultra-peripheral collisions, photon-induced processes, exclusive dilepton production, anomalous magnetic moment, photonuclear dijet production, charged hadron, QGP

1 Introduction

The ATLAS experiment [1] at the Large Hadron Collider (LHC) dedicates part of its annual operational time to the heavy-ion (HI) physics including ultra-peripheral collisions (UPC). The UPC are a unique category of HI collisions, which occur when the distance separating the interacting nuclei exceeds the sum of their radii. The large electromagnetic fields generated by relativistic ions can be considered as fluxes of photons - as described in the Equivalent Photon Approximation formalism [2,3]. Photon-induced interactions occur in both proton-proton, *pp*, and HI collisions. However, in the latter, the cross-sections for a specific process experience a significant increase due to the Z^2 scaling of the photon fluxes (where Z is the atomic number). Furthermore, HI collisions exhibit minimal hadronic pile-up, allowing the identification of exclusive events and triggering on low-p_{T} particles. This exceptional characteristics make UPC an excellent tool for studying rare processes and searching for beyond Standard Model (BSM) phenomena, like axion-like particles in light-by-light ($\gamma\gamma \to \gamma\gamma$) scattering or setting constraints on the anomalous magnetic moment for the tau lepton using exclusive ditau production ($\gamma\gamma \to \tau^+\tau^-$). In the UPC events, photons provide a clean, energetic probe of the partonic structure of the nucleus, analogous to deep inelastic scattering. The photonuclear measurements are important for constraining the photon energy distribution and particle production in Monte Carlo (MC) models such as DPMJET-III [5]. Finally, the photon-induced processes offer a unique opportunity to probe the dynamics of Quantum Chromodynamics (QCD) in extremely asymmetric colliding systems, with energies between those available at RHIC and the LHC. Previous studies by the ATLAS experiment have revealed significant elliptic and triangular flow coefficients in the photonuclear events, indicating the presence of a quark-gluon plasma (QGP). Therefore, it becomes imperative to investigate these events for other potential QGP signatures, including radial flow, strangeness enhancement, and enhanced baryon/meson production.

This review presents the latest findings on ultra-peripheral Pb+Pb collisions from the ATLAS Collaboration. It examines photon-photon induced processes and jet production in UPCs using high-statistics 2018 Pb+Pb data. Additionally, it provides detailed insights into the properties of photonuclear collisions.

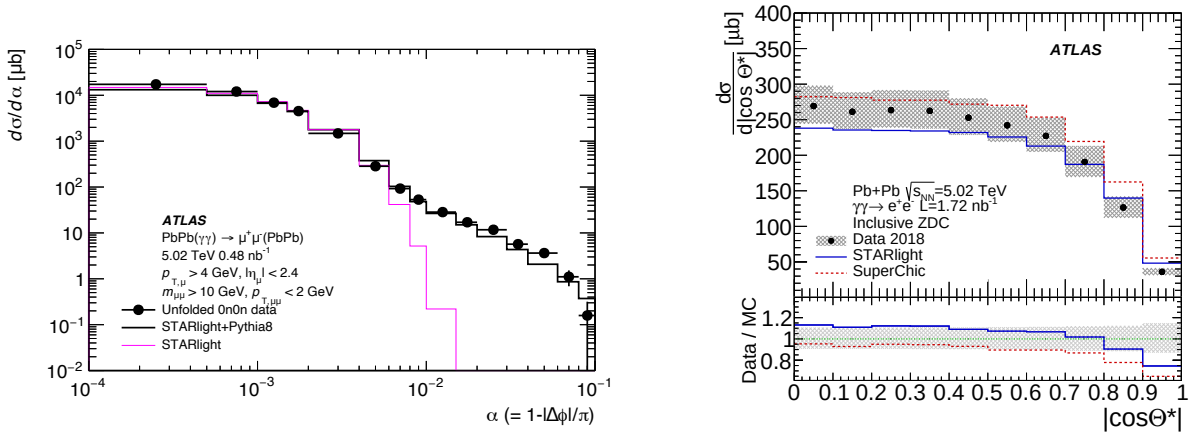

Figure 1: (Left) Differential cross-section as a function of acoplanarity for exclusive $\gamma\gamma \to \mu^+\mu^-$ production in UPC Pb+Pb collisions [6]. Data points are compared with predictions from STARlight and STARlight+PYTHIA8 to account for the FSR contribution. (Right) Differential cross-section measured as a function of m_{ee} for exclusive dielectron production [9], $\gamma\gamma \to e^+e^-$. The bottom panel shows the ratio of the data and the predictions from STARlight and SuperChic.

.

2 Exclusive $\gamma\gamma \to \mu^+\mu^-$ and $\gamma\gamma \to e^+e^-$ production

ATLAS performed a measurement of exclusive $\gamma\gamma \to \mu^+\mu^-$ production [6] in UPC Pb+Pb collisions at $\sqrt{s_{\rm NN}} = 5.02$ TeV with an integrated luminosity of 0.48 nb^{-1}. The fiducial region of the measurement is defined with the final-state muons that are produced in azimuthal angle alignment and have low transverse momenta, $p_{\rm T} > 4$ GeV, and $|\eta| < 2.4$. Moreover, the dimuon mass, $m_{\mu\mu}$, has to be larger than 10 GeV, as well as, the $p_{\rm T}$ for the dimuon system, $p_{\rm T}^{\mu\mu}$, has to be below 2 GeV, to ensure a back-to-back topology. The event selection criteria ensure that each event contains exactly two oppositely charged muons with no additional activity in the detector. Dissociative background from nuclear break up is evaluated to be at the level of 3%.

The integrated fiducial cross-section for the exclusive dimuon production is measured to be: $\sigma = 34.1 \pm 0.3$ (stat.) ± 0.7 (syst.) μb. The prediction from the STARlight [7] MC and STARlight+PYTHIA8 [8] MC are 32.1 μb and 30.8 μb, respectively, in agreement with the measurement. Differential cross-sections are measured as functions of several dimuon variables in the inclusive sample: $m_{\mu\mu}$, dimuon rapidity $y_{\mu\mu}$, scattering angle in the dimuon rest frame cosΘ^*, initial-photon momenta $k_{\rm min}$, $k_{\rm max}$ and acoplanarity, $\alpha = 1 - \frac{|\Delta\phi|}{\pi}$. Figure 1 shows the differential cross section for exclusive $\gamma\gamma \to \mu^+\mu^-$ production as a function of α. The predictions from STARlight and STARlight+PYTHIA8 are compared to the data. In general, a good agrement is found for both MC for $\alpha < 5 \times 10^{-3}$. For larger values of α, the STARlight predictions underestimate the data. This discrepancy arises from the final state radiation (FSR), which is not included in the STARlight calculation. A more accurate representation of the complete α distribution is achieved by integrating STARlight with PYTHIA, which incorporates the FSR contribution.

Exclusive $\gamma\gamma \to e^+e^-$ production was measured [9] by the ATLAS experiment using 1.72 nb^{-1} of Pb+Pb collision data at $\sqrt{s_{\rm NN}} = 5.02$ TeV collected in 2018. The evens exhibit characteristics similar to exclusive dimuon production, where two opposite-sign electrons with low transverse momentum are observed in a back-to-back configuration in the final state. The fiducial region, broader than that of the dimuon measurement, is defined by the following criteria: the electron $p_{\rm T} > 2.5$ GeV, $|\eta| < 2.5$, the dilectron mass ($m_{\rm ee}$) must be above 5 GeV, and the transverse momentum of the dielectron system ($p_{\rm T}^{ee}$) has to be below 2 GeV. A background contribution from dissociative production is estimated using the SuperChic [10] simulation normalised to the α data distribution.

The measured integrated fiducial cross-section for exclusive dielectron production is $\sigma = 215 \pm 1$ (stat.)$^{+23}_{-20}$ (syst.) ± 4 (lumi.) μb. The predictions from STARlight and SuperChic are 196.9 μb and 235.1 μb, respectively, in agreement with the measurement. Differential cross-sections are determined as functions of multiple variables: m_{ee}, absolute dielectron rapidity, $|y_{ee}|$, average electron $p_{\rm T}$, $\langle p_{\rm T} \rangle$ and $|\cos\Theta^*|$. The latter is presented in the right panel of Figure 1. The precision of the measurement

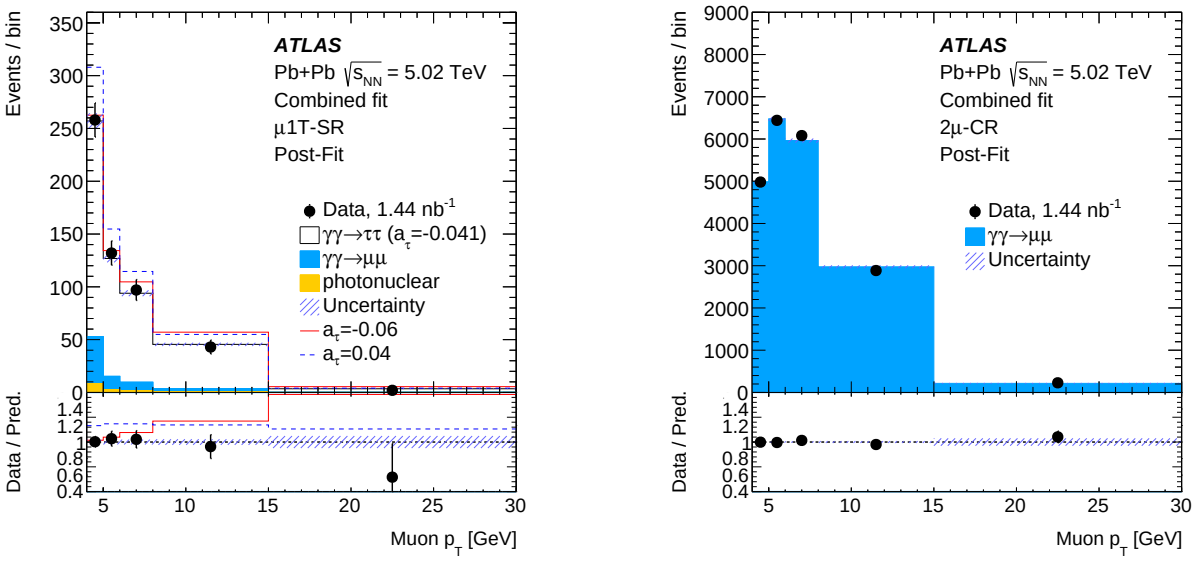

Figure 2: Muon p_{T} distributions in the (left) μ1T-SR and (right) 2μ-CR[11]. Post-fit distributions are shown with the signal contribution corresponding to the best-fit a_τ value (a_τ=-0.042). For comparison, signal contributions with alternative a_τ values are shown.

is dominated by the systematic uncertainties. The MC predictions for the $\gamma\gamma \to e^+e^-$ process from STARlight and SuperChic are compared to the data. Both predictions underestimate or overestimate the data by about 10%. However, SuperChic tends to describe more accurately the shape of the distribution.

3 Exclusive $\gamma\gamma \to \tau^+\tau^-$ production and constraints on a_τ

ATLAS provides the exclusive observation of $\gamma\gamma \to \tau^+\tau^-$ process [11] using data from 2018 Pb+Pb collisions at $\sqrt{s_{\mathrm{NN}}}$= 5.02 TeV with an integrated luminosity of 1.44 nb^{-1}. The measurement of the exclusive production of τ-leptons is used to set new constraints on the anomalous magnetic moment of the τ-lepton, a_τ. The theoretical SM prediction is: $a_\tau^{\mathrm{SM}} = 0.00117721(5)$ [12], which is remarkably smaller than the currently available experimental bounds. Various BSM theories, such as lepton compositeness, supersymmetry, and TeV-scale leptoquarks, etc., predicted modifications to the SM value of a_τ. The most stringent limits on a_τ are currently provided by the DELPHI experiment: $-0.052 < a_\tau < 0.013$ (95% CL) [13].

The identification techniques commonly employed in ATLAS cannot be used for signal τ-leptons due to its very low p_{T} values. Instead, it is required that events considered in the analysis contain one muon from the decay of one of the τ-leptons, and an electron or charged-particle track(s) from the decay of the other τ-lepton. Three distinct signal regions (SR) are defined: muon and electron (μe-SR), muon and one track (μ1T-SR), and muon and three tracks (μ3T-SR). Candidate events are selected with a single muon trigger requiring muon p_{T} above 4 GeV. To ensure the exclusivity of the selected events, a veto on forward neutron activity in the Zero Degree Calorimeter (ZDC) is imposed. Muons selected for the analysis are required to have $p_{\mathrm{T}} > 4$ GeV and $|\eta| < 2.4$, selected electrons have $p_{\mathrm{T}} > 4$ GeV and $|\eta| < 2.47$ and selected tracks should have $p_{\mathrm{T}} > 100$ MeV and $|\eta| < 2.5$. Events containing additional low-p_{T} tracks are rejected. Since different background processes contribute to each signal category, further requirements are introduced in the μ1T-SR (muon and track system $p_{\mathrm{T}} > 1$ GeV) and the μ3T-SR (mass of the three-track system below 1.7 GeV). The main sources of background contributions arise from the exclusive dimuon production with the final-state radiation (FSR) and diffractive photonuclear interactions. The $\gamma\gamma \to \mu\mu$ background is constrained with a dimuon control region, 2μ-CR. It requires exactly two opposite-charge muons with invariant mass above 11 GeV to suppress quarkonia backgrounds and no additional tracks separated from the muons by $\Delta R_{\mu,\mathrm{trk}} > 0.1$.

After applying the event selection, a total of 656 data events were observed in the three signal regions in which the analysis was performed. To measure a_τ, a fit to the muon p_{T} distribution is performed in the three SRs with a_τ being the parameter of interest. Also a control region with events from the $\gamma\gamma \to \mu^+\mu^-$ process is used in the fit to constrain initial-photon fluxes. The fitted muon p_{T} distributions

for the μ1T-SR and 2μ-CR are shown in Figure 2. A very good data-to-prediction agreement is seen for the best-fit value of the a_τ. The $\gamma\gamma \to \tau^+\tau^-$ process was observed with a significance exceeding 5 standard deviations, and a signal strength of $\mu_{\tau\tau} = 1.03^{+0.06}_{-0.05}$ assuming the SM value of a_τ. Figure 3 presents a comparison of the ATLAS measurement of the anomalous magnetic moment of the τ-lepton and previous results obtained at the LEP experiments. The precision of this measurement is similar to the most precise single-experiment measurement by the DELPHI Collaboration [13].

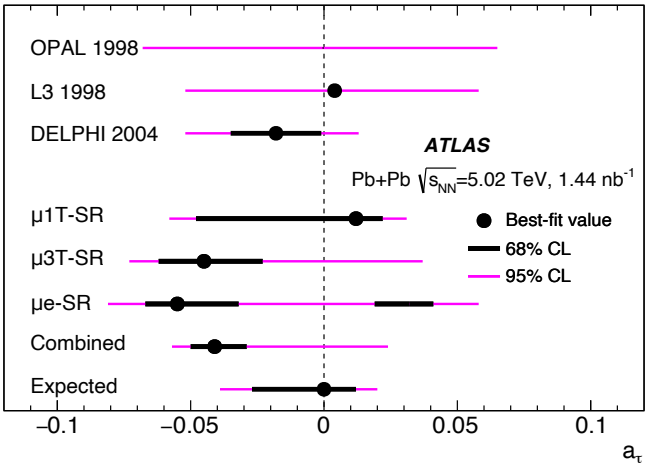

Figure 3: Measurements of a_τ from fits to individual signal regions (including the 2μ-CR), and from the combined fit [11]. Measurements from the OPAL [14], L3 [15] and DELPHI [13] experiments at LEP are also included for comparison.

4 Light-by-light scattering and search for axion-like particles

The light-by-light ($\gamma\gamma \to \gamma\gamma$, LbyL) scattering is a rare phenomenon which proceed via quantum electrodynamics (QED) at the lowest order via a loop of virtual charged fermions or $W^\pm$ bosons. LbyL production can be altered by various BSM phenomena: new particles entering the loop, Born-Infeld extensions of QED, space-time non-commutativity in QED, extra spatial dimensions, etc. Furthermore, the diphoton mass spectrum obtained from the LbyL process can be explored to search for potential neutral axion-like particles, ALP. ALP may contribute to the distribution as a narrow diphoton resonance [16].

LbyL scattering was also measured [17] by ATLAS in UPC Pb+Pb collisions at $\sqrt{s_{\rm NN}} = 5.02$ TeV using a combined 2015+2018 data sample with an integrated luminosity of 2.2 nb^{-1}. The signature of interest is the exclusive production of two photons, each with transverse energy $E_{\rm T}^\gamma > 2.5$ GeV, pseudorapidity $|\eta^\gamma| < 2.4$ and diphoton invariant mass $m_{\gamma\gamma} > 5$ GeV with transverse momentum $p_{\rm T}^{\gamma\gamma} < 1$ GeV. Any extra activity in the detector is vetoed, in particular no reconstructed tracks originating from the nominal interaction point with $p_{\rm T} > 100$ MeV are accepted. The final state photons are aligned in the azimuthal angle ϕ. Back-to-back topology is studied using diphoton acoplanarity, defined as $A_\phi = 1 - \frac{|\Delta\phi|}{\pi}$. Event candidates are expected to have $A_\phi < 0.01$. The main background contribution originates from exclusive production of the electron–positron pairs ($\gamma\gamma \to e^+e^-$). In the measurement, the $\gamma\gamma \to e^+e^-$ background is suppressed with the requirement of no tracks and pixel-tracks reconstructed in the Inner Detector. A remaining dielectron contribution is evaluated using a data-driven method. The second significant background source is gluon-induced central exclusive production (CEP) of photon pairs. The CEP background is evaluated using a dedicated control region in data ($A_\phi > 0.01$) and then extrapolated to the LbyL signal region.

ATLAS established the observation of the LbyL process with 97 events observed in data, while the signal and background expectations are 45 events and 27 $\pm$ 5 events, respectively. The integrated cross-section measured in the fiducial phase space, defined by requirements reflecting the event selection, is $\sigma_{fid} = 120 \pm 17$ (stat.) ± 13 (syst.) ± 4 (lumi) nb. The predictions from the SuperChic v3.0 [18] and from Ref.[19] are 78$\pm$ 8 and 80 $\pm$ 8 nb, respectively. In addition to the integrated fiducial cross-section, ATLAS measured $\gamma\gamma \to \gamma\gamma$ differential cross-sections involving four kinematic variables of the final-state photons. In general, a good agreement between the measurement and SM predictions is found.

ALP may be produced in the photon–photon fusion, $\gamma\gamma \to a \to \gamma\gamma$, followed by the decay to the diphoton pair, where a denotes the ALP field. Thus, a diphoton invariant mass distribution, $m_{\gamma\gamma}$,

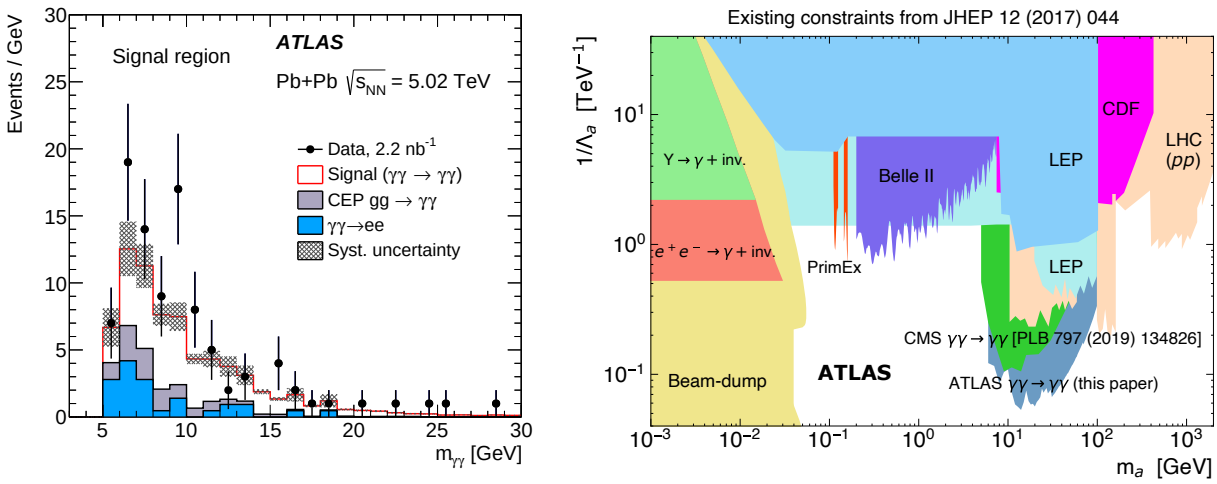

Figure 4: (Left) The diphoton invariant mass for $\gamma\gamma \to \gamma\gamma$ event candidates [17]. The sum of the signal and background expectations are compared to the data. (Right) Compilation of exclusion limits at 95% CL in the ALP-photon coupling ($1/\Lambda_a$) versus ALP mass (m_a) plane obtained by different experiments. The new limit obtained by ATLAS is marked with the label: ATLAS $\gamma\gamma \to \gamma\gamma$ [17]

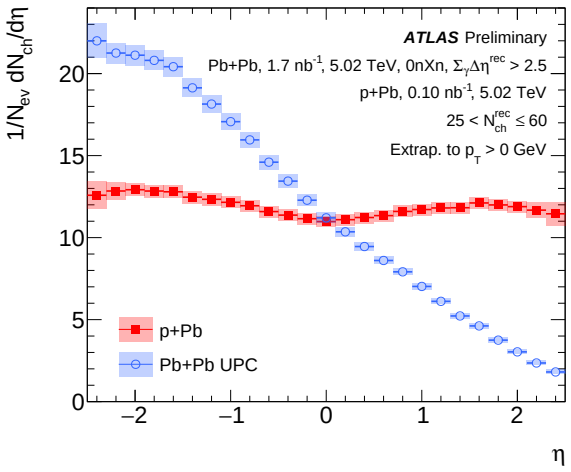

Figure 5: The charged-hadron yields as a function of η extrapolated to $p_{\mathrm{T}} > 0$ GeV for Pb+Pb UPC and p+Pb collisions [23].

presented in the left panel of Figure 4, can be used for ALP searches. The ALP production would result in a resonance peak with diphoton mass equal to the mass of a. The diphoton mass distribution was examined for a mass range between 6 and 100 GeV. No significant excess of events over expected background was found in the analysis. The 95% CL limit was derived for ALP production cross-section and ALP coupling to photons $\frac{1}{\Lambda_a}$ as a function of ALP mass. A summary of the exclusion limits from different experiments together with the new ATLAS constraints is shown in the right panel of Figure 4.

5 Charged hadrons yield measurements in photonuclear events

QGP matter is typically discussed in terms of head-on heavy-ion collisions. However, QGP-like signals have been also observed in smaller systems such as p+Pb, pp, or d+Au. Photons associated with nuclei can break apart the other colliding nuclei, resulting in photon-nucleus or photon-photon interactions. ATLAS measured two-particle azimuthal correlations in the photonuclear events, revealing significant non-zero elliptic (v_2) and triangular (v_3) flow coefficients [20]. The results can be interpreted as indication of a hydrodynamically flowing medium. In Ref. [21], the authors predict that radial flow [22], a signature for

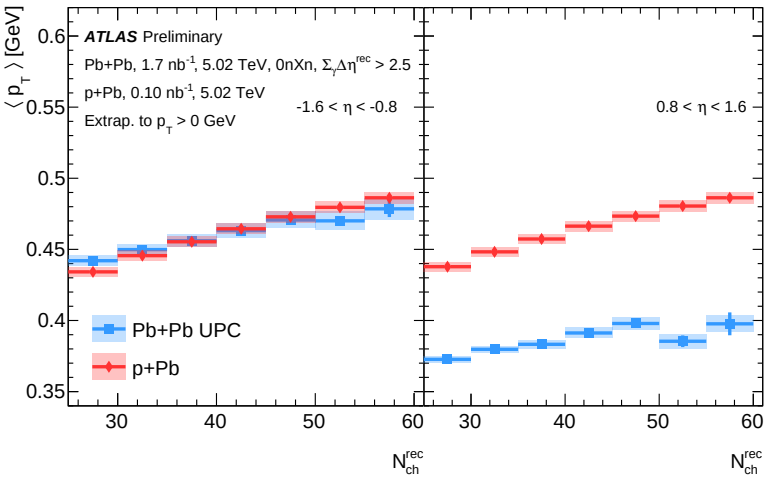

Figure 6: The $\langle p_{\mathrm{T}} \rangle$ of charged-hadron yields as a function of $\mathrm{N}_{\mathrm{ch}}^{\mathrm{rec}}$ in Pb+Pb UPC collisions and p+Pb collisions [23] for $-1.6 < \eta < -0.8$ (left) and $0.8 < \eta < 1.6$ (right). The charged-hadron yields are extrapolated to $p_{\mathrm{T}} > 0$ GeV.

QGP, should be essentially the same in UPC and p+Pb collisions. This can be measured via the mean transverse momentum $\langle p_{\mathrm{T}} \rangle$ of charged and identified particles. To test this prediction, ATLAS performed measurement [23] of inclusive yields of primary charged hadrons as functions of η, p_{T} and in selections of charge particle multiplicity $N_{\mathrm{ch}}^{\mathrm{rec}}$ in Pb+Pb UPC and p+Pb collisions.

The charged-hadron yields in Pb+Pb UPC and p+Pb collisions integrated over p_{T} as a function of η are shown in Figure 5. Negative η corresponds to the direction of the lead nucleus (Pb-going), while positive η corresponds to the direction of the photon (photon-going) and the proton (proton-going) in Pb+Pb and p+Pb collisions, respectively. The distribution in Pb+Pb UPC is highly asymmetric due to the lower energy of the photon compared to the energy per nucleon in the opposing lead nucleus.

Figure 6 shows $\langle p_{\mathrm{T}} \rangle$ for $p_{\mathrm{T}} > 0$ GeV as a function of $\mathrm{N}_{\mathrm{ch}}^{\mathrm{rec}}$ in two η regions, [-1.6,-0.8] and [0.8,1.6], in Pb+Pb UPC and p+Pb collisions. At negative η, $\langle p_{\mathrm{T}} \rangle$ between the two collision systems is comparable. In contrast, on the photon-going side ($\eta > 0$), there is a large difference in the $\langle p_{\mathrm{T}} \rangle$ between the two collision systems for all $\mathrm{N}_{\mathrm{ch}}^{\mathrm{rec}}$. The substantially larger $\mathrm{N}_{\mathrm{ch}}^{\mathrm{rec}}$ at negative η in Pb+Pb UPC and its comparable magnitude in p+Pb may suggest a contribution from radial flow. Further tests measuring the $\langle p_{\mathrm{T}} \rangle$ of identified hadrons are needed to confirm this hypothesis.

6 Photonuclear jet production

ATLAS also performed the measurement of di-jet photoproduction in ultra-peripheral Pb+Pb collisions [24]. The measurement uses data recorded in 2018 with an integrated luminosity of 1.72 nb^{-1}. Photonuclear events are selected using a combination of ZDC and rapidity gap requirements. In particular, events are required to satisfy only a 0nXn condition that requires no neutrons in the photon-going direction and one or more neutrons in the other direction. The jets are reconstructed from particle-flow inputs using the anti-k_{t} algorithm [25] with R = 0.4. Figure 7 shows the triple-differential cross-sections as a function of the photon parton momentum fraction, z_γ (left), the nuclear parton momentum fraction, x_{A}, (right) both cross-sections are presented in different regions of the jet transverse momenta, H_{T}. The z_γ dependence over a narrow x_{A} interval should be determined, primarily, by the photon flux. Thus, results like these should provide an important constraint on theoretical calculations of both the flux and the breakup probability for the photon-emitting nucleus.

7 Summary

This report presents the latest findings on ultra-peripheral Pb+Pb collisions from the ATLAS Collaboration, focusing on photon-photon induced processes and jet production using high-statistics 2018 Pb+Pb data. It also provides detailed insights into the properties of photonuclear collisions. The exclusive e^+e^- and $\mu^+\mu^-$ productions were measured by the ATLAS experiment using UPC data at $\sqrt{s_{\mathrm{NN}}} = 5.02$

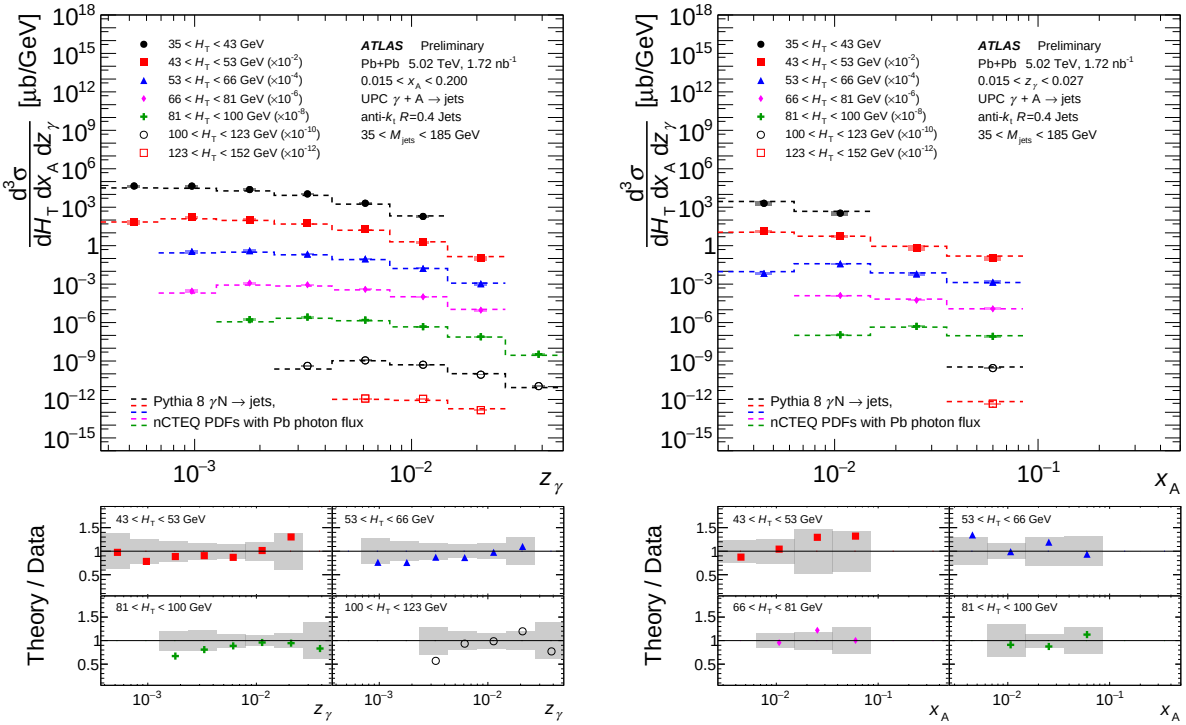

Figure 7: (Left) Triple-differential cross-sections [24], $\mathrm{d}^3\sigma/\mathrm{d}H_T\mathrm{d}x_A\mathrm{d}z_\gamma$, as functions of z_γ for different bins of H_T for events with struck parton energies in the kinematic range $0.015 < x_A < 0.2$. (Right) The same cross-sections as a functions of x_A for different bins of H_T for events with emitted photon energies in the kinematic range $0.015 < z_\gamma < 0.027$.

TeV. The theory predictions from STARlight and SuperChic were compared to the measured fiducial cross-sections and show discrepancies at the level of several percent, with STARlight (SuperChic) underestimating (overestimating) the data. The results of the differential cross-sections provide a reference for other photon-induced processes and for various theoretical approaches to model the photon fluxes. The $\gamma\gamma \to \tau^+\tau^-$ process has been observed in Pb+Pb UPC by the ATLAS experiment, surpassing a 5σ significance. The signal strength is consistent with the Standard Model expectations. The new constraints on the a_τ have been set, and are competitive to the best limits obtained during the LEP era. With the upcoming Run-3 data, an improvement in precision is anticipated. Additionally, the ATLAS experiment has established the presence of $\gamma\gamma \to \gamma\gamma$ scattering, with the results consistent with the Standard Model prediction. The measured invariant mass of the diphoton system was used to set new exclusion limits on axion-like particles. Charged-hadron yields were quantified in UPC photonuclear interactions by ATLAS. Also the mean p_T value of yields measured in η intervals, were measured within selections of $\mathrm{N}_\mathrm{ch}^\mathrm{rec}$. Potential signatures of collectivity including radial expansion were tested via the $\langle p_\mathrm{T}\rangle$ comparison in Pb+Pb UPC and p+Pb collisions. The larger $\langle p_\mathrm{T}\rangle$ at backward compared to forward rapidity in Pb+Pb UPC may suggest the presence of hydrodynamic radial flow. Finally the measurement of the triple-differential cross-section for photonnuclear events were discussed. These results provide an important step towards the goal of a precise limit on nuclear PDFs in this region by quantifying theoretical components, such as the electromagnetic breakup fraction, which are necessary for a precise comparison to theory.

Acknowledgments

This work was partly supported by program "Excellence initiative – research university" for the AGH University of Kraków and by the National Science Centre of Poland under grant number UMO-2021/40/C/ST2/00187.

References

1. ATLAS Collaboration, JINST **3**, (2008) S08003.

2. E. Fermi, Nuovo Cim **2**, (1925) 143.
3. E. J. Williams, Phys. Rev. Journals Archive **45**, (1934) 729.
4. R. Engel, Z. Phys. C **66**, (1995) 203.
5. S. Roesler et al., Advanced Monte Carlo for Radiation Physics, arXiv: hep-ph/0012252, (2001).
6. ATLAS Collaboration, Phys. Rev. **C 104**, (2021) 024906.
7. S.R. Klein et al., Comp. Phys. Comm. **212**, (2017) 258.
8. T. Sjostrand et al., Comp. Phys. Comm. **191**, (2015) 159.
9. ATLAS Collaboration, J. High Energy Phys. **06**, (2023) 182.
10. L. A. Harland-Lang et al., Eur. Phys. J. C **76**, (2016) 9.
11. ATLAS Collaboration, Phys. Rev. Lett. **131**, (2023) 151802.
12. S. Eidelman, and M. Passera, Mod. Phys. Lett. A **22**, (2007) 159.
13. J. Abdallah et al., DELPHI Collaboration, Eur. Phys. J. C **35**, (2004) 159.
14. OPAL Collaboration, Phys. Lett. B **431**, (1998) 188.
15. L3 Collaboration, Phys. Lett. B **434**, (1998) 169.
16. S. Knapen, T. T. Lin, H. K. Lou and T. Melia, Phys. Rev. Lett. **118**, (2017) 171801.
17. ATLAS Collaboration, J. High Energy Phys. **3**, (2021) 243.
18. L. A. Harland-Lang et al., Eur. Phys. J. C **79**, (2019) 39.
19. M. Kłusek-Gawenda et al., Phys. Rev. C **93**, (2016) 044907.
20. ATLAS Collaboration Phys. Rev. C **104** (2021) 014903.
21. W. Zhao et al., Phys. Rev. Lett. **129**, (2022) 252302.
22. U. Heinz, R. Snellings, Ann. Rev. Nucl. Part. Sci. **63**, (2013) 123.
23. ATLAS Collaboration, ATLAS-CONF-2023-059, https://cds.cern.ch/record/2871729 (2023).
24. ATLAS Collaboration ATLAS-CONF-2022-021 https://cds.cern.ch/record/2806461 (2022).
25. M. Cacciari et al., J. High Energy Phys. **04**, (2008) 063.

CERNCOURIER

STRONG INTERACTIONS | MEETING REPORT

Ultra-peripheral conference debuts in Mexico

4 May 2024

Ultra peripheral The UPC23 conference took place in Playa del Carmen, Mexico. Credit: M Rennells

Ultra-peripheral collisions (UPCs) involving heavy ions and protons represent the energy frontier for photon-induced reactions. These high-energy photons can be used to study unique features of quarks and gluons inside nuclei, and can probe electromagnetic and electroweak interactions without the usual backgrounds associated with quantum-chromodynamic processes. The first edition of the international workshop on this subject took place from 10 to 15 December 2023 in Playa del Carmen, Mexico, bringing together about 90 participants, more than a third of whom were early-career researchers. This is the first time that the international UPC community has gathered together, establishing a new international conference series on this active and expanding area of research.

The conference highlighted the impressive progress and diversity of UPC physics, which goes far beyond the initial studies of exclusive pro-cesses. UPC23 covered the latest results from

experiments at RHIC and the LHC, and prospects for the future Electron-Ion Collider (EIC) at Brookhaven National Laboratory. Discussions delved into the intricacies of inelastic photo-nuclear events, including the exciting programme of open charm that is yet to be explored, and examined how UPCs serve as a novel lens for investigating the quark–gluon plasma and other final-state nuclear effects. Lots of attention was devoted to the physics of low-x parton densities – a fundamental aspect of protons and nuclei that photons can probe in a unique way.

Enriched understanding

Among the conference's theoretical highlights, Farid Salazar (UCLA) showed how vector–meson photoproduction could be a powerful method to detect gluon saturation across different collision systems, from proton–nucleus to electron–nucleus to UPCs. Zaki Panjsheeri (Virginia) put forth innovative ideas to study double-parton correlations, linking UPC vector–meson studies to generalised parton distributions, enhancing our understanding of the proton's structure. Ashik Ikbal (Kent State), meanwhile, introduced exciting proposals to investigate quantum entanglement through exclusive J/ψ photoproduction at RHIC.

The conference also provided a platform for discussing the active exploration of light-by-light scattering and two-photon processes for probing fundamental physics and searches for axion-like particles, and for putting constraints on the anomalous magnetic moment of the tau lepton (see CMS closes in on tau g–2).

Energy exploration

Physicists at the LHC have effectively repurposed the world's most powerful particle accelerator into a high-energy photon collider. This innovative approach, traditionally the domain of electron beams in colliders like LEP and HERA, and anticipated at the EIC, allows the LHC to explore photon-induced interactions at energies never before achieved. David Grund (Czech Technical University in Prague), Georgios Krintiras (Kansas) and Cesar Luiz Da Silva (Los Alamos) shared the latest LHC findings on the energy dependence of UPC J/ψ events. These results are crucial for understanding the onset of gluon saturation – a state where gluons become so dense reaching saturation, the dynamical equilibrium where the emission and recombination occurs. However, the data also align with the nuclear phenomenon known as gluon shadowing, which arises from multiple-scattering processes.

David Tlusty (Creighton) presented the latest findings from the STAR Collaboration, which has recently expanded its UPC programme, complementing the energy exploration at the LHC. Klaudia Maj (AGH University of Krakow) presented the latest results on two-photon interactions and photonuclear jets from the ATLAS collaboration, including measurements that may be probing the quark-gluon plasma.

Delegates discussed the future opportunities for UPC physics with the large integrated luminosity expected for Runs 3 and 4 at the LHC

Carlos Bertulani (Texas A&M) paid tribute to Gerhard Baur, who passed away on June 16 last year. Bertulani and Baur co-authored "Electromagnetic processes in relativistic heavy ion collisions" – a seminal paper with more than 1000 citations. Bertulani invited delegates to consider the untapped potential of UPCs in the study of anti-atoms and exotic atoms.

Delegates also discussed the future opportunities for UPC physics with the large integrated luminosity expected for Run 3 and Run 4 at the LHC, with the planned detector upgrades for Run 4 such as FoCal, the recent upgrades by STAR, the sPHENIX programme and at the EIC. Delegates are expecting event selection and instrumentation close to the beam line, for example using "zero degree" calorimeters, to offer the greatest experimental opportunities in the coming years.

The next edition of the UPC conference will take place in Saariselka, Finland in June 2025.

Daniel Tapia Takaki *The University of Kansas.*

UPC 2023 First international workshop on the physics of Ultra Peripheral Collisions

Scientific Topics

Photon-Proton and Photon-Nucleus Physics
Two Photon Physics
Nonlinear And Gluon Saturation
Parton Distribution Developments
Hadronization In Exclusive Processes
Soft Nucleon And Nucleus Interactions
Photoproduction In Events With Nuclear Overlap
UPCs And Future Electron-Ion Colliders

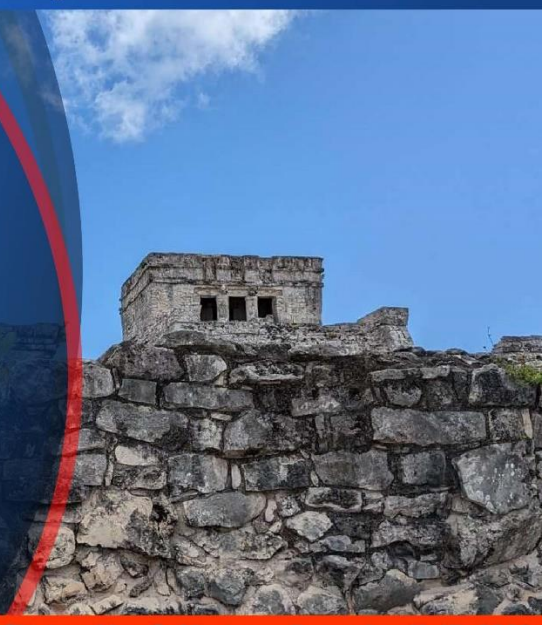

Playa del Carmen (Riviera Maya), Mexico December 11-15, 2023

International Program Committee

Stan Brodsky (Stanford)
Guillermo Contreras (Prague)
David d'Enterria (Geneva)
Victor Goncalves (Pelotas)
Spencer Klein (Berkeley)
Tuomas Lappi (Jyvaskyla), Co-chair
Paul Newman (Birmingham)
Joakim Nystrand (Bergen), Co-chair
Marta Ruspa (Torino)
Eugenio Scapparone (Bologna)
Janet Seger (Omaha)
Anna Stasto (State College)
Peter Steinberg (Upton)
Mark Strikman (State College)
Antoni Szczurek (Krakow)
Daniel Tapia Takaki (Lawrence)
Samuel Wallon (Orsay)

Organizing Committee

Alexander Bylinkin (Bergen)
Martin Hentschinski (Puebla)
Gerardo Herrera (Mexico City), Co-chair
Tommaso Isidori (Lawrence)
Anisa Khatun (Lawrence)
Michael Murray (Lawrence)
John Ralston (Lawrence)
Mario Rodriguez Cahuantzi (Puebla)
Christophe Royon (Lawrence)
Daniel Tapia Takaki (Lawrence), Co-chair

KU I·AN QCD CONAHCYT BUAP Cinvestav UDLAP

The University of Kansas Libraries &
Department of Physics and Astronomy
Lawrence, Kansas

ISSN: 3064 8904
ISSN: 3064-8890